TAMPEREEN TEKNILLINEN YLIOPISTO
TAMPERE UNIVERSITY OF TECHNOLOGY
Julkaisu 845 • Publication 845

Jari Tuominen

Engineering Coatings by Laser Cladding – The Study of Wear and Corrosion Properties

Tampere 2009

Tampereen teknillinen yliopisto. Julkaisu 845
Tampere University of Technology. Publication 845

Jari Tuominen

Engineering Coatings by Laser Cladding – The Study of Wear and Corrosion Properties

Thesis for the degree of Doctor of Technology to be presented with due permission for public examination and criticism in Hermia Auditorium, Hermiankatu 6 A, at Tampere University of Technology, on the 13th of November 2009, at 12 noon.

Tampereen teknillinen yliopisto - Tampere University of Technology
Tampere 2009

ISBN 978-952-15-2252-9 (printed)
ISBN 978-952-15-2324-3 (PDF)
ISSN 1459-2045

ABSTRACT

In the field of surface engineering, laser cladding is an emerging coating method with the quality of high energy density, which enables the production of low diluted and fusion bonded thick metallic coatings on wide variety of metallic base materials with low total heat input. Besides applications where the coating should be deposited on tightly restricted small areas, laser cladding has gained popularity in coating and repair of larger surfaces in massive high value components. However, due to high capital costs and low productivity resulting from the limited amount of power available and low process energy efficiency due to the nature of optical energy, conventional coating methods under constant development are still dominating in many industrial applications. In order to compete with the conventional coating methods, orders of magnitude higher capital costs of lasers and related accessories should be justified/offset by the superiority of the coating quality, extended lifetime of the clad components and/or higher productivity and coating material efficiency.

For that purpose, this thesis studies some essential functional properties of various metallic and metal matrix composite (MMC) coatings produced by modern short-wavelength Neodymium:yttrium-aluminium-garnet (Nd:YAG) and direct high power diode laser (HPDL) cladding techniques. Coatings comprise commercial alloys, which are already familiar and well-established in various engineering applications, as well as novel experimental type alloys, which are rarely studied in the context of laser cladding. Properties of coatings are compared with coatings produced by such rival coating techniques as high-velocity oxy-fuel (HVOF) spraying and plasma transferred arc (PTA) surfacing. Selected wrought, sintered, cast and hot isostatic pressed (HIP) bulk alloys are also used as reference materials. Characterisation and testing of coatings include wet corrosion, hot corrosion, high temperature stability, abrasive wear, sliding wear, residual stresses and thermal fatigue. In order to understand and explain the differences in the behaviour between different coating materials and coating methods, microstructures of the coatings are characterised in details. In addition to coating characterisation, back reflection is studied with novel HPDL cladding process since this area is still rather unknown and critical in developing novel laser sources for cladding and rapid three-dimensional (3D) manufacturing applications.

Determination of back reflection implemented by temperature measurements conducted on several locations in the vicinity of the optics and inside the diode laser head indicated that back reflection from the melt pool and base material towards the laser head exists despite rather long working distance and efficiently absorbed short-wavelength laser beam. This appears particularly intensive during the cladding of single beads where overlapping is not used. The direction of back reflection is dictated by the angle between the surface of the melt pool and incident laser beam, which in turn is influenced by the height of coating layer and tilting angle of laser head. The latter can be adjusted accordingly to avoid harmful back reflection to the critical parts inside the laser head.

In wet corrosion studies in neutral chloride bearing aqueous solution at room temperature (RT), laser cladding process proved to produce impervious Ni-, Cr- and Co-based metallic corrosion barrier coatings, which isolated the less noble base materials completely from the surrounding environment. Inhomogeneous distribution of alloying elements in macro- and micro-level, however, led to preferentially dissolved regions, which were not detected in corresponding wrought alloy. Limited amount of intermixed Fe from the base material characteristics for laser coatings had useful effect on pitting and crevice corrosion resistance.

Distribution of alloying elements in macro- and micro-level together with the amount of dilution dictated how the laser coatings related to the corresponding wrought alloy. By careful control of these characteristics, corrosion properties equivalent to wrought alloy could be obtained.

Ni- and Cr-based laser coatings exposed in air atmosphere to molten sulphate-vanadate compounds showed equivalent or better resistance than commonly used commercial Ni-based wrought alloys. In general, hot corrosion morphology of tested specimens was characterized by thick and relatively dense reaction product layers with the underlying alloy depleted in Cr. Cr-based laser coatings, which consisted of metastable body-centered cubic (bcc) ordered α-Cr and face-centered cubic (fcc) ordered γ-Ni phases, underwent transformation towards equilibrium during the long-term exposure to high temperature. Amount of α-Cr phases and their Cr content increased, and they were prone to molten salt attack.

In low-stress three-body abrasion wear tests, MMC laser coating produced from experimental powder prepared by self-propagating high-temperature synthesis (SHS) showed great potential. Abrasion wear resistance of this coating reinforced with high volume fraction of very fine titanium-molybdenum carbide (Ti, Mo)C particulates approached the qualities of high volume fraction hard metals produced by sintering and HVOF spraying. Among monolithic laser coatings, V-rich Fe-based tool steel showed the best behaviour outperforming for instance several MMC laser coatings. In general, increased hardness of the matrix at the expense of reduced fracture toughness and increased volume fraction of hard carbides was beneficial in this type of test. Due to reheated zones associated with overlapping and inadequate homogenisation of melt, laser coatings suffered from distinctive local differences in wear rates.

Under low-stress dry sliding conditions against quenched & tempered (QT) steels, solid solution strengthened, carbide and intermetallic type Co-based laser coatings outperformed corresponding PTA coatings and HIPped material in wear resistance. These results can be attributed to the higher microhardness values due to lower amount of dilution and differences in microstructure, which both affect the alloys' ability to support the forming oxide layers. Novel Fe-based Nanosteel hardfacing alloy exhibited resistance equivalent to the best Co-based intermetallic type alloys.

Residual stress studies conducted on brittle and ductile hardfacing alloys deposited on various Fe-based base materials indicated that mismatch in coefficients of thermal expansion (CTE) dictate mainly the final residual stress state in coating layer. Even if managed to produce crack-free coating layers from very brittle intermetallic type hardfacing alloy with suitably low CTE by using appropriate preheating, this alloy was very susceptible to cracking when subjected to alternating temperatures as evidenced by low-cycle thermal fatigue tests.

PREFACE

The work presented in this thesis was carried out at the Department of Materials Science, Tampere University of Technology during the years 1999-2009 starting with the project AppliYAG financed by the Finnish Funding Agency for Technology and Innovation (Tekes). The work was conducted under the supervision of Professor Petri Vuoristo to whom I am indebted and wish to express my gratitude for his guidance, patience and advices. Professor Tapio Mäntylä is acknowledged for his guidance in the early stages of my work.

Also, I would like to express my gratitude to my former and present colleagues of Laser Application Laboratory and Surface Engineering Group for motivating me ahead with my work and maintaining good work atmosphere. Thanks are, especially, due to M.Sc. Jyrki Latokartano for his help concerning robots and programming. M.Sc. Paul Hayhurst, M.Sc. Teemu Saarinen and M.Sc. Jyrki Suutala are acknowledged for their collaboration, help and fruitful discussions. Hot corrosion experiments were carried out by M.Sc. Mari Honkanen, whom I would like to thank. M.Sc. Hans Gripenberg, Helsinki University of Technology (Espoo, Finland), is acknowledged for conducting residual stress measurements by hole-drilling. I also wish to express my gratitude to Mr. Mikko Kylmälahti for manufacturing reference samples by thermal spraying.

I am much obliged for the financial support by Tekes, European Commission (the Sixth Framework Program), the Graduate School on New Materials and Processes, Finnish Cultural Foundation (Satakunta Regional Fund), Walter Ahlström Foundation, Kaupallisten ja teknillisten tieteiden tukisäätiö (KAUTE), Andritz Oy, Fortum Service Oy, Kemira Pigments Oy, Kokkola LCC Oy, Kvaerner Power Oy, Laserplus Oy, Luvata Pori Oy, MAN B&W Diesel A/S, Metso Paper Oy, MH Engineering AB, TTT Technology Oy and Wärtsilä Finland Oy.

My dear wife Elena and little son Tommi are most warmly thanked for their endless patience, encouragement and support throughout the preparation of this thesis. Thousand thanks also go to my parents Kari and Sinikka, sister Anu and other support network for all the valuable help you have provided during the course of this work.

Tampere, October 2009

Jari Tuominen

LIST OF SYMBOLS AND ABBREVIATIONS

α	Contact angle (°)
α'	Fine Cr-rich phases in high-Cr NiCr alloy
α-Cr	Body-centered cubic chromium
α_{CTE}	Coefficient of thermal expansion (K^{-1})
α_r	Rotational angle between maximum principal stress and cladding direction (°)
$\alpha(T)$	Thermal diffusivity ($m^2\ s^{-1}$)
α-Ti	Hexagonally close-packed titanium
β	Semi-apical angle of indenter (°)
β_a	Anodic Tafel slope ($V\ cm^2\ A^{-1}$)
β_c	Cathodic Tafel slope ($V\ cm^2\ A^{-1}$)
γ'	Gamma prime phase
γ-Co	Face-centered cubic cobalt
γ-Ni	Face-centered cubic nickel
$d\gamma/dt$	Temperature coefficient of surface tension ($N\ m^{-1}\ K^{-1}$)
$\Delta E/\Delta i$	Slope of linear polarization curve ($V\ cm^2\ A^{-1}$)
ΔG	Gibbs free energy of formation ($kJ\ mol^{-1}$)
ΔH	Enthalpy term ($kJ\ kg^{-1}$)
Δm	Mass of the melted material (base material, coating) (g)
Δs	Clad length (mm)
ΔT	Temperature difference between melt pool and ambient (°C)
ΔT_0	Equilibrium liquidus-solidus interval (= width of the mushy zone) (°C)
ΔT_1	Difference between melting and base material temperature (K)
ΔV	Volume of the melted material (mm^3)
ε-Co	Hexagonally close-packed cobalt
η	Melting efficiency (%)
η-phase	Complex mixed carbide
θ	Angle between vectors V_s and V_b (°)
λ	Primary or secondary dendrite arm spacing (µm)
λ_2	Secondary dendrite arm spacing (µm)
μ	Viscosity of melt pool ($kg\ s^{-1}\ m^{-1}$)
ρ	Density ($kg\ m^{-3}$)
ρ_c	Density of carbide ($kg\ m^{-3}$)
ρ_m	Density of matrix alloy ($kg\ m^{-3}$)
ρ_{mmc}	Density of MMC ($kg\ m^{-3}$)
σ	Stress caused by CTE mismatch (MPa)
σ_i	Residual stress of phase i (MPa)
${}^m\sigma_{ij}$	Macro-residual stress of material consisting of phases i and j (MPa)
σ_j	Residual stress of phase j (MPa)
σ_L	Stress along cladding direction (MPa)
σ-phase	Brittle high-chromium FeCr intermetallic compound
σ_{th}	Thermal or shrinkage stress (MPa)
σ_x	Maximum principal stress (MPa)
$\sigma_{x'}$	Stress in rotated coordinate system (MPa)
σ_y	Minimum principal stress (MPa)
τ_{xy}	Shear stress in principal stress coordinate system (MPa)
$\tau_{x'y'}$	Shear stress in rotated coordinate system (MPa)
υ	Poisson's ratio

υ_c	Poisson's ratio for coating
φ	Rotation angle between cladding direction and measured stress (°)
ψ	Specimen tilt in X-ray stress analysis (°)
ψ_1	Angle between V_{hkl} and V_s (°)
Ø	Wire diameter (mm)
$Ø_d$	Diameter of disc (mm)
$Ø_{id}$	Inner diameter of pipe (mm)
2θ	Diffraction angle in X-ray methods (°)
2D	Two-dimensional
3D	Three-dimensional
a	Lattice parameter (horizontal) in hexagonally close-packed structure (nm)
a	Lattice parameter in cubic structure (nm)
A	Melt cross-sectional area (mm^2)
A_3	Temperature at which ferrite transforms fully to austenite during heating (°C)
A_c	Cross sectional area above the surface of base material (mm^2)
A_i	Atomic mass of the i^{th} element (g)
A_m	Cross sectional area below the surface of base material (mm^2)
$a_{products}$	Chemical activity (concentration) of products
$a_{reactants}$	Chemical activity (concentration) of reactants
c	Lattice parameter (vertical) in hexagonally close-packed structure (nm)
c_1	Crack length (m)
C14	Type of hexagonal crystal structure
$C_{carbide}$	Weight fraction of certain element in carbide
C_D	Weight fraction of certain element in dendritic region
C_{ID}	Weight fraction of certain element in interdendritic region
C_{liquid}	Composition of liquid in equilibrium
C_{matrix}	Weight fraction of certain element in matrix
C_{solid}	Composition of solid in equilibrium
c(T)	Specific heat capacity (J kg^{-1} K^{-1})
d	Plane spacing in X-ray stress analysis (nm)
D	Geometrical dilution (%)
d_1	Dimension of laser spot along cladding direction (mm)
D_b	Diameter of laser spot (mm or m)
D_s	Solute diffusion coefficient in the liquid (m^2 s^{-1})
E	Young's modulus (GPa)
e^-	electron
E^0	OCP when all activities are equal to 1 (V or mV)
E_b	Breakdown potential (V or mV)
E_c	Young's modulus for coating (GPa)
E_{corr}	Corrosion potential (V or mV)
E_p	Measured potential (V or mV)
E_{rp}	Repassivation potential (V or mV)
f	Powder feed rate (g min^{-1})
F	Faraday's constant (96485 C mol^{-1})
f_c	Volume fraction of carbide in initial powder mixture
f_i	Mass fraction of the i^{th} element in the alloy
f_m	Volume fraction of matrix

F_N	Normal indenter load (N)
G	Thermal gradient (°C m^{-1})
G_c	Critical thermal gradient (°C m^{-1})
h	Height of the single bead (mm)
H	Hardness (Pa)
H^+	Hydrogen ion
H_2	Hydrogen gas
H_3O^+	Hydronium, aqueous cation
$H_{abrasive}$	Hardness of abrasive
h_c	Coating height (mm)
$H_{material}$	Hardness of abraded material
i	Current density (mA cm^{-2})
I_{corr}	Corrosion current density (mA cm^{-2})
k	Partition coefficient = C_{solid}/C_{liquid}
K	Wear coefficient
K_1	Constant: 3.27 (μm μA^{-1} cm^{-1} $year^{-1}$)
K_I	Stress intensity factor (kg s^{-2} $m^{-1/2}$ or MPa $m^{1/2}$)
k(T)	Thermal conductivity (W m^{-1} K^{-1})
L	Wear travel length (m)
L_m	Latent heat of fusion (kJ kg^{-1})
M	Molarity or molar concentration
M_s	Start temperature for martensite formation during cooling (°C)
n	Number of electrons in anodic half reaction
N	Number of cycles
n_i	Valence of the i^{th} element in the alloy
O_2	Oxygen gas
P	Delivered laser power (W)
P_c	Power utilized to melt the coating material and weld it to the base material (W)
P_{O2}	Oxygen partial pressure
Q	Net energy flow per area from laser beam (W m^{-2})
R	Ideal gas constant (8.3143 J mol^{-1} K^{-1})
r_1	Beam radius (mm)
R_a	Roughness average
R_{ave}	Average reflectivity (%)
R_p	Reflectivity of beam component parallel to incidence plane (%)
R_s	reflectivity of beam component normal to incidence plane (%)
S	Surface tension number
S-K_a	Intensity peak in EDS spectrum caused by sulphur
t	Cladding time (s)
t_b	Thickness of base material (mm)
T	Temperature (°C or K)
T_1	Room temperature (°C)
T_2	Heat treatment temperature (°C)
$t_{8/5}$	Critical cooling rate (°C s^{-1})
T_c	Cooling rate (°C s^{-1})
T_m	Melting temperature (°C or K)
T_v	Vaporization temperature (°C or K)
V	Wear volume (m^3)
V_b	Traverse speed (m s^{-1} or mm min^{-1})
V_c	Critical growth velocity (m s^{-1} or mm min^{-1})

V_{hkl}	Growth velocity of the dendrite trunk (m s^{-1} or mm min^{-1})
V_s	Growth rate of the solid-liquid interface (m s^{-1} or mm min^{-1})
w	Width of the single bead (mm)
W	Normal load (N)
Z	Atomic number
Ag/AgCl	Silver/silver chloride reference electrode
AISI	American Iron and Steel Institute
Al_2O_3	Alumina
ANSI	American National Standards Institute
ASTM	American Society for Testing and Materials
BaF_2	Barium difluoride
bcc	Body-centered cubic
BN	Boron nitride
BSE	Back-scattered electrons
C_2H_5OH	Ethanol
$CaCO_3$	Calcium carbonate
CaF_2	Calcium difluoride
CaP	Calcium phosphate
$CaSO_4$	Calcium sulphate
CCD	Charge-coupled device
CE	Carbon equivalent
CeO_2	Ceria
cf.	Compare
Cl^-	Chloride ion
CO	Carbon monoxide
CO_2	Carbon dioxide
Co_3Mo_2Si	Laves phase
Co_3W	Intermetallic compound
Co_3W_3C	Mixed carbide
Co_6W_6C	Mixed carbide
Co_7W_6	Intermetallic compound
CoMoSi	Laves phase
COV	Coefficient of variation (%)
cp	Commercially pure
CR	Corrosion rate (μm $year^{-1}$)
Cr_2O_3	Chromia
$Cr_2O_7^{2-}$	Chromium oxide ion
Cr_3C_2	Chromium carbide
Cr^{3+}	Chromium ion
Cr_7C_3	Chromium carbide
$Cr_{23}C_6$	Chromium carbide
CrB	Chromium boride
CrC	Chromium carbide
Cr Kα	X-ray radiation used in stress analysis
CrO_4^{2-}	Chromium oxide ion
$Cr(OH)_3$	Chromium hydroxide
CrOOH	Chromium oxy-hydroxide
$CrVO_4$	Chromium vanadate
CTE	Coefficient of thermal expansion (K^{-1})

CTE_c	Coefficient of thermal expansion for coating (K^{-1})
CTE_s	Coefficient of thermal expansion for base material (K^{-1})
Cu Kα	X-ray radiation used in phase identification
CVD	Chemical vapour deposition
cw	Continuous wave
DIN	German national organization for standardization
EBW	Electron beam welding
EDL	Electrical double layer
EDS	Energy dispersive spectroscopy
e.g.	Exempli gratia
EN	European standard
EPMA	Electron probe microanalysis
et al.	Et alia
etc.	Et cetera
EW	Equivalent weight (g)
EXT-1	Temperature measuring point in leading position
EXT-2	Temperature measuring point in trailing position
fcc	Face-centered cubic
Fe^{2+}	Ferrous ion
Fe_2O_3	Iron oxide
Fe_3O_4	Iron oxide
$FeCl_3$	Iron chloride
FEM	Finite-element modelling
FeOH	Iron hydroxide
FeOOH	Iron oxy-hydroxide
FGM	Functionally graded material
FTC	Fused tungsten carbide
H_2O	Water
HAZ	Heat-affected zone
HCl	Hydrochloric acid
hcp	Hexagonally close-packed
HIP	Hot isostatic pressing
hP12	Pearson symbol for certain hexagonal crystal structure
HPDL	High power diode laser
HRC	Rockwell hardness
HV	Vickers hardness
HVOF	High-velocity oxy-fuel
i.e.	Id est
KCl	Potassium chloride
La_2O_3	Lanthana
LAVA	Commercial simulation software for laser cladding
LP	Laser profilometer
LUT	Lappeenranta University of Technology
M_3C	Mixed metal carbide
M_6C	Mixed metal carbide
M_7C_3	Mixed metal carbide
$M_{23}C_6$	Mixed metal carbide
Me	Metal
Me^{2+}	Metal ion
$Mg(OH)_2$	Magnesium hydroxide

$MgZn_2$	Intermetallic compound between Mg and Zn
MIG	Metal inert gas
MMA	Manual metal arc
MMC	Metal matrix composite
Mo^{3+}	Molybdenum ion
mol.%	Mole percentage
Mo-L_a	Intensity peak in EDS spectrum caused by molybdenum
MoO_3*H_2O	Molybdenum oxy-hydroxide
MoO_4^{2-}	Molybdenum oxide ion
MoS_2	Molybdenum disulfide
$MoSi_2$	Molybdenum disilicide
N_2	Nitrogen gas
Na_2SO_4	Sodium sulphate
NaCl	Sodium chloride
Na:V	Sodium vanadium ratio
NaV_6O_{15}	Sodium vanadyl vanadate
$NaVO_3$	Sodium metavanadate
Nd:YAG	Neodymium:yttrium-aluminium-garnet
Ni^{2+}	Nickel ion
Ni_2W_4C	Mixed carbide
Ni_3Al	Nickel aluminide
$Ni_3V_2O_8$	Nickel orthovanadate
$NiCr_2O_4$	Spinel oxide
NiO	Nickel oxide
$NiSO_4$	Nickel sulphate
NiTi	Nickel titanium intermetallic compound
OCP	Open circuit potential
OH^-	Hydroxide anion
OM	Optical microscopy
$PbSO_4$	Lead sulphate
pH	Acidity or alkalinity level
PID	Proportional integral-derivative
PREN	Pitting resistance equivalent number
PTA	Plasma transferred arc
PTFE	Polytetrafluoroethylene
PVA	Polyvinyl alcohol
PVD	Physical vapour deposition
QT	Quenched & tempered
Ref.	Reference
RT	Room temperature
$S_2O_7^{2-}$	Sulphate ion
SAE	Society of Automotive Engineers
SAW	Submerged arc welding
SDAS	Secondary dendrite arm spacing
SE	Secondary electrons
SEM	Scanning electron microscope
SFTC	Spherical fused tungsten carbide
SHE	Standard hydrogen electrode
SHS	Self-propagating high-temperature synthesis
SiC	Silicon carbide

SiO_2	Silica
SM	Stereomicroscope
SO_2	Sulphur dioxide
SO_3	Sulphur trioxide
SS	Stainless steel
STEM	Scanning transmission electron microscopy
TiB_2	Titanium diboride
TiC	Titanium carbide
TIG	Tungsten inert gas
TiN	Titanium nitride
(Ti, Mo)C	Titanium-molybdenum carbide
TiO_2	Titanium dioxide
TUT	Tampere University of Technology
UNS	Unified numbering system
V_2O_5	Vanadium pentoxide
V_4C_3	Vanadium carbide
V_8C_7	Vanadium carbide
$V_{32}C_{28}$	Vanadium carbide
VC	Vanadium carbide
$VC_{0.88}$	Vanadium carbide
VO_3^-	Vanadium oxide ion
vol.%	Volume percentage
vs.	Versus
W_2C	Ditungsten carbide
WC	Tungsten carbide
WS_2	Tungsten disulfide
wt.%	Weight percentage
XRD	X-ray diffraction
ZrO_2	Zirconia

CONTENTS

1 INTRODUCTION

Different forms of wear and corrosion and their combined effects have annually enormous economic impact on broad range of industries since they cause maintenance, repair and material costs for part replacements as well as losses due to plant shutdowns [1]. Being essentially surface related problem, the field of surface engineering, which includes a wide variety of surface modification, alloying and coating methods, plays a key role in combating mechanical and chemical surface degradation of various engineering components. In contrast to surface modification methods, alloying and coating methods have the advantage of changing surface's composition, which allows, for instance, to design multi-material structures comprising cheap and less noble base materials with required mechanical properties and more expensive and nobler multi-functional coating alloys on the surface to meet the given service conditions. Several methods to manufacture such coatings are available with their own characteristics including capital costs, productivity, wall-plug and process energy efficiencies, selection of coating and base materials, coating integrity, bond and cohesive strength and effects they induce on base material et cetera (etc.). One way to classify these methods is to divide them on the basis of coating thickness they produce. To name a few, electroless and electrolytic plating, chemical and physical vapour deposition (CVD, PVD) are well-established and common methods to manufacture thin wear and/or corrosion resistant films few microns in thickness, whereas thermal and cold spraying, friction surfacing, chrome plating and overlay welding are representative methods to produce thicker coatings from few hundred microns up to several millimetres in thickness [1].

Recently rapidly emerged laser cladding is a process, which belongs to the latter group of coating methods. Analogous with overlay welding, it is a technique, where similar or dissimilar materials, primarily metals, are joined together by fusion. As opposed to gas and arc overlay welding processes, laser cladding utilizes highly concentrated optical energy, which can be sharply focused on the surface of base material leading to orders of magnitude higher energy densities compared with conventional methods. Owing to this, coatings can be produced in a way that only a thin layer of base material melts together with coating material leading simultaneously to fusion bonded and low diluted coatings. Another benefit originating from the high energy density includes short interaction times, i.e. high traverse speeds, between the heat source and base material. This leads to high solidification and cooling rates, which generate fine-grained microstructures as well as limited microsegregation, diminished dissolution of externally added reinforcements, extended solid solubility and phases far from the equilibrium. Moreover, heat input (J/mm) into the base material remains low, which reduces metallurgical changes and distortion. On the other hand, highly concentrated energy combined with high traverse speeds lead also to strong thermal gradients, which cause high tensile residual stresses on coating layer hindering the production of brittle coating materials without cracks. Another drawback addressed to the principal characteristics of light is process energy efficiency, which remains rather low due to reflection of light. All these positive and negative aspects of laser cladding together with related process and material characteristics are attempted to introduce shortly in the following sections.

1.1 Background and milestones in laser cladding

The potential of laser cladding or closely related alloying process, carbide impregnation in this case, was reported already at the end of 60's approximately 9 years after the construction

of the first working laser in 1960 (Figure 1) [2, 3]. In mid 70's the amount of publications and patents concerning pre-placed laser cladding with wires, rods and powders and dynamical feed of wires [4] and few years later dynamical feed of powders started to increase [5]. At late 70's and beginning of 80's laser cladding was adopted by the leading earthmoving vehicle manufacturer and two leading gas turbine manufacturers utilizing continuous wave (cw) mode carbon dioxide (CO_2) lasers, only available lasers at that time to deliver the power level required for laser cladding [5-7]. In spite of the many recognized advantages, it did not receive wider industrial acceptance [8] as for instance laser cutting and welding, which both can be considered as highly efficient "keyhole mode" laser processes accomplished with high intensity focused beam. Main reasons for this slow acceptance of laser cladding relates primarily to low cost efficiency since productivity and process energy efficiency were low due to the nature of heat conduction mode processing and accompanied poor absorption of unfocused CO_2 laser beam to well-shielded molten metals. Secondly, capital costs became high since industrial laser systems capable of laser cladding and related accessories could easily be orders of magnitude greater than conventional coating or overlay welding equipment. Situation has, however, changed. In mid 90's there was an exponential growth at least in laser cladding research including closely related near-net shape 3D manufacturing as measured in a number of published papers [9]. During that time shorter wavelength lasers, cw-mode Nd:YAG and diode, entered the market in kilowatt range and more. Diode lasers, particularly, showed high potential by offering many advantages over other laser systems; low price, small size, high wall-plug efficiency, maintenance-free operation, mobility, which allows cladding treatments on site etc. [10, 11]. With both these lasers productivity in laser cladding was improved significantly. And the growth of laser cladding is expected to continue since lasers are getting more powerful and new potential laser sources like fiber lasers are developed offering similar benefits as diode lasers plus far higher levels of power [12]. In addition to more powerful lasers, novel hybrid laser cladding methods, where additional energy is supplied by the inexpensive electro-magnetic induction or resistive heating, can further increase the productivity even more efficiently without loss in coating quality. From the materials technology point of view, demand for high quality coatings is increasing since service conditions in many processes are getting harsher. Environmental restrictions, for instance, yield higher efficiencies in many combustion processes, which mean higher combustion temperatures. In pulp & paper industries water saving yields closed process water cycles, which mean more highly concentrated and corrosive process waters. With the demands for increasing productivity in mining and crushing operations more wear resistant materials are required etc. In addition, prevailing life cycle thinking and such related issues as the need to enhance material efficiency to save the natural resources also compels the use of high quality coatings, which could be obtained by laser cladding.

1.2 Laser cladding methods

The ultimate objective of laser cladding is, usually, to produce defect-free protective coating fusion bonded to the base material with maximum coating material efficiency and coverage rate allowed by the laser power at hand. This can be implemented by fusing the coating material already pre-deposited on the surface of base material (2-step process) or by feeding it dynamically to the laser-generated melt pool (1-step process).

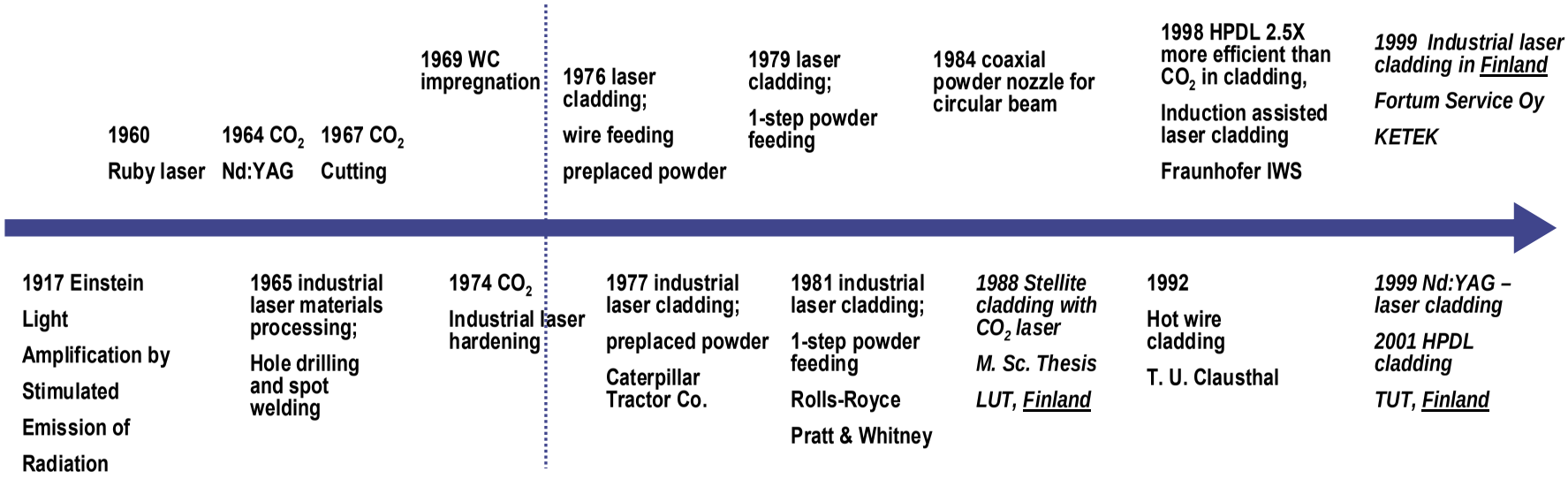

Figure 1. Important global and domestic milestones in laser cladding [2, 3, 13-17].

1.2.1 2-step laser cladding

In 2-step laser cladding, the coating precursor is pre-placed on the base material and subsequently melted by the laser. This pre-placing can be performed by some conventional coating method such as thermal spraying or electroplating or just simply by applying a layer of powder, mat, wire, chip, strip or foil etc. In remelting of previously applied coating the key issue is the bond strength of the coating. It should be high enough to prevent the peeling off of the non-treated coating during subsequent remelting. Consequently, spraying methods, which lead to higher bonding strengths (due to the coating manufacturing mechanisms) than other coating techniques, are preferred. While applying sheets, strips or wires, good thermal contact to the base material should be established to ensure proper wetting and fusion bond. Spot welding and organic binder have been applied for this with success. When using powders they are frequently applied in the form of slurry made of organic binder (e.g. polyvinyl alcohol (PVA)), water and powder in order to agglomerate the powder particles and to fix them on the base material. After spreading the slurry, water is evaporated by a drying process at elevated temperature. In subsequent melting organic binder evaporates and may cause porosity in final coating layer. Contraction of loose powder layer upon melting and associated exposure of base material at the edges of formed bead to the laser beam is another drawback and may cause problems in surface smoothness and dilution while processing large areas by overlapping [18]. Binder loss from the areas adjacent to the molten track may also be a problem [6].

During the formation of the melt pool, laser beam does not interact initially with the base material but with the pre-placed layer. Hence, the heat has to conduct through this loose low conductivity and thermally isolated layer before welding it to the base material. According to model developed by Powell et al. [19], melt front propagates rapidly to interface. At this point solidification starts due to contact with high thermal conductivity base material but fusion bond is not initiated unless there is enough power or interaction time available. Processing parameter window for this stage is rather large and can be utilized for instance in novel laser casting process documented in Ref. [20]. However, to provide that additional power or time to achieve coating with fusion bond, so that excessive dilution is prevented, is rather difficult. This resulted narrow process parameter window for low diluted and fusion bonded coating was claimed for instance in Refs. [21-23]. On the other hand, direct interaction of laser with the pre-placed powder bed may improve energy efficiency due to beam scattering and multiple reflections it induces [24]. This was demonstrated in Ref. [18] where rather high absorptivity of 30% (measured by calorimetry) was reached with CO_2 laser. Mazumder and Li, however, stated earlier that the specific energy (J/mm^2) requirements to melt through a specified pre-placed powder bed depth is almost double that required for a blown powder method [25]. More of these process energy efficiencies are discussed in the section 1.3.2. Another advantage of this pre-placed method is high coating material efficiency. As being 2-step process, its use instead of 1-step process should be, however, justified by other means. One justification could be a limited access for dynamical feed of powder or wire. One such commercial application was developed in Japan where inner surfaces of small diameter pipes ($Ø_{id}$ = 38 mm), used in boiling water reactor type nuclear power plants, were laser clad using pre-placed technique [26].

1.2.2 1-step laser cladding

1-step laser cladding is a process where the coating material, frequently in the form of powder or wire, is fed dynamically into the laser-generated melt pool. In this process, laser beam preheats or melts the fed coating material and a thin layer of base material. Owing to simultaneous movement of laser beam and/or base material, low diluted and fusion bonded bead forms. By overlapping several beads side by side large areas can be covered. Applying several consecutive layers on top of each other, coating thickness can be increased infinitely and the process can be extended to the production of near-net shape 3D structures.

1.2.2.1 Powder feeding

Owing to the wide range of alloys available in powder form and better coupling efficiency of laser beam compared with cold wires, blown powder laser cladding is until now the most utilized 1-step method. In this process, powder feeding can be performed off-axially or coaxially with respect to laser beam as illustrated in Figure 2. In the former process, off-axis nozzle in leading position is normally used due to better powder catchment efficiency it provides (powder stream hits to "uphill") [22]. Powder efficiency can be further improved by using rather high feeding angle between horizontal and nozzle [22]. These off-axis nozzles can be quite simple in structure, circular or rectangular in cross-section and designed in a way that areas difficult to reach can be clad. Few examples of this were given in Refs. [27, 28], where inner surfaces of pipes 50-60 mm in $Ø_{id}$ were laser clad by blown powder method. One of the drawbacks of this off-axis feeding is low reproducibility since small deviations in location of powder delivered with respect to laser beam lead readily to substantial variations in bead geometry, thickness, material efficiency and dilution. On the other hand, off-axis feeding enables to direct the powder flow, for instance, to back part or tail of the melt pool in order to avoid direct contact with laser beam. This is advantage when externally added hard reinforcements, particularly carbides, which absorb laser radiation efficiently, are embedded with as little dissolution as possible. Another disadvantage is its dependence on cladding direction because change in travelling direction in a plane perpendicular to laser beam leads to completely different local cladding conditions if position of the nozzle is not changed "on the fly". Depending on the powder used, short powder–beam interaction times characteristic for off-axis feeding can be benefit or disadvantage. If longer interaction times and higher particle temperatures are preferred, particle velocities can be decelerated with cyclone, which allows the carrier gas to escape before powder stream enters the melt pool. Normally particle velocities range from 1.5 to 2.5 m/s [29-31]. Other factors, which influence on particle preheating, are particle size, composition and morphology (absorption), specific heat capacity (c(T)), the density of the powder cloud (multiple refections), the inclination of the nozzle (traveling distance) and the intensity, the area and energy distribution of the laser beam [32-36].

In coaxial process, cone-shaped powder nozzle surrounds the laser beam and delivers the powder stream coaxially into the beam and melt pool satisfying more or less the Gaussian distribution function in particle concentration. The most significant benefit over off-axis feeding is its independence of cladding direction (omnidirectionality). All directions of the base material movement in a plane perpendicular to laser beam are equivalent. Moreover, powder–beam interaction times are also longer than in off-axis cladding and the passing powder particles attenuate the laser beam and are preheated more efficiently. Besides interaction time laser power attenuation is influenced by particle velocity, powder feed rate, powder density, particle size and angle between powder jet and horizontal [30]. Due to longer interaction times and multiple reflections offered by longer powder cloud, its energy

efficiency could be expected to be higher than in off-axis cladding. Nowadays, several commercial coaxial nozzles developed by research institutes and companies are available for CO_2, Nd:YAG, HPDL and fiber lasers enabling long-term cladding operations with power levels up to ~4-6 kW without interruptions due to overheat and the production of high quality coatings in reproducible manner without any special skills.

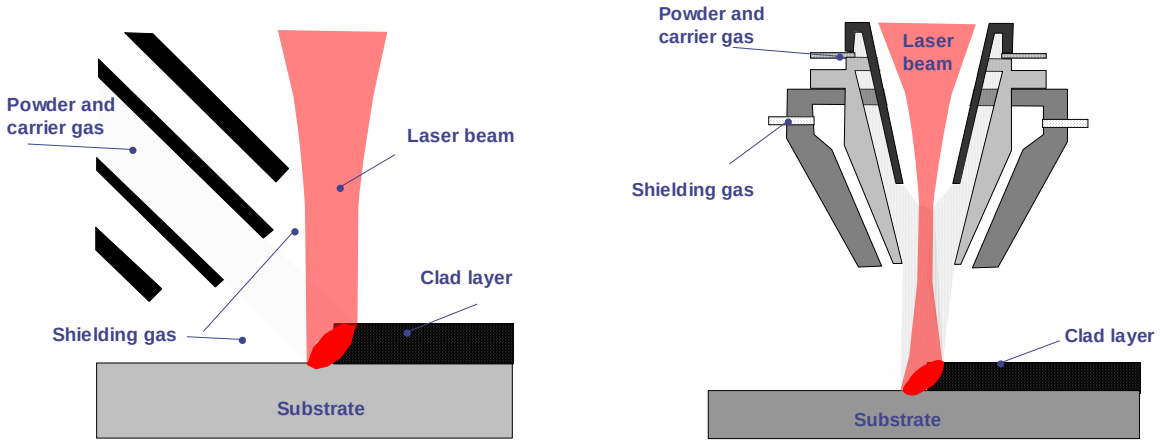

Figure 2. Off-axis and coaxial powder feeding methods in 1-step laser cladding.

In contrast to traditional coaxial laser cladding configuration where the powder cloud surrounds the laser beam, Chivel [37] suggested the method where the powder is delivered vertically into the middle of ring shaped beam, i.e. laser radiation energy is supplied coaxially to a cylindrical powder cloud over the entire surface of this cylinder (Figure 3). According to theoretical calculations, this configuration is claimed to offer ten-fold increase in efficiency measured in J/g compared with traditional coaxial configuration. Prerequisite to implement this configuration is to utilize some non-traditional laser resonator or beam guiding system. Perhaps the most flexible way to implement this is to position diode stacks in a way similar to ring focus laser reported in Ref. [10].

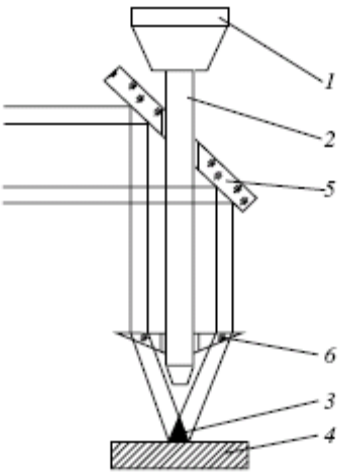

Figure 3. Schematic illustration of laser cladding setup based on ring/cone shaped beam, where the coating material is introduced from the centre of construction. 1. powder hopper, 2. powder nozzle, 3. focal region, 4. base material 5. mirror 6. cone-shaped lens [37].

In general, the main drawback of blown powder laser cladding is the low material efficiency. Values reported range from 10 to 100% but are typically between 40–80%. Material efficiency is strongly dependent on the melt pool dimensions relative to that of powder jet [22, 30]. Powder jet diameter is, in turn, strongly dependent on particle size. Becker and Sepold [38] reported higher material efficiencies while using finer powder. With nano-scale powders powder jet focus diameters as low as 100 μm was reported recently [39]. Use of such a fine powder granulometry necessitates, however, modifications in standard powder feeders and cladding nozzles in order to prevent the agglomeration of powder and resultant blocking and to ensure the constant feed rate. The risk of vaporization increases as well while using such a fine powder [36]. To increase the material efficiency while using standard PTA grade powders (~50-150 μm), which are most often used, powder recycling is, of course, possible but this practice adds extra steps like collecting and sieving and it necessitates efficient shrouding to prevent the oxidation of particles which travel through the beam but does not participate in bead formation [40]. Some change in size distribution compared with original powder may also occur [41]. Another drawback of powder laser cladding is the residual powder and aerosol emissions it releases to the working area. Aerosols, which consist of gas and fine solid or liquid particles, result from vaporization and condensation of cladding materials. Haferkamp et al. [42] characterized these emissions during laser cladding of spherical aluminium-bronze powder (20–75 μm). Observed aerosol rates and amounts of 1.7–2.0 mg/s and 25–28 mg/m^3 exceeded the threshold value for copper smoke in 1.5 minutes. Particle size distribution of these aerosols averaged to 0.13–0.25 μm. In addition to health issues, residual powder emissions influence negatively on facilities and delicate equipment around. In addition to PTA grade powders, HVOF grade (~10-45 μm) is frequently used. It was shown in Ref. [23] that using finer (< 53 μm) grade powder instead of coarse one (63-90 μm) enhances productivity approximately by a factor of 1.6. Another benefit is lower surface roughness, which originates from the particles falling onto mushy zone behind the melt pool and leaving craters and not fully melted powder particles on the surface of bead. Depending on powder manufacturing method, metal powders are spherical (atomizing manufacturing route and/or spheroidizing post-treatment) or irregular (fusing and crushing manufacturing route) in shape. Spherical powders produced by gas atomisation have lower oxygen content and are more expensive than water-atomised powders, which are rougher and irregular in shape. Rougher and oxidized surface was proven to absorb laser radiation more efficiently than smooth spherical less oxdized particles potentially enhancing the process energy efficiency [35].

1.2.2.2 Wire feeding

1-step laser cladding by dynamical feed of wire was introduced in 1976 in patent “Cladding”. Its utilization has, however, lagged behind blown powder method due to narrower range of available alloys, sensitivity of alignment of wire and poorer coupling efficiency for the cylindrical surface of shiny and smooth cold wire as it was already mentioned earlier. In principle, laser cladding by wire feeding can be performed similarly to off-axis blown powder cladding just more attention has to be paid on wire feeding location with respect to laser beam since this process is more sensitive to misalignment. Some authors have stated that the best feeding location, on the basis of bead quality, is the leading edge of the melt pool when the wire is fed from the leading nozzle or from side [43, 44]. This diminishes the shadowing effect which can lead to lack of fusion and unstable melt pool. Naturally, closer attention has to be paid also for the moment when the feed is switched on and off. The main benefits of this process are the high material efficiency, smooth surface finish and the absence, a priori, of residual powder emissions. Wire feed laser cladding experiments have been carried out, for instance, for 316L [44], mild steel [45], NiCrBSi [46], Hastelloys C-276 [47] and C-22 [48],

Inconel 600 [49], Stellite 6 [43], CuAlNi [50] and Cu-30Ni [45, 51] wires varying from 0.2 to 1.7 mm in diameter. To expand the range of alloys, wire and powder feeding can be combined. This was practised in Refs. [52, 53].

1.2.2.3 Strip feeding

As the absorption of randomly polarized laser beam, typical mode of polarization in fiber optic delivered and direct diode lasers, is the highest perpendicularly and at low angles of incidence to the metal surface, it could be expected that the use of flat strip instead of cylindrical wire would lead to better coupling rates and hence better deposition rates. This was suggested by Yelistratov [54], who took the advantage of rectangular nature of the direct diode laser beam and feeding of cold Inconel 625 strip 6 mm in width and 0.4 mm in thickness. In the earlier studies, Luft et al. [55] conducted experiments with amorphous and flexible Stellite strips. Example of modern robotic laser cladding cell equipped with powder, wire and strip feeders as well as short-wavelength Nd:YAG and direct HPDL lasers is shown in Figure 4 [56].

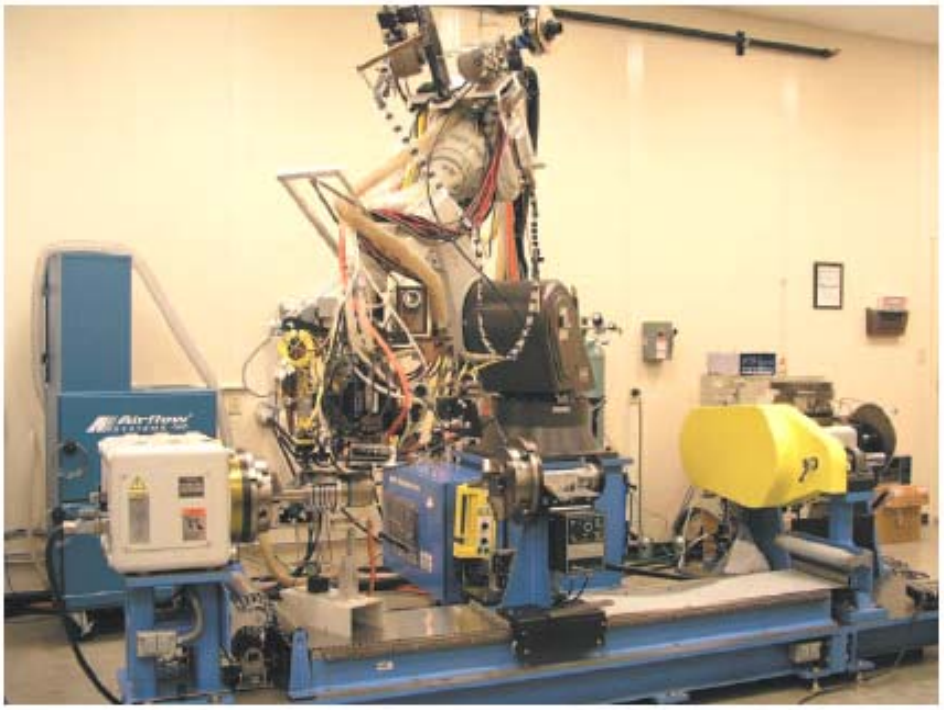

Figure 4. Modern robotic laser cladding cell equipped with powder, wire and strip feeders as well as Nd:YAG and direct HPDL lasers [56].

1.2.3 Hybrid laser cladding

Hybrid laser cladding processes can be understood as a combination of laser and some other heat source contributing additional energy to the process. As the laser energy is relatively expensive and low efficient (wall-plug, process) heat source, some other cheaper form of energy is highly desirable to increase the productivity/deposition rates (kg/h, m^2/h). This additional energy can be brought directly to the coating material and/or alternatively to the base material to be clad. In the former case, the most efficient way to heat the coating material is to heat the wire, rod or strip by means of resistive or inductive heating before it enters the

melt pool. As an example of resistive heating, Bouaifi and Bartzsch [57] combined CO_2 laser and conventional arc welding machine in order to produce Ni-based superalloy coating on mild steel. Before entering the melt pool, wire (Ø = 1.6 mm) was heated up to near its solidus temperature by adjusting voltage and current so that the arc was not initiated. Coatings with low dilution (< 10%) and homogenous chemical composition were produced using trailing wire feed configuration. In consequence of additional energy, laser power could be reduced from 5 kW to less than 3 kW to obtain the same productivity. Hinse-Stern et al. [15] preheated resistively Fe-based cored filler wires (Ø = 2.4–2.8 mm) up to 900-1000°C before entering the rectangular laser beam spot 5–7 mm^2 in size. They stated that preheating provided up to 50% of the process energy required to produce the coating. The net deposition rates up to 3 kg/h were reached with 6 kW CO_2 laser. Wiklund and Flinkfeldt [43] compared the cold and hot wire CO_2 laser cladding processes. When combined with metal inert gas (MIG) power source, deposition rates (kg/h) of Stellite 6 wire (Ø = 1.2 mm) could be increased more than 400% while producing very thick beads up to 5 mm. For the coating thickness of 1 mm and laser power of 5 kW, three times higher traverse speeds could be used compared with cold wire process. Wire was fed from the side (90° angle with respect to traverse direction) at an angle of 50° with respect to horizontal. Distance between the wire feeding nozzle (welding torch) and the surface to be clad was 10 mm. The best place in melt pool to aim the wire was 0.25 x D_b (D_b = diameter of the spot) measured from the leading edge of the spot. With the use of shorter wavelength laser (Nd:YAG), Nurminen et al. [58] achieved deposition rates up to 10 kg/h with Inconel 625 solid wire (Ø = 1.0 mm). They also noted that the solid wires are preferred over the cored filler wires since alloying elements are distributed non-homogeneously and remain unmelted in the final coating layer due to low heat input and coarse alloying elements inside the tube [59].

Besides increasing deposition rates (kg/h, m^2/h), base material heating is beneficial in decreasing the steep thermal gradients associated with laser cladding and hence obtaining crack-free coatings even from the most brittle hardfacing alloys. The most efficient way to conduct base material heating is by means of induction. Depending on the case, stationary induction coils around stationary base material to be heated or movable induction coil in the vicinity of the moving melt pool can be used. As an example of the former case, Beyer et al. [60] reported about 4-fold increase in deposition rate (kg/h) when the base material was preheated to 620°C. For other applications, crack-free coatings of NiCrBSi with 63 HRC and of WC/NiBSi with a volume content of 65% WC particles could be deposited with a traverse speed of up to 10 m/min [60]. For rotationally symmetric components Wetzig et al. [61] eliminated cracking both in base and clad material with simultaneous increase in deposition rates by using leading induction coil. The same kind of approach was adopted by Theiler et al. [62] who produced crack-free MMC clad layers on the outer surface of circular blade. Additionally, high strength magnetic fields associated with induction heating can be utilized in controlling the shape of the individual beads [63] and suppressing the formation of pores [64].

Other hybrid processes studied include laser + PTA hardfacing and laser assisted thermal spraying. In the former one, laser and PTA are not used simultaneously but selectively depending on the contour of the 3D object [60]. The latter one is studied more extensively. Its major advantage is to produce relatively thin (~300 μm) fusion bonded and low diluted metal-based coatings on metallic base materials with low heat input [65-67] and dense ceramic thermal barrier coatings [68-71].

1.3 Laser cladding process characteristics

Laser cladding process characteristics are discussed here under the subsections of laser cladding process parameters, modelling, heat source and melting efficiencies, productivity as well as monitoring and adaptive control.

1.3.1 Laser cladding process parameters

Functional properties and the quality of laser coatings are strongly dependent on chemical composition and microstructure as will be discussed later in section 1.5. Chemical composition is dictated not only by the material selection but also by the control of dilution, which can be defined geometrically or compositionally latter one giving a little bit higher values [27, 72]. Both the microstructure and dilution together with other relevant process results illustrated in chart (Figure 5) created by Ollier et al. [73], and modified by the author, are dependent on laser cladding process parameters, which are chosen on the basis of coating and base materials, the desired coating thickness and available laser characteristics. Consequently, laser cladding parameters can be divided into process and material parameters [74]. Process parameters include actual process parameters, which are variable, fixed laser parameters dictated by the choice of laser and optics and parameters related to the feeding of coating material. Among process parameters, laser power (P), traverse speed (V_b) and feed rate (f) are the principal parameters since they have the largest effect on the process results as will be explained below. By using classical power density – interaction time field, laser cladding is typically carried out in the range of 100–1000 W/mm^2 and interaction times less than 1 s as displayed in Figure 6. Among material parameters, beside surface condition, the most important ones include thermophysical properties, which comprise thermal diffusivity ($\alpha(T)$), thermal conductivity ($k(T)$), density (ρ), melting temperature (T_m), coefficient of thermal expansion (α_{CTE}), latent heat of fusion (L_m) and specific heat capacity ($c(T)$) among which $\alpha(T)$, $k(T)$, ρ, α_{CTE} and $c(T)$ are temperature dependent.

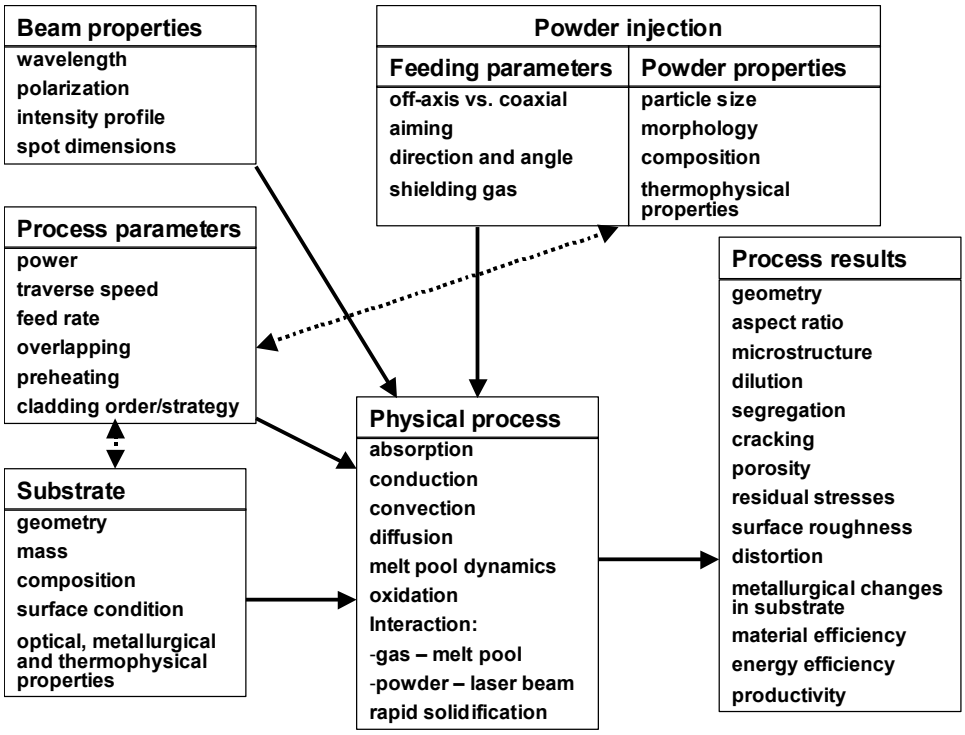

Figure 5. Blown powder laser cladding parameters [18, 73].

Since the dilution and bead or coating geometries vary with different process parameters, it is essential to understand the relationship of the process parameters to the optimal product quality. Considerable experimental and theoretical efforts have been carried out to study this. Low diluted coating with fusion bond, the ultimate goal to be achieved, can be obtained simply by feeding the optimal amount of material (g/mm or g/mm^2) to laser energy used (J/mm or J/mm^2) for a given clad/base material combination. Process parameter window mapped, for instance, against W/mm and g/min for this is rather large, and expands as a function of V_b, in blown powder cladding of Stellite on mild steel assuming that geometrical dilution is allowed, for instance, up to 10%, which is a value typically used to distinguish cladding from the laser alloying process [23, 75]. As in this case, operating windows are always restricted by the dilution, aspect ratio and power limits. What comes to the influence of process parameters on bead or coating geometries, height above the original base material can be increased by increasing f to the limit where the fusion bond is lost while keeping other parameters constant [76]. Simultaneously dilution gets lower as theoretical J/g value decreases [77], whereas thickness of the heat-affected zone (HAZ) surprisingly slightly increases [76].

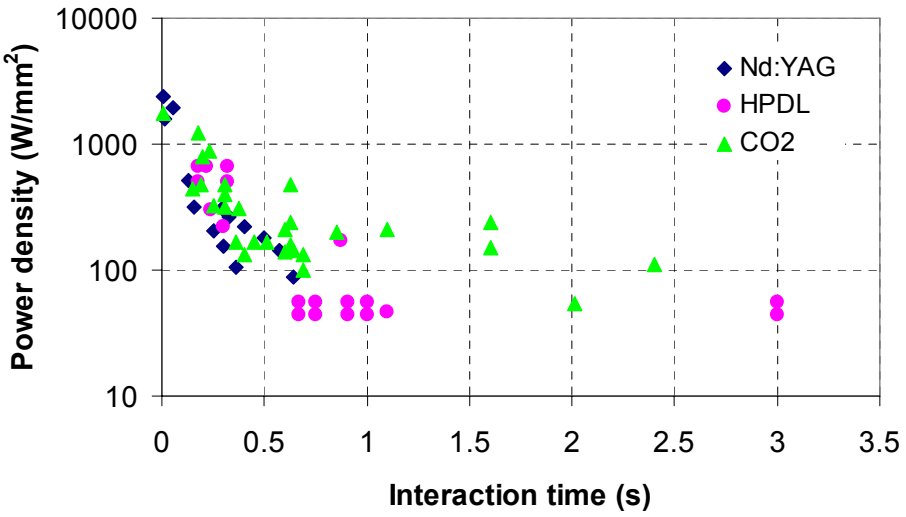

Figure 6. Blown powder laser cladding values (Co-, Ni- and Fe-based alloys on Fe-based base materials because their thermophysical properties do not vary a lot) collected from the literature and mapped against the theoretical power density and interaction time. Note that the power density axis is represented on a logarithmic scale [18, 45-47, 76-83].

Dependencies between height and f [82] and powder feed rate per unit length are linear in blown powder cladding [83]. If powder feed rate is, however, increased beyond the certain threshold value, cross-section of the coating above the original base material surface start to increase at accelerating rate due to multiple scattering of laser beam, which takes place in dense powder cloud coaxially fed into the laser beam. This improvement in absorption enhances the process energy efficiency as explained in Ref. [74]. Other straightforward ways to adjust the bead or coating height is to increase or decrease V_b while keeping other parameters constant. Higher V_b generates thinner and slower V_b thicker bead. Even if theoretical J/g value remains constant, increasing V_b tends to increase dilution as reported in Refs. [38, 76, 77]. This is particularly true for thin beads produced by high traverse speeds. With higher bead heights, dilution is in practice independent of V_b [75]. Height of a single bead cannot be, however, increased infinitely by any means because the aspect ratio

(width/height (w/h)) of the bead affects the formation of inter-run pores between adjacent tracks and thus hinders the formation of defect-free large surface area coating. It was shown by Steen [23] that, in general, aspect ratio (w/h) of single bead should be higher than 5 to avoid such pores or the contact angle (α) defined in Figure 7 should be higher than 100º [83]. Talking about continuous large area coating, the coating height (h_c) must satisfy $h_c<2/3r_l$, where r_l is beam radius, in order to avoid inter-run pores [30]. As the height of the bead is strongly dependent on f and V_b, increasing V_b or decreasing f can increase the aspect ratio [77]. Using wider beam would do the same. Example of this was given in Ref. [27], where 50 mm bead width was obtained by using linear scanning optics. Pelletier et al. [74] and de Damborenea et al. [82] noticed that cross-section and height increases linearly as a function of interaction time, i.e. when V_b decreases. Simultaneously, the depth of HAZ becomes larger since heat input (J/mm) increases. Overlapping defined by bead width and inter-track advance can be used as well to adjust the coating height. By decreasing the inter-track advance, coating height increases [40]. Simultaneously the surface smoothness (periodic variation in coating height) in direction perpendicular to cladding direction decreases minimizing the need for post-machining and increasing material efficiency [22, 84]. At the same time heat-treating effects on previous beads, however, increase. The effect of the third principal process parameter, P, is clear. Bead height increases when P is increased and other parameters are kept constant. Simultaneously, depth of HAZ and dilution become larger [76].

Bead width is primarily dictated by the spot size. However, with low V_b [85] or with high preheat temperature bead width can be wider than the spot size. This is because sufficient energy is available to melt the clad material situated at a distance wider than the beam itself [85]. For the same reason, preheating the base material increases dilution and widens the HAZ [86]. Furthermore, it was observed that bead width increases linearly with P in coaxial cladding [83]. The higher the V_b, the narrower is the single bead. This dependence is also linear [40, 83, 85]. Komvopoulos and Nagarathnam [76] noticed further that the bead width increases when f is increased.

Even if the examples shown here follow mainly the linear relationships between principal process parameters and bead or coating geometries, non-linear dependencies are common when there is change, for example, in absorption as in multiple scattering of laser beam in dense powder cloud. In addition to this, absorption can change due to changes in angle between incident beam and inclined plane (surface of the leading edge of the melt pool) it impinges, which depends on bead thickness and overlapping. V_b is another such factor, which may cause some non-linear dependencies since heat conduction losses to the base material decrease as V_b is increased to extraordinary high levels of 10 000 mm/min, for instance, at the expense of bead and spot width. It may also affect absorption and powder catchment efficiency since narrower beads produced by high V_b let more power and powder to impinge on solid base material. An important question, which arises from the relationships between coating thickness and process parameters, is: is it faster to clad coating with certain thickness by applying two thin consecutive layers instead of one thick? Weerasinghe and Steen [40] noticed that by doubling V_b, bead height (and bead cross-section) decreased by a factor of more than 2 while keeping other parameters constant. This meant that the cladding was energetically more efficient with the slow traverse speeds (~200-800 mm/min). This also suggests that it is faster to clad coating with certain thickness by applying one layer instead of two. This was also confirmed later by the mathematical model developed by Hoadley et al. [22]. Situation, however, changed when V_b was increased from ~800 to ~1200 mm/min. Cladding with the latter speed was now more efficient [40]. The most appropriate way to find

these relationships and simultaneously to reveal the operational window for the process is to create process parameter maps, which usually include vast amount of data presented in simple and concise manner. Creation of such maps involve large amount of cladding experiments where the principal parameters are varied up to their limits. To diminish experimental work, one of the main parameters can be adjusted "on the fly" as in Ref. [83], where the single bead of Ni-based self-fluxing alloy was clad around the rotating carbon steel rod. As a result of 175 analyzed cross-sections, process parameter map displayed in Figure 7 was created.

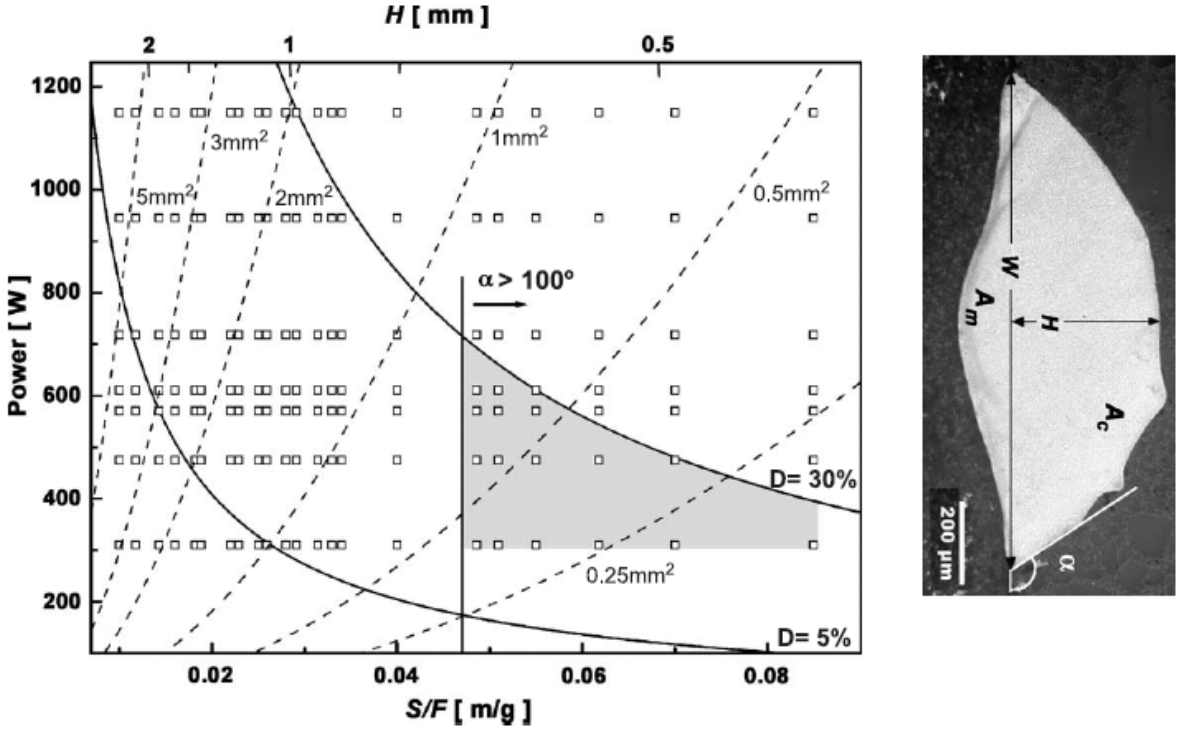

Figure 7. Process parameter map for single bead in coaxial laser cladding. Powder feed rate per unit length increases on lower and bead height on higher horizontal axis from right to left. Solid and dashed curves represent limits for dilution and cross-section area, respectively. Vertical solid line determines the contact angle required for defect-free continuous coating. D is geometrical dilution: (D) = A_m / (A_c + A_m). Operating window is restricted by dilution and contact angle limits [83].

1.3.1.1 Modelling

Since laser cladding process involves three principal process parameters for given beam properties, finding optimal ones for a given coating/base material combination to generate low diluted and fusion bonded coating with desired thickness necessitates usually a series of cladding trials accompanied with some basic metallography. To reduce the amount of experimental work, to help to select the optimal parameters and improve the understanding of the process, modelling has been widely practised. At least two approaches have been utilized; physical models involving large amount of numerical calculations and models based on experimental data. The first approach requires considerations of heat and mass transfers; energy, momentum and mass balance including all the relevant losses [30, 73, 84]; interactions between beam and powder cloud [29, 30]; changes in absorption due to change in incidence angle of beam [30, 87] and multiple reflections in powder cloud; fluid flow due to Marangoni convection [87, 88]; surface tension [31, 84, 89] and phase transformations. Heat

transfer and accompanied temperature fields can be calculated by solving 3D heat conduction equation for moving heat source. This necessitates the knowledge of temperature dependent material properties (k(T), c(T) and ρ) for clad and base materials and net absorption of the laser beam, i.e. how much heat is provided by the beam itself through the powder cloud and how much via preheated powder particles, which participate the bead formation. More realistic melt pool temperatures and temperature fields can be obtained if losses of convection and radiation, energy distribution modified by energy brought by powders [33], L_m (endothermic reaction in melting, exothermic reaction in solidification) and possible exothermic reactions associated with phase formations are taken into account. Heat transfer via Marangoni fluid flow, and powder feeding's influence on it [90], should not be neglected either since it is well known that heat conducts faster in melt pool than predicted by heat conduction equations. In realistic modelling of bead dimensions, at least, powder catchment efficiency, deformation of the melt pool due to powder and gas impact [87], mass transfer due to Marangoni fluid flow and temperature dependent surface tension (and parameters, which influence on it) of the molten clad layer and gravity forces [91] should be known. All these considerations lead to a very complex set of coupled equations, which should be solved three-dimensionally. For these reasons, number of assumptions and simplifications has to be often made reducing the level of correspondence between the mathematical model and reality. Lack of data about temperature-dependent material properties is another factor, which have retarded the creation of reliable 'universal' simulation tool to optimize cladding parameters.

In the earliest attempt to model the blown powder laser cladding, 2D physical model developed by Weerasinghe and Steen [29] estimated the bead dimensions and temperature field in longitudinal direction (along the bead length) when the process parameters were given. They noticed, for instance, that melt pool becomes elongated at high traverse speeds. Attenuation of the laser beam and heat provided by the preheated particles were considered. Later Hoadley and Rappaz [32] proposed also 2D model to define the melt pool shape in transverse cross-section parallel to cladding direction. Accurate melt pool shape and process parameters' influence on it was needed to simulate the solidification velocities and microstructure formation, which are more closely discussed later in section 1.5.1. The model calculated also the clad height when the processing parameters were given and predicted the laser power required to deposit a given clad thickness. Temperature dependent thermophysical properties were used for both the clad and the base material. Latent heat of fusion was included, too. Picasso et al. [30] established 3D model for predicting the process speed and the powder feed rate for the given laser power, beam diameter, geometry of powder stream and clad height. It also gave information about the process energy and powder efficiencies. Their model considered the change in absorption due to bead height (melt pool shape) related change in incidence angle of circularly polarized beam. Kaplan and Groboth [80] created model based on energy and mass balance equations, which permitted the calculation of temperature fields and bead dimensions in transverse cross-section of the bead (perpendicular to cladding direction). Bead dimensions in plane perpendicular to cladding direction were also calculated in Ref. [92]. This model was developed further to commercial simulation software (LAVA) for coaxial laser cladding, which is capable to compute the bead geometries in plane perpendicular to cladding direction when the process and material parameters are given [89, 91]. The required input parameters include laser power, beam diameter, powder feed rate, powder jet focus diameter, traverse speed, particle size and speed, distance between the coaxial nozzle and work piece as well as melting temperatures of base and clad materials. As input data, absorption of laser beam to base material/melt pool and powder particles should be known as well. Output data consists of bead width and height, maximum temperatures on clad

and base materials, powder loss and melt depth below the surface of base material (geometrical dilution) as well as depth of HAZ.

Another comprehensive model for coaxial laser cladding was described by Han et al. [90], who developed model to simulate the melt pool dynamics and dimensions, temperature fields and the geometry of the bead when the process parameters were given. Their results indicated, for instance, that the particle injection has a significant effect on the melt pool flow. Particle injection caused an increase in the maximum fluid flow velocity from 4800 to 18 000 mm/min compared to the situation without powder feed. Furthermore, it was noted that the melt pool temperature increased when the laser power was increased while keeping other parameters constant. The higher the powder feed rate, the lower the melt pool temperature due to attenuation of laser beam. Laser power and powder feed rate influenced also on melt pool length. That is, higher laser powers generated longer and higher powder feed rates shorter melt pools. Cho et al. [93] showed the importance of L_m in modelling by analyzing the time dependent thermal fields with or without it. In simulations where L_m was considered, maximum melt pool temperature decreased together with melt pool and HAZ dimensions as compared with the situation where L_m was neglected.

Laser cladding process modelling, that involves computing the temperature fields, melt dynamics and bead or coating geometries as discussed above, can be supplemented with material modelling. For example, Martukanitz and Babu [94] and Babu et al. [95] attempted to couple heat transfer and fluid flow (process modelling) with thermodynamic and kinetic models (material modelling) to predict the microstructural evolution and stability of WC in different matrix materials. Moreover, 3D temperature distributions can be also supplemented with thermo-mechanical calculations by finite-element model (FEM) to reveal the development of residual stress distributions. These stress and strain fields are computed with the aid of some commercial software like for instance ABAQUS, ANSYS and Sysweld.

1.3.2 Heat source and melting efficiencies

As the energy source in laser cladding is electromagnetic radiation, absorption and energy coupling are in decisive role to determine the heat source and melting efficiencies, i.e. how much of the available laser power actually participates in the cladding process (to heat the base material, to melt the coating material and weld it to the base material) and how much is lost to the surroundings due to back reflection, convection, radiation from the melt pool etc. Together with the available laser power, it dictates the productivity and largely the cost efficiency of the process. There are few ways to measure and compare these efficiencies in laser cladding. One of the most used ways to define the heat source efficiency is to conduct measurements with a calorimeter during cladding. Miyamoto et al. [96] used such method during the 1-step off-axis CO_2 laser cladding of Cu-based powder on Al-based base material. Heat source efficiency was just 10% without powder feed (= remelting), but increased to 30% when Cu powder was fed into the melt pool. This was claimed to be due to oxidation, which took place in melt pool during cladding. Marsden et al. [97] measured CO_2 heat source efficiencies during the off-axis cladding of Stellite 6 powder (30-60 μm) onto mild steel (surface finish was not mentioned). According to calorimetric measurements, heat source efficiency increased from 15% to 25% when the powder feed rate was increased from 5 to 8 g/min while keeping other parameters constant. Frenk et al. [98] noticed later similar enhancement in CO_2 heat source efficiency when the powder feed rate was increased (Stellite 6 on mild steel). With the traverse speed of 500 mm/min, heat source efficiency increased from 16 to 30 % when the powder feed rate was increased from 2 to 8 g/min. With the traverse speed of 1200 mm/min, heat source efficiency increased from 18 to 25 % when the

powder feed rate was increased from 3 to 12 g/min. When the powder feed was increased, coating thickness increased, simultaneously the incidence angle of laser beam changed due to more inclined melt pool. As a consequence of this and linearly polarized beam, the absorption was increased because angle of incidence approached the well-known Brewster angle. These results were verified by conducting laser remelting tests with varying angle of incidence. Absorption increased from 10 to 37.5% when the angle of incidence (= angle with respect to surface normal) was increased from 0 to 80°. Ollier et al. [99] obtained similar results by changing the angle of incidence of linearly polarized CO_2 beam towards "pushing" direction in relation to cladding direction. As a consequence of this, the heat source efficiency increased from 13 to 35 % when the incidence angle was increased from 90 to 150° (with respect to horizontal). Gutu et al. [100] took also the advantage of Brewster angle of linearly polarized CO_2 beam. They developed the optics, which produced circular beam on the surface of base material at very high angles of incidence (70-80˚ with respect to surface normal). At least in surface heating of mild steel, this configuration enhanced the energy coupling by a factor of 2–4 as compared with normal incidence (0˚). They also demonstrated this configuration in cladding by equipping it with vertical off-axis nozzle but efficiency comparison was not made with respect to cladding in normal position. With randomly polarized beams characteristics for fiber-optic delivered beams and direct diode lasers, such positive Brewster effect cannot be utilized. On the other hand, change in incidence angle of beam does not have large influence on absorption assuming that average reflectivity R_{ave} can be estimated as the average value of the reflectivities R_p and R_s according to $R_{ave} = (R_p + R_s)/2$.

Bloehs et al. [101] reported calorimeter studies conducted during the cladding of Stellite 21 powder (45-90 μm) from off-axis nozzle onto milled 16MnCrS5 steel with CO_2 and Nd:YAG lasers. In addition to heat sources (= wavelengths), they studied the influence of traverse speed, power density, surface finish of the base material and different shielding gases. The highest energy coupling rates in CO_2 laser cladding (30–35%) were achieved without shielding gas. Coupling rates with Ar and N_2 were approximately 28%. The lowest coupling rates were achieved with He (21–26%). Heat source efficiencies for CO_2 and Nd:YAG laser cladding were 30 and 60%, respectively, in identical conditions. Increase in traverse speed increased the coupling rates slightly. This was claimed to be due to decrease in bead width, which allowed higher portion of irradiated beam to impinge to oxidized solid surface around the melt pool. Coupling rates also increased when the power density decreased. For high power densities the highly reflective melt pool, resulting in lower coupling rates, occupied most of the laser-irradiated area. Furthermore, coupling rates in CO_2 laser cladding increased slightly in the following sequence as a function of base material surface finish; polished, milled, oxidized, grit-blasted. The positive effect of grit-blasting in CO_2 laser cladding was also reported in Ref [40]. Bloehs et al. [101] calculated also melting efficiencies (ratio of the energy to heat and melt the powder to laser energy used) for CO_2 and Nd:YAG laser cladding. They were approximately 9% for CO_2 and 18% for Nd:YAG. This calculation can be done with equation as follows:

$$\eta = \frac{P_c}{P} = \frac{\Delta m \cdot \Delta H}{t \cdot P} = \frac{\rho \cdot \Delta V \cdot V_b \left(c(T) \cdot \Delta T + L_m\right)}{\Delta s \cdot P} = \frac{\rho \cdot A \cdot \Delta s \cdot V_b \left(c(T) \cdot \Delta T + L_m\right)}{\Delta s \cdot P} = \frac{\rho \cdot A \cdot V_b \left(c(T) \cdot \Delta T + L_m\right)}{P} \quad (1)$$

where,

η = melting efficiency (%)
P_c = power utilized to melt coating material and weld it to base material (W)
P = delivered laser power (W)
Δm = mass of melted material (base material, coating) (g)
ΔH = enthalpy term ($c_p \cdot \Delta T + L_m$) (kJ kg^{-1})
$c(T)$ = specific heat capacity of material melted (base material, coating) (J kg^{-1} K^{-1})
ΔT = difference between melt pool temperature and ambient (K)
L_m = latent heat of fusion of melted material (base material, coating) (kJ kg^{-1})
t = cladding time (s)
ρ = density of melted material (base material, coating) (g mm^{-3})
ΔV = volume of melted material (mm^3)
Δs = clad length (mm)
A = melt cross-sectional area (mm^2)
V_b = traverse speed (mm min^{-1})

Melt pool temperature used in calculations, which was measured by optical pyrometer was 1700˚C. Gedda [20] compared the heat source and melting efficiencies in laser cladding between CO_2 and Nd:YAG laser. According to calorimetric measurements, he stated that 40% of the used CO_2 and 50% of the used Nd:YAG laser power was absorbed by the process while cladding Stellite 21 powder (30-60 μm) on grit-blasted mild steel with off-axis nozzle setup. This small difference in absorption or energy coupling, however, resulted in substantial difference in melting efficiencies as calculated with the equation shown above. P_c for Nd:YAG laser cladding was twice as high as compared with CO_2 laser cladding. This result meant that improved absorption, resulted from the shorter wavelength of the laser beam (1.06 vs. 10.6 μm), was given fully to P_c since the amount of power needed to heat the base material was equal in both processes. Melt pool temperature of 2027˚C was used for both processes. His energy efficiency and redistribution results are summarized in Table 1.

Table 1. Energy redistribution in laser cladding [20].

Distribution	***CO_2***	***Nd:YAG***
Power reflected off the melt	50%	40%
Power reflected off the powder cloud	10%	10%
Power used to heat the base material	30%	30%
Power used to melt the clad layer and weld it to the base material	10%	20%

In addition to CO_2 and Nd:YAG lasers, HPDL devices are increasingly used in laser cladding. Nowotny et al. [16] studied the melting efficiencies of CO_2 and HPDL (940 μm) lasers. According to them, 2.5 times higher CO_2 laser power was needed in comparison with HPDL to obtain single beads of Stellite 21 on mild steel with equal cross-sectional areas. This indicated the beneficial effect of shorter wavelength. Difference in heat source efficiencies between YAG (and other short-wavelength lasers; HPDL and fiber) and CO_2 cladding is much less than predicted by the absorptivity values at RT. This is attributed to the different behaviours when the temperature rises. That is, CO_2 absorptivity increases significantly with a rise in temperature [23, 102], whereas absorptivity for wavelength lower than 1.8 μm slightly falls [102].

Above mentioned values of 13-40% for CO_2 and 50-60% for Nd:YAG laser cladding are rather low compared with heat source efficiencies reported in literature for conventional arc

and electron beam welding processes. Heat source efficiencies in welding processes measured by calorimetric techniques was given by Kou [103] and they were 50-70% for PTA, 60–80% for TIG, 70–80% for MIG, 80–90% for SAW and EBW. Moreover, they are not largely dependent on materials and their surface properties.

In addition to roughening the surface, decreasing the wavelength of the laser beam and utilizing the Brewster angle of linearly polarized beam, it has been reported that using reflective dome, extraordinary high traverse speeds or fine powder particles help to improve efficiencies in laser cladding. As the largest unnecessary loss of energy in laser cladding is the back reflection from the melt pool [20], it is reasonable to attempt to recycle it back to the melt pool. This was described in Refs. [40, 41], where the optical feedback system, which consisted of clean reflecting dome, increased covering rates by a factor of 1.5–1.7 in CO_2 laser cladding. Seefeld et al. [80] found out that with traverse speeds as high as 10 000 mm/min substantially higher covering rates were achieved compared with normal traverse speeds used in traditional laser cladding (300–1500 mm/min). With Nd:YAG laser power of just 1.2 kW, Stellite 21 coating layer, 0.5 mm in thickness on mild steel, was laser clad with a rate of 0.23 m^2/h. Drawback of this high traverse speed cladding technique enabled by high power density (= small spot, D_b = 0.8 mm) was the low powder catchment efficiency, which was just 15–35 %. Partes et al. [104] verified that this improved efficiency resulted from the diminished heat conduction losses to the base material as well as increased energy input into the powder cloud. This latter effect was due to thicker powder cloud and associated increase in absorption due to multiple reflections. Thicker powder cloud resulted from the higher powder feed rate since f/v (g/mm) was kept constant. They also found out that the use of finer powder particles (10–45 μm) instead of coarse ones (45–150 μm) enhanced melting efficiency further by a factor of two. Pelletier et al. [74] noted similar increased absorptivity as a function of powder feed rate due to multiple reflection phenomenon as discussed earlier. Sears [105] suggested that improved absorptivity results from the denser powder cloud, which returns more reflected energy back to the surface. Another factor, which has been reported to enhance the melting efficiency is the possible energy release due to exothermic reaction, which takes place in melt pool. For instance, some carbides (TiC), borides (TiB_2) and intermetallics (Ni_3Al) [106] have large negative formation enthalpies, which could improve the process efficiency to some extent.

1.3.2.1 Productivity

Productivity or other commonly used term, deposition rate, is strongly related to the amount of absorbed laser power, which mainly depends on the laser power available and factors discussed above. Deposition rates in laser cladding collected from the literature are plotted in Figure 8. They concern the cladding trials of monolithic Fe-, Ni- and Co-based alloys on Fe-based base materials. It can be seen that short-wavelength lasers and hybrid processes increase productivity significantly. The following net deposition rates can be selected: ~0.5 kg/h with 3 kW CO_2 + reflective dome, off-axis blown powder process [23]; 1.4-1.9 kg/h with 4 kW HPDL, cold wire process [45]; 1.9 kg/h with 4 kW HPDL, cold strip process [54]; 3 kg/h with 6 kW CO_2, hot wire process [15]; 4.5 kg/h (Stellite 6 assuming that solid wire) with 5 kW CO_2, hot wire process [43]; 10 kg/h with 4.4 kW Nd:YAG, hot wire process, [58]. For the sake of comparison, deposition rates for TIG (dilution 5-10%) are up to 2 kg/h, for PTA (dilution 5–30 %) up to 7 kg, for MIG (dilution 10-25%) up to 10 kg/h, for SAW (dilution 15-35%) up to 70 kg/h and for electroslag up to 350 kg/h [107]. These reported values for conventional welding processes are effective rates meaning that any necessary breaks in the deposition process such as changing electrodes are taken into account. They can be considered

also as net rates since filler forms consist mainly of wires, rods, strips and tubes excluding the PTA process where the filler is in powder form.

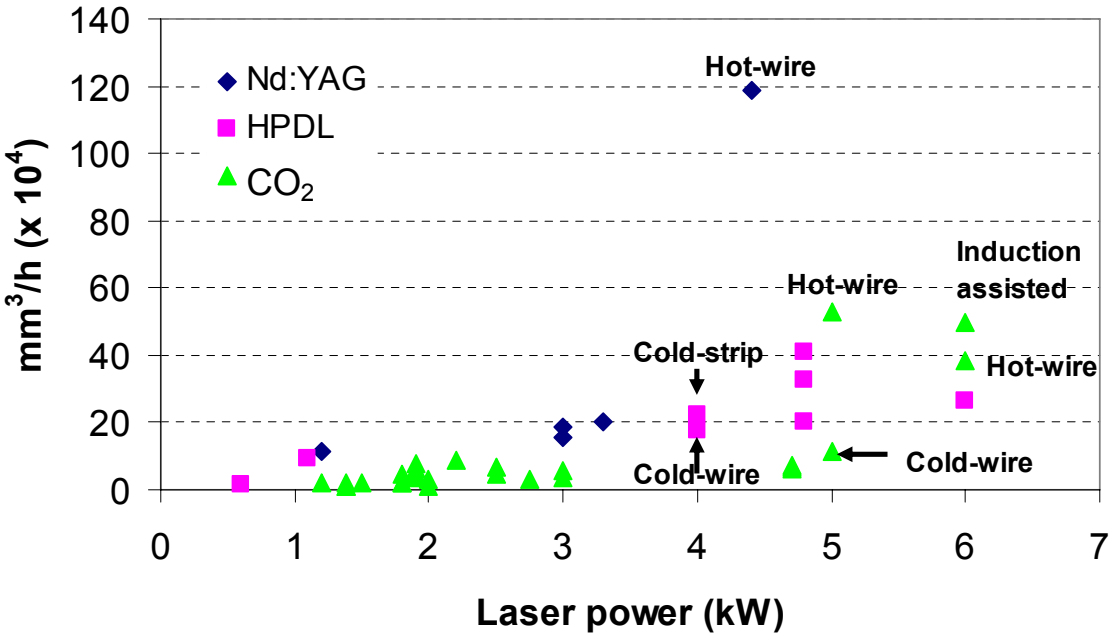

Figure 8. Deposition rates expressed in mm^3/h for blown powder cladding process unless otherwise denoted [15, 18, 23, 43, 45, 54, 58, 61, 79-81].

1.3.3 Monitoring and adaptive control

Depending on the size and geometry of the base material, heat accumulates at various rates as laser cladding proceeds. Due to limitations in heat conduction, particularly vulnerable sites for this are the edges, corners and thin sections. Due to overheating, melt pool temperature and size increases, which lead to excessive dilution, deeper HAZ and wider and thicker bead if process parameters are kept constant. This can be, fortunately, prevented by the adaptive control of the process where one or more of the principal cladding parameters are adjusted on-line. In practice, the most straightforward way to implement this closed-loop process is to adjust the laser power on the basis of signal measured from the surface of the melt pool after which the signal is sent to the well-established proportional integral-derivative (PID) controller that compares it to a preset value. Non-contact and fast optical pyrometers and photo-diodes based on the Planck's radiation law are used to create this signal by measuring the emitted radiation. 2-colour and multi-wavelength pyrometers are preferred since they measure temperatures close to actual temperatures without elaborated calibrations. Owing to the calculation method, they are less sensitive to variations in actual emissivity, which depends on several factors including material, temperature, oxidation and surface finish. In order to diminish the sensitivity to variations in working distance, coaxial type mounting of sensors is preferred.

Several studies have been performed to find out the melt pool temperature during cladding and reveal its dependence on the process parameters. Sallamand and Pelletier [108] and Pelletier et al. [109] measured temperatures in the range of 1800–2000ºC by 2-colour pyrometer in cladding of MMCs on Cu and Al-based base materials. Miyamoto et al. [96]

recorded temperatures above 1700ºC while cladding Cu-based powder on Al. Salehi and Brandt [110] reported values around 1800ºC while cladding Ni-based superalloy on mild steel. Doubenskaia et al. [111] used multi-wavelength pyrometer which spot diameter was 0.8 mm. Temperature was around 2200°C in pulsed Nd:YAG cladding of WC-Co(30 vol.%)-CuAl on steel. Bi et al. [112] applied a germanium photo-diode sensor integrated coaxially to the laser beam in coaxial cladding nozzle while depositing martensitic stainless steel on mild steel. Temperature signal (volts) increased when laser power and powder feed rate was increased and traverse speed was decreased while keeping other parameters constant. In another study to find out the effect of process parameters, Doubenskaia et al. [111] utilized 1-colour pyrometer. An increase in laser power and decrease in powder feed rate was noted to increase the non-true temperature. Apart from principal process parameters, Bloehs et al. [113] noticed the influence of shielding gases and carbide additions on melt pool temperature as a result of different coupling rates.

To compare the applicability of 2-colour pyrometer and photo-diode in laser cladding, Salehi et al. [114] studied their response to changes in process parameters. Analogous with results in Ref. [112], the optical emission detected by the photo-diode increased with an increase of powder feed rate even if the actual temperature of the melt decreased. Sun et al. [115] noticed the linear dependence between melt temperature and laser power while cladding Stellite 6 on martensitic stainless steel.

In one of the earliest publications concerning adaptive control, Grünenwald et al. [116] implemented closed-loop process by adjusting laser power on the basis of signal obtained via 2-colour pyrometer. Bloehs et al. [113] demonstrated the applicability of adaptive control in cladding of shaft 16 mm in diameter. With constant output power, linear increase in dilution occurred as the cladding advanced. When the set point of the melt temperature was fixed to 1725°C, laser power decreased when the cladding proceeded. This resulted in constant dilution. Salehi and Brandt [110] proved that closed-loop cladding process based on coaxial 2-colour pyrometer and PID controller, which adjusted the laser power, led to more uniform dilution and HAZ compared to open-loop process in cladding of Ni-based alloy on mild steel 10 mm in thickness. Bi et al. [112] presented closed-loop controlled process, which was based on photo-diode. In cladding of thin axis 7 mm in diameter, excessive dilution was prevented by adjusting the laser power when cladding proceeded.

In another approach, cameras are used to measure the melt pool dimensions. For instance, Hu and Kovacevic [117] utilized an infrared image acquisition system based on coaxially mounted CCD camera (800 frames/s) to measure the melt dimensions in 3D-manufacturing. PID controller kept the width of the melt pool constant by adjusting the laser power. Besides providing control signal, high-speed video cameras are applied to reveal the melt pool dynamics and melt pool-powder jet and melt pool–base material interaction zones. In one of the few published papers, Miyamoto et al. [96] photographed melt pool from side with high-speed video camera (4000 frames/s, halogen lamp illumination) during the 1-step off-axis cladding of Cu-based powder on Al-based base material. Photos revealed counter-clockwise melt flow in front and clockwise melt flow behind the centre of melt pool (cladding direction from right to left) due to temperature and surface tension gradients. Velocity of the flow was estimated to be in the range of 600–900 mm/min. According to numerical model developed by Ollier et al. [99] melt flow followed the same pattern for Stellite 6 on mild steel. Maximum melt flow velocities were attained at the surface and they were approximately 54 000 mm/min (traverse speed 250 mm/min). Results were verified by recording the melt pool from above

with high-speed video camera. It appeared that melt flowed from the front of the melt pool to the back side of the melt pool and from the hot center to the cooler edges. The maximum velocities were attained at the surface in the range of 30 000–60 000 mm/min [73].

Apart from the optical methods, Li and Steen [72] developed a fast dual-frequency electromagnetic sensor (response time 5 ms) for non-contact dilution monitoring, which was based on changes in electrical conductivity and magnetic permeability of clad layer as a function of dilution. For efficient operation, clad and base materials should have large differences in electric and magnetic properties. In addition, sensor should be mounted well behind the melt pool since for proper operation temperature should be below Curie temperature (~770˚C) hindering its use for control purposes.

1.4 Materials in laser cladding

As discussed earlier in section 1.3.1, materials and their thermophysical properties comprise one group of cladding parameters. The most common group of materials utilized in laser cladding are described here under the headings base and coating materials.

1.4.1 Base materials

Laser coatings can be deposited onto a wide range of engineering metals including ferrous and non-ferrous metals and alloys. They differ greatly in thermophysical, optical and metallurgical properties influencing the selection of cladding strategy, parameters and coating material. In the following sections, different types of base materials and effects of laser cladding on them (= cladability) and vice versa are discussed shortly.

1.4.1.1 Fe-based

The most common group of engineering metals are Fe-based covering over 80% by weight of all the use of engineering metals [3] forming naturally the largest group of base materials subjected to laser cladding. They can be further subdivided into carbon-manganese (C-Mn) steels (= mild steels), alloy steels, stainless steels, tool steels and cast irons.

Carbon-manganese steels. Low carbon C-Mn steels (0.05–0.25%C) consisting of ferrite and pearlite possess good cladability and even thick structures can be laser clad without additional preheat. During heating cycle certain thickness of base material undergoes austenization and pearlite dissolution, which leads to formation of martensite in HAZ during rapid cooling inherent to laser cladding. Hardening and related cold or hydrogen cracks as well as decrease in ductility is avoided due to low carbon content. Potential sources of dissolved hydrogen in HAZ could be the moisture in consumables, shielding gases and environment or the unclean surface of the base material. Instead, hot cracking may become a problem in HAZ if sulphur (S) and phosphorus (P) contents are high and Mn low. Rapid thermal cycles and low heat input may, however, hinder or prevent fully the segregation of impurities and thus the formation of such cracks. To author's knowledge formation of hot cracks in HAZ has not been reported in the context of laser cladding. S and P may, however, diffuse to clad layer due to intermixing causing hot cracks in it. This can be eliminated by using less hot-crack sensitive intermediate layer between base and clad materials as described in Ref. [27]. As carbon content increases the weldability of medium (0.25–0.60%C) and high carbon steels (0.60–2.11%C) decreases and additional preheating becomes necessary to slow down the critical cooling rates ($t_{8/5}$) and suppress the formation of hard and brittle martensite in HAZ. This was realized in study made by Wetzig et al. [61], where crack formation in HAZ of AISI 1043 (0.43%C) was eliminated with the use of induction heating as part of cladding process.

Hardenability, cladability and possible preheat temperature within carbon steels can be estimated using carbon equivalent equations developed for traditional arc welding. Common for all the carbon steels is relatively high melting temperature enabling the production of low diluted single layer coatings. Thermal conductivities are moderate and CTEs low. Latter promotes the formation of tensile residual stresses in coating layers, which usually have higher CTEs.

Alloy steels. Besides C and Mn, alloy steels include small amounts of Cr, Mo, V, Ni etc. Most of the alloying elements increase hardenability and risk of cold cracks in HAZ. The most frequently used alloy steels are QT steels. Typical examples, and potential targets for laser cladding include boiler tubes in power plants, pistons in diesel engines and paper mill rolls.

Stainless steels. Austenitic stainless steels possess the best cladability among stainless steels, i.e. deleterious phase transformations do not take place in HAZ rendering the use of preheat or elevated working temperatures unnecessary. In addition to this, high CTE inherent to austenitic stainless steels acts against the formation of tensile residual stresses in coating layer during cooling. This decreases the probability of crack formation during the production of hard and brittle coatings. Moreover, the inter-granular carbide precipitation (= sensitization) is not quite probable due to low heat inputs and rapid thermal cycles neglecting the subsequent solution annealing. Austenitic stainless steels have higher susceptibility to hot cracking than carbon steels because S and P segregates more easily in austenite. Austenitic stainless steels have low thermal conductivities, which causes lower heat conduction losses. This leads to higher dilution than in cladding onto mild steel with identical process parameters [118]. Due to low $k(T)/\alpha_{CTE}$ ratio austenitic stainless steels are the most distorted by the heat among Fe-based base materials. Numerous laser cladding applications concerning austenitic stainless steels due to poor sliding, friction, erosion and cavitation-erosion properties can be named; sealing faces in various valves used in power plants, chemical plants, oil refineries, diesel engines etc., boiler tubes in power plants [119, 120], rotor blades in pulp screen machinery [3] etc. Martensitic stainless steels are widely used in applications where a combination of moderate corrosion resistance and high strength is needed. Owing to high amount of alloying elements these steels harden in air leading to the fact that preheating is not enough to prevent the formation of martensite in HAZ during laser cladding. If application requires, post-weld heat treatment is needed to temper the martensite in HAZ. Usually, it is more straightforward to laser clad martensitic stainless steels in annealed condition and submit the laser clad component afterwards to annealing, quenching and tempering. Low CTE inherent to these steels, however, increases the risk for crack formation in coating layer during such treatment and cladding, too. Typical examples of base materials made of martensitic stainless steels, and potential targets for laser cladding, include steam turbine blades [121-125], diesel engine valve stems and spindles, piston rods and grinding segments in wood grinders, propellers [126], pump impellers [126], pressing dies for glass [127], land- and off-shore-based well drilling and oil extraction equipment [6, 128] as well as cutlery. Ferritic stainless steels possess corrosion properties between austenitic and martensitic stainless steels. During laser cladding grain growth may take place in HAZ leading to embrittling. Low heat input and rapid thermal cycles, however, limit the grain growth as well as the precipitation of carbides, nitrides and σ-phase which are deleterious for toughness and corrosion performance [3].

Tool steels. Owing to their high strength, toughness and wear resistance, tool steels are widely applied in components that are subjected to very high loads. According to working temperature, they are subdivided into hot and cold work tool steels. Former represents significantly easier cladability in tempered condition due to higher ductility. Similar to

martensitic stainless steels, most of the grades are air hardenable requesting preheat, prolonged cooling and subsequent heat treatment in order to avoid cold cracks in HAZ and guarantee the ductility in working environments. As an example of brittleness, Wetzig et al. [61] reported on cracks in HAZ of AISI O2 cold work tool steel as a consequence of thermal cycles induce by laser cladding. Potential applications for laser cladding and repairing includes non-ferrous metal and plastic moulds [78, 129, 130], dies [130-134], rolls [130], punches and other metal forming tools [131].

Cast irons. Cast irons can be subdivided roughly to ductile, grey, white, malleable and alloy cast irons. Owing to their microstructures and mechanical properties, they all respond differently to laser cladding. The most difficult ones to be laser clad are grey, white and alloy cast irons possessing limited ductility and thus the great risk of crack formation in HAZ due to tensile shrinking stresses formed on cooling. One example of this was given by Wiklund and Kaplan [135]. Ductile and malleable cast irons tolerate more stresses and they can be laser clad even without preheat. Hardening of HAZ depends mainly on carbon content in the matrix (= the amount of pearlite) since graphite does not dissolve readily due to limited diffusion time caused by rapid thermal cycles inherent to laser cladding. Graphite flakes in grey cast irons are, however, more susceptible to dissolution than graphite spheroids in ductile cast irons forming carbides and martensite in HAZ [3]. Dilution control is more difficult than in steels because cast irons have moderate melting temperatures. This may also lead to excessive porosity in coating layer due to degassing if released carbon is allowed to react with dissolved oxygen from the atmosphere [136]. High intermixing may also increase the hardness and decrease the corrosion resistance of the coating due to formation of carbides in coating layer. It is also possible that thin layer of brittle ledeburite forms at the melted region of base material [42]. Thermal conductivities and CTEs of the cast irons are typically: 40-50 W/m·K, 10.9-11.4 x 10^{-6} 1/K (20-500°C) for gray cast iron; 25-33 W/m·K, 11.3-12.0 x 10^{-6} 1/K (20-500°C) for ductile cast iron and 13-40 W/m·K, 11.8-18.2 x 10^{-6} 1/K (20-500°C) for alloy cast iron. Potential laser cladding applications of cast irons include cylinder liners [136, 137], cylinder heads, piston rings [135, 136], crankshafts, brake rotors [138] and drums, paper mill rolls, extrusion screws, cement feed screws, drawing tools [42], guide shoes [139] and pump impellers.

In conclusion, defects described in literature concerning traditional welding metallurgy are seldomly or hardly ever reported in the context of Fe-based base materials subjected to laser cladding. This can be explained by the low heat input inherent to laser cladding, which leads to narrow HAZ. On the other hand, laser cladding trials are frequently conducted on small size base materials where constraints and thus the stress factors remain low. However, to authors experience base material defects particularly related to hardening in HAZ are common in massive base materials.

1.4.1.2 Al-based

The second most studied base materials subjected to laser cladding are cast and wrought Al alloys. These alloys have been extensively used in automotive, marine and aerospace applications due to their low density (~2.7 g/cm^3), high strength-to-weight ratio and good corrosion resistance. Nevertheless, low hardness and poor wear properties have limited their use in many applications. Therefore, several types of laser coatings including AlSi-, AlSiCuNi- [28], AlCu- [140], AlNb- [141], Cu-based alloys [142-144], Al- and Cu-based MMCs [145] and direct injection of carbides (SiC, TiC) [146-148] have been applied. As can be noticed, potential coating materials are restricted mainly to Al-based alloys, Al-based

MMCs and directly injected carbides since Al has the disadvantage to form brittle intermetallics with basically all the elements (Ni, Cr, Co, Mo, Fe, Ti, Cu), which are used in traditional coating materials to improve the surface properties. The abundant formation of such intermetallics as NiAl, $NiAl_3$, $FeAl_3$, Fe_2Al_5 impairs, for instance, bond strength and other mechanical properties significantly [149]. Moreover, dilution control would be difficult due to large differences in melting temperatures between base and traditional coating materials. Compared with steels Al alloys are more difficult to laser clad because of poor laser beam coupling (= high reflection) and high thermal conductivity. It should be also mentioned that laser cladding on Al alloys, which are precipitation hardened (cast 300, wrought 2000, 6000–8000 series) leads to dissolution of these precipitates (Al_2Cu, Al_2CuMg, Mg_2Si, $MgZn_2$) in HAZ destroying the earlier heat treatment locally [3]. Al alloys, which contain Mg (T_v~1100°C) and Zn (T_v~900°C) vaporize readily causing pores in laser clad layer. Furthermore, injected SiC particles react with Al matrix forming Al_4C_3 and Al_4SiC_4 carbides, which are deleterious for mechanical properties [147, 150]. Potential applications, some of them already commercialized, include cladding of valve seats inside the cylinder head of the internal combustion engine made of Al [28, 142-144], pistons [28], cylinder bores [151], heads and blocks and repair of corroded areas in structural airframe [152] as well as various undersea marine components [153].

1.4.1.3 Ni-based

Ni-based superalloys strengthened by precipitates, solid solution atoms or dispersed oxides possess excellent corrosion and oxidation resistance and mechanical properties at high temperatures. They are widely applied as wrought and cast alloys in harsh environments including for instance gas turbines, diesel engines, metal forming tools, pumps and various off-shore components. Due to high material costs, repairing of these parts with Ni-based superalloys, for example, by laser becomes desirable. Actually, laser cladding and repairing of turbine blades made of Ni-based superalloys started the industrial utilization of laser cladding at the beginning of 80's. Since those days utilization has continued and developed together with advances in materials to repairing and 3D manufacturing of directionally solidified and single crystal superalloy base materials. These sophisticated alloys were needed to meet the higher temperatures and mechanical loads encountered in more efficient gas turbines [154]. With appropriate selection of coating material (narrow solidus-liquidus temperature interval) and careful control of solidification conditions by choice of process parameters, it is possible to grow epitaxial layers on single crystal alloy and avoid undesirable grain boundaries and stray grains [154, 155]. From the cladability point of view, Ni-based superalloys have moderate melting temperature, moderate CTE and low thermal conductivity. Precipitation-hardened grades should be laser clad in solution-annealed state and conduct ageing after the cladding since precipitates dissolve in HAZ due to thermal cycle induced by laser [156]. Owing to segregation of impurities and formation of low melting point phases, low heat input or even external cooling is preferred in order to prevent liquation cracks in HAZ [156]. In addition to variety of gas turbine components, valve seats, valve spindles and pistons in diesel engines are potential targets for laser cladding.

1.4.1.4 Ti-based

Titanium and its alloys with qualities of high strength-to-weight ratio, rather low density, biocompatibility and excellent corrosion resistance find their applications in gas turbine engines, airframes, automotive components, marine equipment, human spare parts and various components in chemical industry. Similar to Al alloys, their wear resistance is poor. This is mainly due to high coefficient of friction against themselves and other metals, which is

attributed mainly to the low c/a ratio in hcp α-Ti [148]. In order to overcome this drawback, laser cladding experiments have been conducted. It has been proved that efficient ways to improve the wear properties are laser cladding of Ti-based MMCs (TiB-Ti) [157] and direct injection of hard particles (SiC, TiC, TiN, WC) [146, 158]. Owing to its high affinity to oxygen, nitrogen and hydrogen, effective inert gas shielding implemented by trailing gas shield nozzle or shielding gas chamber must be applied. Potential laser cladding applications include the repair of high value gas turbine components [159, 160].

1.4.1.5 Mg-based

Magnesium alloys have the lowest density (~1.8 g/cm^3) of engineering metals and higher strength-to-weight ratios than many Al alloys making them potential structural metals in automotive and aerospace applications where the weight reductions are highly desired [161]. The main obstacles for their use are, however, poor wear properties and corrosion resistance against chlorides and some acids. Laser cladding has been applied to overcome these problems. Coatings applied have been usually Al-based alloys [162] or MMCs [163-165] since Al has compatible temperature ranges for melting and it is one of those few elements, which exhibits certain degree of solid solubility with Mg [166]. Problems caused by low melting temperature and formation of intermetallics can be overcome by using intermediate layers. Yue et al. [167] managed to produce stainless steel clad layers on Mg-based alloy by using intermediate layers of brass and copper. Direct injection of carbides (SiC, Cr_3C_2) without metal matrix has also been practised [168, 169]. The use of typical coating materials is excluded because they include elements, which form intermetallics with Mg. From the processing point of view, efficient gas shielding is required since molten Mg is highly reactive with oxygen and nitrogen. Similar to Al, Mg alloys possess low melting points, high CTEs and thermal conductivities [161].

1.4.1.6 Cu-based

Wrought and cast Cu and its alloys can be subdivided roughly into pure copper (Cu), brasses (CuZn), bronzes (CuSn), aluminium bronzes (CuAlFe/Ni) and cupro-nickels (CuNi). Their utilization is mainly based on high thermal and electrical conductivities, low coefficient of friction, decorative appearance, immunity to microbiological attack and good corrosion resistance especially in marine environments. These alloys have been subjected to laser cladding for the reasons of low hardness, poor wear [170, 171] and cavitation-erosion resistance [172, 173]. Ni-based alloys have been proved to be good coating candidates for Cu-based materials since Ni forms solid solution with Cu in any proportions. This results in good interfacial bonding without brittle intermetallics [170, 172]. Directly injected [174] and in-situ synthesized carbides as well as Cu-based alloys [50] are also applied. High reflectivity and thermal conductivity impede the cladding process, but preheating and associated oxidation improves the energy coupling. In the case of brass, evaporation of Zn may cause porosity in coating layer. In cold worked grades, HAZ softens due to thermal cycle. Potential targets for laser cladding include Cu-based casting moulds, soldering bits, electrical discharge machining electrodes [171], marine propellers [48] and other propulsion and seawater handling systems [50], nozzles and tuyeres, which inject air, oxygen and fuel in blast furnaces and smelters [175].

1.4.1.7 Others

In addition to the most typical engineering metals discussed above, laser cladding has been studied on selected MMCs, structural ceramics, polymers and elastomers. MMCs studied include SiC reinforced Al- [176] and Mg- [177] as well as carbon fiber reinforced Mg-based

bulk alloys [178]. Laser coatings including AlZn [177] and AlSi [178, 179] have been applied to enhance their wear and corrosion performance. Mg-alloys reinforced with hard particles are particularly vulnerable to galvanic corrosion due to formation of cathode/anode pairs since Mg is the most active metal in galvanic series of metals, for instance, in seawater.

In electronics, circuit boards are manufactured on insulators made of Al_2O_3. Conventional manufacturing methods, however, limit the minimum width of the circuit to 100 μm. To increase the packaging-density, Li et al. [180] utilized high beam quality of fiber laser in micro-cladding of electronic pastes (silver, ruthenium) on Al_2O_3. Due to complex chemical reactions layers were strongly bonded to the alumina.

Elastomers are widely used as sealing surfaces but they suffer from high coefficient of friction in dry sliding conditions. Rombouts et al. [181] produced recently low-friction polymer laser coatings reinforced with solid lubricants.

1.4.2 Coating materials

Wide variety of coating materials based on metal alloys is suitable for laser cladding. Their properties, cladability and applications are discussed shortly in the following sections, which are classified according to the main elemental constituent present.

1.4.2.1 Co-based

The most popular group of coating materials in laser cladding comprise Co-based hardfacing alloys, which are widely used in sliding wear applications particularly at elevated temperatures and often simultaneously exposed to corrosive media. Their excellent high temperature hardness, galling and corrosion resistance are attributed to the allotropic nature of Co as well as alloying elements including C, Cr, Mo, W, Ni and Si on the basis of which they are subdivided to solid solution strengthened, carbide and intermetallic type alloys. Solid solution strengthened with Cr, Mo and/or W, low carbon grade Stellite 21 and Ultimet, are probably the most widely used and versatile alloys in laser cladding. They are relatively soft and ductile enabling the production of crack-free coatings even on massive components without preheating. They have good machinability and they work-harden during machining. Work hardening and related phase transformation (fcc γ-Co to hcp ε-Co) is dependent on alloying elements. Elements including Cr, Mo, W and Si, which diminish the stacking fault energy of Co matrix, favour the phase transformation and work hardening, whereas Fe, Ni and Mn increase the stacking fault energy and thus stabilize the metastable fcc-structure [182]. For that reason, dilution should be kept low when deposited on steels. Compared with carbide type Co alloys, crevice corrosion resistance in chloride bearing solution is far better due to Mo [183]. Their CTEs lie between C-Mn steels and austenitic stainless steels and melting temperaturs are somewhat lower. Applications of Co-based laser coatings include various sealing surfaces of fluid and engine valves and valve seats, pump shafts and gas turbine parts found in the chemical processing, oil, gas and power industries [113, 184-186].

Owing to higher carbon content (1-3 wt.%) carbide-type Co-based alloys are harder, more brittle and wear resistant than solid solution strengthened ones since carbide formers, Cr, W and Co, form various amounts of $M_{23}C_6$, M_7C_3 and M_6C type mixed carbides. Depending on the carbide content, they can be further subdivided to hypo- and hypereutectic alloys with respect to (Co, Cr)–$Cr_{7-x}Co_xC_3$ system [187]. They differ greatly in microstructure. Hypoeutectic alloys consist of γ-Co dendrites and interdendritic $(Cr, Co, W)_7C_3$ eutectic

carbides together with γ-Co. For carbon contents higher than ~2.5 wt.% they are hypereutectic and consist of M_7C_3 carbides in an interdendritic Co-based matrix [184]. Grades harder than Stellite 6 necessitates the use of preheat to avoid cracking.

Intermetallic type hardfacing alloys exhibit high hardness and sliding wear properties at room and elevated temperatures due to the formation of hard and brittle thermally stable CoMoSi Laves phases in ductile Co-based matrix. These alloys are very brittle and prone to cracking. Their CTEs are at level of steels excluding austenitic stainless steels. Hypoeutectic T-900 and newly developed T-401 are more ductile than hypereutectic T-800 and T-400.

1.4.2.2 Ni-based

This important group of laser coating materials can be divided further on the basis of their use. In applications where high strength, excellent corrosion and high temperature oxidation resistance is required NiCr, Monel (NiCu) and various superalloys including Inconel (NiCrMo), Nimonic (NiCr), Incoloy (NiCrFe), Hastelloy (NiMo) [47] and sophisticated single-crystal type alloys (CMSX-4) become applicable. They possess good cladability on Fe-based base materials owing to nickel's ability to form solid solution with Fe, high ductility and melting point, which is lower than in Fe-based base materials excluding cast irons. Precipitation hardened grades need to be aged after cladding since intermetallics such as $Ni_3(Al, Ti)$ (γ´) or inter-granular carbides do not have time to form during rapid thermal cycle. Hot cracking susceptibility increases at the presence of S and/or Nb. Additional preheat is not needed due to high ductility. It can be even detrimental by prolonging the time for segregation. Among numerous potential applications of Ni-based laser coatings, laser cladding of deep gas well equipment [47], large mining components [188], power plant boiler panels and tubes [119], gas turbine blades [154] and flame faces of diesel engine exhaust valves can be named [189].

Ni-based hardfacing alloys, classified according to the major hard phase present, include for instance carbide type Nistelle (NiCrMoW), silicide type Nucalloy (NiCrSiW) and boride type Deloro and Colmonoy self-fluxing alloys (NiCrBSi). Carbide and silicide type alloys, developed to replace more expensive Co-based hardfacing alloys, are more suitable to sliding wear applications, whereas harder grade self-fluxing alloys can also be applied in abrasive wear applications. In general, carbide and silicide type alloys have, however, lower sliding wear properties than Co- and Fe-based hardfacing alloys, whereas boride type alloys have better abrasion resistance than Co-based alloys. Complex microtructure of NiCrBSi coatings consist for instance of γ-Ni, CrB, Cr-rich M_7C_3 type carbides, $M_7(CB)_3$ carbo-borides and nickel silicides Ni_5Si_2. In addition to providing hard particles, Si and B are added to decrease the melting point. Harder grades possess limited ductility requesting the use of additional preheat to avoid cracks.

1.4.2.3 Fe-based

Fe-based coating materials are further classified to stainless steels, tool steels, Fe-based hardfacing alloys and Hadfield steels.

Austenitic stainless steels are used in laser cladding to increase the corrosion resistance of less noble base materials. They are suitable for laser cladding because of high ductility and since rapid solidification inherent to laser cladding favours austenite formation and simultaneously suppress the ferrite content in the final microstructure [190]. This is important because ferrite contents are detrimental to corrosion resistance, ductility and they may transform to brittle σ-phases later at elevated service environments [3]. On the other hand, ferrite solidification

mode and small ferrite contents (3–8 vol.%) diminish tendency for solidification/hot cracking because impurities, S and P, are less soluble in austenite than in ferrite, and segregate more easily in austenite [3]. Solidification and phase contents in final microstructure depend also strongly on composition. This can be roughly estimated by using Schaeffler diagrams constructed for arc welding processes in terms of ferrite promoting Cr and austenite promoting Ni equivalents [3]. Some difficulties may, however, arise in laser cladding of austenitic SS, which affect the coating properties. Weerasinghe et al. [191] showed that 316L is susceptible to liquation cracking during laser cladding. Associated overlapping heat-treated the previous bead where liquation of low melting point boundary films took place resulting in cracks. Ferrite contents were observed to vary between 0–16% depending on the location in clad. They also found interdendritic cracks when high traverse speeds (>1200 mm/min) were used. Sensitization due to carbon pick-up and heat treatments due to overlapping passes did not occur. Anjos et al. [190] laser clad 254 SMO on mild steel. Fully austenitic structure was obtained. According to Ni and Cr equivalents it was expected as compared with 316L. They also found out that some microsegregation took place during solidification. Cr and Mo segregated to interdendritic regions. Li et al. noticed the same in Ref. [192]. Pan et al. [193] remelted AISI 321. They observed that when the solidification rates increased, the solidification mode changed from primary δ-ferrite to primary austenite. Thus, the amount of δ-ferrite increased towards the coating/base material interface. Austenitic SS laser coatings are used in piston rods of hydraulic cylinders and in boiler panels and tubes in power plants [119].

Martensitic stainless steels are relatively inexpensive alternatives to applications where moderate corrosion and wear resistance is enough. Depending on exact chemical composition of the alloy and cooling rates as-laser-clad microstructure consists of Cr-rich carbides, martensite, retained austenite or bainite. Crack-free coatings are usually obtained without preheat [78, 194] due to martensitic transformation and associated volume expansion, which acts against formation of tensile residual stresses during cooling. Tempered areas may form in heat-treated areas due to overlapping resulting in periodic variations in microhardness [194]. In addition to post-clad heat treatment, austenite can be transformed to martensite under heavy wear conditions [195]. Potential applications are for instance large mining components [188].

Ferritic stainless steels are rarely studied in the context of laser cladding. In one of the few studies, Li et al. [196] noticed that as-laser-clad superferritic stainless steel consisted of ferrite without harmful σ–phase, which did not precipitate during cooling. They also noted that Cr and Mo were slightly segregated at the dendrite boundaries.

Owing to their low price, high hardness and excellent wear and impact resistances, tool steels are very important group of coating materials in laser cladding. Excellent wear properties are based on the high volume fraction of fine, in-situ formed, vanadium- or chromium-rich carbides and network of mixed carbides (Fe, W, Mo, Cr) at grain boundaries in martensite or austenite matricises or mixture of these depending on the exact chemical composition and thermal cycles. Retained austenite in final microstructure is usually detrimental to wear resistance but beneficial in impact resistance due to increased ductility and fracture toughness [197]. It can be, however, transformed to martensite by subsequent tempering or cryogenic cooling leading to higher hardness and changes in wear resistance [85, 131, 198, 199]. Transformation of austenite into martensite may also take place under wear conditions as mentioned above [195]. Zhang et al. [197] and Wang et al. [130] ranked laser clad tool steels in accordance with abrasion wear resistance in the following order starting from the best; 15V, 10V, 9V and M4. Similar to martensitic stainless steels volume expansion during cooling

helps to produce crack-free coatings even without preheat or just with modest preheat (~200ºC). In this case too, previously clad beads respond to heat treatment caused by overlapping, which leads to periodic variations in microstructure and hardness [130].

Fe-based hardfacing alloys containing various amounts of C, Cr, W, Si, B, Ni, Mo and Mn have been developed mainly to offer an alternative to more expensive Co- and Ni-based alloys and secondly to replace the use of Co in radioactive nuclear power plant environments. Compared with tool steels, these alloys contain far higher amounts of alloying elements, especially Cr, providing better corrosion resistance. Several commercial alloys are available such as Norem (austenite), Tristelle and recent Nanosteel (ferrite) together with whole lot of experimental ones developed by research institutes studying the laser cladding [200-206]. These alloys have been widely tested in overlay welded and laser clad condition and compared to Co-based and other relevant alloys. For instance, Norem alloys have exhibited sliding wear properties similar to Co-based alloys (St 6 and 21) at low temperatures but at higher temperatures (>180°C) sliding wear properties proved to be inferior [207, 208]. Persson [186] tested laser clad Norem in high-load sliding contact at RT and up to 250°C and observed sliding properties similar to St 21 at RT, but inferior properties at elevated temperatures (>180°C). Excellent sliding wear properties at RT results from the strain induced austenite to martensite transformation. This transformation does not take place at higher temperatures. Alloys made of Fe-Cr-Mn-C and Fe-Cr-W-Mn-C developed by Singh and Mazumder [200] and Choi and Mazumder [201], respectively, outperformed Stellite 6 in sliding wear resistance latter being better. Kagawa and Ohta [202] in turn developed abrasion wear resistant laser coatings comparable to Ni-hard alloy cast iron. Depending on the exact composition and cooling characteristics microstructure of the laser clad Fe-based hardfacing alloys may consist of fine or even nanostructured and homogeneously distributed Cr-rich complex carbides type $M_{23}C_6$, M_6C, M_3C, M_7C_3 and M_3C_2 in ferritic, austenitic or martensitic matrix or mixtures of these. These alloys respond readily to post-clad heat treatment offering coating properties to be widely adjusted. In addition to low cost, austenitic Norem alloys have advantage of comparable CTE to austenitic stainless steels [209]. Potential laser cladding applications include sealing surfaces of valves in nuclear power plant [186, 207] as well as various pump and turbine components due to good cavitation-erosion resistance [207].

Hadfield steels are austenitic manganese steels (12-19%Mn, 1.1-1.4%C, 0-2.5%Cr), which work-harden readily during plastic deformation. They are widely used under impact wear conditions but their resistance against pure abrasion is not so good if work hardening does not occur [210]. Pelletier et al. [211, 212] laser clad such coating (12%Mn, 1.2%C) on low carbon steel. Under cold rolling subjected to austenitic clad layer, hardness increased from 200-350 to 650-800 HV and austenitic structure transformed to ferrite or martensite or mixture of these. Potential applications are various earth and rock engaging equipment used for instance in agriculture, mining, oil well drilling and civil engineering.

1.4.2.4 Cu-based

As already mentioned in section “Al-based base materials”, Cu-based alloys including CuNi [213], CuNiSiBFe [142], CuNiSiFeCoMoCr [142] and CuNiSiVCrFeAlP [143] have been found the most suitable for laser cladding in order to improve wear and high temperature properties of Al-based alloys. This is due to the copper’s higher solid solubility (~6.0 wt.%) in Al than other elements (Ni, Co, Fe) [214] and lower melting point of Cu-based alloys, which helps to keep the interface zone narrow and formation of brittle AlCu type

intermetallics relatively low. Another motivation to use Cu-based alloys as coating materials is their advantage of low friction in various sliding contacts. These low friction bearing alloys laser clad on mild and stainless steels have been produced for instance by Galun et al. [215] and Yakovlev et al. [216] using alloys based on CuAlBi, CuBiSn and CuSn. Yakovlev et al. [216] resolved the low load-carrying capacity of soft CuSn matrix by reinforcing its inner part with nanostructured WC/Co and leaving the top surface as pure soft matrix as required. In other examples of Cu-based coatings on Fe-based base materials, Zeng et al. [217] produced Cu bead on mild steel and Bruck [27] CuNi on carbon steel. The former one was noticed to remain its low electrical resistivity [217]. Despite their low (Cu and Fe) mutual solubility, interface defects like cracking was not reported. Possible embrittling due to intermetallics could be overcome by applying Ni as intermediate layer.

1.4.2.5 Al-based

Al-based coatings are mainly AlSi alloys [153, 218, 219] or Al with small amounts of intermetallic formers including Nb [141], Cr [220] and Cu [140] etc. They are applied mainly on Al-based base materials in order to increase the hardness and wear resistance. Another interesting group of potential coating materials of this class are AlSn-based bearing alloys, which exhibit low friction [215]. Due to formation of brittle intermetallics Al-based coatings cannot be laser clad on steels. Gilkes managed to laser clad Al on steel without melting the steel by using very high power density, which led to plasma formation. They called it laser plasma deposition [23].

1.4.2.6 Ti-based

Repairing and building of various expensive gas turbine components made of different $\alpha + \beta$ Ti alloys are the main applications of Ti-based alloys in the context of laser cladding [159, 160]. In addition, there is need for high quality titanium laser coatings on components made of more conventional structural materials exposed to various aggressive environments found in chemical, petrochemical and marine industries due to their excellent corrosion resistance. However, owing to their high melting point and ability to form brittle intermetallics, production of defect-free coatings directly, for example, on steels is impossible. To overcome this problem, intermediate layer made of Ni could be used because formed intermetallics are not as brittle as with Fe. Another difficulty arises from their affinity to atmospheric elements such as oxygen and nitrogen, which lead to undesired increase in hardness and brittleness. Therefore, efficient shielding with inert gases (Ar, He) is prerequisite to obtain pure high quality Ti-based coatings. The trailing shoes or closed shielding gas chambers are used for this purpose.

1.4.2.7 Metal matrix composites

Metal matrix composites (MMC) constitute probably the most studied group of coating materials in laser cladding. They consist of ductile metal matrix providing fracture toughness, transferring mechanical stresses to reinforcements and holding them together, and hard reinforcements providing high stiffness, hardness and wear resistance [221]. Hard reinforcements are refractory (high melting point) carbides, borides, nitrides or oxides, which preferably do not melt but mix with the molten matrix or base material. Frequently used refractories are WC, TiC, Cr_3C_2, SiC, VC, B_4C, TiB_2, TiN, Al_2O_3, ZrO_2 and Cr_2O_3. They differ in physical, thermal and mechanical properties influencing the choice of cladding strategy, choice of metal matrix, microstructural development and functional properties like wear and corrosion. Their potential applications include rock and trash crushers, excavator

teeth, teeth of rock bits, chutes, dies, extrusion and cutting tools, grinding tools, metal-forming tools and road construction equipment.

There are several different ways to produce MMCs by laser cladding. Perhaps the most used one is to make mechanical powder mixture of hard discontinuous particles and metal matrix and feed it to the cladding nozzle from single hopper. Due to possible differences in densities between hard particles and metal matrix, some gravitational segregation may take place in powder hopper, especially in disc-type powder feeders. This can be prevented by using fluidised-bed powder feeders or by feeding hard particles and metal matrix simultaneously from the separate powder hoppers and let them mix later in the cladding nozzle. It is also possible to inject hard particles straight into the molten base material without metal matrix addition. In addition to above-mentioned external addition methods, hard reinforcements can also be synthesized in-situ through reactions in liquid melt pool and in solid state during subsequent cooling. This in-situ synthesis can be implemented, for example, by feeding pure carbide forming metal or compound powders and graphite powder simultaneously together with the metal matrix. In-situ formed MMCs exhibit some advantages like "cleaner" interfaces (no brittle phases) between carbide and matrix, as compared with carbides produced by external addition methods.

The properties of MMCs produced by laser cladding depend on the type, size, morphology, amount and distribution of the hard particles as well as the feature of the interface between the binding metal and the hard particle (= bonding between particle and matrix) and their dissolution. In addition to different types of hard particles, several kinds of metal matrix alloys can be chosen in order to achieve various property requirements such as wear, impact, corrosion, erosion, friction, heat resistance, heat conduction, ductility etc. Most of the hard particles used in laser cladding are carbides and borides. Single carbide powder particle can be binderless or with binder. In the former case, single powder particle consists of single carbide, which can be spherical (cooled by spraying) or angular (crushed). They can be without coating or dense-coated typically with Ni or Co. These binderless powders are manufactured by carburizing elemental metal powder or by fusing metal and carbon. Fused powder particles are very dense. In latter case (with binder) single powder particle consists of several small carbides and the binder. These powders are typically used in thermal spraying. They are manufactured first by carburising metal powder in order to produce carbide (or through chemical reactions) and subsequently by sintering and crushing or agglomerating (spray drying) and sintering in order to combine carbides and binder. Sintered powders are angular and quite dense; whereas agglomerated powders are spherical and relatively porous. These powders can also be dense-coated. Coating is applied to carbide particles in order to improve wetting and to avoid oxidation and decarburization during thermal spaying. It may also protect the carbide in laser cladding, since carbides show very high absorptivity to laser beam compared to metals. Another carbide powder manufacturing method, which should be mentioned, is a self-propagating high-temperature synthesis (SHS) [222]. In this case, single powder particle consists of very small carbides and the binder. Carbides have a size ranging from less than 1 μm up to few micrometers. These powders are dense and they are angular in shape.

Some essential crystallographic, thermophysical and mechanical properties of most frequently used hard particles in MMCs produced by laser cladding are tabulated in Table 2.

Table 2. Some essential properties of hard reinforcements at RT. The values given are an average found from the literature [222].

	WC	**W_2C**	**VC**	**Cr_3C_2**	**TiC**	**SiC**	**TiB_2**
Density (g/cm^3)	15.8	17.2	5.7	6.7	4.9	3.2	4.5
T_m (℃)	2870	2730	2830	1810	3067	2545	2980
Mean CTE x 10^{-6} (1/K)	4.2		6.2	7.9	6.4	3.3	6.8
Thermal conductivity (W/m·K)	63		39	19	21	41-145	24
E (GPa)	670		430	372	460	475	522
Specific heat (J/kg·K)	179		531	546	557	669	625
Electrical resistivity ($\mu\Omega$•cm)	22		60	75	68	> 1500	12
Hardness (GPa)	22		27	14	32	26	30
Crystal structure	hexagonal	hcp	fcc	orthorhombic	fcc	fcc hcp	hcp

Change of Gibbs free energy of formation governs the thermal stability of the hard particle. The higher the negative value of energy, the more stable the particle. Change of Gibbs free energy of formation for some common particles is shown as a function of temperature in Figure 9. It is notable that W_2C is more stable at high temperatures than WC, and Ti-based particles are the most stable ones. SiC is the least stable at high temperatures. It usually dissociates and dissolves easily at high temperatures into the melt pool. Therefore, SiC is mainly used together with low melting point Al matrix, which enables low melt pool temperatures. Their density levels correspond, too. Despite mentioned thermal stabilities of WC and W_2C, laser cladding experiments showed that W_2C dissolves easier, for example, to nickel matrix than WC does [223, 224]. In consequence of this, MMCs produced from WC powders showed better abrasion wear resistance than MMCs from WC/W_2C powders [224]. Consequently, chemical stability and kinetics of dissolution of the hard particle with respect to metal matrix should be taken into account when the risk of dissolution (and cracking tendency + wear properties) is considered. For example, Gassmann [225] studied the influence of matrix material on the dissolution kinetics of fused WC/W_2C powder (45-125 μm). He found out that NiBSi-matrix dissolved carbide less than Stellite 21 matrix. Nowotny et al. [226] reported on similar result, i.e. WC dissolved more heavily in Stellite 21 than in NiBSi. Lou et al. [227] showed that the chemical composition of the matrix had strong influence on the

interface between WC and matrix and stability of WC. They HIPped WC-12Co (agglomerated & sintered) in Stellite 21, PM10V tool steel and M3/2 high-speed steel. They stated that dissolution of WC took place already at the solid state. The angular details of WC particles in Stellite 21 and HSS matrices were rounded by dissolution into the matrix and the formation of thick interface layer, while WC particles in the PM10V matrix retained their initial surface morphology and shape. Solubilities of some common carbides in Ni, Co and Fe are shown in Table 3.

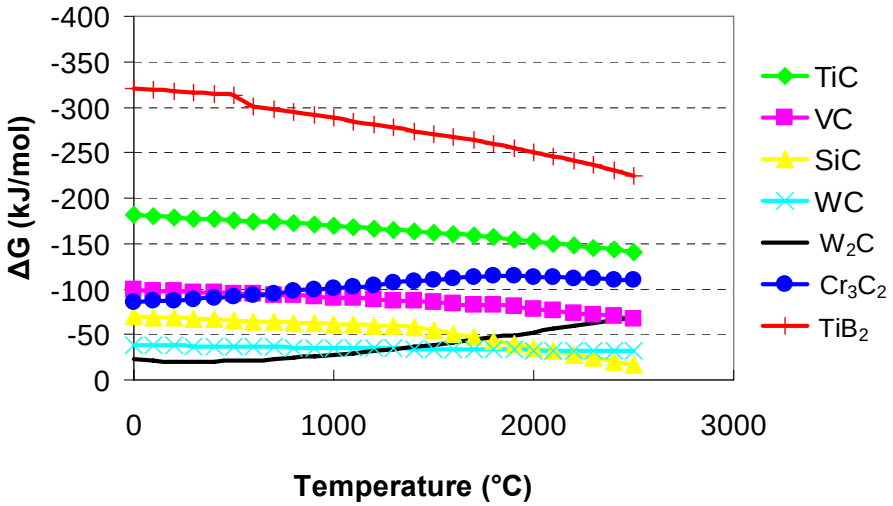

Figure 9. Change of Gibbs free energy of formation (M+C → MC) of some common hard reinforcements used in MMCs by laser cladding. The more negative the energy value, the higher the stability of the carbide/boride. Energy values were computed using Outokumpu HSC Chemistry 4.0 software [228].

Table 3. Solubilities of some common carbides in Ni, Co and Fe at 1250 °C [229].

Solubilities of the Carbides in the Iron-Group Metals at 1523 K

	Solubility [wt % (mol %)]		
Carbide	Cobalt	Nickel	Iron
WC	22 (7.9)	12 (3.9)	7 (2.2)
TiC	1 (1.0)	5 (4.9)	<0.5 (<0.5)
VC	6 (5.6)	7 (6.6)	3 (2.7)
NbC	5 (2.9)	3 (1.7)	1 (0.53)
TaC	3 (.93)	5 (1.6)	0.5 (0.15)

According to theoretical kinetic calculations and visual observations conducted by Babu et al. [95], WC particles dissolved more rapidly in Fe than in Ni liquid.

Temperature during manufacturing of MMC is an important parameter influencing the kinetics of dissolution [221]. Melt pool temperature in the laser cladding depends on cladding parameters, which in turn depend on the melting temperature of the matrix and base material. The higher the melt pool temperature, the higher the risk for particle dissolution into the matrix [116]. The lower the melting temperature of hard particle, the higher the risk of dissolution into the matrix. Therefore, Ni-, Co- and Fe-based self-fluxing alloys (low melting temperature) are often used as matrix materials. Chromium carbide has the lowest melting temperature of the used reinforcements. It usually melts and dissolves partly or fully into the melt pool, and precipitates in various forms (usually as needles) of CrC (Cr_7C_3 etc.) during cooling. Dissolution and formation of carbides embrittles the matrix, which increases cracking tendency. Dissolution and precipitation of carbides in the matrix is not necessarily detrimental to wear resistance.

Refractory carbides used in MMCs can be divided into two mayor types: the interstitial carbides and the covalent carbides. Interstitial carbides include TiC, VC, Cr_3C_2 and WC. In this case, the carbon atom has a much smaller size than the host metal atom, allowing it to nest in the interstices of the lattice, which is generally arranged in a close-packed structure. Bonding in interstitial carbides is partly covalent and ionic, but mostly metallic, which explains why the interstitial carbides closely resemble metals. SiC and B_4C are covalent carbides. The carbon atom is only slightly smaller than the Si atom and the bonding is essentially covalent [222].

Tungsten carbide exists as WC, W_2C and WC_{1-x}. Tungsten mono-carbide has a very narrow range of homogeneity ($WC_{0.98}$-$WC_{1.00}$). If dissolution takes place, it forms mixed carbides during cooling, which embrittle the matrix. For example, such extremely brittle phases as Co_6W_6C, Co_3W_3C, Fe_3W_3C and Ni_2W_4C form, depending on the used metal matrix, whereas, for example, TiC exists as a single homogenous carbide phase with a wide range of stoichiometry ($TiC_{0.47}$ to $TiC_{0.99}$). Dissolved TiC recrystallizes to dendritic TiC and does not lead to matrix embrittlement in the same way as WC does [230]. Those WC particulates, which are partially dissolved, form epitaxially grown dendrites around them [231]. This combines hard particles strongly with the matrix. It is claimed that good combination between WC particles and matrix can help to resist the “pull-out” force on the WC particles for example under the abrasive wear [232]. In addition to brittle complex carbide phases mentioned above W_2C phases have been found to form around dissolved WC. Li et al. [233] identified them to be bar-like α-W_2C and blocky β-W_2C. Like complex carbide phases W_2C is very brittle and its corrosion and wear resistance are also inferior to that of WC. Furthermore, W_2C is chemically less stable than WC [222], which explains the differences in dissolution behaviour as reported earlier.

Vanadium carbide exists as VC and V_2C. Its stoechiometry range is $VC_{0.73}$ to $VC_{0.99}$. It is most often used with Fe-based matrix. For example, Herrera et al. [234] injected VC (10 μm) particles into AISI 1045. Microstructure consisted of α-Fe matrix with dispersed cubic VC_x carbides, mainly V_8C_7 and V_4C_3, which were probably produced by the partial dissolution of VC in the melt during cladding and its subsequent precipitation. They also noted that substantial mass transfer occurred across the carbide/matrix interface: the content of vanadium dissolved in the α-Fe matrix was found to be between 11 to 23 wt.%, whereas the amount of substitutional iron in V_8C_7 carbides reached 50 wt.%. No complex carbides or Fe-V intermetallic compounds were detected. Ebner et al. [235] injected VC into AISI M2 tool steel. The process parameters were chosen in way that nearly all the injected particles were

dissolved in the melt. The microstructure consisted of tool steel matrix and V-rich MC_{1-x} mono-carbides, which precipitated directly from the melt. Microanalyses revealed that mono-carbides dissolved appreciable amounts of other alloying elements. Especially tungsten entered the mono-carbides, which caused tungsten depletion in the matrix. They also noted that NbCs dissolved significantly smaller amounts of other alloying elements than V-rich mono-carbides. Vanadium carbides were also used together with AISI H13 [236] and AISI M4 tool steels [237]. The latter one showed very high resistance against abrasive wear.

Cr_3C_2 is an intermediate carbide having carbon chains with C-C distance approximately 0.165 nm running through distorted metal lattice where Cr atoms are at the corners of trigonal prisms and carbon atoms in the center of the prisms. It can also exist as $Cr_{23}C_6$ and Cr_7C_3. Tassin et al. [238] laser alloyed 316L with Cr_3C_2 (5 μm). It was noted that carbides melted and precipitated during cooling as M_7C_3 (M=Fe or Cr) carbides. Cr_3C_2 dissolved completely as it does in majority of the reports found, especially when the original carbide size is small. In sliding wear tests TiC–316L was better than Cr_3C_2–316L. Kim and Kim [239] pre-placed Cr_3C_2 (3-5 μm) on AISI 420 martensitic stainless steel. XRD revealed the presence of retained Cr_3C_2 and precipitated Cr_7C_3 in laser clad layer. Precipitated carbide size is usually small due to rapid cooling inherent to laser cladding, i.e secondary carbides do not have time to grow. Thus, the process is advantageous for the dispersion of fine carbides [239]. Kumar and Goswami noticed that laser clad Ni20Cr-Cr_3C_2 (60/40) had better abrasion wear resistance than Ni20Cr-WC (60/40) [240].

Volume fraction. In general, the abrasion wear resistance of MMC is directly related to the volume fraction of hard particulates. Consequently, larger volume fractions result in higher wear resistance. Exceptions, however, exist in Fe-based matrices where the amount of hard particulates may influence the amount of retained austenite in the matrix [241]. In consequence of dissolution of carbides, carbon content of the matrix increases decreasing the martensite start temperature (M_s). Relation between the volume fraction of hard particulates and abrasion wear resistance can be explained by wear mechanism, which is usually microcutting of the softer binder matrix. Higher volume fraction of hard particulates decrease the mean free path between the hard particulates and the area of soft matrix exposed to abrasives becomes smaller. Increasing volume fraction of hard particulates, however, leads to coating defects like brittle cracks, pores and possibly uneven distribution of hard particulates. A cracking tendency, especially, increases together with the volume fraction of hard particulates. Maximum volume fractions achieved in laser cladding were reported to be up to 80% (TiC/Ni-AISI 410S) without major coating defects [230]. FGM structures bear even higher volume fractions as described by Liu and DuPont [242]. They produced crack-free TiC-Ti MMC FGMs onto Ti6Al4V. The amount of TiC on the top layer was up to 95 vol.%. In earlier study, Nowotny et al. [226] found that 45-50 vol.% WC/W_2C in NiBSi matrix could be produced crack-free. In the case of Stellite 21 the maximum useful content of WC/W_2C was lower; 35-40 vol.%. Coating, which contained 40 vol.% WC exhibited equivalent resistance to the abrasive wear as traditional cemented tungsten carbides [230]. In another study, abrasive wear tests showed that wear rates of laser clad WC/Co(45-90μm)-NiBSi (60/40 wt.%) MMC were comparable with that of sintered WC/Co (90/10) hard metal [243]. In addition to volume fraction, it is essential that hard particulate is very well bonded to the matrix as already explained earlier. Therefore, it would be desirable that some dissolution of particulate would occur in order to prevent “pull-out” of the particulate from the matrix. According to several publications larger volume fractions of hard particulates are beneficial in sliding wear resistance, too. Volume fraction of hard particulates may also have

influence on absorbed laser energy. In SiC injection an increase in the amount of particles resulted in higher total absorbed laser energy, which means that laser power should be adjusted accordingly [158].

Carbide size. Carbide sizes found in MMC coatings produced by laser cladding differ from 20 nm up to 1 mm [244-247]. Due to overheat during the flight and later in melt pool, coarse carbides dissolve less than fine ones because they offer smaller surface area to volume ratio [158]. According to literature, in sliding wear conditions fine carbides are preferred to the coarse ones. Generally, coarse carbides are better than fine ones in abrasive wear conditions. Large carbide size means that binder phase must be removed to a greater depth before particulate can be removed and, therefore, larger particles are more resistant to "pull-out". Carbide size with respect to size of abrasives plays also an important role. It would be preferable that the size and hardness of the reinforcement particles are higher than those of the common abrasives [205]. Axén and Zum Gahr [198] studied the effect of carbide size (3 vs. 30 μm) on the abrasion wear resistance of TiC – AISI O2 MMC produced by laser. Coarser TiC behaved better in most cases despite larger mean free path between individual particles with identical volume fractions of TiC. Van Acker et al. [248] studied the influence of carbide particle size on sliding, mild abrasive and severe abrasive wear resistance. They used spherical fused WC/W_2C of three different size distributions in ductile NiB matrix: 1) 14-70 μm, 2) 48–109 μm and 3) 116–207 μm. They found out that small carbides were beneficial in sliding wear test, whereas size did not matter in mild and severe abrasive wear tests. In addition to small carbide size, increase in carbide volume fraction was favourable for the sliding wear resistance. They stated that cohesion (bonding) of the matrix to the carbides was worse for larger carbides than for finer ones. The fact that this decohesion was found only in the coatings reinforced with coarse carbides could be an explanation for the higher sliding wear compared to the coatings reinforced with finer carbides. In a study by Laroudie et al. [249] it was noted that small TiC particles tend to cluster leaving quite large bare matrix areas vulnerable to abrasives.

Morphology. Morphology of the powder particle depends on manufacturing route of the powder as explained earlier. In general, fused powders with high cohesion dissolve less than porous ones leading to better coating performance. For instance, according to study by Cerri et al. [250], MMC produced from dense-coated single crystal WC (powder 45-90 μm, carbides 45-90 μm) and NiBSi showed better abrasion wear resistance than sintered and dense-coated WC (powder 45-90 μm, carbides 30-50 μm). Agglomerated WC (powder 45-90 μm, carbides <10 μm) showed the worst abrasion wear resistance. The abrasion resistance of MMCs with 42 and 63 vol.% proved to be better than that of other widely used abrasion resistant Ni-hard material. Another study states that crushed angular WC particles outperformed spherical fused WC/W_2C particles in abrasion wear resistance, because spherical carbides dissolved comparatively more into the matrix [224]. WC dissolved less in Ni-matrix than W_2C as already mentioned earlier. In Ref. [248] it was claimed that spherical carbide shape minimizes crack initiation at sharp edges of the cemented carbides, thus decreasing the cracking tendency compared to angular ones. Gassmann [225] studied the influence of carbide morphology on dissolution kinetics in Stellite 21 and NiBSi matricises. Carbide powders were: 1) WC-17Co, Co-coated, agglomerated, powder 20-50 μm, carbide < 6 μm; WC melt carbide, $100\%WC/W_2C$, powder 45-125 μm and 3) WC/Ni melt carbide, Ni-coated, $92\%WC/W_2C$-8%Ni, powder 25-125 μm. He concluded that powder no. 1 dissolved most in Stellite 21, whereas powder no. 2 dissolved least in the same matrix. This was explained by the difference in particle size and integrity. He explained further that Ni-coating

on WC/W_2C (powder no. 3) accelerated dissolution, because Ni had diffused partly into the carbide already during the powder manufacturing. Hence, according to this study, dense-coating can actually be detrimental to carbide dissolution in melt pool. Nowotny et al. [226] compared the carbide morphology and its influence on abrasion wear resistance. They used the following powders in NiBSi and Stellite 21 matrices: 1) WC-12Co, agglomerated, 45–90 μm and 2) WC/W_2C, fused, non-clad, angular, 45–90 μm. They did not notice any difference in abrasion wear between powders 1 and 2 in NiBSi matrix.

Metal matrix. There are innumerable amount of metal alloys, which can be used in MMCs produced by laser cladding. In order to diminish the cracking tendency, most frequently encountered defect in laser coatings, metal matrix should be soft and ductile. Furthermore, melting temperature should preferably be low in order to avoid high melt pool temperatures and decrease the carbide dissolution. For the above-mentioned reasons Fe-, Ni- and Co-based self-fluxing alloys including only low amounts of carbide, silicide and boride forming elements should be used. In applications where corrosion resistance is not an issue low cost Fe-based alloy systems are excellent alternatives. In addition to low cost, Fe-based matrix is beneficial in preventing cracks due to similar CTE to Fe-based base materials and possible expansion of the matrix during cooling due to martensitic transformation. Expansion due to martensitic transformation decreases or prevents the formation of tensile stresses during cooling. For example, Gassmann et al. [230] produced crack-free MMCs (TiC – AISI 410 SS on austenitic stainless steel) up to 45 vol.% TiC. Using the transformation induced expanding during cooling Hidouci et al. [251] managed to decrease cracking tendency by adding 20 and 30 vol.% unstabilised ZrO_2 (1 μm) on $MoSi_2$ cladding layer. In melt pool zirconia remains solid. During cooling, it does not remain tetragonal but transforms to a stable monoclinic form. This transformation of particles, provided they are greater than a critical size, causes an increase in volume (5%), which acts against tensile stresses produced during cooling. Axén and Zum Gahr [198] studied the effect of matrix hardness on the abrasion wear resistance of TiC – AISI O2 MMC against SiC. They concluded that the higher the matrix hardness, the higher the wear resistance.

Abrasive. Axén and Zum Gahr [198] studied the effect of abrasive (SiC) size (200, 135, 75, 20 μm) on the abrasion wear resistance of TiC – AISI O2 MMC. It was noted that the larger the abrasive, the higher the wear rate. Clad layers were TiC(45-50 vol.%, 30 μm)-AISI O2 and TiC(50-55 vol.%, 3 μm). Abrasive wear depends also on the hardness of the abrasively acting solids relative to that of the wearing material. According to this, abrasive wear occurs at low level for abrasives softer than and high level for abrasives harder than the wearing material [198].

Besides material parameters as discussed above, process parameters importantly affect the quality of final clad layer. One can control the extent of the dissolution of the particulates by choosing appropriate nozzle setup and parameters related to the velocity of the particles and the interaction time in laser beam/melt pool.

Positioning of powder flow. Injection location in relation to laser beam affects particulate dissolution. It can be significantly diminished by injecting particulates from, for example, trailing off-axis nozzle into the back part of the laser beam, because particles spend less time in the melt and some particles do not cross the laser beam at all [158, 252]. Kloosterman [158] demonstrated this by injecting SiC particles into Ti6Al4V. By changing the position of the particle flow from behind to beyond the centre of the laser beam, there was a transition from

modest to considerable dissolution of SiC particles. It should be however mentioned that Ti6Al4V has very low thermal conductivity (7.1 W/m·K at RT), which enables to elongate the melt pool along beam scanning direction [253]. For instance, the size of the elongated laser melt pool (which is the best place for injection) in Al-Si alloy (Al-12Si: 141-155 W/m·K at 25°C) is extremely small proven by the finite element analysis [254]. For the sake of comparison, typical metal matrix materials used in laser cladding have the following thermal conductivity values (W/m·K) at RT: Stellite 21 (12.7), 316L (13.2), H13 (17.2), Inconel 625 (13.9) and NiCrBSi (Deloro 60) (15.0).

Particle velocity. Interaction time of particles with laser beam is determined by the particle velocity and travelling distance. Interaction time should preferably be as low as possible (particle velocity as high as possible) without excessively disturbing the melt pool, because carbides, in particular, absorb short-wavelength laser beam efficiently. Even if the interaction times are usually in the order of milliseconds, there can be considerable increase in temperature due to high absorption of carbide particles (for SiC~90%) at a wavelength of 1.06 μm (Nd:YAG). According to Kloosterman [158] particle velocities are usually in the range of 1–2 m/s. He found out that particle velocity of ~1.2 m/s resulted in a temperature increase of ~2000°C in the case of SiC particle with a diameter of 80 μm, injected from the off-axis nozzle into the centre of the laser beam. Particle velocity can be adjusted by changing the carrier/shielding gas flow rate or pressure. Vreeling et al. [255] measured the SiC (80 μm) particle velocities from the off-axis nozzle. The mean velocity of the particles showed a linear increase with carrier gas flow rate. A nozzle diameter of 1.7 mm increased the velocity by a factor of about 1.5 with respect to nozzle diameter of 2.3 mm. Overall, particle velocities varied in the range of 2.5–5.0 m/s. Anandkumar et al. [150] studied the influence of particle (SiC) velocity on carbide dissolution in AlSi matrix. When the injection velocity was low, excessive dissolution of SiC in the melt pool occurred. On the contrary, for high injection velocity, dissolution of SiC was very limited and the microstructure of the coatings consisted essentially of undissolved SiC particles in the matrix. The velocity of the injected particles was varied in the range of 0.5-5.0 m/s by opening and/or closing the gas outlet of the cyclone. Lin [34] made temperature analysis of the powder (AISI 304) streams in coaxial CO_2 laser cladding. He found out that the higher the particle velocity, the lower the particle temperature. Stream velocity of 2 m/s produced maximum temperature of 1600°C at a distance of 20 mm from the nozzle exit, whereas the velocity of 6 m/s produced maximum temperature of 1000°C. The influence of particle size on particle heating was also calculated: 45 μm and 105 μm particles heated up to 1200°C and 900°C, respectively.

Traverse speed. In general, traverse speed in laser cladding defines the lifetime of the melt pool if laser beam spot size and power are kept constant. Melt pool lifetime, in turn, defines the interaction time of hard particulates in the melt pool before solidification. Thus, traverse speed has definite influence on carbide dissolution behaviour. Pelletier et al. [109] reported that if the reinforcement is only in contact for a brief time with the molten metal, chemical reactions between matrix and carbides are reduced. Abboud and West [256] noticed earlier that increasing the traverse speed leads to lower degree of carbide dissolution. It should be, however, to bear in mind that increasing traverse speed leads to lower coating thickness. If coating thickness needs to be more or less constant, laser power and powder feed rate should be increased accordingly to keep the specific energy constant (J/mm^2). If the traverse speed is increased and specific energy is kept constant, the melt pool length increases and the interaction time may not decrease. This was confirmed by Pei et al. [253] who conducted comprehensive finite element analyses (FEA) on the melt pool length

on Ti6Al4V. They noticed that melt pool length extends along scanning direction when traverse speed increases and specific energy is kept constant (J/mm^2). This holds true for the materials, which have relatively low thermal conductivities. Same FEA analysis on Al-8Si showed that the influence of increasing traverse speed on melt pool elongation was extremely small. It should be realized that the extension of laser melt pool is determined by thermo-physical properties like thermal conductivity (6.7 for Ti6Al4V and 121 W/m·K for AlSi alloy) [254].

1.4.2.8 Functionally graded materials

By using two or more powder hoppers and/or wire feeders simultaneously, it is possible to produce laser clad MMC or monolithic beads with graded composition along bead length or depth. In the latter case more than one consecutive layer is usually needed, whereas the former one can be obtained readily within single bead. Production of these functionally graded materials (FGM) is realised by varying the powder or wire feed rate of each feeding unit in synchronisation with translation movement. Examples of varying volume fraction of hard particulates along coating depth are given in Refs. [62, 242, 257], where TiC and WC/Cr_3C_2 contents in Ti-based and NiBSi matrices, respectively, increased gradually from the bottom layer to top layer up to 95 and 70-80 vol.%. Contrast to multi-layer coatings with increasing hard particulate content, Pei et al. [253] and De Hosson and Ocelik [254] manage to produce graded MMC along coating depth by single layer. This was obtained by feeding WC or SiC particulates into the Ti6Al4V melt pool via trailing off-axis nozzle just behind the laser beam. This permitted the particles to penetrate in the melt to certain depths and remain there during solidification resulting in increased carbide content from the bottom to the top surface of the melt pool. Due to low thermal diffusivity of Ti6Al4V, it was easier to elongate the melt pool by increasing the traverse speed compared with for example Al-based base material. Using also one layer technique, Syed et al. [258] produced gradient metal alloy coating via simultaneous feed of wire (Ni) and powder (Cu). With formed compositional gradient (Cu content increased towards the surface) it was possible to clad CuNi on H13 tool steel. Examples of graded structures along bead length are given, for instance, in Refs. [205, 259]. Shortly, laser cladding is feasible method to manufacture graded structures to tailor specific materials for their functional performance in particular applications, to clad pairs with low mutual solubility and decrease differences in thermophysical and mechanical properties between clad and base materials.

1.4.2.9 Solid lubricants

Besides hard particulates like carbides, oxides and nitrides, various hexagonal (with high c/a ratio) or soft, low shear strength solid lubricants can be embedded in load-carrying metal matrix by laser cladding in order to decrease the high coefficient of friction and wear, for example in the cases of austenitic SS, Al and Ti alloys. Despite being atmospheric dependant, they are roughly classified according to the operating temperature at which they exhibit the lowest friction. Low temperature (<500ºC) solid lubricants include for instance molybdenum and tungsten disulfides (MoS_2, WS_2), silver (Ag) and graphite, whereas hexagonal boron nitride (BN) and calcium difluoride (CaF_2) constitute the high temperature (>500ºC) solid lubricants. Their embedding as original chemical compound is more difficult than the embedding of hard particulates because most of them oxidize readily and decompose below the melting temperatures of potential matrix metals. For instance, MoS_2 (T_m = 1185ºC, ρ = 5.1 g/cm^3) particles (<10 μm) clad with Ni dissociated in pre-placed laser cladding leading to various sulfides with matrix materials, which, nevertheless, possessed low friction [260]. Wolfe et al. [252], however, managed to embed fine <1 μm WS_2 (T_m = 1250ºC, ρ = 7.5 g/cm^3) particles together with Cr_3C_2 into Inconel 625 matrix by injecting them to the trailing

edge of the melt pool, thus avoiding the direct interaction with the laser beam. Instead of direct injection of solid lubricant particles, Yakovlev et al. [261] produced MoS_2 layers by laser cladding first Mo layer, which was later submitted to heated chamber fulfilled with sulphur vapour. Courant et al. [262] succeeded in leaving graphite (T_m = 3675ºC, ρ = 2.2 g/cm^3) inclusions in Ti matrix by pre-placed pulsed laser cladding technique. Significant amounts of TiC formed as well. Ag (T_m = 960ºC, ρ = 10.5 g/cm^3) was tried as solid lubricant together with CaF_2/BaF_2 in multi-material alloy consisting of 20(Ni20Cr)-50(Cr_3C_2)-15(Ag)-15(CaF_2/BaF_2) in vol.% [263, 264]. Owing to its immiscibility to NiCr matrix, Ag segregated to the surface of the coating during solidification. CaF_2 (T_m = 1418ºC, ρ = 3.2 g/cm^3) seemed to be stable since it remained in final microstructure. Similar observations were made by Wang et al. [265], who embedded CaF_2 in Al_2O_3 matrix on Al_2O_3 base material. In addition to enhance sliding contacts, CaF_2 is efficient flux and purifier extensively used to increase fluidity of melt and eliminate gas and impurities [266]. Shehata et al. [267] and Molian and Hualun [268] applied hexagonal BN (T_m = 3000ºC, ρ = 2.3 g/cm^3) to tool steel and Ti, respectively. In both cases, majority of BN decomposed and formed new hard phases with matrix elements leading to better wear resistance.

1.4.2.10 Rare-earth element additions

Similar to hard refractory reinforcements and solid lubricants, rare-earth elements, frequently as oxides (CeO_2, La_2O_3, Y_2O_3), can be externally added to the metallic or MMC laser coatings during cladding. Due to their high chemical activity (large atomic radius, low electronegativity (Ce, La)) with impurity atoms like O, S (hot cracks), H (cold cracks) and N they are predominantly used as purifying agents. This purification (deoxidation, desulfuration) occurs during cladding as part of the formed high melting point reaction products float to the surface of melt pool and clean off the clad layer as molten slag, leading to final coating with less inclusions and possibly the reduced tendency to crack formation. In addition, it has been observed that these additions have effects on scale of the microstructure and functional properties of coatings. For instance, Wang et al. [269-271] noticed that additions (< 10 wt.%) of CeO_2 and La_2O_3 in NiCrBSi refine the microstructure, decrease the coefficient of friction as well as improve the microhardness, sliding wear and corrosion resistances. Zhao et al. [272] reported similar positive effects on corrosive wear of Ni + WC MMC. Enhancement in wear properties is attributed mainly to the hard reaction products including complex carbides, silicides, borides and oxides, which remain in the final coating [273]. Apart from adding CeO_2 and La_2O_3 to Ni-based alloys, Li et al. [274] mixed nano-Y_2O_3 with Co-based alloy. They obtained oxide dispersion strengthened (ODS) alloy, which showed great potential at elevated temperatures. Yttria addition influenced also on solidification since texture was greatly diminished.

As distinct from rare-earth additions, reactive transition metal Hf was added to Ni-based superalloys. Rapid solidification inherent to laser cladding extended its solid solubility, which led to the considerable improvements in oxidation-resistance properties at elevated temperatures due to its positive effect on adherence and stability of the protective oxide layer (Al_2O_3) on metal surface [275].

1.4.2.11 Intermetallics

Similar to externally added or in-situ synthesized hard particulates various intermetallics are used to reinforce wide variety of metal matrices. Ternary CoMoSi Laves type phases and binary nickel silicides were shortly mentioned in the context of Tribaloy and Nucalloy hardfacing alloys. Other intermetallics widely studied in laser cladding include chromium

(Cr_3Si, $Cr_{13}Ni_5Si_2$) [276, 277], tungsten (W_5Si_3, W_2Ni_3Si) [278], molybdenum ($MoSi_2$, Mo_2Ni_3Si) [279, 280] and titanium silicides (Ti_5Si_3, Ti_2Ni_3Si) [281]. Due to inherent large negative free energies of formation (Cr_3Si in Ni-Cr-Si system, $MoSi_2$ in Mo-Si system, Ti_5Si_3 in Ni-Ti-Si system), they form in-situ from pure precursor elements by precipitation during solidification and cooling. Final microstructure usually consists of intermetallic primary dendrites (e.g. Cr_3Si) in ternary metal matrix (e.g. Ni-Cr-Si). In general, intermetallic silicides are characterized by high melting temperature (1770ºC; Cr_3Si, 2030ºC; $MoSi_2$, 2120ºC; Ti_5Si_3), high oxidation resistance and they retain high hardness and strength at elevated temperatures due to strong covalent-dominated covalent-metallic atomic bonds. This latter feature provides excellent capability to resist plastic deformation leading to excellent sliding wear resistance also at elevated temperatures. On the other hand, the ductility close to zero limits their use as coatings and necessitates the use of high preheat in order to obtain crack-free coating layers. Ignat et al. [279] and Hidouci et al. [282] circumvent the need for this high preheat by utilizing allotropic transformation of ZrO_2 (from tetragonal to monoclinic) and associated 4-5% volume expansion during cooling to decrease the cracking tendency by adding un-stabilized ZrO_2 (1-10 um, 10-20 vol.%) particles into the alloy. Another important group of intermetallics manufactured by laser cladding comprises low density Ni- [283, 284], Fe- [285] and Ti-aluminides [286, 287]. Potential high temperature applications include gas turbines, heat exchangers, turbocharger rotors, valves and furnace elements [279]. Apart from intermetallics for high-temperature applications, versatile intermetallic compound, NiTi, and its laser cladding is frequently studied in the context of liquid handling systems and medical applications due to its excellent resistance against cavitation-erosion [288] and biocompatibility [289].

1.4.2.12 Others

High solidification rates inherent to short interaction time laser glazing process have enabled the production of thin amorphous layers with unique properties (corrosion) on surfaces of various metals [290] and ceramics. There is also interest and possibility to produce thick amorphous metal coatings by 1-step laser cladding [291, 292]. Traverse speeds in the range of 2400–3000 mm/min were high enough to produce single amorphous beads made of $Ni_{66}Cr_5Mo_4Zr_6P_{15}B_4$ and $Fe_{57}Co_8Ni_8Zr_{10}Si_4B_{13}$ (in at.%) alloys, which contain such glass-forming elements as P, B and Si. Overlapping, however, heat-treated the previous beads resulting in crystallized zones in continuous coating layer.

Oxide ceramics are widely used coating materials especially at high temperatures. Their laser cladding on metallic base materials is, however, almost impossible due to lack of solid solubility, extreme brittleness, large differences in melting temperatures and poor wetting characteristics. In one of the rare publications, Nowotny et al. [293] succeeded in 1-step cladding of Al_2O_3/TiO_2 layers on aluminium. Due to chemical nature of bonding between Al_2O_3 and Al and mechanical bonding, bond strengths achieved were at the level of 40–60 MPa. Another approach was presented by Zhou et al. [294], who produced Al_2O_3 layers on aluminium base material through exothermic reaction of $2Al+1.5SiO_2 = Al_2O_3+1.5Si$. A few studies have shown that bioceramic calcium phosphate (CaP) coatings can be laser clad on human implant materials, Ti6Al4V [295-297] and 316L [298], in order to promote bone growth over the surface of the implant.

1.5 Laser coating characteristics

As briefly mentioned in section 1.3.1 functional properties and the quality of laser coatings are strongly dependent on chemical composition and microstructure. In this section, laser coating characteristics are discussed under the subsections of microstructure formation, coating defects, corrosion and wear properties, residual stresses and mechanical properties.

1.5.1 Microstructure formation

Besides chemical composition, it is often microstructure characterized by phase and growth morphology, which controls the functional properties and the quality of the final coating obtained. The microstructure formed is largely dependent on solidification process and chemical composition of the coating alloy. In laser cladding, microstructure formation frequently falls in the category of rapid solidification since growth rates of the solid-liquid interface (V_s) are often >600 mm/min [299]. Typically, three kinds of microstructures are detected in laser coatings; planar, cellular and dendritic. The latter two are usually columnar in shape. They grow perpendicular to temperature isotherms, i.e. along the steepest temperature gradient. In cubic metals, crystallographic effects influence the grain growth by favoring the growth along preferred crystallographic directions. These preferred directions are <100> directions, which is usually seen in XRD pattern taken from the surface of fcc-ordered alloy parallel to coating/base material interface as the strongest peak arises from the plane (002) instead of plane (111), which would give the strongest peak if randomly oriented. In practice, this means that growth direction remains essentially perpendicular to coating/base material interface (direction [001]) except for the very top surface where the growth is parallel to coating/base material interface (direction [100]) due to a minimum velocity criterion given by equation 2 (Figure 10) [300]:

$$V_{hkl} = \frac{V_b \cos\theta}{\cos\psi_1} \qquad (2)$$

V_{hkl} = growth velocity of the dendrite (m s^{-1})
V_b = traverse speed (m s^{-1})
θ = angle between V_s and V_b (°)
ψ_1 = angle between V_{hkl} and V_s (°)

These different types of microstructural growths depend strongly on the local shape of the solid-liquid interface, which in turn depends on solidification conditions, which are determined by thermal gradient (G, °C/m) and solidification speed (V_s, m/s) at the solid-liquid interface. The latter is the same as the growth rate of the solid-liquid interface mentioned earlier. Solidification conditions (G and V_s) are dependent on processing conditions and they vary as a function of depth of the formed bead as shown in Figure 10 and explained in caption. V_s is dependent on the traverse speed of the cladding process (V_b) and angle θ. Angle θ depends on the shape of the melt pool, which is determined by heat flux. Heat flux depends on the traverse speed (V_b), dimension of the laser beam spot along cladding direction (d_1) and temperature dependent thermophysical properties of the alloy, namely the diffusion coefficient for heat ($\alpha(T)$, mm^2/s), i.e. thermal diffusivity ($\alpha(T) = k(T) / (\rho \bullet c(T))$). The higher the traverse speed (V_b) in relation to factor $\alpha(T)/d_1$, the more elongated the melt pool [301]. This also means that V_s cannot be increased indefinitely since the angle θ stays large with high V_b even on the surface. Consequently, V_s would never reach the V_b at high traverse speeds [302]. Thermal gradient (G), in turn, depends on the traverse speed (V_b), temperature difference between melt pool and base material as well as thermal conductivity [303]. The

following general trends regarding the variation in G were identified; when V_b increases, G increases; when the base material is preheated, G decreases and when the thermal conductivity increases, G decreases. Examples of magnitudes of V_s and G was given by Frenk and Kurz [81], who calculated values for V_s and G for the different traverse speeds (V_b) at the solid-liquid interface of Stellite 6 throughout the coating thickness. With the traverse speed of 100 mm/min average values of V_s and G were 84 mm/min and $2 \cdot 10^5$ K/m. Increasing traverse speed to 10 000 mm/min, increased average values of V_s and G to 8400 mm/min and $1.5 \cdot 10^6$ K/m. These values gave cooling rates of 280 and $2.1 \cdot 10^5$ K/s since cooling rate (T_c) is defined by: $T_c = G \cdot V_s$.

Talking about the planar front growth, according to solidification theory, it becomes possible when G/V_s ratio is high. These conditions are encountered at the bottom of the melt pool. When G/V_s ratio starts to decrease, planar solid-liquid interface destabilizes leading to cellular, dendritic and again cellular growth in this sequence. The critical growth velocity (or thermal gradient) after which the planar growth destabilizes and cellular and dendritic growth starts is given by:

$$V_c = \frac{GD_s}{\Delta T_0} \qquad (3) \qquad \text{or} \qquad G_c = \frac{\Delta T_0 V_s}{D_s} \qquad (4)$$

Where,

V_c = critical growth velocity (m s^{-1})
G_c = critical thermal gradient (°C m^{-1})
G = thermal gradient (°C m^{-1})
D_s = solute diffusion coefficient in the liquid (m^2 s^{-1})
ΔT_0 = equilibrium liquidus-solidus interval (= width of the mushy zone) (°C)

It can be seen that the wider the mushy zone of the alloy with given G, the lower the V_c. This means that the wider the mushy zone, the narrower the planar front zone near the coating/base material interface. Planar microstructure would be highly desirable throughout the coating since it is free of microsegregation and grain boundaries. Planar growth is also possible with very high growth rates since ΔT_0 approaches zero (= partition coefficient (k) approaches unity), but these velocities are not usually achieved in laser cladding. For typical laser coating alloys and used cladding parameters planar growth zone is just couple of microns in thickness and majority of the coating microstructure consist of cellular or dendritic columns.

Another form of above equation, which gives the conditions for planar growth, is:

$$\frac{G}{V} > \frac{\Delta T_0}{D_s} \qquad (5)$$

It can be seen that conditions are fulfilled the best at the coating/base material interface where the G/V ratio is at maximum.

This destabilization of solid-liquid interface and the initiation of cellular and dendritic growth are closely related to the constitutional supercooling, which takes place in liquid near the solid-liquid interface. With growth velocities higher than V_c solid-liquid interface rejects

solute atoms ahead of the solid-liquid interface. Simultaneously, solute profile forms in liquid near the solid-liquid interface so that the solute content is the highest near the solid-liquid interface and decreases going further into the liquid. Width of this composition profile is defined by D_s/V_s. As the composition of the liquid changes, also liquidus temperature changes. In the case of $k < 1$, (k is partition coefficient = C_{solid}/C_{liquid}) liquidus temperature decreases when the solute content increases. Consequently, liquidus temperature becomes lower near the solid-liquid interface compared to the liquid further away. Depending on the actual thermal gradient across the solid-liquid interface, certain portion of the liquid with increased solute content may experience a temperature, which is below its liquidus temperature. In this case of thermal gradient G, that portion of liquid is said to be constitutionally supercooled. In consequence of this, nucleation ahead of the solid-liquid interface takes place, i.e. planar front growth destabilizes and cellular and dendritic growth starts. This nucleation ahead of the interface may also lead to change from columnar to equiaxed growth [304]. These are often called stray grains. In transverse cross-section perpendicular to cladding direction, they are easily mixed with the dendrites growing parallel to coating/base material interface. Convection movements in melt pool may also fragment dendrites and initiate the formation of stray grains or mix the orientations of columnar trunks.

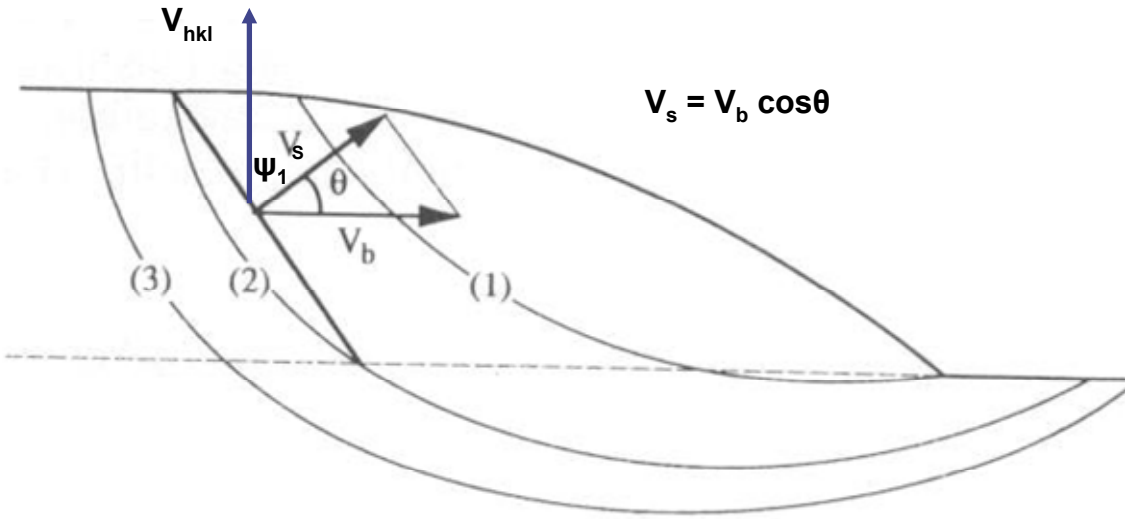

Figure 10. Transverse cross-section parallel to cladding direction cut through the centerline of the single bead. Solidification speed (V_s) depends on traverse speed (V_b) and angle θ between vectors V_s and V_b; $V_s = V_b \bullet \cos \theta$. Since the angle θ is 90° at the bottom and approaches 0° at top of the melt pool, solidification speed is at minimum at the bottom and maximum at the top of the melt pool, i.e. V_s increases from the bottom to the free surface of the coating. In contrast, thermal gradient (G) is at maximum at coating/base material interface and minimum at the top of the coating, i.e. G decreases from the bottom to the free surface of the coating. G and V_s define also the local cooling rate (T_c) since $T_c = G \bullet V_s$ (°C/s). It increases from the bottom to the free surface of the coating.

In addition to the type of microstructural growth (= shape of the grains), V_s and G affects the scale of the microstructure via cooling rate T_c. Frenk and Kurz [81] noted that secondary dendrite arm spacing λ_2 followed $\lambda_2 \bullet T_c^{1/3}$ = constant relationship when Stellite 6 was laser clad with traverse speeds of 100–10 000 mm/min. This relationship does not differ much from the frequently used general $\lambda^2 \bullet V_s$ = constant relationship given in Ref. [299], where λ is the

primary or secondary dendrite arm spacing. Scale of the microstructure, in turn, affects the hardness of the alloy. For instance, Frenk and Kurz [184] obtained 30% higher hardness values for laser clad hypoeutectic Stellite 6 alloy (λ_2 = 0.5–0.8 μm) compared with corresponding cast microstructure (λ_2 = 15–20 μm) despite lower carbide (M_7C_3) fraction (carbide fraction decreased when traverse speed was increased). Traverse speed in this laser cladding experiment was exceptionally high; 10 000 mm/min. Positive effect of the finer scale of the microstructure on hardness and yield strength can be explained via Hall-Petch grain boundary strengthening equations, which are based on the observation that grain boundaries impede efficiently the dislocation movements. If compared with other overlay welding techniques, Monson and Steen [305] reported on the following cooling rates deduced from SDAS of Stellite 6; 9 for oxyacetylene, 46 for TIG, 112 for PTA and 3045 K/s for laser cladding.

1.5.1.1 Microsegregation

Microsegregation, which appears as compositional differences between dendrite cores and interdendritic regions, takes place during solidification. Principle is that the solute atoms, which decrease the temperature of the alloy segregates to interdendritic regions, i.e. solute is rejected by the solid/liquid interface and builds up ahead of the advancing front. Equilibrium partition coefficient (k) for these alloying elements is less than 1 ($k = C_{solid}/C_{liquid}$). According to equilibrium binary phase diagrams, such solute atoms as Nb (<23.2 wt.%), Mo (<47.7 wt.%) and Cr segregates to interdendritic regions when alloyed with pure Ni. Similarly, Cr (<42.4 wt.%) and Mo (<38.0 wt.%) segregate into interdendritic regions when alloyed with pure Co. Presence of other alloying elements may, however, change the segregation behaviour. If the solute increases the temperature of the alloy, it segregates to dendrite core and its $k > 1$. The more the k deviates from 1, the more severe the segregation. In other words, the larger the temperature interval between solidus and liquidus, the larger the segregation. In rapid solidification, partition coefficient is, however, dependent on growth rate of the solid-liquid interface (V_s). When the growth rate increases, k approaches unity (and width of the solute profile becomes smaller), i.e. temperature interval between liquidus and solidus approaches zero. The most immediate consequence of this dependence of k on growth rate is that at high solidification rates, less solute redistribution occurs with the result that the solidified structure is more uniform in composition [306]. They can be further reduced by solid-state diffusion during subsequent post-heat treatment or immeadiately during slow cooling [103]. In bcc ordered structures, this homogenization is easier than in fcc structures [103].

1.5.1.2 Macrosegregation

Macrosegregation stands for compositional differences in macro-level in final coating layer. It depends on mass transport in melt pool, which is in turn dependent on stirring motions known as Marangoni convection originating from the steep thermal gradients, which cause surface tension gradients [307]. The magnitude of this convection depends primarily upon the surface temperature gradients. Thus, processing with beam where the power density is non-homogeneously distributed increases temperature gradients and the magnitude of fluid flow producing more homogeneous compositional distribution [308]. Besides Marangoni convection, gravitational force and impact of the powder jet [90] affect the fluid flow. In laser cladding fluid flow velocities are typically several times greater than the traverse speeds as was discussed in sections 1.3.1.1 and 1.3.3 resulting in homogeneous compositional distributions. With increased traverse speeds non-homogeneous distributions have been reported [309]. This was encountered in situation where the coating was prepared from pure

Fe, Cr and Ni powders. Influence of convection on liquid homogenization is often described with surface tension number S [310]:

$$S = \frac{\left(d\gamma/dT\right) Q D_b}{\mu V_b k(T)} \qquad (6)$$

$d\gamma/dt$ = temperature coefficient of surface tension (N m^{-1} K^{-1})
Q = net energy flow per area from laser beam (W m^{-2})
D_b = laser beam diameter (m)
μ = viscosity (kg s^{-1} m^{-1})
V_b = traverse speed (m s^{-1})
k(T) = thermal conductivity (W m^{-1} K^{-1})

When S is low, convection is negligible, and mass transport in the melt pool is predominantly diffusive resulting in non-homogeneous compositional distribution. When S is high, convection plays a dominant role and homogeneous compositional distribution can be expected.

1.5.2 Coating defects

The selection of improper process parameters, cladding strategy and/or coating/base material pair may lead to coating defects such as cracks, pores/voids, excessive dilution and compositional non-homogeneity. Cracks encountered in laser coatings can be divided to brittle cracks caused by limited ductility and hot or liquation cracks caused by low melting temperature phases, which form in consequence of segregation during solidification. Brittle cracks evolve during cooling when hot coating material tries to undergo shrinkage but is prevented by the constraints imposed by the relatively cool and rigid base material. If the resulting tensile stresses exceed the ultimate tensile strength of the alloy and all the deformability is utilized, brittle cracks perpendicular to coating/base material interface develop relieving tensile residual stresses but also offering free path from surrounding environment to the base material. According to Ref. [116], preheating is an efficient way to eliminate the formation of such cracks. Porosity in laser clad layers may originate from inter-run pores, which form between two overlapped beads, solidification/shrinking cavities and/or gas evolution [40]. Formation of inter-run pores was discussed in section 1.3.1. Shrinking cavities in interdendritic regions occur during solidification when dendrite arms grow together and block the melt to enter the interdendritic regions [166]. Gas evolution or degassing occurs in melt pool due to chemical reaction, which leads to voids spherical in shape. Typical reaction is $C + O_2 \rightarrow CO_2/CO$, which is often met in MMCs and coatings on cast irons. In the former case, the void formation is related to the dissociation of carbide. That is, dissolved oxygen, which originates from the atmosphere, moisture or oxidation of the powder, reacts with C resulting in CO/CO_2 gas. If duration of the melt pool is too short for degassing, gas pores remain in the final coating [22]. Pores may also originate from vaporization of carbides due to high absorptivity of laser beam [243]. In order to diminish gas pore formation, powders can be preheated in oven to remove the moisture or cladding can be conducted in shielding gas chamber or by using additional shielding gas shoe around the melt pool. Powders can also be mixed with small amounts CaF_2, which leads to lower amount of pores in coating as discussed in section 1.4.2.9 [266]. The reason why any type of porosity should be eliminated is its negative influence on mechanical properties since pores may act as initiation sites for

cracks as will be discussed in section 1.5.6.2 [311]. In certain applications their existence may, however, be advantageous. In lubricated conditions micropores in the coating/surface may act as pockets for lubricating oil as suggested by Belmondo and Castagna [312], who introduced pores on purpose on MMC coatings by using Si powder in pre-placed laser cladding process. Evaporation temperature of Si is lower than the melt pool temperature. The results showed that Si powder was excellent for this purpose, because it evaporates rapidly during laser cladding process and forms uniform distribution of micropores inside the coating. Dilution and compositional non-homogeneties were discussed earlier in sections 1.3.1, 1.5.1.1 and 1.5.1.2.

1.5.3 Corrosion properties

Key questions concerning corrosion properties of laser coatings are; how they protect, usually, the less noble base material underneath and how their corrosion properties relate to the corresponding bulk alloys and coatings manufactured by conventional methods. These issues are discussed here under the sections of wet or aqueous corrosion and high temperature corrosion.

1.5.3.1 Wet corrosion

Several authors have studied the wet corrosion properties of various laser coatings. Weerasinghe et al. [191] compared the wet corrosion properties of laser clad, wrought and manual arc deposited 316L. In long-term immersion tests in aqueous $FeCl_3$ solution, laser coating outperformed wrought and welded ones in pitting corrosion resistance. In stress-corrosion cracking test, laser coating compared well with wrought 316L. It was also noted in intergranular corrosion tests that as-laser-clad 316L was not in sensitized condition. In potentiodynamic polarization tests carried out by Dutta Majumdar et al. [313], laser clad 316L outperformed corresponding conventionally processed bulk alloy in pitting corrosion resistance in NaCl solution. Cooper et al. [314] compared seawater corrosion behaviour of wrought and laser remelted Inconel 625 in long-term immersion tests. Wrought Inconel 625 was better since the chemical composition of the remelted one was inhomogeneous in micro-level due to slight microsegregation of solute atoms during solidification. They suggested subsequent heat treatment to homogenize the structure and improve the corrosion properties. Subsequent heat treatment, indeed, is efficient method to homogenize the fine microstructures as reported by Kujanpää and David [315] in the context of laser welding of high Mo austenitic SS.

Li et al. [192, 196] and Anjos et al. [190] tested the corrosion properties of superferritic (UNS S44700, Fe-29Cr-4Mo) and superaustenitic SS (254 SMO) produced by laser cladding and compared them with corresponding bulk alloys. In both cases microsegregation of Cr and Mo was detected. The localized corrosion performances were studied by potentiodynamic anodic polarization in NaCl, $FeCl_3$ and HCl (not for 254 SMO) solutions as well as long-term immersion tests in acidified $FeCl_3$ (ferritic, 254 SMO) and NaCl (254 SMO) solutions. Ferritic laser coating exhibited passive behaviour very similar to commercial alloy in polarization tests but suffered from slight pitting corrosion in long-term immersion (commercial reference alloy was not tested in long-term immersion). In anodic polarization tests in NaCl, dendrite cores, which depleted Cr and Mo dissolved preferentially, whereas in $FeCl_3$ and HCl Cr- and Mo-rich areas dissolved more. Similar to corresponding bulk alloy, austenitic laser coating did not suffer from pitting in anodic polarization tests but pits formed in long-term exposure and they were smaller and more numerous than in bulk alloy ($FeCl_3$). Influence of microsegregation was also studied by Nakao and Nishimoto [316]. They

remelted cast AISI 904L, Incoloy 825 and 625 alloys with traverse speeds from 500 to 6000 mm/min. Subsequent corrosion tests indicated that laser remelted structures exhibited improved corrosion resistance compared with cast structures. This was due to less amount of microsegregation. Elemental analyses revealed that solute atoms, Cr and Mo, were distributed more homogeneously in micro-level compared with cast structures. It was also noticed that the higher the traverse speed in remelting, the lower the amount of microsegregation as already explained in section 1.5.1.1. Since the production of large area coating involves always overlapping and associated remelting and reheating of previous beads, which leads to such microstructural changes as microsegregation or sensitizing, there might be local differences in corrosion rates between overlapped and central areas of beads. This has been studied at least in the cases of AISI 420 [317], 304L [318], 321 [319], Fe-10Cr-13P-7C [290], zirconium alloy [320], AlSi [290] and Al-2014-T6 alloys [321, 322]. Various corrosion tests provided evidence that overlapped areas in AISI 420, 304L, 321 and Al-2014 were more sensitive to pitting corrosion than other areas. In Zr-alloy, Fe-Cr-P-C and AlSi accelerated corrosion took place near the overlapped regions.

Besides compositional inhomogeneties in micro-level, dilution is one of the key factors influencing the corrosion performance since noble corrosion resistant alloys are usually applied on less noble base materials. Influence of dilution by Fe was tested by Crook [323], who diluted tungsten inert gas (TIG) welded Ultimet alloy (Co-26Cr-9Ni-5Mo-3Fe-2W-0.8Mn-0.3Si-0.08N-0.06C in wt.%) with various amounts of AISI 1040 and 316L. Corrosion tests were carried out in several aqueous solutions at different temperatures. Results showed that dilution was detrimental in all the test conditions and intermixing with AISI 1040 had a much stronger negative effect on corrosion resistance than intermixing with 316L.

1.5.3.2 High temperature corrosion

In high temperature corrosion tests, laser coatings have been exposed to various gas atmospheres and molten salts. Zhang et al. [324], for instance, studied the hot corrosion properties of laser remelted Co-based self-fluxing alloy against molten lead sulphate ($PbSO_4$) at 700-900°C. They found out that sulphur ions penetrated into the coating along dendrite and interdendrite grain boundaries. Secondary dendrite arms, however, retarded significantly the penetration rate. Uusitalo [325] examined the high temperature corrosion of laser clad high-Cr NiCr coatings and compared them with corresponding HVOF sprayed coatings in chlorine containing gaseous (550°C, HCl) and molten salt (550°C, $40Na_2SO_4$-$40K_2SO_4$-10NaCl-10KCl in wt.%) environments. Laser coatings prevented the penetration of gaseous corrosive species into the base material and coating in gas environment. Laser coatings outperformed HVOF coatings also in molten salt environments. Cr-rich phases were, however, prone to chlorine attack under molten salt in oxidizing conditions. Longa and Takemoto [326] compared the hot corrosion properties of thermal sprayed (flame spraying, arc spraying, low-pressure plasma spraying) and superficially laser remelted high-Cr NiCr coatings against Na_2SO_4-V_2O_5 (15/85 mol.%) in air at 900°C. As opposed to sprayed coatings, penetration of molten salt compounds was prevented by laser remelting. Longa-Nava et al. [327] compared the hot corrosion properties of flame, low-pressure plasma sprayed and superficially laser remelted NiCrAl coatings against Na_2SO_4 and Na_2SO_4-$NaVO_3$ (70/30 mol.%) in SO_2/O_2 atmosphere at 900°C. They found out that laser remelted one was more resistant than the same coatings in the as-sprayed condition. Wang et al. [328] compared the hot corrosion properties of cast and laser remelted Ni-based superalloy against Na_2SO_4-NaCl (75/25 mol.%) at 900°C. Laser remelted outperformed the cast one by a factor of 2-3. In cast alloy significant sulfidation and oxidation took place along grain boundaries. Internal attack was absent in laser remelted alloy.

1.5.4 Wear properties

Similar to corrosion properties, wear properties of laser coatings are discussed here mainly in comparison with corresponding bulk alloys and coatings manufactured by conventional methods. They are subdivided here into sliding, abrasion, impact, erosion and cavitation erosion wear.

1.5.4.1 Sliding

In the preceding section 1.5.1 it was discussed that the scale of the microstructure follows the $\lambda^2 \bullet V_s$ = constant relationship, i.e. the higher the growth rate (V_s), the smaller the scale and the higher the microhardness. Therefore it could be expected that higher V_s has positive influence on sliding wear resistance as suggested by Archard wear equation V = KWL/H, where V is the wear volume (m^3), K wear coefficient, W normal load (N), L = wear travel length (m) and H hardness (Pa) [329]. Despite its positive influence on microhardness Frenk and Kurz [184] observed that the scale of the microstructure did not affect the sliding wear resistances of equally diluted Stellite 6 laser coatings in dry conditions against WC/Co (90/10 wt.%) hard metal under severe wear regime (1 MPa). This was due to stress cycles (fatigue), which destroyed the microstructure of Stellite 6 underneath the exposed surface in pin-on-disc sliding wear test, and oxide layers, which formed between mating surfaces. Simultaneously, it was, however, noted that finer microstructure exhibited lower coefficient of friction than coarser one. Influence on work hardening was negligible. Effect of the scale of the microstructure may, however, be beneficial in other wear conditions since wear behaviour depends strongly on the tribological system.

Similar to the scale of the microstructure, dilution affects the microhardness and potentially sliding wear. This was shown by Frenk and Kurz [184], who studied the influence of Fe dilution on dry sliding wear resistance of Stellite 6 against hard metal. The higher the dilution, the lower the resistance and microhardness. Increase in Fe content from 1.2 to 4.0 wt.%, for instance, doubled the wear rates. Also coefficient of friction increased. Besides decrease in microhardness, intermixed Fe from the base material affected negatively on work hardening since it increased the stacking fault energy and stabilized the metastable fcc-structure as discussed in section 1.4.2.1. De Hosson and De Mol van Otterloo [185] reported later on similar results for Stellite SF20 in dry and wet fretting conditions against 316L. In other study, Xu et al. [330] deposited Stellite 6 on martensitic stainless steel with laser and TIG. Compared with TIG clad layers, which exhibited the geometrical dilutions of 41-46%, less diluted laser coatings (4–7 %) showed more than two times higher resistances against AISI D2 tool steel in dry block-on-ring tests.

In another study by Xu et al. [331], laser and PTA was used to deposit NiCrBSi clad layers. In dry block-on-ring tests against GC15 bearing steel, coefficients of friction were 0.42-0.48 for laser and 0.51-0.58 for PTA clad layers. Wear losses for laser coating were 54 times lower than that for PTA coating. The amounts of Fe dilution were not mentioned but the maximum hardnesses were 730 for laser and 500 HV for PTA coating. Sha and Tsai [194] compared AISI 420 coatings produced by laser and SAW. Laser and SAW coatings consisted of eight and four consecutive layers, respectively. In dry sliding wear tests against hardened steel laser coating exhibited superior wear properties to SAW coating. This originated from the differences in microstructure and hardness. Hardness of the as-laser-clad coating was 600 HV compared with 370 HV for tempered SAW coating. Preheating and tempering were necessary to obtain crack-free coatings in SAW process, whereas laser coating was produced crack-free without pre- or post-heat treatments.

1.5.4.2 Abrasion

Influence of microstructure on abrasive wear was studied by Atamert and Bhadeshia [332]. They deposited several layers of Stellite 6 with manual metal arc (MMA), TIG and laser to obtain different scales in microstructure. MMA coatings had the coarsest microstructure (primary arm spacing; 14-20 μm) and the lowest hardness, whereas the laser coating exhibited the finest microstructure (8-12 μm) and the highest hardness. Against Al_2O_3 abrasive MMA coating was the worst one, whereas TIG and laser coatings exhibited twice lower wear rates. With harder SiC abrasives, all the coatings showed similar wear rates. Compared with HIPped tool steels Zhang et al. [197] observed that laser clad tool steels were slightly less resistant to abrasive wear (Al_2O_3). Similarly, Colaco et al. [199] found out that as-sintered AISI M42 tool steel was better than laser remelted and laser remelted + tempered ones in abrasion wear resistance. De Beurs and De Hosson [195] compared the abrasive wear of conventionally hardened + slightly tempered and laser remelted AISI D6 tool steel. They stated that abrasive wear rates did not differ significantly. Among MMCs Zhu et al. [247] tested abrasive wear of NiCrBSi reinforced with coarse WCs produced by laser cladding and atomic hydrogen welding. The abrasive wear results showed that laser coatings had superior wear resistance to welded coatings.

Effects of Fe dilution on abrasive wear properties have been studied for laser clad Co-based hardfacing alloys and tool steels. In contrast to sliding wear, De Mol van Otterloo and De Hosson [333] observed that abrasion wear resistance of laser clad Stellite grades 21, 6, 1, 20 and SF20 on 316L base material actually increased with dilution in spite of decrease in hardness. They explained that this improvement took place due to change in wear mode, i.e. from more severe microcutting and microcracking caused by Al_2O_3 particles to milder microcutting and microploughing, because dilution improved the fracture toughness of the coatings. These results contradict with studies carried out by Crook [323], who tested the effects of dilution on wear properties of solid solution strengthened low carbon Co-based Ultimet alloy (TIG), which was diluted with AISI 1040 and 316L. Abrasion wear resistance of Ultimet alloy reduced substantially with increased dilution. Colaco et al. [199] studied the effect of Fe dilution on AISI M42 tool steels. They found out that this material tolerated Fe up to 45 wt.% before abrasion wear resistance started to decrease significantly.

1.5.4.3 Impact

Besides pure abrasion, resistances against impact-abrasion, impact-wear and impact are highly needed in applications such as crushing, mining and excavation. Zhang et al. [197] conducted impact resistance tests for laser clad and HIPped tool steels. Compared to HIPped ones, laser clad tool steels exhibited 3–4 times higher impact resistances. Aihua et al. [334] conducted impact-wear tests (valve against valve seat) at elevated temperature for laser clad NiCrBSi and CoCrW self-fluxing alloys. Laser clad NiCrBSi alloy processed at high laser traverse speed produces better impact-wear resistance than laser clad at low traverse speeds or plasma sprayed + vacuum induction fused. The reasons for this were claimed to be the laser coating's higher microhardness, finer microstructure and the precipitation of hard phase particles (Ni_3B and $Cr_{23}C_6$) at the test temperature of ~780˚C.

1.5.4.4 Erosion

Erosive wear is frequently encountered, for instance, in steam turbines due to water droplet erosion, in combustion engines due to fuel injection and in pumps and coal/sand slurry pipelines due to slurry-erosion. Coulon et al. [121] studied water droplet erosion of laser

coatings under the impact velocities of 600 m/s and incidence angle of 90°. They reported that laser clad Stellite 6 outperformed forged and cast bulk Stellites of the same grade. This result suggested that laser clad Stellite 6 was more ductile than corresponding bulk alloys since at high angles of incidence brittleness and fatigue dominates the wear [335]. At low angles erosive wear is mainly controlled by the hardness [335]. In addition to water droplets, influence of such erosive solid particles as quartz (SiO_2) and alumina (Al_2O_3) carried by gas jet was studied. Oberländer and Lugscheider [336], for instance, compared the erosion resistance of laser clad and PTA welded NiCr alloy coatings against quartz erosives impacting the surface at a velocity of 118 m/s at an incidence angle of 30°. Coatings produced by laser cladding showed erosion resistances ~8-14% higher than that of the coatings produced by PTA welding. This better erosion resistance of laser coatings was claimed to be a result of finer microstructure, smaller and more finely distributed hard phases, supersaturation of the solid solution phases, and the lower degree of dilution. Pelletier et al. [212] conducted solid particle erosion tests for laser clad Hadfield manganese steel and compared the properties with bulk Ti6Al4V, 316L, Ni-22%Cr-Fe-Mo and plasma sprayed carbide coating. Laser clad coating outperformed all the reference materials at every tested angle (30-90°) except 316L at 90°. Wear rates were nearly independent of particle impact angle due to the peculiar structure, which consisted of hard work-hardened surface layer and ductile structure underneath offering great potential in erosion applications.

As the slurry-erosion (erosive particles are entrained in flowing liquid) is often met in applications where the incidence angles are low like in pipelines, high hardness becomes desirable. For that reason MMCs are applied and studied. Tucker et al. [13] measured slurry-erosion rates for laser clad MMCs including different volume fractions of WC in Co-based matrices, TiC in Stellite 6, $MoSi_2$ in Stellite 6 and directly injected $MoSi_2$ in AISI 304. Slurry-erosion rates for laser clad MMCs at an incidence angle of 20° were higher than that for commercial sintered hard metal (WC-Co, 88/12 in vol.%), which contained higher amount of carbides, but significantly less than for bulk Stellite 6. Among laser clad MMCs Co-based matrices reinforced with WC proved to be the best ones. It was also noted that the higher the volume fraction of WC, the better the slurry erosion resistance. TiC-Stellite 6 (50/50 vol.%) was just slightly better than Stellite 6 since TiC particles tended to break into many pieces under test conditions. Another poor performance of TiC was reported by Duraiselvam et al. [337], who studied the slurry-erosion resistance of WC and TiC reinforced NiAl laser coatings. Higher wear rates were due to the presence of unmelted and partially melted TiC particles in the matrix, which acted as initiation sites for erosive attack. Jiang and Kovacevic [338] conducted slurry-erosion tests (SiO_2 in water, 25 m/s) for laser clad FeCrBSi, NiCr-Cr_3C_2, WC/W_2C-Co and bulk AISI 4140 with impact angles 30-90°. Laser clad FeCrBSi exhibited the lowest wear rates. Its resistance was further improved by cryogenic cooling, which refined the microstructure.

If the liquid in slurry includes corroding elements, their combined effects may further increase wear rates. A synergy develops between both mechanisms. Usually these wear rates are higher than the sum of corrosion and erosion rates alone. Erosion-corrosion studies have been subjected to Ni-based self-fluxing alloys with and without externally added reinforcements. According to laboratory and field tests, Wang et al. [339] noticed that erosion-corrosion rates for laser clad NiCrBSi was about twice less than that for AISI 420 stainless steel. Resistance of such coating can be further increased by post-heat treatment at 550°C for 1.5 hours, which increases the hardness due to precipitation of hard borides [340]. Among MMCs, NiCrBSi

reinforced with Cr_3C_2 outperformed WC even if the latter was harder than the former one [341].

1.5.4.5 Cavitation erosion

Cavitation erosion is a common cause of failure in liquid and steam handling systems, which is caused by the repeated generation and collapse of cavities (i.e. bubbles) in a liquid near to the surface of a material. When bubbles collapse, shock waves and micro-jets are emitted causing pressure pulses on material nearby. The repetitive attack by these pressure pulses leads to fatigue, fracture and loss of material. Collapse of bubbles arises from sudden change in flow or from vibration. The material surface degradation due to cavitation is severe in many common engineering systems made from austenitic and martensitic stainless steels, cast irons, brasses and Al-alloys e.g. in hydraulic turbines and pumps, pipes and valves, mining drills, diesel engine cylinders, turbine blades in marine industry, ship propellers, and high speed ultrasonic mixing systems in food and pharmaceutical industries [288, 342, 343]. Nevertheless, only a few research groups so far have focused on improving cavitation erosion resistance of different base materials by means of laser cladding. Coatings made of Ni- and Fe-based self-fluxing alloys [173, 343-345], Ni-based superalloys [172], NiAl [125], NiAl reinforced with TiC [125] and 316L reinforced with WC [342, 346] have all given encouraging results. On MMCs it is worth to mention that fine WC particulates outperformed coarse ones and in-situ synthesized TiCs externally added ones.

1.5.5 Residual stresses

As laser cladding is conducted with high intensity and short interaction times, i.e. heating occurs very locally, large thermal gradients arise between molten clad material, adjacent bead and solid base material, which temperature remains relatively low during processing. On rapid cooling large tensile stresses develop because adjacent bead and cold base material restrict contraction in cooling clad material. Magnitude of these shrinkage stresses can be estimated with equation [347]:

$$\sigma_{th} = E\alpha_{CTE}\Delta T_1 \tag{7}$$

σ_{th} is shrinkage or thermal stress (MPa), E is Young's modulus (GPa), α_{CTE} is CTE (K^{-1}) and ΔT_1 is difference between melting temperature and base material during processing (K). These large tensile stresses, which develop in final coating layer, are often undesirable from a performance standpoint. In particular, tensile stresses can have detrimental effect on fatigue, tensile, wear [329] and corrosion properties [348], not to mention integrity of coatings. For these reasons, their magnitudes and factors affecting them should be known. The magnitude and sign of developing stresses depend on the difference in CTEs between the coating and base material, difference in temperature between melt pool and base material during processing [22], cooling rates, mechanical properties (E, yield strength) of both materials, solid-state phase transformations, which involve changes in volume as well as rigidity (thickness) of base material. For example, if CTE of coating (CTE_c) is higher than that of base material (CTE_s); larger the difference in CTEs, the higher the tensile stress in coating layer. If $CTE_c < CTE_s$; larger the difference in CTEs, the lower the tensile stress in coating layer. As ΔT_1 decreases while using preheat, it is an efficient way to decrease the tensile stresses in coating in both given situations [349]. If $CTE_c < CTE_s$, tensile residual stresses in coating layer can be even converted into compressive ones as was shown by Dekumbis [349], who post-heated Stellite 6 on austenitic SS at 900˚C for 4 hours. Prerequisite for this is to use high

enough temperature and long enough time during which all the stresses are relieved through plastic deformation and creep. Assuming that deformation of base material and phase transformation related volume changes do not take place, resultant stress sign and magnitude can then be estimated with equation [350]:

$$\sigma = \frac{(CTE_c - CTE_s)(T_2 - T_1)E_c}{1 - \upsilon_c} \quad (8)$$

where σ is residual stress (MPa), T_2 heat treatment temperature (°C), T_1 room temperature (°C), E_c Young's modulus for coating (GPa) and υ_c Poisson's number for coating. It suggests that tensile residual stresses cannot be removed fully by post-heat treatment if $CTE_c > CTE_s$. Moreover, use of preheat decreases cooling rates effectively, which allows more time for plastic deformation and creep to occur. Both these tend to relax, at least to some extent, evolving stresses [22]. It has also influence on rates at which tensile stresses develop. As the tensile stresses in coating layer develop during cooling, possible martensitic transformation and associated volume expansion start to counteract against developing tensile stresses at martensite start temperature (M_s). This can even result compressive stresses in coating layer of AISI P20 tool steel as described by Chen and Xue [351]. Van Brussel and De Hosson [352] observed that these compressive stresses may, however, turn into tensile ones. They observed that each new overlapped bead exerted tensile force upon previous bead by which the compressive stresses disappeared. Some of the residual stresses of various laser coatings on different base materials found from the literature are shown in Table 4.

1.5.6 Mechanical properties

Several types of mechanical test methods have been applied to various laser coating/base material combinations and laser-manufactured 3D-structures to reveal their suitability in applications under different types of static and dynamic mechanical loads. These static and dynamic mechanical properties are discussed here separately.

Table 4. Maximum residual stresses in laser coatings collected from the literature. Signs (+) and (-) denote tensile and compressive, respectively [22, 351, 353-357].

Coating	*Base material*	*Residual stress (MPa)*	*Method*
Stellite 6	X2CrNiMo 18 12	+100 - +350 -550 - -350[1]	XRD
Stellite 6	Aust. SS	+100 - +500	Layer removal
Stellite 6	Fe37	+600	Crack compliance
Stellite 6	Mart. SS	+600 - +1000	Layer removal
Stellite 6	C-steel	+150 - +350	XRD
Stellite 21	AISI 316L	+100 - +150 -200 - -150[2]	XRD
AISI 304	Mart. SS	+200 - +300	Layer removal
AISI P20	AISI P20	-300 - -150	Hole drilling
CuNiFeSi	AlSiMg	+50 - +200	Crack compliance, XRD

[1)] after post-heat treatment (900˚C, 4h)
[2)] after post-heat treatment (900˚C, 1h)

1.5.6.1 Static

Undoubtedly, the most important mechanical property is the bond strength between the coating and the base material since it determines whether the coating remains on base material in operation conditions or not. Owing to the welding nature of laser cladding process de-bonding at the coating/base material interface due to shear stresses along or tensile stresses normal to interface is hardly ever encountered if process parameters are chosen so that joint defects (= lack of fusion) at the interface are absent. A few bending, cold rolling and direct pull tests have confirmed this and additionally proved the superiority of laser clad coatings over thermal sprayed coatings. For instance, study by Pelletier et al. [109] showed that 4-point bending tests subjected to Al-based MMC laser clad on Al caused vertical crack in coating instead of crack along coating/base material interface. Recent 4-point bending tests by Hjörnhede and Nylund [358] revealed that Fe-based hardfacing alloy laser clad on low-alloyed steel tube tolerated the strains up to 15% without signs of de-bonding, while coatings deposited by arc spray and HVOF processes de-bonded after the strains of 1.4–1.9% and 0.8-1.8%, respectively. In another study by Pelletier et al. [211, 212], Hadfield steel laser clad on low carbon steel survived very high deformations caused by cold rolling without de-bonding. Same method was also used by Hidouci et al. [359], who generated high deformations on Ni-based superalloy laser clad on H11 tool steel. Despite high deformations de-bonding was not observed. Cadenas et al. [360] used direct pull test normal to interface for WC-17Co laser clad onto AISI 1043. Bond strength exceeded the tensile strength of the used epoxy adhesive, which was 60 MPa. The laser coating outperformed clearly the corresponding plasma sprayed coating, which showed the interfacial bond strength of 50 MPa. According to Hjörnhede and Nylund [358], bond strength of laser coatings exceeded 69 MPa (strength of adhesive) in contrast to interfacial strength of 55-61 MPa for HVOF coating and cohesive strength of 38 MPa for arc sprayed coating.

In addition to bending tests and tensile pull tests normal to coating/base material interface, tensile tests parallel to interface inducing large shear stresses at interface have been used. In a comprehensive study by Niederhauser [361], solid solution strengthened CoCr and FeCr hard-facing alloys laser clad on medium carbon steel were tested in this way both longitudinally and transversally in relation to cladding direction. Together with 2 or 3 consecutive layers of coating, tensile specimens included the unaffected base material and HAZ, which consisted of tempered martensite due to the heating effect of subsequent passes. Results confirmed the excellent bonding between coating and base material, since de-bonding was never observed. It was also encouraging to note that yield and ultimate tensile stresses exceeded the values obtained with base material alone. Even if the base material alone exhibited the highest ductility (~23%), elongation values were still considerable for laser clad specimens (~10% for CoCr and ~18% for FeCr) taking into account the hardening of HAZ. In fact, in-situ tempering of HAZ during cladding played a key role in ductility. This was revealed by the test subjected to specimen, where HAZ comprised some untempered martensite. Elongation was just 5% in this case.

Occasionally, in spite of visually defect-free joint between laser clad coating and base material, issue of low bond strength and de-bonding may arise if interface region includes brittle and low-strength phases in consequence of incompatible metallurgy. As mentioned in section 1.4.1.2. Al is metal, which forms variety of intermetallic compounds with elements (Fe, Ni, Co, Cr, Ti, Cu) commonly found in coating alloys. One representative example of the formation of intermetallics and its influence on mechanical properties including bond and impact strength was given by Wang et al. [149, 362, 363], who laser clad Cu-based Al-Fe bronze and FeCrNiBSi onto Al-13%Si alloy. Due to abundant formation of Cu_xAl_y and Fe_xAl_y

intermetallics at the interface zone, bond strengths as low as 15–40 and 17–110 MPa was measured by direct pull test. According to Ref. [161], tensile strengths for corresponding base materials and clad alloys alone are in the range of 300-400 MPa (for cast and wrought Al-13%Si) and 500-1000 MPa (for wrought CuAlFe), respectively. For the sake of comparison tensile strengths for $FeAl_3$ and Fe_2Al_5 are just about 15–17 MPa. As the tensile tests were carried out in vacuum chamber of SEM, dynamical observations confirmed the initiation and propagation of cracks at the interface zone. Formation of brittle intermetallics led also to poor impact performance since cracks parallel to coating/base material interface formed at the interface zone. From the metallurgical point of view, Al-Si alloys are more suitable for Al base materials as shown by Pei et al. [219], who found out that bond strength between Al-40Si clad track and Al-12Si base material exceeded the tensile strength of base material alone.

As laser cladding process generates heavily textured grain structures, anisotropic mechanical properties can be expected. This anisotropic behaviour is better shown in experiments where specimen consists of coating structure alone. Situation, where the coating structure alone has to be under the influence of mechanical load is encountered in 3D-components produced by rapid laser manufacturing. Due to increasing attention subjected to 3D rapid manufacturing, several studies on the mechanical behaviour of these laser clad structures can be found. Commonly the strength and ductility depend on test direction in relation to manufacturing direction. Yield and ultimate tensile strength values for the laser clad structures are typically higher in direction parallel to cladding direction (= perpendicular to growth direction and grain orientation) than in direction perpendicular to cladding direction (= parallel to growth direction and grain orientation), whereas ductility is higher in direction perpendicular to cladding direction. This applies at least to Ni-based superalloys like Inconel 625 and 690 (fcc) [364, 365], austenitic stainless steels (fcc) [365] and some titanium alloys [159]. In addition to textured grain structures, residual stresses and interface zones may play a role. The yield and tensile strength values of laser clad structures along both directions are often significantly higher than corresponding cast and comparable to wrought alloys assuming that joint defects are absent, although the ductility may be slightly lower in direction parallel to cladding direction [364, 365]. It is claimed that high strength values can be attributed to fine grain structure (Hall-Petch grain size refinement) characteristic for rapid solidification since fine grain structures result in increased strength according to Hall-Petch effect (grain boundaries act as barriers to dislocation movement). Depending on the alloy in question, such subsequent heat treatments as stress relief or precipitation hardening may enhance further the mechanical properties of laser clad structures as in Inconel 718 [159].

A lot of efforts have been put to study the mechanical properties of MMCs produced by laser cladding. In this case, it is not only the interfacial strength between the coating and base material, but also the bond strength between the externally added or in-situ synthesized hard particles and metal matrix, which determines the mechanical behaviour of coating. Obviously, high bond strength between particles and matrix is preferred, since hard particles primarily receive the high contact loads caused by various hard abrasives and simultaneously protect the softer matrix against wear. These internal bond strengths between particles and matrix have been evaluated for several particle/matrix combinations using the same mechanical test methods as mentioned above. For example, Galvan et al. [367] conducted tensile tests for in-situ synthesized TiB in Ti6Al4V matrix inside vacuum chamber of SEM. Tensile tests indicated strong interface between TiB needles and matrix since de-bonding was not observed. Vreeling [147] noticed that injection of WC into Ti6Al4V decreased the tensile strength and ductility considerably compared with original base material alone. This was related to the reaction products of W_2C and TiC, which surrounded the primary WC particles,

since these phases were the initiation sites for fractures and cleavage [147, 254]. Reaction products played also a key role in the failure of SiC/Al-10Si MMC under the tensile stress since de-bonding of reaction product Al_4C_3 from the AlSi matrix was the predominant fracture initiation mechanism [147]. Mehlmann et al. [368] tested matrix-particle adhesion by bending Ti (cp) reinforced with B_4C. Tests showed that crack in the layer did not follow any particular preferred path, indicating very good adhesion between B_4C and the matrix. Apart from matrix-particle adhesion studies, Li et al. [369] conducted tensile tests on TiC-64Fe36Ni samples in order to find out the effect of volume content of TiC on strength and ductility. As expected, the strength increased significantly with increasing TiC reinforcement, whereas ductility dropped.

1.5.6.2 Dynamic

Both laser clad coating/base material systems and laser-manufactured 3D-structures alone have been subjected to low- and high-cycle fatigue tests. This is an important issue to be explored because laser cladding generates large residual stresses on final component and it is known that residual stresses influence significantly on fatigue life of component. Moreover, fluctuating loads lead to fractures already under stresses which are well below the ultimate tensile or even yield strength limits of the material and it is claimed that 70-90 % of all the fractures encountered in various machines are fatigue ones [166].

For instance, Niederhauser [361] conducted fatigue tests for CoCr and FeCr hardfacing alloys laser clad on medium carbon steel. Test specimens consisted again of 2 or 3 consecutive layers of coating, HAZ and unaffected base material. Fatigue tests were carried out in tensile-compression mode parallel to coating/base material interface. They stated that for low strain amplitudes, the base material alone exhibited longer fatigue life, whereas for high strain amplitudes coating/base material system showed longer fatigue life. This behaviour was related to the tensile residual stresses formed in the coating during cladding. It was noted that residual stresses survived low strain amplitudes but vanished during high strain amplitude tests. In other words, residual stresses had greater negative influence on fatigue life when the coating/base material system underwent low strain loading cycles. Interface region proved to be again very strong since crack initiation started either in the unaffected base material (CoCr) or laser clad coating (FeCr).

Several studies have shown equal or even better fatigue strengths for laser-manufactured 3D-components than for corresponding alloys produced by conventional methods. To name a few, Nowotny et al. [160] found out that as-laser-manufactured 3D-structure made of Ti6242 alloy outperformed corresponding reference material in high-cycle fatigue tests. Kelbassa et al. [370] performed high-cycle fatigue tests for laser-manufactured and subsequently heat-treated (aged) 3D-structures made of Inconel 718. Laser manufactured and aged structure proved to be as good as corresponding heat-treated forged material.

Cyclic mechanical loads in a structure can be induced not only by the external forces, but also by the thermal changes alone or together with external mechanical forces. Thermally induced cyclic loads become significant in coating/base material systems if there is large difference in CTE between coating and base material, and especially if the construction is rigid. Even if the CTE mismatch is absent strong cyclic thermal gradients may generate loads, which lead to failure. Possible applications where laser coating/base material systems could be subjected to thermal cycling can be encountered for example in combustion engines, gas and steam turbines, moulds, metal forming tools and hot rolling mill rollers. Yet, surprisingly few publications, which deal with thermal fatigue of laser coatings, can be found. In one of the

few studies Felberbaum et al. [311] conducted high-cycle thermal fatigue tests (1100°C -> 200°C -> 1100°C etc.) for laser clad CMSX-4 Ni-based superalloy on top of cast single crystalline CMSX-4 base material (no difference in CTEs, but steep thermal gradients due to induction heating). They noticed that cracks, in consequence of thermal cycling, initiated from such defects as micropores, oxides and hot tears, which located in solute-rich interdendritic regions. Astapchik et al. [371] tested two grades (soft and hard) of laser remelted NiCrAlBSi coatings on Ti alloy. In low-cycle thermal fatigue test (700°C -> compressed air, etc.) harder one, which was worse, survived 25-50 cycles without cracking. Blank et al. [213] conducted FEM simulations for stress and strain for CuNi laser coatings on cast Al alloy during thermal cycling (300-400°C -> water quenching). Beyond certain critical temperature the base material close to the interface was plastically deformed with each cycle. After the first 10–20 cycles, stress cycle in coating and base material stabilized and it became independent of the initial residual stress state.

1.6 Objectives of the present work

Laser cladding is an emerging and versatile coating method to produce thick metallic and metal matrix composite (MMC) coatings traditionally on small work pieces or confined areas in massive components. With the development of more powerful laser sources and hybrid cladding techniques, repairing and coating of larger surfaces in massive high value components become more cost efficient. Yet, primarily due to high capital costs of lasers, conventional coating methods, also under constant development, are still dominating in many industrial applications. Lasers have taken great advance in cladding but not yet done breakthrough as in welding and cutting. In order to compete with the conventional coating methods, orders of magnitude higher capital costs of lasers and related accessories should be justified/offset by the superiority of the coating quality, extended lifetime of the clad components and/or higher productivity and coating material efficiency.

Objectives of this present work are to study some essential functional properties of coatings produced by modern short-wavelength Neodymium:yttrium-aluminium-garnet (Nd:YAG) and direct high power diode laser (HPDL) cladding techniques, and to compare them with coatings produced by other coating techniques such as high-velocity oxy-fuel (HVOF) spraying and plasma transferred arc (PTA) overlay welding. Properties of coatings are also compared with selected wrought, sintered, cast and hot isostatic pressed (HIP) bulk alloys. Coating materials comprise traditional and widely used commercial metal alloys with and without refractory reinforcements as well as novel experimental type alloys, which are rarely studied in the context of laser cladding. Characterisation and testing of coatings include wet corrosion, hot corrosion, high temperature stability, adhesive wear, abrasive wear, residual stresses and thermal fatigue. Wet corrosion tests focus on integrity of the coating, i.e. how well the noble coating alloys protect the less noble base material underneath, and resistance against localized forms of corrosion, i.e. pitting and crevice corrosion in chloride bearing environments. Wet corrosion properties have crucial influence on service lifetime of various components in pulp and paper as well as off-shore industries. Similar to wet corrosion, objectives in hot corrosion tests are to study the coatings' ability to protect the less noble base material against molten salt compounds of Na, V and S at high temperatures. Long-term exposure to high temperature provides additional information about high temperature stability of metastable phases frequently detected in laser coatings. These tests have significance for coating applications in combustion chambers of diesel engines burning heavy fuel as well as oil- and waste-fired boilers in power plants. In tests against pure abrasion, large group of

metal alloys reinforced with different types of refractory carbides are tested in order to find out dissociation of carbides and associated embrittlement of matrix as well as dependencies between wear resistance and morphology, type, size and volume fraction of carbides. Information derived from results are beneficial for powder and coating manufacturers as well as end users, who deal, for instance, with chutes, extruders, rock crushers and various earth moving equipment. Objective of adhesive wear tests against quenched and tempered structural steels is to provide information about coatings' ability to resist galling in dry conditions. These conditions are encountered in situations where lubrication is whether absent or inadequate due to process requirements, or lubrication is blocked by accident, or in the beginning of various start procedures when lubrication film has not yet developed between mating surfaces. Residual stress and low-cycle thermal fatigue tests focus mainly on brittle Tribaloy hardfacing alloy based on intermetallics and applicability in conditions where temperature fluctuates up and down like, for instance, in combustion engines, various metal forming tools and situations where the clad component is subjected to post-clad heat treatments. In addition to coating characterisation, efforts are made to clarify back reflection in novel direct HPDL cladding process since this area is still rather unknown but critical in developing novel laser sources for cladding and rapid 3D-manufacturing applications.

2 EXPERIMENTAL PROCEDURES

This chapter introduces 1-step laser cladding processes and materials studied in this work and describes the characterisation and testing methods of the coatings and reference materials.

2.1 Laser cladding processes and facilities

Two types of continuous wave, short-wavelength, industrial lasers were used in coating production; Nd:YAG and direct HPDL.

2.1.1 Nd:YAG

Nd:YAG laser cladding experiments were performed with 4 kW Haas HL4006D lamp-pumped laser, which was equipped with step-index glass fiber 15 m in length and 600 µm in diameter. Processing end of the fiber was supplied with BEO welding optics, which consists of collimator, semi-transparent mirror, camera and a pair of water-cooled plane convex quartz lenses. Focal length of the lower, focusing, lens was 200 mm. Coax 8 commercial coaxial powder feeding nozzle (Fraunhofer IWS, Dresden, Germany) was installed to welding optics. It consists of water-cooled jacket, inner and external nozzles, which form a circumferential channel with the gap of 250 µm between them at the nozzle tip. Flowing along this channel, powder and carrier gas converged to cone-shaped stream with the same central axis as the laser beam. Its focal point was 13 mm below the nozzle tip after which the powder stream was more or less straight or slightly dispersed. The inner nozzle had a channel with minimum inside diameter of 4.5 mm at the nozzle tip through which the laser beam and shielding gas passed. The positive pressure of this shielding gas prevented the particles from flowing up to the protection lens. Before entering the nozzle, powder feeder and carrier gas transported the powder stream through a nylon hose to a splitter, which split the powder into four streams. During cladding experiments focal position of the beam was above the base material and inside the coaxial nozzle resulting in spot diameters of 1.8–4.5 mm at the surface of base material. The processing head and the laser beam were kept at 90° in relation to base material surface. They were manipulated with Fanuc S-700 six-axis robot system with a capacity of 30 kg payload at wrist.

Since the laser cladding experiments were conducted out of focus, the resulting intensity distribution in beam cross-section measured with a Primes beam analyser based on hollow needle technique was not exactly “top-hat” but more like Gaussian as shown in Figure 11. According to 86% rule, diameter of the beam was 1.8 mm in this case.

2.1.2 Direct HPDL

HPDL cladding experiments were carried out using 6 kW Rofin-Sinar DL060H2 direct diode laser, which was mounted on KUKA KR 125 six-axis robot system with a capacity of 125 kg payload at wrist. Diode laser was equipped with optics, which had the focal length of 461 mm. In order to get the highest possible power density (W/mm^2), the rectangular shape of the delivering beam was focused to a spot size of 22 x 5 mm^2. To achieve a maximum 6 kW laser power it was operated with wavelengths of 808 (3100W) and 940 nm (2850W). Consequently, the maximum power density available with this configuration was ~55 W/mm^2. This was clearly lower than power densities used in Nd:YAG experiments (190–390 W/mm^2). Figure 12 displays the intensity distribution and dimensions of the rectangular beam in focus. Intensity profile was “top-hat” along the slow axis and Gaussian along the fast axis.

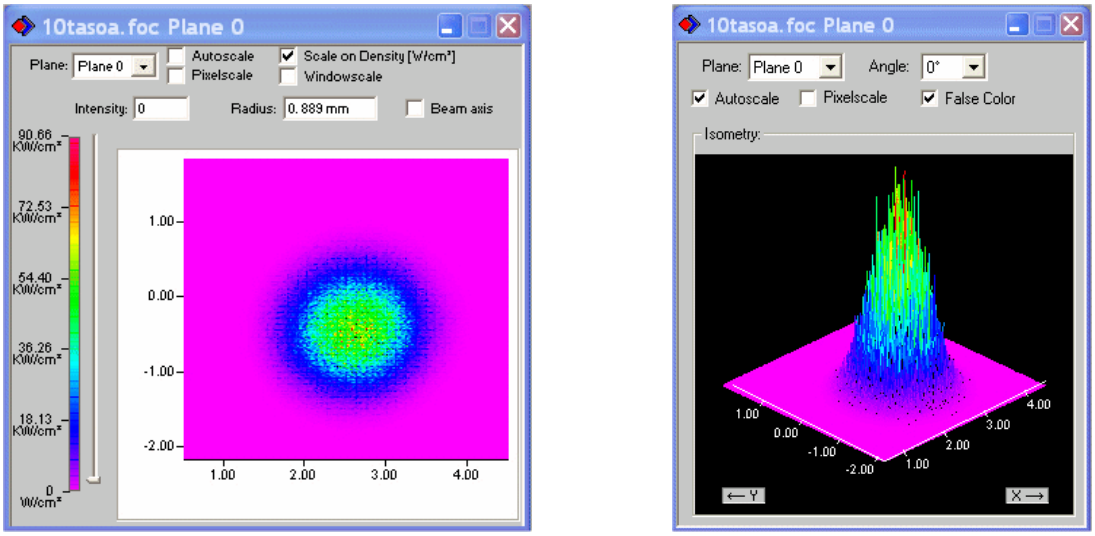

a) b)

Figure 11. Intensity distribution of Nd:YAG laser beam measured at plane 13 mm below the nozzle tip; a) plane and b) spatial distribution.

Two types of powder feeding nozzles were applied; off-axis and coaxial type. Off-axis nozzle (DLR Stuttgart, Germany) consisted of a cyclone and two concentric flat nozzles. In the cyclone carrier gas and powder particles were partly separated after which they fell more or less gravitationally to the flat nozzle, where the powder stream was spread to a width of the larger dimension of the beam spot (slow axis). The nozzle was positioned at an angle of 60 degrees with respect to the surface of base material. The tip of the nozzle was located at a distance of 30 mm from the base material. The shielding gas shrouded the powder stream in order to protect the powder particles and melt pool from oxidation and to obtain more focused powder stream in direction, which corresponded to the narrower dimension of the beam spot (fast axis). Experimental setup for off-axis nozzle configuration is shown in Figure 13. Coaxial type powder feeding nozzle (Fraunhofer IWS, Dresden, Germany) consisted of water jacket, two opposite rectangular powder channels and large rectangular channel in the centre for shielding gas and laser beam as illustrated in Figure 14. Powder channels injected the powder stream at an angle of 65 degrees with respect to the surface of base material. The nozzle was positioned at a distance of 15 mm from the base material.

In order to produce constant transport of powder for both cladding processes, Medicoat Duo (Medicoat AG, Mägenwil, Switzerland) disc type powder feeder equipped with two hoppers and type 5850S mass flow controllers by Brooks Instrument (Brooks Instrument, Hatfield, USA) was used. They were calibrated for argon (Ar) and nitrogen (N_2). Ar (ρ = 1.78 kg/m^3), which is heavier than N_2 (ρ = 1.25 kg/m^3), was used in these experiments as carrier and shielding gases, because it has higher viscosity (better for carrying particles), enthalpy of ionization (less likely to form plasma) and it is more inert than N_2 (no nitrides). In YAG cladding with Coax 8 nozzle carrier and shielding gas flow rates were 6 and 15 l/min, respectively. In HPDL cladding with off-axis nozzle carrier and shielding gas flow rates were 6 and 26-50 l/min, respectively. In HPDL cladding with coaxial type nozzle carrier and shielding gas flow rates were 6 and 50 l/min, respectively. Powder deliveries with respect to laser beam were aligned with the help of oxidized spot shoot by the lasers in pulsed mode.

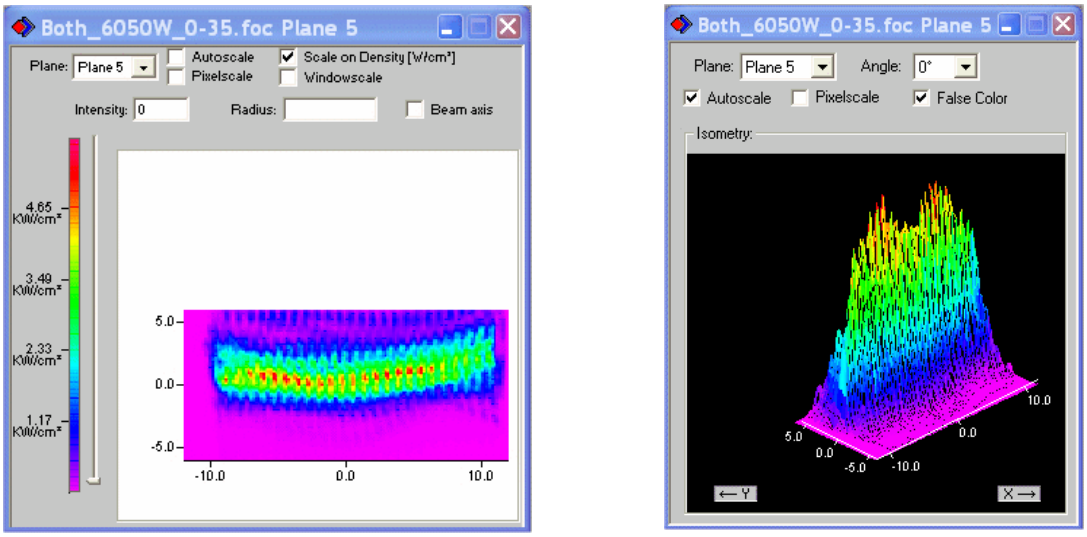

a) b)

Figure 12. Intensity distribution of HPDL laser beam measured at focal plane; a) plane and b) spatial distribution.

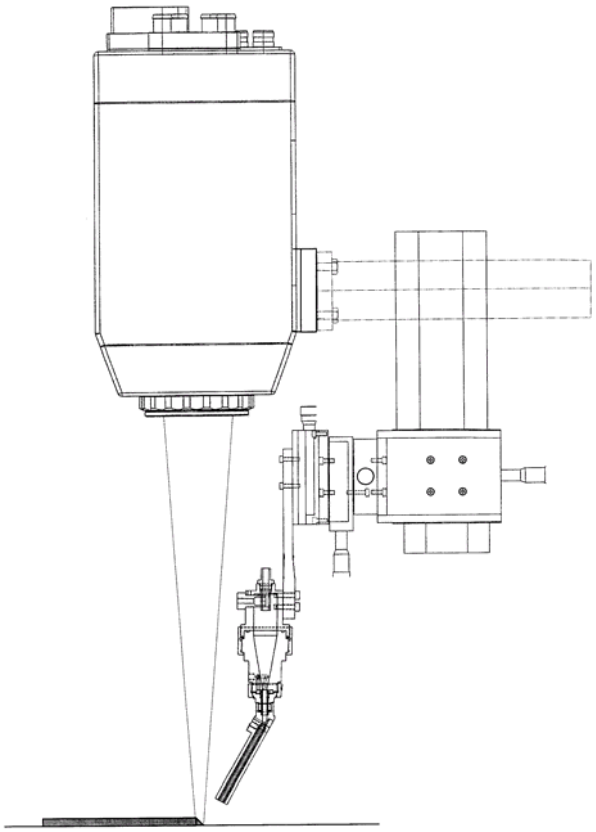

Figure 13. Experimental setup of off-axis HPDL cladding process.

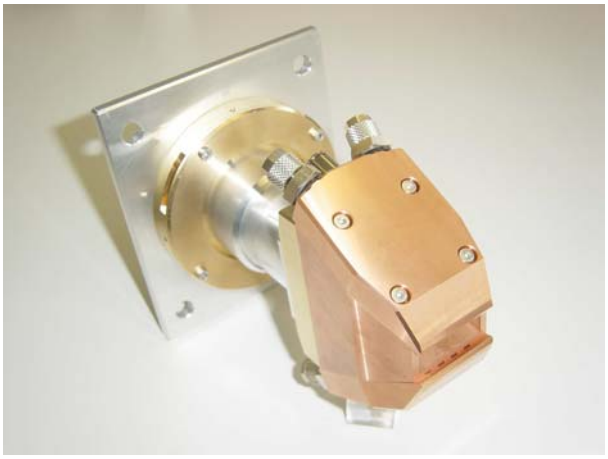

Figure 14. Coax 11 coaxial type powder feeding nozzle (Fraunhofer IWS) for diode laser.

2.1.2.1 Back reflection measurements

In order to study the back reflection during various HPDL cladding situations, temperature monitoring and control system built in-house in close cooperation with laser manufacturer was utilized. It consists of several temperature sensors on different locations as shown later in section 3.1. Four internal temperature sensors, type NTC, were fixed inside the laser head. They were named in this study as 808_T1, 808_T2, 940_T3 and 940_T4 according to the prisms they were fixed. Two external thermocouples, type PT100, were mounted on the bottom frame of the laser head in the vicinity of the optics. They were named as EXT-1 and EXT-2. Another external thermocouple, type PT100, was fixed to the off-axis powder nozzle. Temperature values during processing were recorded and stored by the data acquisition system written in LabVIEW software. Recording interval was 1 s.

2.2 Studied materials

This section introduces laser coating and reference materials selected for various corrosion, wear, residual stress and thermal fatigue studies.

2.2.1 Wet corrosion

Laser coatings studied in wet corrosion tests included Ni-based Inconel 625, Alloy 59, Cr-based SX-717 and Co-based Stellites 21 and 6. Reference materials consisted of wrought Inconel 625, 316L, martensitic SS (EN 1.4731) and Ti grade 2. Inconel 625 and Stellite 21 were also tested in PTA overlay welded and Stellite 6 in HIPped conditions. Chemical compositions and manufacturing methods are summarized in Table 5. PTA overlay welding and HIPping were carried out by the experienced industrial workshops. Process parameters for these were classified. Inconel 625 was sprayed with HVOF gun at Tampere University of Technology as will be explained in section 2.3.4.

2.2.2 Hot corrosion

Three commercial Ni- and Cr-based alloy powders were chosen for hot corrosion tests. They were produced mainly by HPDL using off-axis setup. Refence bulk alloys consisted of Inconel 625, Inconel 718, Nimonic 80A and 42CrMo4 QT steel as tabulated in table 6.

Table 5. Manufacturing methods and compositions (wt.%) of test materials exposed to wet corrosion.

Material	Condition	Ni	Cr	Mo	Nb	Fe	Si	Co	C	Mn	W	Particle size	Base material
Inconel 625[1]	HPDL	Bal.	21.5	8.9	3.8	1.2	0.5		0.01			53–150 µm	Fe52, t = 20 mm
Inconel 625[1]	PTA	Bal.	22.1	9.0	3.6	0.9	0.5		0.01			53–150 µm	Fe52, t = 30 mm
Inconel 625[1]	HVOF	Bal.	22.3	9.1	3.4	0.8	0.5		0.02			10–45 µm	Fe37, t = 10 mm
Inconel 625[1]	HVOF + laser	Bal.	22.3	9.1	3.4	0.8	0.5		0.02			10–45 µm	Fe37, t = 10 mm
Inconel 625[2]	Wrought	Bal.	22.5	9.0	3.6	3.6	0.1			0.2			
Alloy 59[1]	Nd:YAG	Bal.	23.6	15.6		0.2	0.1		0.01	0.2		45–150 µm	Fe52, t = 20 mm
Stellite 21[1]	Nd:YAG	2.8	28.3	5.3		1.0	0.9	Bal.	0.3	0.7		53–150 µm	Fe52, t = 30 mm
Stellite 21[1]	PTA	2.8	28.3	5.3		1.0	0.9	Bal.	0.3	0.7		53–150 µm	Fe52, t = 30 mm
Stellite 6[1]	Nd:YAG	1.7	28.3			1.6	1.1	Bal.	1.1		4.4	53–150 µm	Fe52, t = 20 mm
Stellite 6[2]	HIP	1.7	30.1	0.6		1.0	0.8	Bal.			5.4		
SX-717[1]	HPDL	42.5	Bal.	2.5			1.2					75–150 µm	Fe52, t = 20 mm
Austenitic SS[3]	Wrought	10.1	16.9	2.1		Bal.	0.7			1.8			AISI 316L
Martensitic SS[3]	Wrought		11	1.0		Bal.	2.1		0.4	0.6			EN 1.4731
Mild steel[3]	Wrought					Bal.							Fe37
Ti grade 2[3]	Wrought	Ti-0.08C-0.03N-0.25O-0.015H-0.3Fe (max. values)											

1) according to analysis certificate provided by the supplier
2) according to EDS area analyses
3) nominal composition

Table 6. Manufacturing methods and compositions (wt.%) of test materials exposed to hot corrosion.

Material	Condition	Ni	Cr	Mo	Nb	Fe	Si	Co	C	Mn	B	Al	Ti	Particle size	Base material
SX-707[1]	HVOF	45	Bal.	3			1							10-45 µm	42CrMo4
SX-707[1]	HPDL	45	Bal.	3			1							75-150 µm	42CrMo4
SX-717[1]	HPDL	42.5	Bal.	2.5			1				0.5			75-150 µm	42CrMo4
Inconel 625[1]	HPDL	Bal.	22	9.0	4	1	0.5			0.4				53-150 µm	42CrMo4
Inconel 625[2]	Wrought	Bal.	22.5	9.0	3.6	3.6	0.1			0.2		0.2	0.2		
Inconel 718[3]	Wrought	Bal.	19.0	3.1		17	0.4	1		0.4		0.6	0.9		
Nimonic 80A[3]	Wrought	Bal.	19.5			3	1	2	0.1	1		1.4	2.3		
42CrMo4[3]	Wrought		1	0.2		Bal.	0.2		0.4	0.7					

1) according to analysis certificate provided by the supplier
2) according to EDS area analysis
3) nominal composition

2.2.3 Abrasion wear

Several different types of commercial alloys including Co-based (solid solution strengthened, carbide and intermetallic type) hardfacing alloys, tool steels, Fe-based hardfacing alloy with ability to form amorphous and nanoscale structures from the company Nanosteel and different combinations of interstitial type hard refractory carbides (WC, WC/W_2C, VC, CrC) and metal matrices (NiCrBSi, Stellites, tool steel) were laser clad for abrasion wear tests. In addition to these, experimental type (Ti, Mo)C-based powders manufactured by SHS and recycled WC powder produced from the used hard metal by disintegrator milling were used as precursors for laser coatings. Reference materials comprised HVOF sprayed WC-CoCr coatings, sintered WC-CoCr hard metal and Ni-hard wear resistant cast iron, which are widely used in abrasive wear conditions.

Compositions of the used materials are tabulated in Table 7. Metal matrix / hard carbide combinations, ratios and hard carbide details including production method, shape, density and integrity as well as phases present are listed in Table 8. Phases present were identified by XRD method. Shape and integrity of the carbides was revealed by SEM micrographs, which

are shown in Figures 15-27. Metal matrix / hard carbide powder mixtures were prepared by weighing the desired amount of matrix and carbide powders and mixing them in plastic bottle placed in the mechanical mixer named Turbula for 3–4 hours.

HVOF coatings were sprayed with Diamond Jet Hybrid 2700 spray gun at Tampere University of Technology. The sintered hard metal was supplied by Fraunhofer Institut für Keramische Technologien und Sinterwerkstoffe (FhG-IKTS), Dresden, Germany. SHS powders were manufactured at VTT Processes, Tampere, Finland. Recycled hard metal powder was manufactured at Tallinn Technical University, Tallinn, Estonia.

Table 7. Compositions (wt.%) and manufacturing methods of abrasion wear test materials.

Material	Condition	Ni	Cr	Mo	Nb	Fe	Si	Co	C	Mn	B	W	V	Particle size
Tribaloy T-800[1]	Nd:YAG		18	28			3.4	Bal.						63-150 µm
Stellite 1[1]	Nd:YAG	1.1	30.8			1.3	1.2	Bal.	2.2			12.4		53-150 µm
Stellite 6[1]	Nd:YAG	1.7	28.3			1.6	1.1	Bal.	1.1			4.4		53-150 µm
Stellite 12[1]	Nd:YAG	1.1	28.9			1.1	1.2	Bal.	1.4			8.0		53-150 µm
Stellite 21[1]	Nd:YAG	2.8	28.3	5.3		1	0.9	Bal.	0.3	0.7				53-150 µm
Ralloy WR10[1]	Nd:YAG		12.5	1.1		Bal.	0.4		2.3	0.4			4.0	50-150 µm
Ralloy WR6[1]	Nd:YAG		5.3	1.3		Bal.			2.9				11.5	50-150 µm
Nanosteel[1]	Nd:YAG		22.6	6.6		Bal.	1.6		1.5	3.8	4.2	8.4	Zr 0.8	50-150 µm
SX-707[1]	Nd:YAG	45	Bal.	3			1							75-150 µm
Inconel 718[1]	Nd:YAG	Bal.	19.9	3.1	5.3	18.6								45-120 µm
Colmonoy 42-P2[1]	Nd:YAG	Bal.	9.5			2.7	3.1		0.4		1.6			63-150 µm
Metco 12C[1]	Nd:YAG	Bal.	10			2.5	2.5		0.15					45-125 µm
Metco16C[1]	Nd:YAG	Bal.	15.8	2.3		3.3	4.4		0.50		4.0			45-125 µm
Diamalloy 2001[1]	Nd:YAG	Bal.	17.0			4.0	4.0		1.0		3.5			45-125 µm
Amperit522.2[1]	Nd:YAG							11.2	5.7			Bal.		44-88 µm
Amperit522.3[1]	Nd:YAG							11.1	5.5			Bal.		5-44 µm
WOKA 9604[1]	Nd:YAG								4.0			Bal.		38-72 µm
Durmat SFTC[1]	Nd:YAG								3.8			Bal.		45-90 µm
Durum FTC[1]	Nd:YAG								3.9			Bal.		63-90 µm
Durmat VC[1]	Nd:YAG								8.2				Bal.	45-106 µm
SHS 1377[2]	Nd:YAG	(Ti, Mo)C – Ni (50/50 wt.%)												45-125 µm
SHS 1378[2]	Nd:YAG	(Ti, Mo)C – Stellite 6 (50/50 wt.%)												45-125 µm
SHS 1380[2]	Nd:YAG	(Ti, Mo)C – Ni (35/65 wt.%)												45-125 µm
SHS 1389[2]	Nd:YAG	(Ti, Mo)C – Stellite 6 (20/80 wt.%)												45-125 µm
SHS 1436[2]	Nd:YAG	(Ti, Mo)C – Colmonoy 42-P2 (50/50 wt.%)												45-125 µm
Metco 31C-NS[1]	Nd:YAG	Bal.	16			3.3	3.9		0.9		2.9			45-125 µm
								12.7	5.5			Bal.		45-125 µm
Metco 70C-NS	Nd:YAG	chromium carbide												30-106 µm
Recycled WC[2]	Nd:YAG	WC-14Co-8Fe (Instead of Fe, Ti was detected in binder by EDS)												45-125 µm
Ni-hard	Cast	wear resistant cast iron (FeNiCrMnSiC)												
Austenitic SS[3]	Wrought	10.1	16.9	2.1		Bal.	0.7			1.8				AISI 316L
Mild steel[3]	Wrought													Fe37
Amperit 559.074[1]	HVOF		8.1					5.9	5.5			Bal.		
Amdry 5843[1]	HVOF		4.2					10.3	5.2			Bal.		
WC-6Co-8Cr[2]	Sintered	sintered WC-6Co-8Cr												

1) according to analysis certificate provided by the supplier
2) according to supplier
3) nominal composition

Besides comparing the abrasion wear resistance of different types of laser coatings (Co-based hardfacing alloys, tool steels, WC-NiCrBSi, WC-CoCr, CrC-NiCrBSi, CrC-CoCr and (Ti, Mo)C SHS) between themselves and how their resistance relate to the reference materials, several other things can be compared. Influence of carbide size can be studied by comparing the wear behaviour of the following coatings: 1) Metco 16C + Amperit 522.2 (50/50 vol.%) 44-88 µm vs. Metco 16C + Amperit 522.3 (50/50 vol.%) 5-44 µm and 2) Stellite 21 + Amperit 522.2 (50/50 vol.%) 44-88 µm vs. Stellite 21 + Amperit 522.3 (50/50 vol.%) 5-44 µm.

Table 8. MMC powder combinations, ratios and hard particulate details.

Powder	*Wt.%*	*Vol. %*	*Carbide type*	*Integrity*	*Shape*	*Phases*	*Density (g/cm³)*	*Carbide size*
NiCrBSi + WC/Co (Metco 31C-NS)	63/35	~78/22	agglomerated	porous	spherical	WC	14.4[1]	45-125 µm powder < 15 µm angular carbides
NiCrBSi + WC (Diamalloy 2001 + Durum WC FTC)	31/69	~50/50	fused & crushed	dense	angular	WC, W_2C (46/54)	16.6[2]	63-90 µm
NiCrBSi + WC/Co (Metco 12C + Amperit 522.2)	55/45	~70/30	dense-coated	dense	roundish	WC	14.6[1]	44-88 µm
NiCrBSi + WC/Co (Metco 16C + Amperit 522.2)	34/66	~50/50	dense-coated	dense	roundish	WC	14.6[1]	44-88 µm
NiCrBSi + WC/Co (Metco 16C + Amperit 522.3)	34/66	~50/50	dense-coated	dense	roundish	WC	14.6[1]	5-44 µm
NiCrBSi + WC/Co (Colmonoy 42-P2 + Amperit 522.3)	15/85	~25/75	dense-coated	dense	roundish	WC	14.6[1]	5-44 µm
NiCrBSi + WC (Metco 12C + Durmat SFTC)	51/49	~70/30	fused	dense	spherical	WC, W_2C, W (40/60)	16.6[3]	45-90 µm
NiCrBSi + WC (Metco 12C + Woka 9604)	51/49	~70/30	fused & crushed	dense	angular	WC, W_2C (43/57)	16.6[2]	38-72 µm
NiCrBSi + WC Metco 16C + recycled WC	57/43	~70/30	milled, sintered & crushed	dense	angular	WC	13.3[1]	45-125 µm powder < 5 µm angular carbides
CoCrMoNi + WC/Co (Stellite 21 + Amperit 522.2)	36/64	~50/50	dense-coated	dense	roundish	WC	14.6[1]	44-88 µm
CoCrMoNi + WC/Co (Stellite 21 + Amperit 522.3)	36/64	~50/50	dense-coated	dense	roundish	WC	14.6[1]	5-44 µm
NiCrBSi + CrC(Metco 16C + Metco 70C-NS)	72/28	~70/30	sintered & crushed	dense	angular	Cr_3C_2, Cr_7C_3, $Cr_{23}C_6$	6.7	30-106 µm
CoCrWC + CrC Stellite 6 + Metco 70C-NS	70/30	~65/35	sintered & crushed	dense	angular	Cr_3C_2, Cr_7C_3, $Cr_{23}C_6$	6.7	30-106 µm
FeCrVMoC + VC Ralloy WR6 + Durmat VC	75/25	~70/30	N/A	porous	roundish	V_4C_3, V_8C_7, $VC_{0.88}/V_{32}C_{28}$	5.7	45–106 µm
Ni + (Ti, Mo)C Nickel + (Ti, Mo)C SHS 1380	65/35	~50/50	SHS	dense	angular	(Ti, Mo)C	4.9[4]	45-125 µm powder < 3 µm square carbides
Ni + (Ti, Mo)C Nickel + (Ti, Mo)C SHS 1377	50/50	~35/65	SHS	dense	angular	(Ti, Mo)C	4.9[4]	45-125 µm powder < 3 µm square carbides
CoCrWC + (Ti, Mo)C Stellite 6 + (Ti, Mo)C SHS 1389	80/20	~70/30	SHS	dense	angular	(Ti, Mo)C	4.9[4]	45-125 µm powder < 2 µm roundish carbides
CoCrWC + (Ti, Mo)C Stellite 6 + (Ti, Mo)C SHS 1378	50/50	~37/63	SHS	dense	angular	(Ti, Mo)C	4.9[4]	45-125 µm powder < 2 µm roundish carbides
NiCrBSi + (Ti, Mo)C SHS 1436 Colmonoy 42-P2 + (Ti, Mo)C	50/50	~40/60	SHS	dense	angular	(Ti, Mo)C	4.9[4]	45-125 µm powder < 2 µm roundish carbides

1) calculated on the basis of volume fraction of WC and binder
2) calculated on the basis of WC/W_2C volume fraction, which was calculated from the integrated areas of peaks WC $\left(10\bar{1}1\right)$ vs. W_2C $\left(10\bar{1}1\right)$ and WC $\left(11\bar{2}0\right)$ vs. W_2C $\left(11\bar{2}0\right)$
3) calculated on the basis of WC/W_2C volume fraction, which was calculated from the integrated areas of peaks WC $\left(10\bar{1}1\right)$ vs. W_2C $\left(10\bar{1}1\right)$ and WC $\left(11\bar{2}0\right)$ vs. W_2C $\left(11\bar{2}0\right)$. W was neglected.
4) 4.9 g/cm^3 is value for TiC. It gives too high value for carbide in volume fraction calculations since (Ti, Mo)C is denser than TiC

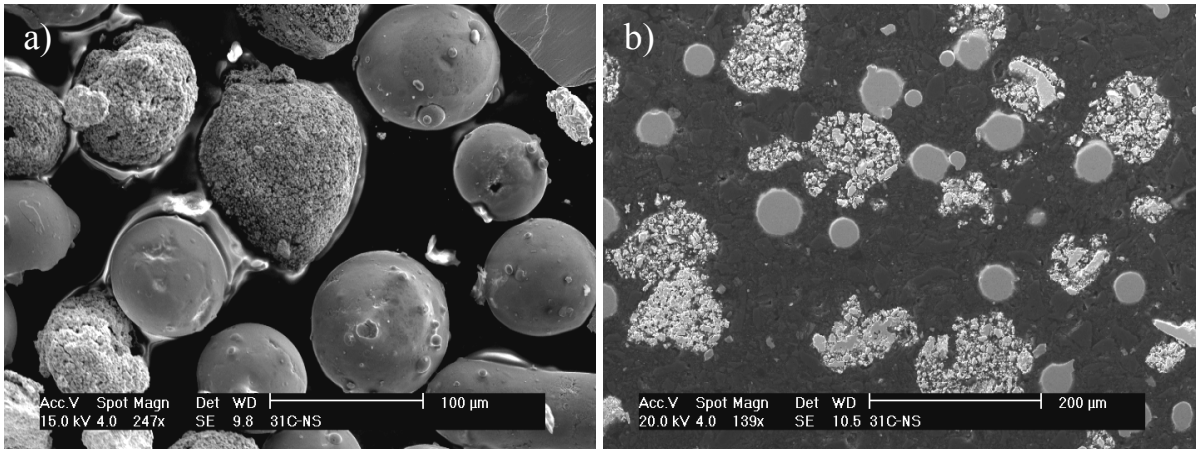

Figure 15. Metco 31C-NS powder blend: a) morphology and b) cross-section. This powder is a mechanical blend of gas atomized NiCrBSi (spherical dense particles) and small WC particulates agglomerated with Co binder (spherical porous particles).

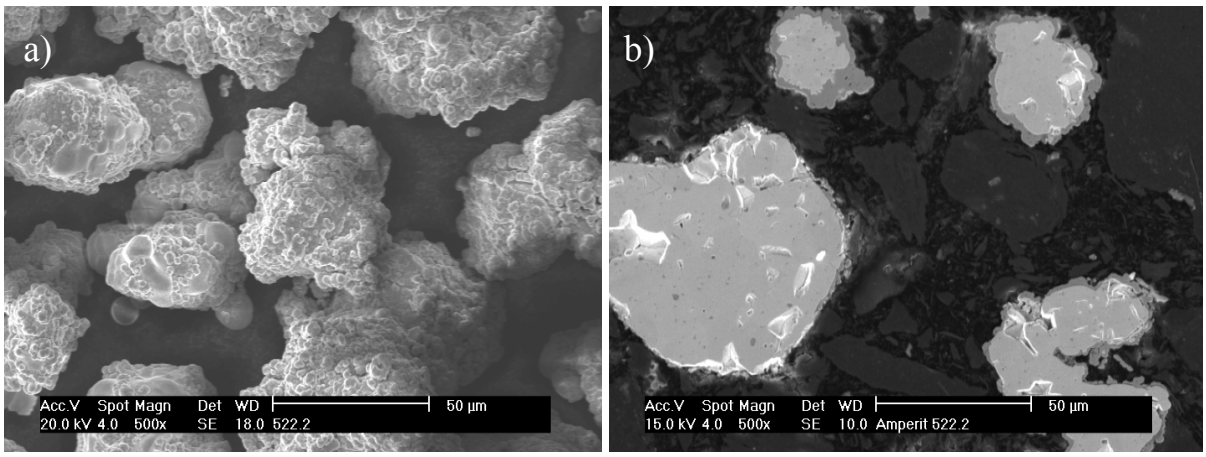

Figure 16. Amperit 522.2 WC/Co dense-coated powder: a) morphology and b) cross-section. Co coating around WC is clearly seen in cross-section image.

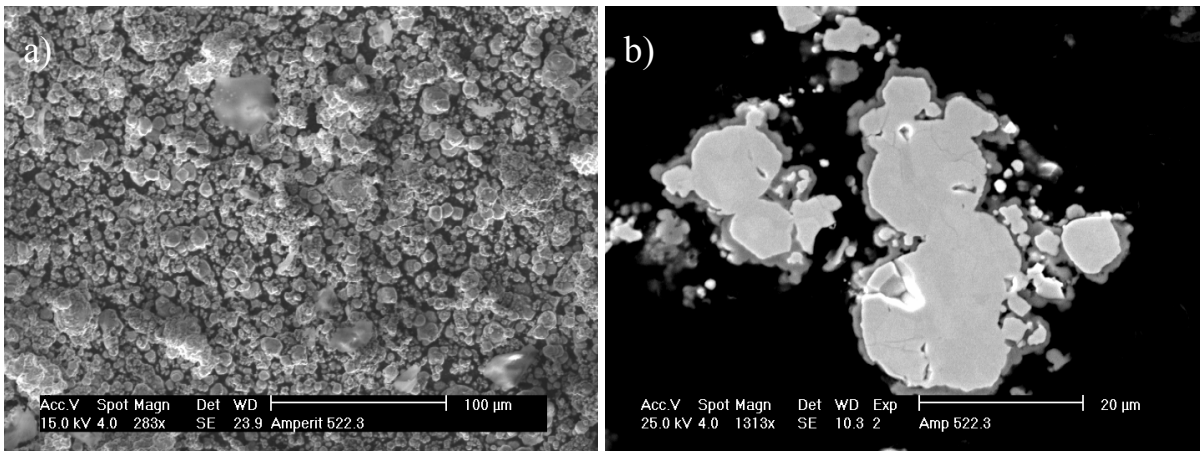

Figure 17. Amperit 522.3 WC/Co dense-coated powder: a) morphology and b) cross-section. Co coating around WC is clearly seen in cross-section image.

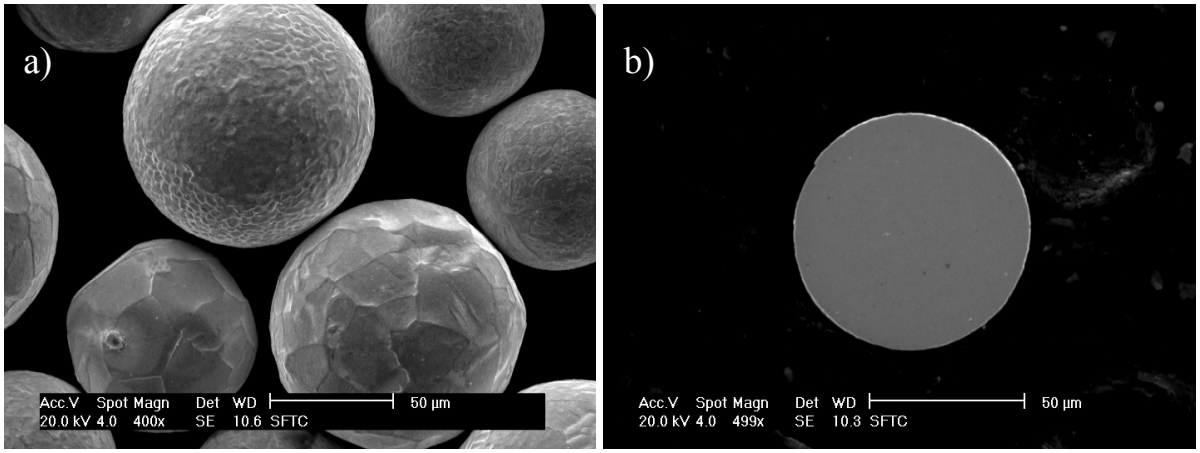

Figure 18. SFTC WC/W_2C/W powder: a) morphology and b) cross-section.

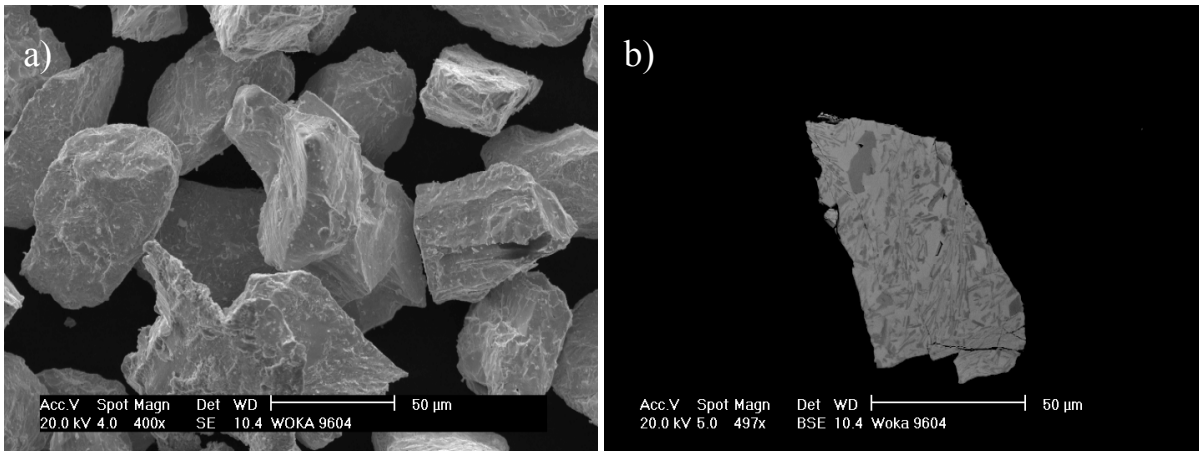

Figure 19. WOKA 9604 WC/W_2C powder: a) morphology and b) cross-section. Microstructure consists of WC needles in W_2C matrix. This powder is nearly identical to Durmat FTC WC/W_2C powder.

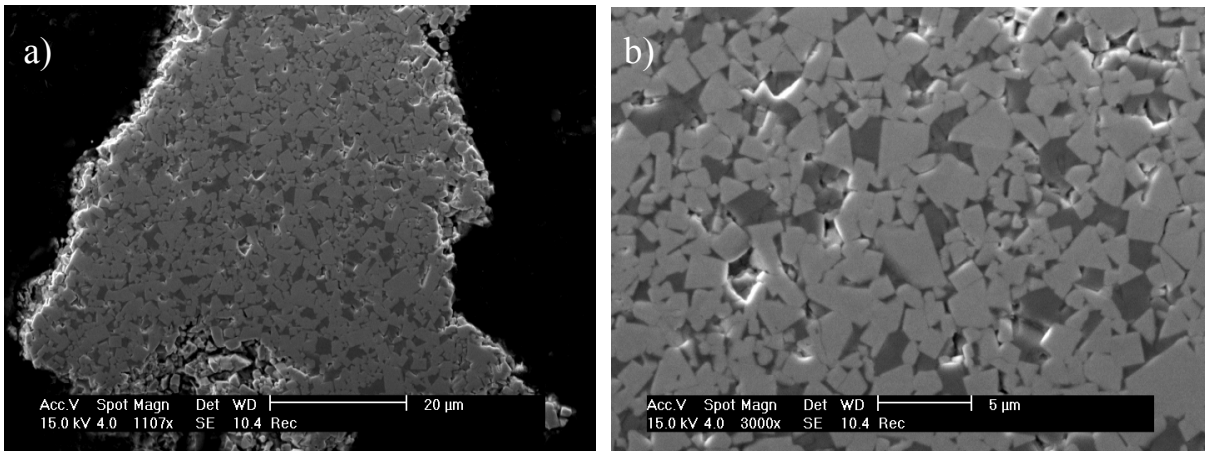

Figure 20. Recycled WC-14Co-8Fe powder: a) lower and b) higher magnification cross-section. According to EDS analysis taken from the cross-section binder consists of Co and Ti. Fe was not detected.

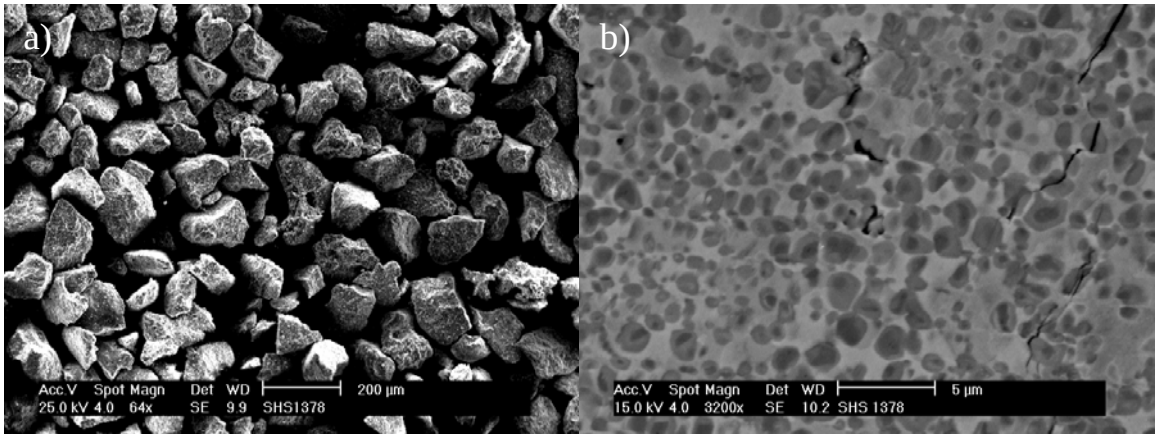

Figure 21. SHS 1378 powder (Ti, Mo)C – Stellite 6 (50/50 wt.%): a) morphology and b) cross-section. Dark phases are (Ti, Mo)C. They are round in shape. Diameter of (Ti, Mo)C phases vary between 0.5–1.8 µm.

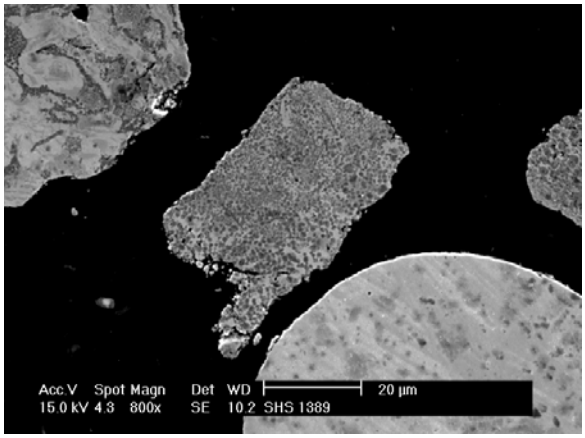

Figure 22. SHS 1389 powder (Ti, Mo)C – Stellite 6 (20/80 wt.%); cross-section. This powder is a mechanical blend of SHS 1378 (angular particles) and gas atomized Stellite 6 (spherical particles).

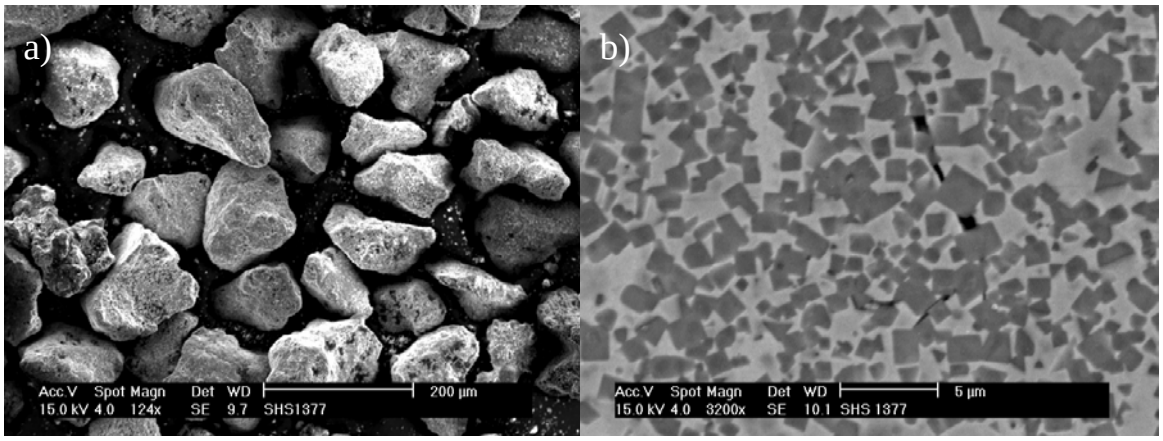

Figure 23. SHS 1377 powder (Ti, Mo)C – Ni (50/50 wt.%): a) morphology and b) cross-section. Dark phases are (Ti, Mo)C. They are rectangular or square in shape. Diagonal of rectangles vary between 0.5–2.8 µm. According to image analysis volume fraction of (Ti, Mo)C is approximately 57%.

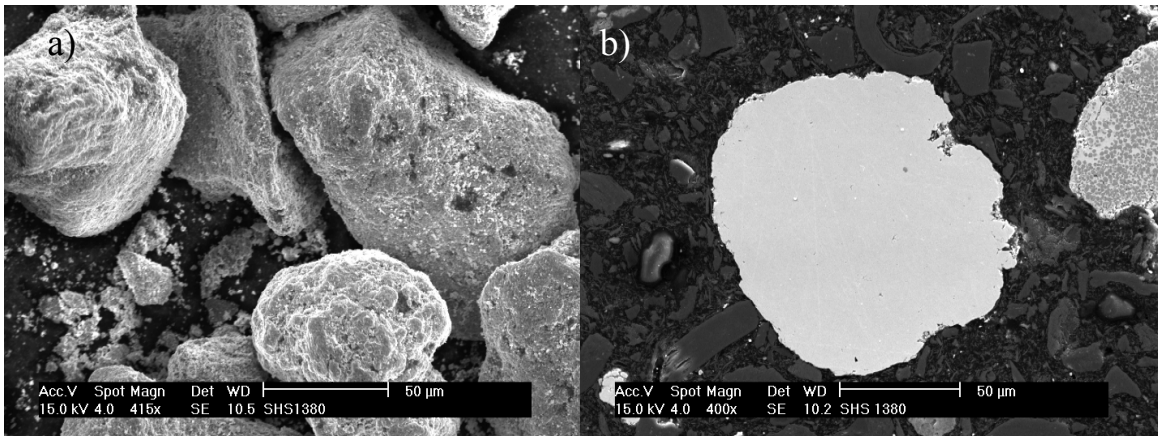

Figure 24. SHS 1380 powder (Ti, Mo)C – Ni (35/65 wt.%): a) morphology and b) cross-section. This powder is a mechanical blend of SHS 1377 and Ni.

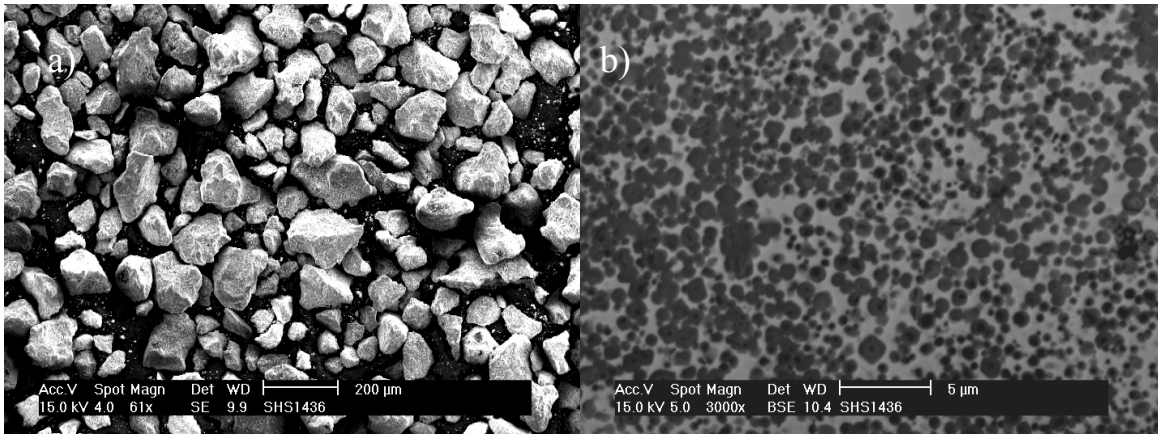

Figure 25. SHS 1436 powder (Ti, Mo)C – NiCrBSi (50/50 wt.%): a) morphology and b) cross-section.

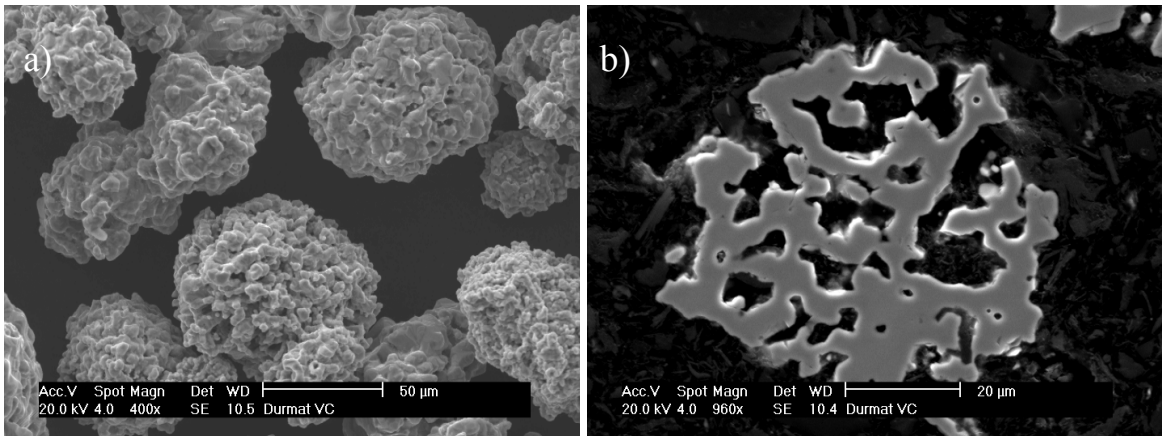

Figure 26. Durmat VC powder: a) morphology and b) cross-section.

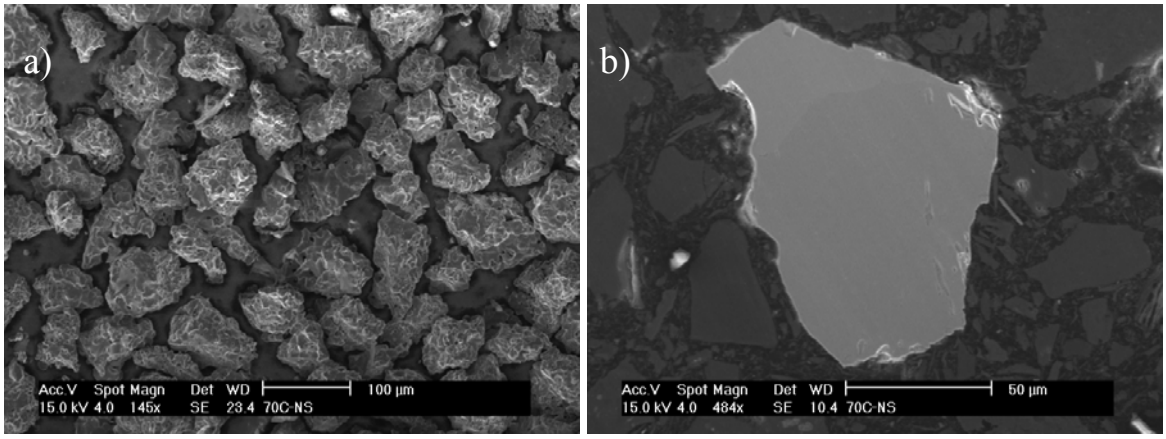

Figure 27. Metco 70C-NS CrC powder: a) morphology and b) cross-section.

Influence of matrix material can be studied by comparing the wear behaviour of the following coatings: 1) Metco 16C + Amperit 522.3 (50/50 vol.%) 5-44 µm vs. Stellite 21 + Amperit 522.3 (50/50 vol.%) 5-44 µm; 2) Metco 16C + Amperit 522.2 (50/50 vol.%) 44-88 µm vs. Stellite 21 + Amperit 522.2 (50/50 vol.%) 44-88 µm.

Influence of carbide morphology can be studied by comparing the wear behaviour of the following coatings: 1) Metco 12C + Amperit 522.2 (70/30 vol.%) 44-88 µm vs. Metco 12C + Durmat SFTC (70/30 vol.%) 45-90 µm vs. Metco 12C + Woka 9604 (70/30 vol.%) 38-72 µm.

Influence of carbide dissolution can be studied by comparing the wear behaviour of the following coatings: 1) Colmonoy 42-P2 + Amperit 522.3 (25/75 vol.%) 5-44 µm low laser power vs. Colmonoy 42-P2 + Amperit 522.3 (25/75 vol.%) 5-44 µm high laser power and 2) Metco 16C + recycled WC (70/30 vol.%) 45-125 µm low laser power vs. Metco 16C + recycled WC (70/30 vol.%) 45-125 µm low laser power.

Influence of carbide volume fraction can be studied by comparing the wear behaviour of the following coatings: 1) SHS 1378 vs. SHS 1389 and 2) SHS 1377 vs. SHS 1380.

2.2.4 Sliding wear

Similar to abrasion wear studies, several different types of Co-based hardfacing alloys including solid solution strengthened, carbide (hypo- and hypereutectic) and intermetallic type grades as well as Fe-based hardfacing alloy from the company Nanosteel were selected for sliding wear tests. Co-based hardfacing alloys of Stellite 21 and T-800 were also overlay welded with PTA method. Additionally, hypoeutectic carbide type Stellite 6 was manufactured with HIP process. Among experimental type materials, laser coatings were prepared from the selected SHS powders shown together with other alloys in Table 9.

2.2.5 Residual stresses

Co-based solid solution strengthened Stellite 21 and intermetallic type Tribaloy T-800 was chosen for residual stress measurements. They were laser clad on mild, martensitic and austenitic stainless steels, which all differ in their CTEs. Martensitic (EN 1.4731) and austenitic (21-12N) grades are typical valve materials used in combustion engines. Chemical compositions and CTEs of materials are listed Table 10.

Table 9. Manufacturing methods and compositions (wt.%) of sliding wear test materials.

Material	Condition	Ni	Cr	Mo	Nb	Fe	Si	Co	C	Mn	B	W	Particle size
T-800[1]	Nd:YAG		18	28			3.4	Bal.					63-150 µm
T-800[1]	PTA		18	28			3.4	Bal.					63-150 µm
T-400[1]	Nd:YAG		9.6	29.4			2.8	Bal.					63-150 µm
Stellite 1[1]	Nd:YAG	1.1	30.8			1.3	1.2	Bal.	2.2			12.4	53-150 µm
Stellite 6[1]	Nd:YAG	1.7	28.3			1.6	1.1	Bal.	1.1			4.4	53-150 µm
Stellite 6[2]	HIP	1.7	30.1	0.6		1.0	0.8	Bal.				5.4	bulk
Stellite 21[1]	Nd:YAG	2.8	28.3	5.3		1	0.9	Bal.	0.3	0.7			53-150 µm
Stellite 21[1]	PTA	2.8	28.3	5.3		1	0.9	Bal.	0.3	0.7			53-150 µm
Nanosteel[1]	Nd:YAG		22.6	6.6		Bal.	1.6		1.5	3.8	4.2	8.4 + Zr 0.8	50-150 µm
(TiC,Mo)-St 6[3]	Nd:YAG	(Ti, Mo)C – Stellite 6 (20/80 wt.%)											45-125 µm
(TiC,Mo)-St 6[3]	Nd:YAG	(Ti, Mo)C – Stellite 6 (50/50 wt.%)											45-125 µm
(TiC,Mo)-Ni[3]	Nd:YAG	(Ti, Mo)C – Ni (35/65 wt.%)											45-125 µm

1) according to analysis certificate provided by the supplier
2) according to EDS area analysis
3) according to data provided by the supplier

Table 10. Chemical compositions (in wt.%) and CTEs of residual stress test materials. For Stellite 21 and T-800 compositions are according to certificate provided by the powder supplier. For base materials values are nominal compositions.

Material	Ni	Cr	Mo	Fe	Si	Co	C	Mn	Particle/ Base material size	CTE ($1/K \times 10^{-6}$)
Stellite 21	2.8	28.3	5.3	1.0	0.9	Bal.	0.3	0.7	53–150 µm	14.2 (20-600°C)[1]
T-800		18	28		3.4	Bal.			63–150 µm	12.6 (20-500°C)[2]
Fe52				Bal.	0.5		0.2	1.6	100 x 60 x 20 mm^3	12.7 (20-500°C)[1]
Aust. SS	11	21.5		Bal.	1.0		0.2	1.3	$Ø_d = 46$, $t_b = 20$ mm	16.7 (20-600°C)[3]
Mart. SS		11		Bal.	2.2		0.4	0.6	$Ø_d = 33$, $t_b = 20$ mm	12.1 (20-600°C)[3]

1) according to Ref. [372]
2) according to Ref. [373]
3) according to data provided by the supplier

2.2.6 Thermal fatigue

Ni-based Inconel 625, Cr-based SX-717 as well as intermetallic type Co-based Tribaloy T-800 are alloys, which are frequently used at high temperatures. They were laser clad on mild and/or austenitic stainless steels (21-12N) and submitted to low-cycle thermal fatigue tests. Chemical compositions of powders and base materials are shown in Table 11. According to Tobe et al. [374] CTEs for SX-717 and Inconel 625 at 100°C are 11.7 and 13.8 x 10^{-6} K^{-1}, respectively. CTEs for base materials were shown in Table 10.

2.3 Coating characterisation

Material characterization devices and methods are described in the following sections.

2.3.1 Microscopy

Optical microscopy (OM) with magnification range of 5–100X was used in the examination of polished and polished and etched microstructures. Two systems were used; Versamet 3 (Union Co., Japan) and Leica DM 2500 M (Leica Microsystems, Switzerland). Resolutions for OM pictures were 2048 x 1536 Pixels. Scanning electron microscopy (SEM/ESEM,

Model XL-30, Philips, Eindhoven, Netherlands) was used both in secondary (SE) and back-scattered elecron (BSE) modes with higher magnifications (20–10000X). Resolutions for SEM pictures were 712 x 532 Pixels. Energy dispersive spectrometer (EDS, Model DX-4, EDAX International, New Jersey, USA) was used in qualitative and quantitative elemental analyses. The EDS detector was equipped with a thin polymer window for the detection of light elements ($Z \geq 5$) including carbon ($Z = 6$) and oxygen ($Z = 8$). Quantitative chemical analyses were conducted in semi-quantitative standardless manner.

Table 11. Chemical compositions (in wt.%) of thermal fatigue test materials. For Inconel 625, SX-717 and T-800 powders compositions are according to certificate provided by the supplier. For base materials values are nominal compositions.

Material	Ni	Cr	Mo	Nb	Fe	Si	Co	C	Mn	Particle/Base material size
Inconel 625	Bal.	21.5	8.9	3.8	1.2	0.5		0.01		53–150 µm
SX-717	42.5	Bal.	2.5			1.2				75–150 µm
T-800		18	28			3.4	Bal.			63–150 µm
Fe52					Bal.	0.5		0.2	1.6	$Ø_d$ = 44 mm, t_b = 20 mm
Aust. SS	11	21.5			Bal.	1.0		0.2	1.3	$Ø_d$ = 46 mm, t_b = 20 mm

2.3.2 X-ray diffraction

In order to reveal crystal structures and phases present in studied materials, X-ray diffractometer (Siemens D500, Karlsruhe, Germany) was used at a scanning rate of 1°/min (step size 0.02°, step time 1.2-2.4 s) using monochromatic Cu K_α radiation at 40 kV and current of 30 mA. The scanning angle 2θ covered a range of 10/20–80°.

2.3.3 Microhardness

Vickers microhardness measurements were carried out with Shimadzu (Shimadzu, Kioto, Japan) and Matsuzawa MMT-X7 microhardness testers using indentation loads of 300 and 1000 g.

2.3.4 Wet corrosion

In order to study the corrosion properties, find out corrosion mechanisms and test the suitability of coatings as corrosion barriers, wet corrosion tests were performed. They consisted of open circuit potential (OCP) and potentiodynamic cyclic polarization measurements. In OCP measurements the surface of the sample was exposed to 3.5 wt.% NaCl solution (0.6 M NaCl) at RT for 7 days. Solution was prepared using analytical grade NaCl (Oriola Oy, Espoo, Finland) and tap water. Solution was not aerated or de-aerated before or during the test. During the exposure, OCP of the coating/base material system or wrought alloy was measured as a function of time with respect to Ag/AgCl (+0.207 V vs. SHE) reference electrode (Schott Geräte GmbH Model B2820; 3M KCl) using high internal resistance voltmeter (Fluke 79, >10 MΩ) in order to avoid changing the potential of the working electrode during the potential measurement. The first OCP value was measured after 1 min, the second after 20 min, the third after 1 h of exposure and the rest in every 24th hour. The surface area of the coating exposed to the electrolyte was approximately 3.5 cm^2. Exposure area was positioned so that it covered the overlapping areas between adjacent tracks even in HPDL clad coatings where the inter-track advance was 15 mm. The exposed area was restricted by plastic tube, which was glued to the surface of the sample and filled with the NaCl solution so that the solution volume to specimen area ratio was approximately 0.14 ml/mm^2. Other end of the tube was kept closed during the test in order to prevent the evaporation of the solution, which was not replenished or changed during the test time. This

rather simple “zero-current” test is widely used among coating researchers to reveal if there is any connection between the electrolyte and the base material through the coating assuming that there is clear potential difference between coating and base material alone.

Potentiodynamic cyclic polarisation measurements were performed in 3.5 wt.% NaCl solution at RT using CMS 100 Electrochemical Measurement System (Gamry Instruments Inc., Warminster, USA), which consists of computer-controlled potentiostat (PC4) and software. Solution was prepared again using analytical grade NaCl and tap water and it was not aerated or de-aerated before or during the test. Three-electrode electrochemical cell was EG&G PARC Model K0235 flat cell (Figure 28) in which a 1 cm^2 area of flat coating surface was exposed to the NaCl solution (initial pH ~7). It consists of a glass cylinder horizontally sandwiched between two flat blocks. One block had a circular opening of 11 mm in diameter against which the studied coating surface was pressed. The point of contact between corrosion cell and coating surface was sealed with a knife-edged Teflon (PTFE) gasket, which is more likely to promote crevice corrosion than for example elastomer-type gaskets or so called Avesta corrosion cell configuration, which is used when crevice conditions need to be fully eliminated. It should be, however, emphasized that the cell used here was not true crevice corrosion cell. The potentials were measured with respect to the Ag/AgCl (+0.207 V vs. SHE) reference electrode (Schott Geräte GmbH Model B2820; 3M KCl), which was connected to the sample through a salt bridge. The coating samples were finished by wet grinding using ANSI 1200 grit SiC paper (P4000). Right after the grinding and rinsing in ethanol, prepared sample was mounted to a cell and exposed to the electrolyte. After 60 minutes exposure in the electrolyte, the potential was started to increase at a rate of 0.5 mV/s from –800 mV. The scanning direction was reversed when +1000 mV was reached. A platinum electrode was used as a counter electrode for current measurement. The corrosion current densities (I_{corr}) were extracted using the linear polarization and Tafel extrapolation methods with the aid of Gamry Echem Analyst software. Also in this test, the exposed area included overlapped regions. Five measurements were done per sample. After each measurement sample was prepared again by wet grinding. Exposed surfaces were finally studied with SEM.

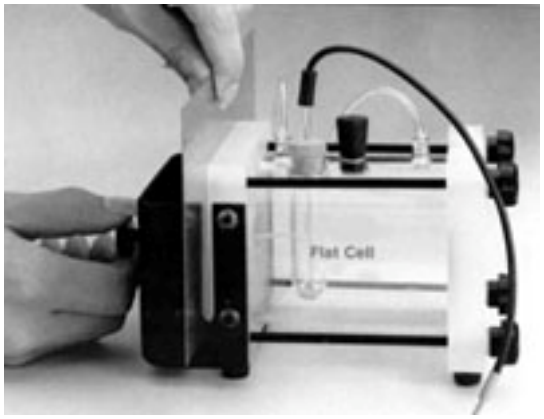

Figure 28. EG&G PARC Model K0235 flat specimen cell.

OCP measurements were conducted exclusively to Inconel 625 materials. Laser coatings were produced with HPDL using off-axis setup described earlier. Laser cladding parameters were 6 kW, 400 mm/min and 113 g/min. Inter-track advance was 15 mm. HVOF sprayed coating was produced with Diamond Jet Hybrid 2700 (Sulzer-Metco, Wohlen, Switzerland) spray gun with following parameters; oxygen 150 $L.min^{-1}$, propane 70 $L.min^{-1}$, air 360 $L.min^{-1}$, nitrogen

13 L.min^{-1}, powder feed rate 60 g/min, spraying distance 230 mm, surface speed 100 m/min and advance per revolution 5 mm/r. These parameters were recommended by the manufacturer of the spray gun. Remelting of the HVOF sprayed coating was conducted with Nd:YAG laser equipped with hardening optics where integrating mirror focused the beam to a spot size of 10 x 8 mm^2. Remelting parameters were 4 kW and 1900 mm/min. Inter-track advance was 8 mm.The experienced industrial workshop supplied the PTA overlay welded coating. Weld surfacing parameters were not available.

In addition to coatings mentioned above, several other coatings were tested in cyclic potentiodynamic polarization tests. In order to study the influence of dilution, Inconel 625 HPDL coatings were prepared also with powder feed rates of 104 and 77 g/min while keeping other parameters constant. All the other laser coatings, except SX-717 (HPDL), were produced with Nd:YAG laser equipped Coaxial 8 cladding nozzle as described earlier. Following parameters were used: Alloy 59; 3 kW, 1000 mm/min, 27 g/min, 2.0 mm, D_b = 4.5 mm; Stellite 21; 3 kW, 1000 mm/min, 27 g/min, 2.5 mm, D_b = 4.5 mm and Stellite 6; 0.8 kW, 700 mm/min, 5 g/min, 1.0 mm, D_b = 1.8 mm. Parameters for reference PTA (Inconel 625, Stellite 21) and HIPped (Stellite 6) alloy were not available.

Total thickness of the as-overlay-welded PTA coating was 2.9 mm of which 2.3 mm was above and 0.6 mm below the surface of original base material. Approximately 0.7 mm was ground away before OCP and polarization measurements.

2.3.5 Hot corrosion

Within the hot corrosion studies, prepared coating and bulk specimens were covered with a controlled amount of Na_2SO_4–V_2O_5 synthetic salt (Na_2SO_4 from Merck KGaA, V_2O_5 from J. T. Baker) and placed on alumina crucibles in Lindberg/Blue M vertical tube furnace, which is shown in Figure 29. Ceramic tube, 75 mm in inner diameter and 1500 mm in length, was used as the reaction chamber. The lower end of the tube was closed. Alumina crucibles were placed on the plates constructed with three holes for the outlet passage of gas and one big hole for the central tube, which held the plates and conveyed the inlet gas downwards to the bottom of tube. The central tube was 10 mm in outer diameter and 2 mm in wall thickness. The temperature in the reaction chamber was measured by thermocouples mounted in the vicinity of alumina crucibles. Every 100 hours the mixture of Na_2SO_4–V_2O_5 in powder form and liquid ethanol (C_2H_5OH, T_v = 79°C) of approximately 100 mg at a time was added on top of specimens. This gave contamination flux rate around 0.67 mg/cm^2·h. The furnace was always cooled down before the salt addition. Inlet gas was air and it was blown to the reaction chamber along the central tube at a rate of 1 l/min during the test.

Two salt compositions were used: 1) 50Na_2SO_4-50V_2O_5 in wt.%, which was 56Na_2SO_4-44V_2O_5 in mol.%, (Na:V; 1.27) and 2) 15Na_2SO_4-85V_2O_5 in wt.%, which was 18Na_2SO_4-82V_2O_5 in mol.%, (Na:V; 0.22). According to equilibrium phase diagram shown in Figure 30 [375], they both were in molten state during the tests since the test temperatures ranged from 650 to 850°C. In order to identify the formed sodium vanadyl vanadates, the salt mixtures were kept alone at 650°C for 5 hours in stagnant air after which they were cooled slowly to RT in furnace. Further, XRD was used to determine the compounds formed. The procedure revealed the presence of NaV_6O_{15} (Na:V; 1:6, T_m = 625°C) and Na_2SO_4 in salt (Na:V; 1.27). Salt (Na:V; 0.22) formed only NaV_6O_{15}. This $Na_2O{\cdot}V_2O_4{\cdot}5V_2O_5$ sodium vanadyl vanadate, commonly known as 1.1.5 NaVV, is one of the most frequently found compounds deposited on the exhaust valves of large diesel engines burning heavy fuel [376]. As Bryers explained,

these sodium vanadyl vanadates could be formed between Na_2SO_4 and V_2O_5 by reaction [377]:

$$xNa_2SO_4 + yV_2O_5 = (Na_2O)_x \cdot yV_2O_5 + xSO_3 \quad (9)$$

The reaction in the experiment described above was apparently not finished after 5 hours at 650°C, as Na_2SO_4 was still present in salt (Na:V; 1.27). EDS analyses taken from the salt (Na:V; 0.22) confirmed that sulphur reacted fully into SO_3.

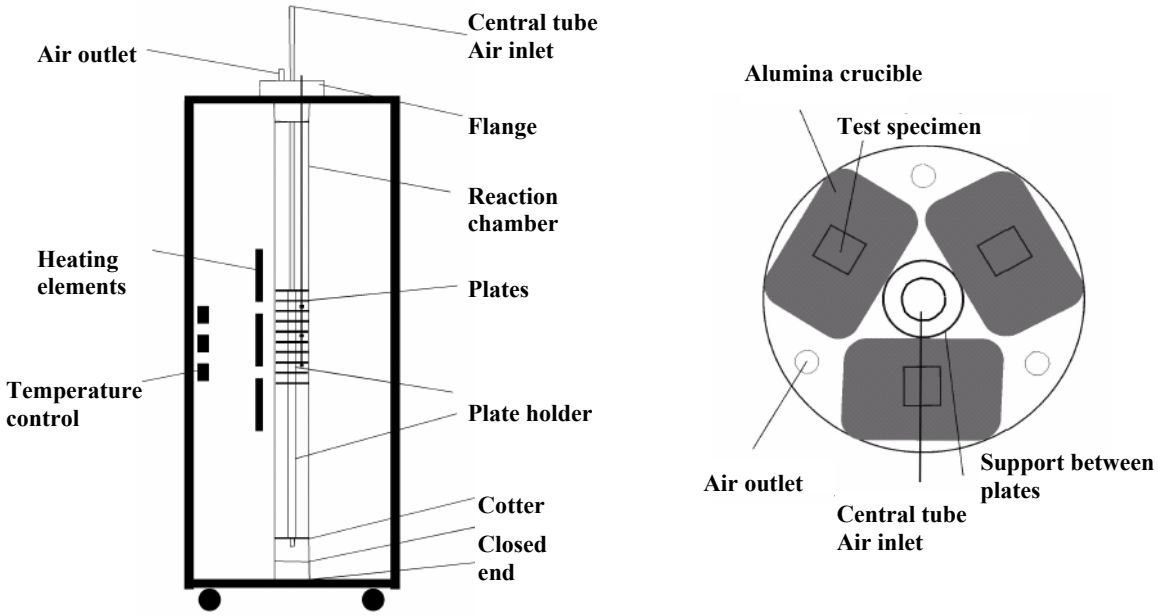

Figure 29. Schematic drawings of vertical tube furnace and alumina crucibles on plates.

1-step HPDL cladding process with off-axis nozzle configuration and HVOF spraying were used to prepare the hot corrosion test specimens. Single beads 20 mm in width were laser clad on grit-blasted 42CrMo4 QT steel (AISI 4142) plates 20 mm in thickness. They were in annealed condition (250 HV_1). As there was no continuous coating, overlapped zones were not tested. Laser cladding parameters were; 4.8 kW, 300-350 mm/min and 68–100 g/min. SX-707 coating was sprayed with Diamond Jet Hybrid 2700 HVOF spray gun onto alumina (grit 32) grit-blasted 42CrMo4 QT steel plate 10 mm in thickness. Spraying parameters used were; oxygen 240 $L.min^{-1}$, propane 70 $L.min^{-1}$, air 375 $L.min^{-1}$ and powder feed rate 60 g/min. They were hotter than those described earlier in section 2.3.4.

Two specimens of each material were prepared for hot corrosion tests by cutting the coating samples and bulk pieces to the size of 10 x 15 x 10 mm^3. Before that the laser coatings were ground with grinding machine. The HVOF sprayed coating and wrought samples were ground manually with SiC paper grit 600. In order to prevent the material loss from the backside of the samples and make it easier to measure the thickness losses after the test, the backsides of each test specimen were finally HVOF sprayed with the layer of SX-707 to the thickness of 0.4 mm. Before and after the test, the sample thickness was measured from the interface of backside coating to the free surface of the ground/corroded test coating. Thickness measurements, average of 12 measurements at different locations, were performed with

optical microscope equipped with a measuring table with an accuracy of 1 μm. Schematic cross-section of the test specimen is shown in Figure 31.

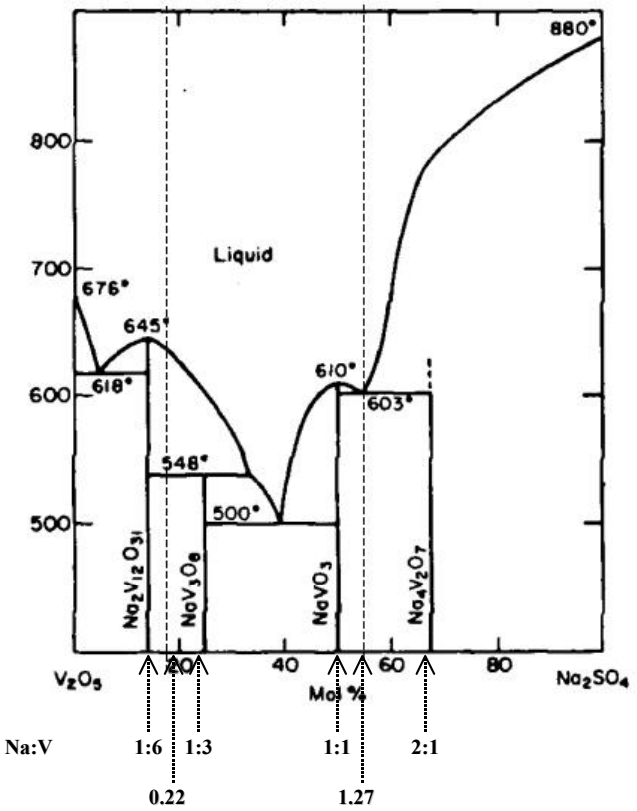

Figure 30: Phase equilibrium for Na_2SO_4-V_2O_5 [375]. Vertical axis is temperature in degrees Celcius.

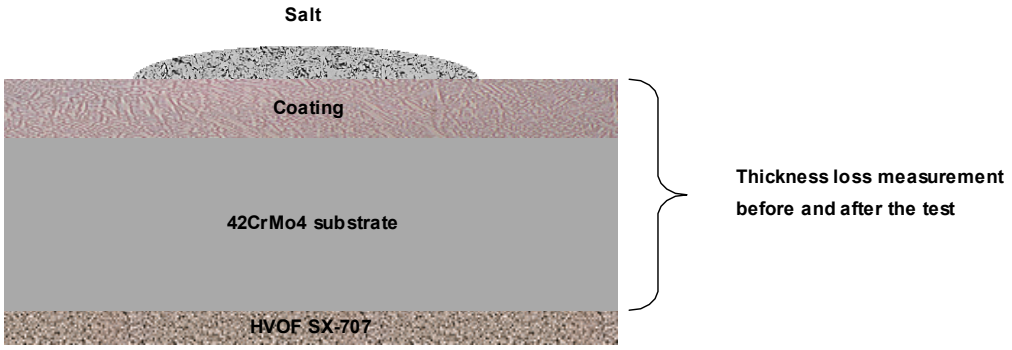

Figure 31. Schematic drawing of hot corrosion test specimen.

After the hot corrosion tests, the specimens were mould into cold-setting resin. Resin buttons were then cut in halves to reveal the cross sections. During the metallographic preparation, the specimens were next ground and polished in dry condition in order to prevent the dissolution of possible water-soluble reaction products like sulphates of Na and Ni. The prepared cross-sections were then carburized and examined by SEM and EDS (semi-quantitative analysis).

In order to identify the phases present in reaction product layers and selected laser coatings, XRD scans were performed. In the case of high-Cr NiCr laser coatings, phase identification was performed before and after test at different depths starting from the coating surface. After the identification of the phases, relative volume fractions of the phases were estimated from the integrated intensities of diffraction peaks by direct comparison method presented in Ref. [378]. Two peaks per phase were taken into account in order to diminish the influence of possible texture. This experiment together with SEM and EDS studies was carried out to examine the high temperature stability of the coatings.

2.3.6 Abrasion wear

Abrasion wear tests were conducted with a rubber-wheel abrasion test device, a modified version of ASTM G65, where crushed dry quartz (SiO_2) sand abrasives flow between the surfaces of the rotating rubber wheel and the test specimen. The basic construction of the device and principle of this low-stress three-body abrasion wear test are schematically illustrated in Figure 32. In this test, specimens with length of 50, width of 20 and height of 20-22 mm were pressed against the rotating rubber wheel with a load of 23 N. Rotation was along the longest dimension of the specimen. Surface speed of the rubber wheel was 1.64 m/s. The test time was one hour, which equals to the total wear length of 5904 m. Five specimens were tested simultaneously. Each specimen was abraded 12 minutes in each of the positions (five specimen positions altogether) to eliminate possible differences in wear characteristics between each specimen holder and sand feeder. After every 12 minutes their weight losses were measured with an accuracy of 1 mg. The abrasive feed rate used in these tests was approximately 20–25 g/min per test specimen. According to measurements conducted with laser diffractometer, grain size distribution of the quartz sand was: d_{10} = 139 µm, d_{50} = 285 µm, d_{90} = 470 µm. Its average hardness on Mohs scale is 7, corresponding to hardness values of 750-1200 HV [329]. SEM image of the as-received angular quartz sand is shown in Figure 33.

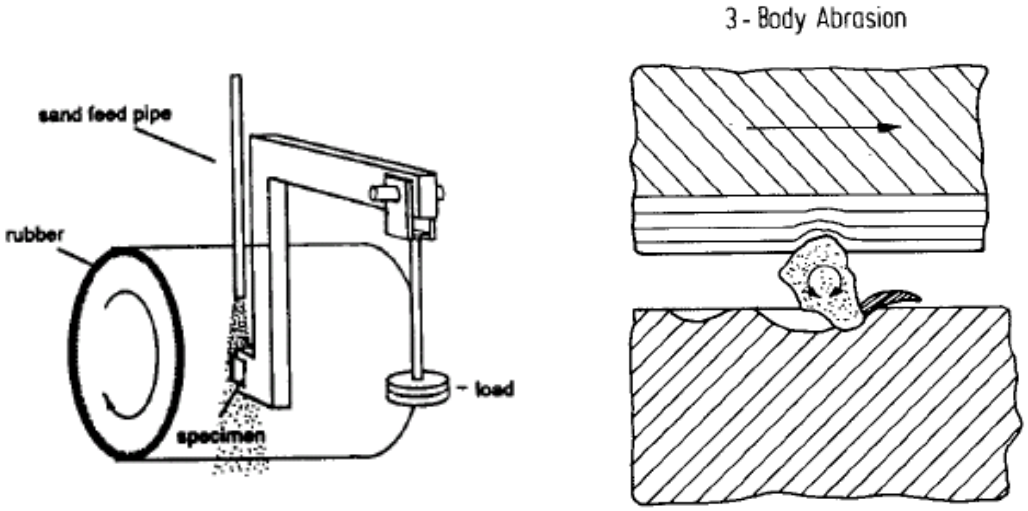

Figure 32. Basic construction of the rubber wheel abrasion wear test device and principle of three-body abrasion.

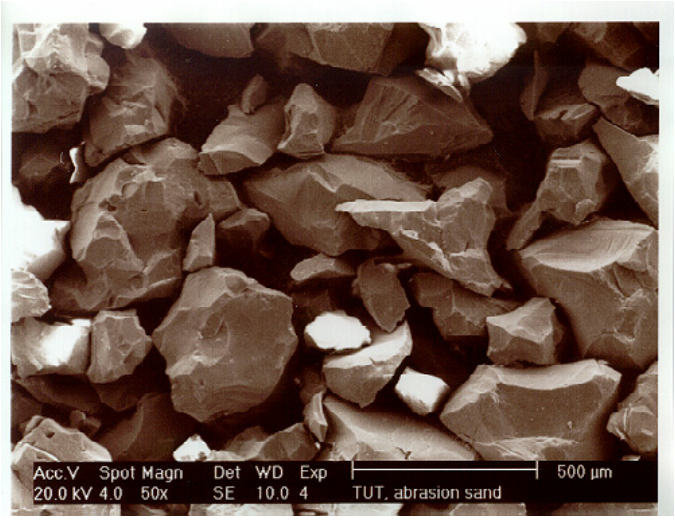

Figure 33. SEM image of the as-received quartz sand used in rubber wheel abrasion tests.

Laser coatings were deposited directly onto the wear test specimens (50 x 20 x 20 mm^3) made of mild steel. Each specimen consisted of four consecutive layers deposited in sequence shown in Figure 34. After each deposited layer specimen was let to cool down for some time without additional cooling. Nd:YAG and Coax 8 cladding nozzle was used with parameters in the range of 700–1000 W, 700 mm/min and 5–10 g/min. First layer was deposited with the highest and the last one with the lowest laser power. Diameter of the laser beam spot was approximately 1.8 mm. Inter-track advances were 1.0 and 1.4 mm. Additional preheat was not applied, i.e. cracks were allowed to form. Three specimens per alloy and MMC were produced. After the cladding and prior to tests, specimens were ground manually with 80-600 SiC paper in order to reduce the surface roughness. In the case of MMCs, this treatment did not fully level the surface. The layer to be removed to level the surface would have been ~80 µm in coatings manufactured with inter-track advance of 1 mm. After these specimens were abrasion wear tested, some of the most promising ones were submitted to diamond wheel grinding in order to level the surface to the point where no already tested surface remained and subsequently was tested again. This was done in order to study the influence of overlapping and possible microstructural changes on wear behaviour.

Exceptions to previous description were that MMC coatings produced from Metco 16C + Amperit 522.2 (50/50 vol.%), Metco 16C + Amperit 522.3 (50/50 vol.%), Stellite 21 + Amperit 522.2 (50/50 vol.%), Stellite 21 + Amperit 522.3 (50/50 vol.%) and Colmonoy 42-P2 + Amperit 522.3 (25/75 vol.%) consisted of just one layer and they were clad along the shortest dimension of the specimen. Nd:YAG and Coax 8 cladding parameters were 900 W, 680 mm/min and 8-10 g/min. Diameter of the laser beam spot was approximately 1.8 mm. Inter-track advance was 0.7 mm. No additional preheat was applied. Tribaloy T-800 coatings were deposited on 316L plates (100 x 60 x 20 mm^3) from which the abrasion wear test specimens were cut so that the rubber wheel rotated perpendicular to cladding direction. Nd:YAG and Coax 8 cladding parameters were 1600 W, 420 mm/min and 24 g/min. Diameter of the laser beam spot was approximately 4 mm. Inter-track advance was 2 mm. Preheat of 500˚C, measured with 2-colour pyrometer, was used to eliminate the cracks.

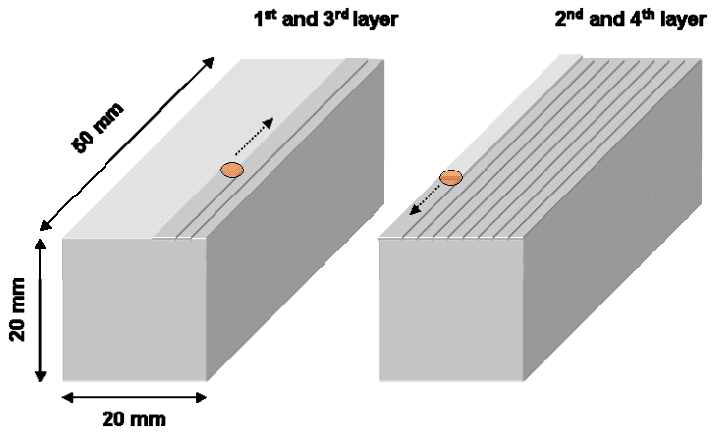

Figure 34. Sequence of laser cladding on abrasion wear test specimens.

After the abrasion wear tests, wear scars were examined with SEM. In addition to this, the profiles of the wear scars were measured from the diamond wheel ground specimens along the direction perpendicular to wear direction using UBM-Microfocus Compact (UBM Messtechnik GmbH, Ettlingen, Germany) laser profilometer (LP) possessing lateral and vertical resolutions of 1.0 and 0.06 µm, respectively. Tested specimens were also sectioned perpendicular to cladding, i.e. to wear direction for metallographic studies.

2.3.7 Sliding wear

The sliding wear properties of the selected laser coatings and reference alloys were defined in dry condition at RT by using block-on-ring type test device. The principle of the test method and the dimensions of the block and ring are shown in Figure 35. In these tests, the rings were made of 42CrMo4 (DIN 1.7225, SAE 4140) and 34CrMo4 steels, which are typical mass-produced QT steels widely used in construction of miscellaneous apparatus in mechanical engineering, engine and vehicle construction. They were heat-treated to hardness values of 30 (42CrMo4) and 60 HRC (34CrMo4) prior to wear tests. Surface roughness values (R_a) estimated with LP were 0.3–0.6 µm across the width of the rings. This measuring direction was perpendicular to grinding marks and sliding direction. Wear specimen blocks were cut from the laser clad Fe52 plates to dimensions of 25 x 12 x 6 mm^3 in a way that the sliding direction was parallel to the cladding direction. Before the test the surface of the coating in wear block was ground with grit 600 SiC paper (P1200) to the level where no as-laser-clad surface remained. In the block, the grinding marks ran randomly in relation to sliding direction. During the test, the block slid against the rotating ring under a load of 57 N. Initial Hertzian stresses caused by the line contact between the block and the ring were 80-110 MPa indicating the absence of plastic yielding. These values were calculated according to formula described in ASTM G77. Normal load, block width, ring diameter, Poisson´s ratios and Young's modulus of the block and ring were needed for calculations. These rather low values obtained were considered as maximum stresses subjected to coatings since in this type of test, the nominal contact stress decreases due to increasing contact area when the test proceeds. The surface speed of the ring was 140 m/min. The test time was limited to 90 minutes, because longer test might have revealed the base material beneath the least wear resistant coatings. The test procedure was intermitted after the first 4, 30, 60 and 90 minutes for weighing the blocks. The rings were weighed only once after the 90 minutes test was completed. In order to reveal any changes in wear behaviour, temperature of the block was monitored during the test with K-type thermo-element (Ø = 0.5 mm), which was placed

between the block and the sample holder. After the first 90 minutes, the test was continued another 30 minutes during which the temperature of the block was measured with the same thermocouple, now, welded to the block. All the tests were carried out in normal laboratory atmosphere. The ambient temperature varied between 21 and 22 ºC and the relative humidity between 12 and 29%. Wear test results were reported mainly as the volume losses for both the blocks and the rings according to standard ASTM G77. In order to study the wear mechanisms the worn surfaces were analysed with SEM, EDS, XRD and LP. The wear debris was collected from a sheet of paper, which was placed under the ring during the test and examined subsequently with SEM.

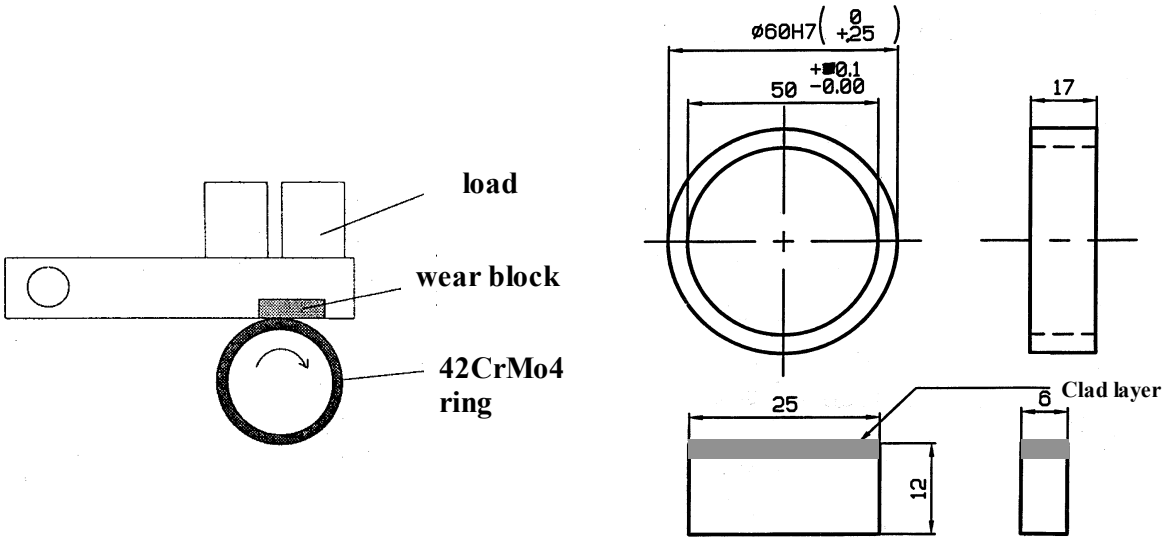

Figure 35. The principle of the block-on-ring sliding wear test device and the dimensions of the block and ring.

One layer laser coatings for sliding wear tests were prepared by depositing Stellite 21, Stellite 1 and Tribaloy T-800 onto mild steel (Fe52) plates (100 x 60 x 20 mm^3) from which the wear blocks were cut. Nd:YAG and Coax 8 cladding nozzle was used with parameters in the range of 1500–1800 W, 420 mm/min and 15–24 g/min. Diameter of the laser beam spot was approximately 4 mm. Inter-track advance was 2 mm. Additional preheat of 460-500ºC was applied for Stellite 1 and T-800 to eliminate the cracks.

Nanosteel, Stellite 6 and (Ti, Mo)C-based wear blocks were cut from laser clad samples, which consisted of 4 consecutive layers. These coatings were produced with Nd:YAG and Coax 8 cladding nozzle using parameters 700–1000 W, 700 mm/min and ~5 g/min. The first layer was deposited with the highest and the last one with the lowest laser power. Diameter of the laser beam spot was approximately 1.8 mm. Inter-track advances were 1.0 and 1.4 mm. Additional preheat was not applied, i.e. cracks were allowed to form.

Stellite 21 and T-800 were also overlay welded with PTA on planar surface of Fe52 discs 30 mm in thickness and 105 mm in diameter. Parameters are not available but both of the coatings were crack-free. Process parameters for HIPped Stellite 6 are not available either.

2.3.8 Residual stresses

For residual stress measurements three separate T-800 and two Stellite 21 specimens were prepared. The first T-800 coating was laser clad on Fe52 plate, the second on austenitic and

the third on martensitic SS discs. Preheat and elevated working temperature of 500°C was used. Stellite 21 coatings were laser clad on austenitic and martensitic SS discs without preheat. All the base materials were 20 mm in thickness. X-ray stress analyses were conducted with XStress 3000 stress analyser (Stresstech Oy, Vaajakoski, Finland) shown in Figure 36, which consisted of a goniometer, central unit and portable computer with calculation program. The $\sin^2\psi$ -method was applied with specimen tilts of $\psi = \pm 0°, \pm 14.1°, \pm 20.1°, \pm 24.9°, \pm 29.1°, \pm 32.9°, \pm 36.5°$ and $\pm 40°$. ψ-oscillation $\pm 5°$ was used to increase measuring volume and decrease the error. Measurements were done along φ-directions of 0° and 90° corresponding transverse and longitudinal directions in relation to cladding direction. Peak shifts of each tilt were calculated using cross-correlation equation and the slope of $d/\sin^2\psi$ was determined with the least squares method. Both coatings and all the base materials were measured with Cr Kα radiation at 30 kV, 6.7 mA and 10 s exposure times. The diameter of the measuring area was 3 mm. The diffraction peaks used were CoMoSi and Co_3Mo_2Si Laves phases for T-800 with 2θ values of 150-153° and fcc-Co (220) for Stellite 21 with 2θ values of 128-130°. Normal elastic constants (T-800: E = 240 GPa, ν = 0.3 and St 21: E = 211 GPa, ν = 0.3) were utilized in all calculations as constants for Laves phases were unknown. In order to define the residual stress as a function of depth, material was removed electrolytically (Struers Movipol 3) from the coating and base material underneath. Changes in elastic constants and diffraction peaks at the interface were accounted, accordingly. The advantage of this method of layer removal over mechanical methods is that no new stress components were introduced. A disadvantage, however, is that some preferential etching takes place due to two phase structure (T-800) and inhomogeneous distribution of intermixed Fe particularly in overlapping areas, i.e. surface becomes possibly rougher and rougher after each etching. The removed layer thickness was determined with Trimos TVM 600 vertical height measuring instrument (Trimos S.A., Chavannes, Switzerland). The diameter of the measuring tip in Trimos was 8 mm. Each minimum and maximum stress value given in figures concerning XRD method in section 3.6 is the average value of 5 measurements. Minimum and maximum values were calculated on the basis of errors, which originated from the non-ideal $d/\sin^2\psi$ plots as shown in Figure 36. After each measurement the sample was randomly shifted a couple of millimetres before the measurement was repeated.

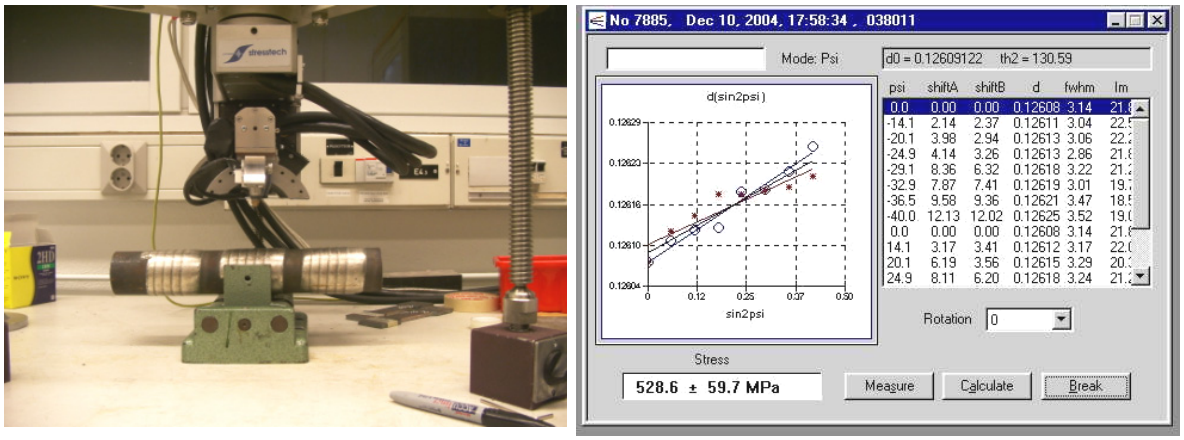

Figure 36. XStress 3000 stress analyser and the slope of $d/\sin^2\psi$ plot measured from Stellite 21 laser coating. Due to non-ideal plot the error for 528.6 MPa was ± 59.7 MPa.

In order to check the reliability of X-ray method from one phase only (T-800), reference stress measurements were made with a high-speed circular micro-hole drilling method

(MTS3000) at the University of Technology in Espoo, Finland. In this method, cylindrically shaped micro-hole was drilled step by step into the specimen surface. The stepping motors were computer-aided and controlled via printed circuit boards. Adjustment of the hard metal drilling tool 1.6 mm in diameter and the drilling process was controlled with an online CCD camera. The low feed rate (~60 μm/min) in addition with a high cutting rate of 300 000 revolutions per minute guaranteed a stress free drilling process with negligible heat development. The residual stresses in the coatings were locally relieved due to this material removal, deforming the surface around the drilled micro-hole. The relaxed surface strains were measured for every drilling step (step increased from 10 to 80 μm in Stellite 21 and from 20 to 50 μm in T-800 as drilling proceeded) by strain gauge rosette (HBM RY61S 1.5/120), which was glued so that one of the three measuring grids coincided with the cladding direction. Using calibration curves and material constants (E, ν) the measured surface strains were converted to the nominal strains at the bottom of the drilled hole for every drilling step. Finally, principal stresses for each drilling depths were calculated with RESTAN-software using Kockelmann method [379]. Stresses along longitudinal and transverse directions in relation to cladding direction were later solved analytically using equations:

$$\sigma_{x'} = \sigma_x \cos^2 \alpha_r + \sigma_y \sin^2 \alpha_r + \tau_{xy} 2 \cos \alpha_r \sin \alpha_r$$
$$\tau_{x'y'} = -(\sigma_x - \sigma_y)\cos \alpha_r \sin \alpha_r + \tau_{xy}(\cos^2 \alpha_r - \sin^2 \alpha_r) \qquad \text{(10 and 11)}$$

Where, α_r was rotational angle between maximum principal stress σ_x and $\sigma_{x'}$ (= σ_L = stress along cladding direction), σ_y was minimum principal stress and τ_{xy} shear stress. $\tau_{x'y'}$ was shear stress in coordinate system, which was rotated by angle α_r.

T-800 on austenitic and martensitic SS was laser clad with Nd:YAG equipped with Coax 8 with parameters; D_b = 4 mm, 1800 W, 420 mm/min and 24 g/min. Inter-track advance was 2 mm. Tribaloy T-800 on mild steel was clad with parameters: D_b = 4 mm, 1800 W, 420 mm/min and 20 g/min. Inter-track advance was 3 mm. Stellite 21 on austenitic and martensitic SS was laser clad with parameters; D_b = 4 mm, 1600 W, 800 mm/min and 17 g/min. Inter-track advance was 2 mm.

2.3.9 Thermal fatigue

Low-cycle thermal fatigue tests for the selected crack-free as-laser-clad coating/base material pairs were conducted with the help of induction heater and Fanuc S-700 six-axis robot system. Minac 18/25 single (EFD Induction, Skien, Norway) induction heater (10–40 kHz) was equipped with pancake coil and ECU 1167 control unit, which included PID regulator for temperature control. The principle of the test is provided in Figure 37. At first, the laser clad disc was mounted on robot arm after which the K-type thermoelement (Ø = 0.5 mm) was welded with thermocouple attachment unit onto the surface of disc as illustrated in Figure 38. After that, the robot started to move the sample between pancake induction coil and water spray. Heating was administered under the disc as shown in Figure 37. After the desired temperature was reached as measured on the surface of the disc, PID control switched off the heating and robot moved the heated sample under the water spray. Similar to heating, cooling was administered under the disc as shown in Figure 37. After the desired number of cycles was reached, the test was finished and the surface of the the coating was studied with Novex P-10 (Arnhem, the Netherlands) stereomicroscope (SM) in order to observe possible cracks generated during the test. Afterwards, longitudinal (plane parallel to free surface of the coating) and transverse (perpendicular to cladding direction) cross-sections were prepared for SEM and OM studies.

With given setup, used robot program and induction parameters coating/base material pairs encountered thermal cycles, which consisted of rapid heating up to approximately 685ºC and rapid cooling back to 16–18ºC. Heating from 16–18ºC to approximately 600ºC took place in 50 seconds (12ºC/s), whereas cooling from 650ºC to 100ºC lasted about 10 seconds (55ºC/s). Time interval between peak temperatures was 200 s. Holding time above 600ºC was approximately 60 s. Temperature-time-cycle is illustrated later in section 3.7.1.

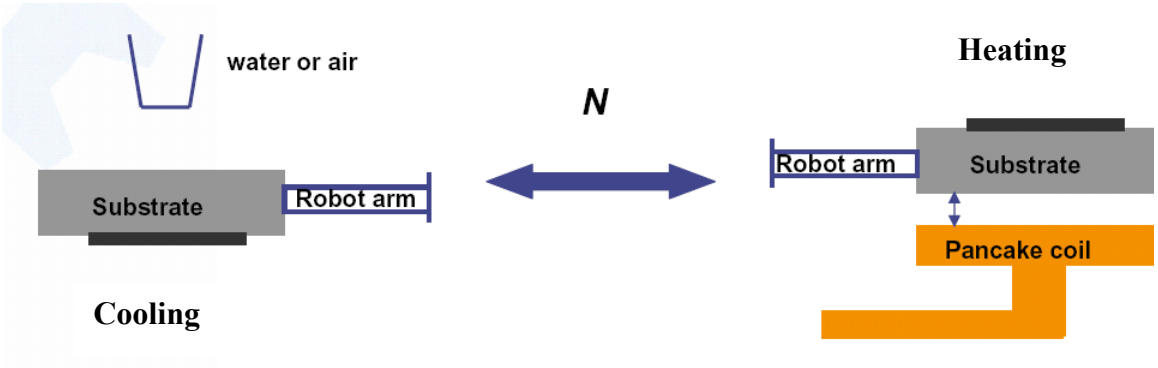

Figure 37. Experimental setup for thermal fatigue test.

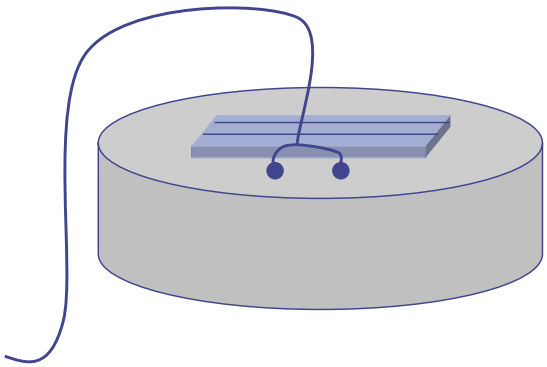

Figure 38. K-type thermoelement welded on the surface of base material next to laser coating.

The selected laser coatings were laser clad on the selected base materials, which were in the form of discs. These discs were 20 mm in thickness and 44-46 mm in diameter. Coatings were laser clad on the planar, grit-blasted, surfaces of the discs as shown in Figure 38. Nd:YAG laser equipped with Coax 8 coaxial nozzle was used. Inconel 625 and SX-717 coatings on mild steel were laser clad without preheat with the following parameters; D_b = 1.8 mm, 900 W, 700 mm/min and 4-6 g/min. Inter-track advance was 0.7 mm. T-800 on mild steel was clad with parameters: D_b = 1.8 mm, 700 W, 400 mm/min and 3 g/min. Inter-track advance of 0.7 mm and preheat of 500ºC were used. T-800 on austenitic SS was laser clad with parameters; D_b = 4 mm, 1700 W, 400 mm/min and 18 g/min. Inter-track advance of 2 mm and preheat of 500ºC were used.

2.4 Summary of the experimental procedures

Studied materials, coating methods, manufacturing methods of reference bulk materials, characterization and test procedures are roughly summarized in flow chart shown in Figure 39.

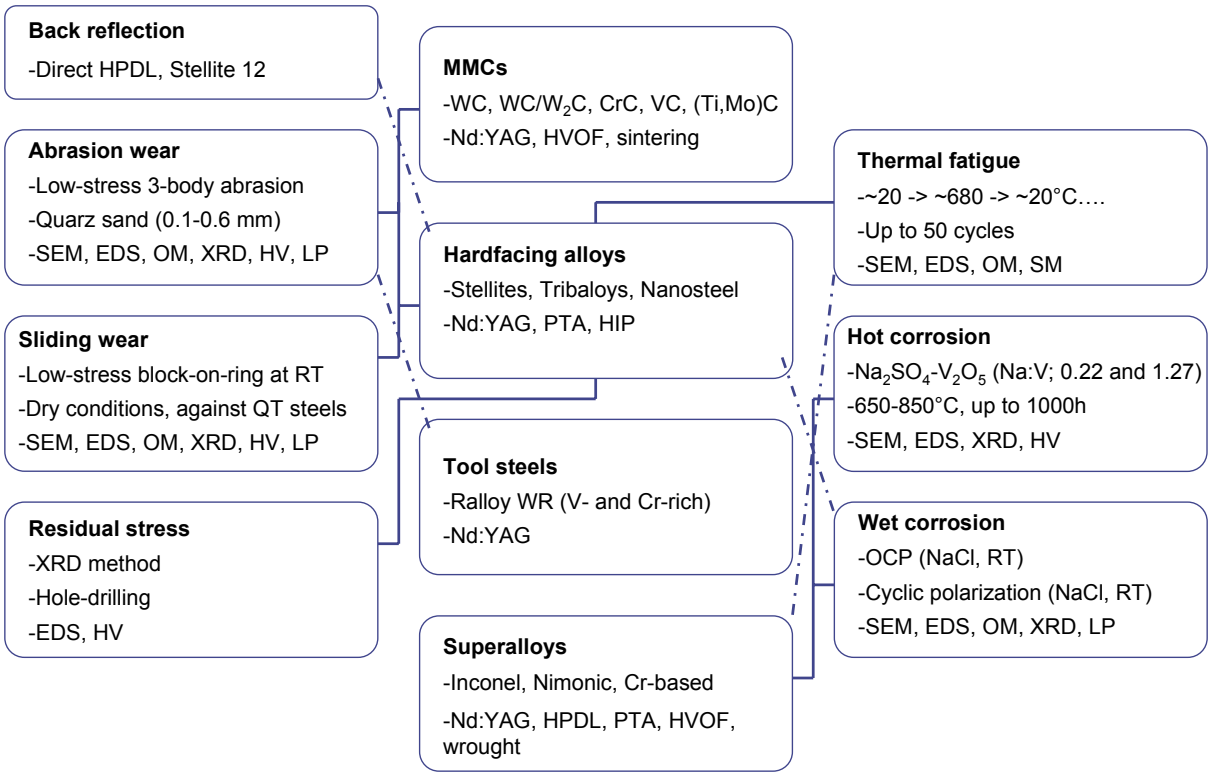

Figure 39. Flow chart concerning the experimental procedures.

3 RESULTS

The results presented in this thesis consist of back reflection characteristics and various essential functional properties of laser coatings with respect to reference coatings and bulk alloys produced by other means. The back reflection characteristics are focused exclusively on blown powder cladding process based on 6 kW direct HPDL, which utilises wide laser beam geometry. The functional properties of laser coatings comprise studies of wet corrosion, hot corrosion, abrasive wear, sliding wear, residual stresses and thermal fatigue.

3.1 Back reflection characteristics

As mentioned in the experimental section, the temperature monitoring and control system was built in-house for the diode laser. It was utilized to measure the temperatures on several different locations during three various cladding situations in order to study the direction of back reflection. In the first situation, single beads of Stellite 12 were laser clad with off-axis setup onto the planar surface of massive mild steel block (947 x 228 x 154 mm^3), which surface condition was milled. Cladding powder was PTA grade Stellite 12. Cladding parameters were 4.8 kW, 300 mm/min and 75 g/min. Each bead had the length of ~300 mm, i.e. beam was on 1 minute. The objective of this first experiment was to study the influence of tilting of the laser head on the direction of back reflection during cladding in order to define the tilting angle, which directs the least amount of reflected laser beam inside the laser head. Before cladding experiments, three reference cladding trials (1 minute each) were performed without base material in order to create reference temperature curves for comparison purposes. The distance from the optics to the floor, which was the target, was approximately 1.5 m. This was expected to produce conditions which did not cause any temperature increase inside the laser head due to back reflection. With an accuracy of 0.1°C, temperature curves measured inside the laser head during 1 minute were identical. Another reference curves were made by melting the planar surface without powder injection. Altogether six situations were studied including three real cladding situations with the base material:

1) Cladding without base material, no tilting
2) Melting, laser head was perpendicular to surface
3) Melting, laser head was tilted +2.5º with respect to surface normal
4) Cladding, laser head was perpendicular to surface
5) Cladding, laser head was tilted +2.5º with respect to surface normal
6) Cladding, laser head was tilted +5.0º with respect to surface normal

The results from the first set of experiments are illustrated in Figure 40. As it can be seen from the measured maximum temperature values, it is very clear that when the base material was used underneath the laser beam, maximum temperature values in each measuring locations increased, even inside the laser head, due to back reflection. It was also very obvious that if the laser head was tilted +2.5º or +5.0º towards the “pulling” direction, temperature values inside the laser head increased. This suggest that to protect the laser head in single bead cladding situations, it is better to keep it perpendicular to the surface of the base material or tilt it towards the “pushing” direction. The latter may, however, cause some problems to the off-axis nozzle, because the beam reflects more strongly towards it.

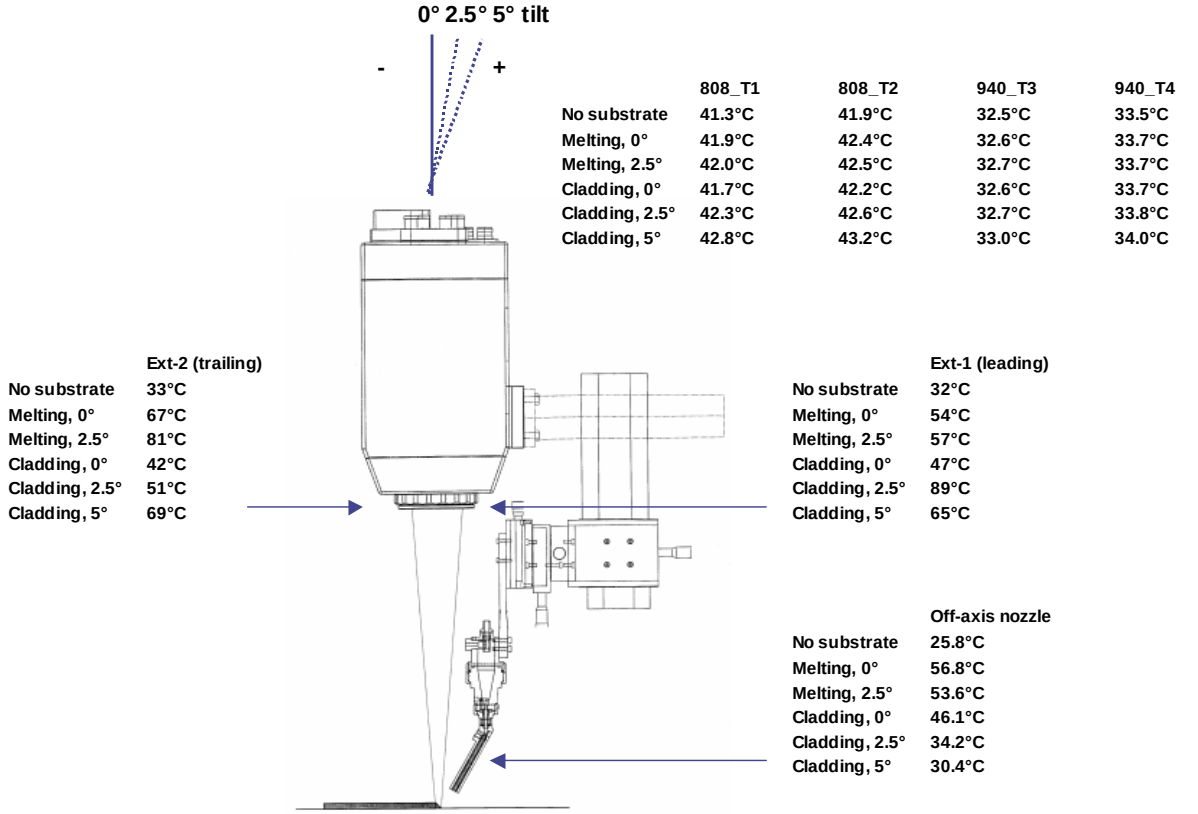

Figure 40. Maximum temperature values measured during single bead cladding trials.

In the second set of experiments, instead of single beads, continuous coating layer including overlapping was laser clad using the same off-axis nozzle configuration as in previous experiment. Base material in this experiment was mild steel rod 50 mm in diameter. Its surface condition was turned. Cladding powder was again PTA grade Stellite 12. Cladding parameters were the same; 4.8 kW, 75 g/min and 300 mm/min. Inter-track advance was 10 mm per revolution, which means that the overlapping was approximately 50%. With these parameters, coating 1.7 mm in thickness was obtained. Laser head was tilted +2.5º towards the "pulling" direction. Reference temperature curves were again created by running the robot program with beam on without base material. This was repeated twice. The following temperatures were recorded during the reference measurements at the moment of 8 minutes: 808_T1 (54.1 and 54.2ºC), 808_T2 (59.6 and 59.6ºC), 940_T3 (44.2 and 44.4ºC) and 940_T4 (41.6 and 41.6ºC). Total beam on time in these experiments was 8 minutes 47 seconds.

The results from the second set of experiments are shown in Figures 41 and 42. As it can be deduced from the temperature curve measured inside the laser head (Figure 41), the situation was now better than in single bead cladding. After approximately 9 minutes of continuous cladding, the highest temperature increase, which was measured in position 808_T1 was just 0.8ºC (+1.5%). In the same position, after 1 minute single bead cladding, the temperature increase was 1.0ºC (+2.4%). This favourable result can be attributed to the overlapping. As shown in Figure 42, temperature curve measured by the first external sensor (EXT-1) in leading position revealed that after the first full revolution when the overlapping started, the back reflection changed its direction strongly. This is due to change in melt pool shape due to overlapping.

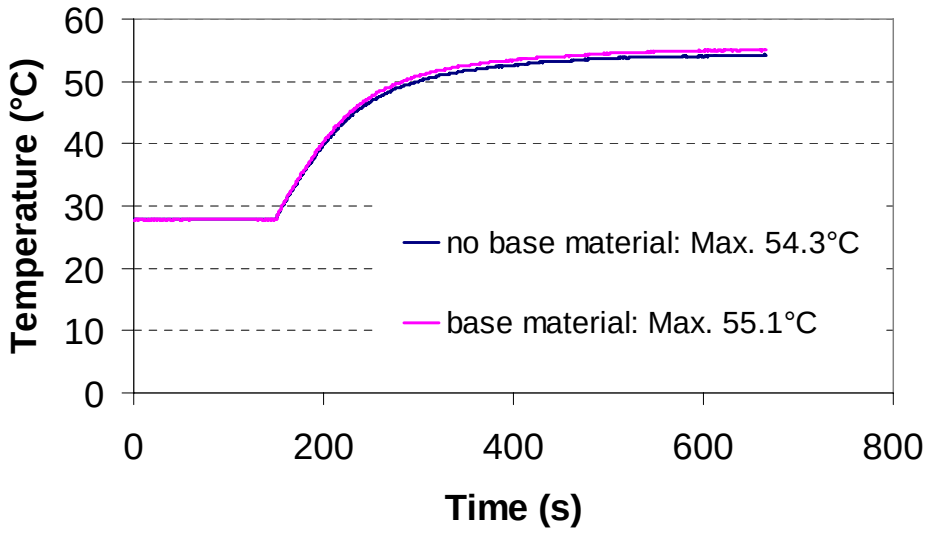

Figure 41. Influence of base material on temperature sensor 808_T1.

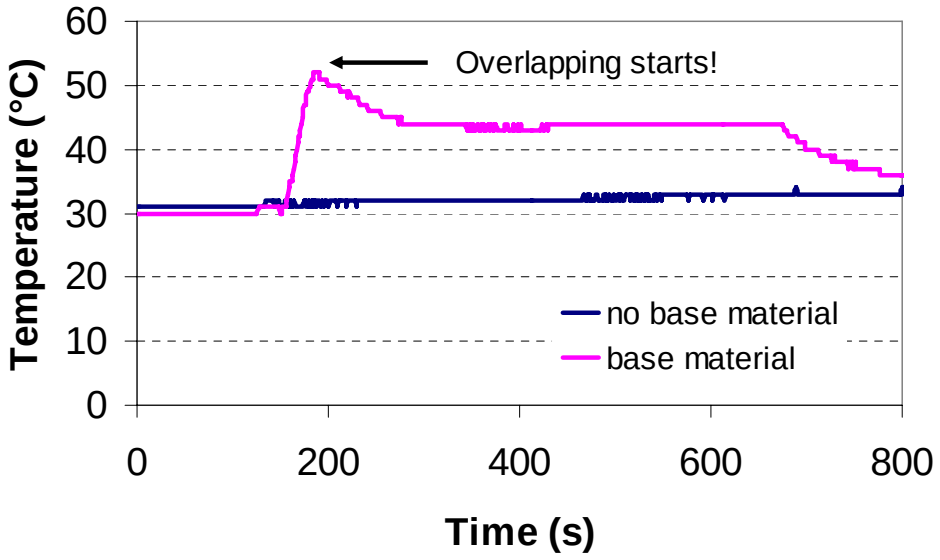

Figure 42. Influence of base material on temperature sensor EXT-1 (leading).

In the third set of experiments, off-axis powder feeding nozzle was changed to coaxial type one. With this nozzle, single beads were laser clad on block of milled mild steel. These experiments, including cladding parameters, were basically the same as those described in the first set of experiments. Laser head was just tilted also towards the "pushing" direction. Altogether six following situations were studied:

1) Cladding without base material, no tilting
2) Cladding, laser head was perpendicular to surface
3) Cladding, laser head was tilted +2.5º with respect to surface normal
4) Cladding, laser head was tilted +5.0º with respect to surface normal
5) Cladding, laser head was tilted -2.5º with respect to surface normal
6) Cladding, laser head was tilted -5.0º with respect to surface normal

The results from the third set of experiments are shown in Table 12. As it can be seen from the maximum temperature values measured inside the laser head, they follow the same trend as those in the first experiments with off-axis powder feeding nozzle. Tilting the laser head towards the "pulling" direction increased the temperatures inside the laser head. It is important to point out that back reflection inside the laser head was totally eliminated when the laser head was tilted -5.0º towards the "pushing" direction. If two different nozzles, off-axis and coaxial type, are compared, with used parameters and bead thickness, coaxial type nozzle generated conditions which caused less back reflection inside the laser head in single bead cladding. This is obviously due to larger amount of material between melt pool and laser head to block the back reflection.

Table 12. Maximum temperatures measured inside the laser head during single bead trials using coaxial type nozzle.

Test	***808_T1***	***808_T2***	***940_T3***	***940_T4***
Cladding, no base material	41.3ºC	41.8ºC	32.6ºC	33.2ºC
Cladding, 0º	41.8ºC	42.0ºC	32.5ºC	33.4ºC
Cladding, +2.5º	42.2ºC	42.3ºC	32.6ºC	33.4ºC
Cladding, +5.0º	42.3ºC	42.4ºC	32.5ºC	33.4ºC
Cladding, -2.5º	41.7ºC	42.0ºC	32.6ºC	33.4ºC
Cladding, -5.0º	41.4ºC	41.8ºC	32.6ºC	33.4ºC

3.2 Wet corrosion properties

Wet corrosion properties of the selected alloys were evaluated by means of open circuit potential (OCP) and cyclic polarization measurements in aqueous 3.5 wt.% sodium chloride (NaCl) solution at room temperature (RT). Results are shown separately in the following sections. All the potentials quoted here are referred to the silver/silver chloride (Ag/AgCl) reference electrode.

3.2.1 Open circuit potential measurements

OCP measurements were performed for exposed Inconel 625 coatings produced by different methods in order to test their suitability as corrosion barrier coatings. Wrought Inconel 625 and grit-blasted Fe37 were used as reference materials. Compositions of the tested Inconel 625 alloys are tabulated in Table 13. They are the average values of three energy dispersive spectroscopy (EDS) area measurements taken from the vicinity of the exposed area. Representative microstructures of high power diode laser (HPDL) clad, plasma transferred arc (PTA) overlay welded, high-velocity oxy-fuel (HVOF) sprayed, HVOF sprayed + laser remelted and wrought Inconel 625 are shown in Figures 43–48. OCP curves for the tested materials are displayed in Figure 49.

Table 13. Chemical compositions of the tested Inconel 625 coatings and wrought alloy in weight percentage (wt.%.).

Material	***Ni (wt.%)***	***Cr***	***Mo***	***Nb***	***Fe***	***Si***	***Al***	***Ti***
Laser (HPDL)	61.0	20.6	7.8	3.6	6.0	0.7	0.1	0.2
PTA	45.8	16.0	7.8	3.6	25.1	0.8	0.2	0.3
Wrought	60.1	22.5	9.0	3.6	3.6	0.1	0.2	0.2
HVOF	62.9	20.5	10.4	3.8	1.4	0.6	0.2	0.2
HVOF + laser	64.6	19.6	9.7	3.5	1.5	0.6	0.2	0.6

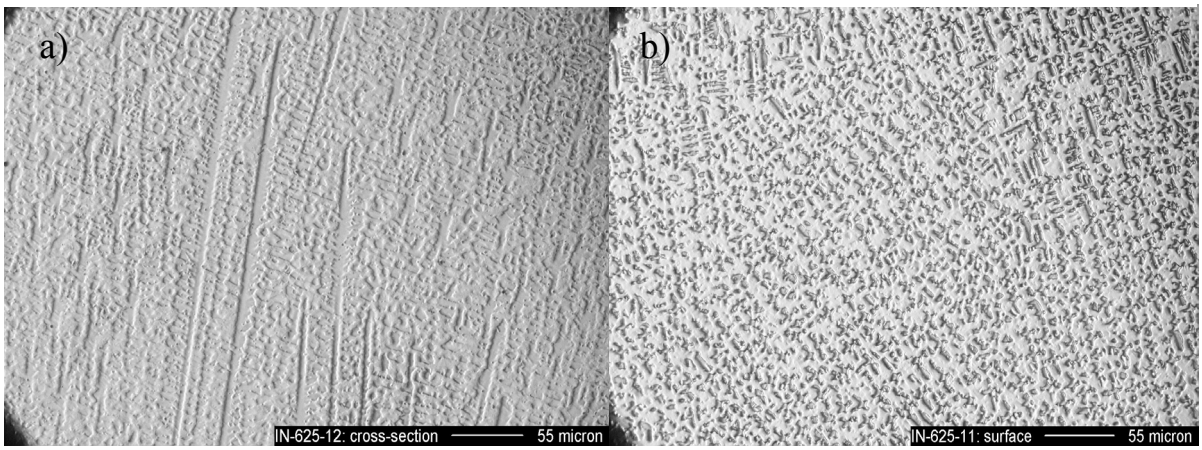

Figure 43. Optical micrographs taken from the a) etched transverse (perpendicular to cladding direction) and b) longitudinal (parallel to the plane of the free surface of the coating) cross-sections of HPDL clad Inconel 625 (6.0 wt.% Fe). Microstructure consists of directionally solidified face-centered cubic (fcc) ordered Ni-based solid solution. Columnar grains characterized with very short secondary arms grow nearly parallel to the direction of build towards the surface of coating. As distinct from the original powder and wrought Inconel 625, highest intensity in X-ray diffraction (XRD) scan was measured from the plane (200) indicating texture along preferred <100> direction typical for fcc structures. Diameter of the columnar grains measured from the longitudinal section is 3–7 μm in diameter. Differential etching arises from the compositional differences between dendrite cores and interdendritic regions.

3.2.1.1 Reference materials

As illustrated in Figure 49, two dissimilar reference wrought alloys exhibited totally different behaviour in chloride-bearing aqueous solution at RT. OCP value for Inconel 625 started to change from –220 mV to more positive direction immediately after the exposure reaching the steady state (-30 mV) approximately in 48 h. According to Nernst equation (equation 12), this means that the concentration and activity of the dissolved metal ions (Ni^{2+}, Cr^{3+}, Mo^{3+}) from the metal lattice to electrical double layer (EDL) decreased as a function of time. This means also that it took approximately 48 h to transform the previously formed oxide layer into a passive film that inhibits or stabilizes the anodic ($Me \rightarrow Me^{2+} + 2e^-$) and cathodic ($2H^+ + 2e^- \rightarrow H_2$, or $2H_3O^+ + 2e^- \rightarrow 2H_2O + H_2$, $O_2 + 2H_2O + 4e^- \rightarrow 4OH^-$) reactions to lower level (both cathodic reactions are possible because the solution, which was neutral, was not purged) (both these cathodic reactions make electrolyte more alkaline). Thermodynamical calculations conducted for NiCrMo system in H_2O solution at RT suggest that this insoluble passive film

consists of oxides, oxy-hydroxides and hydroxides ($NiCr_2O_4$, Cr_2O_3, MoO_3*H_2O and $Cr(OH)_3$). As opposed to Inconel 625, OCP value for Fe37 started to change from –600 mV to

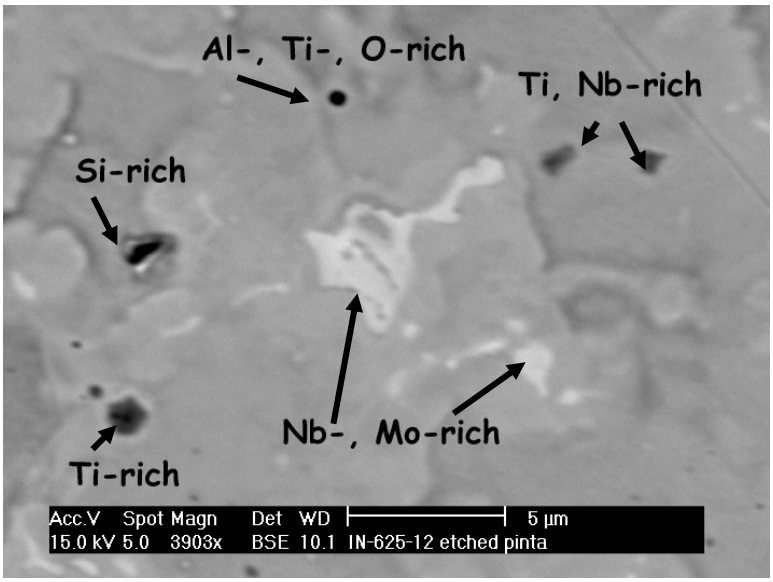

Figure 44. High magnification back-scattered electron (BSE) image of the etched surface (longitudinal cross-section) of the HPDL clad Inconel 625 coating (6.0 wt.% Fe). In addition to abundant Mo- and Nb-rich areas, some Si-, Ti-, TiNb- and AlTiO-rich phases were observed. Due to small amounts of Al and Ti in original powder, the precipitation of fcc ordered gamma prime (γ') ($Ni_3(Al, Ti)$) could have been possible. Elemental maps, however, revealed that AlTi-rich areas did not contain Ni but O. It is not surprise since Al and Ti have high oxygen affinity. In addition, the precipitation of γ' is very sluggish process, which excludes such precipitation during fairly rapid cooling inherent to laser cladding. Ti- and TiNb-rich areas irregular in shape are probably carbides.

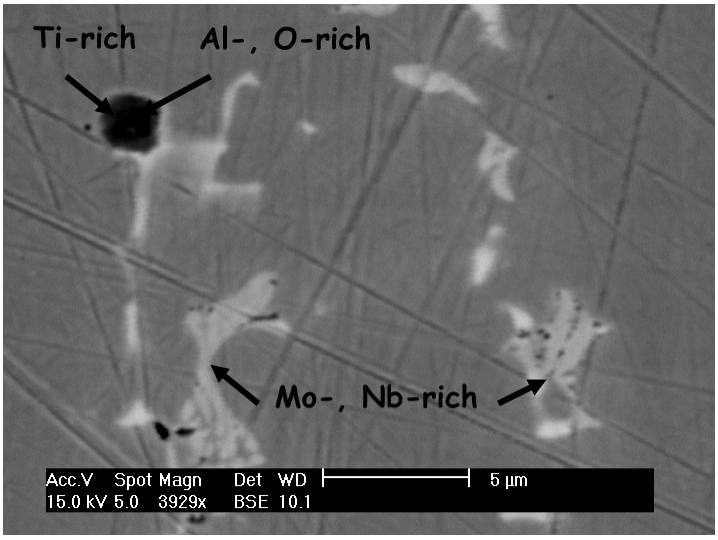

Figure 45. BSE-image of the longitudinal cross-section of the PTA overlay welded Inconel 625 coating. Analogous with laser clad alloy, Mo- and Nb-rich segregated areas as well as AlTiO-rich phases were found.

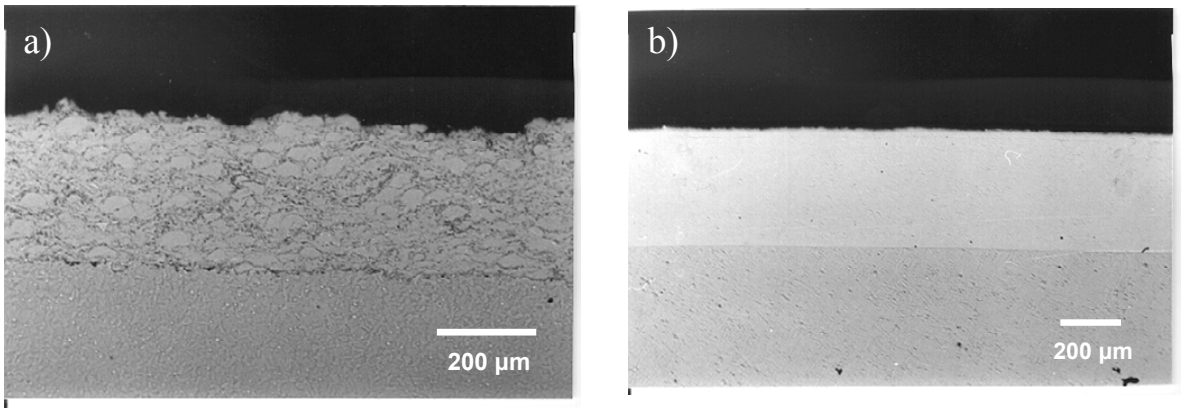

Figure 46. Optical micrographs of the a) HVOF sprayed and b) HVOF sprayed + laser remelted (transverse cross-section parallel to remelting direction) Inconel 625 coatings. Thickness of the HVOF sprayed coating is 300 µm. Oxide layers at splat boundaries are clearly seen. Thickness of this particular remelted coating is 400 µm. Fusion bond was generated. This quite heavily diluted remelted coating (D = 25%) is similar to less diluted tested one.

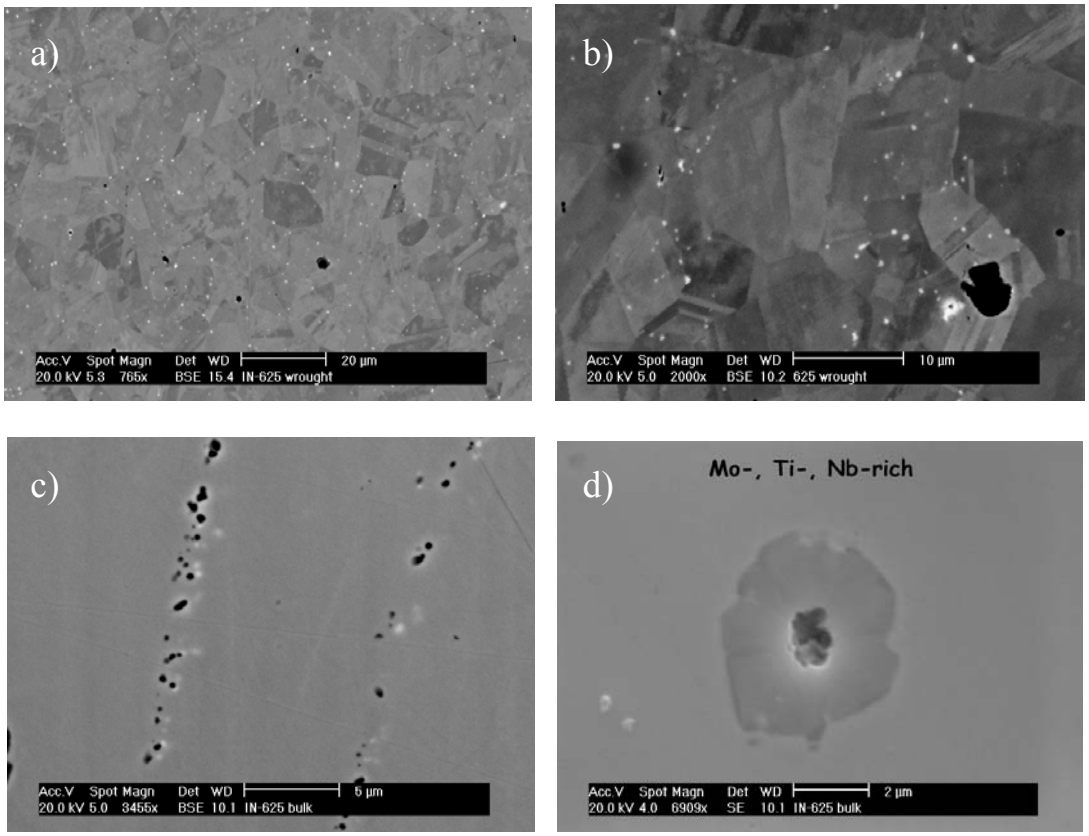

Figure 47. High magnification BSE and SE images of the wrought Inconel 625. Alloy consists of nearly equiaxed fcc ordered grains with homogeneous chemical composition. Tiny bright dots in images (a) and (b) taken from the etched surface were rich in Mo and Nb. They are probably remnants of microsegregation, which occurred during the fusion and subsequent solidification of alloy and which remained and perhaps became smaller in subsequent forming process. In the same images, larger black dots are rich in Ti. Some tiny black dots lined up in image (c) could be grain boundary carbides. Dot in image (d) was rich in Mo, Ti and Nb.

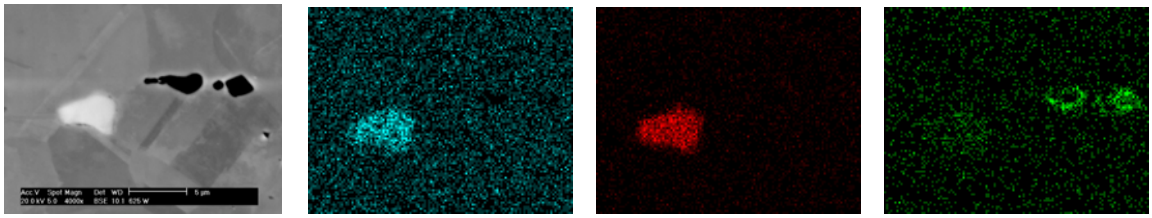

Figure 48. Elemental maps of wrought Inconel 625 alloy revealing remnants of segregated Mo and Nb as well as Ti-rich areas.

more negative direction immediately after the exposure reaching the steady state (-700 mV) already during the first 1 h of the test. Decreasing OCP means that the concentration and activity of the dissolved metal ions (Fe^{2+}) from the metal lattice to the EDL increased as a function of time. The formed porous and loose corrosion products, iron oxy-hydroxides (FeOOH) and iron oxides (Fe_2O_3, Fe_3O_4), on the surface did not protect the metal. Instead, corrosion continued after 1 h at a constant rate. This resulted potential difference of ~700 mV (steady state OCP values for Inconel 625 and Fe37) was then utilized in evaluation of the imperviousness of the coatings manufactured by different methods.

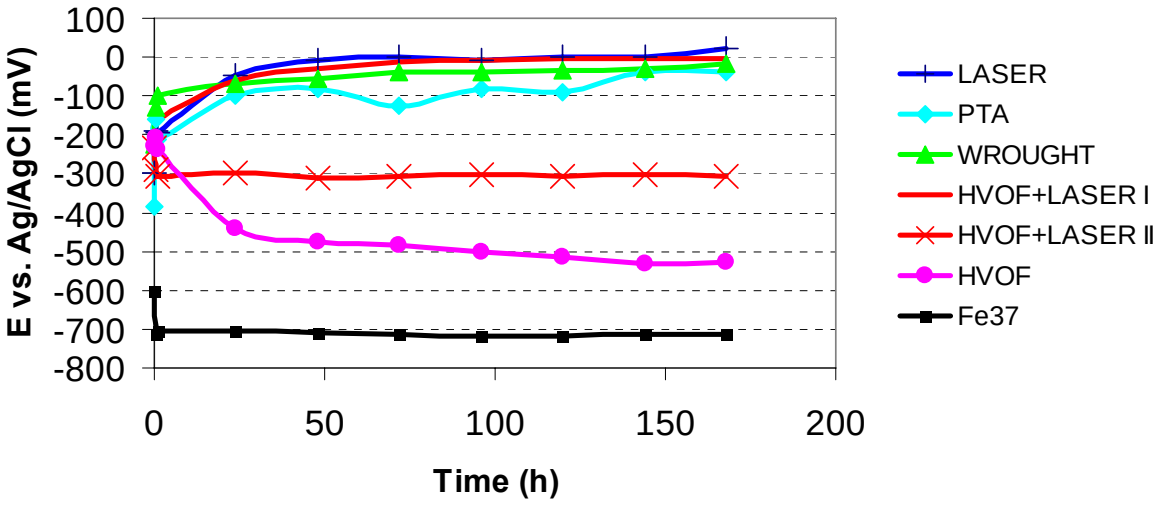

Figure 49. OCP curves for wrought, PTA overlay welded, HPDL laser clad, HVOF sprayed and HVOF sprayed + laser remelted Inconel 625 alloys measured in 3.5 wt.% NaCl solution at RT.

$$E_p = E^0 - \left(\frac{RT}{nF}\right)\ln\left(\frac{a_{products}}{a_{reactants}}\right) \qquad (12)$$

where,

$a_{products}$ = chemical activity (concentration) of products
$a_{reactants}$ = chemical activity (concentration) of reactants
E_p = measured potential (V or mV)

E^0 = OCP when all activities are equal to 1 (V or mV)
R = ideal gas constant (8.3143 J mol^{-1} K^{-1})
T = temperature (K)
n = number of electrons in anodic half reaction
F = Faraday's constant (96485 C mol^{-1})

3.2.1.2 Coatings

As displayed in Figure 49, OCP value for HVOF sprayed coating started to change to more negative direction, i.e. towards to its base material value, immediately after exposure to the 3.5 wt.% NaCl solution, indicating active corrosion behaviour similar to Fe37 alone. It was also noted that after a couple of hours from the beginning of the test, first corrosion products appeared more or less evenly on the whole surface of the exposed coating. Owing mainly to splat boundaries and perhaps to interconnected pores and microcracks characteristic for sprayed coatings, the electrolyte reached the base material fast and corroded it, as illustrated in Figure 50. If the sprayed coating structures are compared before and after the exposure as in the SE images in Figures 51a and b, it can be seen that the coating itself has corroded selectively. It is evident that the deterioration of the coating has initiated along splat boundaries and corroded the coating nearby.

Laser clad, remelted and PTA overlay welded coatings responded differently compared with HVOF coating. In these cases OCP started to change to more positive direction after exposure to electrolyte indicating passive corrosion behaviour similar to corresponding wrought alloy. Distinctively lower OCP measured for PTA coating may originate from the relatively high amount of dilution. Anyhow, after one week of exposure all the surfaces of the exposed areas were still free of any visible corrosion products, which prove that these coatings restricted the base material from the electrolyte perfectly.

HVOF coatings, which were remelted with improper parameters (HVOF + laser II in Figure 49) allowed the electrolyte to pass the coating through a single interconnected pore causing crevice corrosion-like behaviour (Figure 52). Corrosion products appeared from the base material through this single pore to the surface after a couple of hours from the beginning of the test. At the same time it was noted that OCP values decreased like in the case of sprayed coating being however 200 mV more positive than values of sprayed coating/base material system. After the electrolyte reached the base material, the less noble Fe37 started to dissolve as positive ions ($Fe = Fe^{2+} + 2e^-$) to electrolyte inside the crevice. According to crevice corrosion theory [348], this anodic reaction was maintained by the cathodic reaction outside the crevice ($2H^+ + 2e^- \rightarrow H_2$, $O_2 + 2H_2O + 4e^- \rightarrow 4OH^-$). Increased amount of positive ions (Fe^{2+}) attracted the negative chloride ions (Cl^-) to crevice. Formed iron chlorides ($Fe^{2+}2Cl^-$) were hydrolyzed by water, which led to iron hydroxide (FeOH) corrosion products and H^+Cl^- ions ($Fe^{2+} + 2Cl^- + 2H_2O \rightarrow Fe(OH)_2 + 2Cl^- + 2H^+$ and $Cr^{3+} + H_2O \rightarrow Cr(OH)^{2+} + H^+$). Formed hydrogen ions in the crevice increased the acidity of the electrolyte inside the crevice with respect to the outside of crevice increasing further the dissolution (= the ratio of hydrogen ions to hydroxyl ions increased). Together with galvanic effects involved like in this case, the base material deteriorates rapidly due to single interconnected pore in the coating layer. Improper laser remelting parameters stand here for too hot or too cold parameters. When too hot remelting parameters were used single interconnected pores tended to form in central parts of tracks and overlapped regions. Too cold remelting parameters tended to leave interconnected paths in overlapped regions (track width was 10 mm, inter-track advance was 8 mm).

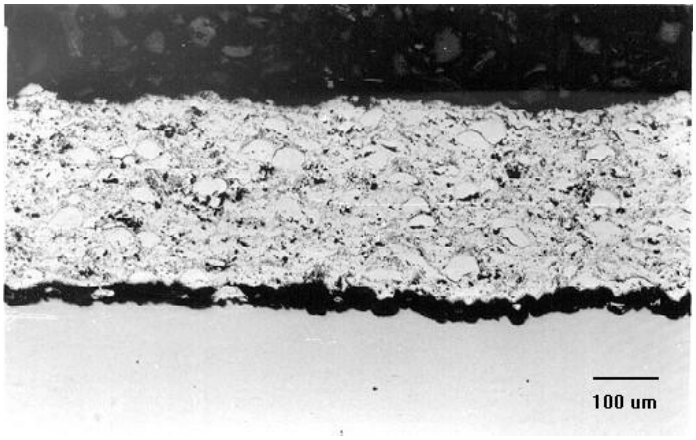

Figure 50. Optical micrograph of HVOF sprayed Inconel 625 exposed to 3.5 wt.% NaCl for 7 days.

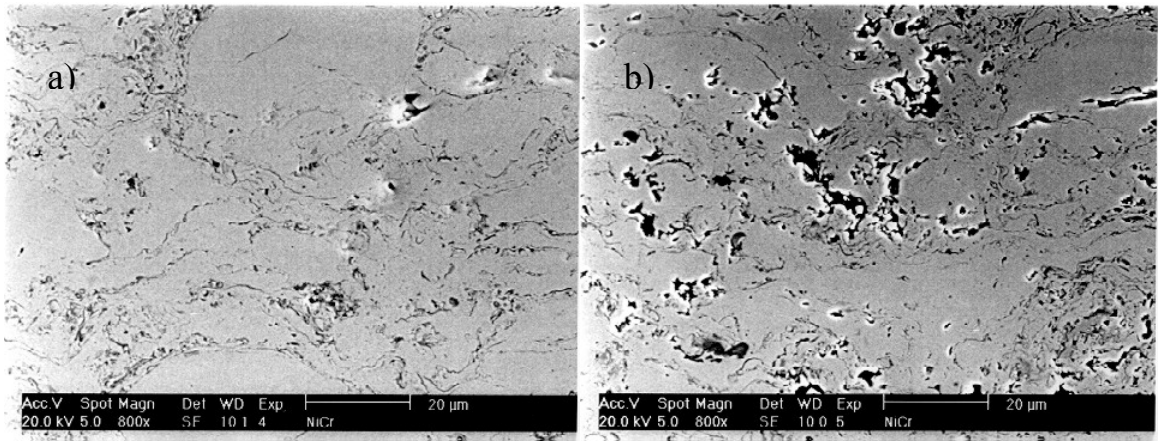

Figure 51. SEM images of HVOF sprayed Inconel 625 a) before and b) after the exposure to 3.5 wt.% NaCl for 7 days.

3.2.2 Cyclic polarization measurements

Potentiodynamic polarization tests were performed for Ni-based Inconel 625, Alloy 59, Cr-based SX-717 and Co-based Stellite 21 and Stellite 6 alloys produced by different methods in order to reveal the possible differences in corrosion mechanisms and define the corrosion rates (CR) in given circumstances. Wrought austenitic and martensitic stainless steels (SS) and titanium were used as reference materials. Five polarization tests were conducted for each material. Representative potentiodynamic polarization curves for Inconel 625, Stellite 21 and Stellite 6 alloys are given in Figures 53–55. Compositions of the tested alloys are listed in Table 14. They are the average values of three EDS area measurements taken from the vicinity of the exposed area. The corrosion (E_{corr}), breakdown (E_b) and repassivation (E_{rp}) potentials together with the corrosion current densities (I_{corr}) of the tested materials are summarized in Table 15. They are the average of five measurements. Calculated CRs (µm/year) are shown in Figures 56 and 57.

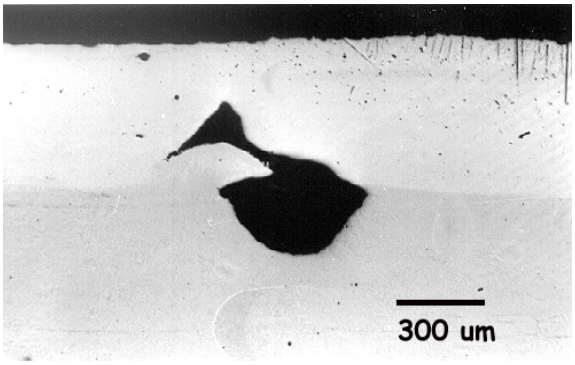

Figure 52. Optical micrograph of HVOF sprayed + laser remelted Inconel 625 exposed to 3.5 wt.% NaCl for 7 days.

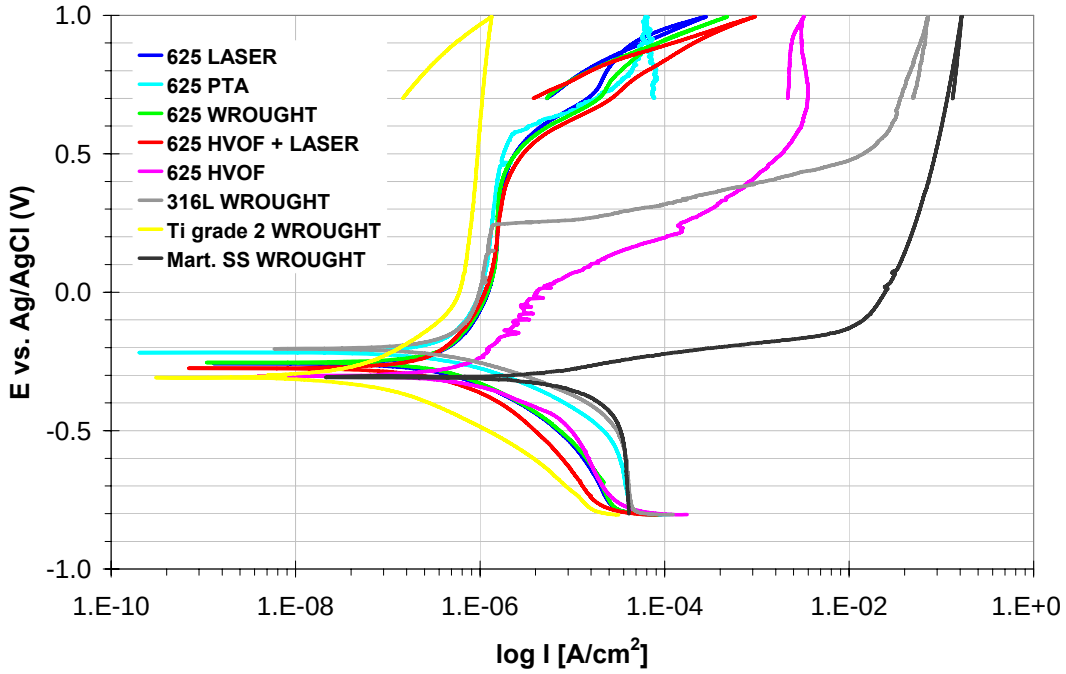

Figure 53. Representative potentiodynamic polarization curves for wrought, PTA overlay welded, HPDL laser clad (6.0 wt.% Fe), HVOF sprayed and HVOF sprayed + laser remelted Inconel 625 alloys measured in 3.5 wt.% NaCl solution at RT. Potential scans started from –0.8 V and ended to the same point. For the sake of clarity reverse scans are shown only up to +0.7 V. Wrought 316L, martensitic SS and Ti grade 2 were used as reference materials. Curve measured from Ti reveals that oxygen evolution at ~+580 mV (pH 7) did not affect the current density.

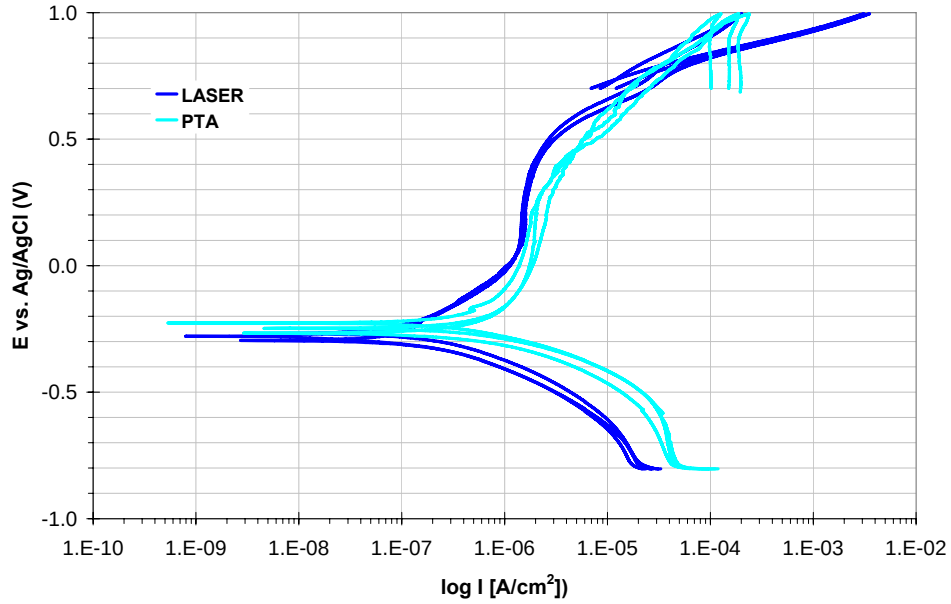

Figure 54. Representative potentiodynamic polarization curves for PTA overlay welded (3) and Nd:YAG laser clad (3) Stellite 21 alloys measured in 3.5 wt.% NaCl solution at RT.

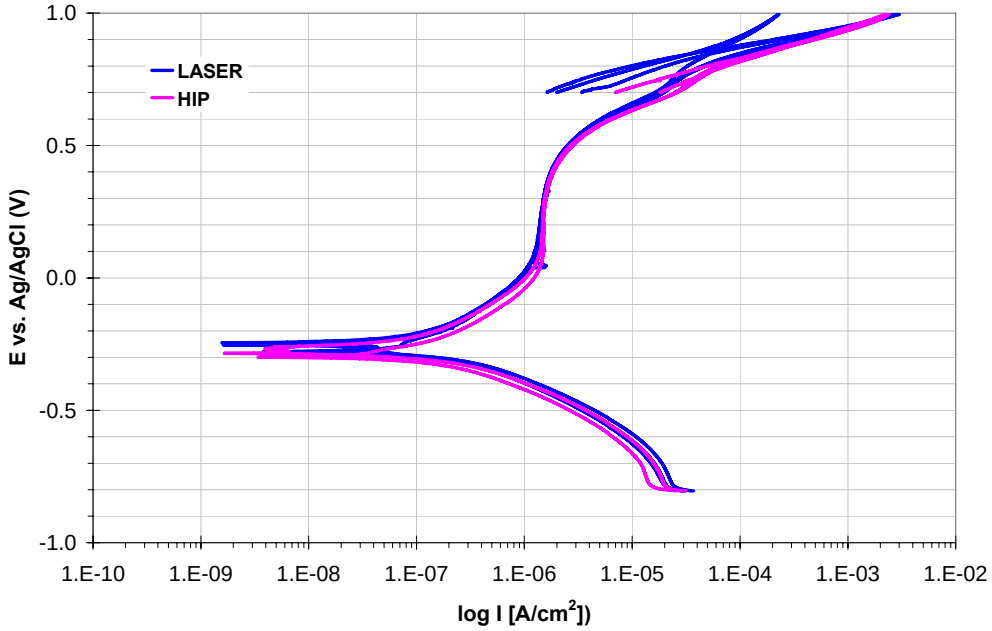

Figure 55. Representative potentiodynamic polarization curves for hot isostatic pressed (HIP) (3) and Nd:YAG laser clad (3) Stellite 6 alloys measured in 3.5 wt.% NaCl solution at RT.

Table 14. Chemical compositions of the tested alloys in wt.%.

Material	*Ni*	*Co*	*Cr*	*W*	*Mo*	*Nb*	*Fe*	*Si*	*Mn*	*Al*	*Ti*
In625 Laser	61.0		20.9		7.8	3.6	6.0	0.7			
In625 Laser	56.6		18.8		9.1	4.6	9.4	0.7	0.3	0.4	0.3
In625 Laser	49.5		17.1		7.9	4.4	19.4	0.7	0.6	0.4	0.2
In625 PTA	45.8		16.0		7.8	3.6	25.1	0.8		0.2	0.3
In625 Wrought	60.1		22.5		9.0	3.6	3.6	0.1		0.2	0.2
In625 HVOF	62.9		20.5		10.4	3.8	1.4	0.6		0.2	0.2
In625 HVOF + laser	64.6		19.6		9.7	3.5	1.5	0.6		0.2	0.2
Alloy59 Laser	58.4		21.7		16.0		2.5	0.3	0.6	0.6	
SX-717 laser	35.8		48.3		2.8		12.0	1.2			
St 21 laser	3.1	60.4	27.4		5.7		1.3	1.2	0.9		
St 21 PTA	2.0	47.1	20.4		4.7		24.0	1.1	0.7		
St 6 laser	2.0	62.6	28.9	3.5	0.5		1.6	1.0			
St 6 HIP	1.7	60.5	30.1	5.4	0.6		1.0	0.8			
316L Wrought	10.1		16.9		2.1		Bal.	0.7	1.8		
Mart. SS Wrought			11.0		1.0		Bal.	2.1	0.6		
Ti grade 2 Wrought											Bal.

I_{corr} values expressed in Table 15 were determined both by the polarization resistance (= linear polarization) and Tafel extrapolation methods. In polarization resistance method, linear portion of the potential-current density curve within ±20 mV of the E_{corr} extracted from the potentiodynamic polarization curve was used. Representative example of such curve for Inconel 625 (6.0 wt.% Fe) laser coating is illustrated in Figure 58.

I_{corr} was then calculated using Stern-Geary equation [348]:

$$\frac{\Delta E}{\Delta i} = \frac{\beta_a \beta_c}{2.3(i_{corr})(\beta_a + \beta_c)} \qquad (13)$$

where:

$\Delta E/\Delta i$ = slope of the curve ($V \cdot cm^2\ A^{-1}$)
β_a = anodic Tafel slope (ΔE/decade of i) ($V \cdot cm^2\ A^{-1}$)
β_c = cathodic Tafel slope (ΔE/decade of i) ($V \cdot cm^2\ A^{-1}$)

In Tafel extrapolation method, I_{corr} values were calculated by iteration with the help of Gamry Elchem Analyst software from the Tafel plots within ±200 mV of the E_{corr} extracted from the measured potentiodynamic polarization curves.

I_{corr} values obtained with both methods were then related to uniform CRs (µm/year) by the following equation (Faraday´s law):

$$CR = \frac{K_1(I_{corr})EW}{\rho} \qquad (14)$$

Table 15. E_{corr}, E_b, E_{rp} and I_{corr} values of the tested alloys exposed in 3.5 wt.% NaCl solution at RT. Values are the average of five measurements. Those E_{rp} values, which showed exceptionally high COV, were average of less than five because potential scan was occasionally stopped before E_{rp} was reached.

Material	***Method***	***Fe (wt.%)***	***E_{corr} (mV)***		***I_{corr} (±20mV) ($\mu A/cm^2$)***		***I_{corr} (±200mV) ($\mu A/cm^2$)***		***E_b (mV)***		***E_{rp} (mV)***		***Hysteresis***
			AVE	***COV***	***AVE***	***COV***	***AVE***	***COV***	***AVE***	***COV***	***AVE***	***COV***	
In-625	Wrought	3.6	-252	5.6%	0.031	17.6%	1.12	31.6%	-		+333	23.4%	Neg.
In-625	Laser	6.0	-262	2.0%	0.039	16.9%	1.32	27.8%	+567	10.4%	+135	79.9%	Neg.
In-625	Laser	9.4	-238	3.7%	0.042	25.5%	1.56	23.2%	+374	11.0%	+113	93.2%	Neg.
In-625	Laser	19.4	-224	8.7%	0.038	28.3%	1.33	33.4%	+491	34.0%	-6	25.9%	Neg.
In-625	PTA	25.1	-226	7.6%	0.046	29.4%	1.04	36.4%	+514	9.3%	-68	86.2%	Pos.
In-625	HVOF+laser	1.5	-213	5.8%	0.023	17.2%	0.78	26.3%	-		+299	34.5%	Neg.
In-625	HVOF	1.2	-297	3.1%	0.077	12.0%	2.31	7.7%	+5	20.3%	-199	4.6%	Neg.
Alloy59	Laser	2.5	-234	7.9%	0.033	10.5%	0.84	26.9%	-		+488	7.8%	Neg.
SX-717	Laser	12.0	-221	5.4%	0.011	30.4%	0.23	36.9%	-		+499	29.8%	Neg.
St 21	Laser	1.3	-270	4.2%	0.026	46.0%	0.59	42.6%	-		+463	6.8%	Neg.
St 21	PTA	24.0	-254	8.1%	0.051	16.9%	1.68	31.5%	+332	6.7%	-198	46.5%	Pos.
St 6	Laser	1.6	-268	8.4%	0.019	23.2%	0.25	72.3%	-		+483	9.8%	Neg.
St 6	HIP	1.0	-289	5.4%	0.034	42.4%	0.81	66.8%	-		+361	30.6%	Neg.
316L	Wrought	Bal.	-194	7.2%	0.034	31.1%	0.98	15.8%	+263	31.2%	-255	52.5%	Pos.
Mart SS	Wrought	Bal.	-307	6.0%	0.69	19.7%	9.26	31.0%	-223		-		Pos.
Ti grade 2	Wrought	-	-307	0.9%	0.005	32.0%	0.10	47.0%	-		+265	58.5%	Neg.

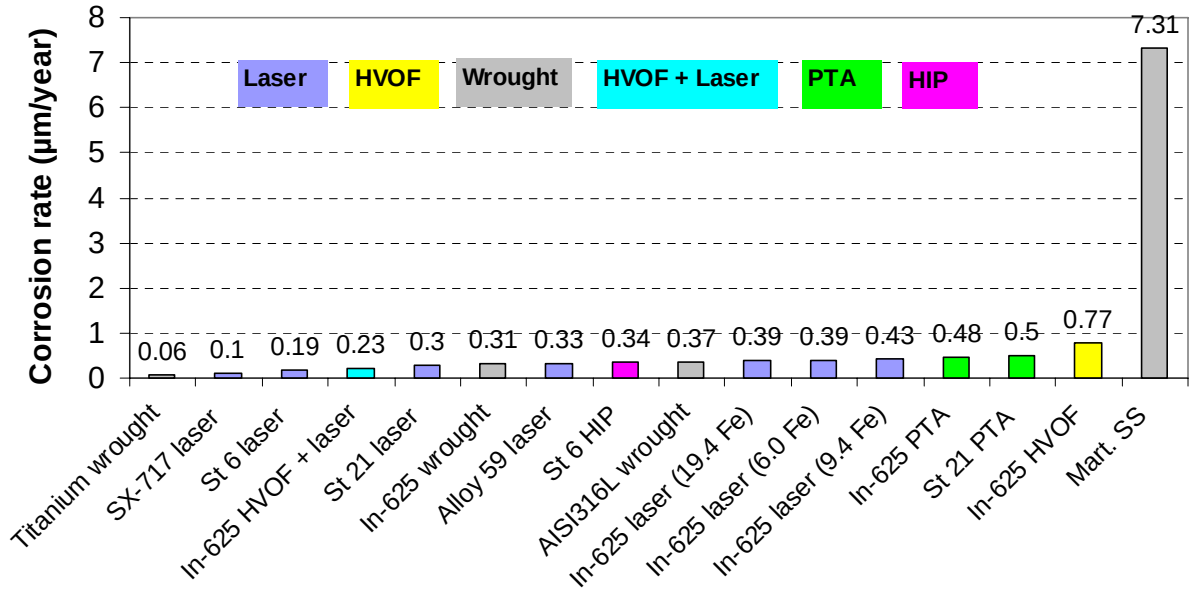

Figure 56. Corrosion rates calculated from the linear polarization data extracted from the potentiodynamic cyclic polarization curves (within ±20 mV of the E_{corr}).

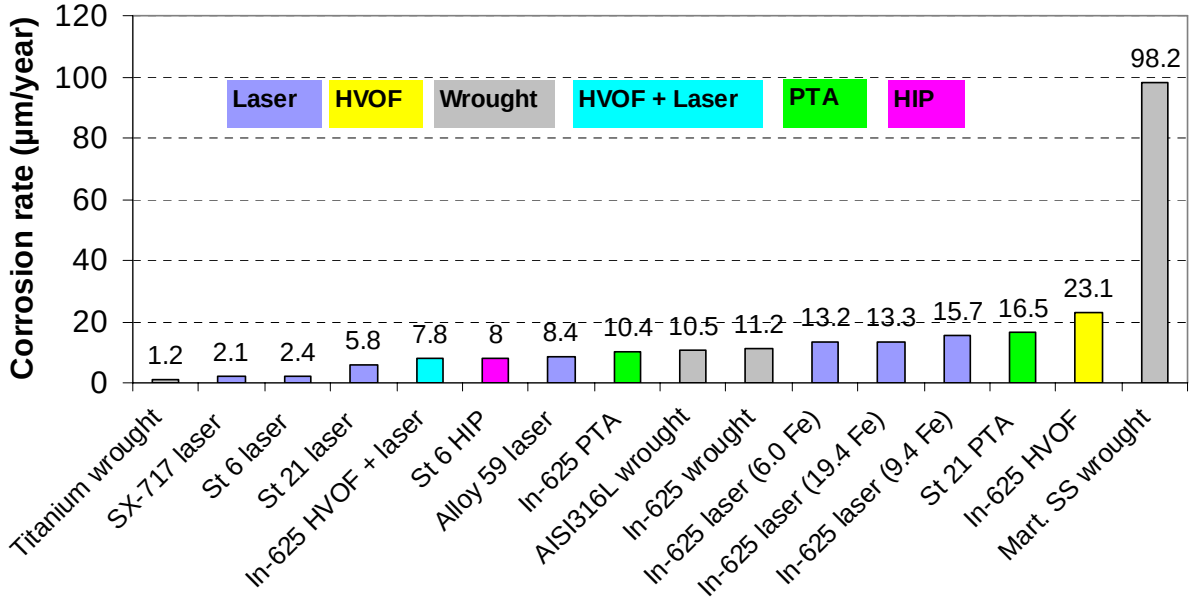

Figure 57. Corrosion rates calculated from the I_{corr}, which were obtained from the Tafel plots (within ±200 mV of the E_{corr}) created by Gamry Elchem Analyst software.

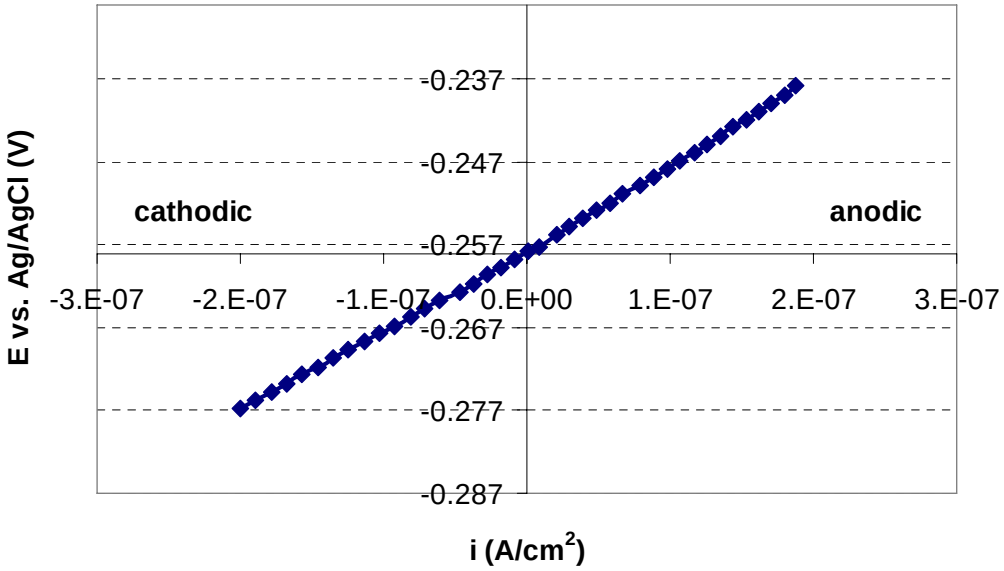

Figure 58. Linear polarization curve for laser clad Inconel 625 (6.0 wt.% Fe) within ±20 mV of the E_{corr}. The applied potential (V) is plotted against the current density (A/cm^2). Potential step was 1 mV per step.

where:

CR = corrosion rate (μm year^{-1})
K_1 = 3.27 (μm μA^{-1}·cm^{-1}·year^{-1})
EW = equivalent weight of the alloy (g)
I_{corr} = corrosion current density (μA cm^{-2})
ρ = density (g cm^{-3})

Equivalent weights (EW) were calculated according to EDS analyses (= dilution was taken into account) with equation 15 assuming that all the major elements were oxidized and participated in corrosion:

$$EW = \frac{1}{\sum \frac{n_i f_i}{A_i}} \qquad (15)$$

where:

EW = equivalent weight of the alloy (g)
n_i = valence of the ith element in the alloy
f_i = mass fraction of the ith element in the alloy
A_i = atomic mass of the ith element (g)

The lowest valence values of 2 (= number of electrons taking part in the reaction) were used for the main elements Ni, Co and Fe, whereas the valence values of 3 for Cr, 3 for Mo, 3 for Nb and 4 for Si were used for alloying elements. Composition fractions lower than 1 wt.%

were neglected. The following EWs were obtained; 25.87 for Inconel 625, 26.09 for Alloy 59, 21.03 for SX-717, 25.06 for Stellite 21, 25.37 for Stellite 6, 26.10 for 316L, 24.97 for martensitic SS and 15.96 for titanium.

Nominal densities of 8.44 for Inconel 625, 8.60 for Alloy 59, 8.31 for Stellite 21, 8.46 for Stellite 6, 8.0 for 316L, 7.7 for martensitic SS and 4.54 g/cm^3 for titanium were used. Thus, influence of dilution was neglected. If it is assumed that Fe decreases the density of clad layer, then corrosion rates should be higher than reported particularly for heavily diluted coatings.

Comparing the CRs given by the linear polarization and Tafel extrapolation methods, the former gives order of magnitude lower values as shown in Figures 56 and 57. Rank of the materials, however, is pretty much the same. The level of CRs achieved with linear polarization method are in good agreement with the results obtained by Al-Fozan and Malik [380], who immersed wrought 304L, 316L and Inconel 625 alloys in slowly flowing (12 l/h) natural seawater at RT for 1–2 years. Especially when it is taken into account that 3.5 wt.% NaCl is considered to be more aggressive towards metals than natural sea water due to the absence of denser calcareous ($CaCO_3$, $Mg(OH)_2$) corrosion products on the surface of the exposed alloy, which decelerate the corrosion [381]. CRs in Ref. [380] were 0.37-0.55 μm/year for 304L, 0.05–0.24 μm/year for 316L and 0.05-0.07 μm/year for Inconel 625. CRs calculated here by the linear polarization method gave 0.37 μm/year for wrought 316L and 0.31 μm/year for wrought Inconel 625.

Accuracy of the used electrochemical test configuration and repeatability of the results it gives can be evaluated by comparing the curves in Figures 54 and 55 and coefficient of variation (COV = standard deviation divided by the average) values in Table 15. On the basis of average E_{corr} and standard deviation, COV for E_{corr} was as low as 5.6% in average. Average COV for I_{corr} measured by the linear polarization method was 24.9%, whereas it was 34.8% defined by the Tafel extrapolation method conducted with Gamry Elchem Analyst software. The results (rank) given by the linear polarization can be therefore considered more reliable. There were no differences in COV values between coating and wrought alloys.

3.2.2.1 Ni-based alloys

Among Inconel 625 alloys, the HVOF sprayed coating/base material system exhibited corrosion resistance inferior to laser clad, laser remelted, PTA overlay welded and wrought alloys. As illustrated in Figure 53, HVOF sprayed sample shows conspicuously high anodic current densities and a distinctive increase in it after narrow passivation area (from E_{corr} to +5 mV) already at about +5 mV. Such behaviour relates to connection rapidly established between Fe37 base material and chloride-bearing electrolyte through the coating layer. Due to lack of protecting and passive oxide films at the coating/base material interface, potential increase removes substantial amounts of Fe^{2+} ions from the base material through the sprayed coating layer resulting in high current densities. However, despite the absence of Cr in base material, there is clear attempt to passivate in the coating/base material system, which does not take place, for instance, in martensitic SS containing 11 wt.% Cr (Figure 53). This attempt to passivate and orders of magnitude lower anodic current densities compared with martensitic SS can be attributed to the presence of sprayed Inconel 625 coating layer. For some reason, rather strong secondary passivation takes place in transpassive region and negative hysteresis loop generates. Current densities in this region are, however, three orders of magnitude higher than in other Inconel 625 alloys. Despite negative hysteresis, E_{rp}, which

describes the alloy's ability to repair the protective oxide film, set to the level as low as –200 mV. It can be also pointed out that E_{corr} (-297 mV) was the lowest and I_{corr} the highest among Inconel 625 alloys (Table 15). CRs (μm/year) shown in Figures 56 and 57 were calculated on the basis of composition of Inconel 625 even if the mild steel base material participated strongly in anodic reaction as confirmed by the transverse cross-section of the tested sample (Figure 59), which reveals severe localized deterioration in base material resembling signs caused by pitting or crevice corrosion. Obviously, interconnected paths formed crevices, which led to the observed deterioration. It is also observed that coating surface is damaged. This can be related to the distinctive increase in current density and breakdown of slight passivation, which is readily lost due to non-continuous passive film or imperfections in it due to surface defects like pores, inter-splat boundaries and gaps between non-fused particles or due to lack of Cr in consequence of oxidation. Interior of coating remained surprisingly intact and crevice corrosion under the gasket was absent.

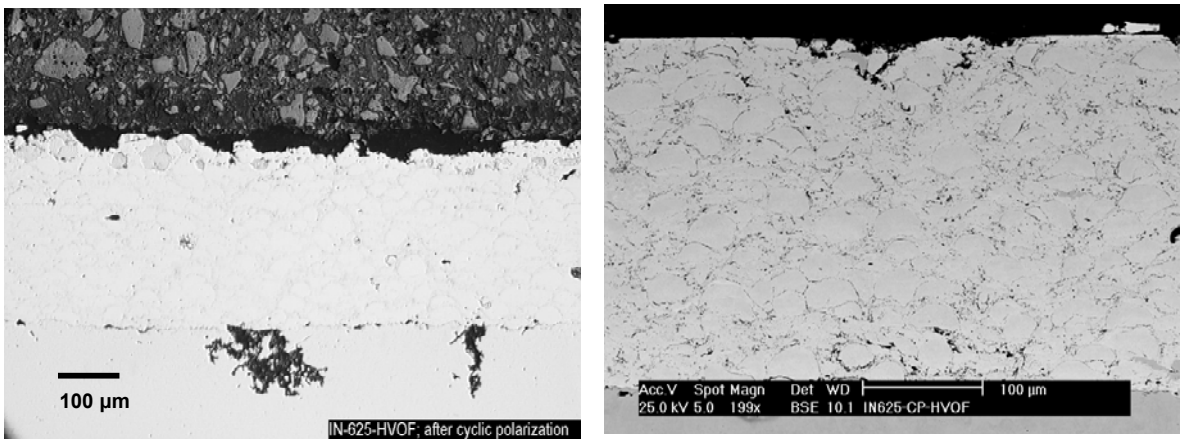

Figure 59. HVOF sprayed Inconel 625 after potentiodynamic polarization test.

Laser clad (6.0 wt.% Fe), remelted, PTA overlay welded and wrought Inconel 625 exhibit substantially wider passivation region, lower anodic current densities and higher E_{corr} compared to the HVOF coating. For instance, passivity of laser clad coating (6.0 wt.% Fe) is maintained until about +450-+600 mV, where slight increase in current density takes place. In this case, increase in current density is not due to abrupt breakdown of passivity caused by chlorides like in reference wrought 316L (Figure 53), which suffered from severe pitting corrosion in central regions of exposed area and crevice corrosion under the gasket, but mainly transformation of passive films (Cr_2O_3, $NiCr_2O_4$, CrOOH and MoO_3*H_2O) to soluble oxide ions (CrO_4^{2-}, $Cr_2O_7^{2-}$, MoO_4^{2-}). According to potential-pH diagram for NiCr system in H_2O (Figure 60a), which unfortunately neglects the effects of chlorides, insoluble Cr_2O_3 and $NiCr_2O_4$ transform to soluble oxides at +425 mV when pH is 7 at RT. Mo apparently increases this potential when pH is 7 or less as suggested in Figure 60b and chlorides decrease it because passivation region gets narrower and moves towards more alkaline solutions as explained in Ref. [382] for Cr. Reference curves measured from titanium reveal that oxygen evolution ($2\ H_2O \rightarrow O_2 + 4H^+ + 4e^-$), which should start on test sample surface at +580 mV, did not have influence on measured current densities and verifies the above soluble-insoluble transformation explanation for the current density increase. Surface examination after the test with SEM supported the interpretation of polarization curves (no clear breakdown potential, negative hysteresis) since exposed surfaces proved to be free of corrosion pits. Instead, it was observed that slight crevice corrosion occurred under the gasket and potential increase in

transpassive region dissolved the exposed surface non-uniformly as shown in optical macrographs in Figure 61. The latter was due to non-homogeneous distribution of intermixed Fe from the base material. Elemental maps taken from the ground surface (Figure 62) affirmed the existence of Fe "waves" due to intermixing between coating and base material. Fe content in these "waves" was approximately 7.8 wt.% compared to 3.5 wt.% in other regions in the coating where the average Fe content was 6.0 wt.%. Existence of such waves is quite surprising since the exposed surface was at a distance of 1.5 mm from the coating/base material interface, intensity distribution of the used laser beam was homogeneous in direction perpendicular to cladding direction and interaction time of the beam was as high as 0.75 s leaving plenty of time for rapid homogenization of the melt pool by intense Marangoni convective flows. On the other hand, homogeneous intensity distribution may have also led to slower convective flows due to lower temperature gradients. Similarly, HPDL clad coating, which contained 9.4 wt.% Fe, suffered from this macrosegregation but not the most heavily diluted coating (19.4 wt.% Fe). This could be perhaps explained by the surface tension number (S) given in equation 6 in section 1.5.1.2. The higher the S, the more vigorous the convection, i.e. the more homogeneous is the composition of the melt pool. As increased dilution was produced by lowering the powder feed rate (f) and keeping other parameters constant, melt pool temperature was likely to rise, which in turn reduced the melt viscosity (μ). As μ decreases, the convection is more severe as suggested by the equation 6. Intermixed Fe from the base material may also have decreased the μ since Inconel 625 with rather high Mo content possesses high μ. In addition, higher melt pool temperature caused by decreased f has definitely elongated the melt pool, thus leaving more time for melt homogenization. Moreover, Fe dilution increases temperature coefficient of surface tension (dγ/dT) (2.7% increase when Fe content increases from 6.0 to 19.4 wt.% and 4.8% from 6.0 to 25.1 wt.%). But on the other hand, temperature increase decreases dγ/dT.

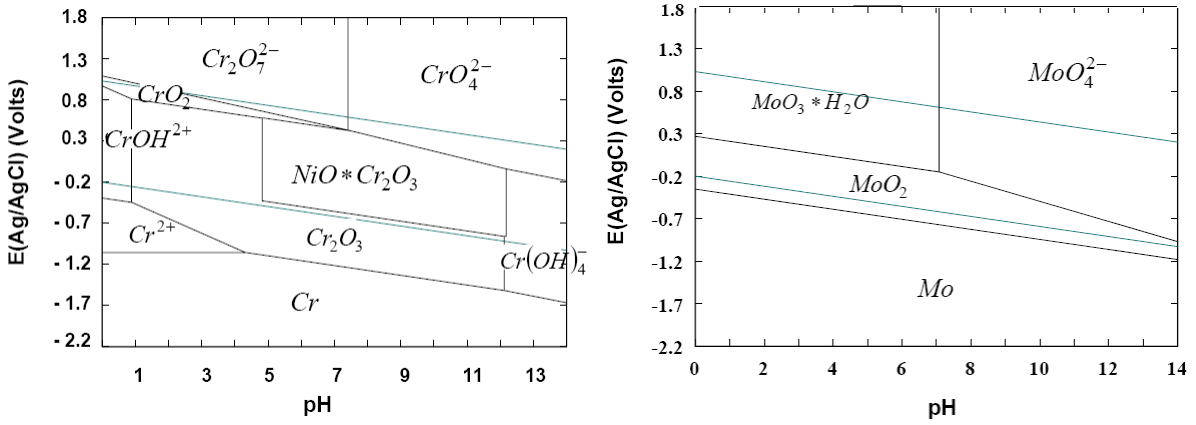

a) b)

Figure 60. Potential-pH diagrams for a) Cr-Ni-H_2O and b) Mo-H_2O systems at 25ºC showing insoluble and soluble reaction products. Initial pH of the solution was ~7. Dotted lines express the stability limits for water. Above the upper dotted line oxygen evolution on the metal surface starts. Below the lower dotted line hydrogen evolution takes place. At pH 7 oxygen evolution starts at +580 mV. At pH 7 insoluble chromium oxide layers transform to soluble products at +425 mV. At pH < 7 Mo reaction product is still insoluble at 1800 mV. At pH > 7 insoluble Mo oxide layer transforms to soluble products at already -200 mV [228].

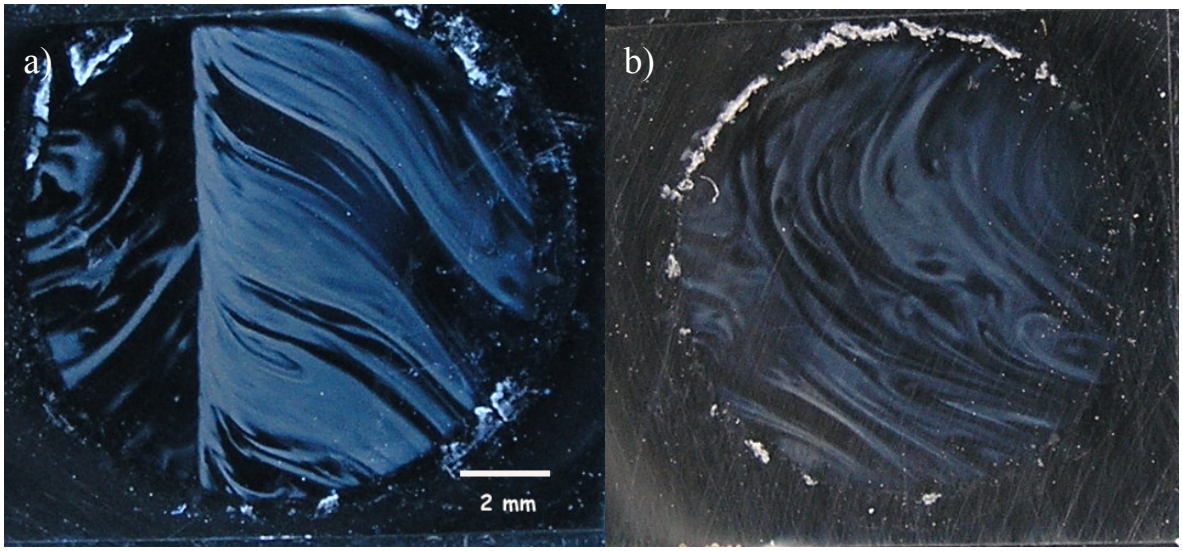

Figure 61. Cyclic polarization tested surface of HPDL clad a) Inconel 625 (6.0 wt.% Fe) and b) Inconel 625 (9.4 wt.% Fe) coatings. Signs of slight crevice corrosion under the gasket and Fe "waves", which were profoundly dissolved with respect to other regions are clearly seen in both macrographs. Overlapped region is seen in macrograph (a), where the cladding direction was from top to bottom. Inter-track advance proceeded from right to left.

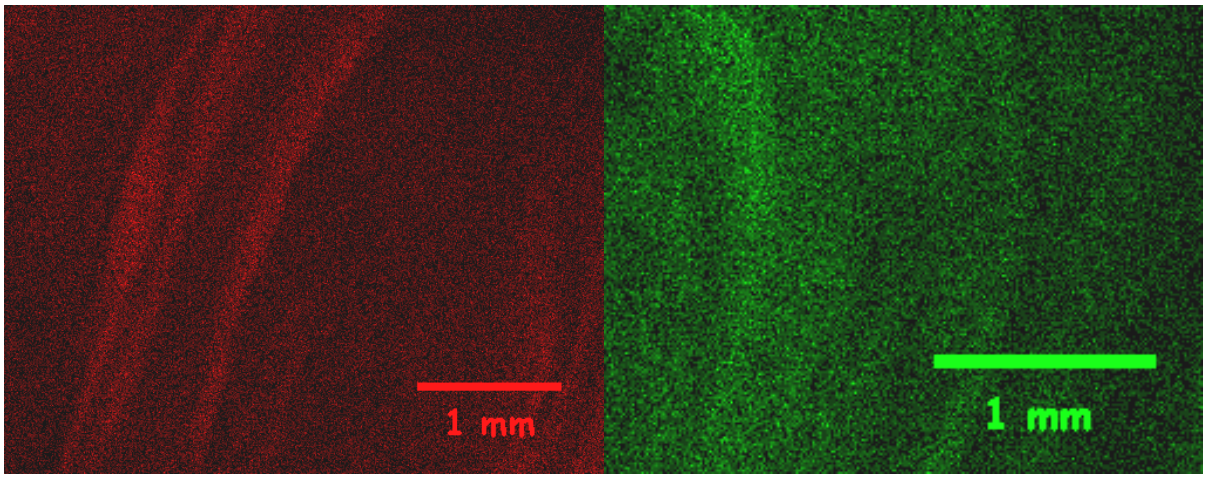

Figure 62. Elemental maps of Fe taken from the surface of ground (P4000) Inconel 625 (6.0 wt.% Fe) laser coating.

In addition to this inhomogeneous composition and corrosion in macro-level, SEM examination revealed non-uniform composition in micro-level due to microsegregation, which led to the preferentially dissolved areas as well. As shown in Figure 63, Mo and Nb segregated to interdendritic regions forming Mo- and Nb-rich regions during rather slow solidification characteristics of HPDL cladding with wide rectangular beam geometry and low power density. According to EDS point analyses, segregation of Nb was stronger than segregation of Mo. The segregation of Cr was negligible. These results are in good agreement with the results reported by DuPont et al. [383], who measured alloy partition coefficients ($k = C_{solid}/C_{liquid}$) of 0.46–0.54 for Nb and 1.05 for Cr in Nb-bearing Ni-based superalloys. The more the k is below 1, the higher the solute's tendency to segregate into interdendritic regions and the more it is above 1, the higher the solute's tendency to segregate into dendrite cores.

According to Tinoco [384], Mo and Nb segregate to the interdendritic regions and Cr to dendrite cores in Inconel 625. He also showed that the degree of segregation for Nb decreases as the cooling rate increases. Knorovsky et al. [385] studied the segregation of Cr, Nb, Mo and Fe in Inconel 718. He found out that Nb and Mo segregate strongly to interdendritic regions whereas Cr and Fe weakly to dendrite cores. In samples studied here, the regions where Mo and Nb contents were lower (dendrite cores) dissolved preferentially as illustrated in SEM micrographs in Figure 63. Such profoundly dissolved regions either in macro- or micro-level were not detected, for instance, in wrought Inconel 625 indicating homogeneous elemental distribution. The degree of segregation in this laser coating was, however, small enough to survive these conditions without pitting corrosion. Dendrite cores with low Mo became susceptible to pitting corrosion since pitting usually starts in regions, which deplete Mo. According to common pitting resistance equivalent number (PREN) equations, Nb also enhances pitting corrosion resistance indicating that its microsegregation is detrimental.

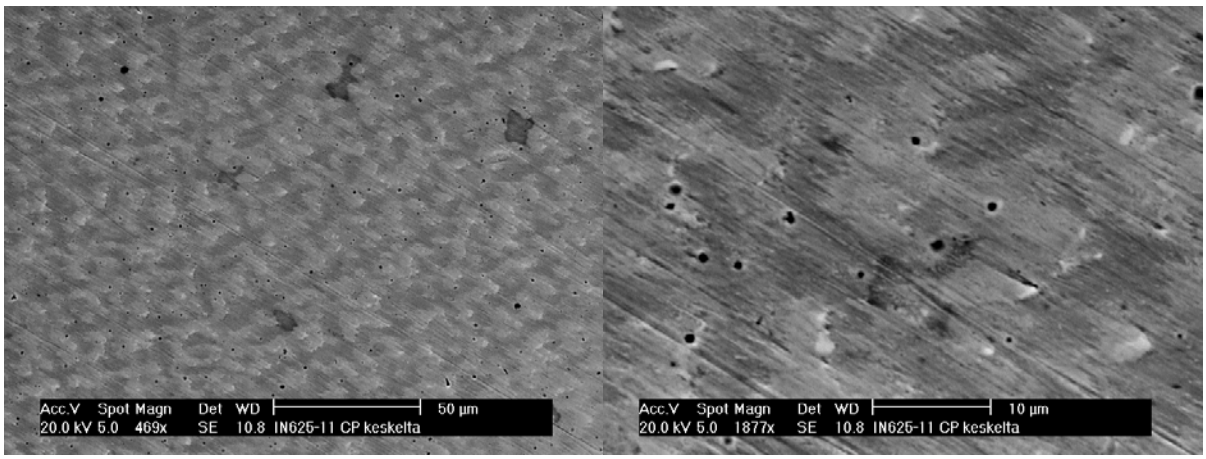

Figure 63. SEM image of the polarization tested surface of laser clad Inconel 625 (6.0 wt.% Fe). Light interdendritic regions are rich in Mo and Nb due to microsegregation. Dark dendrite cores are preferentially dissolved. Average composition of the light interdendritic region is Ni-19.4Cr-11.7Mo-7.7Nb-1.2Si-4.1Fe in wt.%. Average composition of the dark dendrite core is Ni-20.8Cr-8.2Mo-2.5Nb-0.6Si-4.9Fe in wt.%. Thus, C_{ID}/C_D for Nb was 3.1 and C_{ID}/C_D for Mo was 1.4. The widths of the segregated areas vary approximately from 5.6 to 8.3 µm. According to interaction volume simulation carried out by Edax Electron Flight Simulator, X-rays generate in the ball shape volume, which is 2.1 µm in diameter when the accelerating voltage is 20 kV. Thus, EDS point analyses can be considered reliable. Nominal composition of the Inconel 625 was used in simulation.

The influence of dilution (6.0 vs. 9.4 vs. 19.4 wt.% Fe) on corrosion resistance of Inconel 625 was studied in the case of HPDL clad coatings. In laser coating where Fe content was 19.4 wt.%, distinct E_b similar to wrought 316L was observed in three (+355, +442 and +678 mV) measurements out of five. Otherwise, the current density started to increase gradually at about +450 mV. The examination of the exposed surfaces revealed severe crevice corrosion under the gasket but central part of the surface was free from corrosion pits. In this coating, Fe was homogeneously distributed across the surface. Similarly, in laser coating where the Fe content was 9.4 wt.% clear E_b was observed in three (+390, +327 and 404 mV) measurements out of five. However, increase in current density was not as rapid as in coating with higher dilution (19.4 wt.% Fe) but definitely more obvious than in less diluted coating (6.0 wt.% Fe) or wrought alloy as shown in Figure 64. Central part of the exposed surface was again free from

corrosion pits, but moderate crevice corrosion under the gasket was observed. In this coating analogous with less diluted (6.0 wt.% Fe) one, Fe was distributed unevenly across the exposed surface. Obviously, the higher the amount of Fe in Inconel 625 and consequently the lesser amounts of Cr, Ni and Mo, the lower the resistance against localized corrosion and particularly against crevice corrosion since Fe impairs the properties of protective oxide layer. Even the least diluted coating (6.0 wt.% Fe) showed slight crevice corrosion under the gasket, which was not detected in wrought alloy, where the Fe content was 3.6 wt.%. As tabulated in Table 15, Fe also affected E_{rp}, which dropped with Fe increase. CRs calculated on the basis of I_{corr} showed no significant differences. It could have been anticipated that the most diluted coating exhibits the highest CR at E_{corr} but this was not the case perhaps due to homogeneous Fe distribution.

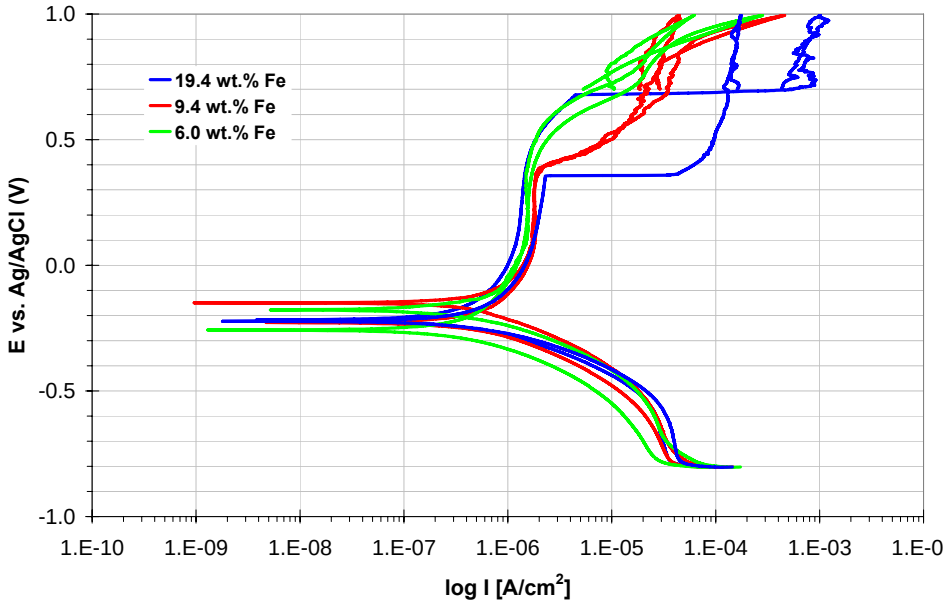

Figure 64. Representative potentiodynamic polarization curves for HPDL laser clad Inconel 625 coatings with different amounts of Fe measured in 3.5 wt.% NaCl solution at RT.

The advantage of low Fe content was further ascertained in the case of laser remelted Inconel 625 coating, which seemed to be superior to laser clad coatings and equivalent to or even better than wrought alloy. Fe content of this ~0.3 mm thick coating was just 1.5 wt.% showing nearly negligible dilution and it was evenly distributed across the exposed surface. Cyclic polarization curves revealed gradual increase in current density at +450-+600 mV similar to wrought alloy and the least diluted (6.0 wt.% Fe) laser coating. E_{rp} was at the level of E_{rp} measured for wrought alloy and clearly better than for more diluted laser coatings. CRs at E_{corr} were even lower than those for wrought alloy as shown in Figures 56 and 57. SEM examination of exposed surface revealed that neither pitting nor crevice corrosion occurred. Contrary to largely microsegregated HPDL coatings and more analogous with wrought alloy, preferentially dissolved areas were hardly detected as illustrated in Figure 65. This was attributed to the low amount of microsegregation due to high solidification rates, which originated from the high traverse speed (1900 mm/min) and low interaction time (0.25 s). This coating was not as susceptible to pitting corrosion as HPDL clad coating because Mo and Nb were more homogeneously distributed. Furthermore, low Fe content improved its resistance against crevice corrosion.

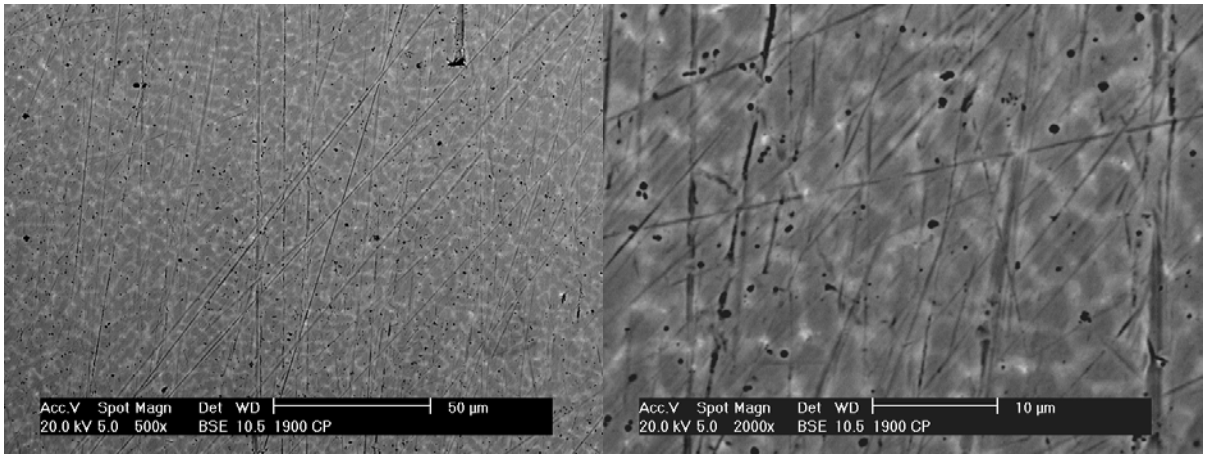

Figure 65. SEM image of the polarization tested surface of HVOF sprayed + laser remelted Inconel 625. Light regions are rich in Mo and Nb due to microsegregation. Dark regions are preferentially dissolved. Average composition of the light region is Ni-19.5Cr-9.6Mo-3.3Nb-0.6Si-1.6Fe. Average composition of the dark region is Ni-19.3Cr-9.2Mo-2.4Nb-0.5Si-1.5Fe. C_{ID}/C_D for Nb was 1.4 and C_{ID}/C_D for Mo was 1.04 indicating lower microsegregation compared with HPDL coatings. The widths of the segregated areas vary approximately from 1.3 to 1.7 µm. This arises error in compositional analysis by giving too low values for Mo and Nb in segregated regions.

In PTA overlay welded Inconel 625 coating distinctive increase in current density was observed 4 times out of 5 measurements. This increase was more abrupt than in curves measured from wrought alloy or the least diluted HPDL coating (6.0 wt.% Fe) but slighter than in wrought 316L or the most diluted HPDL coating (19.4 wt.%). Increase in current density occurred at potentials between +460-+580 mV, which is notably higher than in HPDL coatings containing 9.4 and 19.4 wt.% Fe. This is quite surprising since Fe content of this PTA overlay welded coating was as high as 25.1 wt.%. SEM examination of the exposed surface revealed that Fe was evenly distributed across the surface, central part of the area was free from corrosion pits and severe crevice corrosion took place under the gasket as illustrated in Figure 66. Moreover, considerably higher microsegregation was detected especially for Nb than in HPDL coatings suggesting slower solidification rates (Figure 67). Contrary to HPDL coatings Nb- and Mo-rich areas included less Cr than other areas (i.e. Cr segregated to the dendrite cores). This may explain the finding that the dendrite cores (Nb- and Mo-depleted areas) dissolved just slightly more than interdendritic (Nb- and Mo-rich) areas. Apart from other studied Inconel 625 materials, positive hysteresis loop was generated indicating perhaps crevice corrosion since corrosion pits were not detected. E_{rp} was also lower indicating poorer ability to re-heal its protective oxide layer.

Another Ni-based alloy, which showed excellent corrosion performance was laser clad Alloy 59. This high Mo content (16 wt.% Mo) and low diluted (2.5 wt.% Fe) coating was manufactured with Nd:YAG laser equipped with Coax 8 cladding nozzle. Equivalent to best Inconel 625 coatings and wrought alloy, gradual increase in current density started at +450 mV but E_{rp} of +490 mV was even higher than for wrought Inconel 625 alloy. This coating did not suffer from pitting or crevice corrosion under the gasket.

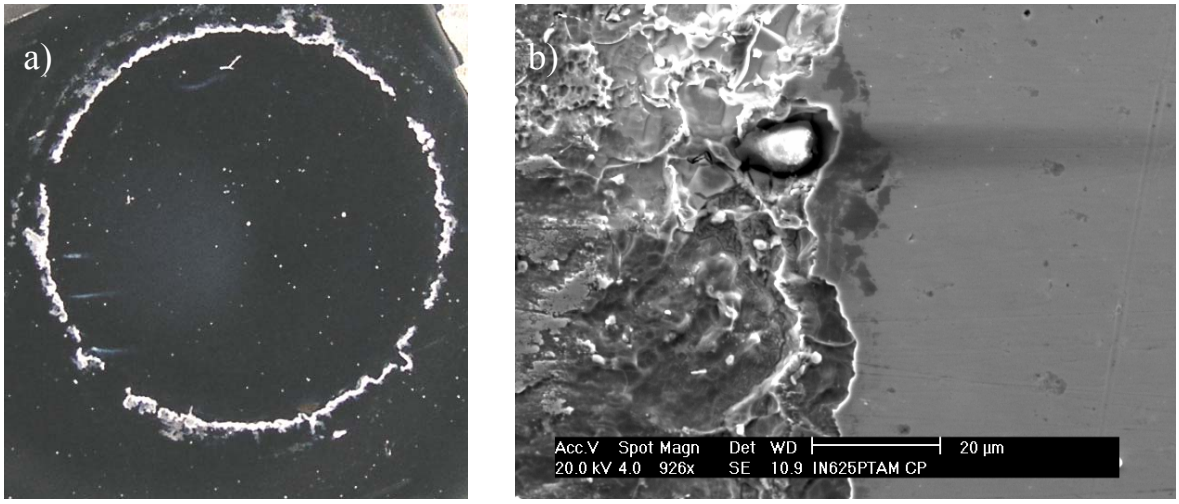

Figure 66. Polarization tested surface of Inconel 625 PTA; a) macrograph and b) SEM image showing severe crevice corrosion under the gasket. Diameter of the exposed area is 11 mm.

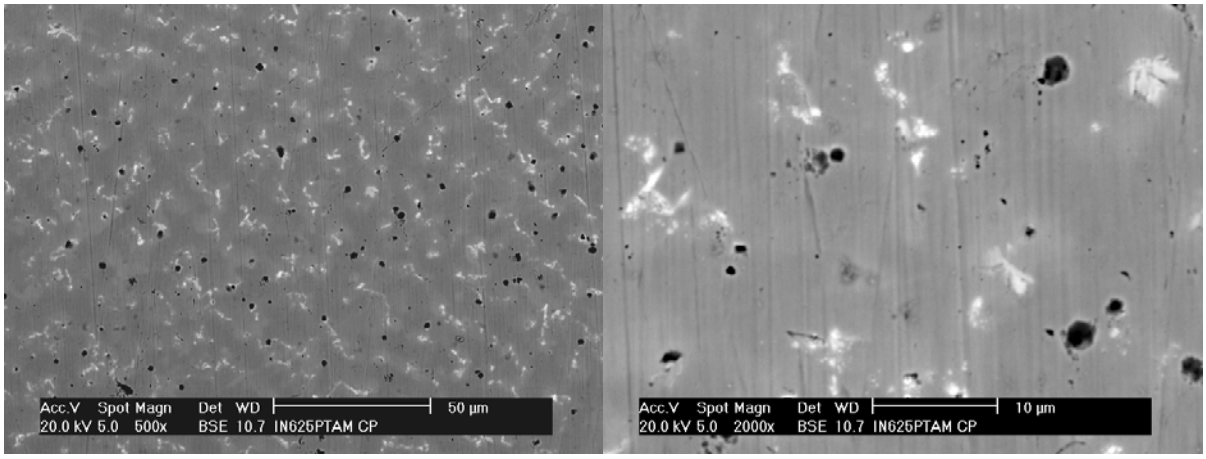

Figure 67. SEM image of the polarization tested surface of PTA overlay welded Inconel 625. Light interdendritic regions are rich in Mo and Nb due to microsegregation. Dark dendrite cores are preferentially dissolved. Average composition of the light region is Ni-11.9Cr-10.5Mo-32.2Nb-0.6Si-14.7Fe. Average composition of the dark region is Ni-16.5Cr-6.9Mo-1.8Nb-0.6Si-24.7Fe. C_{ID}/C_D for Nb was 17.9 and C_{ID}/C_D for Mo was 1.5. The widths of the segregated areas vary approximately from 6.6 to 13.2 µm. This confirms the reliability of EDS point analyses. Black dots are rich in Ti and Nb. Cr and Fe segregated to the dendrite cores since alloy partition coefficients are 1.05 for Cr and 1.02 for Fe in Inconel 625 [383]. PTA coating has higher susceptibility to pitting corrosion than laser coating because Mo and Nb were more severely segregated. Segregation of Cr to dendrite cores may, however, balance this a bit.

High-Cr NiCr (SX-717) laser coating even if heavily diluted (12 wt.% Fe) outperformed Ni-based alloys in corrosion resistance, that is, no signs of crevice or pitting corrosion was detected. Slight increase in current density started at noticeably higher potential (+560 - +780 mV), anodic current densities and I_{corr} were lower and E_{rp} higher than in Inconel 625 or Alloy 59. Ni-rich phases were more susceptible to corrosion than Cr-rich phases (cf. hot corrosion properties in section 3.3.1.2).

3.2.2.2 Co-based alloys

Stellite 21 laser coating (Nd:YAG, 1.3 wt.% Fe) exhibited potentiodynamic polarization curves nearly identical to wrought and low diluted Inconel 625 and Alloy 59 laser coatings including slight increase in current density between +450-+500 mV. E_{rp} was equivalent to Alloy 59 and substantially higher than those for the best Inconel 625 alloys. I_{corr} values settled between remelted and wrought Inconel 625. In addition, Stellite 21 laser coating was immune to crevice corrosion under the gasket and pitting corrosion. Instead, SEM studies of exposed surface revealed preferentially dissolved areas in micro-level, where Cr- and Mo-rich interdendritic regions, in consequence of microsegregation, dissolved considerably less than dendrite cores as shown in Figure 68. Consequently, dendrite cores became susceptible to pitting corrosion due to lack of Mo and Cr. In given conditions, Mo and Cr contents were, however, high enough to resist pitting. According to EDS point analyses, C_{ID}/C_D for Mo was 3.8 and for Cr 1.4. Overlapped areas, where the scale of the microstructure is clearly coarser, were revealed by dissolution as shown in Figure 69a.

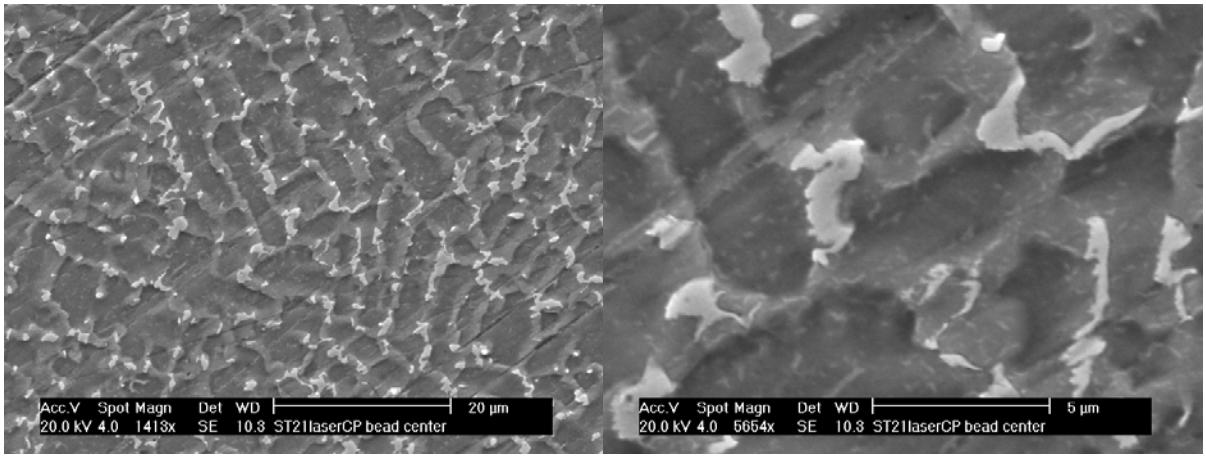

Figure 68. SEM image of the polarization tested surface of Stellite 21 laser coating. Light regions are rich in Mo and Cr due to microsegregation. Dark regions are preferentially dissolved. Average composition of the light region is Co-34.9Cr-15.0Mo-2.3Ni-1.4Si-0.9Fe, whereas the dark region is Co-25.4Cr-4.0Mo-3.4Ni-1.1Si-1.2Fe in wt.%. C_{ID}/C_D for Mo was 3.8 and for Cr 1.4. The widths of the segregated regions are less than 1.0 µm. Small size and uneven surface quality may have caused some error in quantitative EDS analyses (EDS point analysis; 20 kV, tilt 0º). According to interaction volume simulation carried out by Edax Electron Flight Simulator, X-rays generated in the ball shape volume, which was 2.2 µm in diameter. Nominal composition of Stellite 21 was used in simulation.

Compared with more heavily diluted PTA coating (24.0 wt.% Fe), laser coating showed substantially better corrosion performance as shown in Figures 54, 56 and 57 and in Table 15. Anodic current densities were distinctively higher for PTA coating and slight increase in current density took place at potential range as low as +230-+400 mV indicating Fe's detrimental effect on passive film. Moreover, E_{rp} was significantly higher for laser than that for PTA coating. Similar to PTA overlay welded Inconel 625, Stellite 21 PTA coating possessed positive hysteresis loop. Instead of severe crevice corrosion under the gasket observed in PTA overlay welded Inconel 625, Stellite 21 PTA coating exhibited slight pitting corrosion in the central regions of the exposed areas while crevice corrosion under the gasket was absent (Figures 69b and 70). This susceptibility to pitting can be attributed to the higher dilution and microsegregation. If polarization curves for PTA overlay welded Inconel 625

(25.1 wt.% Fe) and Stellite 21 (24.0 wt.% Fe) are compared (Figure 71), it can be noted that Stellite 21 possessed higher anodic current densities and increase in it took place at lower potentials. E_{rp} was also substantially lower for PTA overlay welded Stellite 21.

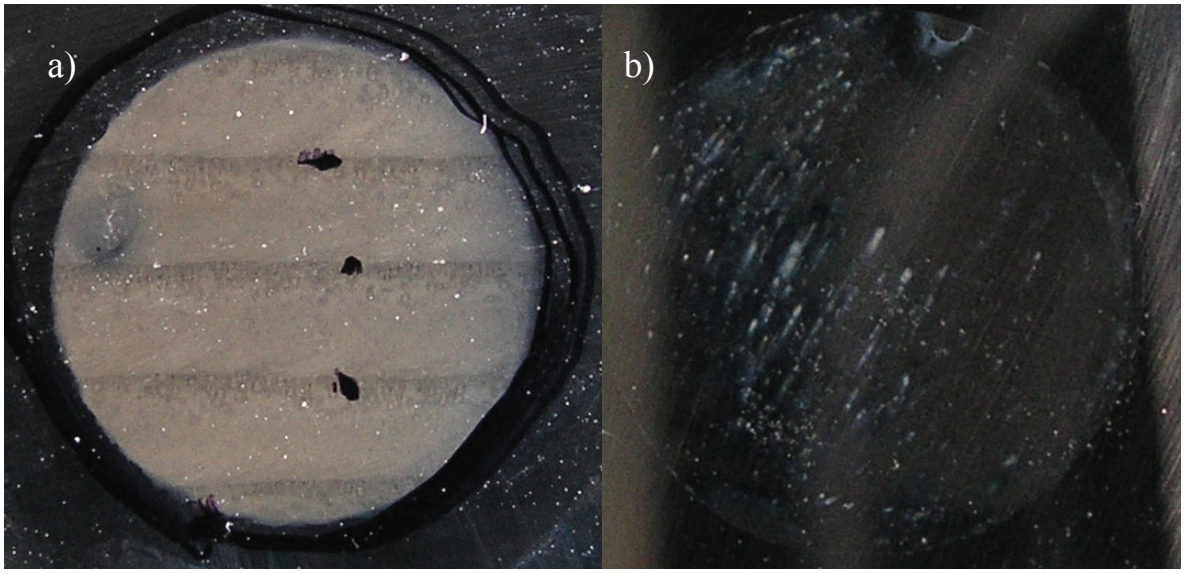

Figure 69. Optical macrographs of cyclic polarization tested surface of a) laser clad and b) PTA overlay welded Stellite 21. Inter-track advance in laser cladding was 2.5 mm. Three black dots shown on the surface of laser coating are pen marks. Corrosion pits are clearly seen on the surface of PTA overlay welded coating.

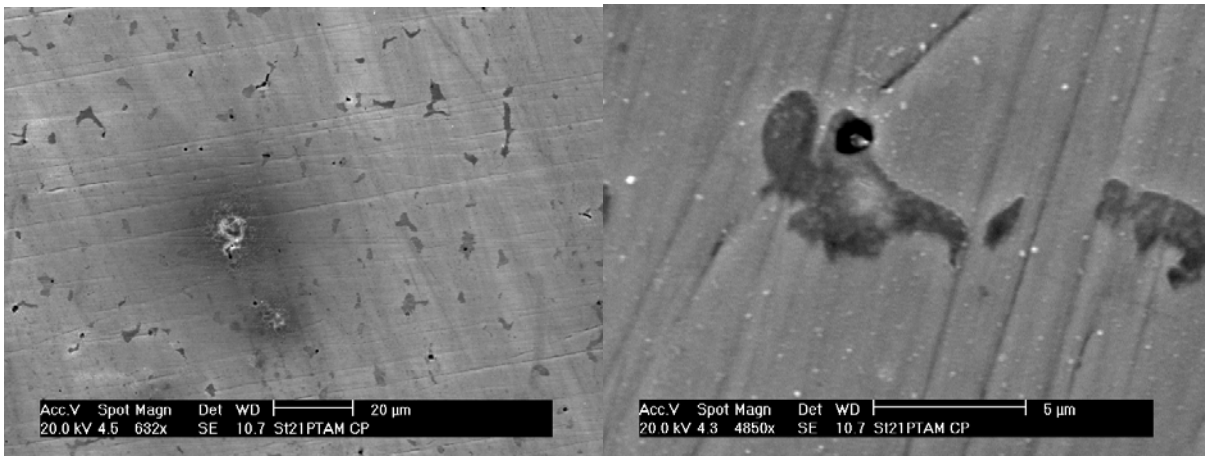

Figure 70. SEM images of the polarization tested surface of PTA overlay welded Stellite 21. Dark regions are rich in Mo and Cr. Average composition of the dark region is Co-32.2Cr-17.8Mo-1.4Ni-1.4Si-16.8Fe. Average composition of the light region is Co-20.3Cr-4.4Mo-2.7Ni-1.3Si-23.3Fe. Widths of these dark regions vary approximately from 2.0 to 3.0 µm. Corrosion pits are clearly seen in lower magnification micrograph.

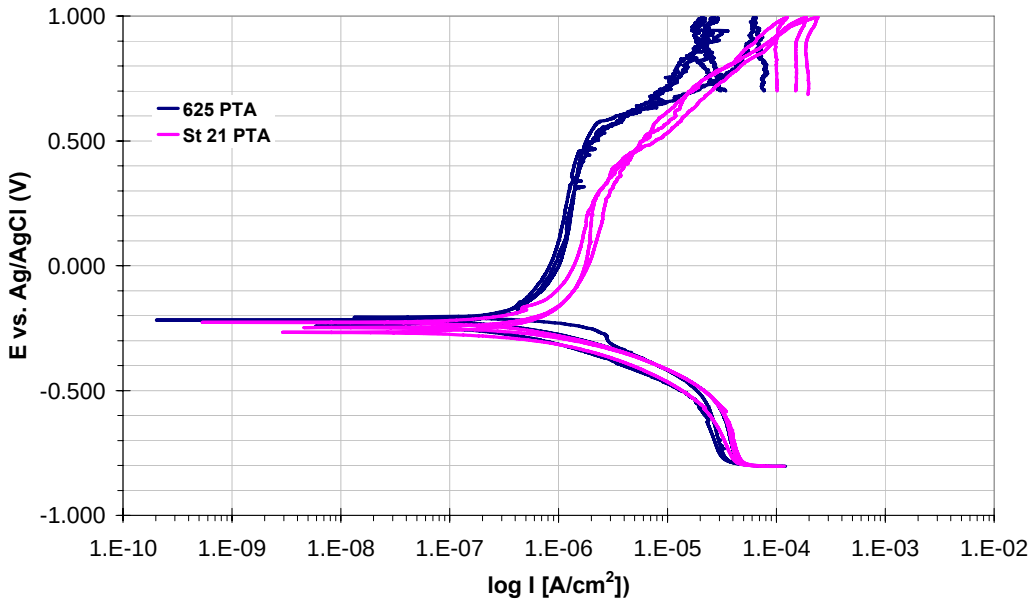

Figure 71. Representative potentiodynamic polarization curves for PTA overlay welded Inconel 625 (3) and Stellite 21 (3) coatings measured in 3.5 wt.% NaCl solution at RT.

Low diluted Stellite 6 coating (1.6 wt.% Fe) produced by Nd:YAG laser showed corrosion performance comparable with Stellite 21 in given circumstances, that is, anodic current densities and E_{rp} were nearly identical and increase in current density occurred at +450-+550 mV. SEM examination of the exposed surface revealed that crevice corrosion under the gasket and pitting corrosion in central regions was absent. Instead, analogous with Stellite 21 laser coating, preferentially dissolved areas were detected as displayed in Figure 72. That is, Cr- and W-rich interdendritic regions consisting of fcc-Co and carbides were less attacked than Cr- and W-depleted dendrite cores.

Compared with Stellite 6 produced by HIPping (1.0 wt.% Fe), laser coating exhibited identical polarization curves except for E_{rp}, which was lower for HIPped alloy (Figure 55, Table 15). Similar to laser coating, Cr-depleted matrix was more severely dissolved than Cr-rich carbides (Figure 73). Crevice and pitting corrosion was absent. Apart from the interconnected network of carbides in laser coating, discrete spherical carbides were found from the HIPped alloy and matrix contained more W than carbides.

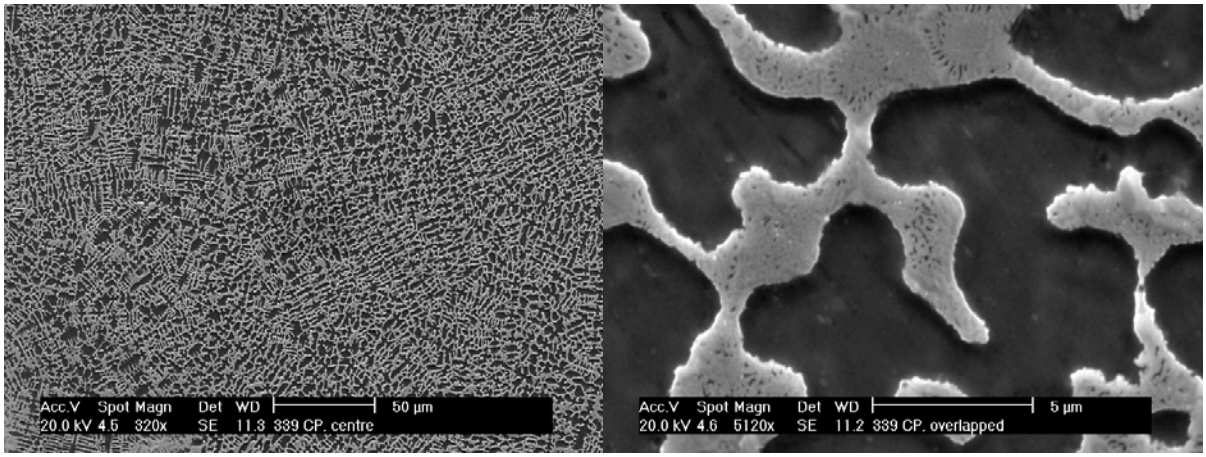

Figure 72. SEM images of the polarization tested surface of Stellite 6 laser coating. Light interdendritic regions are mixture of Cr-rich M_7C_3 carbides and small amounts of fcc Co. Dark Co (fcc) matrix is preferentially dissolved. Average composition of the interdendritic region is Co-40.0Cr-7.5W-1.6Ni-0.6Si-0.5Mo-1.2Fe, whereas for the matrix it is Co-23.9Cr-3.8W-2.4Ni-0.9Si-0.1Mo-2.0Fe in wt.% (EDS point analyses, 15 kV). C_{ID}/C_D for Cr was 1.7 and for W 2.0. Overlapped regions were coarser than central regions of bead.

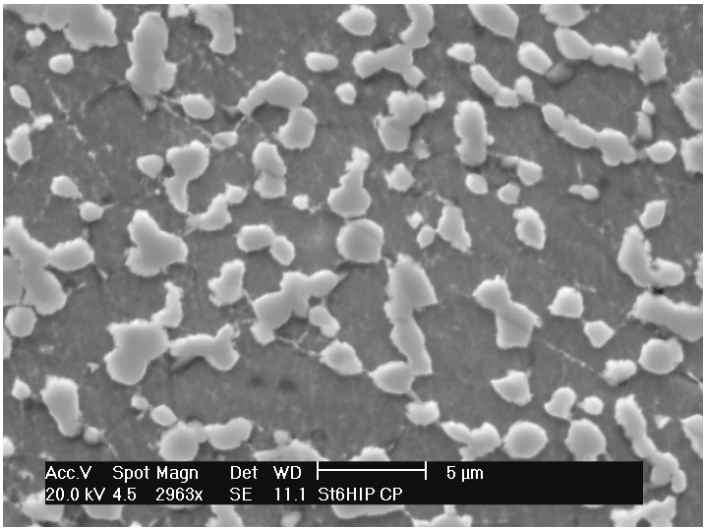

Figure 73. SEM image of the polarization tested surface of HIPped Sellite 6. Light regions are Cr-rich carbides. Dark matrix is preferentially dissolved. Average composition of the carbides is Co-77.3Cr-3.3W-0.4Ni-0.1Si-0.5Mo-0.3Fe (EDS point analyses, 15 kV). Average composition of the dark matrix is Co-20.8Cr-6.7W-2.2Ni-1.0Si-0.4Mo-1.2Fe. $C_{carbide}/C_{matrix}$ for Cr was 3.7 and for W 0.5. As opposed to Stellite 6 laser coating W content is higher in matrix than in carbides. This is due to W's tendency to segregate into interdendritic liquid during solidification, which takes place in laser cladding. On the contrary Cr content in carbides is much higher than in laser coating.

3.3 Hot corrosion properties

In hot corrosion tests, the selected metal alloys were mainly exposed to Na_2SO_4-V_2O_5 (50/50 wt.%) (Na:V=1.27) salt in air at 650°C for 1000 hours. They comprised Cr- (SX-707, SX-717) and Ni-based (Inconel 625) laser coatings, HVOF sprayed Cr-based (SX-707) coating and wrought Ni- (Inconel 625, Inconel 718, Nimonic 80A) and Fe-based (42CrMo4) alloys. In order to study the influence of salt composition, HVOF sprayed SX-707 and wrought Nimonic 80A were exposed to Na_2SO_4-V_2O_5 (15/85 wt.%) (Na:V=0.22) in air at 650°C for 1000 hours. The influence of temperature was studied by exposing HVOF sprayed SX-707 to Na_2SO_4-V_2O_5 (15/85 wt.%) (Na:V=0.22) in air at 650, 750 and 850°C for different periods of time (100–1000h). Chemical compositions of the laser coatings revealing the magnitudes of dilution are tabulated in Table 16. They are the average values of three EDS area measurements taken from the transverse cross-sections of as-laser-clad coatings near the surface to be exposed. According to thickness loss measurements given in Figure 74, all the tested laser coatings and HVOF coating exhibited good resistance to hot corrosion. The resistances of these coatings appeared to be even slightly better than that of wrought Nimonic 80A and much better than that of other wrought reference alloys. The average COV of all the measurements was 17%. The highest COV, 58%, and the lowest, 0%, were calculated for SX-717 and Inconel 625 laser coatings, respectively. Average coating thicknesses (2 samples per coating, 12 measurements per sample) before and after the test were 717 µm (11 µm STDEV) and 657 µm (9 µm STDEV) for Inconel 625 laser, 396 µm (8 µm STDEV) and 345 µm (10 µm STDEV) for SX-707 HVOF and 1093 µm (9 µm STDEV) and 1054 µm (11 µm STDEV) for SX-717 laser.

Hot corrosion morphology of the tested alloys was generally characterized by thick and relatively dense reaction product layers with the underlying alloy depleted in Cr. These reaction product layers were found to consist mainly of Ni, Cr, V and O, which formed compounds like nickel ortho- ($Ni_3V_2O_8$) and chromium vanadates ($CrVO_4$) as revealed by XRD measurements. The former one was the major phase in reaction product layers on Ni-based whereas the latter one was the major one on Cr-based alloys. $CrVO_4$ was found mainly in the vicinity of metal surface and $Ni_3V_2O_8$ on the outermost areas of corrosion product. Cr- and Ni-sulphides or protective oxide layers like NiO, Cr_2O_3 and $NiCr_2O_4$ were not detected. Melting temperatures of $Ni_3V_2O_8$ and $CrVO_4$ are 1220 and 810°C, respectively [386]. This suggests that the reaction product layers remained solid underneath the regularly added salt layer. Na was nearly absent since only some small traces were detected in reaction product layers. Microstructures before and after the tests as well as reaction product layers of the tested materials are shown and discussed in greater detail in sections 3.3.1 and 3.3.2.

Influence of salt composition on thickness losses is shown in Figure 75a. It reveals that salt, which contained higher fraction of V_2O_5 was more corrosive than salt (Na:V=1.27). Figure 75b shows the influence of temperature and time on thickness losses. It can be noticed that the higher the temperature and longer the exposure time, the more severe the deterioration. Temperature increase from 650 to 850°C increased the thickness loss at least by a factor of 5. It can be further observed that deterioration rates in HVOF sprayed SX-707 were more like accelerating rather than constant or decelerating at all the test temperatures.

Table 16. Average chemical compositions of the as-laser-clad coatings in wt.%. Inconel 625 contained also 0.5 wt.% Mn.

Material	***Ni***	***Cr***	***Mo***	***Nb***	***Fe***	***Si***	***Al***	***Ti***
SX-707 (HPDL)	41.0	49.0	3.0		6.0	1.0		
SX-717 (HPDL)	41.0	53.0	3.0		2.0	1.0		
Inconel 625 (HPDL)	62.6	20.9	8.9	3.8	2.6	0.4	0.1	0.2

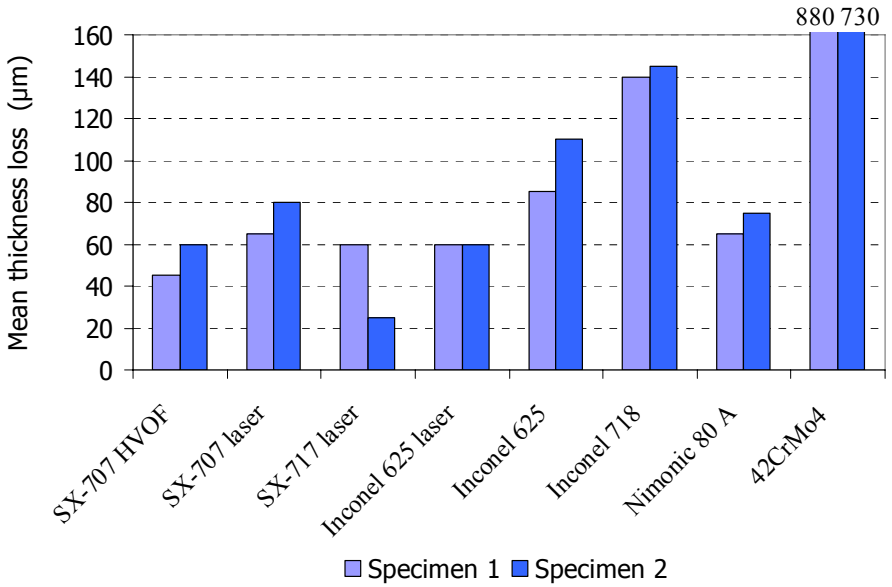

Figure 74. Thickness loss measurements taken from the alloys exposed to Na_2SO_4-V_2O_5 (50/50 wt.%) (Na:V=1.27) in air at 650℃ for 1000 h. Possible internal penetration is not taken into account.

3.3.1 Coatings

The results concerning the coatings Inconel 625 laser, SX-717 laser, SX-707 laser and SX-707 HVOF are shown and discussed below.

3.3.1.1 Inconel 625 laser

Microstructure of Inconel 625 coating produced by HPDL was presented earlier in Figures 43 and 44 in section 3.2.1. Hot corrosion test specimen studied here was essentially the same except for lower compositional dilution, which was only 2 % calculated according to equation given in Ref. [27]. Heavily and increasingly diluted zone in the coating next to interface was neglected in calculation. Width of this zone at the centre of bead was 160 µm according to EDS line scan analysis. Microhardness of the coating was ~250 $HV_{0.3}$. Another difference between wet and hot corrosion specimens was the base material. In this case, where the coating was laser clad on high carbon equivalent 42CrMo4 (CE = 0.68), underneath the clad, i.e. in the outermost layer of the base material, hardened HAZ was developed. In this zone, the temperature arose well above the A_3 temperature and the pearlite/ferrite structure transformed into austenite. Upon subsequent fast cooling, this new phase underwent a further phase transformation and became martensite at M_s temperature and below (M_s = 315°C for AISI 4340). Due to absence of subsequent passes (overlapping) or the second layer,

martensite did not become tempered. Hardness of this zone, which reached to a depth of 1.2 mm, was ~635 HV_1.

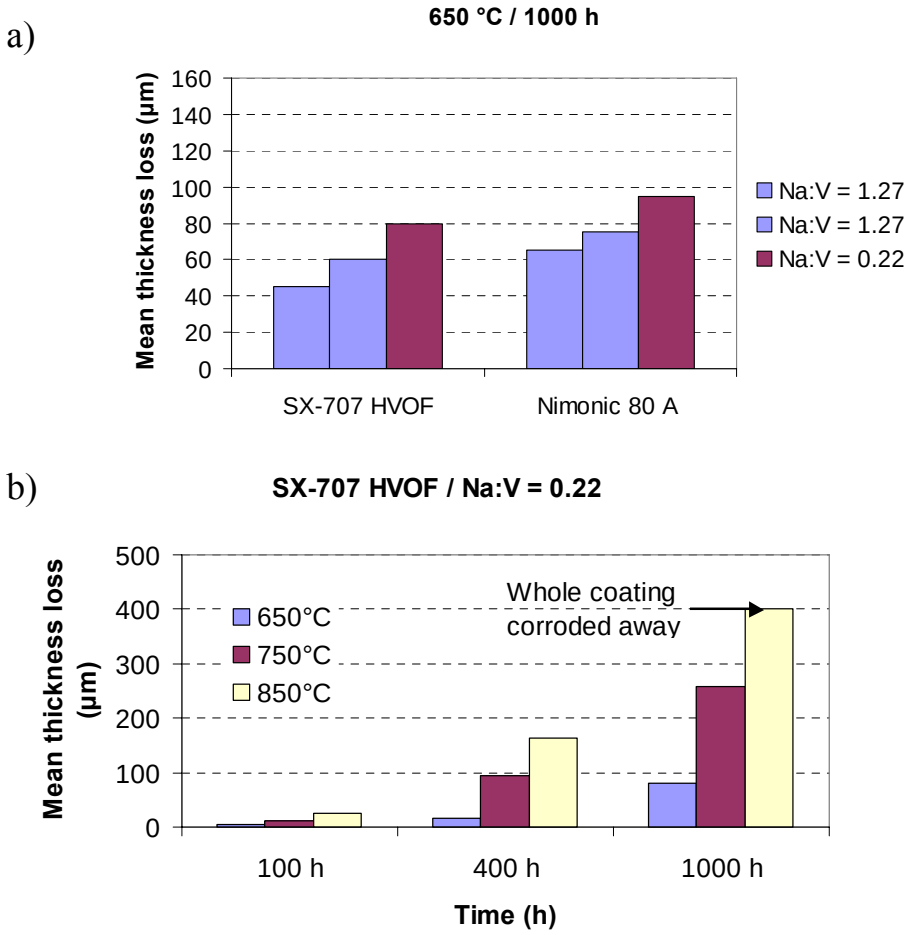

Figure 75. Influence of a) salt composition and b) temperature and time on mean thickness loss.

In hot corrosion test, the surface of Inconel 625 laser coating deteriorated uniformly as illustrated in Figure 76. Reaction product layer was stratified to several thin layers unlike that found in Cr-based coatings, which will be discussed later. Despite Cr-rich reaction product layer next to coating alloy, no distinct Cr-depleted zone was detected in the coating as revealed by BSE-image in Figure 76b and EDS line scan analysis in Figure 77. It is still noteworthy to point out that annealing at 650°C for 1000 hours did not homogenize the microsegregated Nb and Mo in the clad layer as evidenced by the EDS point analyses taken from the bright and dark phases before and after the exposure. This could be attributed to their larger atomic radii compared with Ni and Cr, which would hinder their solid-state diffusion in fcc crystal structure. For the sake of comparison, Kujanpää and David [315] managed to homogenize Mo in fcc-ordered iron austenite at 1150°C during the period of 16 minutes as discussed earlier in section 1.5.3.1. Precipitation of γ' phase could be other possible change in microstructure and their transformation further to orthorhombic Ni_3Nb but the examination of these was neglected here.

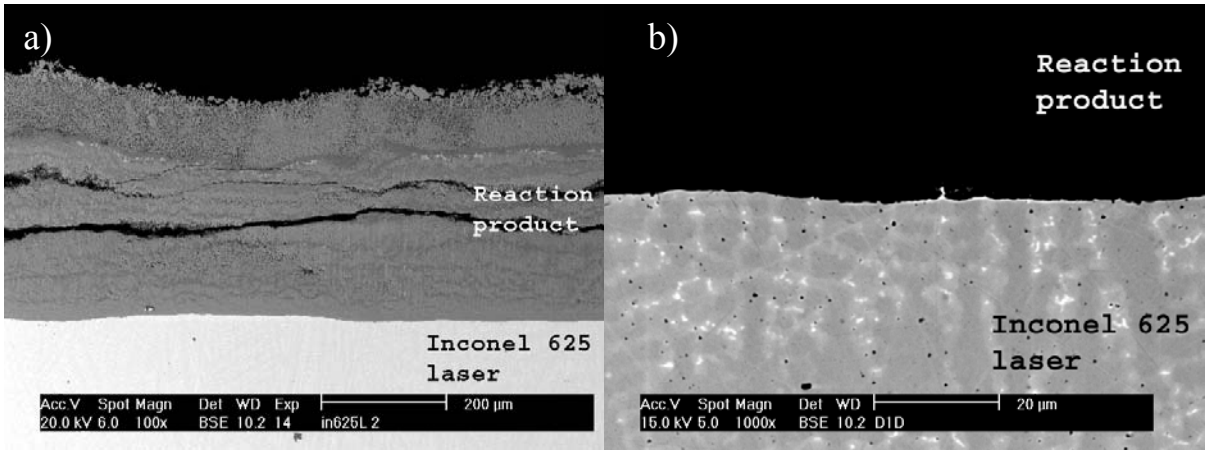

Figure 76. BSE image of transverse (perpendicular to cladding direction) cross-section of Inconel 625 laser coating reacted at 650℃ in air with Na_2SO_4–V_2O_5 (50/50 wt.%) (Na:V = 1.27) on the surface.

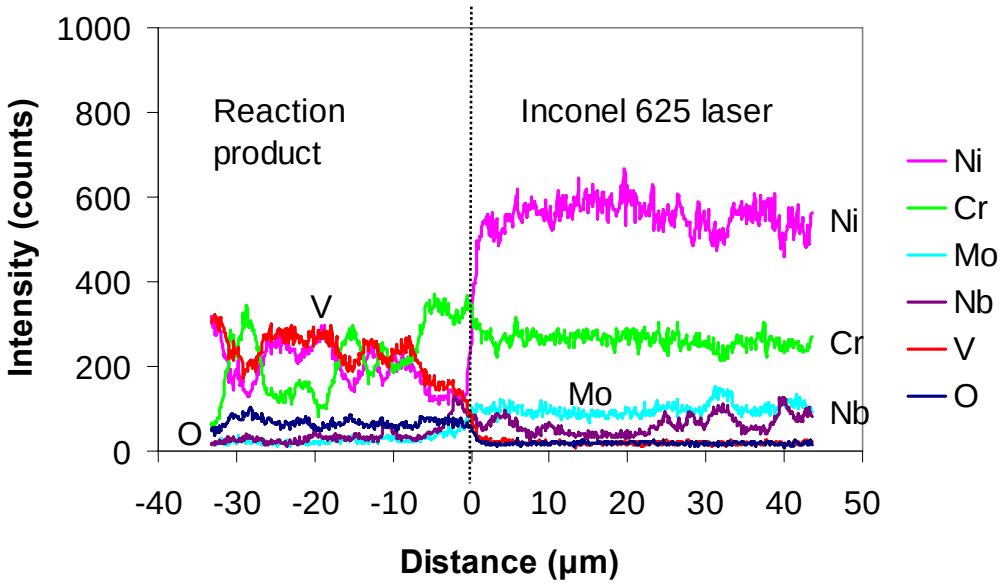

Figure 77. EDS line scan analysis along the cross-section of tested Inconel 625 laser coating.

3.3.1.2 SX-717 laser

This Cr-based laser coating exhibited very dense and crack-free dendritic (longer secondary arms than in Inconel 625) microstructure strongly bonded to the base material as illustrated in Figure 78. Compared with cellular columnar grains observed, for instance, in laser clad Inconel 625, such long secondary arms are claimed to be important for retarding the migration of sulphur ions into the alloy during the hot corrosion process [324]. In consequence of selective solidification and eutectic reaction, segregation of phases occurred as revealed by the high magnification BSE-image in Figure 78b. The average composition of Cr-rich dendritic phase, which was identified as bcc ordered α-Cr, was 35Ni-59Cr-3Mo-1Si-2Fe in wt.% on the basis of EDS point analyses. Interdendritic region, which consists of α-Cr and fcc ordered Ni-rich γ-phase, showed the composition of 47Ni-48Cr-2Mo-1Si-2Fe in wt.%. Compositions of these areas were not detected to vary as a function of depth of the coating. Obviously, the alloy exhibited extended solid solubility since Cr-rich α-phase dissolved much

more than just ~2 wt.% Ni as suggested by the eutectic binary Ni-Cr equilibrium phase diagram shown in Figure 79 [387]. Due to very fine-scale microstructure particularly in interdendritic regions, the volume fraction of the phases present was attempted to estimate using direct comparison method presented in Ref. [378]. The pairs of (200)γ and (110)α and (111)γ and (200)α reflections shown in Figure 80 were considered. On the basis of this calculation, as-laser-clad coating contained 47 vol.% of α-phase and 53 vol.% of γ-phase. Compositional dilution was only 2%. Microhardness of the coating was 575–590 $HV_{0.3}$ (552–562 HV_1). Small black dots irregular in shape shown in Figure 78b are probably shrinking cavities because they are found only in the interdendritic regions. Gas pores can be excluded since they would have been spherical in shape [166].

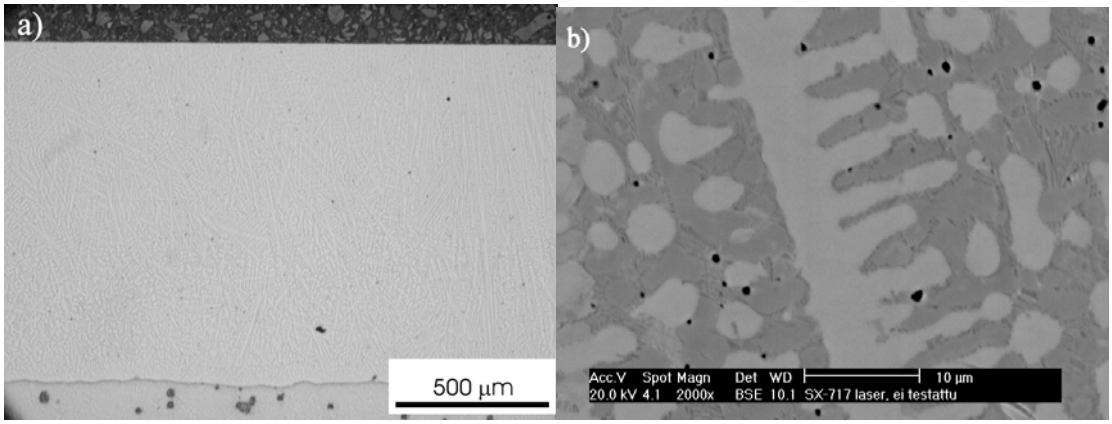

Figure 78. SX-717 laser coating; a) optical micrograph and b) BSE image. Light areas are rich in Cr and Mo compared to composition of initial powder, i.e. dendrites are α-Cr, whereas interdendritic regions consist of (α + γ) eutectic.

In hot corrosion tests, this Cr-based laser coating possessed the highest resistance among the tested alloys. The surface exposed to the salt deteriorated uniformly and the reaction product layer was rather dense in the vicinity of coating surface as illustrated in Figure 81. Elemental maps and EDS line scan analysis (Figures 81 and 82) revealed that the reaction product layer was rich in Cr in this area, whereas outermost layers were rich in Ni. High magnification BSE-images revealed that coating regions rich in Cr and Mo were more heavily attacked than Ni-rich regions. These Cr- and Mo-rich regions appear dark in Figures 83-84. It was also observed that during annealing at 650°C for 1000 h, Cr-rich phases enriched further with Cr as could be expected on the basis of equilibrium binary phase diagram. The average composition of the Cr-rich α-phase was now 32Ni-63Cr-3Mo-1Si-1Fe in wt.% compared with 35Ni-59Cr-3Mo-1Si-2Fe before the test. The average composition of the interdendritic region was 48Ni-47Cr-2Mo-1Si-2Fe in wt.% compared with 47Ni-48Cr-2Mo-1Si-2Fe before the test. It was also noted that the amount of α-phase increased during the test. If the volume fractions were 47α-53γ (%) before the test, they were 55α-45γ (%) after the test. Binary phase diagram suggests that the equilibrium chemical compositions (wt.%) of the α- and γ-phases at 650°C are 2Ni-98Cr and 68Ni-32Cr. With the initial composition of 44.3Ni-55.7Cr (wt.%) volume fractions of α- and γ-phases should have been 40% and 60%, respectively. This direct comparison method with the selected peaks gives obviously too high values for α-Cr and too low values for γ-Ni. It does not, however, change the observation that the amount of Cr-rich α-phase increased during annealing. In addition to EDS point analyses, another finding which may support the increase of Cr content in α-phase (and decrease of Cr in γ-phase) was the

change in lattice parameters (a). It was noted that the lattice parameter of γ-phase decreased 1.2% during the test from 0.3590 nm to 0.3548 nm. Lattice parameter of pure Ni is 0.3523 nm. Equivalent atomic radius of Ni is 0.1377 nm and Cr 0.1420 nm. In contrast, the lattice parameter of α-phase changed just 0.2%. Another factor noteworthy to point out is the amount of Fe. EDS analyses suggest that interdiffusion did not take place between coating and base material during annealing. Hardness profiles before and after the test are illustrated in Figure 85. It indicates that microhardness (HV_1) decreased only on outer surface of coating layer.

Tomita et al. [388] annealed PTA overlay welded NiCr (50/50) clads at 500–750 °C. They also observed increase in α-phase but also the precipitation of fine Cr-rich α'-phases. According to them, α-phases precipitated in γ-phases next to grain boundaries growing inside γ-phases. Fine Cr-rich α'-phases precipitated in γ-phases as well.

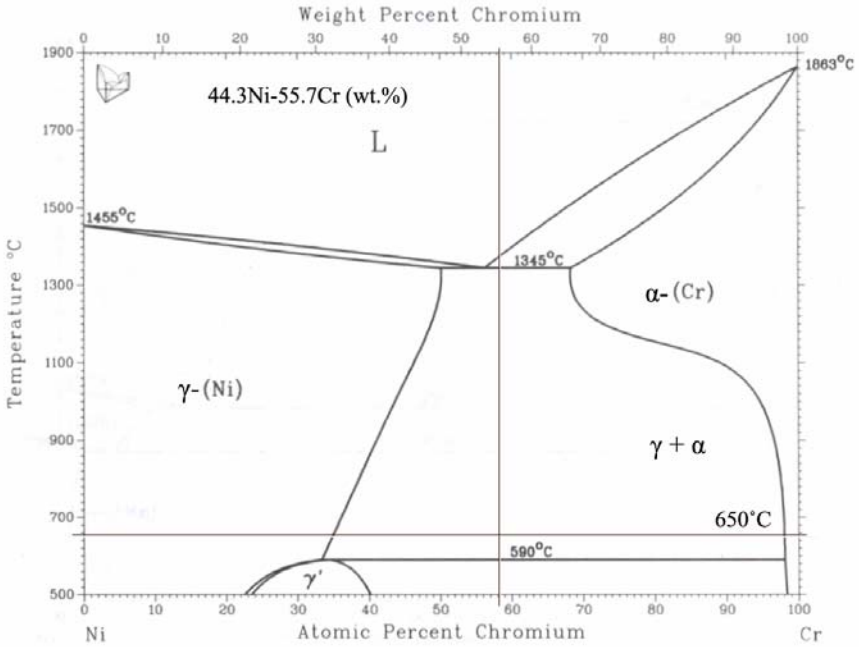

Figure 79. Eutectic binary equilibrium phase diagram for Ni-Cr. SX-717 is hypereutectic alloy having a composition to the right of the eutectic point. In equilibrium, liquid 44.3Ni-55.7Cr (wt.%) starts to solidify at 1371˚C. At this temperature solid α-Cr (32Ni-68Cr) starts to form (dendrites). Temperature drops and concentrations of phases follow liquidus and solidus. At eutectic temperature 1345˚C equilibrium exists between solid α-Cr (35Ni-65Cr) and liquid (47Ni-53Cr). According to lever rule, their weight fractions are 16% α-Cr and 84% liquid, i.e. the weight fraction of α-Cr is 16% and eutectic (α-Cr + γ-Ni) 84%. When cooling continues eutectic reaction takes place; liquid -> α-Cr and γ-Ni (this is interdendritic region). γ-Ni or α-Cr forms the matrix for interdendritic region. The one, which is not the matrix takes the form of, for example, plates (widmanstätten). At 650˚C eutectic matrix consists of 34% α-Cr and 66% γ-Ni in weight fractions. Overall, taking into account α-Cr primary dendrites, phase weight fractions in equilibrium at 650˚C are 37% α-Cr and 63% γ-Ni, which is in volume fractions 40% α-Cr and 60% γ-Ni.

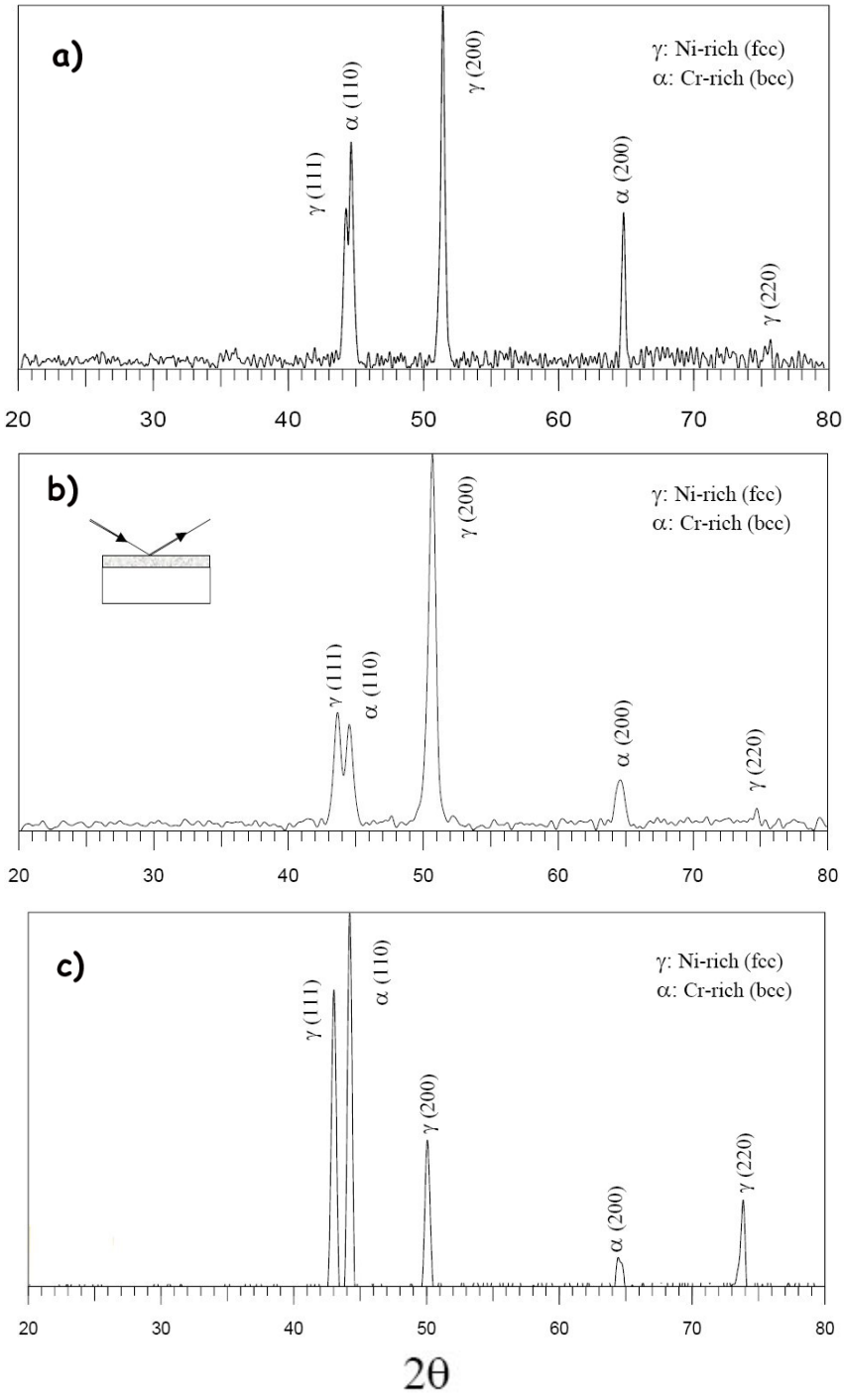

Figure 80. X-ray diffraction patterns of SX-717: a) hot corrosion tested laser coating and b) as-laser-clad coating and c) powder. Distance from the coating/base material interface to the surface of the ground coating was 990 μm in both cases.

3.3.1.3 SX-707 laser

Compared with hypereutectic SX-717 alloy, composition of SX-707 is more like eutectic (46.9Ni-53.1Cr in wt.%) due to higher Ni and lower Cr contents. Nevertheless, microstructure consisted of Cr-rich dendrites analogous with SX-717 alloy. Cr-rich dendrites contained 52 wt.% Cr and 42 wt.% Ni, whereas interdendritic areas contained 46 wt.% Cr and 48 wt.% Ni. Owing mainly to compositional dilution of 6 %, microhardness in the range of 460–470 $HV_{0.3}$ was substantially lower than that in laser clad SX-717. Degradation of the coating was similar

to SX-717 laser coating. Thickness loss was notably higher than in the SX-707 HVOF coating, most likely due to higher Fe content as a result of dilution. Reaction product layer was very similar to that observed on top of SX-717 laser coating.

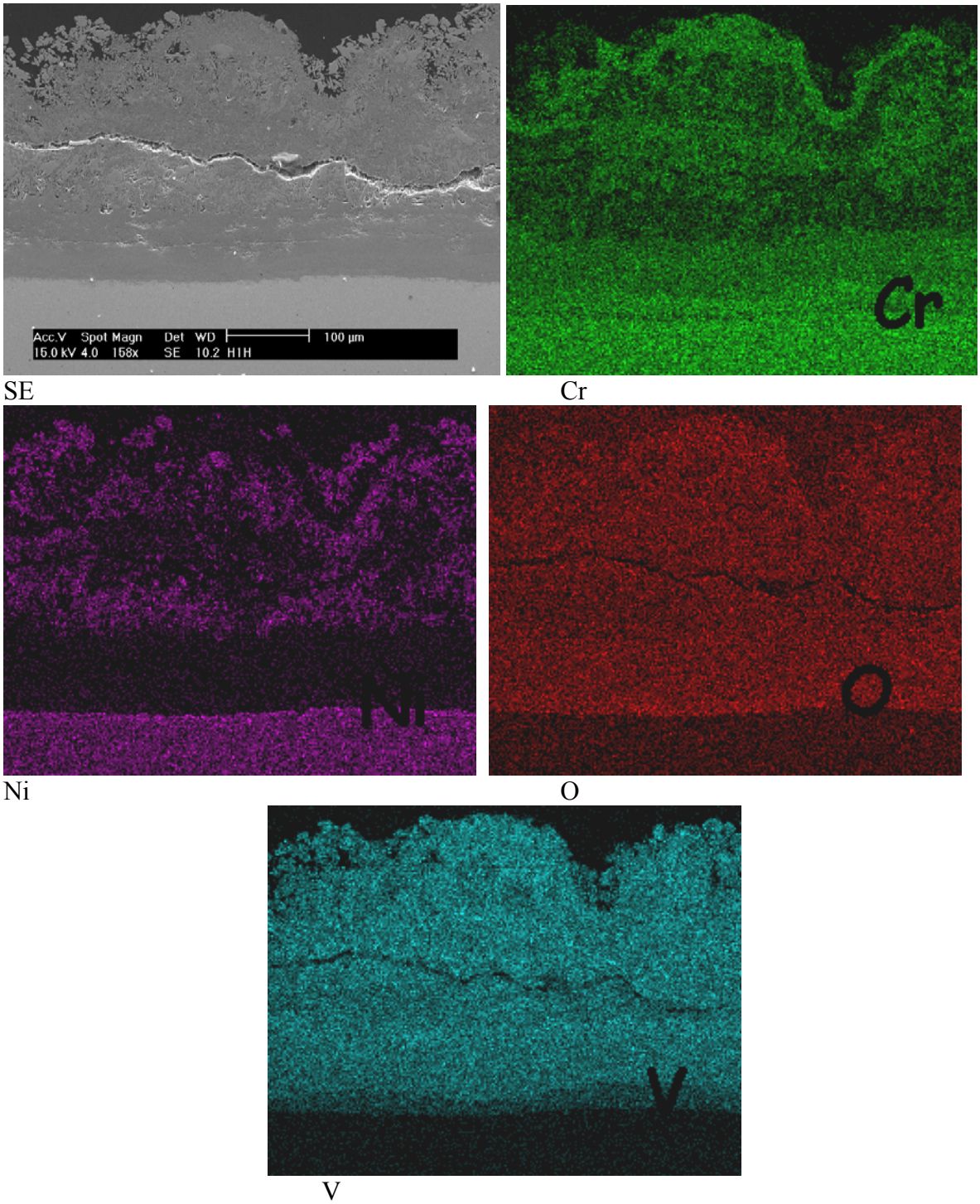

SE Cr

Ni O

V

Figure 81. Reaction product layers on top of SX-717 laser coating exposed to Na_2SO_4-V_2O_5 (50/50 wt.%) (Na:V=1.27) in air at 650°C for 1000 h . Narrow Cr-depleted layer can be seen in elemental map of Cr.

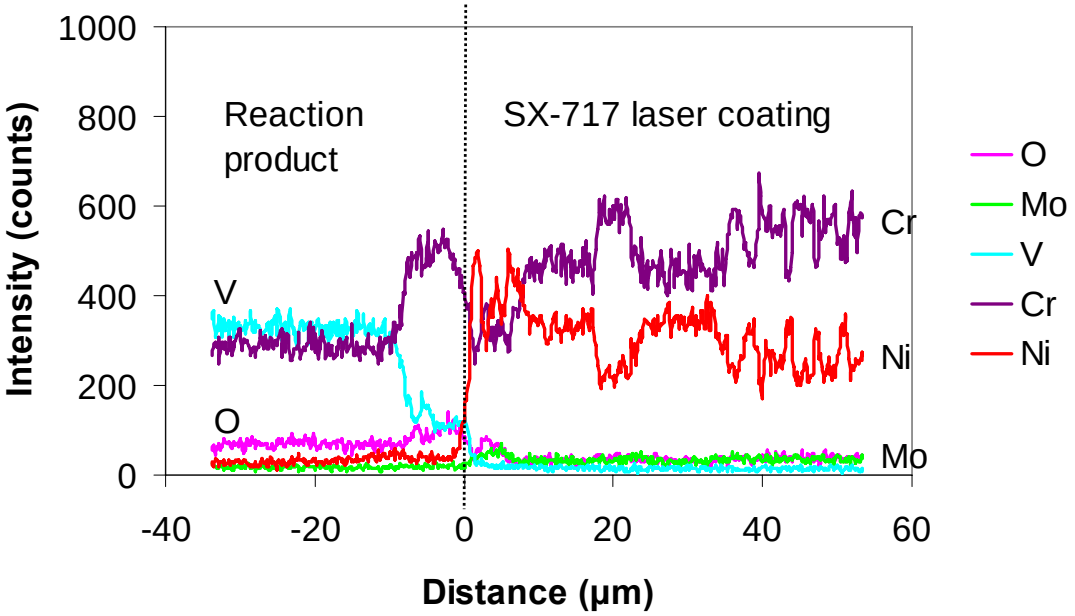

Figure 82. EDS line scan analysis of SX-717 laser coating exposed to Na_2SO_4-V_2O_5 (50/50 wt.%) (Na:V=1.27) in air at 650 °C for 1000 h.

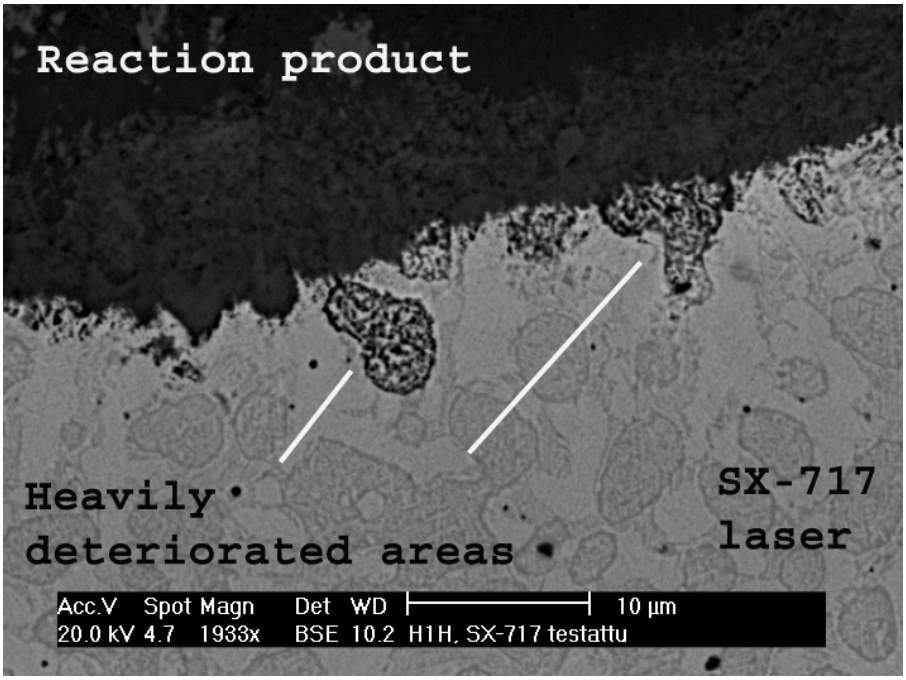

Figure 83. Transverse cross-section of SX-717 laser coating reacted at 650 °C in air with Na_2SO_4–V_2O_5 (50/50 wt.%) (Na:V = 1.27) on the surface.

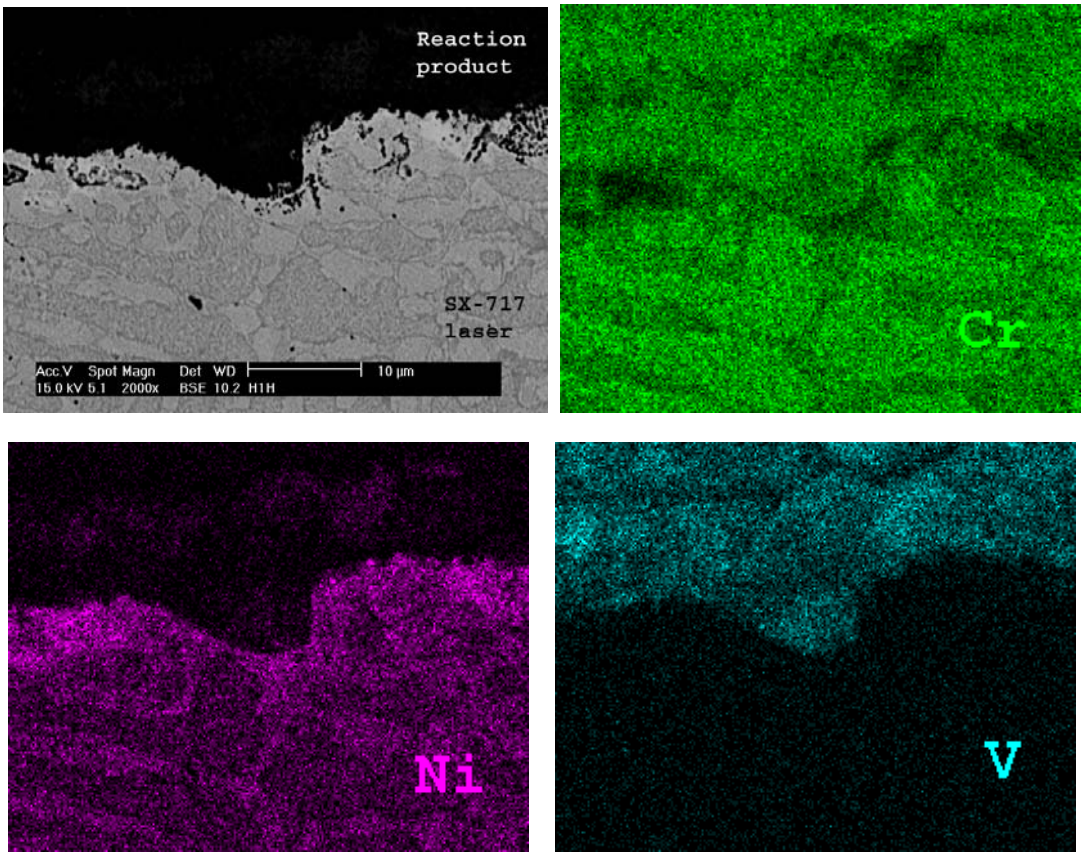

Figure 84. Elemental maps of SX-717 laser coating exposed to Na_2SO_4-V_2O_5 (50/50 wt.%) (Na:V=1.27) in air at 650 °C for 1000 h.

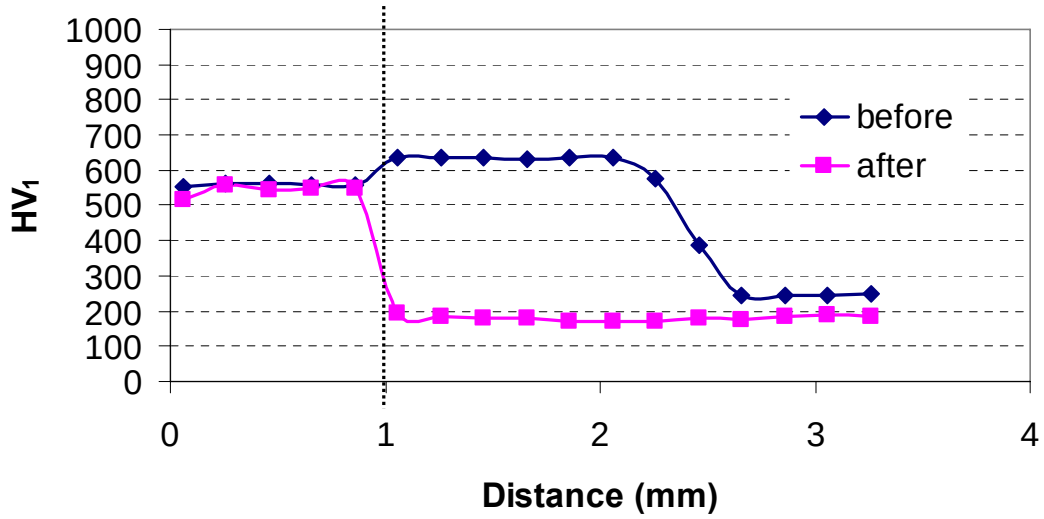

Figure 85. Microhardness profiles of SX-717 laser coating before and after the test.

3.3.1.4 SX-707 HVOF

HVOF spraying method produced layered coating microstructure typical for sprayed metallic coatings as shown in Figure 86. Inter-splat boundaries can be clearly distinguished due to oxide layers at splat boundaries. Most of the splats are wide and relatively flat, however, surprisingly high amount of round not fully melted splats were detected. General impression was that the coating was not very dense. Microhardness of the coating was 490–510 $HV_{0.3}$.

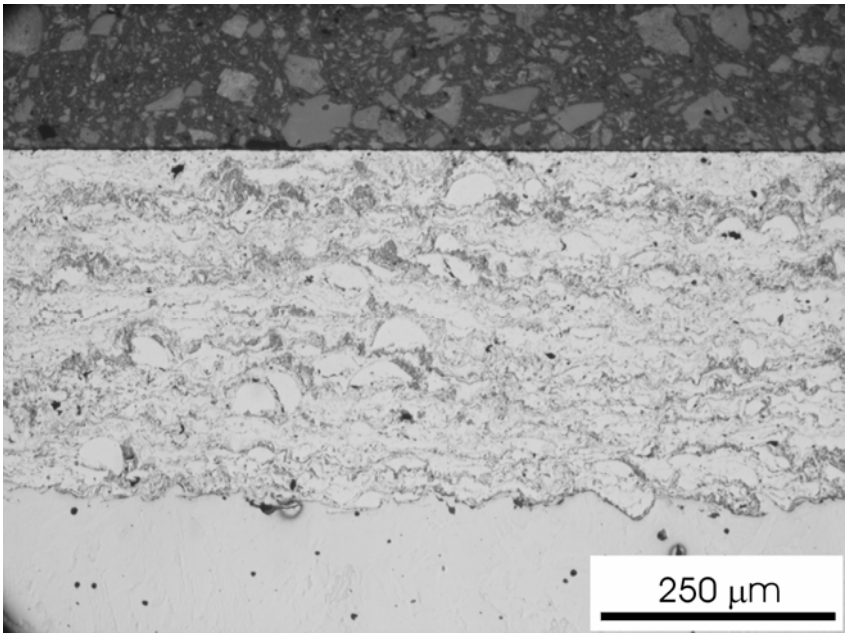

Figure 86. Optical micrograph of SX-707 HVOF coating before the test.

The deterioration of the HVOF coating was not uniform. Some wide and shallow pits were easily detected on the coating surface beneath the reaction product layer, which was rather dense in the vicinity of coating surface as shown in Figure 87. The reaction product layer was very similar to that observed on top of SX-717 laser coating. That is, the light areas in the reaction product layers were rich in Ni, V and O, whereas the dark areas were rich in Cr, V and O. Most importantly, it seemed that elements of salt did not penetrate through the splat boundaries into the coating and base material, which indicates that the coating was dense enough to keep it intact in this particular test environment. Due to the overlap of intensity peaks of Mo-L_a and S-K_a in EDS spectrum, it was difficult to be conclusive was there any S in the coating. Cr-depleted layer in the vicinity of coating surface was revealed by EDS line scan analysis shown in Figure 88.

3.3.2 Wrought alloys

The results concerning wrought alloys Inconel 625 and Nimonic 80A are shown and discussed below.

3.3.2.1 Inconel 625

Microstructure of wrought Inconel 625 before the test was presented earlier in section 3.2.1 in Figures 47 and 48. In hot corrosion test, the deterioration of the surface was uniform, that is,

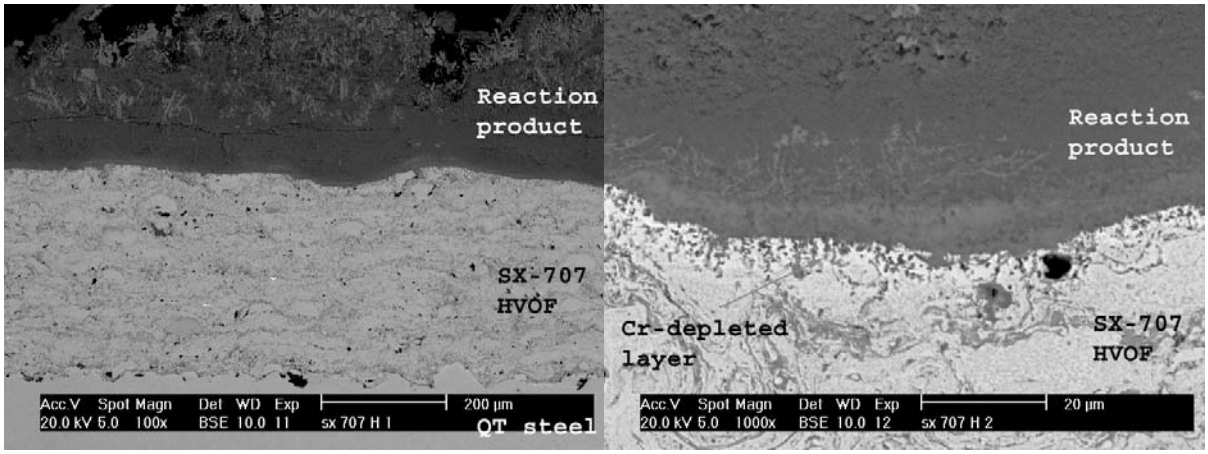

Figure 87. BSE images of reaction product layers and SX-707 HVOF coating exposed to Na_2SO_4-V_2O_5 (50/50 wt.%) (Na:V=1.27) in air at 650°C for 1000 h.

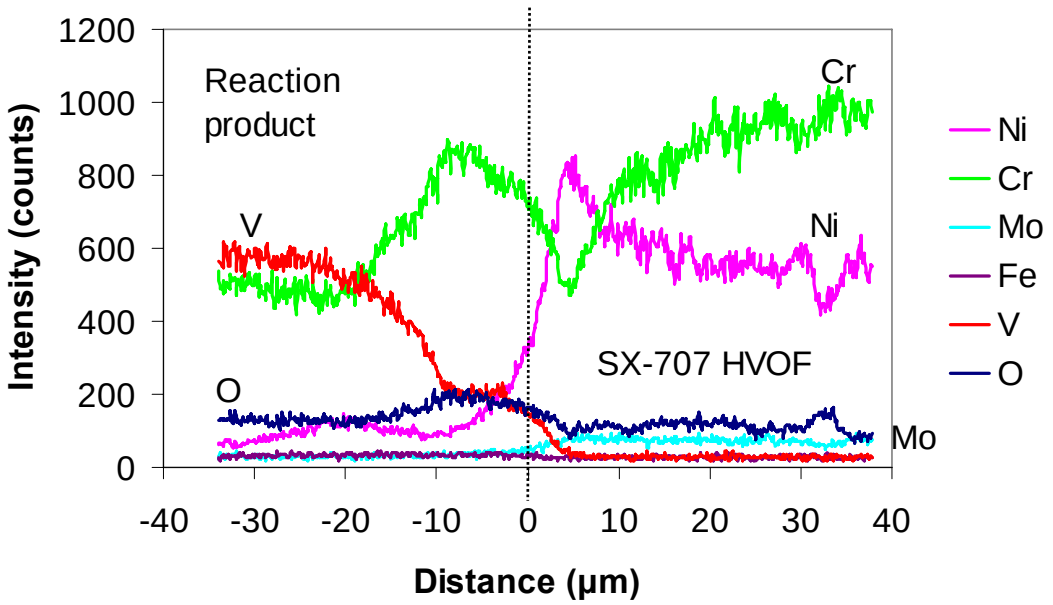

Figure 88. EDS line scan analysis of reaction product layers and SX-707 HVOF coating exposed to Na_2SO_4-V_2O_5 (50/50 wt.%) (Na:V=1.27) in air at 650°C for 1000 h.

no preferential grain boundary attack was detected, as shown in Figure 89. Instead, distinct and uniform Cr-depleted layer, approximately 3 µm in thickness, was formed in the alloy just beneath the reaction product layer as shown in Figures 89b and 90. Such a distinctive Cr-depleted layer was not observed in Inconel 625 laser coating as explained earlier in section 3.3.1.1. Another difference between wrought and laser clad alloys can be found in reaction product layers. As opposed to laser coating, reaction product layers of wrought alloy included discrete Nb- and Mo-rich areas as shown in Figure 89b. In addition, the Cr-rich reaction product layer in the vicinity of metal surface was not as obvious as in laser coating. It was also interesting to note that laser coating exhibited substantially better resistance as revealed by mean thickness loss measurements (Figure 74). This could be perhaps attributed to the Mo, which is detrimental to resistance against sulphate-vanadates, or better to its distribution in the alloy.

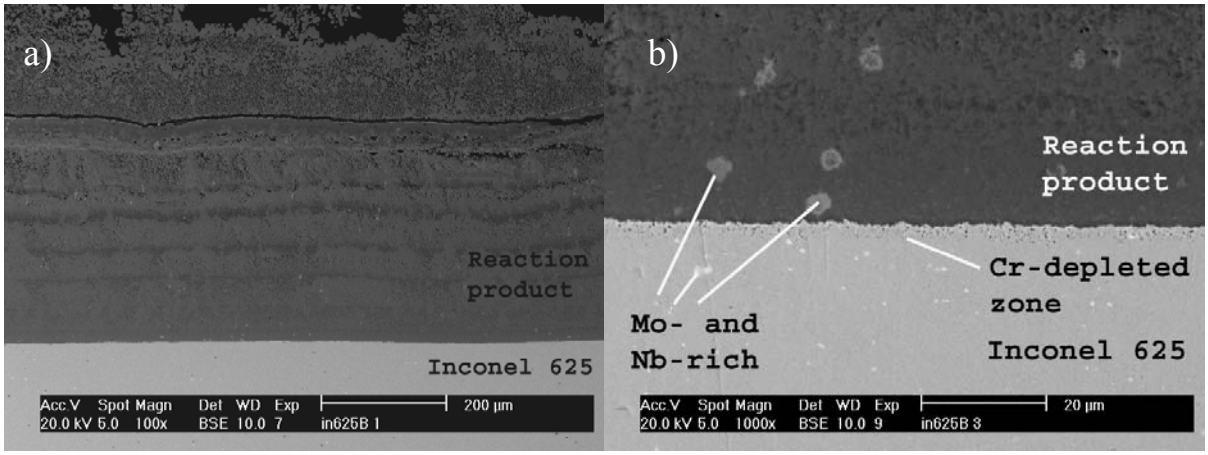

Figure 89. Cross-section of wrought Inconel 625 reacted at 650℃ in air with Na_2SO_4–V_2O_5 (50/50 wt.%) (Na:V = 1.27) on the surface.

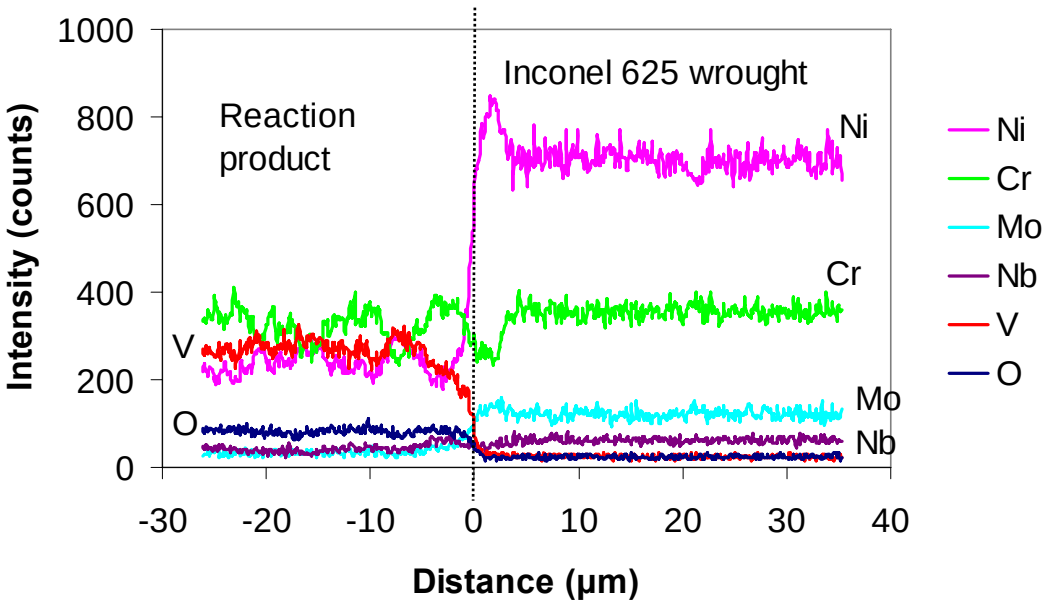

Figure 90. EDS line scan analysis of the tested wrought Inconel 625.

3.3.2.2 Nimonic 80A

The deterioration of Nimonic 80A was uniform across the specimen surface. The reaction product layer in macro-level was clearly divided into rather dense Cr-rich layer near the salt/alloy interface and porous upper layer, which was rich in Ni. The layer next to alloy surface was strongly stratified as shown in Figures 91 and 92, and Cr-rich reaction product layer right next to alloy surface was not as distinctive as in Cr-based alloys and laser clad Inconel 625. Cr-depleted layer, approximately 7-13 µm in thickness, was formed in the alloy next to reaction product interface. The grain boundaries, which contained carbides (frequently $M_{23}C_6$) and are clearly seen in Figure 91b, did not contain any corrosive species. Instead, S was detected on the bottom of Cr-depleted layer indicating that internal sulfidation caused by Na_2SO_4 has taken place. In this case, S cannot be mixed with Mo since Nimonic 80A does not contain Mo.

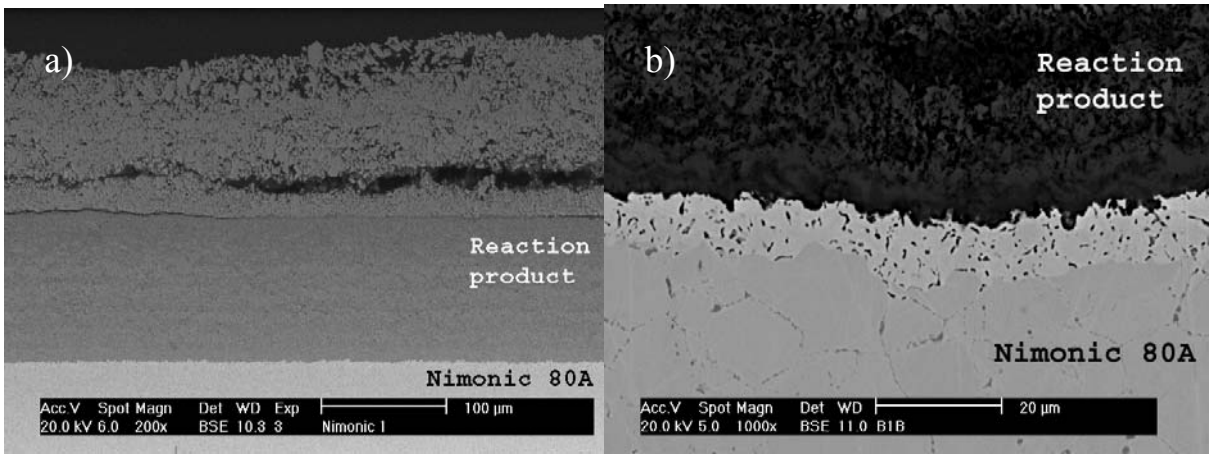

Figure 91. Cross-section of wrought Nimonic 80A reacted at 650 ℃ in air with Na_2SO_4–V_2O_5 (50/50 wt.%) (Na:V = 1.27) on the surface.

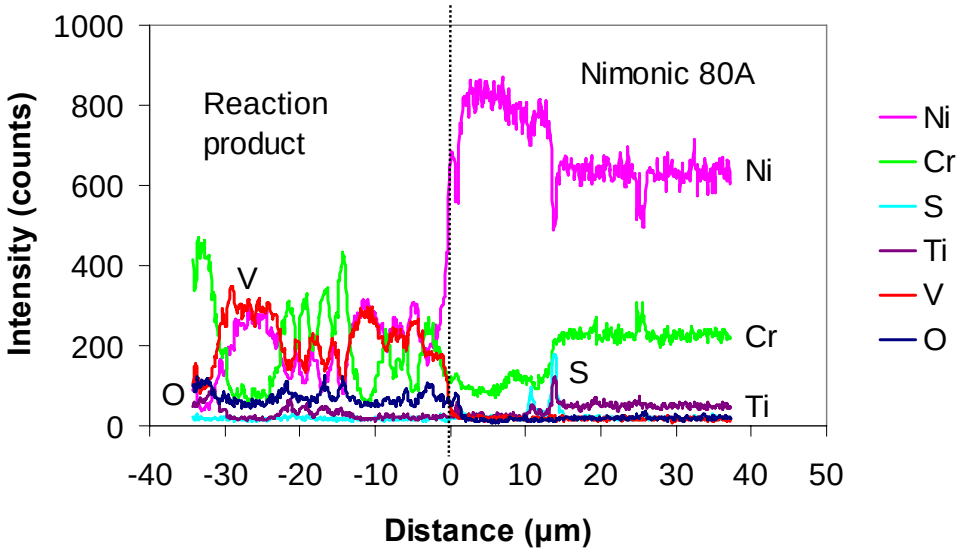

Figure 92. EDS line scan analysis of wrought Nimonic 80A exposed to Na_2SO_4-V_2O_5 (50/50 wt.%) (Na:V=1.27) in air at 650 ℃ for 1000 h.

3.4 Abrasion wear properties

Different types of laser coatings and reference materials were tested in low-stress three-body abrasion wear test using angular silica (750–1200 HV, 0.1–0.6 mm) as an abrasive. The test results for the manually ground materials are expressed as mass and volume losses in Figures 93 and 94. The results are the average of three measurements. The highest and lowest COV, 38.6% and 2.2% was calculated for laser clad SHS 1380 ((Ti, Mo)C – Ni 35/65 wt.%) and Metco 31C-NS (NiCrBSi-WC/Co 65/35 wt.%), respectively. The average COV of all the measurements was 20.3%. COV for manually flat ground, i.e monolithic alloys, was 19.7% and for samples (MMCs) where some as-laser-clad surfaces remained in the valleys between beads 20.5%. Volume losses for monolithic alloys were calculated using mass loss values and nominal densities of the alloys found in the literature or densities given by the supplier of the powder. Volume losses for MMCs were calculated using densities given by the law of mixture between the matrix and the hard particulates [389]:

$$\rho_{mmc} = f_c \cdot \rho_c + (1 - f_c) \cdot \rho_m \qquad (16)$$

where,

ρ_{mmc} = density of MMC (kg m^{-3})
f_c = volume fraction of carbide in initial powder mixture
ρ_c = nominal density of carbide found in literature, given by the supplier or calculated by the author (kg m^{-3})
ρ_m = nominal density of matrix alloy found in literature or given by the supplier (kg m^{-3})

Volume loss approximation based on ρ_{mmc} given by the equation 16 is valid if the volume fraction of carbides in the coating corresponds to volume fraction of carbides in initial powder mixture, no dissolution of primary carbides and no preferential wear has taken place, i.e. matrix and carbides have exhibited uniform wear. These assumptions were hardly ever true as will be discussed in the following sections.

Vickers microhardness values of the tested materials are illustrated in Figure 95. For laser coatings they were taken vertically and horizontally in relation to coating/base material interface with an increment of 0.1 mm, load of 10 N (HV_1) and loading/indentation time of 10 s. Values given in Figure 95 are the average of at least 30 measurements taken horizontally from the uppermost coating layer (1 or 4 layers altogether) covering more than one reheated zones associated with overlapping. Measurements were not taken under the wear scar, so they can be considered as initial hardness values. Measurements in vertical direction reached into the HAZ in the base material.

In addition to bulk or average microhardness values (HV_1), microhardness measurements were conducted separately on the matrix and carbides in MMCs with a load of 3 N ($HV_{0.3}$). The average values of five measurements taken randomly across the coating cross-section are reported in Table 17, which summarizes also the coating characterization results including major carbide phases present, volume fraction of primary carbides and estimated fracture toughness of the coatings. The phases present in the coating were identified using XRD method together with SEM and EDS. XRD patterns were taken from the manually ground non-tested surfaces of the coatings. Volume fractions of primary carbides were measured using SEM and OM micrographs taken from the transverse cross-sections of the coatings and Adobe Photoshop 6.0. Analyzed area covered the full thickness of the coating in the case of carbides initially larger than 5 μm in diameter. In the case of smaller carbides, several higher magnification micrographs taken from the representative areas in the coating were used. Fracture toughness of the coatings were grouped into low, moderate, high and excellent by detecting the possible crack initiation from the corners of Vickers pyramid indentation at a load of 10 N and measuring their lengths since the stress intensity factor (K_I) closely related to the fracture toughness can be calculated with equation [390]:

$$K_I = \frac{F_N}{(\pi \cdot c_1)^{3/2} \cdot \tan\beta} \qquad (17)$$

Where, F_N (N) is the normal indenter load, c_1 is the crack length (m) and β is 68° for a Vickers diamond. The longer the crack length, the lower the K_I and fracture toughness.

According to volume losses illustrated in Figure 94, tested materials can be classified roughly into three groups. First group, exhibiting the lowest wear resistance, consists of laser coatings made of monolithic Co-based hardfacing alloys, Cr-based SX-707, Ni-based Inconel 718 and tool steel WR10 as well as wrought alloys Fe37 and 316L. For this first group of materials abrasion conditions were hard since the average hardness of the abrasive was clearly higher ($H_{abrasive}/H_{material} > 1.2$) than the hardness of the tested materials. The rank of Stellites and their resistances with respect to wrought 316L were in good agreement with the results obtained by De Mol van Otterloo and De Hosson [333].

The second group of materials, exhibiting significantly better resistance, comprise laser coatings made of various MMCs, monolithic Fe-based Nanosteel hardfacing alloy and WR6 tool steel as well as cast Ni-hard alloy. This group of materials is discussed more in details in the following sections.

The third group of materials, showing the best abrasion wear resistance, consists of high volume fraction (~75 vol.%) WC-based cemented carbides (hard metals) manufactured with HVOF spraying or sintering.

3.4.1 NiCrBSi + WC

As displayed in Figure 94, NiCrBSi + WC laser coatings exhibited wide range of volume losses (10–40 mm^3) in the second group of materials depending on the type and volume fraction of carbides as well as the hardness of the matrix used. Obviously, the hardest matrix alloys, Diamalloy 2001 (58-60 HRC) and Metco 16C (58-60 HRC), reinforced with high volume fractions (50 vol.%) of coarse fused WC/W_2C (Durmat FTC) (Figure 96) and fine dense-coated WC particulates (Amperit 522.3), respectively, exhibited the lowest volume losses but were still far from the third group of the tested materials. Consequently, the softest matrix material, Metco 12C (30 HRC), reinforced with low volume fraction (30 vol.%) of coarse dense-coated WC particulates (Amperit 522.2) exhibited the highest wear volume. The rest of the results, however, are not so straightforward. For the reasons, which will be explained further, Metco 16C reinforced with high volume fraction (50 vol.%) of coarse dense-coated WC particulates (Amperit 522.2), for instance, was inferior to many others. Interestingly, moderately hard matrix, Colmonoy 42-P2 (36 HRC) reinforced with the highest volume fraction (75 vol.%) of fine dense-coated WC particulates (Amperit 522.3) was worse than Metco 16C + Amperit 522.3 (50/50 vol.%). This suggests that the matrix hardness played a key role in abrasion wear resistance in given conditions. Ready made blend of NiCrBSi and small WC particulates loosely agglomerated with Co binder (Metco 31C-NS) turned out to be inapplicable in laser cladding since the coating obtained suffered from serious pore formation and cracking due to severe carbide dissolution. Instead, the results obtained from the recycled WC were encouraging from the cladability and wear resistance point of view. In the following subsections, attempt is made to explain these results by studying the effects of size, volume fraction, dissolution and morphology of carbides on matrix alloys, wear mechanisms and wear resistances of the coatings.

3.4.1.1 Influence of carbide size

Influence of carbide size on abrasion wear resistance, carbide dissolution and microhardness can be found out by comparing the results obtained for Metco 16C + Amperit 522.2 (44-88 μm) (50/50 vol.%) and Metco 16C + Amperit 522.3 (5-44 μm) (50/50 vol.%). These coatings were laser clad with identical parameters. Abrasion wear results and microhardness values are summarized in Table 18. Representative micrographs taken from the transverse cross-sections

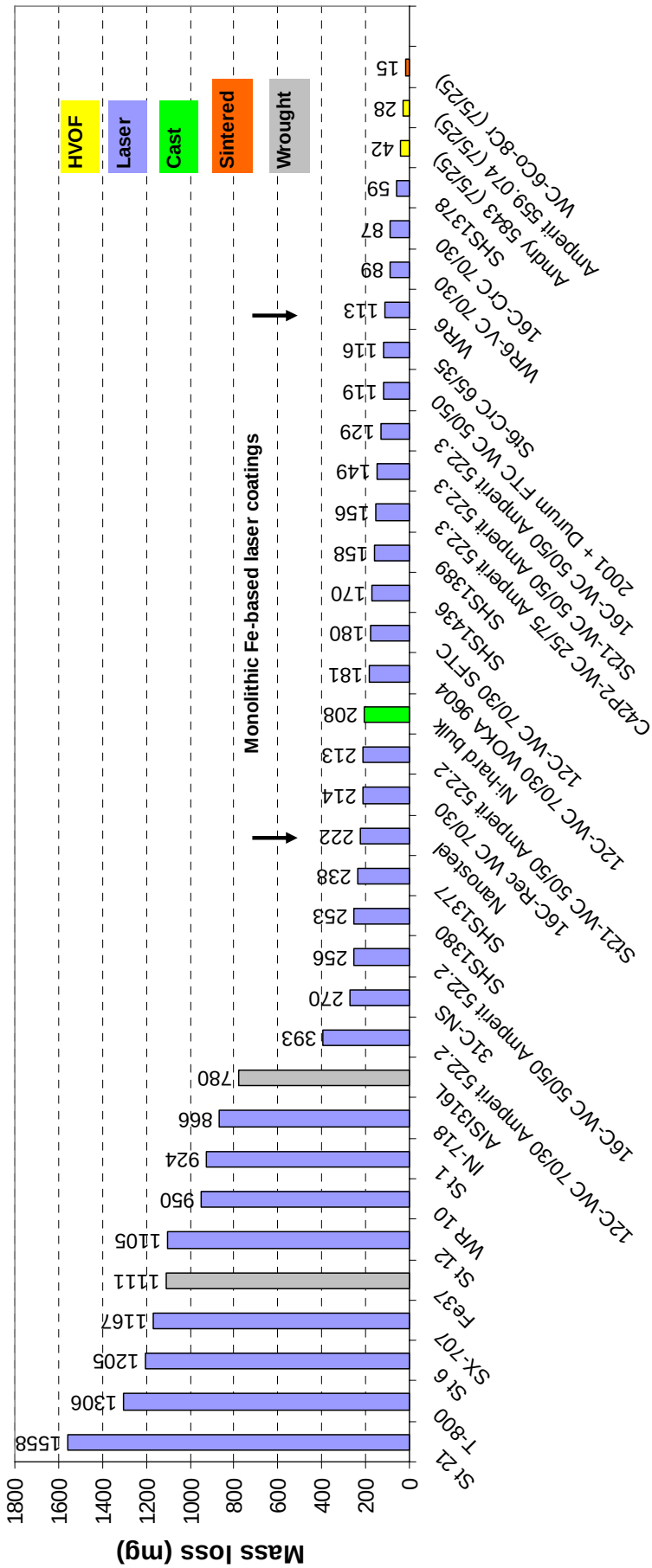

Figure 93. Rubber wheel abrasion wear test results expressed as mass loss. Results are the average of three measurements. Average Fe content on the surface of T-800 one layer laser coating was 1.5 wt.%.

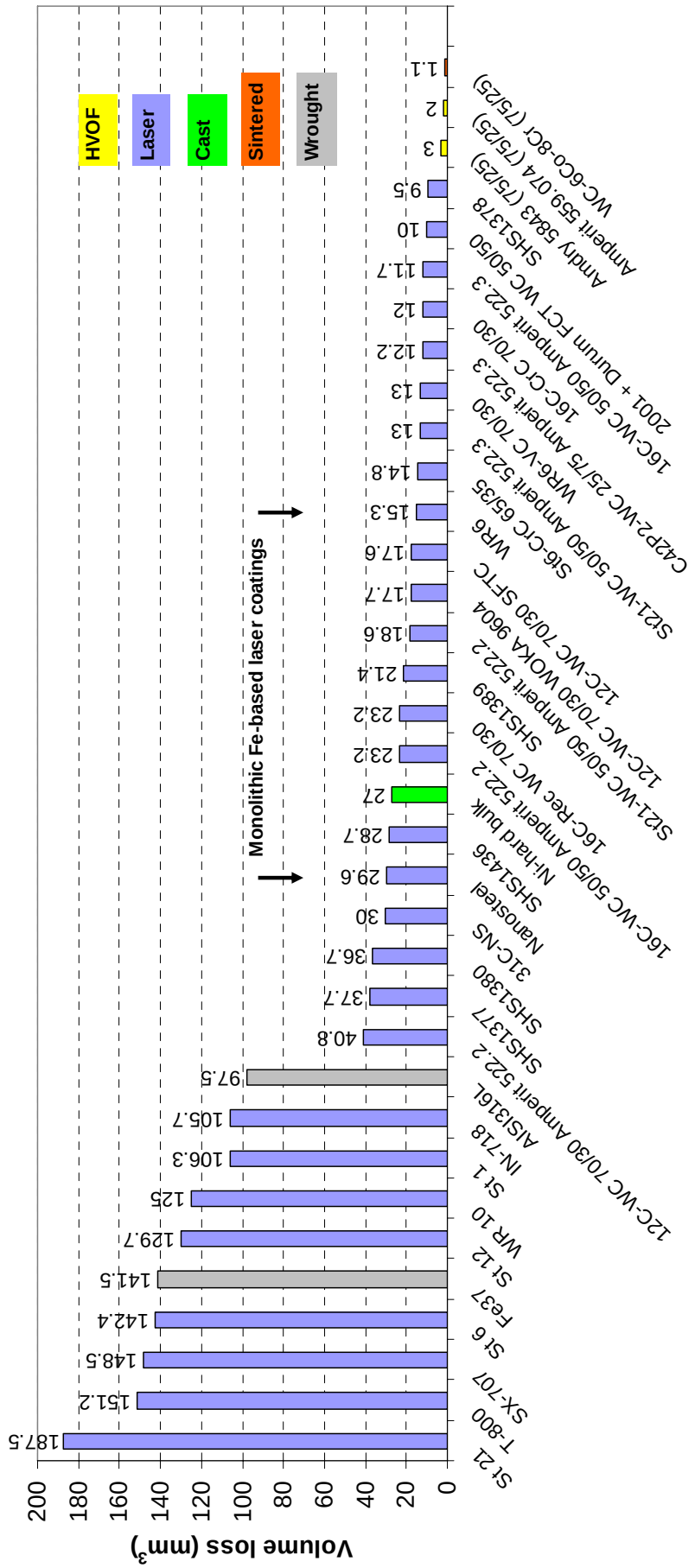

Figure 94. Abrasion wear test results expressed as volume loss. Results are the average of three measurements. Volume losses for (Ti, Mo)C SHS laser coatings are slightly overestimated because Mo in carbides was not taken into account.

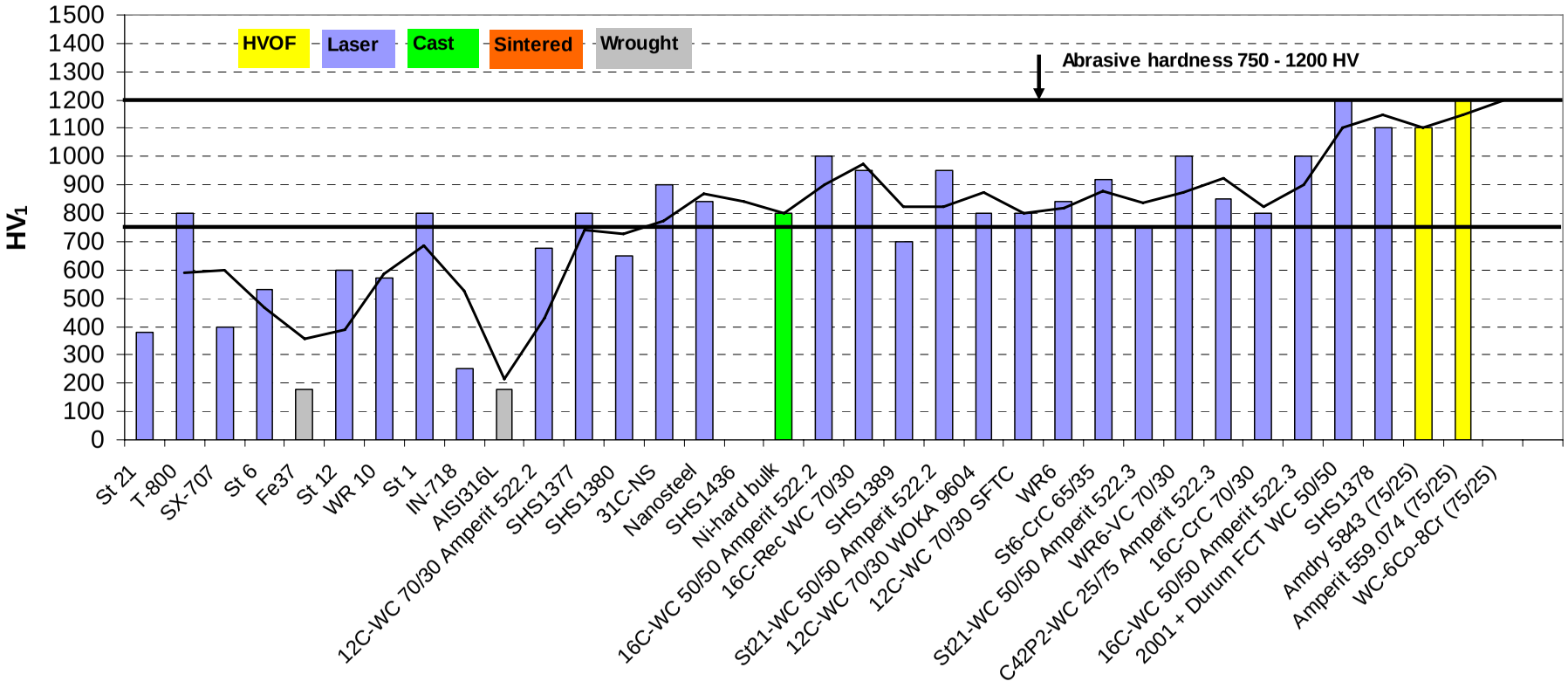

Figure 95. Vickers microhardness values (HV_1). Materials are ranked in decreasing volume loss order (cf. Figure 94).

Table 17. Summary of the Fe-based monolithic and MMC laser coating characteristics. Coatings are sorted in descending order with respect to wear resistance according to volume loss. Carbide microhardness values could not be measured from the finest carbide grades; (Ti, Mo)C SHS carbides and Amperit 522.3 dense-coated WC (5–44 µm)

Coating	***Primary carbide volume %***	***Major phases***	***Cracks initiated in the matrix under the load of 10 N (HV_1) / Fracture toughness***	***HV_1 bulk***	***$HV_{0.3}$ carbide***	***$HV_{0.3}$ matrix***
SHS 1378 (Ti, Mo)C – St 6 (50/50 wt.%)	64	(Ti, Mo)C	No / Excellent	1100	N/A	N/A
Diamalloy 2001 + Durum FTC WC (50/50 vol.%)	50	WC, W_2C	Yes / Moderate	1240	2090	900
16C + Amperit 522.3 (50/50 vol.%)	24	WC	Yes / Moderate	1030	N/A	1020
16C + 70C-NS (70/30 vol.%)	20	Cr_3C_2, Cr_7C_3	Yes / Moderate	840	1500	870
C42-P2 + Amperit 522.3 (25/75 vol.%)	50	WC	Yes / High	850	N/A	750
WR 6 + VC (70/30 vol.%)	20	VC	No / Excellent	1030	1940	840
St 21 + Amperit 522.3 (50/50)	7	WC, Co_6W_6C, Co_3W_3C	Yes / High	760	N/A	1000
St 6 + 70C-NS (65/35)	17	Cr_3C_2, Cr_7C_3	No / Excellent	920	1590	830
WR 6	10	VC	No / Excellent	840	N/A	
12C + WC SFTC (70/30)	24	WC, W_2C	Yes / High	810	2420	570
12C + WC WOKA 9604 (70/30)	38	WC, W_2C	Yes / High	820	1950	650
St 21 + Amperit 522.2 (50/50)	31	WC, Co_6W_6C, Co_3W_3C	Yes / High	960	1350 cracked	880
SHS 1389 (Ti, Mo)C – St 6 (20/80 wt.%)	26-60	(Ti, Mo)C	No / Excellent	750	N/A	N/A
16C + recycled WC (70/30)	24	WC	Yes / Moderate	970	1580	800
16C + Amperit 522.2 (50/50)	41	WC	Yes / Moderate	990	1280 cracked	900
SHS 1436	60	(Ti, Mo)C	N/A	N/A	N/A	N/A
Nanosteel	N/A	N/A	Yes / High	840	N/A	N/A
31C-NS	N/A	N/A	Yes / Low	1010	N/A	N/A
SHS 1380	37-51	(Ti, Mo)C	No / Excellent	520	N/A	N/A
SHS 1377	62	(Ti, Mo)C	No / Excellent	780	N/A	N/A
12C + Amperit 522.2 (70/30)	35	WC	Yes / High	680	1230 cracked	570

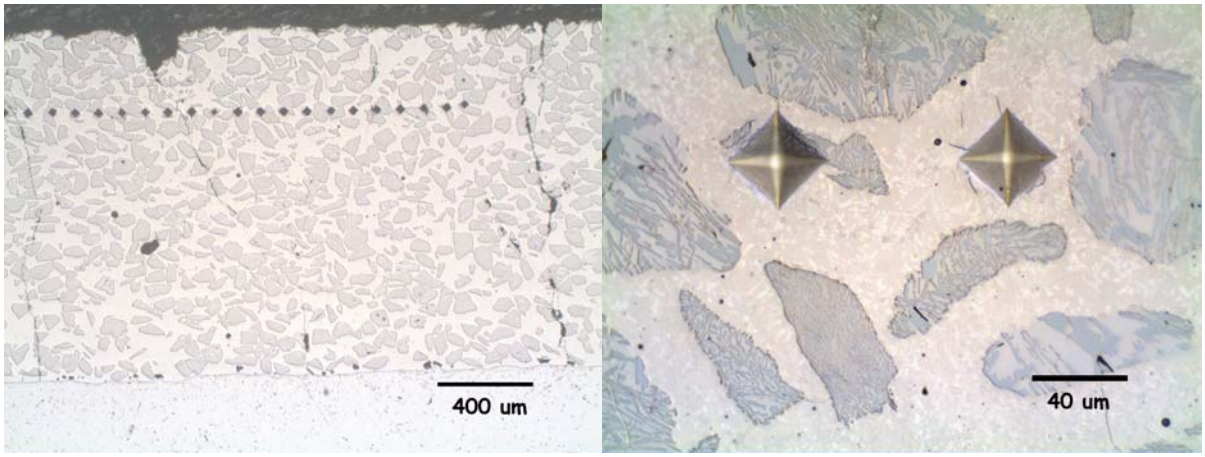

Figure 96. Optical micrographs taken from the transverse cross-section (perpendicular to cladding direction) of Diamalloy 2001 + Durum FTC WC (50/50 vol.%) coating. Vertical cracks are seen. All the cracks propagated through carbides, which indicated good interfacial bond between the matrix and carbides. According to image analysis, volume fraction of primary carbides was approximately 50 %. Carbide microstructure consisted of WC needles (dark) in W_2C matrix (light).

(parallel to cladding direction) together with high magnification SEM micrographs taken from the wear scars are illustrated in Figures 97-101.

Table 18. Influence of carbide size on abrasion wear resistance and microhardness.

Coating	***Volume ratio***	***Carbide size (µm)***	***Mass loss (mg)***	***STDV***	***COV (%)***	***Volume loss (mm^3)***	***HV_1***	***$HV_{0.3}$***
Metco 16C* + *Amperit 522.2	(50/50) (59/41)[1]	44-88	256	46	18	23.2 23.5[2]	990	900[3] 1280[4]
Metco 16C* + *Amperit 522.3	(50/50) (76/24)[1]	5-44	129	41	32	11.7 13.6[2]	1030	1020[3] N/A[4]

1) volume ratio of matrix to primary carbides according to image analysis
2) volume loss calculated on the basis of matrix/carbide volume ratio in coating measured with image analysis
3) matrix microhardness
4) carbide microhardness

First of all, it should be mentioned that fine dense-coated primary WC particulates (5-44 µm) were much more non-homogeneously distributed in the matrix compared with corresponding coarse carbides (44-88 µm). This can be observed from the micrographs in Figures 97 and 99. Evidently, the coating reinforced with fine carbides consisted of nearly primary carbide-free areas and areas with high primary carbide contents. According to image analyses carried out on the cross-section from the free surface of coating to coating/base material interface, the average volume fraction of fine primary carbides was 24%. This is substantially lower than 41 vol.% measured from the coating reinforced with coarser carbides. XRD curves measured from the manually ground surfaces (Figure 102), however, suggest that there was not significant differences in volume fractions at least on the very top surface of the coating, which met the wear conditions. Microhardness values measured from the matrix suggest that fine carbides dissolved more severely into the matrix because its hardness was clearly higher for coating reinforced with fine carbides (900 vs. 1020 $HV_{0.3}$). This was expected because

coarser carbides offer smaller surface area to volume ratio than fine carbides. Furthermore, some of those nearly primary carbide-free areas may have resulted from the reheating associated with overlapping. This would explain at least partly the primary carbide-free areas, non-homogeneous distribution and low volume fraction measured from the cross-section image.

Concerning wear resistances, it is clear that the coating reinforced with fine carbides exhibited approximately twice better resistance than coating reinforced with coarse carbides. Explanations for this can be found from the higher matrix hardness and shorter mean free path between carbides assuming that primary carbide (fine) content was equal to coating reinforced with coarser carbides. The role of the matrix hardness is important since wear mechanism was mainly microcutting or microploughing of matrix as evidenced in Figures 98 and 101. This increase in microhardness results from the dissolution of carbides into the matrix and subsequent precipitation of secondary carbides, which are shown in Figures 97 and 100 for both coatings, just in lesser degree for coarser carbides as proved by the microhardness measurements. These complex secondary carbides, usually the type Ni_2W_4C, are very hard and brittle but obviously enhance the wear resistance of the matrix in these wear conditions as results suggest. Here, complex secondary carbides contained also substantial amount of Cr. Similar to matrix hardness, mean free path between carbides is important since the shorter the mean free path between carbides, the less matrix is exposed to abrasives. It is also known that mean free path between carbides decrease when carbide content increases. With equal amounts of carbides, coating reinforced with finer carbides posses the shorter mean free path between carbides [390]. These two factors, microhardness of the matrix and mean free path between carbides, would then explain the results.

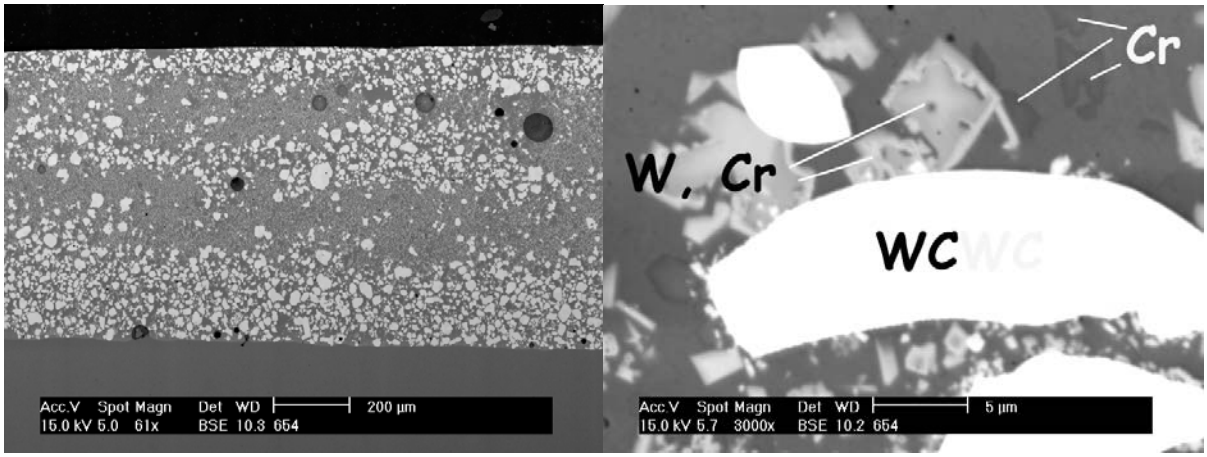

Figure 97. BSE images taken from the transverse cross-section (parallel to cladding direction) of Metco 16C + Amperit 522.3 (50/50 vol.%) coating. Fine carbides are non-homogeneously distributed in the matrix. Large spherical dark areas in lower magnification image are gas pores resulting probably from the formation of CO/CO_2 in consequence of dissociation of carbides and subsequent reaction with oxygen from the atmosphere. Such pores were not detected in coating reinforced with corresponding coarse carbides. In high magnification image the brightest areas are primary WCs, grey areas are precipitated secondary carbides rich in W and Cr, the darkest areas are rich in Cr (perhaps CrB) and the rest is the matrix. EDS area measurement taken from the vicinity of free surface of the coating gave the following composition (wt.%): 3.3Si-51.1W-1.2Mo-7.5Cr-1.8Fe-6.2Co-27.6Ni-1.3Cu. Fe content indicates very low dilution in this 1 layer coating.

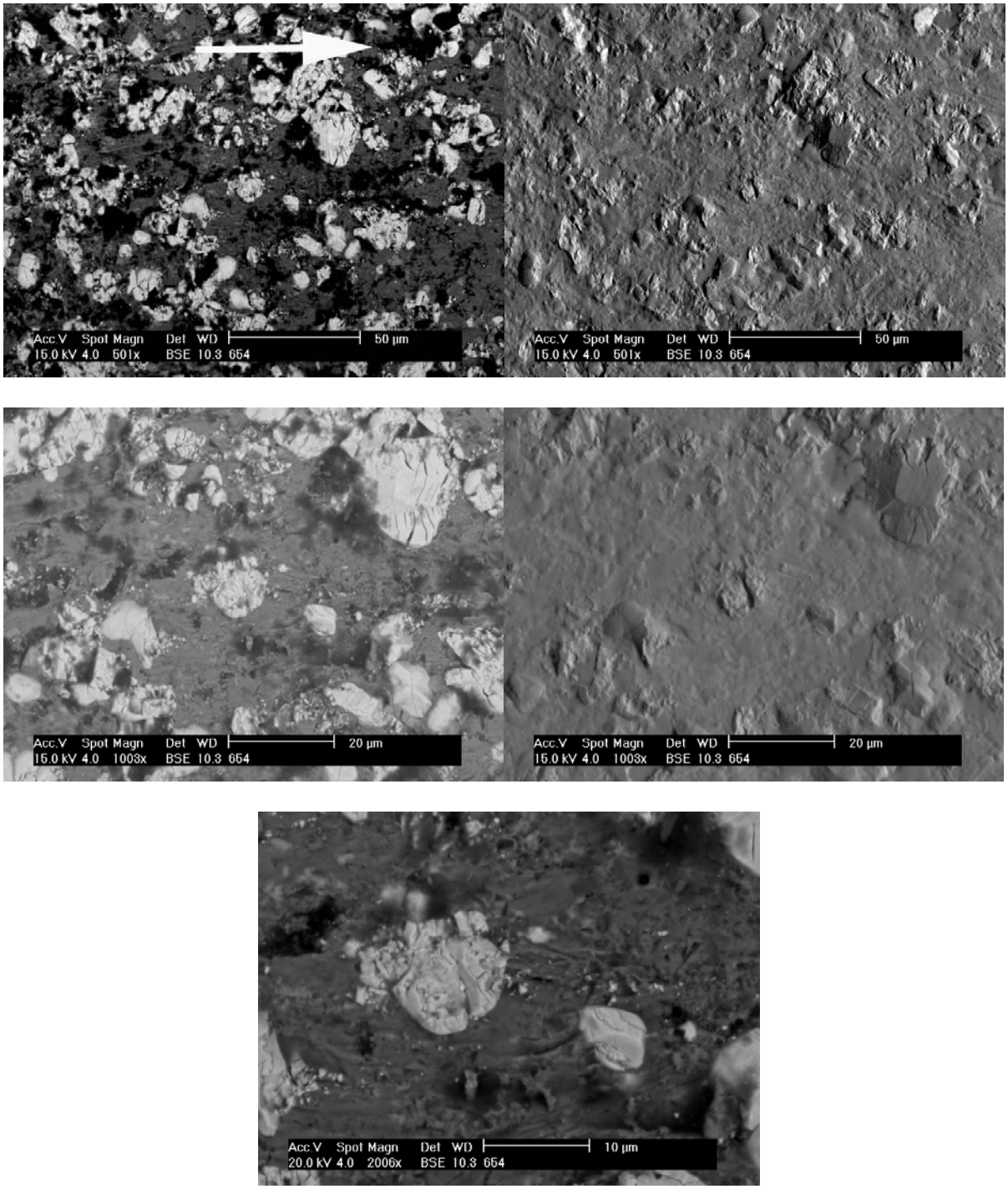

Figure 98. SEM micrographs taken from the wear scar of Metco 16C + Amperit 522.3 (50/50 vol.%) coating. Arrow indicates the rubber wheel rotation direction. Matrix wore down particularly at front of carbides in relation to wear direction. Signs of plastic flow on the matrix surface suggest the wear by microploughing and cutting. Carbides were severely cracked.

According to SEM micrographs taken from the wear scars, matrices have worn down profoundly in both cases leaving the carbides upraised as explained above. Owing to partial dissolution of primary carbides, they were very well bonded to the matrix and carbide "pull-outs" were not detected. Most of the carbides were, however, severely cracked and fragmented under the used abrasion conditions. It was also noted that coarse dense-coated

WC particulates cracked regularly under the Vickers indentation loads of 10 and 3 N. As a result of this, average carbide hardness value was as low as 1280 $HV_{0.3}$. Frequently, these cracks propagated along grain boundaries inside individual carbide. Grain boundaries can be seen in high magnification BSE image illustrated in Figure 99. According to Pierson [222], this kind of low fracture toughness may originate from the chemical impurities at grain boundaries.

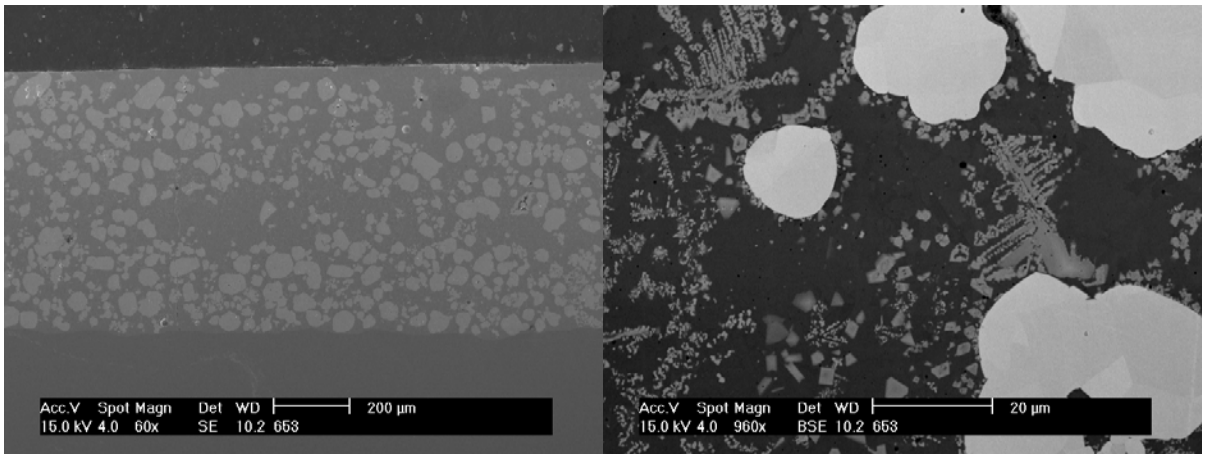

Figure 99. SEM images taken from the transverse cross-section (parallel to cladding direction) of Metco 16C + Amperit 522.2 (50/50 vol.%) coating. EDS area measurement taken from the vicinity of free surface of the coating gave the following composition (wt.%): 3.6Si-52.6W-1.6Mo-5.7Cr-2.6Fe-8.4Co-23.9Ni-1.5Cu. Fe content indicates very low dilution in this 1 layer coating. Grain boundaries inside individual WC particulates are visible in high magnification BSE image.

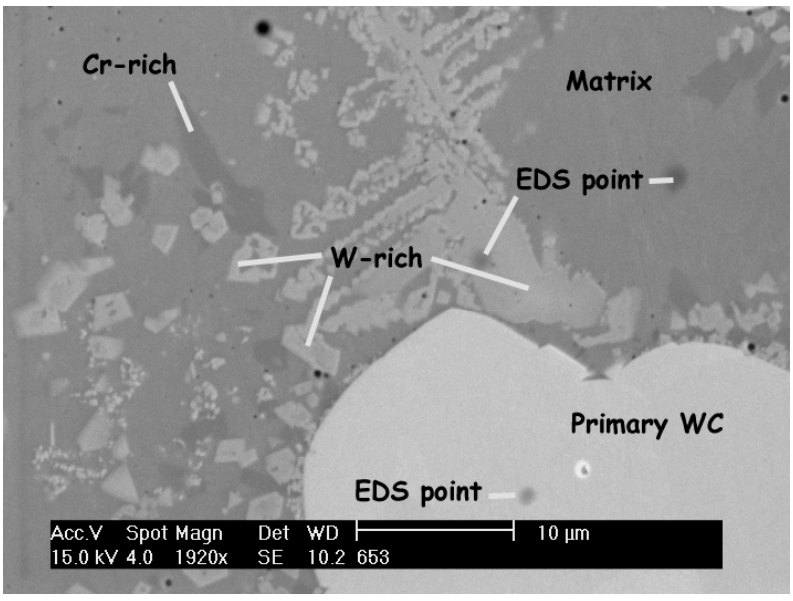

Figure 100. SEM image taken from the transverse cross-section (parallel to cladding direction) of Metco 16C + Amperit 522.2 (50/50 vol.) coating at the distance of 350 µm from the coating/base material interface. According to EDS point analysis the composition of the precipitated secondary carbide is 6Si-44W-6Mo-16Cr-3Fe-6Co-19Ni in wt.%. Co coating around WC dissolved into the matrix. Composition of the matrix was Ni-21.5Co-12.0Fe-8.2Cr-2.9Cu-1.6Si-0.5Mo in wt.%.

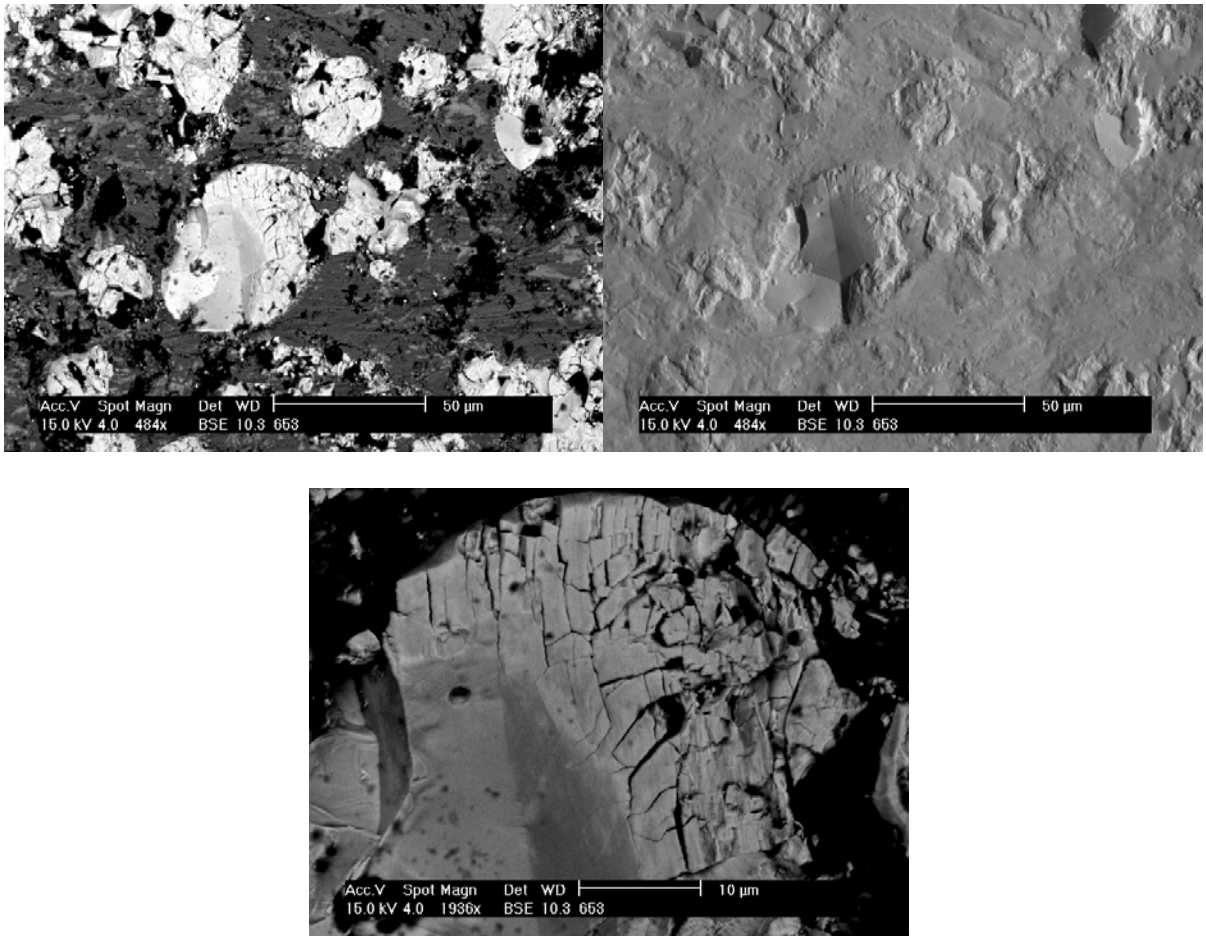

Figure 101. SEM micrographs taken from the wear scar of Metco 16C + Amperit 522.2 (50/50 vol.%) coating. Rubber wheel rotation direction was from left to right. Carbides are severely cracked and fragmented.

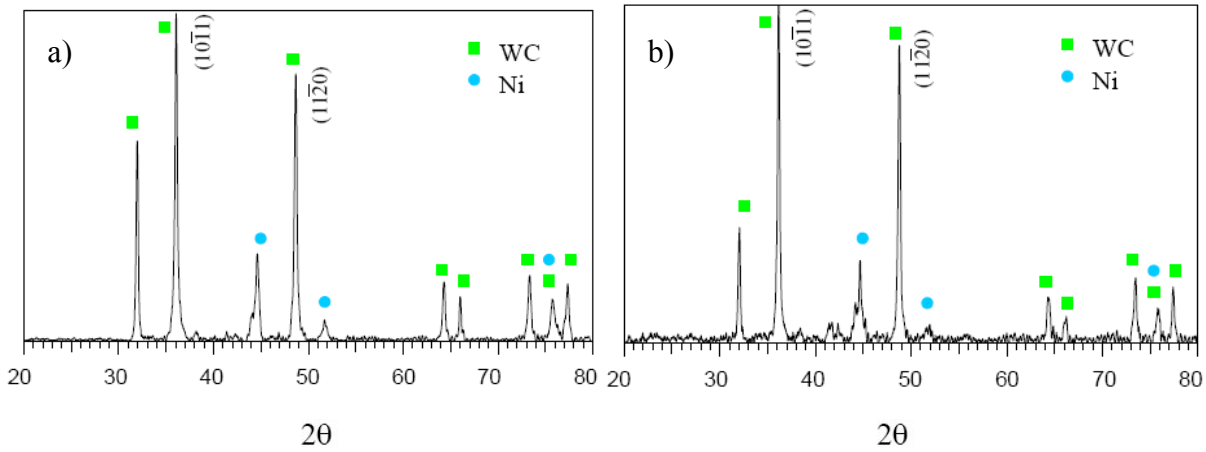

Figure 102. XRD patterns measured from a) Metco 16C + Amperit 522.3 and b) Metco 16C + Amperit 522.2 coatings.

3.4.1.2 Influence of carbide dissolution

Colmonoy 42-P2 + Amperit 522.3 (25/75 vol.%) (5-44 µm) was laser clad with low (900 W) and high laser powers (1000 W). This allowed studying the effect of carbide dissolution on wear resistance and microhardness. All the other parameters were kept constant. The wear and microhardness results are summarized in Table 19. The representative micrographs taken from the transverse cross-sections (parallel to cladding direction) are illustrated in Figures 103-105.

Table 19. Influence of carbide dissolution on abrasion wear resistance and microhardness.

Coating	***Volume ratio***	***Carbide size (µm)***	***Mass loss (mg)***	***STDV***	***COV (%)***	***Volume loss (mm^3)***	***HV_1***	***$HV_{0.3}$***
C42-P2 + Amperit 522.3 low power	(25/75) (45/55)[1]	5-44	186	64	35	14.5 15.4[2]	805	733[3] N/A[4]
C42-P2 + Amperit 522.3 high power	(25/75) (50/50)[1]	5-44	156	50	32	12.2 13.4[2]	850	752[3] N/A[4]

1) volume ratio according to image analysis
2) volume loss calculated on the basis of average matrix/carbide volume ratio in coating measured with image analysis
3) matrix microhardness
4) carbide microhardness

Higher laser power increased carbide dissolution as expected. This was proved by the volume fraction and matrix hardness measurements. This higher dissolution led to better resistance against abrasive wear. XRD patterns are displayed in Figure 106. Similar trend in wear resistance was obtained for Metco 16C + recycled WC (70/30 vol.%) coating. The coatings laser clad with low and high power showed average mass losses of 241 and 214 mg, respectively. SEM micrographs taken from the wear scar of Metco 16C + recycled WC (70/30 vol.%) coating manufactured with high laser power is shown in Figure 107. The binder made of Ti and Co kept the small WC particles well together.

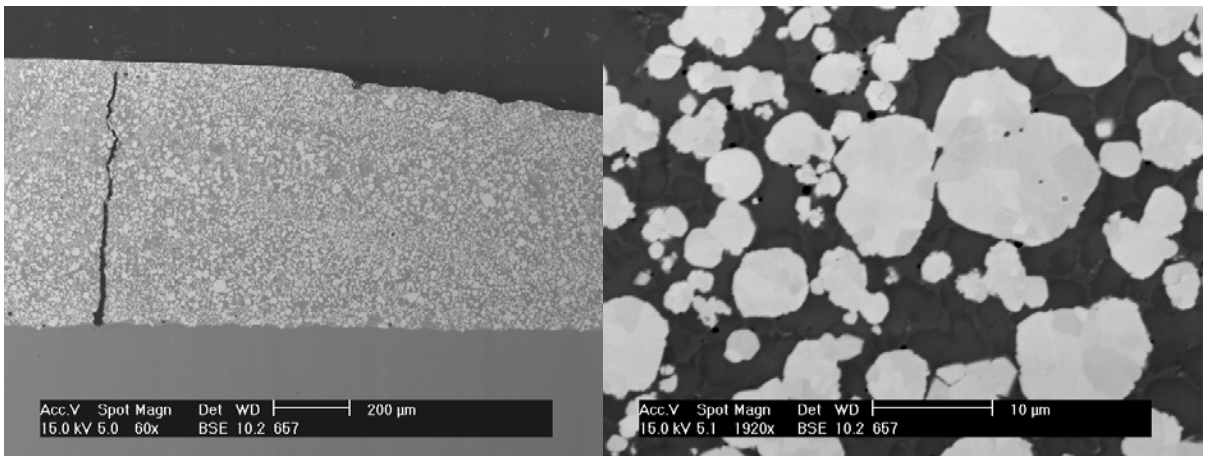

Figure 103. BSE images taken from the transverse cross-section (parallel to cladding direction) of Colmonoy 42-P2 + Amperit 522.3 (25/75 vol.%) coating (low power). EDS area analysis from the vicinity of free surface of the coating gave the following composition (wt.%): 3.1Si-64.2W-2.3Cr-1.4Fe-12.4Co-16.6Ni. Fe content indicates very low dilution in this 1 layer coating.

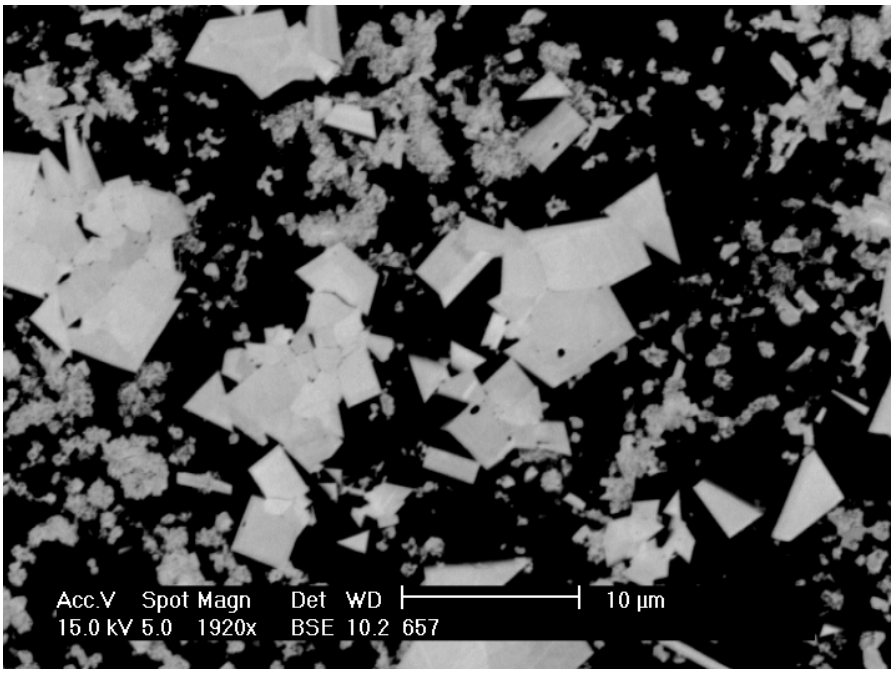

Figure 104. BSE image taken from the transverse cross-section (parallel to cladding direction) of Colmonoy 42-P2 + Amperit 522.3 (25/75) coating (low power) at the distance of 300 µm from the coating/base material interface. According to EDS point analysis the composition of the sharp edged carbide corresponded to the composition of the primary carbide. Composition of the precipitated carbide was 3.0Si-63.5W-3.6Cr-8.3Fe-8.5Co-13.0Ni in wt.%. Composition of the matrix was Ni-19.6Co-21.1Fe-11.3W-2.1Cr-1.9Si in wt.%.

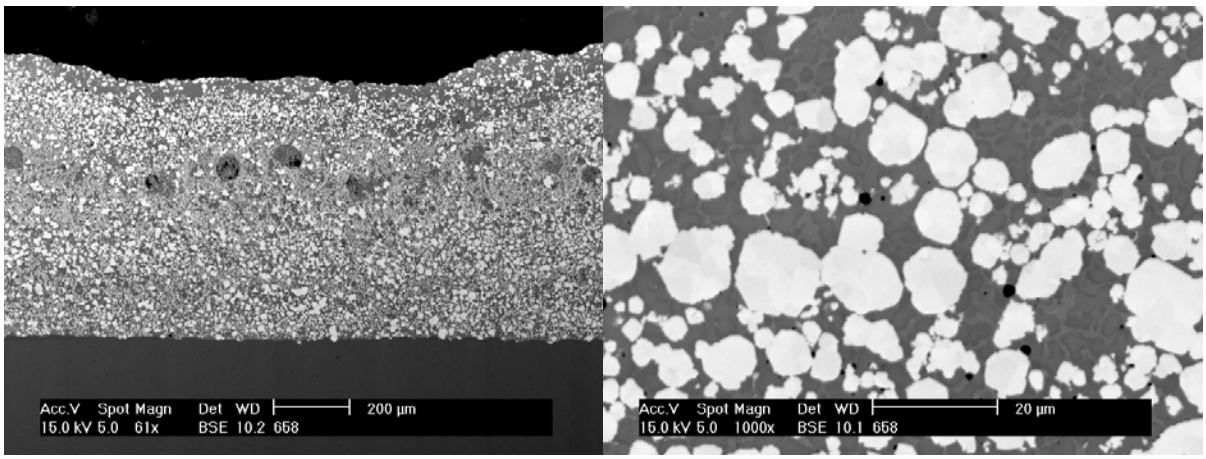

Figure 105. BSE images taken from the transverse cross-section (parallel to cladding direction) of Colmomoy 42-P2 + Amperit 522.3 (25/75) coating (high power). Large spherical dark areas in lower magnification image are gas pores. Such pores were not detected in coating laser clad with low power.

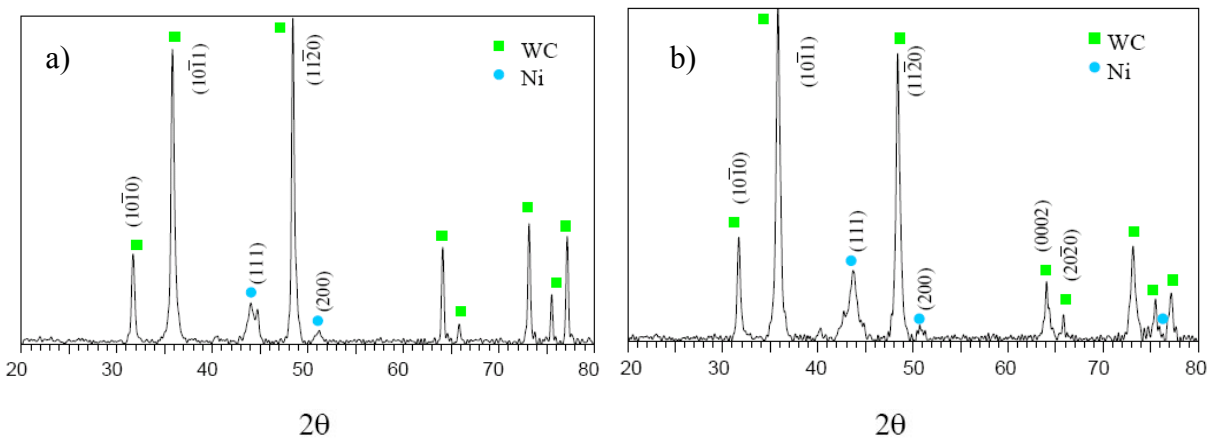

Figure 106. XRD patterns measured from Colmonoy 42-P2 + Amperit 522.3 (25/75 vol.%) coatings laser clad with a) low and b) high laser power.

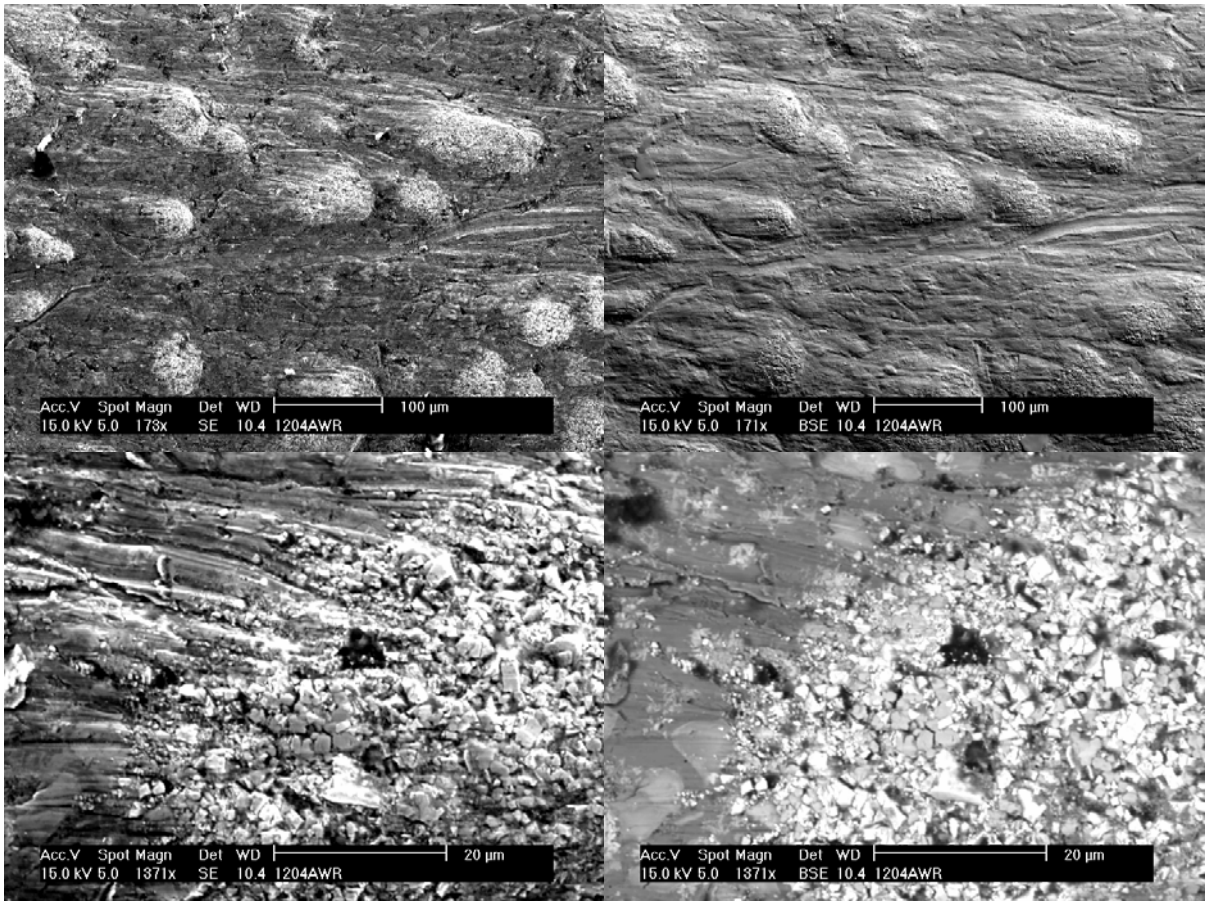

Figure 107. SEM micrographs taken from the wear scar of Metco 16C + recycled WC (70/30 vol.%) coating. Rubber wheel rotated from right to left. Matrix wore down profoundly by microploughing and –cutting as evidenced by signs of plastic flow. Small carbides inside recycled WC powder particles were well bound together by TiCo matrix.

3.4.1.3 Influence of carbide morphology

Influence of carbide morphology on abrasion wear resistance and carbide dissolution was studied by mixing dense-coated WC, spherical fused WC/W_2C/W and angular fused WC/W_2C with Metco 12C (30 HRC ~ 304 HV). These carbides had nearly equal size distributions, which excluded the influence of carbide size on dissolution and wear behaviour. All three different coatings were laser clad with identical parameters. Abrasion wear results and microhardness values are summarized in Table 20. Representative micrographs taken from the transverse cross-sections (perpendicular to cladding direction) together with high magnification SEM micrographs taken from the wear scars are illustrated in Figures 108-112. Wear scar for Metco 12C + Amperit 522.2 (70/30 vol.%) was essentially similar to one displayed in Figure 101. For that reason, it is not shown here.

Table 20. Influence of carbide morphology on abrasion wear resistance and microhardness.

Coating	***Volume ratio***	***Carbide size (µm)***	***Mass loss (mg)***	***STDV***	***COV (%)***	***Volume loss (mm^3)***	***HV_1***	***$HV_{0.3}$***
Metco 12C* + *Amperit 522.2	(70/30) (65/35)[1]	44-88	393	52	13	40.8 37.8[2]	678	568[3] 1225[4]
Metco 12C* + *Durmat SFTC	(70/30) (76/24)[1]	45-90	180	50	28	17.6 18.6[2]	810	570[3] 2420[4]
Metco 12C* + *Woka 9604	(70/30) (62/38)[1]	38-72	181	23	12	17.7 16.5[2]	820	650[3] 1950[4]

1) volume ratio according to image analysis
2) volume loss calculated on the basis of average matrix/carbide volume ratio in coating measured with image analysis
3) matrix microhardness
4) carbide microhardness

According to image analysis conducted on transverse cross-sections (perpendicular to cladding direction), average primary carbide volume fractions varied from 24 (SFTC) to 38% (Woka 9604). Fortunately, volume fractions of dense-coated WC and angular fused WC/W_2C were nearly the same (35 vs. 38 vol.%) enabling to make some comparative study. On the basis of mass and volume losses, it is evident that coatings reinforced with angular fused WC/W_2C exhibited more than twice better abrasion wear resistance than coating reinforced with dense-coated WC. This substantial difference in resistance can be explained by comparing the microhardness values and wear scars. Bulk microhardness of the coating reinforced with angular fused carbides was clearly higher (820 vs. 678 HV_1). This partly originates from the slightly higher volume fraction of primary carbides and higher matrix hardness but mainly from the difference in behaviour of the primary carbides under the indentation load. Namely, dense-coated WC particulates cracked severely under the both indentation loads (10 and 3 N) as already explained in section 3.4.1.1. Some of those carbides were cracked along grain boundaries even without any external load (except sample preparation) as illustrated in higher magnification micrograph in Figure 108. With a load of 3 N average microhardness of the dense-coated WC was just 1225 $HV_{0.3}$ compared to 1950 $HV_{0.3}$ for angular fused carbides. Wear scar studies revealed that dense-coated WC particulates cracked also more severely under used abrasive conditions than angular fused ones. If the matrix microhardness values are compared, matrix reinforced with angular fused carbides exhibited higher values (568 vs. 650 $HV_{0.3}$). This suggests that angular fused WC/W_2C carbides dissolved more abundantly to matrix than dense-coated WCs. XRD curves measured from both of the coatings (Figure 113a and c) confirmed this as the integrated areas of unnamed peaks, which belong presumably to precipitated mixed carbides are larger for

coating reinforced with angular fused carbides.. It is known that W_2C is chemically [222] and thermodynamically less stable than WC (at least temperatures below ~1400C°) (Figure 9). For this reason it may have had higher degree of dissolution in Ni-based matrix. Also angularity and associated sharp corners may have enhanced the dissolution further. This dissolution behaviour is in good agreement with results reported in Refs. [223, 224, 391]. Wear behaviour, however, contradicts with rubber wheel abrasion wear results reported by Huang et al. [224]. In their study, coating reinforced with less dissolved WC particulates exhibited better abrasion wear resistance than coating reinforced with WC/W_2C and angular WC particulates survived the test without fragmentation. Their crushed WC particulates were produced by carburisation of elemental W without subsequent dense-coat processing. Manufacturing process of WC particulates used here before dense-coating process is unknown but commercially the carburisation of elemental W is the most important and thus the most probable method in this case. Luft et al. [391] used visually and compositionally identical powder in their studies and they called it agglomerated and dense-coated.

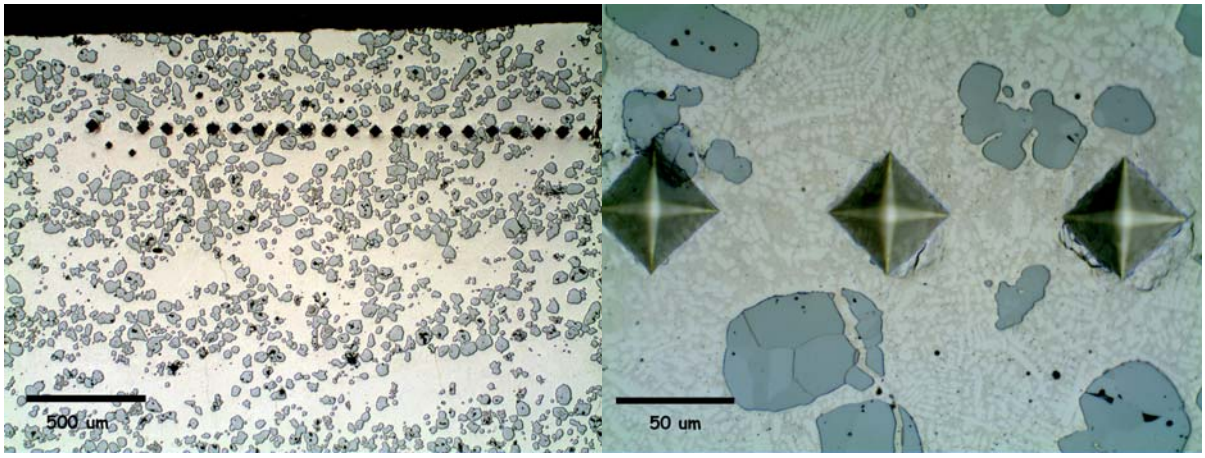

Figure 108. Optical micrographs taken from the transverse cross-section (perpendicular to cladding direction) of Metco 12C + Amperit 522.2 (70/30 vol. %) coating. Some of the WC particles were cracked along grain boundaries even without any additional mechanical load (except sample preparation).

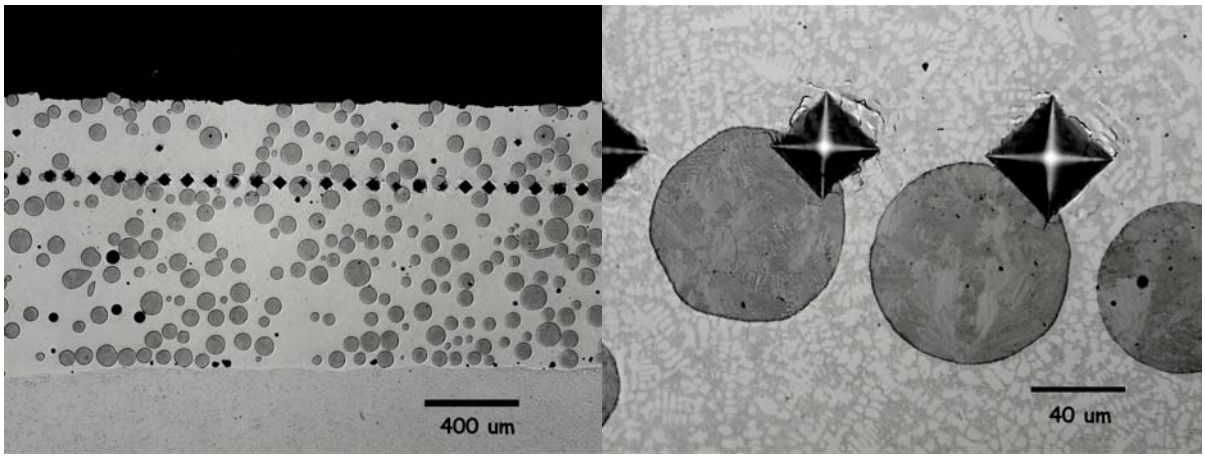

Figure 109. Optical micrographs taken from the transverse cross-section (perpendicular to cladding direction) of Metco 12C + $WC/W_2C/W$ SFTC (70/30 vol.%) coating.

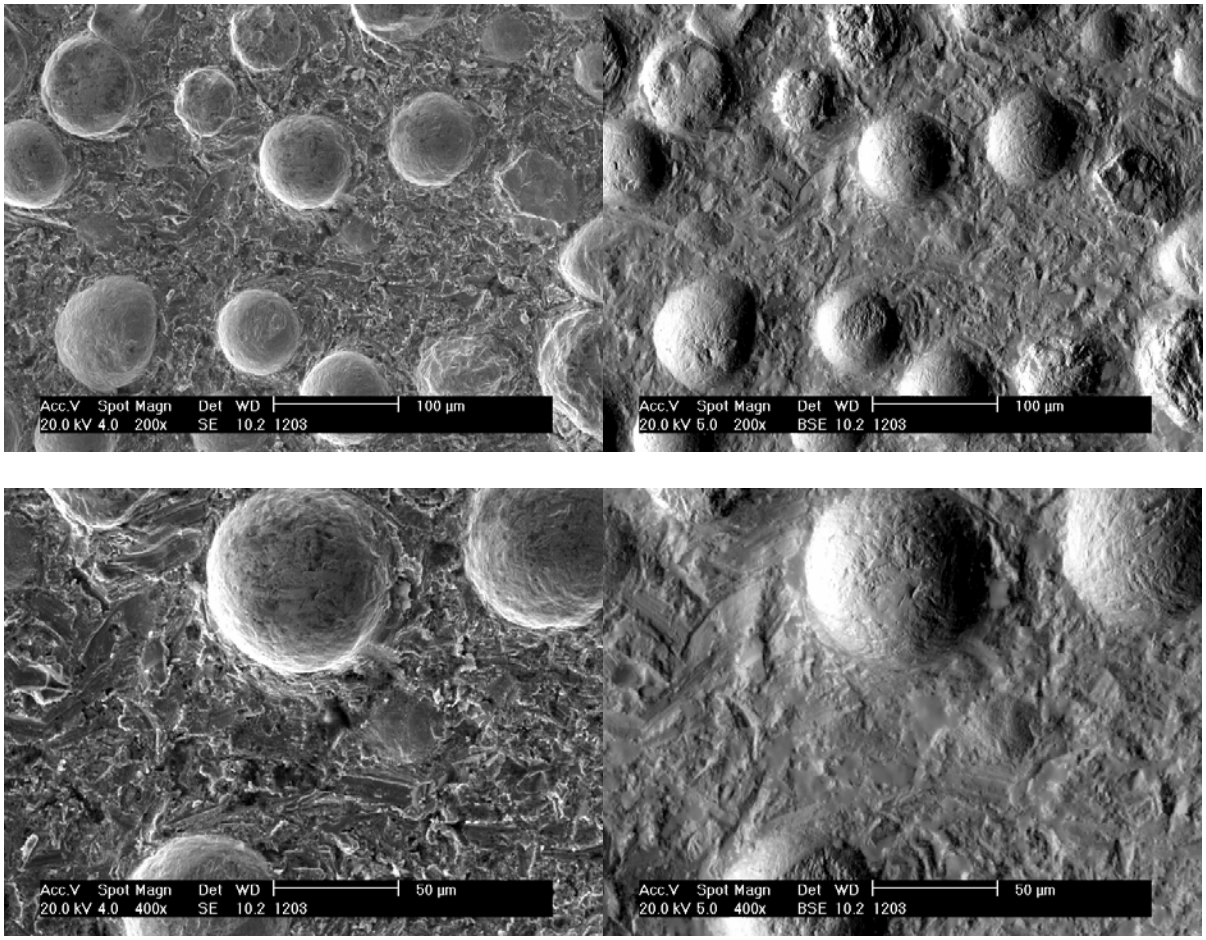

Figure 110. SEM micrographs taken from the wear scar of the Metco 12C + WC/W_2C/W SFTC (70/30 vol.%) coating. Rubber wheel rotation direction was from left to right. Some of the carbides are split in two in plane parallel to surface. Majority of the carbides are, however, intact. Signs of plastic flow are seen on the surface of matrix.

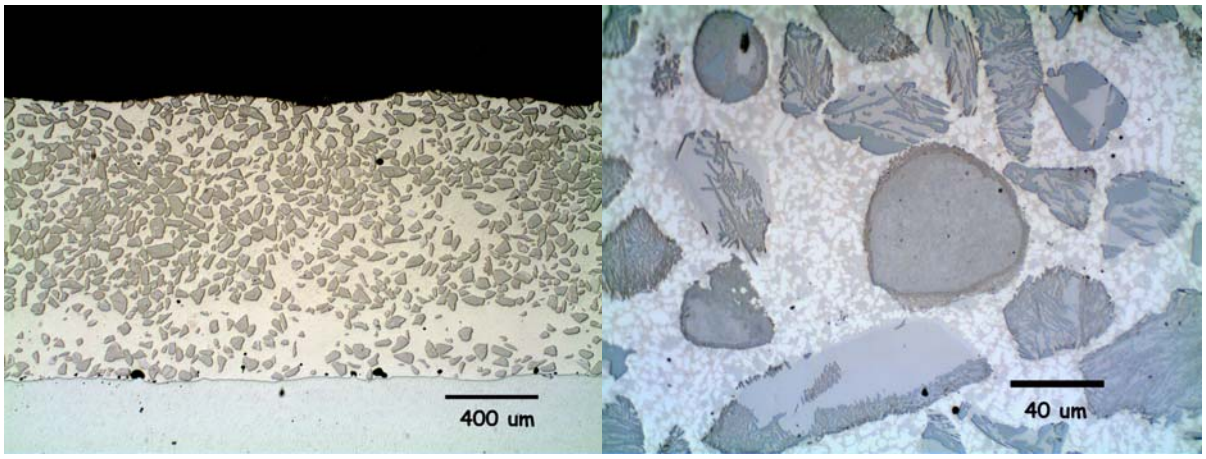

Figure 111. Optical micrographs taken from the transverse cross-section (perpendicular to cladding direction) of Metco 12C + WC/W_2C Woka 9604 (70/30 vol.%) coating. Carbide microstructure consists of WC needles (dark) in W_2C matrix (light).

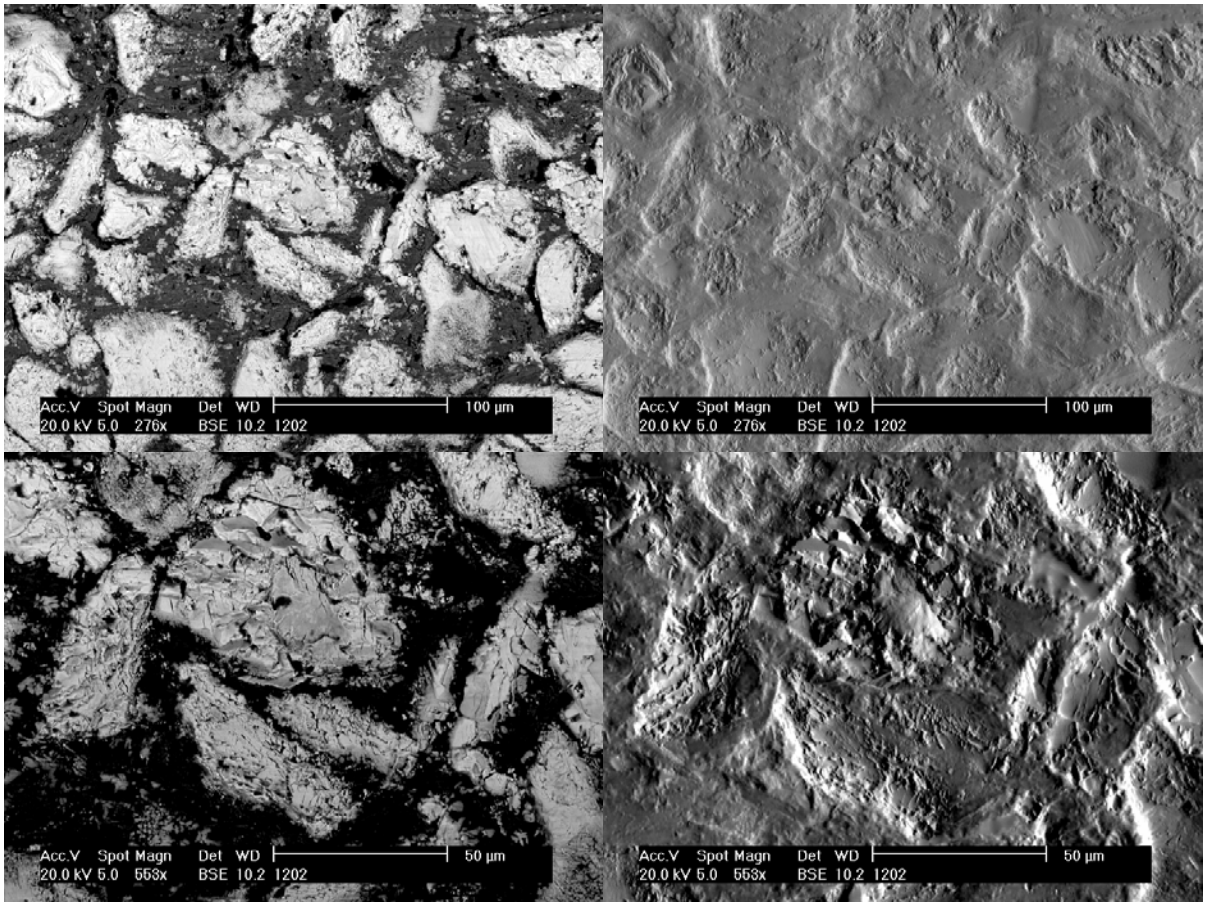

Figure 112. SEM micrographs taken from the wear scar of Metco 12C + WC/W_2C Woka 9604 (70/30 vol.%) coating. Rubber wheel rotation direction was from left to right. Carbides are much more severely damaged than SFTC ones but not as badly as dense-coated WCs.

Comparison between fused carbides (angular vs. spherical) is more difficult because of different volume fractions of primary carbides in coatings (24 vs. 38 vol.%). This difference may have originated from the incomplete mixing of powders or mechanical segregation in powder hopper since microhardness values do not indicate any excessive dissolution of spherical carbides, which would have decreased the primary carbide content. Assuming that matrix and carbides exhibited uniform wear, volume losses suggest that spherical fused carbides are better because they showed just slightly higher volume losses (18.6 vs. 16.5 mm^3) despite notably lower volume fraction of carbides. SEM micrographs taken from the wear scars, however, reveal that matrix has worn down much more profoundly in coating reinforced with spherical carbides. This increases the difference in real wear volumes since wear volume of coating reinforced with spherical fused carbides increases. The reason for this higher degree of matrix wear in coating reinforced with spherical carbides can be found from dissolution. Angular fused carbides may have dissolved more severely due to sharp corners as revealed by large difference in matrix hardness values (570 vs. 650 $HV_{0.3}$) and the integrated areas of unnamed peaks in Figure 113. On the other hand, it may have also resulted exclusively from the higher carbide content (24 vs. 38 vol.%). According to WC/W_2C volume fraction calculations based on integrated areas of peaks $WC\left(10\bar{1}1\right)$ vs. $W_2C\left(10\bar{1}1\right)$ and $WC\left(11\bar{2}0\right)$ vs. $W_2C\left(11\bar{2}0\right)$, amount of WC with respect to W_2C increased in both coatings. WC/W_2C for spherical fused WC/W_2C/W powder was 40/60, whereas in coating it was 45/55. In angular fused WC/W_2C powder relation was 43/57 and in coating 60/40. Both of

these examples indicate the faster dissolution of W_2C over WC and higher susceptibility of angular fused ones to dissolution. Concerning carbide hardness, it was observed that spherical fused carbides exhibited significantly higher hardness than angular fused ones (2420 vs. 1950 $HV_{0.3}$). This resulted almost equal bulk hardness values (810 vs. 820 HV_1) despite notably lower carbide content. Wear scar images also speak for spherical carbides since they remained predominantly intact, whereas angular ones cracked. Spherical shape together with high hardness and existence of W could explain this difference in cracking. For instance, spherical ones may have softened the impact of abrasives by receiving them in less steep/high angles even if the attack angle is not so crucial in three-body abrasive wear where abrasives are free to rotate. And cubic (bcc) W could have increased their fracture toughness.

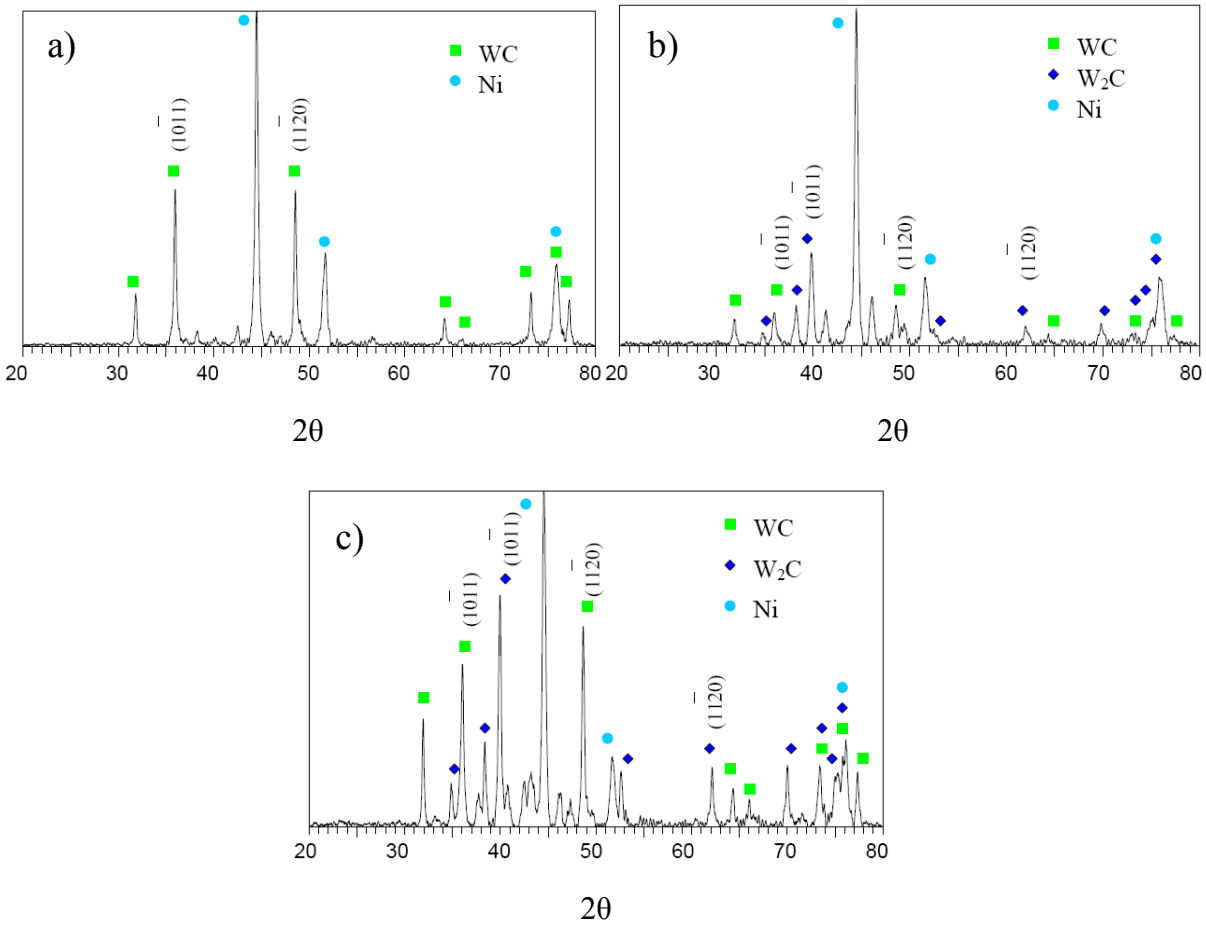

Figure 113. XRD patterns measured from a) Metco 12C + Amperit 522.2 (70/30 vol.%), b) Metco 12C + SFTC (70/30 vol.%) and c) Metco 12C + Woka 9604 (70/30 vol.%) coatings.

3.4.2 Stellite 21 + WC

Similar to study in section 3.4.1.1, Amperit 522.3 and 522.2 dense-coated WC particulates were mixed with Stellite 21 matrix with ratio of 50/50 in vol.%. This allows comparing the influence of matrices.

3.4.2.1 Influence of matrix material

Influence of matrix material on wear resistance, carbide dissolution and microhardness was studied by mixing equal volume fractions of fine and coarse dense-coated WC with Ni-based

Metco 16C and Co-based Stellite 21. These coatings were laser clad with identical parameters. Abrasion wear results and microhardness values are summarized in Table 21. Representative micrographs taken from the transverse cross-sections (parallel to cladding direction) of Stellite 21 + Amperit 522.3 (50/50 vol.%) and Stellite 21 + Amperit 522.2 (50/50 vol.%) coatings are illustrated in Figures 114 and 115. Corresponding Metco 16C coatings were already displayed in Figures 97 and 99 in section 3.4.1.1.

Table 21. Influences of matrix material on abrasion wear resistance and microhardness.

Coating	***Volume fraction***	***Carbide size (µm)***	***Mass loss (mg)***	***STDV***	***COV (%)***	***Volume loss (mm^3)***	***HV_1***	***$HV_{0.3}$***
Metco 16C* + *Amperit 522.3	(50/50) (76/24)[1]	5-44	129	41	32	11.7 13.6[2]	1030	1020[3] N/A[4]
Stellite 21* + *Amperit 522.3	(50/50) (93/7)[1]	5-44	149	24	16	13.0 16.9[2]	760	1000[3] N/A[4]
Metco 16C* + *Amperit 522.2	(50/50) (59/41)[1]	44-88	256	46	18	23.2 23.5[2]	990	900[3] 1280[4]
Stellite 21* + *Amperit 522.2	(50/50) (69/31)[1]	44-88	213	31	15	18.6 20.0[2]	960	880[3] 1345[4]

1) volume ratio according to image analysis
2) volume loss calculated on the basis of average matrix/carbide volume ratio in coating measured with image analysis
3) matrix microhardness
4) carbide microhardness

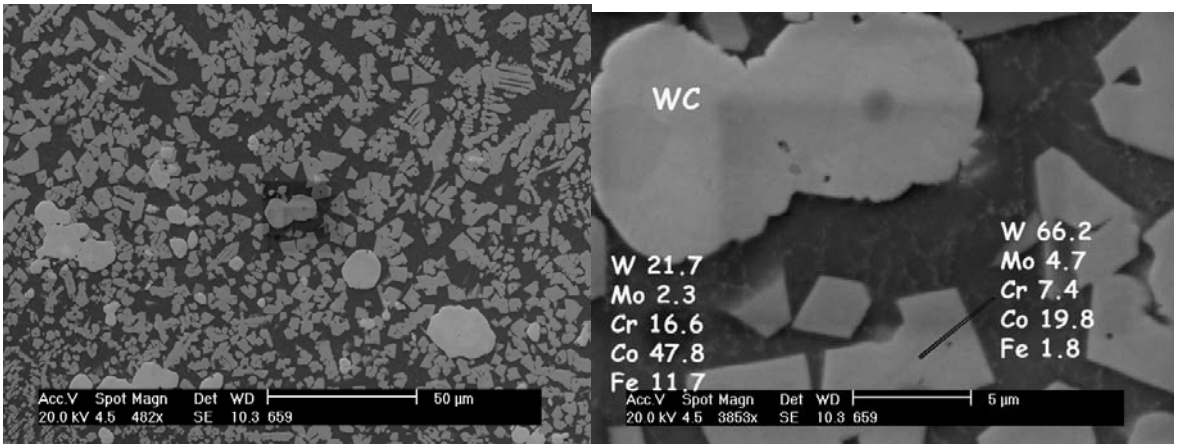

Figure 114. BSE images taken from the transverse cross-section (parallel to cladding direction) of Stellite 21 + Amperit 522.3 (50/50 vol.%) coating. Only a small amount of primary carbides retained (7 vol.%). According to EDS point analysis the composition of the precipitated secondary carbide was 4.8Mo-7.4Cr-1.8Fe-19.8Co-66.2W in wt.%. Composition of the matrix was 2.3Mo-16.6Cr-11.7Fe-47.8Co-21.7W in wt.% at the distance of 800 µm from the coating/base material interface. Fe content indicates rather high dilution in this 1 layer coating.

Metco 16C (58–60 HRC ~ 685–736 HV) alone is harder and is expected to have better abrasion wear resistance than Stellite 21 (32 HRC ~ 321 HV). When mixed with equal amount of WC, only a small difference in abrasion wear resistance was observed. This can be

attributed to the matrix microhardness values, which were almost equal in consequence of higher degree of carbide dissolution in CoCr- than in NiCr-based matrix. This result is in good agreement with the results obtained by Nowotny et. al. [226] and Gassmann [225], who observed faster dissolution kinetics for WC in CoCr than in NiBSi. Nowotny et al. [226] suggested that it was due to higher solubility of WC in Co than in Ni as was shown in Table 3, where the solubility of WC in Co at 1250ºC is nearly 2 times higher than in Ni. On the other hand, Babu et al. [95] showed that dissolution kinetics do not go along with solubility values shown in Table 3. Precipitated complex secondary carbides were identified as type Co_6W_6C (η-phase) (M_6C) and Co_3W_3C (η-phase) (M_3C) complex carbides as illustrated in Figure 116.

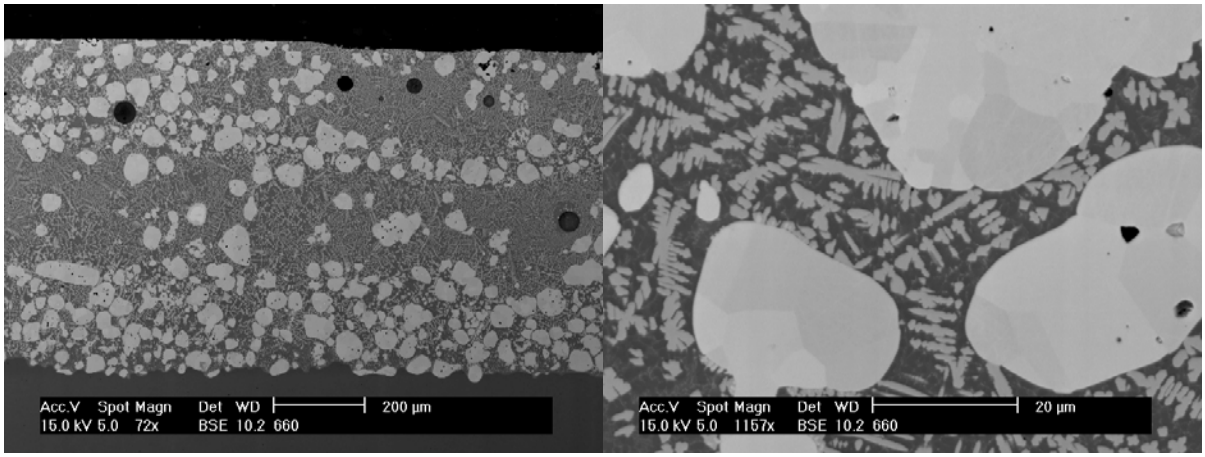

Figure 115. BSE images taken from the transverse cross-section (parallel to cladding direction) of Stellite 21 + Amperit 522.2 (50/50 vol.%) coating. Significantly higher amount of primary carbides retained (31 vol.%). According to EDS point analysis the composition of the precipitated secondary carbide was 3.7Mo-6.6Cr-5.8Fe-20.1Co-1.3Ni-62.4W in wt.%. Composition of the matrix was 2.6Mo-16.7Cr-16.2Fe-40.8Co-2.1Ni-20.6W in wt.% at the distance of 600 µm from the coating/base material interface. EDS area analysis from near the free surface of the coating gave the composition of 2.0Mo-6.8Cr-6.2Fe-21.4Co-0.7Ni-62.7W in wt.%. Fe contents indicate rather high dilution in this 1 layer coating.

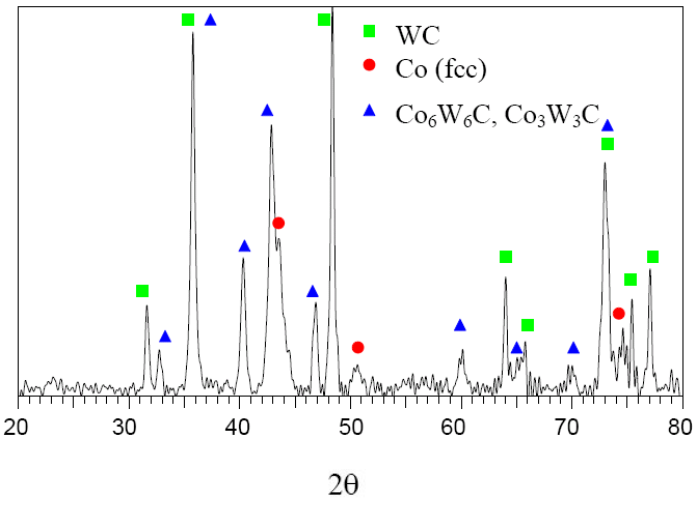

Figure 116. XRD pattern measured from Stellite 21 + Amperit 522.3 coating (50/50 vol.%).

3.4.2.2 Influence of carbide size

Similar to study in section 3.4.1.1, effect of carbide size on abrasion wear resistance, carbide dissolution and microhardness can be found out by comparing the results obtained for Stellite 21 + Amperit 522.2 (44-88 μm) (50/50 vol.%) and Stellite 21 + Amperit 522.3 (5-44 μm) (50/50 vol.%). These coatings were laser clad with identical parameters. Abrasion wear results and microhardness values are summarized in Table 22. Representative micrographs taken from the transverse cross-sections (parallel to cladding direction) were shown earlier in Figures 114 and 115.

Table 22. Influence of carbide size on abrasion wear resistance and microhardness.

Coating	***Volume fraction***	***Carbide size (μm)***	***Mass loss (mg)***	***STDV***	***COV (%)***	***Volume loss (mm^3)***	***HV_1***	***$HV_{0.3}$***
Stellite 21 + Amperit 522.2	(50/50) (69/31)[1]	44-88	213	31	15	18.6 20.0[2]	960	880[3] 1345[4]
Stellite 21 + Amperit 522.3	(50/50) (93/7)[1]	5-44	149	24	16	13.0 16.9[2]	760	1000[3] N/A[4]

1) volume ratio according to image analysis
2) volume loss calculated on the basis of average matrix/carbide volume ratio in coating measured with image analysis
3) matrix microhardness
4) carbide microhardness

Analogous with results reported in section 3.4.1.1, coating reinforced with fine dense-coated WCs exhibited significantly better resistance against abrasive wear than coating reinforced with corresponding coarse carbide. This result verifies the earlier results and emphasizes the role of matrix hardness in wear resistance.

3.4.3 NiCrBSi + CrC

Metco 16C (58–60 HRC ~ 685–736 HV) matrix alloy reinforced with 30 vol.% of CrC (30-106 μm), which consisted mainly of orthorhombic Cr_3C_2 and lower amounts of hexagonal Cr_7C_3 and cubic $Cr_{23}C_6$, was one of the best laser coatings studied here in abrasion wear resistance despite its low initial carbide volume fraction. Due to low melting temperature of CrC (T_m for Cr_3C_2 is 1810ºC), carbides melted and dissolved into the matrix decreasing further the amount of retained primary carbides. Re-heated zones associated with overlapping, particularly, suffered from dissolution/melting. These areas were nearly free of primary carbides. According to image analysis, average volume fraction of primary carbides in the coating was approximately 20%. In addition to primary carbides, microstructure of the coating contained precipitated secondary carbides in Ni-based (fcc) matrix as revealed by the high magnification BSE images taken from the transverse cross-section (Figure 117). These secondary carbides were nearly equiaxed or needle-like in shape. Needle-like secondary Cr-rich carbides (light grey) are shown in higher magnification BSE image in Figure 117. According to elemental maps illustrated in Figure 118, dark areas were rich in Cr and contained more Mo than light areas. C was not detected in these areas. According to XRD, secondary carbides were mainly the type Cr_7C_3. Some vertical cracks and spherical pores were also detected from the transverse cross-section perpendicular to cladding direction. Vickers pyramid indentation at a load of 10 N initiated cracks in the matrix, which propagated both along the primary carbide / matrix interfaces and through primary carbides as illustrated in Figure 119. This was the first coating so far where the cracks propagated distinctively

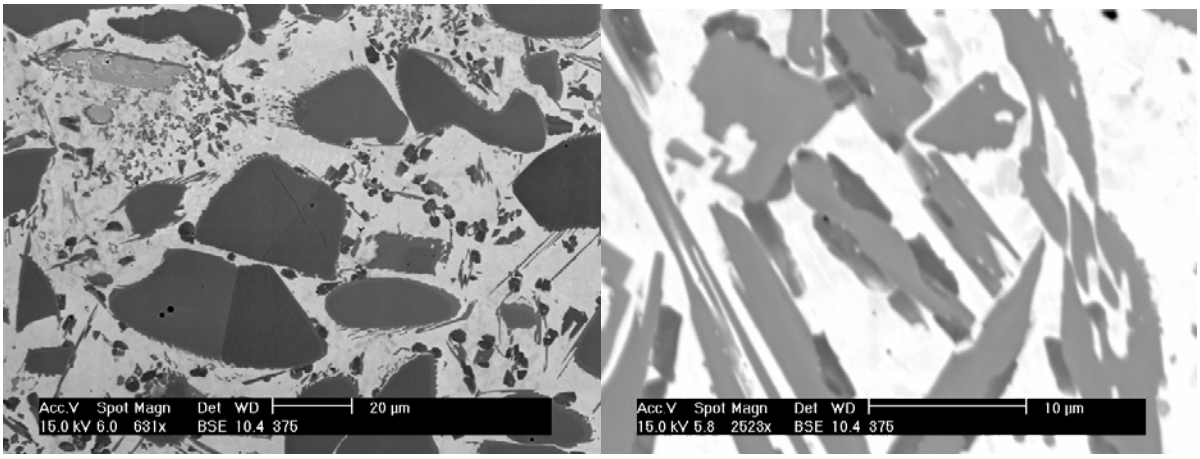

Figure 117. BSE images taken from the transverse cross-section (perpendicular to cladding direction) of Metco 16C + 70C-NS (70/30 vol.%) coating.

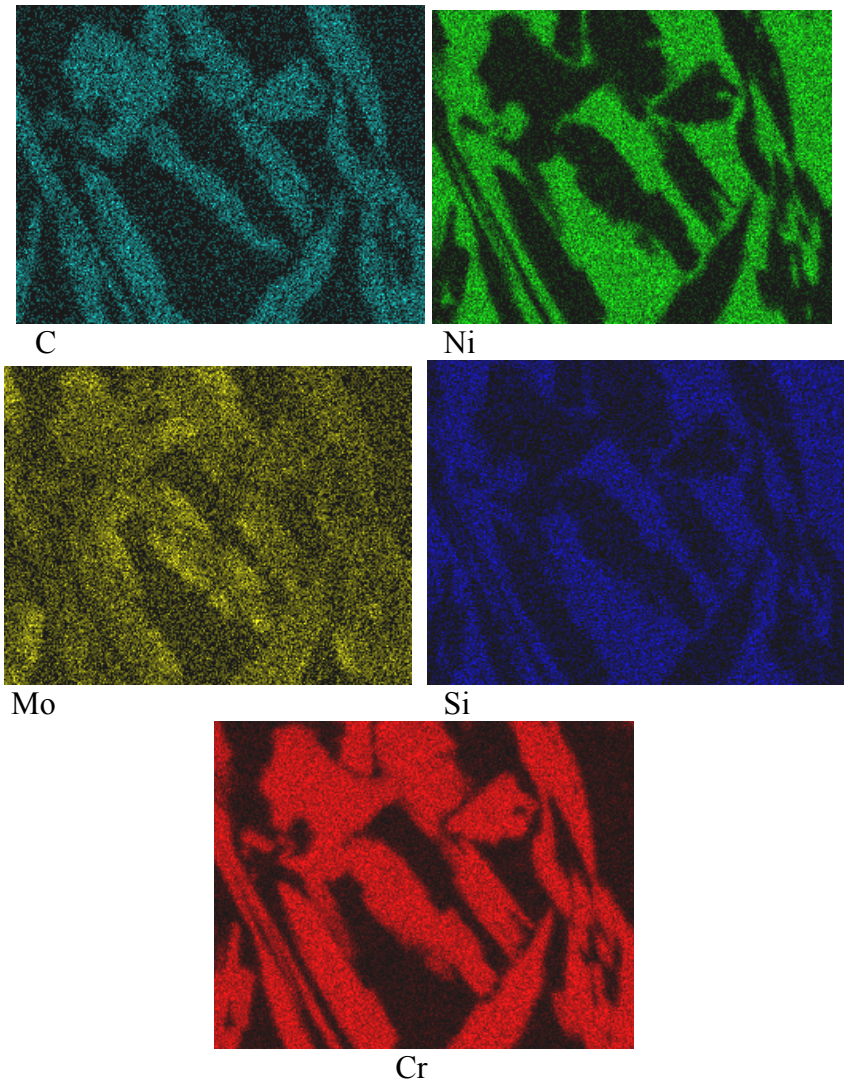

Figure 118. Elemental maps taken from the secondary carbides shown in high magnification image in Figure 117.

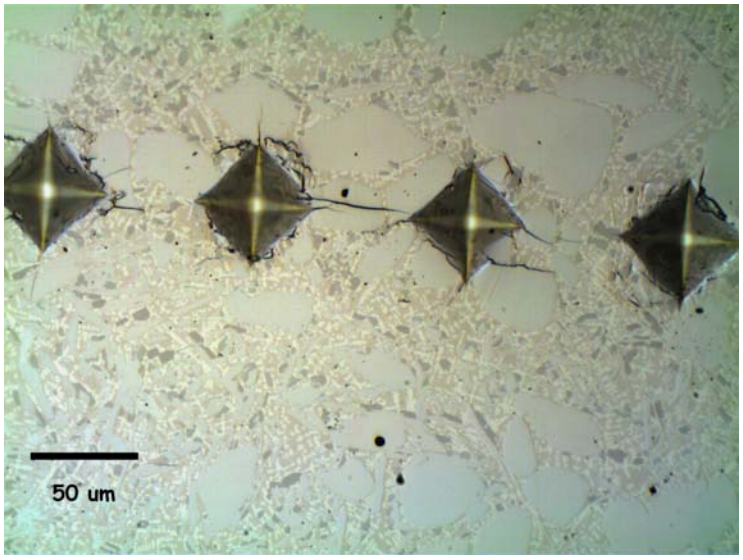

Figure 119. Optical micrograph taken from the transverse cross-section (perpendicular to cladding direction) of Metco 16C + 70C-NS (70/30 vol.%) coating. Vickers pyramid indentation at a load 10 N initiated cracks, which propagated along matrix/ primary carbide interfaces as well as through carbides.

along carbide/matrix boundaries. Indentation load of 3 N on primary carbides did not initiate cracks indicating good fracture toughness.

Explanations for the excellent resistance against abrasive wear can be sought from the microhardness values and wear mechanisms revealed by the SEM micrographs taken from the wear scar (Figure 120). Microhardness values for Metco 16C reinforced with CrC and WC are summarized in Table 23.

Table 23. Abrasion wear losses and microhardness values of Metco 16 reinforced with CrC and WC.

Coating	***Volume fraction***	***Carbide size (µm)***	***Mass loss (mg)***	***Volume loss (mm^3)***	***STDV***	***COV (%)***	***HV_1***	***$HV_{0.3}$***
Metco 16C* + *CrC	(70/30) (80/20)[1]	30-106	87	12.0 11.9[2]	15	17	840	870[3] 1500[4]
Metco 16C* + *recycled WC	(70/30) (76/24)[1]	45-125	214	23.2 24.1[2]	5	2	970	800[3] 1580[4]
Metco 16C* + *Amperit 522.3	(50/50) (76/24)[1]	5-44	129	11.7 13.6[2]	41	32	1030	1020[3] N/A[4]
Metco 16C* + *Amperit 522.2	(50/50) (59/41)[1]	44-88	256	23.2 23.5[2]	46	18	990	900[3] 1280[4]

1) volume ratio according to image analysis
2) volume loss calculated on the basis of average matrix/carbide volume ratio in coating measured with image analysis
3) matrix microhardness
4) carbide microhardness

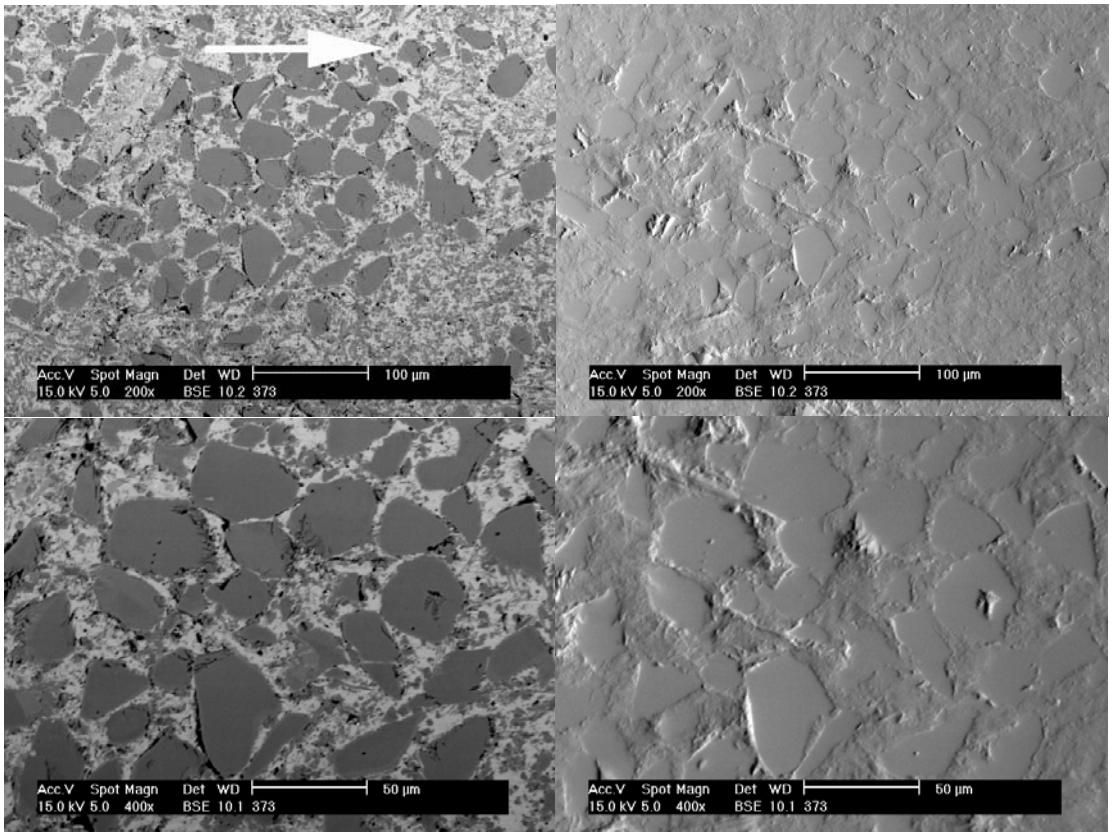

Figure 120. SEM micrographs taken from the wear scar of the Metco 16C + 70C-NS (70/30 vol.%) coating. Arrow indicates the rubber wheel rotation direction. Matrix has worn down profoundly at the front side of the carbides in relation to wear direction. Primary carbides are predominantly intact without signs of scratches or cracks.

There are not significant differences in microhardness values, which could explain the excellent resistance of Metco 16C reinforced with CrC. In fact, bulk hardness was the lowest among comparable coatings. Instead, there was large difference in wear mechanisms at least compared with Amperit 522 dense-coated WC powders. Namely, primary CrC particulates remained predominantly intact without signs of scratches and cracks. This was somewhat surprising since CrC particulates were not extraordinarily hard as proved by the hardness measurements but apparently hard enough to resist silica (750-1200 HV).

CrC behaved also well in Stellite 6 matrix, but not as good as with Metco 16C if wear resistance is considered. Abrasion and microhardness values are summarized in Table 24. Representative micrographs taken from the transverse cross-sections (perpendicular to cladding direction) together with high magnification SEM micrographs taken from the wear scar are illustrated in Figures 121-122. It is worth to point out that this was the first coating discussed so far where the indentation load of 10 N did not initiate cracks in the matrix.

3.4.4 Tool steels

Two different tool steel compositions were laser clad and tested, WR10 (Fe-12.5Cr-1.1Mo-4.0V-2.3C in wt.%) and WR6 (Fe-5.3Cr-1.3Mo-11.5V-2.9C in wt.%), the latter being substantially better in abrasion wear resistance (950 vs. 113 mg). At the same time, it was the best monolithic laser coating studied here. According to XRD analysis WR10 powder consisted predominantly of austenite, whereas laser coating consisted of austenite,

Table 24. Influence of matrix material on abrasion wear resistance and microhardness.

Coating	***Volume fraction***	***Carbide size (µm)***	***Mass loss (mg)***	***Volume loss (mm^3)***	***STDEV***	***COV (%)***	***HV_1***	***$HV_{0.3}$***
Metco 16C + CrC	(70/30) (80/20)[1]	*30-106*	87	12.0 11.9[2]	15	17	840	870[3] 1500[4]
Stellite 6 + CrC	(65/35) (83/17)[1]	*30-106*	116	14.8 14.2[2]	26	24	920	830[3] 1590[4]

1) volume ratio according to image analysis
2) volume loss calculated on the basis of average matrix/carbide volume ratio in coating measured with image analysis
3) matrix microhardness
4) carbide microhardness

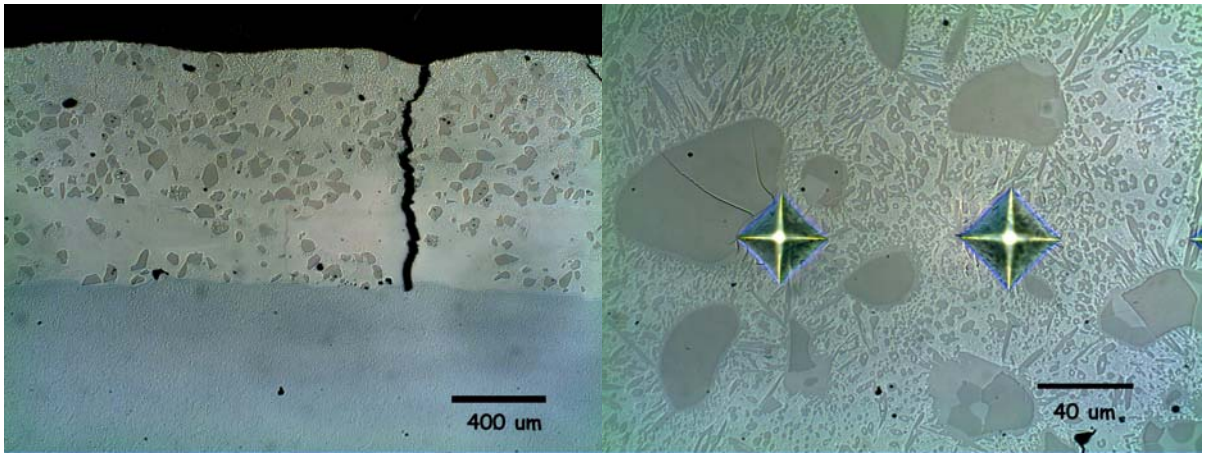

Figure 121. Optical micrographs taken from the transverse cross-section (perpendicular to cladding direction) of Stellite 6 + 70C-NS (65/35 vol.%) coating.

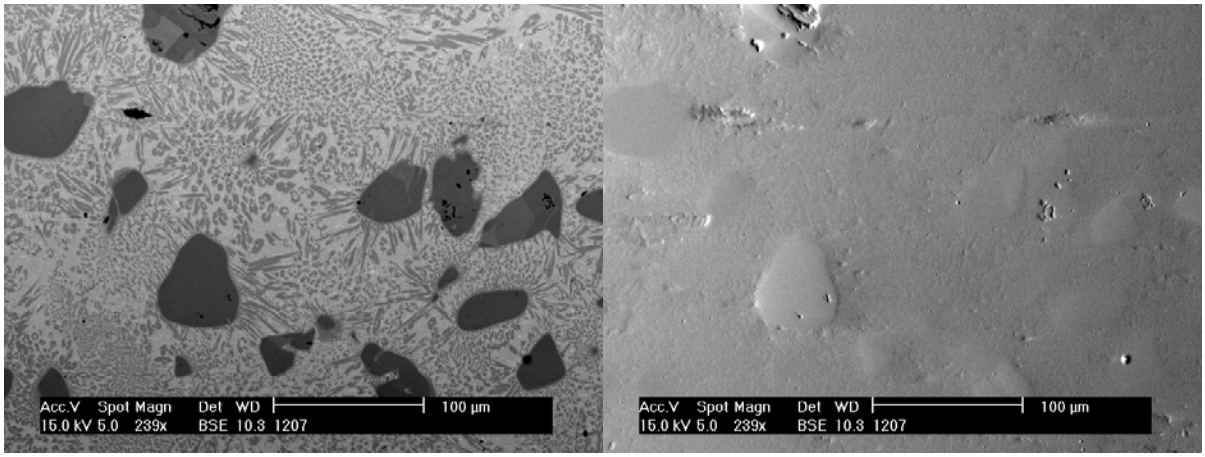

Figure 122. SEM micrographs taken from the wear scar of Stellite 6 + 70C-NS (65/35 vol.%) coating. Rubber wheel rotated from left to right.

martensite/ferrite and only small amounts of VC (actually the peaks coincided with V_4C_3, V_8C_7 and $VC_{0.88}/V_{32}C_{28}$). Austenite to martensite/ferrite ratio, as evaluated roughly from the integrated peak areas (γ(111) vs. α(110)), was 9 for powder and 1.3 for laser coating. These peaks were the highest ones and no preferred orientation was detected. Microhardness of this coating was approximately 560 HV_1. According to XRD analysis WR6 powder consisted of austenite, VC and small amounts of martensite/ferrite. WR6 laser coating consisted of fine, round and star-like, VCs (~10 vol.%, 0.6–2.0 µm in diameter), network of FeCrVMo-carbides in a matrix of austenite and martensite/ferrite. Austenite to martensite/ferrite ratios were 3.2 and 0.6 for powder and laser coating, respectively. These ratios are overestimated since one of the VC peaks overlaps with γ(111). The best and most often used peaks to evaluate austenite to martensite ratios are α(200) and γ(220). Unfortunately α(200) peak was so weak that its integrated intensity could not be measured. Average microhardness of the WR6 laser coating was 848 HV_1. Nital (4%) etching revealed reheated zones associated with overlapping, which were approximately 40 HV_1 harder than non-reheated zones (870 vs. 830 HV_1). This hardness increase originated probably from the transformation of austenite to martensite due to reheating. Despite high hardness, this alloy was the only laser coating among the second group of abrasion wear tested materials that survived the cladding without cracking (even without preheat). This resulted from the volume expansion associated with martensite formation during cooling, which acted against tensile stresses that formed during cooling. Vickers pyramid indentations (3 and 10 N) did not initiate cracks indicating excellent fracture toughness. Representative micrographs of WR6 laser coating is shown in Figure 123. Reheated and non-reheated zones together with hardness values are illustrated in Figure 124. SEM micrographs taken from the wear scar are shown in Figure 125. In contrast to MMCs discussed above, deep and long scratches caused by angular silica particles are clearly seen. VCs were definitely too small and mean free path between them was too high to prevent apparent wear mechanisms, micro-ploughing and –cutting, to occur.

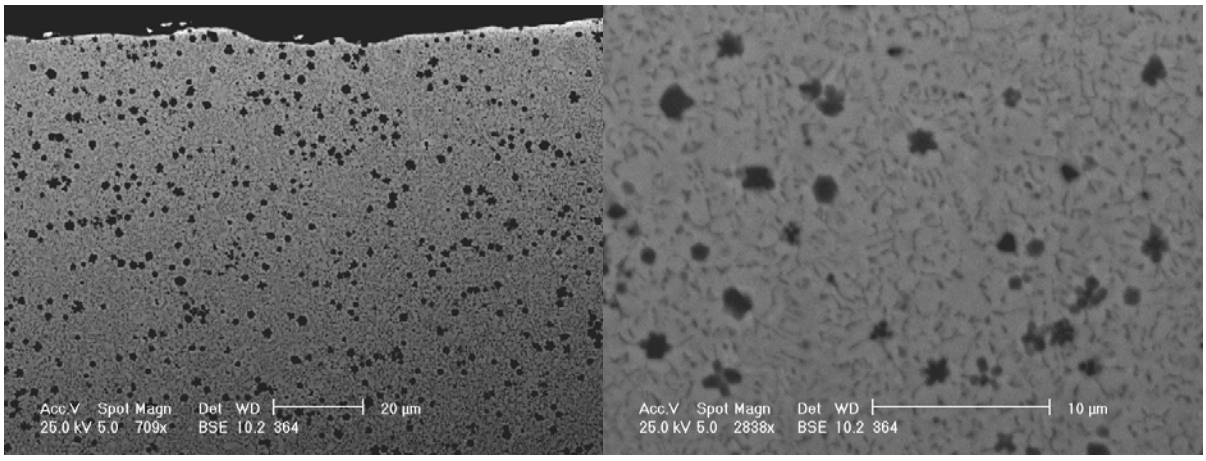

Figure 123. SEM micrograph of WR 6 tool steel laser coating. Volume fraction of vanadium carbides is approximately 10% according to image analysis. Carbides are 0.6-2.0 µm in diameter.

Abrasion wear resistance of WR6 tool steel was further enhanced by adding externally 30 vol.% of coarse VC particulates (45–106 µm). Optical micrograph of this coating is shown in Figure 126. Mass and volume losses decreased from 113 to 89 mg and from 15.3 to 13 mm^3. This improvement was, however, rather modest. VC addition increased bulk hardness of the

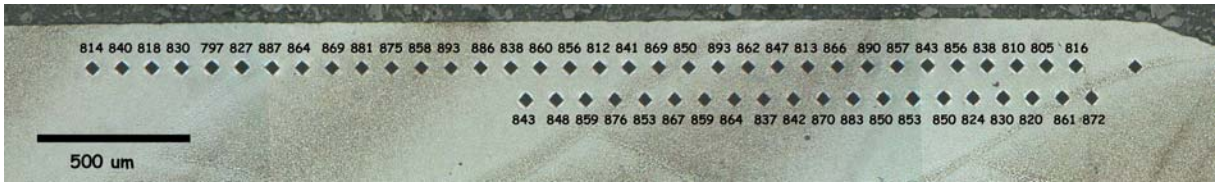

Figure 124. Optical micrograph of etched transverse (perpendicular to cladding direction) cross-section of WR6 tool steel laser coating. Reheated zones and increased microhardness values are clearly seen.

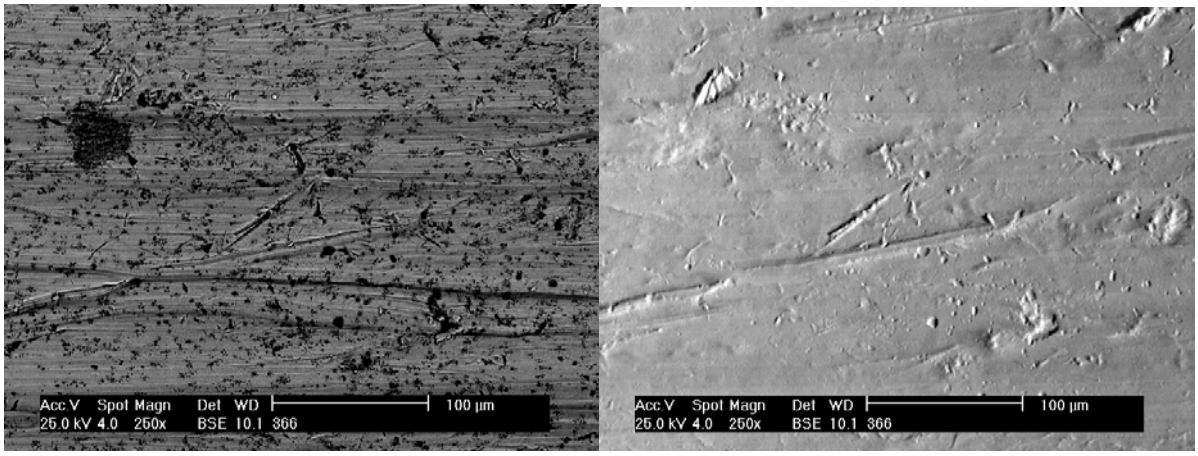

Figure 125. SEM micrographs taken from the wear scar of the WR6 laser coating. Rubber wheel rotation direction was from left to right. In contrast to MMCs deep and long scratches/grooves are clearly visible.

coating from 850 to 1030 HV_1 thanks to high hardness of the externally added VCs (1940 $HV_{0.3}$). Matrix hardness was 840 $HV_{0.3}$. According to XRD, WR6 laser coating reinforced with VCs contained significantly lower amount of martensite/ferrite than WR6 laser coating alone. Austenite to martensite/ferrite ratio was 3.6 compared with 0.6 for WR6 laser coating alone. Due to peak overlapping discussed above, these values are overestimated particularly for WR6 reinforced with externally added VCs. If comparison is made on the basis of integrated peak areas of $\gamma(200)$ vs. $\alpha(110)$, austenite to martensite/ferrite ratios for WR6 alone and WR6 reinforced with externally added VCs are 0.16 and 0.56, respectively. This comparison indicates lower martensite/ferrite content in WR6 reinforced with externally added VCs. Those reheated zones with increased hardness were not detected either. Similar to other MMCs, matrix wore more than carbides and they were tightly bonded to the matrix as revealed by the SEM images taken from the wear scar (Figure 127). Fracture toughness remained high since Vickers pyramid indentation at a load 10 N did not initiate any cracks in the matrix.

3.4.5 (Ti, Mo)C - MMC

(Ti, Mo)C laser coatings were prepared from the powders, which were manufactured with SHS technique. As a result of SHS and subsequent crushing, individual powder particles (45–125 µm), angular in shape, contained spherical or cubic (Ti, Mo)C particulates less than approximately 3 µm in diameter/diagonal. Matrix materials were Stellite 6, nickel and Colmonoy 42-P2 (NiCrBSi). (Ti, Mo)C particulates were spherical in Stellite 6 (Figure 21)

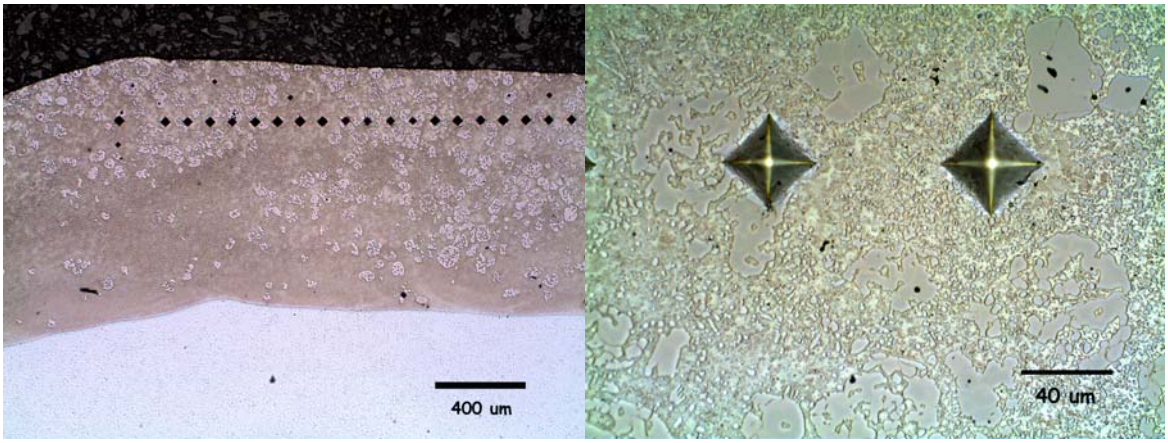

Figure 126. Optical micrographs taken from the transverse cross-section (perpendicular to cladding direction) of WR6 + VC (70/30 vol.%) coating. Vickers pyramid indentation at a load 10 N did not initiate any cracks indicating excellent fracture toughness compared with many other MMCs produced in this study.

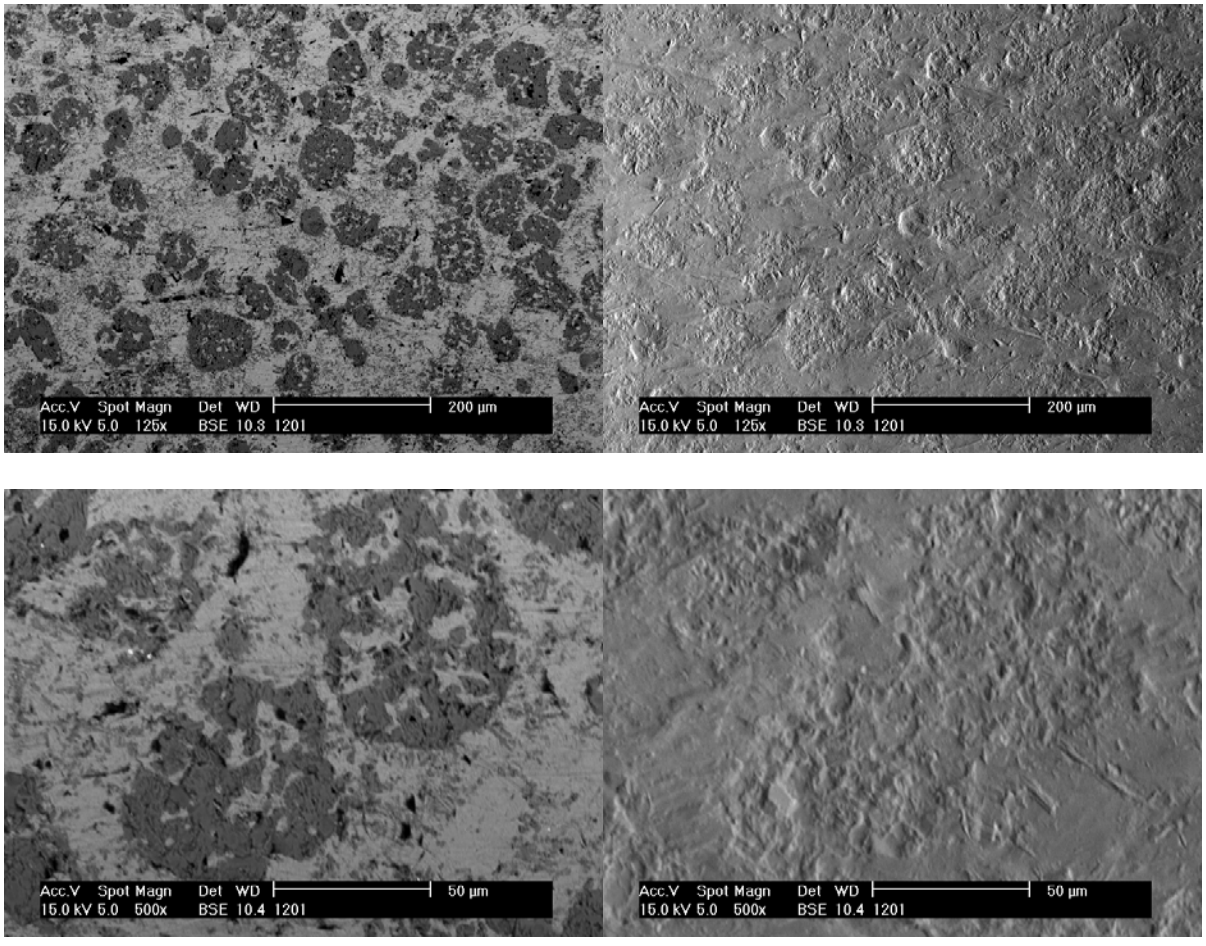

Figure 127. SEM micrographs taken from the wear scar of the WR6 + VC (70/30 vol. %) laser coating. Rubber wheel rotation direction was from left to right.

and cubic in nickel matrix (Figure 23). Particulates in Colmonoy 42-P2 powder resembled particulates in nickel matrix just the corners were rounded (Figure 25).

3.4.5.1 (Ti, Mo)C – Stellite 6

Two different mass ratios were used; (Ti, Mo)C – Stellite 6 (50/50 wt.%) (SHS 1378) and (Ti, Mo)C – Stellite 6 (20/80 wt.%) (SHS 1389). The latter one was obtained by mixing the desired amounts of SHS 1378 and Stellite 6 powders. Laser coating made of SHS 1378 powder exhibited the best resistance against abrasive wear in used conditions among all the laser coatings tested. Owing to high volume fraction of fine and hard (Ti, Mo)C particulates, approximately 64 vol.% according to image analysis, coating was characterized with the bulk hardness of 1100 HV_1 and very short mean free path between particulates. The representative micrographs of SHS 1378 laser coating in low and high magnifications are illustrated in Figures 128 and 129. It was observed that during solidification some carbides tended to form carbide chains or strings, which are seen on the right hand image in Figure 129. In general, Vickers pyramid indentation at a load of 10 N did not initiate cracks in the matrix, but in the vicinity of these carbide chains, some cracks formed and they propagated along the chains. Occasional large pores as well as vertical cracks were also detected. XRD patterns were identical for powder and coating which means that no additional phases formed during cladding. This was expected since possibly dissolved TiCs recrystallizes to dendritic TiC. XRD patterns for SHS 1378 powder and laser coating are shown in Figure 130. In addition to (Ti, Mo)C and fcc-Co, hcp-Co was also detected.

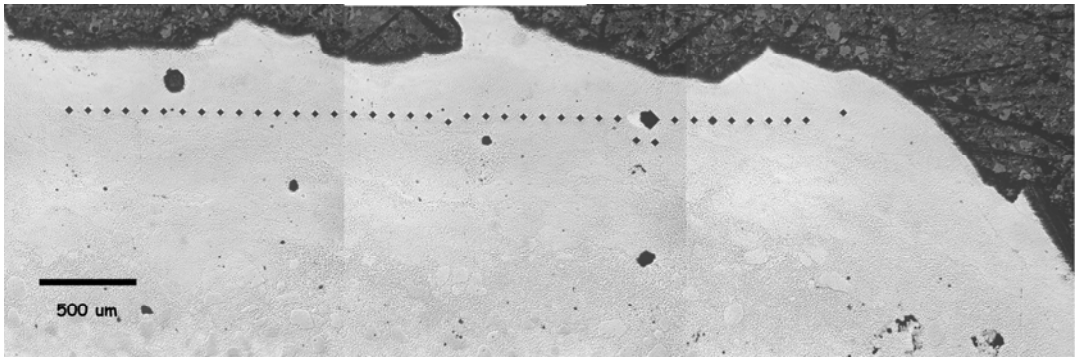

Figure 128. Optical micrograph taken from the transverse cross-section (perpendicular to cladding direction) of as-laser-clad SHS 1378 coating. Large black dots are pores. Some large particles at the lower end of the image have experienced incomplete melting. Due to exceptionally high melt viscosity irregularities formed on the surface.

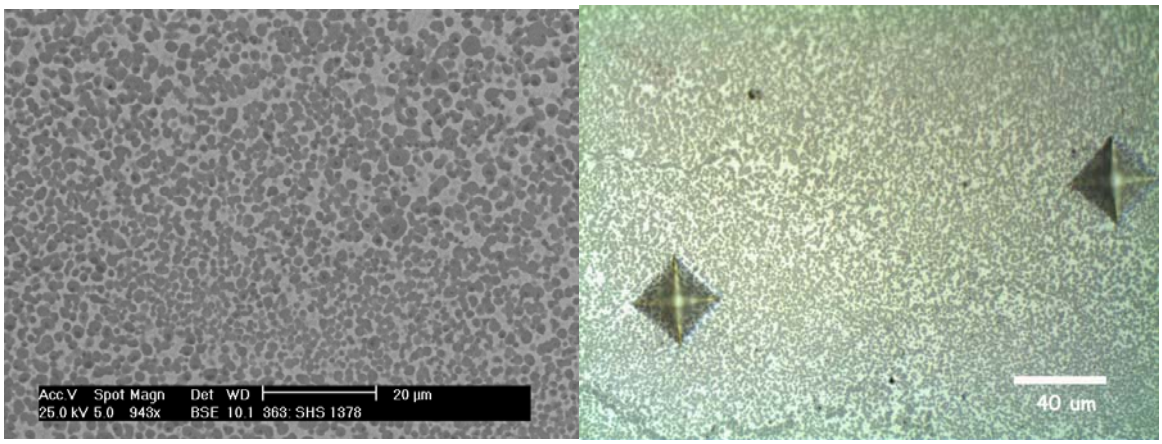

Figure 129. SEM and optical micrographs taken from the transverse cross-section (perpendicular to cladding direction) of SHS 1378 laser coating. Carbide chains/strings are seen in optical micrograph.

Despite short mean free path between (Ti, Mo)C particulates Stellite 6 matrix wore down at the front of carbides in relation to wear direction as displayed in Figure 131. Carbide surfaces were free from scratches. Some of them cracked but not as severely as dense-coated WCs (Amperit 522) and fused WC/W_2Cs (Woka 9604) discussed earlier.

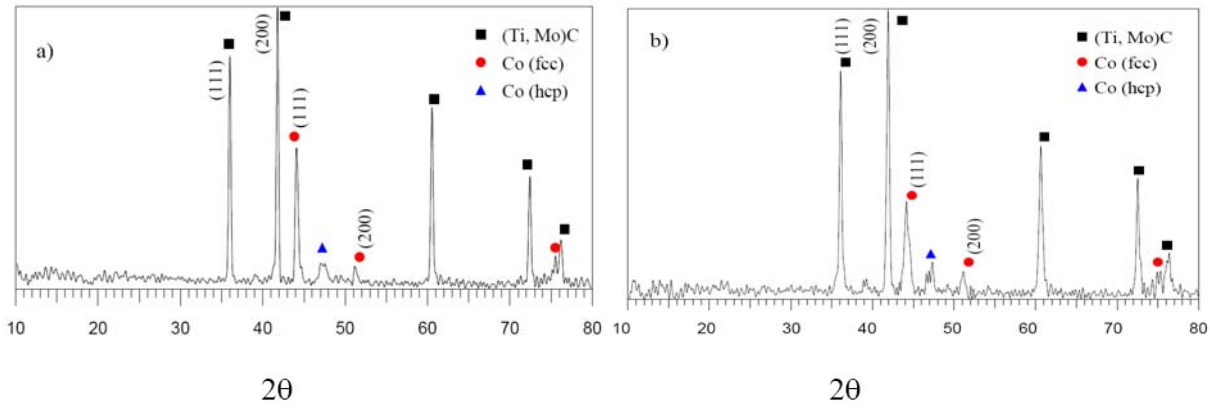

Figure 130. XRD patterns measured from SHS 1378 a) powder) and b) coating.

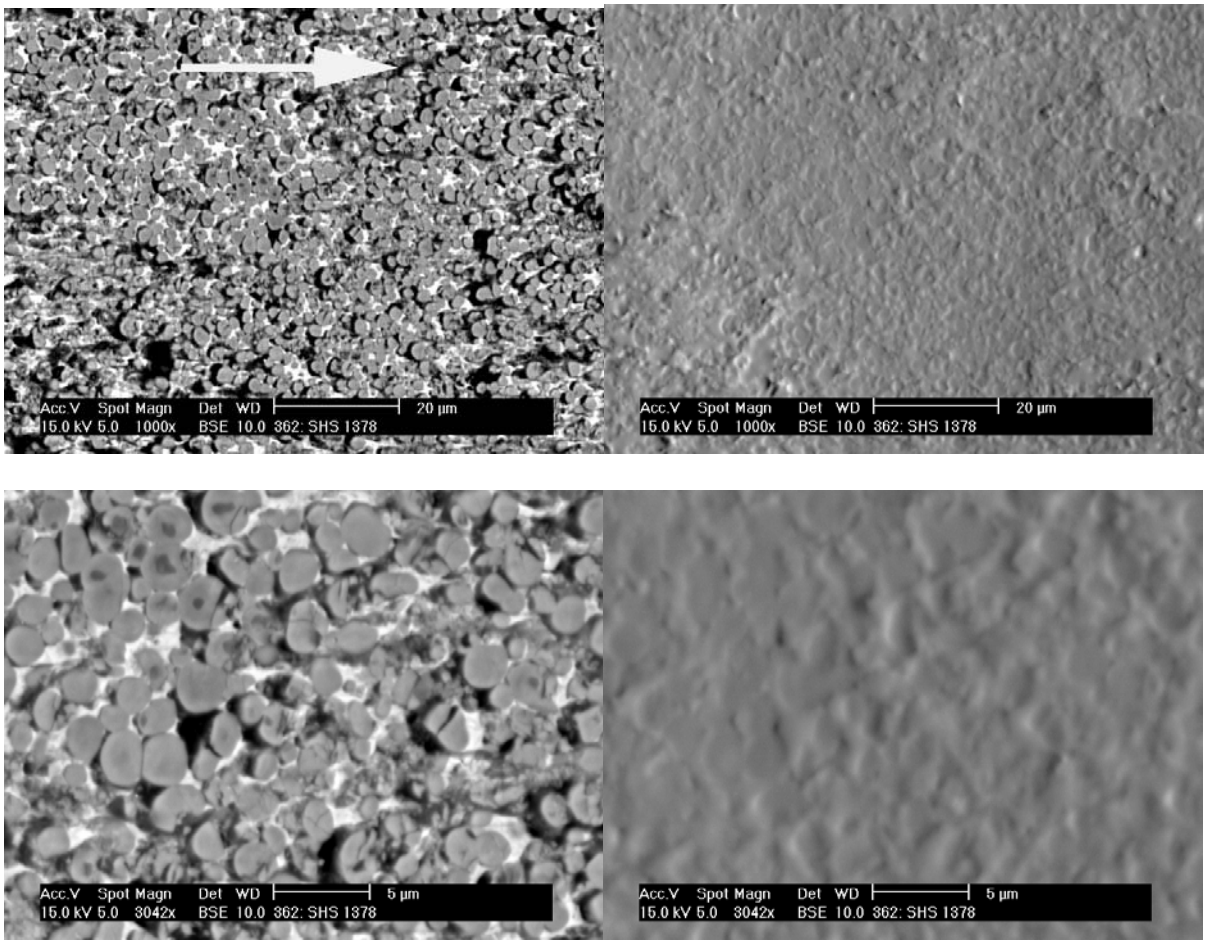

Figure 131. SEM micrographs taken from the wear scar of SHS 1378 laser coating. Arrow indicates the rubber wheel rotation direction.

3.4.5.2 (Ti, Mo)C – Ni-based matrices

With pure nickel as matrix two different mass ratios were used; (Ti, Mo)C – Ni (50/50 wt.%) (SHS 1377) and (Ti, Mo)C – Ni (35/65 wt.%) (SHS 1380). The latter one was obtained by mixing the desired amounts of SHS 1377 and Ni powders. Due to low matrix hardness (~200 HV), coatings made of these powders, were among the worst MMC laser coatings studied here. Carbide volume fractions varied largely in coating made of SHS 1380. This resulted from the incompletely melted or mixed single SHS 1377 particles found in the coating. One representative example is shown in Figure 132. Similar feature was observed in coating made of Co-based SHS 1389, which was also the blend. These incompletely melted or mixed powder particles had better wear resistance than other areas as revealed by the SEM image taken from the wear scar of SHS 1389 in Figure 133. Carbide chains or strings were observed again and they were susceptible to cracking as illustrated in Figure 132.

Another Ni-based (Ti, Mo)C coating was prepared from the powder; (Ti, Mo)C – Colmonoy 42-P2 (50/50 wt.%) (SHS 1436). Due to higher matrix hardness (36 HRC ~ 355 HV), this coating outperformed (Ti, Mo)C – Ni coatings clearly in wear resistance, but was still worse than even SHS1389 ((Ti, Mo)C – St 6 (20/80 wt.%)). This result emphasizes again the role of matrix hardness in given abrasive conditions.

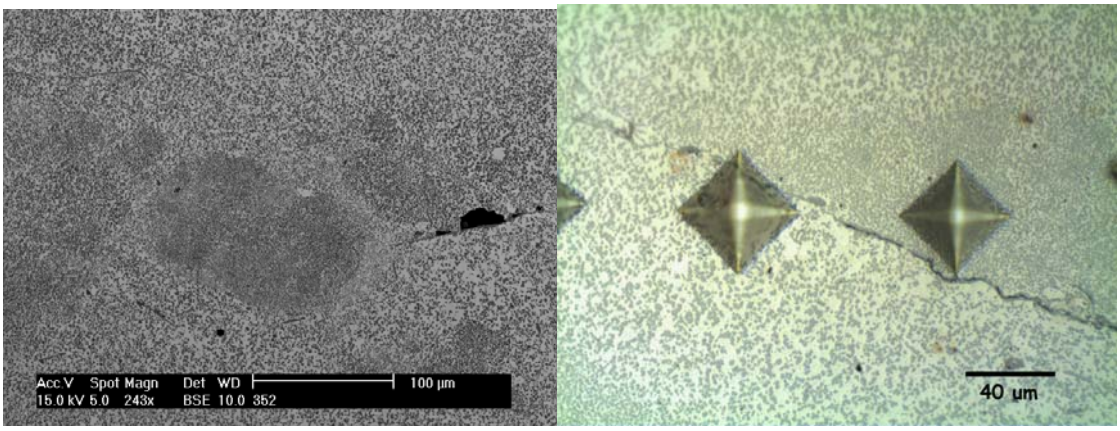

Figure 132. SEM and optical micrographs of the transverse cross-section (perpendicular to cladding direction) of SHS 1380 coating. Carbide chain/string is seen in optical micrograph. Vickers pyramid indentation at a load 10 N cracked it. Original powder was the blend of SHS 1377 and Ni. For the reason of incomplete melting of single SHS 1377 powder particles, there are regions with high (51 vol.%) and low carbide (37 vol.%) fractions.

3.4.6 Local differences in wear rates

In order to reveal the possible local differences in wear rates, 13 different types of already tested laser coatings consisting of 4 consecutive layers were submitted to diamond wheel grinding, where they were levelled until the wear scar or no as-laser-clad surface remained. Due to low peak-to-valley distances in vertical direction originated from the overlapping and low volume losses occurred during testing, layer thicknesses need to be removed were so low that the flat ground surface intersected the outermost clad layer. After the abrasion wear tests, surface line profiles were measured in direction perpendicular to cladding and wear direction using laser profiler. The length of the profile was 10 mm covering several reheated zones associated with overlapping. Some of the coatings were also cut transversely perpendicular to wear direction and cross-section samples were prepared. Abrasion wear test results of these diamond wheel ground surfaces are expressed as volume losses in Figure 134. Most of the

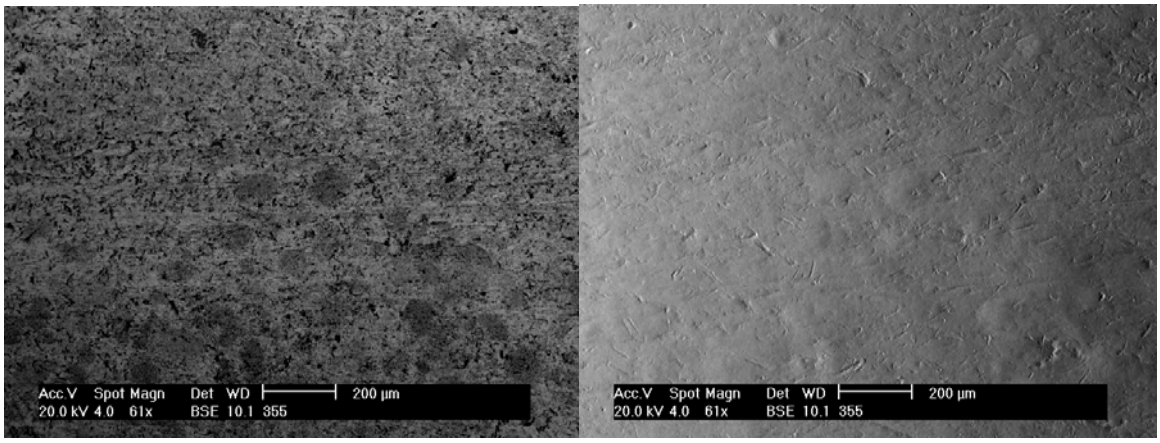

Figure 133. SEM micrographs taken from the wear scar of SHS 1389 coating. Rubber wheel rotation direction was from left to right. Incompletely melted or mixed single SHS 1378 particles are seen.

coatings exhibited lower volume losses when ground flat. WR6 and SHS 1378 laser coatings were tested twice. Abrasion wear resistance of the latter one approached to those of high volume fraction (~75 vol.%) WC-based cemented carbides. It is also notable that WR6 reinforced with externally added VCs outperformed substantially WR6 alone.

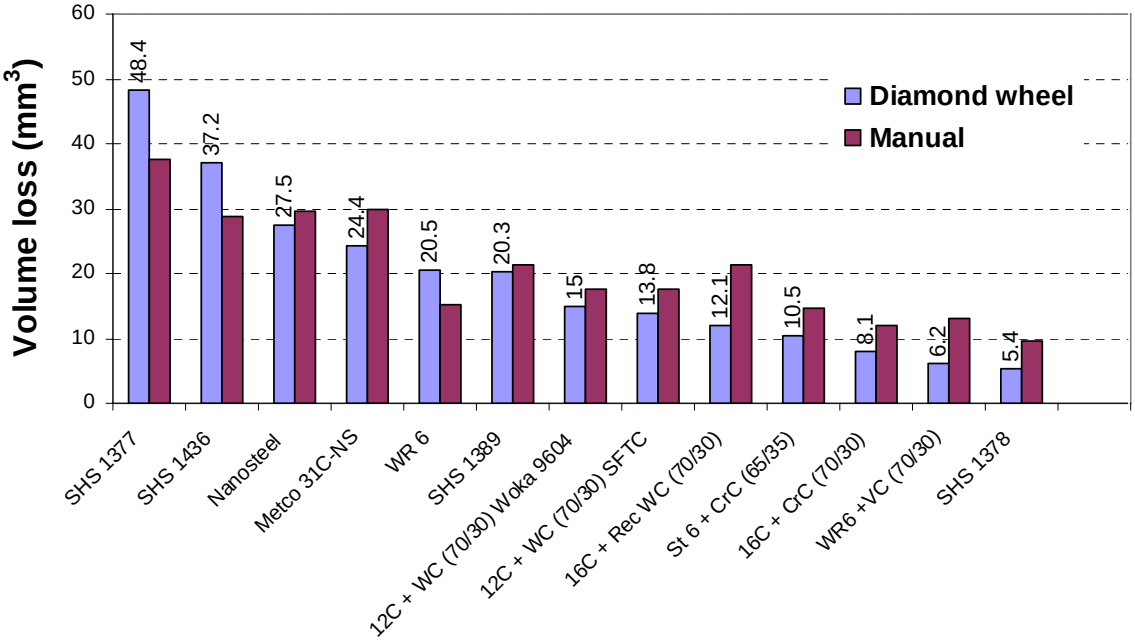

Figure 134. Rubber wheel abrasion wear results for diamond wheel ground laser coatings. Results for WR6 (COV 6.9%) and SHS 1378 (COV 23.6%) are the average of two measurements. All the other coatings were tested only once. Volume losses for (Ti, Mo)C SHS laser coatings are slightly overestimated because Mo in carbides was not taken into account.

3.4.6.1 (Ti, Mo)C coatings

Surface profiles were measured from the tested SHS 1377 ((Ti, Mo)C – Ni (50/50 wt.%)) and SHS 1389 ((Ti, Mo)C – St 6 (20/80 wt.%)) coatings. Both of these coatings were laser clad with inter-track advance of 1.4 mm. Surface profile measured from SHS 1377 revealed very smooth peaks and large peak-to-valley distances in vertical direction, which were approximately 250 μm. Regular distance between valleys was approximately 1.2 mm and between peaks approximately 1.3 mm. Surface profiles measured from SHS 1389 revealed distinctively sharper peaks than in SHS 1377. Peak-to-valley distances in vertical direction were approximately 45 μm. Regular distance between valleys was approximately 1.4 mm. These results suggest that overlapped areas (width of the valleys were narrower than widths of the peaks) exhibited higher wear rates than central parts of the beads.

3.4.6.2 Fe-based coatings

As explained earlier in section 3.4.4, WR6 laser coating consisted of harder reheated and softer non-reheated zones. Widths of the reheated zones were 0.7–0.8 mm, whereas widths of the non-reheated zones were 0.4–0.7 mm. According to surface profiles, valleys appeared at the regular interval of 1.4 mm, which was also the inter-track advance used in cladding. Widths of the peaks (reheated zones) were 0.7–0.8 mm. Widths of the valleys (non-reheated zones) were 0.4–0.6 mm. This indicates that reheated zones exhibited better wear resistance than non-reheated zones as could be expected on the basis of microhardness values. Peak-to-valley distances in vertical direction were very low; 14 μm.

Similar to WR6, Nanosteel laser coating generated regular wear pattern. This coating was laser clad with inter-track advance of 1 mm. Optical micrographs revealed that peaks appeared at the interval of 1 mm and they were located at the overlapped regions. This suggests that reheated zones were hardened. Horizontal hardness measurements confirmed the increased hardness in reheated zones. These reheated zones were approximately 0.3 mm in width and 910 HV_1 in hardness. Hardness of the non-reheated zone was 780 HV_1. Average hardness of the coating was 840 HV_1.

3.4.6.3 NiCrBSi + WC coatings

Surface profile studies were made for Metco 12C + Woka 9604 (70/30 vol.%), Metco 12C + WC SFTC (70/30 vol.%) and Metco 16C + recycled WC (70/30 vol.%) coatings. Inter-track advance in laser cladding was 1 mm for all the coatings. All the coatings except Metco 12C + WC SFTC (70/30 vol.%) generated regular wear pattern, which corresponded to the inter-track advance used. Representative example is shown in Figure 135, where regular wear pattern generated on the surface of Metco 12C + Woka 9604 (70/30 vol.%) coating. Valleys coincided well with overlapped regions, which suffered from lower primary carbide content similar to cases reported in Refs. [223, 225, 283, 392, 393]. Gassmann [225] suggested that Marangoni flow is not efficient enough to transport carbides to the remote edges of the bead, and thus homogenize the structure when high volume fraction of WCs is used. This together with excessive dissolution of carbide due to reheating could explain this. Such a low carbide content areas were not observed in Metco 12C + WC SFTC (70/30 vol.%) coating where the true carbide volume fraction was 24%.

3.4.6.4 CrC-based coatings

According to surface profile measured and cross-section prepared from Stellite 6 + CrC (65/35 vol.%) laser coating, distinct regular wear pattern generated. Valleys appeared at the distance of 1 mm, which corresponded to the inter-track advance used in cladding. It was already earlier mentioned in section 3.4.3 that coatings reinforced with CrC suffered from

excessive carbide dissolution in reheated zones. These valleys coincide well with the reheated zones.

Figure 135. Regular wear pattern on the surface of laser clad Metco 12C + WC Woka 9604 (70/30 vol.%). Distance between the valleys is 1 mm.

3.5 Sliding wear properties

Sliding wear properties of the selected alloys were evaluated by conducting low-stress block-on-ring tests in dry condition at RT as described in section 2.3.7. Low-stress originates from the rather low load of 57 N, which induced initial Hertzian stresses in the range of 80–110 MPa. The selected alloys consisted of Co-based laser and PTA overlay welded coatings, HIPped Co-based alloy, Fe-based Nanosteel and (Ti, Mo)C-based MMC laser coatings. Laser-hardened 42CrMo4 was used as reference material. The sliding wear resistances were measured by weighing the wear blocks during and after the 90 minutes testing time, whereas the rings were weighed just once when the test was completed. In the following, the results are, however, reported as the volume losses in cubic millimetres (mm^3) for both the block and the ring. Block scar volume was calculated from the block scar width after 90 minutes testing time according to formula expressed in standard ASTM G77 and ring scar volume was calculated from the mass loss of the ring. The reported values are the average of three measurements for the tests against 42CrMo4 ring (30 HRC). Tests against 34CrMo4 (60 HRC) were conducted only once. The calculated maximum and minimum COV in tests against 42CrMo4 ring were 15% for T-800 PTA and 2% for T-400 laser coating. For all the blocks the average COV was 7%.

The results of the test series against 42CrMo4 and 34CrMo4 rings are presented in Figures 136 and 137. Average microhardness values before the test and Fe contents, which reveal the magnitude of compositional dilution in coatings, are tabulated in Table 25. Generally, there is trend that the higher the initial microhardness of the test block, the lower the wear scar volume in the block but there are also few exceptions, which makes the ranking of materials on the basis of initial microhardness values unreasonable. Not surprisingly, MMCs, which contained fine (<3 μm) (Ti,Mo)C particulates, exhibited the lowest wear against both rings. At the same time, ring counterparts, however, subjected to severe wear. If to evaluate the results on the basis of total wear volume (both the block and the ring included) the group of alloys comprising intermetallic type Tribaloys, carbide type Stellite 1 and Fe-based Nanosteel showed the best behaviour. This kind of classification is relevant because adherence between these coatings and the counterparts were negligible. For instance, very low wear volume of the ring, which mated against laser-hardened 42CrMo4, resulted from the strong material transfer from the block to the ring. To continue classification, the tested materials can be roughly divided also to those, which exhibited severe, moderate or mild wear regimes in given conditions. Stellite 21, for instance, belongs to the first, Stellite 6 to the second and the rest to the third group. Block temperatures measured during the test, shown in Figures 138 and 139, supports this classification well together with the measured mass losses as a function of distance given in Figure 140. If different manufacturing methods are compared, laser

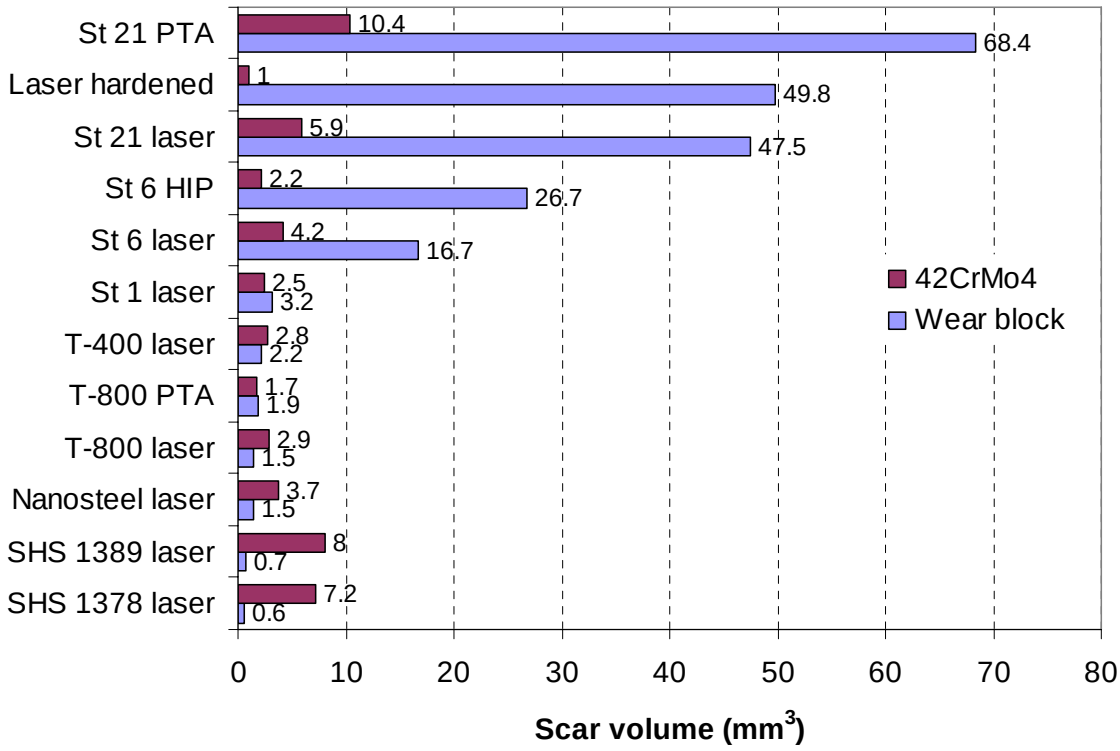

Figure 136. Sliding wear test results against 42CrMo4 ring (30 HRC). SHS 1389 is (Ti, Mo)C – Stellite 6 (20/80 wt.%). SHS 1378 is (Ti, Mo)C – Stellite 6 (50/50 wt.%).

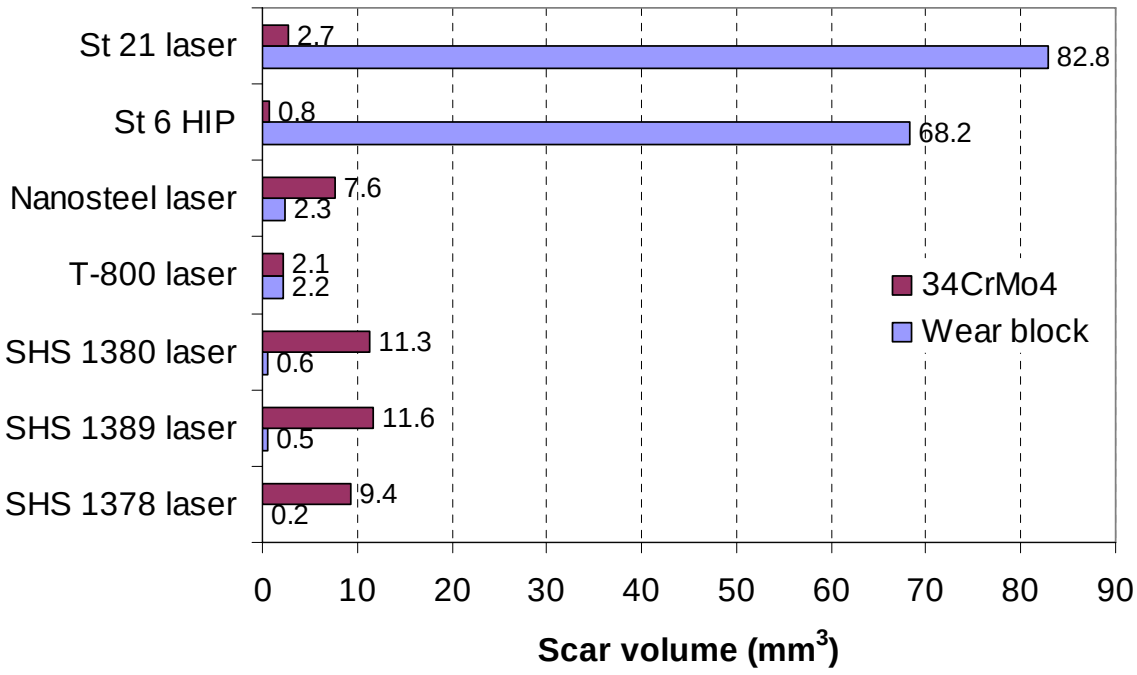

Figure 137. Sliding wear test results against 34CrMo4 ring (60 HRC). SHS 1380 is (Ti, Mo)C – Ni (35/65 wt.%).

Table 25. Average microhardness values before the test and Fe contents of the tested alloys. Dilution in multi-layer coatings was negligible.

Material	***HV_1***	***Fe (wt.%)***
Stellite 21 PTA	300	24.0
42CrMo4 laser-hardened	700	Bal.
Stellite 21 laser	400	1.3
Stellite 6 HIP	540	1.0
Stellite 6 laser (multi-layer)	530	1.6
Stellite 1 laser	780	1.3
Tribaloy T-400 laser	710	1.7
Tribaloy T-800 PTA	640	16.0
Tribaloy T-800 laser	800	0.4
Nanosteel laser	800	Multi-layer
SHS 1380	660	Multi-layer
SHS 1389	700	Multi-layer
SHS 1378	1100	Multi-layer

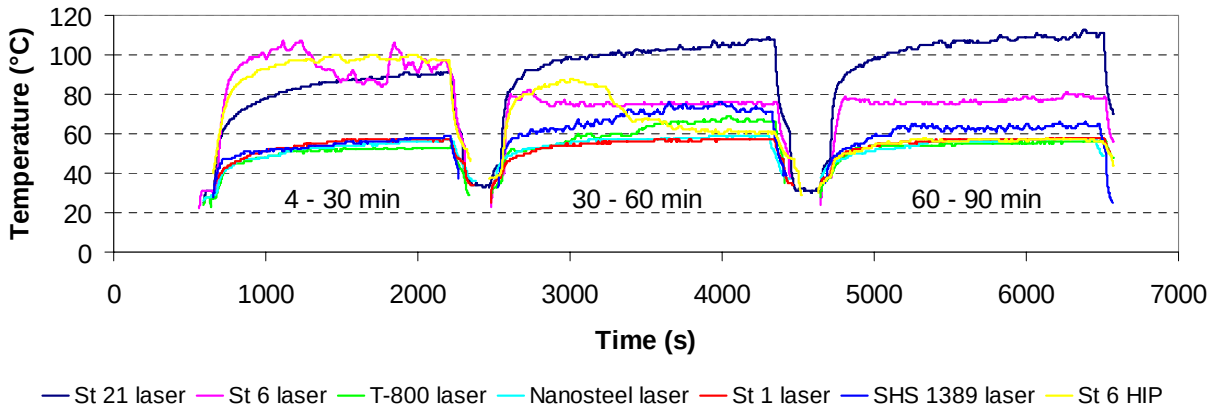

Figure 138. Block temperatures measured during the test (4–90 min) against 42CrMo4 (30 HRC) ring. SHS 1389 is (Ti, Mo)C – Stellite 6 (20/80 wt.%). Recording interval was 1 s.

outperformed PTA (Stellite 21 and T-800) and HIP (Stellite 6) clearly. Sliding wear resistance of laser coatings was 1.3–1.4 times better than PTA coatings and 1.6 times better than corresponding HIPped alloy under the wear test conditions used. All these aspects are discussed in greater detail in the following sections.

3.5.1 Stellite 21

The microstructure of low diluted solid solution strengthened Stellite 21 laser coating (1.3 wt.% Fe) consisted of fcc ordered directionally solidified dendritic γ-Co as revealed by metallographic and XRD studies. The secondary dendrite arm spacing was approximately 3 µm. The average hardness of the coating was approximately 400 HV_1 in as-laser-clad condition. According to microhardness measurements and XRD studies, work hardening or allotropic crystal structure transformation from γ-Co (fcc) to ε-Co (hcp) did not take place in surface to be tested during the preparation of the wear test blocks. In sliding wear tests against

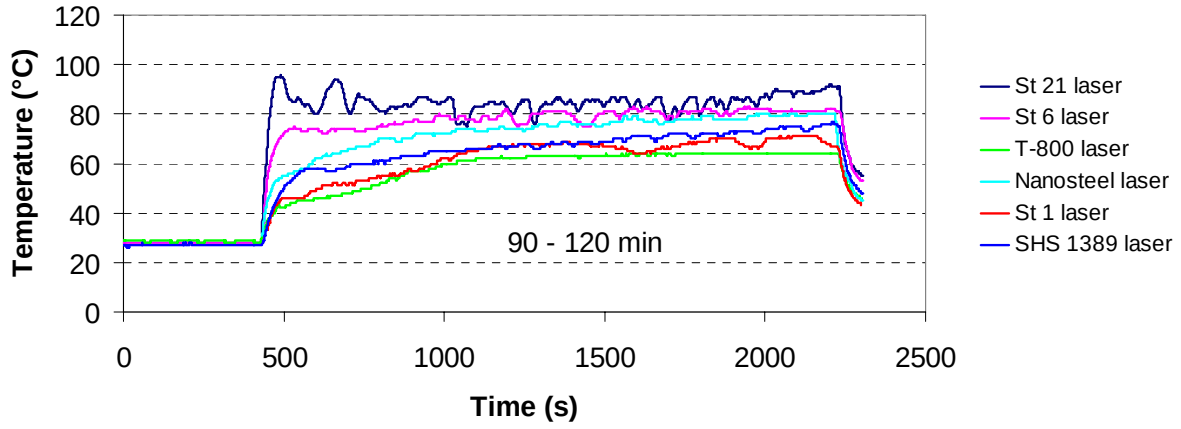

Figure 139. Block temperatures measured during the period of 90–120 min against 42CrMo4 (30 HRC) ring. Recording interval was 1 s.

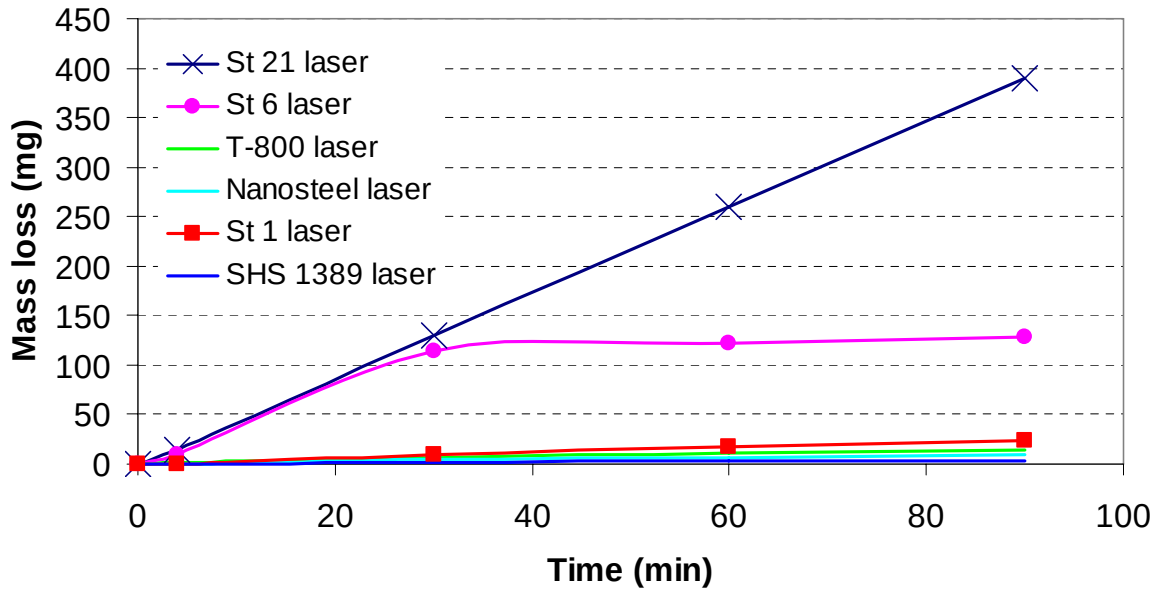

Figure 140. Mass losses of the blocks as a function of time (= sliding distance) against 42CrMo4 ring. Despite decreasing nominal contact pressure over the contact region during the test, Stellite 21 showed constant wear rate. Stellite 6 exhibited strongly decreasing and the rest slightly decreasing wear rates.

42CrMo4 (30 HRC), the average wear volume of 47.5 mm^3 was the third highest among the tested materials leaving only the laser hardened 42CrMo4 and heavily diluted PTA overlay welded Stellite 21 (24.0 wt.% Fe) behind. Despite decreasing nominal contact pressure over the contact region during the test, this coating exhibited the constant wear rate between 0–90 minutes as shown in Figure 140. During this time period, no visible oxide layer (by naked eye) formed either on the block or ring. Simultaneously, the temperatures measured from the block increased to the level of 110°C, which was the highest among the tested alloys. In additional test between 90-120 minutes, the oxide layer, however, formed. Simultaneously, wear mechanism changed from severe to mild due to decreased nominal contact pressure on

the surface and reduced plastic deformation, which allowed oxide layer to form [394]. For that reason, temperature remained rather low (80-90°C) during the period of 90–120 minutes as displayed in Figure 139. In other alloys this last period showed always higher temperatures compared with previous ones due to better weld joint between the thermocouple and the block. Block temperature, however, fluctuated strongly as a function of time during that last period. This indicated occasional peeling off and reformation of oxide films.

Transverse cross-section prepared from the 90 min tested coating revealed slight subsurface deformation as illustrated in Figure 141. That is, the grains at the very top of the tested surface aligned towards the sliding direction of the ring. It was also noted that the microhardness of the coating increased from initial 400 to 460–480 HV_1. This work-hardened zone reached the depth of 0.3 mm. At the depth of 40 µm, microhardness was as high as 510-560 $HV_{0.3}$. Nevertheless, XRD measurements conducted on the tested surface did not reveal, at least severe allotropic fcc -> hcp transformation. There is, however, some uncertainty because diffraction peak of hcp ordered Co (0002) overlaps with the fcc Co peak (111) since their 2θ values are 44.8° and 44.2°, respectively. The highest peak of randomly oriented hcp ordered Co should have arisen at 2θ = 47.6°. This peak was absent for sure. Large scale fcc -> hcp transformation may have, however, occurred in the beginning of the test where the initial Hertzian stress was at maximum. Due to progressive wear, allotropically transformed alloy may have worn away and was not clearly revealed by XRD. In fact, this could also explain the constant wear rates throughout the test assuming that fully hcp ordered Co possess better sliding wear resistance.

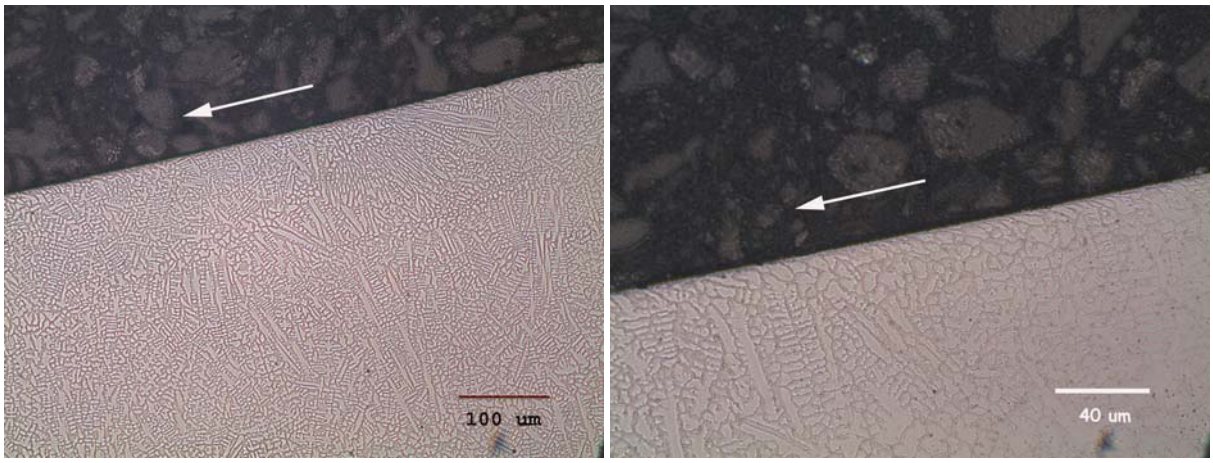

Figure 141. Optical micrographs showing slight subsurface deformation in etched Stellite 21 laser coating after severe dry sliding wear against 42CrMo4 steel. Transversal cross-section is parallel to cladding direction. White arrow indicates the sliding direction. Work-hardened zone reached the depth of 0.3 mm. Within that zone microhardness was 460–480 HV_1.

The SEM examination of the worn surfaces (90 minutes test) showed that significant transfer of material and cold welding or galling took place when Stellite 21 laser coating slid against 42CrMo4 steel. Several patches and stripes of material, which contained Fe up to 20 wt.%, were discovered on the surface of coating. One typical example is shown in Figure 142a. The surface was also plastically deformed. Oxygen was detected, but it was obvious that continuous and thick oxide layer was absent. The worn ring surface shown in Figure 142b contained adhered coating alloy, which was partly fractured and worn away together with ring material. This fractured wear debris may have promoted some abrasive wear even if deep

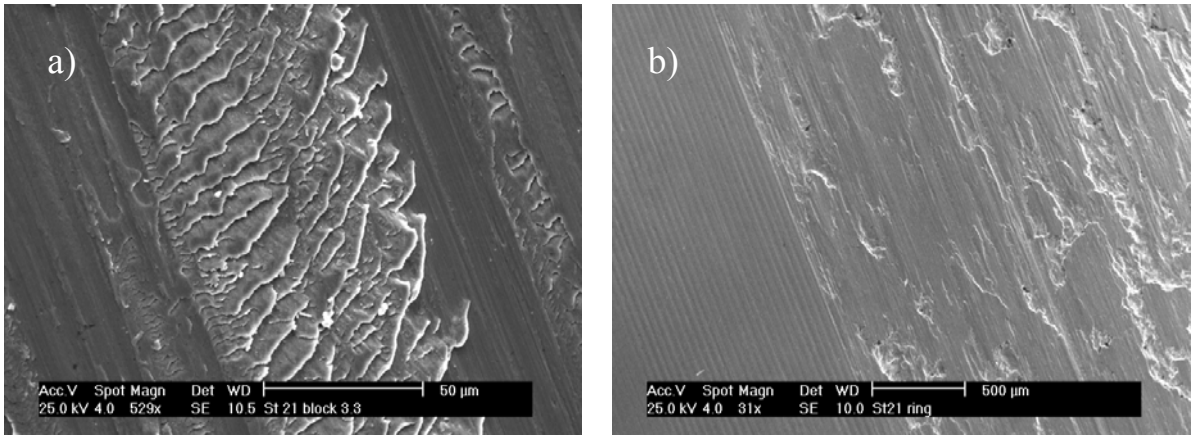

Figure 142. SEM micrographs of the sliding wear tested surfaces of a) Stellite 21 laser coating and its b) 42CrMo4 ring counterpart.

grooves were missing. The amount of oxygen detected on the ring surface was noticeably smaller than, for instance, on the surface of ring against T-800 as will be described later.

Large amount of metallic wear debris was collected under the ring, which slid against the Stellite 21 laser coating. They consisted exclusively of thick Fe-based metallic platelets varying 20–200 µm in length as presented in Figure 143. Their surface was covered with plastically deformed Co-based "tongues" indicating strong galling before detachment. Basically, the platelet detaches from the ring when the adhesive forces at the junctions between the block and the ring are stronger than the cohesive strength of the ring alloy. However, according to delamination theory there is also fatigue cycling involved in the formation of such plate-like wear particles, which are typical in severe wear regime [394, 395]. Rotating ring inevitably underwent such fatigue cycling.

Compared with more heavily diluted and considerably softer PTA overlay welded Stellite 21, laser coating exhibited 1.4 times better sliding wear resistance. Besides lower microhardness, this could be attributed to the weaker ability to work-harden since Fe is known to increase the

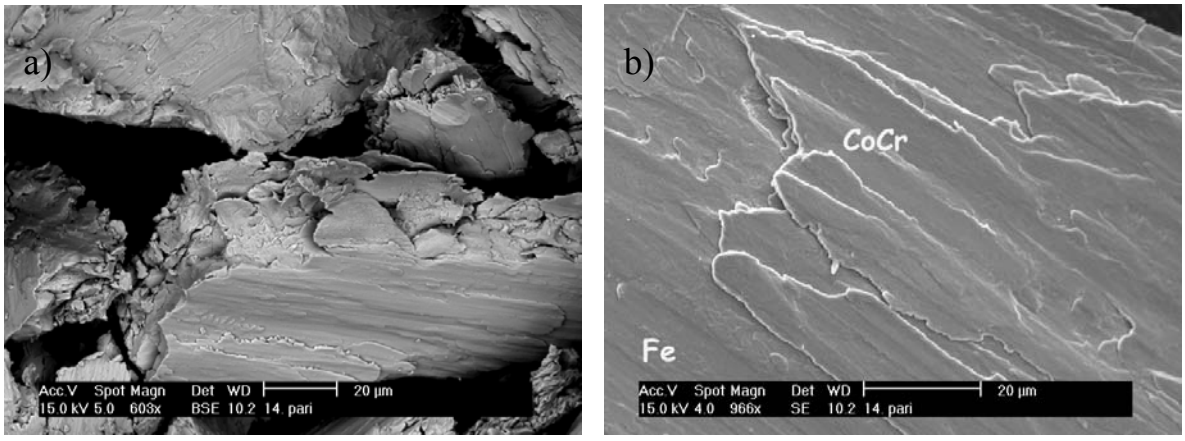

Figure 143. Wear debris of Stellite 21 laser coating against 42CrMo4 (load, 57 N; sliding velocity, 140 m/min); a) thick platelets and b) detail of plastically deformed Co-based "tongues" on the surface of Fe-based platelet.

stacking fault energy and to stabilize the fcc ordered structure. According to microhardness measurements, work-hardened zone exhibited, however, the hardness of ~390 $HV_{0.3}$. Hardness increase from 300 to 390 $HV_{0.3}$ was at same level as that measured from the less diluted laser coating (from 400 to 510-560 $HV_{0.3}$). Yet, it should be kept in mind that nominal contact pressure was somewhat lower at the end of the test due to higher wear volume compared with corresponding laser coating. On the basis of this, its ability to work-harden was not diminished. Analogous with laser coating, PTA overlay welded one exhibited constant wear rate throughout the test and oxide layer did not form at any stage. Wear block temperature was not monitored.

3.5.2 Stellite 6

Low diluted carbide type Stellite 6 laser coating (1.6 wt.% Fe), which consisted of interconnected network of interdendritic carbides and fcc ordered γ-Co dendrites as illustrated in Figure 144a, showed substantially better sliding wear resistance than Stellite 21. Obviously, this was attributed to higher hardness (400 vs. 530 HV_1) resulting from the carbides, which volume fraction was in the range of 34–40% according to image analysis carried out on the etched surface. These values are, however, overestimated since interdendritic regions included also some γ-Co and γ-Co dendrites were dissolved more severely. According to literature concerning Stellite 6 laser coatings [396], these carbides were the type M_7C_3 (M = Co, Cr, W). Frenk et al. [396] reported that their weight fraction is typically around 10% in laser coatings. According to Atamert and Bhadeshia [332], volume fraction of carbides in Stellite 6 is typically 20-30%. Other phases found from the carbide type Stellite laser coatings include $M_{23}C_6$ carbide and intermetallic Co_3W [185]. Existence of M_7C_3 could not be confirmed by XRD since the peaks identified with certainty belonged to strongly textured fcc ordered γ-Co as shown in Figure 145. The highest peak of Cr_7C_3 (as well as $Cr_{23}C_6$) overlaps with the fcc ordered γ-Co (111) at ~2θ = 44°. Intermetallic Co_3W was absent or under the detection limit of XRD. The secondary dendrite arm spacing in this coating was approximately 2 μm and W was predominantly bound to carbides as suggested by EDS point analyses (15 kV). C_{ID}/C_D for W and Cr was 2.0 and 1.7, respectively. In sliding wear tests, wear rates decreased strongly when the nominal contact pressure over the contact region decreased during the test. This can be attributed to the formation of thick and low friction oxide layer, which restricted partly the contact between mating metal surfaces. According to temperatures measured from the block, oxide layer formed in the beginning of the test period 30–60 min as shown in Figure 138. Visual inspection of the surfaces made after 60 minutes supported this interpretation. Signs of oxide layers were also observed already after 30 minutes testing time but significant and continuous oxide layer formation was absent. Temperature measurements during the period of 4–30 min verified that there were alterations in friction, which suggests the formation and peeling off of the oxide layer. Analogous with Stellite 21 laser coating, work-hardened zone was developed under the wear scar. Microhardness values measured from the work-hardened zone were in the range of 610-670 $HV_{0.3}$. Frictional heat was notably higher in the beginning of the test compared with Stellite 21 laser coating. This may have originated from the possible fcc -> hcp transformation in Stellite 21 laser coating since it is more probable for Stellite 21 than Stellite 6 as elements like Cr and W, which decrease the stacking fault energy are strongly bound with carbides in Stellite 6 laser coating.

Despite similar or even slightly higher hardness (530 vs. 540 HV_1), HIPped Stellite 6 alloy exhibited sliding wear resistance inferior to Stellite 6 laser coating. This can be attributed to the differences in microstructure. As the laser coating consisted of network of interconnected carbides in fcc ordered γ-Co, HIPped alloy contained tiny (1–2 μm) discrete carbides irregular

or spherical in shape as illustrated in Figure 144b. According to XRD shown in Figure 145, these carbides could be the type M_3C_2, $M_{23}C_6$, M_7C_3 and Co_6W_6C. Intermetallics, Co_3W or Co_7W_6, were not revealed by XRD. Other distinctive difference compared with laser coating, was the high amount of hcp ordered ε-Co in the matrix, which indicates slower cooling rates. Volume fraction of carbides was in the range of 30–36%, which is in good agreement with Stellite 6 laser coating. Tungsten was, however, less bound to carbides than in laser coating since $C_{carbide}/C_{matrix}$ for W in HIPped alloy was 0.7, whereas for laser coating it was 2.0 (C_{ID}/C_D). Similar trend for W was obtained by Frenk et al. [81, 396], who reported on W contents of 5 wt.% in M_7C_3 and 4.4 wt.% in Co matrix of Stellite 6 laser coating. As the partition coefficient of W in Co-Cr-W-C system is 0.775 at 1660K [396], it segregates strongly into the liquid (= interdendritic regions) during solidification like in laser cladding. Such solidification segregation did not occur in HIPping, which did not experienced melting and liquid state. Due to lack of segregation the magnitude of solid solution strengthening was probably higher in HIPped than in laser clad alloy. As the W should decrease the stacking fault energy and promote the allotropic fcc –> hcp transformation, stronger work hardening could have been expected. On the other hand, Cr content in the matrix was lower than in laser coating (Cr decreases stacking fault energy as well). Anyway, hardness values in work-hardened zone (520-560 $HV_{0.3}$) were distinctively lower than in corresponding laser coating (610-670 $HV_{0.3}$). This can be related, at least partly, to the nominal contact stresses since the cross-sections were prepared from the samples, which were tested 90 minutes. HIPped alloy wore more severely during this time, so the nominal contact pressure, which influenced under the wear scar was lower in the case of HIPped alloy compared with laser coating. Similar to laser coating, wear rates decreased strongly during the test. This decrease in wear rate (= change in wear regime) and accompanied oxide formation just occurred later, i.e. under lower stresses, compared with laser coating. During the period of 4–30 min of the test, temperature of the HIPped block was approximately 100°C without fluctuations. Temperature dropped significantly not until midway through the period of 30–60 min as displayed in Figure 138. This indicates that the network of hard interdendritic carbides characteristics for laser coating provided more rigid structure to support oxide layers and to resist plastic deformation caused by higher contact stresses.

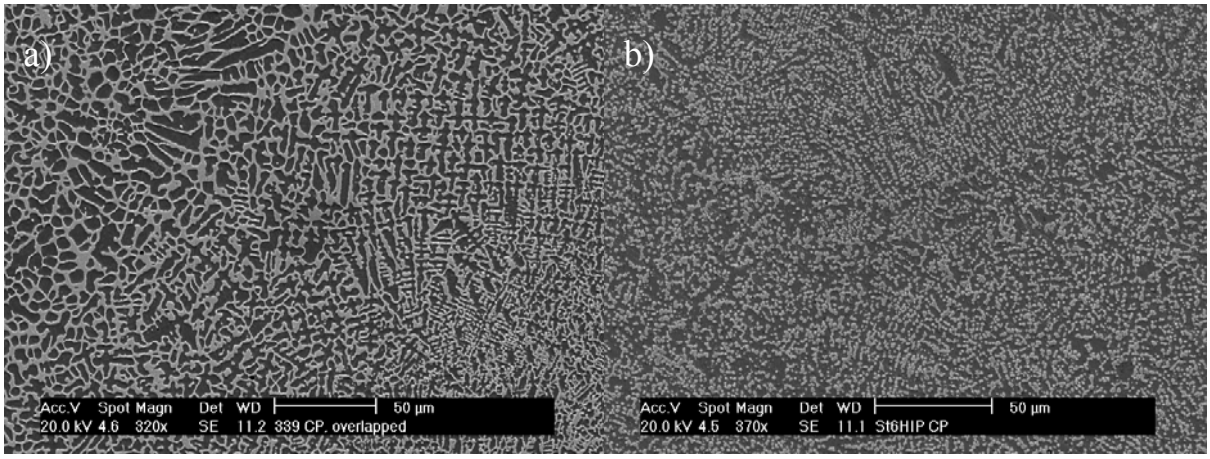

Figure 144. SEM micrographs taken from the longitudinal cross-sections (plane parallel to coating/base material interface) of a) laser clad and b) HIPped Stellite 6 alloys.

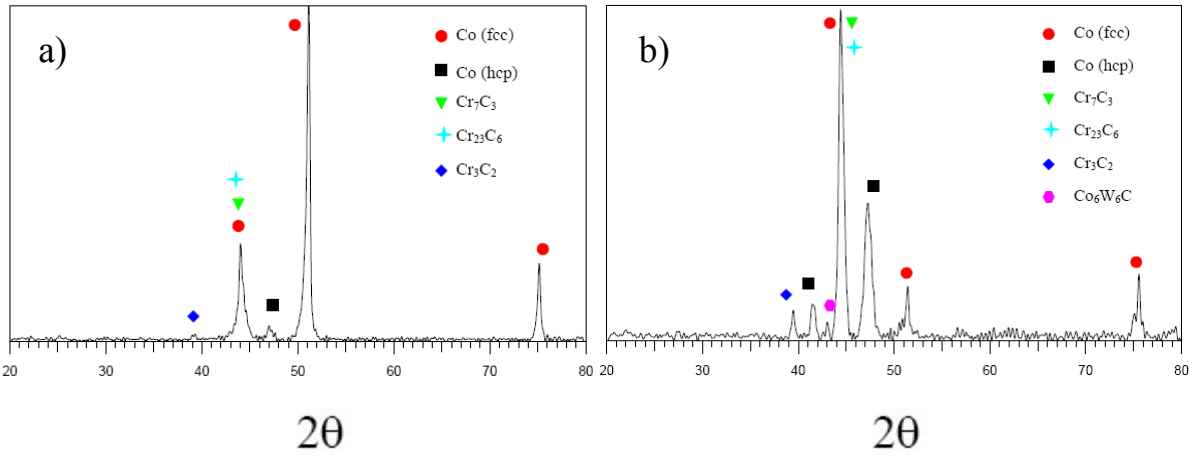

Figure 145. XRD patterns measured from the manually ground a) laser clad and b) HIPped Stellite 6 alloys.

3.5.3 Tribaloy T-800

This pore and crack-free hypereutectic intermetallic type laser coating consisted of light and dark regions as illustrated in BSE images taken from the transverse cross-section (perpendicular to cladding direction) in Figure 146. Light regions, which were rich in Mo and Si compared to the dark matrix, were identified as hcp ordered Co_3Mo_2Si and/or CoMoSi Laves phases, which are the type $MgZn_2$ (C14 or hP12) [397]. In the central regions of the beads, these intermetallics were nearly spherical approximately just 5 µm or less in diameter. In overlapped regions, they were feather-like and distinctively coarser than spherical colonies in central regions as seen in Figure 147. For the sake of comparison, mean sizes of primary Laves phases in as-cast Tribaloys were reported to be 17-25 µm and with higher solidification rates in casting 9 µm [398]. Despite this difference in microstructure, laser coating exhibited uniform microhardness in both directions; parallel and perpendicular to coating/base material interface. According to elemental maps taken from the transverse cross-sections, Cr and intermixed Fe from the base material were mainly found in the dark matrix, which consisted of fcc ordered Co-based solid solution and Laves phases particularly in overlapped regions. According to Halstead and Rawlings [397] and Gnanamuthu [398], Cr is typically partitioned about one-third in the Laves phase and two-thirds in the solid solution. XRD patterns showed that the highest peak intensity in laser coating was measured from the Laves phases, whereas the Co-based matrix gave the highest peak intensity in T-800 powder. Halstead and Rawlings [397] reported that the faster the solidification in casting, the higher the volume fraction of primary Laves phases. According to image analysis the amount of Laves phases in laser coating was around 54–57 vol.%, which is in good agreement with the results concerning as-cast T-800 reported in Refs. [397, 399].

In sliding wear tests, intermetallic type hardfacing alloys including T-800 responded differently to dry sliding conditions than solid solution strengthened Stellite 21 and carbide type Stellite 6 discussed earlier. Due to rapid formation and rather tightly bonded oxide layers between mating surfaces and particularly on top of coating, low diluted T-800 laser coating exhibited one of the lowest wear volumes among the studied monolithic alloys and one of the lowest frictional heats. These oxide layers, which formed already during the first 4 minutes of the test, on the top of T-800 laser coating are illustrated in Figure 148. As can be seen in Figure 148a, there are, however, some signs of oxide layer spalling. According to EDS

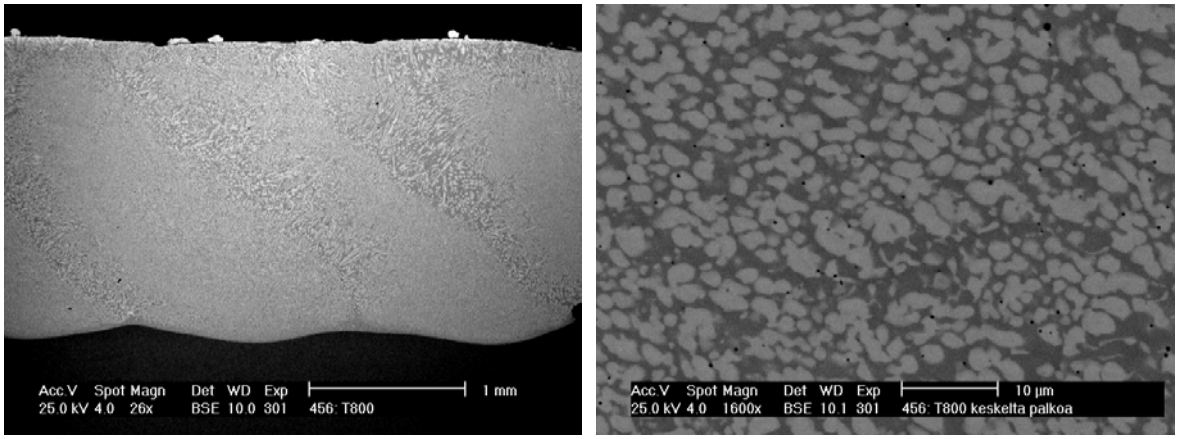

Figure 146. BSE images of transverse cross-section (perpendicular to cladding direction) of T-800 laser coating. Higher magnification is taken from the central region of the bead.

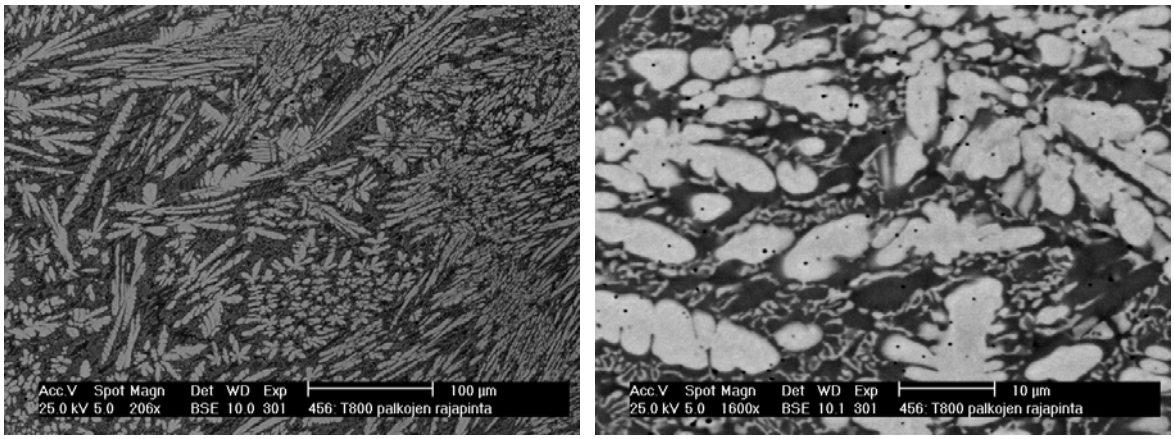

Figure 147. Low and high magnification BSE images of overlapped zones in T-800 laser coating.

analyses, these oxides contained elements of Fe, Co, Mo, Cr and Si. The regions between the oxide layers consisted of elements of T-800 with traces of O, but not adhered Fe from the ring. Some occasional iron splats were, however, detected as one shown in Figure 149, but this was very rare. Oxide layers were also observed on the top of the worn ring surface, which was relatively smooth. EDS analyses taken from the worn ring showed Fe and O and traces of Mo and Cr. Co was not detected from the ring surface. This surface examination proved that the oxide layers separated the sliding surfaces and only occasional direct metallic contact took place.

The amount of wear debris collected under the ring, which slid against T-800 laser coating, was very small. This is consistent with the wear volume results. Wear debris consisted predominantly of finely divided dust-like oxides including elements of Fe (52 wt.%) and smaller amounts of O (16%), Co (16%), Mo (9%), Cr (5%) and Si (1%). This elemental analysis indicated that it originated mainly from the ring, which is in accordance with the volume loss results obtained for T-800 and T-400 laser coatings. Large metallic particles were not detected. This kind of fine wear debris is typical for mild wear regime.

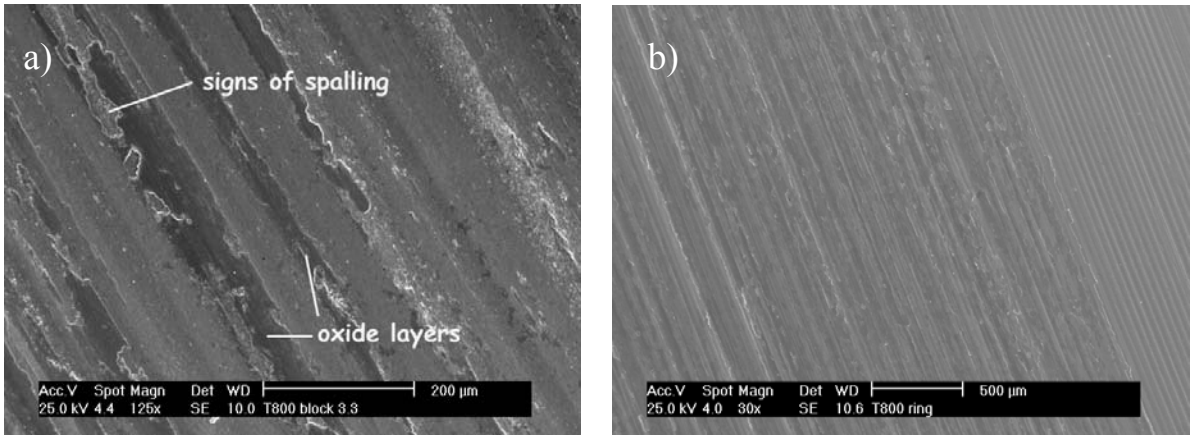

Figure 148. SEM micrographs of the tested surfaces of a) T-800 laser coating and b) 42CrMo4 ring counterpart.

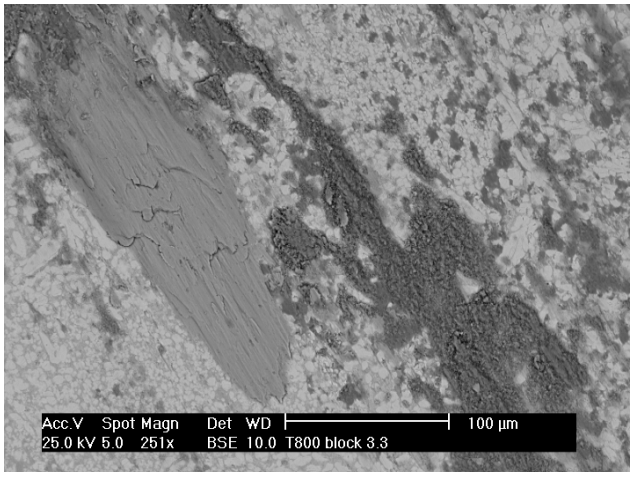

Figure 149. BSE image of the tested surface of T-800 laser coating. The lightest regions are Laves phases, plastically deformed gray splat is adhered Fe from the ring and the darkest regions are oxide layers.

More heavily diluted (0.4 vs. 16.0 wt.% Fe) PTA overlay welded T-800 coating exhibited 1.3 times higher volume loss than corresponding laser coating. Figure 150 shows the microstructure of the PTA overlay welded coating. Owing to higher heat input and slower solidification and cooling rates, the resulting microstructure of the weld overlay was much coarser than that of laser coating. The hardness values of PTA welded deposit (800 vs. 640 HV_1) were generally lower than those of laser coating owing to higher dilution (16 wt.% Fe). According to image analysis, the amount of Laves phases in PTA coating was around 57–64 vol.%, which was slightly higher than that in laser coating. XRD patterns of PTA and laser coatings are shown in Figure 151. They suggest that PTA coating contains less Laves phases than laser coating. Due to higher dilution the amount of Laves phases in PTA coating could be expected to be lower. As XRD pattern was taken from the larger surface area than image analysis, its results are considered more reliable.

Wear debris collected under the ring, which slid against T-800 PTA was similar to wear debris of laser coating except for few large fractured metallic platelets 80-350 µm in length and 50-160 µm in width shown in Figure 152a. EDS analysis taken from the platelet showed mainly Fe (42 wt.%) and smaller amounts of O (19%), Mo (15%), Co (12%), Cr (11%) and Si

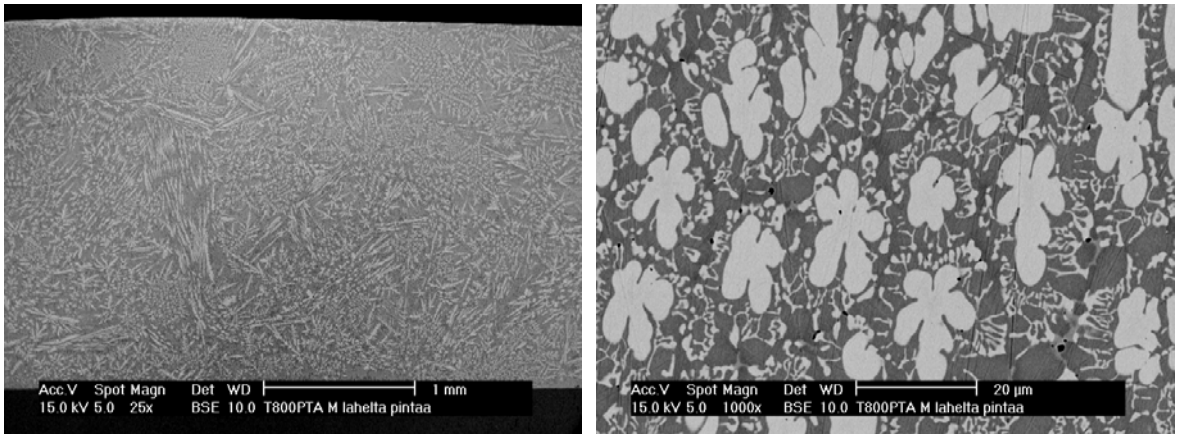

Figure 150. BSE images of transverse cross-section (parallel to oscillation direction) of T-800 PTA coating.

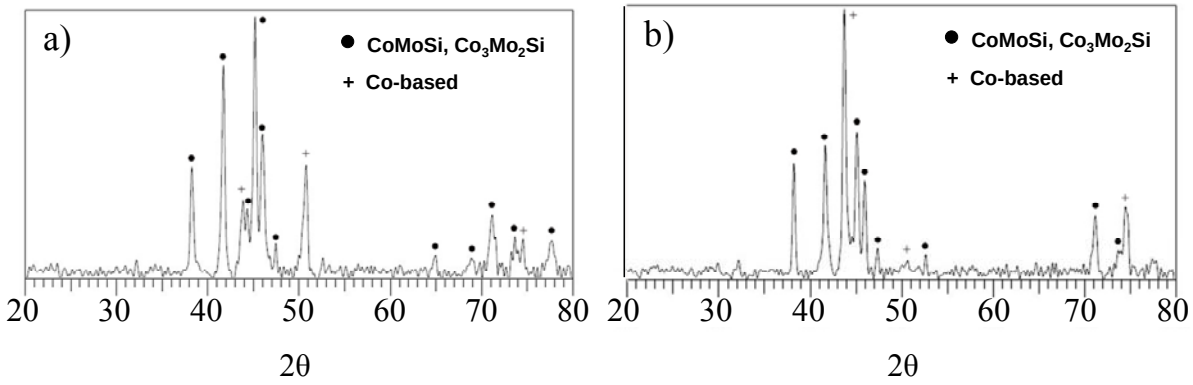

Figure 151. XRD patterns measured from T-800 a) laser and b) PTA coatings.

(2%). These platelets were obviously detached from the ring. On the basis of elemental mapping, light areas in Figure 152b were oxygen-free and rich in cobalt. Other areas were covered with oxides of Co, Mo, Fe and Si. This indicates that unlike in T-800 laser coating there was some Co transfer from the matrix of PTA coating to the ring.

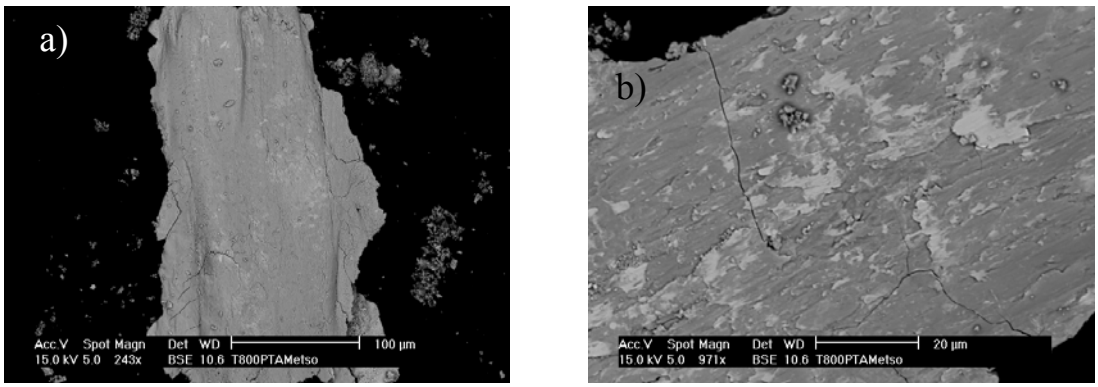

Figure 152. Wear debris of T-800 PTA coating against 42CrMo4 ring (load 57 N; sliding velocity, 140 m/min); a) large platelet and dust-like debris; b) detail of plastically deformed platelet surface, light regions are oxygen free and rich in Co.

3.6 Residual stresses

Residual stress measurements were conducted on Tribaloy T-800 and Stellite 21 laser coatings on different base materials. T-800 was laser clad on mild steel, martensitic and austenitic stainless steels 20 mm in thickness using preheat of ~500°C. Stellite 21 was laser clad on martensitic and austenitic stainless steels without preheat. To get the residual stress profiles by XRD method, material was removed by electrolytic polishing layer by layer until the base material was met and further. To verify the results obtained with XRD, hole-drilling method was applied on T-800 coating on martensitic and Stellite 21 on martensitic and austenitic stainless steels.

3.6.1 Tribaloy T-800 and Stellite 21

Residual stress profiles measured from T-800 on mild steel by XRD method using Laves phase peaks are illustrated in Figure 153. Owing to the manual surface grinding (~0.2 mm was removed from the as-laser-clad surface before measurement), large compressive residual stresses generated to a depth of 0.1 mm on the surface. Otherwise, the coating was slightly in tension (<+100 MPa). For instance, at the depth of 0.4 mm, average longitudinal residual stress of 5 measurements was +74 MPa (STDEV 31 MPa). The magnitude of tensile stress was not dependent on measuring direction in relation to cladding direction.

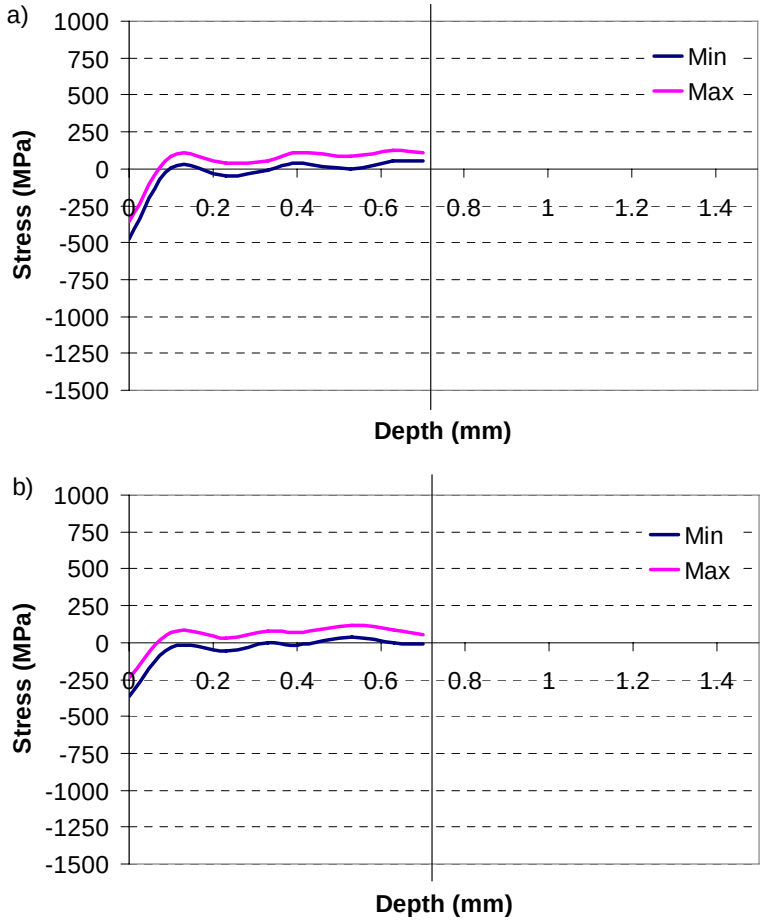

Figure 153. Residual stress profiles along a) longitudinal and b) transverse directions in relation to cladding direction measured from T-800 laser coating on mild steel. Measurements were conducted with XRD method. The layer thickness removed by electrolytic polishing varied from 70 to 130 µm. Average removed thickness was 100 µm.

Similar to T-800 on mild steel, T-800 on martensitic SS was in tension except for the surface where the large compressive residual stresses (0.4 mm ground away) existed as shown in Figure 154. The magnitude of tensile stress is noticeably higher than in coating on mild steel. It is also noteworthy to point out that hardened HAZ beneath the coating was in compression. Base material hardness before cladding was ~340 HV_1 and after ~750 HV_1 in HAZ. Volumetric expansion associated with hardening of HAZ may have increased the tensile stress in coating compared with coating on mild steel. There is also larger difference in CTEs between coating and base material in this case compared with mild steel. Error of measurement is clearly larger (larger difference between minimum and maximum values) compared with T-800 on mild steel. This can be attributed to the quality of etched/polished surface. Overlapped areas were more heavily etched in this case, which caused uneven surface. This can be, in turn, attributed perhaps to the more unevenly distributed Fe. The average Fe content of the coating on martensitic SS was 1.7% wt.%. Fe content was not measured from the coating on mild steel but microhardness values suggest that coating on mild steel was more heavily diluted since its average hardness was 680 HV_1 compared with 820 HV_1 in coating on martensitic SS. Low error of measurement obtained from the base material verifies this influence of surface condition on error since the etched base material surface was very smooth.

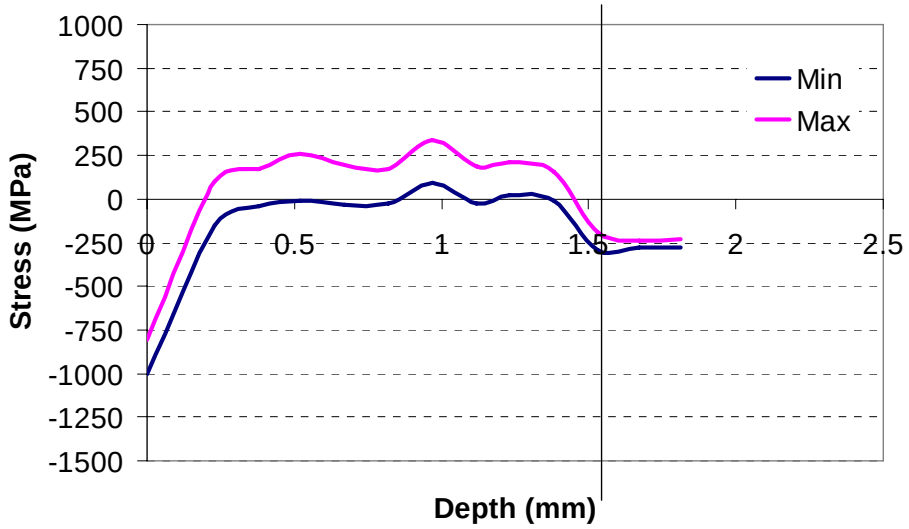

Figure 154. Residual stress profile along longitudinal direction measured from T-800 laser coating on martensitic stainless steel. Measurements were conducted with XRD method. The layer thickness removed by electrolytic polishing varied from 110 to 230 µm. Average removed thickness was 150 µm.

Residual stress profiles of T-800 on martensitic SS obtained via hole-drilling method showed also compressive stresses on the ground surface and tensile stresses deeper in the coating (Figure 155). Magnitude of tensile stresses is in accordance with the results obtained by XRD method. High tensile peaks under compressive surface result from counterbalancing stresses. This zone was probably etched away in XRD measurements and not shown in profiles (Figures 153 and 154) due to larger steps between measurements (~100-150 µm vs. ~20-50 µm). Rotational angles (α_r) between maximum principal stresses and stresses along cladding (longitudinal) direction varied from 20 to 30° depending on the depth.

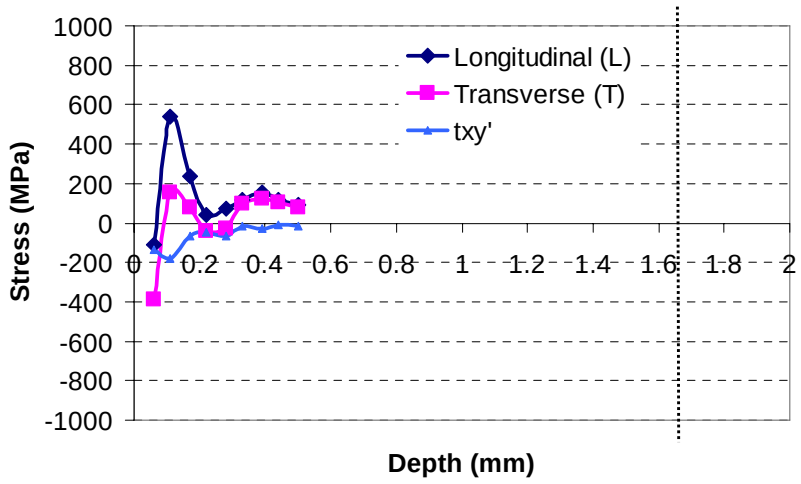

Figure 155. Residual stress profiles measured from T-800 laser coating on martensitic SS. Measurements were conducted using hole-drilling method.

Contrary to previous results, T-800 on austenitic SS was predominantly in compression as shown in Figure 156, whereas the base material beneath the coating was in tension. This can be attributed to the difference in CTEs between coating and base material. During cooling the base material with higher CTE underwent larger shrinking than coating causing compressive stress in it.

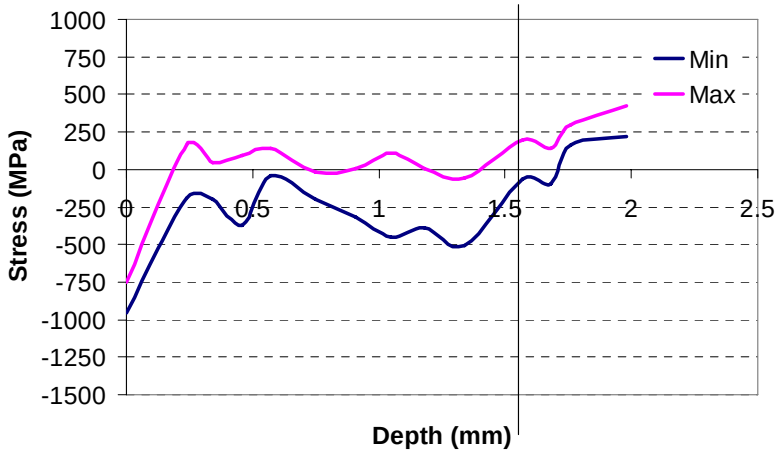

Figure 156. Residual stress profile along transverse direction measured from T-800 laser coating on austenitic SS. Measurements were conducted with XRD method. The layer thickness removed by electrolytic polishing varied from 80 to 240 µm. Average removed thickness was 150 µm.

For the sake of comparison average strain values (average of three measuring grids) obtained during hole-drilling for T-800 and Stellite 21 laser coatings are illustrated in Figure 157. They confirm the influence of CTE difference between coating and base material. Stress values calculated with Kockelmann method for the hole-drilled Stellite 21 gave values of 200-800 and 400-900 MPa on austenitic and martensitic base materials, respectively. Values are unrealistically high since yield strength of Stellite 21 is 517 MPa [400]. Calculation method

used is known to give too high values if stresses are higher than 60% of the yield strength. According to XRD method, residual stresses on the surface of as-laser-clad Stellite 21 on martensitic and on austenitic stainless steels were ~ +500 MPa and ~ +100 MPa, respectively. These values are in good agreement with values found from the literature and reported earlier in section 1.5.5. Average Fe content in Stellite 21 on martensitic SS was 1.2 wt.% and on austenitic SS 1.9 wt.%.

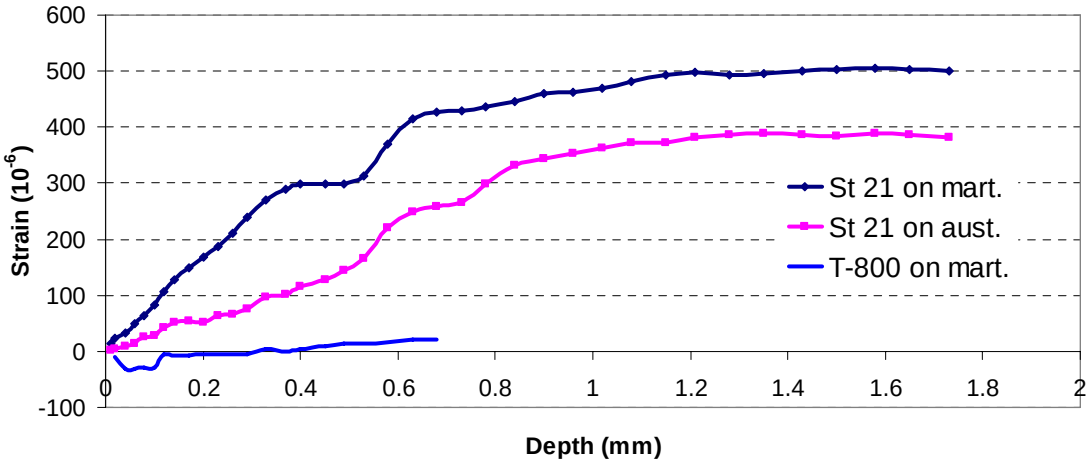

Figure 157. Average strain values recorded during hole-drilling process for different coating/base material pairs.

3.7 Thermal fatigue properties

To study the influence of possible CTE mismatch between coating and base materials as well as ductility of the coating, a series of low-cycle thermal fatigue tests were conducted on different coating/base material pairs. These pairs included Inconel 625, SX-717 and T-800 on mild steel and T-800 on austenitic SS. Thickness of the base material was 20 mm in each case. All the coatings were in as-laser-clad condition.

3.7.1 Inconel 625

Initially defect-free, i.e. no interface defects except one oxidized semi-molten powder particle, low diluted (Fe content 1–2 wt.%) Inconel 625 laser coating on mild steel survived at least 50 cycles without cracking. Thermal cycles this coating encountered are illustrated in Figure 158. After 50 cycles the test was stopped.

3.7.2 SX-717

Two Cr-based SX-717 laser coatings on mild steel with different magnitudes of dilution were tested. Coating, which Fe content was 6–7 wt.% survived at least 32 cycles similar to those shown in Figure 158. After 32 cycles the test was stopped. Coating with lower amount of Fe (1–2 wt.%) survived at least 50 cycles. After 50 cycles the test was stopped. Both of these coatings were initially defect-free except several micropores in interdendritic regions as was shown in Figure 78b in section 3.3.1.2. Nominal CTE for this alloy was 11.7 x 10^{-6} K^{-1} (at 100°C), which does not deviate much from CTE of mild steel. It was also important to note that micropores in interdendritic regions did not act as stress raisers and initiate cracks as reported in Ref. [311].

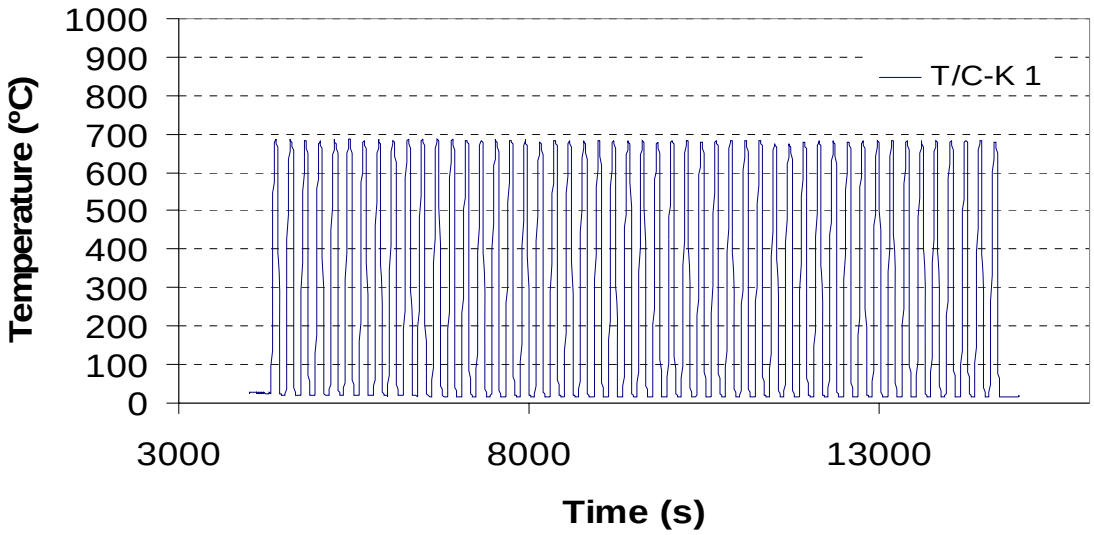

Figure 158. Thermal cycles encountered by Inconel 625 laser coating on mild steel. Average peak temperature was 685ºC. Heating period from 18ºC to peak temperature lasted approximately 70 s. Cooling period from the peak temperature back to 18ºC lasted approximately 60 s.

3.7.3 Tribaloy T-800

Initially defect-free T-800 laser coatings were tested on mild steel and austenitic SS. Coating on mild steel was more heavily diluted (28–29 Fe wt.%) than coating on austenitic SS (3–4 wt.% Fe). Despite high dilution and low mismatch in CTEs (T-800: 12.6 (20-500°C) vs. Fe52: 12.7 (20-500°C)), T-800 on mild steel survived only 1 cycle but cracked severely during the next 5 cycles. Similarly, low diluted T-800 on austenitic SS survived only 1 cycle but cracked severely during the next 5 cycles. In the latter case, cracks perpendicular to coating/base material interface observed on transverse cross-section continued to base material, which was initially in tension as was shown in Figure 156.

4 DISCUSSION

In this chapter, the obtained results are discussed separately for back reflection measurements, wet corrosion, hot corrosion, abrasion wear, sliding wear, residual stress and thermal fatigue studies.

4.1 Back reflection characteristics

As the traditional blown powder laser cladding process suffers from low productivity and cost efficiency in large area applications, one way to overcome this is to use high power levels of short-wavelength laser beam produced by relatively cheap and efficient laser sources. Direct high power diode lasers (HPDL) fulfill these criteria well. Despite short-wavelengths, energy couplings in liquid state surface treatments including cladding are typically rather low as discussed in section 1.3.2. For instance, in Nd:YAG cladding 50% of the delivered laser power reflects off the melt pool and powder cloud [20]. For this reason, using high levels of power, back reflection targeted to laser itself and cladding tool should be considered. Direct HPDLs, particularly, are vulnerable to back reflection due to their open structure. There is clear path for the reflected beam to enter, for instance, inside the laser head in various surface treatment processes.

The studies conducted here were carried out to define the direction of back reflection in 1-step blown powder laser cladding process while using direct HPDL equipped with off-axis or coaxial type powder feeding nozzles. In-house built temperature monitoring system was utilized in measurements. It measured temperatures on several locations including prisms inside the laser head. In cladding experiments, the coating alloy was Stellite 12, which does not usually oxidize but remains rather shiny and smooth during processing. As the oxidation improves absorption, cladding conditions in this study can be considered harmful for laser head and nozzles because high reflection was expected. According to temperature measurements, it was noted that despite rather long working distance of ~0.5 m, back reflection indeed increased the temperatures inside the laser head while using laser power of 4.8 kW. The amount of back reflection inside the laser head depended on the incidence angle of laser beam with respect to the surface of the melt pool. As the leading edge of the melt pool, which shape depends on factors like bead height, melt pool length and perhaps the melt viscosity, reflects the beam forward towards the direction where cladding proceeds, laser head should be tilted towards “pushing” direction in order to avoid additional heating inside the laser head. This was particularly true for single bead cladding. It was proved that tilting the laser head towards the “pushing” direction as much as 5.0°, temperature increase inside the laser head due to back reflection was fully eliminated. This was obtained while using coaxial type cladding nozzle. Off-axis cladding configuration was not tested in “pushing” position. During large area coating application, where the beads were deposited side by side with 50% overlapping, heating inside the laser head diminished because the shape of the leading edge of the melt pool changed. Due to 50% overlapping bead height increased and melt pool inclined directing the reflected beam more towards the direction where the inter-track advance proceeded. This result was obtained while using off-axis nozzle. Coating thickness was 1.7 mm in these large area experiments.

If two different nozzles, off-axis and coaxial type, are compared in single bead cladding, with used parameters and bead thickness, the coaxial type nozzle generated conditions which caused less back reflection inside the laser head. This was obviously due to larger amount of

material between the melt pool and laser head to block the back reflection. As the coaxial type nozzle provided better shielding for the melt pool than off-axis nozzle, the total amount of back reflection was probably higher while cladding with coaxial type nozzle. This also speaks for the more efficient blocking of back reflection in case of coaxial type nozzle.

4.2 Wet corrosion properties

Wet corrosion studies consisted of open circuit potential (OCP) and potentiodynamic cyclic polarization measurements both in aqueous 3.5 wt.% NaCl solution at room temperature (RT). OCP measurements proved that defect-free Inconel 625 laser coatings were true corrosion barrier coatings, which restricted the less noble mild steel base material perfectly from the surrounding environment. Plasma transferred arc (PTA) overlay welding produced also impervious coating layers but high-velocity oxy-fuel (HVOF) sprayed coating allowed the solution to penetrate into the base material and corrode it quickly. Coating itself was corroded selectively since areas adjacent to oxidized splat boundaries were degraded. Dent et al. [401] noticed similar degradation in HVOF sprayed NiCrMoB coating exposed to 0.5 M H_2SO_4, especially when significant oxidation occurred during spraying. According to Edris et al. [402], these areas suffered from Cr depletion since Cr was oxidized predominantly to Cr_2O_3 but also to spinel $NiCr_2O_4$. Consequently, local galvanic pairs were generated inside the coating structure. Another galvanic pair was generated between the coating and base material due to established electrolyte connection. Since the NiCrMo alloy occupies much higher position than Fe in the galvanic series in seawater [348] (as well as in 3.5 wt.% NaCl as shown by OCP measurements in Figure 49), the former became cathode and the latter anode, i.e. coating was cathodically protected, which accelerated the base material corrosion further. Corrosion performance of HVOF coating was, however, improved significantly by subsequent laser remelting. With optimal parameters, perfect corrosion barrier coatings with low dilution and fusion bond were produced. In addition, undesired oxide layers in the as-sprayed structure disappeared probably by floating and accumulating at the surface during solidification. One of the benefits of this 2-step process was that relatively thin coatings (0.3-0.4 mm) with low dilution and fusion bond could be obtained. Corrosion barrier coating in aqueous environments does not necessarily have to be very thick and the production of thin and low diluted coating by 1-step method is difficult. With the inter-track advance of 8-9 mm, i.e. with overlapping of approximately 10-20%, and traverse speed of 1900 mm/min, coverage rates of 0.9-1.0 m^2/h were reached with a 4 kW Nd:YAG laser. This rather high coverage rate originates exclusively from the low thickness since melting efficiencies, 17-22%, for this process was not any spectacular compared for instance with 26-33% calculated for 1-step HPDL cladding. In these calculations, the melt pool temperatures were assumed to be between 1350-2000°C. Compared with thicker coatings produced by 1-step method, thinner laser remelted coatings were, however, more susceptible to coating defects. Interconnected paths were formed in overlapped areas due to too cold parameters and/or lack of overlapping. With too hot parameters single interconnected pores formed even on the centre of remelted tracks. Such single interconnected paths were never encountered in thicker Inconel 625 coatings produced by 1-step cladding on mild steel. Despite their low frequency of occurrence and small size in diameter in plane parallel to coating/base material interface, transverse cross-sections prepared from the exposed coatings revealed that these singe interconnected pores lead to severe and rapid deterioration in base material mainly via mechanism familiar from crevice corrosion.

In general, these exposure tests were not very harsh for Inconel 625 alloy. For this reason, there could not be detected any differences in behaviour between wrought, PTA overlay

welded and laser coatings in spite of remarkable differences, for instance, in dilution and microsegregation. PTA coating was exception since its OCP curve showed clearly lower potentials compared with other impervious coatings. This was due to significantly higher Fe content in coating in consequence of dilution.

In cyclic polarization measurements, far higher amount of alloys produced by different methods were tested. These tests revealed clearer differences in their corrosion performance than in OCP measurements. The results are discussed here starting from the Ni-based alloys.

Ni-based alloys tested comprised Inconel 625 and Alloy 59. Inconel 625 coatings were produced with 1-step HPDL cladding, PTA overlay welding, HVOF spraying and laser remelting of HVOF sprayed coating. Wrought Inconel 625 was used as reference material. Cyclic polarization curves and microstructural studies indicated that impervious coatings outperformed clearly the HVOF sprayed coating for the same reasons as explained already earlier. HPDL clad coatings, which exhibited higher amount of Fe in consequence of dilution, macrosegregation of Fe and microsegregation of Mo and Nb than wrought alloy, was inferior to wrought alloy. This was evidenced by the microstructural studies and characteristics extracted from the polarization curves. For instance, HPDL clad coating, which exhibited the lowest amount of Fe (6.0 wt.%) among HPDL coatings, showed lower repassivation (E_{rp}) potential than wrought alloy, which contained 3.6 wt.% Fe. In addition to this, characterization of tested surfaces revealed that HPDL coating suffered from slight crevice corrosion under the gasket, preferential dissolution of macrosegregated areas and dendrite cores, which were depleted in Mo and Nb. All these characterized aspects were absent in wrought alloy. The difference in performance between HPDL coatings and wrought alloy increased when the dilution of the coating increased. More heavily diluted laser coatings (9.4 and 19.4 wt.% Fe) exhibited lower E_b and E_{rp} as well as more severe crevice corrosion under the gasket. Evidently, Fe was very detrimental to crevice corrosion resistance of Inconel 625 alloy. As the initial Fe content of the powder was 1.2 wt.%, the compositional dilution of the coating, which included 6.0 wt.% Fe, was approximately 5%. In 1-step HPDL cladding even lower compositional dilutions were obtained without loosing fusion bond as evidenced in hot corrosion studies where compositional dilutions were approximately 2%. This kind of extremely mildly diluted HPDL coating would have managed better in polarization tests than coatings studied here. On the other hand, considering real applications, it would be safer to use little bit too hot parameters rather than too cold ones to secure fusion bond. As these HPDL coatings were manufactured with rather low power density and high interaction time rather high microsegregation of Mo and particularly Nb to the interdendritic regions took place. This microsegregation behaviour was in good agreement with the results presented by Tinoco [384], who reported on segregation of Mo and Nb to interdendritic regions and Cr to dendrite cores in Inconel 625. This microsegregation was, however, not so severe that it would have caused initiation of corrosion pits in areas depleted in Mo, which is often reported in the context of arc welded alloys exposed to chloride bearing environments. Microsegregation can be, however, diminished by using higher traverse speeds and shorter interaction times. Laser remelted Inconel 625 characterized with low dilution and microsegregation showed behaviour equivalent to wrought alloy. These two samples could be still tested in harsher environments to verify their equivalent resistance. Whitney et al. [403] noticed recently that laser clad Ni-based superalloys (Inconel 625, Alloy 59 and C-276) exhibited lower pitting resistance at elevated temperature in chloride bearing environments as compared to the same alloy in wrought condition. This was attributed to the microsegregation, which was absent in wrought alloys.

Co-based alloys subjected to cyclic polarization measurements included Stellite grades 21 and 6. Stellite 21 was manufactured by Nd:YAG laser cladding and PTA overlay welding. Stellite 6 was prepared by Nd:YAG cladding and HIPping. According to data extracted from the polarization curves, low diluted Stellite 21 laser coating (1.3 wt.% Fe) exhibited behaviour similar to wrought Inconel 625 and low diluted Inconel 625 and Alloy 59 laser coatings. E_{rp} was even better than that for wrought Inconel 625. It was also immune to crevice corrosion under the gasket and pitting corrosion in used conditions. SEM studies, however, revealed preferentially dissolved areas in micro-level, where Cr- and Mo-rich interdendritic regions in consequence of microsegregation dissolved considerably less than dendrite cores. As opposed to Inconel 625, chromium tended to segregate to the interdendritic regions instead of dendrite cores. Similar Mo segregation in laser clad Stellite 21 was reported in Refs. [186, 361] but segregation of Cr was not mentioned. When the both key elements Cr and Mo segregate to the interdendritic regions, this makes dendrite cores exceptionally vulnerable to pitting. In fact, PTA coatings which suffered from higher dilution and microsegregation than laser coating suffered from pitting corrosion.

Compared with almost equally diluted Stellite 6 laser coating (1.6 wt.%), the used cyclic polarization conditions did not reveal any major differences. According to Rogne et al. [183], Stellite 21 has higher critical crevice corrosion temperature in chloride bearing solutions than equally diluted Stellite 6, which does not contain Mo. It could be anticipated that dendrite cores in Stellite 6 become susceptible to pitting not only due to lack of Mo but also due to decreased Cr content because part of the Cr is bound to interdendritic carbides. HIPped Stellite 6 (1.0 wt.% Fe) exhibited even lower Cr content in the matrix than laser coating in dendrite cores (~20.8 vs. 23.9 wt.%). Nevertheless, data extracted from the polarization curves did not show any major differences. E_{rp} was, however, higher for laser coating (+483 vs. +361 mV). As the HIPped Stellite 6, closely reminding the one studied here, showed in Ref. [404] significantly lower current densities and higher E_b than cast Stellite 6 in 3.5 wt.% NaCl polarization tests at RT, it can be assumed that Stellite 6 laser coating would be far better than corresponding cast alloy.

4.3 Hot corrosion properties

Hot corrosion studies revealed that Ni and Cr in the tested alloys built up rather dense corrosion products, nickel ortho- ($Ni_3V_2O_8$) and chromium ($CrVO_4$) vanadates, on the exposed surfaces in comparison with Fe in Fe-based wrought alloy. These continuous and compact oxide layers, particularly $CrVO_4$, clearly reduced the diffusion of oxygen and other agents from the Na_2SO_4-V_2O_5 salt and environment inwards to the metal resulting in the reduction of the kinetics of the anodic reactions ($Ni \rightarrow Ni^{2+} + 2e^-$, $Cr \rightarrow Cr^{3+} + 3e^-$) at the alloy/salt and cathodic reactions in molten salt (for instance $S_2O_7^{2-}$ and VO_3^- are reduced [327]) and/or at the salt/atmosphere interface ($½O_2 + 2e^- \rightarrow O^{2-}$). As the melting temperatures of $Ni_3V_2O_8$ and $CrVO_4$ are 1220 and 810°C, respectively [386], they might have remained solid underneath the regularly added salt layer since each salt addition involved cooling down the sample. These reactions were not, however, fully prevented since even with one of the best alloys studied here, SX-707 HVOF exposed to salt (Na:V = 0.22), deterioration was more like accelerating rather than constant or decelerating as a function of time as was shown in Figure 75b. It could have been expected that increase in the corrosion product thickness would have decreased the corrosion rates despite regular salt addition.

If trying to describe what actually may have happened on the surfaces of the alloys in the test, initially, Ni- and Cr-based alloys were covered with thin but dense protective oxide layers, which were formed after grinding procedure since the oxygen activity (= partial pressure, P_{O2}) in air at RT (P_{O2} = 0.2 atm) readily exceeded the equilibrium values to oxidize Ni to NiO (P_{O2} = 10^{-74} atm, $2Ni + O_2 = 2NiO$, ΔG = -423 kJ) and Cr to Cr_2O_3 (P_{O2} = 10^{-124} atm, $4/3Cr + O_2 = 2/3Cr_2O_3$, ΔG = -705 kJ). In addition to these, protective spinel oxides like $NiCr_2O_4$ may have formed (P_{O2} = 10^{-112} atm, $1/2Ni + Cr + O_2 = 1/2NiCr_2O_4$, ΔG = -636 kJ). It is also possible that protective oxide layers developed further on the top of test alloys in the beginning of the hot corrosion test. At the test temperature of 650˚C in reaction chamber, oxygen activity should have been more than 10^{-18} atm for Ni to form NiO, 10^{-30} atm for NiCr to $NiCr_2O_4$ and 10^{-34} atm for Cr to form Cr_2O_3. Equilibrium oxygen activities at 650˚C were obtained from the phase stability diagrams of ternary Ni-O-S and Cr-O-S systems calculated with "Outokumpu HSC Chemistry® 4.0 for Windows" –software (Figure 159). In the reaction chamber atmosphere at 650˚C, the oxygen partial pressure was presumably higher than the pressure needed to form protective oxide layer at least in the case of Cr, particularly when the air was constantly blown to the reaction chamber and elevated temperature enhanced the reaction rates.

Another question is, was the oxygen activity high enough beneath the molten salt. As Lai explained [405], the reaction kinetics of hot corrosion is often characterized by an initial incubation state with a relatively low rate of reaction and a later stage with rapid materials degradation by oxidation and/or sulfidation. In other words, the initial stage involves frequently a formation of a protective oxide layer of reaction products on the metal. On the other hand, oxygen activity may have been locally too low at the metal/salt interface to form the protective oxide layers. In fact, molecular oxygen solubility in Na_2SO_4–V_2O_5 salt is low according to Rapp [406] (oxidizing solute is predominantly dissolved SO_3) and environment is often reducing at the metal/salt interface promoting sulfidation attack. Signs of this were observed in wrought Nimonic 80A, where some sulphur was detected below alloy surface as was mentioned in section 3.3.2.2. However, irrespective of whether the protective oxide layer formed in the beginning of test or not, at later stage the salt mixture finally fluxed or dissolved the protective oxide layers away and prevented their reformation, which enabled the corrosion, i.e. reactions between alloy, atmosphere and salt, to proceed.

According to studies in Refs. [407, 408], sodium sulphate salt's ability to flux and thus prevent the formation of protective oxide layers depends strongly on acid/base character of the molten salt. Acid/base character is in turn determined by the salt composition and the surrounding gas atmosphere. Salt is acidic when its oxygen ion (O^{2-}) activity is low and dissolved SO_3 from the atmosphere is high. Salt is basic when its oxygen ion activity is high and dissolved SO_3 is low. V_2O_5 additions tend to decrease oxygen ion activity and increase the melt acidity and corrosion rates [409]. Rapp [407] has shown that solubility of certain metal oxide decreases to certain minimum when the molten salt acidity increases. This can be described in diagrams where the molten salt acidity is on x-axis and solubility of oxide on y-axis (Figure 160). After that solubility minimum, oxide solubility starts to increase when the molten salt acidity increases. At solubility minimum, oxide is nearly stable and does not react with the molten salt. Different oxides have their solubility minima at different points on x-axis. Obviously, these minima conditions were not met in the present study since deterioration tended to proceed. Depending on the melt acidity, dissolution of oxide layer can occur in acidic or basic ways. In acidic fluxing, metal oxide decomposes into positive metal ions and negative oxygen ions:

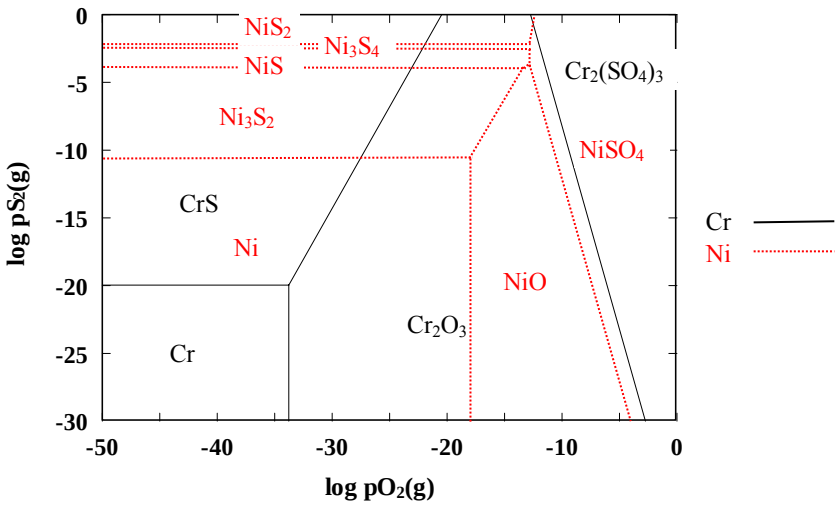

Figure 159. *Superimposed phase stability diagram of the (Ni-Cr)-O-S system at 650℃. Sulphur activity increases upwards on y-axis and oxygen activity to the right on x-axis [228].*

$$MO = M^{2+} + O^{2-} \quad (18)$$

In the case of chromium and nickel oxides acidic fluxing and precipitation of corrosion products caused by Na_2SO_4-V_2O_5 can be presented as follows [327, 410]:

$$Cr_2O_3 + 3Na_2SO_4 = Cr_2(SO_4)_3 + 3Na_2O \quad (19)$$
$$Cr_2O_3 + 2NaVO_3 = 2\mathbf{CrVO_4} + Na_2O \quad (20)$$
$$Cr_2O_3 + V_2O_5 = 2\mathbf{CrVO_4} \quad (21)$$
$$Cr_2O_3 + Na_2O{\cdot}V_2O_5 = \mathbf{CrVO_4} + Na_2O \quad (22)$$
$$3NiO + V_2O_5 = \mathbf{Ni_3V_2O_8} \quad (23)$$
$$3NiO + Na_2O{\cdot}V_2O_5 = \mathbf{Ni_3V_2O_8} + Na_2O \quad (24)$$

This acidic fluxing and prevention of formation of protective oxide layers is maintained by the ”negative solubility gradient” in molten salt as explained in Ref. [407] making metal vulnerable to continuous oxidation via precipitated corrosion products. In basic fluxing precipitated corrosion products would have been for instance $NaNiO_2$, Na_2CrO_4 and $NaCrVO_4$ [408, 410].

On the basis of these chemical reactions and reaction product layers determined with XRD, acidic fluxing of Ni and Cr oxides have taken place in the present experiments even if the tests were carried out in air atmosphere, which was deficient in SO_2/SO_3. In the beginning of the test and after every addition of salt, environment may have been, however, enriched with SO_2/SO_3 momentarily according to reaction equation 9 shown in section 2.3.5. Acidic fluxing is also supported by the fact that V_2O_5 content was relatively high in molten salt. When V_2O_5 content was increased, hot corrosion of materials became more severe as was displayed in Figure 75a. This also speaks for acidic fluxing since acidity of molten salt increases when V_2O_5 content increases as mentioned above. Since solubility of oxides is strongly dependent on acid/base character of salt, which is influenced by the surrounding gas atmosphere, materials may behave differently for example in real combustion environments, which

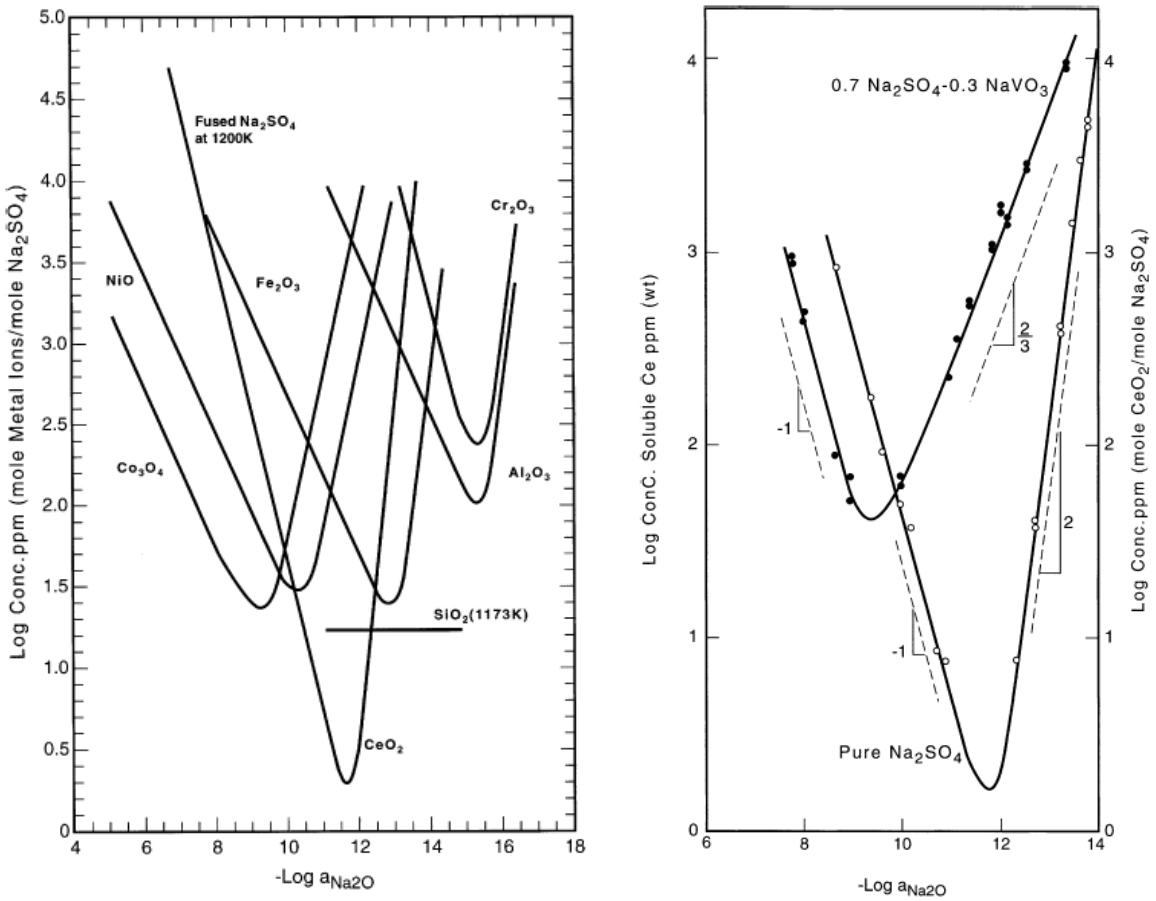

Figure 160. Solubilities of various oxides in a) molten Na_2SO_4 at 1200K and b) and influence of vanadate addition. Salt acidity increases on x-axis from left to right [407].

contains SO_2/SO_3. For that reason the field tests after initial screening are essential stage in the development and selection of combustion zone materials including laser coatings.

According to Nicholls' model [411], which evaluates the vanadic hot corrosion resistance of materials at temperatures between 535–700°C on the basis of alloy composition, alloys tested here should have been ranked in the following order: SX-707 laser (100 µm/500h), SX-717 laser (110), Nimonic 80A wrought (150), Inconel 625 wrought (220), Inconel 718 wrought (220), Inconel 625 laser (250) and 42CrMo4 (533). Values in brackets are thickness losses per 500h calculated with the model. In general, they are clearly higher than in experimental results obtained here. These differences arise from the differences in used salt compositions, perhaps contaminant flux rates (mg / cm^2·h) and gas environment. Salt in his experiments was $20Na_2SO_4$-$40V_2O_5$-$10NaVO_3$-$15CaSO_4$-$15NiSO_4$ in wt.%. Atmosphere was flowing mixture of air and SO_2. The results obtained in this study obeyed fairly well the rank except Inconel 718 wrought and Inconel 625 laser. According to experimental results achieved here, Fe was much more detrimental than that predicted by the model. This can be seen in the rank of Inconel 718 (17 wt.% Fe) and in rather low thickness loss of 42CrMo4 compared, for instance, with Nimonic 80A. Inconel 625 laser coating, in turn, behaved "too well" in experiments (Figure 161). It showed surprisingly low amount of degradation compared with Inconel 625 wrought alloy. Significant difference in resistance cannot be explained exclusively by the chemical analyses, which were (wt.%): Ni-20.9Cr-8.9Mo-3.8Nb-2.6Fe-

0.5Mn-0.4Si-0.2Ti-0.1Al for Inconel 625 laser and Ni-22.5Cr-9.0Mo-3.6Nb-3.6Fe-0.2Mn-0.1Si-0.2Ti-0.2Al for Inconel 625 wrought. It can be, however, noted that Fe content was slightly higher in wrought alloy. On the other hand, the amount of Cr was lower in laser coating. Differences in these elements are, however, quite small. As explained in Ref. [410], oxides of Mo, V and W in salt decrease the oxygen ion activity of salt, i.e. to increase the salt acidity, which in turn increases corrosion. As it was observed, reaction product layers on top of wrought Inconel 625 contained Mo-rich areas, which were not detected in the case of Inconel 625 laser coating. Thus, one of the reasons for the superiority of laser coating over wrought alloy could be the change in melt acidity. Obviously, molten salt dissolved more Mo out of the structure where Mo was more evenly distributed (wrought alloy). Microsegregation of Mo perhaps led to better hot corrosion resistance. Another difference, which should be considered, is the microstructure. As it was shown in Figure 47, wrought alloy contained perhaps some grain boundary carbides. These may have suffered internal oxidation and sulfidation as described in Ref. [328], thus allowing reactive elements to penetrate into the alloy and deplete it from Cr. This could have occurred in the very top surface layer where Cr was depleted as was shown in Figure 89b. Any preferential grain boundary attack below that Cr depleted layer was not detected.

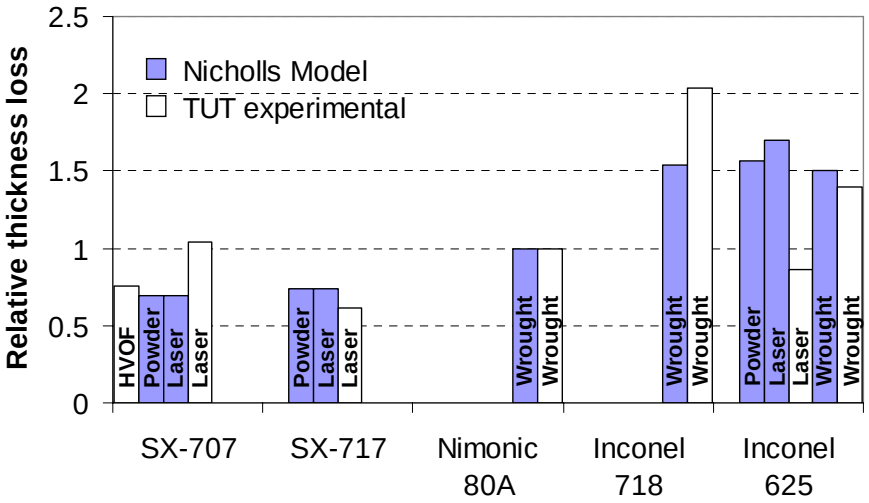

Figure 161. Comparison of experimental results and results calculated with Nicholls' model at 650 ℃. In both series, relative thickness loss of 1 was given to Nimonic 80A wrought.

About high-Cr NiCr laser coatings, despite their low mean thickness losses, particularly in low diluted condition, their high temperature stability was rather low. In consequence of extended solid solubility obtained during rapid solidification for γ-Ni and α-Cr phases, their volume fractions and compositions changed towards the equilibrium during the test at 650°C for 1000h. That is, the amount of α-Cr phases and their Cr content increased. As these α-Cr phases were susceptible to hot corrosion in used environments, applicability of these high-Cr NiCr laser coatings can be questioned.

4.4 Abrasion wear properties

Low-stress three-body abrasion-wear studies using angular silica (750–1200 HV, 0.1–0.6 mm) as an abrasive was conducted with rubber wheel abrasion test device for various metallic monolithic and metal matrix composite (MMC) laser coatings. Other well-known high abrasion resistant coatings and bulk materials including cast Ni-hard alloy and high volume

fraction WC-based cemented carbides (hard metals) produced by HVOF spraying and sintering were used as reference materials. Besides comparing laser coatings between themselves and reference alloys, influence of carbide volume fraction, carbide size, carbide morphology as a result of different powder manufacturing methods and dissolution of carbides into the matrix were studied. In general, all the laser coatings studied here were inferior to high volume fraction hard metals. Volume fraction of hard WC particulates in these reference hard metals was as high as ~75%. The best laser coatings, which approached the qualities of these, were various MMCs and monolithic Fe-based alloys (WR6 and Nanosteel), which outperformed substantially, for instance, monolithic Co-based hardfacing alloys with similar hardness. As the amount of material removed from the surface in abrasion is largely dependent on the depth of indentation of abrasives into the surface, which in turn depends on the hardness of the surface [329], the results suggest that there was difference in wear mechanisms between Fe-based (WR6 and Nanosteel; ~840 HV_1) and the hardest Co-based alloys (Stellite 1 and T-800; ~800 HV_1). Instead of microploughing and –cutting detected at least on the surface of WR6 tool steel, apparently more brittle Co-based hardfacing alloys suffered also from microcracking and associated detachment of larger fragments, which inevitably led to higher wear rates than pure microcutting and –ploughing as explained in Ref. [329]. Otherwise these results cannot be explained. Such detaching fragments were indeed found on the wear scar of T-800 shown in Figure 162 despite its compressive residual stress state as was reported in section 3.6.1. Nanosteel may have also suffered from microcracking since it was slightly less abrasion resistant than WR6 tool steel despite similar microhardness. Fracture toughness studies conducted with Vickers pyramid indentation load supported this deduction.

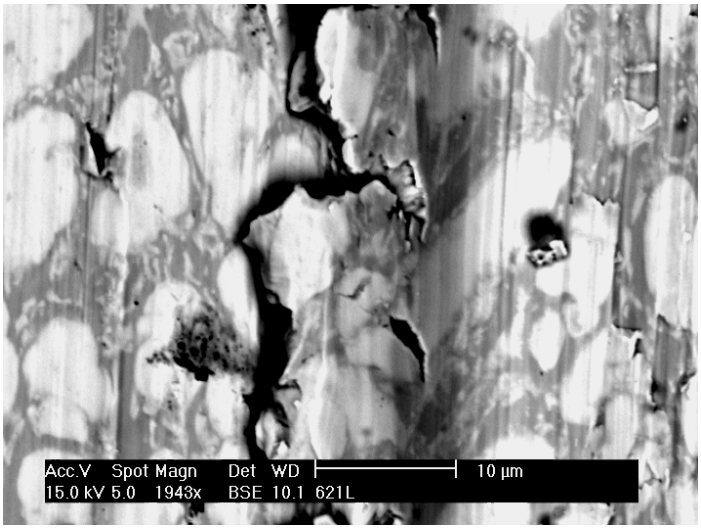

Figure 162. SEM micrograph taken from the wear scar of abrasion wear tested T-800 laser coating. Rubber wheel rotated along the vertical dimension of the micrograph. Bright areas are hcp-ordered Laves phases. Material is removed by brittle fracture.

Compared with monolithic alloys, ranking of MMC laser coatings in reliable way was far more difficult. This resulted from the difficulty to calculate the correct volume losses due to wide range of hard particulate densities (~4.9-16.6 g/cm^3) used, detected dissolution of carbides and related changes in matrix density, differences in degree of preferential wear of softer matrix alloy and possible improper mixing of precursor powders or mechanical segregation in powder hopper, which both might have led to deviated carbide volume

fractions in comparison with the intended original powder mixture. Densities of MMCs (ρ_{mmc}) could have been determined reliably by removing pieces of coating and weighing them in air and in liquid with known density as was practised in Ref. [337] but still preferential wear of softer matrix and different behaviour of carbides would have caused difficulties to get the correct volume losses. However, certain general trends based on the characterization of microstructures, wear scars and mass loss values could be observed. For instance, hardness of the matrix alloy played a crucial role in wear behaviour. No matter was it obtained purposefully by the selection of harder grade matrix alloy or was it the result of excessive carbide dissolution and subsequent precipitation of mixed carbides in the matrix; the harder the matrix, the higher the wear resistance. The first example of this was Colmonoy 42-P2 (NiCrBSi, 36 HRC) reinforced with Amperit 522.3 (dense-coated WC/Co). This coating was laser clad with low and high laser powers. High laser power generated coating with lower amount of primary carbides (50 vs. 55 vol.%) and harder matrix (750 vs. 730 $HV_{0.3}$), which led also to better abrasion resistance. Even better performance was obtained when significantly harder Metco 16C (NiCrBSi, 58-60 HRC) was reinforced with same but lower amount of Amperit 522.3. Average primary carbide content of this coating was just 24% but the matrix hardness was as high as 1020 $HV_{0.3}$. The third example concerns (Ti, Mo)C particulates as SHS 1436 (Colmonoy 42-P2 + (Ti,Mo)C (~40/60 vol.%)) outperformed SHS 1377 (Ni + (Ti,Mo)C (~35/65 vol.%)). These observations were relevant as the wear was subjected profoundly to the matrix because abrasive silica was softer than any of the carbides used and all the carbide types were tightly bound to the matrix due to partial dissolution as carbide "pull-outs" were not found in any of the coatings.

This result or finding that increased matrix hardness is beneficial should be interpreted with care since rubber wheel abrasion test creates conditions, which are rarely met in real applications. According to Hutchings [329], soft and compliant rubber as a support for abrasives gives conditions, which treats hard and brittle materials with low fracture toughness more kindly than hard and rigid supports often encountered, for instance, in two-body abrasion wear situations. In other words, harder matrices can be detrimental in real wear conditions where abrasives penetrate deeper into the brittle matrix due to higher load or where large abrasives impact the surface causing cracks and brittle fractures, which accelerate the wear rates. Thus, ranking of MMC laser coatings could change dramatically in more realistic wear conditions.

In this perspective, the most appropriate coatings could be those, which were characterized with high fracture toughness; Stellite 6 reinforced with (Ti, Mo)C or CrC, tool steel WR6 reinforced with VC and softer grades of NiCrBSi reinforced with fused spherical WC/W_2C/W particulates. From the dissolution and embrittlement of the matrix point of view chemically and thermodynamically more stable WC would be preferable over WC/W_2C, but dense-coated tungsten mono-carbide used in this study turned out to be the most brittle one. They were broken up severely during the wear process and under indentation loads of 3 and 10 N. Particularly vulnerable sites for cracking were grain boundaries. Pierson [222] suggested that chemical impurities at grain boundaries may provoke cracking. Manufacturing method of this dense-coated powder is unknown but such impurities as for instance sulphur at grain boundaries could have been originated from the low quality carbon black, which is mixed with elemental tungsten in carburization [413]. This is commercially the most important manufacturing method of tungsten mono-carbides [413]. The influence of subsequent dense-coat processing on impurities at grain boundaries is unknown, too. Coating around WC particulates was probably prepared by a reduction of metal salt solution in hydrogen atmosphere. Huang et al. [224] used tungsten-mono carbides manufactured by carburisation

of elemental W without dense-coated layer. In their rubber wheel abrasion studies (silica, 333 N) tungsten mono-carbides survived the test without cracking and outperformed more heavily dissolved spherical fused WC/W_2C particulates. Consequently, it is not relevant to prejudge all the available tungsten mono-carbides simply on the basis of this study especially when it was noticed that powder manufacturer finished the production this Amperit 522 couple of years ago. Yet, higher fracture toughness of fused WC/W_2C and particularly $WC/W_2C/W$ and substantially better abrasion wear resistance was some sort of surprise since hcp-ordered W_2C is frequently considered very brittle and more or less undesirable in wear applications compared with simple hexagonal WC [225].

Another clear trend, the beneficial effect of fine carbide size can also be related to the increased matrix hardness. Metco 16C and Stellite 21 matrices were reinforced with fine and coarse WC/Co particulates and in both cases the coating reinforced with finer carbides were significantly better. Mean free path between carbides may have also played a role especially in Metco 16C since with equal volume fractions finer carbides leave less amount of matrix exposed to hard abrasives as mean free path between carbides decreases [390]. In situations where possible carbide dissolution did not harden the matrix; the higher the volume fraction of primary carbide in the coating, the higher the wear resistance. This was certainly evidenced by the results from SHS 1378 and SHS 1389, where carbide dissolution and precipitation of mixed carbides did not harden the matrix. These coatings contained 64 and 26-60 vol.% of (Ti, Mo)C particulates in Stellite 6 matrix and the former one was significantly better than the latter. This can be attributed also to the differences in mean free path between carbides. The higher the volume fraction of carbides, the shorter the mean free path between them and smaller the surface area of softer matrix exposed to the hard abrasives [390].

Concerning the results in pure low-stress three-body abrasion, the best one among laser coatings was MMC where Stellite 6 matrix was reinforced with very fine (< 2 μm) (Ti, Mo)C particulates spherical in shape (SHS 1378). Volume fraction of these particulates in the coating was approximately 64%, which corresponded very well to the original powder (63 vol.%) produced by self-propagating high-temperature synthesis (SHS). This observation together with XRD analysis and Vickers pyramid indentation load studies suggested that coating did not suffer from the deleterious dissolution and precipitation of brittle mixed carbides or reduced matrix's fracture toughness. This can be attributed to the nature of TiC, which have high thermal stability and very low solubility in cobalt as presented in Figure 9 and Table 3. These features enable to use very fine carbide granulometry even in the case of external addition of reinforcements as proved here. In spite of low solubility, (Ti, Mo)C particulates were very strongly bound to the matrix as detached carbides were not detected in wear scar studies. Some of the carbides were, however, cracked but mainly the material was removed from the matrix particularly in front of carbides in relation to wear direction. As the matrix material alone was very poor in abrasion resistance, excellent results here can be attributed to the high volume fraction of nearly nano-scale hard particulates, which left very short mean free path between carbides exposed to abrasives. With even higher volume fraction of similar (Ti, Mo)C particulates, for instance, in tool steel matrix, abrasion wear properties of hard metals could be perhaps reached. Decreasing melt viscosity due to higher carbide content would, however, limit the cladability and low solubility of TiC in Fe weaken the interfacial bond between carbides and matrix. Another potential matrix alloy could be one of those hardest NiCrBSi grades.

Other well succeeded laser coatings were the hardest NiCrBSi (Metco 16C and Diamalloy 2001) alloys reinforced with high volume fraction (50%) of coarse and angular fused

WC/W_2C and fine dense-coated WC particulates, Metco 16C reinforced with coarse CrC and tool steel WR6 reinforced with coarse VC particulates. Latter two exhibited particularly high potential since initial volume fractions of hard particulates were only 30 vol.%. In Metco 16C CrC particulates remained intact, i.e. no scratches, cracks or fragmentations were detected after the wear tests. Hence, CrC particulates exhibited high enough hardness and fracture toughness to survive in used conditions as opposed to brittle tungsten mono-carbides. Matrix was not particularly hard compared with Metco 16C reinforced with WCs. Vickers indentation load of 10 N initiated however cracks which propagated along matrix/carbide boundaries indicating exceptional interface brittleness not found from any other hard particulate-matrix combinations studied in this work.

4.5 Sliding wear properties

In sliding wear studies, different types of Co-based hardfacing alloys (solid solution strengthened, carbide, intermetallic), Fe-based Nanosteel alloy and (Ti,Mo)C reinforced MMCs produced by laser cladding were tested against QT steels in dry condition at RT. PTA overlay welded coatings, laser-hardened steel and HIPped bulk alloy were used as reference materials. Under used circumstances solid solution strengthened Stellite 21 exhibited severe adhesive wear throughout the test, whereas the carbide type hypoeutectic Stellite 6 in the beginning of the test, where the nominal contact pressure was high, a severe adhesive wear and later mild oxidative wear. The harder coatings including carbide type Stellite 1, intermetallic types Tribaloy T-800 and T-400, Fe-based Nanosteel alloy and (Ti,Mo)C reinforced MMCs exhibited mild oxidative wear throughout the test. Reasons for this kind of behaviour can be found in mechanical properties of the alloys including hardness, yield strength and capacity for plastic flow (ductility), particularly at elevated temperatures due to generation of frictional heat.

Stellite 21, which has the highest capacity for plastic flow (9% elongation at RT [400]), obviously the lowest yield strength and hardness among the tested materials, underwent high plastic deformation during the test evidenced by the worn surface examination. Such plastic deformation together with little mechanical support by the relatively soft coating (even if work-hardened) prevented the formation of tightly bonded oxide films, which led to direct metallic contact, strong interfacial adhesion and high frictional heat. Some superficial work hardening took place during the sliding contact proved by the microhardness measurements. XRD studies, however, did not reveal large scale allotropic transformation from γ-Co (fcc) to ε-Co (hcp) after the 90 minutes testing time. Such allotropic transformation may have occurred in the beginning of the test where the Hertzian stress was at maximum but this was not studied. Due to progressive wear, allotropically transformed alloy may have worn away and was not revealed clearly by XRD after the test was completed. This could explain the constant wear rates throughout the test assuming that hcp ordered Co possess better sliding wear resistance. Hcp ordered Co, indeed, should possess at least lower ductility than fcc ordered Co since hcp structure has limited ductility due to fewer slip systems compared with cubic close-packed structure (fcc), which is more ductile. According to Persson [186], galling resistance and friction qualities can be improved significantly if easily sheared hcp {0001} basal planes supported by work-hardened zone orient parallel to the worn surface. He noticed complete fcc -> hcp transformation (hcp peaks at $2\theta = 41.7°$, 44.8° and 47.6° were detected) in Stellite 21 laser coating subjected to self-mating sliding contact under high loads of 200-2200 N. Apparently, low-load (58 N) sliding contact condition used in these experiments did not induce such allotropic transformation and plane orientation except perhaps in the beginning of test when the nominal contact pressure was high. Moreover, according to Ref.

[414] T-800 should exhibit only 3 to 7 times better sliding wear resistance than Stellite 21 in dry conditions against 4620 steel ring under high loads of 670 and 1330 N. In this study, in low-load sliding contact, T-800 showed more than 30 times better sliding wear resistance. This can be explained by the absence of severe fcc to hcp transformation in Stellite 21 under low-load condition. Aoh et al [415] noticed that PTA overlay welded Stellite 6 was 11-16 times better than Stellite 21 in high temperature sliding wear resistance against hardened tool steel when low load and high sliding speed was used. When the load was increased and sliding speed was dropped, Stellite 6 was just 1.2-1.6 times better than Stellite 21. Sliding wear test parameters used here were apparently not favourable for Stellite 21. As the post-machining (turning, grinding) is frequently practiced on laser coatings such favourably oriented hcp planes may develop during post-machining and generate better sliding properties.

In harder coatings tightly bonded oxide films, which were supported by the hard coating alloy underneath, formed readily already during the first 4 minutes of the test and survived throughout the test. Such oxide films effectively separated the sliding surfaces and prevented the formation of adhesive metallic junctions leading to low frictional heat and wear rates. In intermetallic type Co-based hardfacing alloys, the best alloys tested here, high hardness, high yield strength and low capacity for plastic flow originated from the strong covalent-dominated covalent-metallic atomic bonds between atoms in ternary CoMoSi Laves phases and hcp ordered structure. Due to these bonds, hcp ordered, $MgZn_2$ (C14) type Laves phases did not loose their strength and hardness at elevated temperatures. From the sliding wear performance and economical points of view, Fe-based hardfacing alloy containing Cr, W, Mo, B, Mn, Si, C and Zr from the company Nanosteel exhibited high potential. It was nearly as good as excellent T-800 when the total wear loss is considered (block + ring). High hardness of this alloy (~800 HV_1) originates from the high volume fraction of fine and complex $M_{23}(BC)_6$ and $M_7(CB)_3$ borocarbides cubic in shape predominantly in refined α-Fe (bcc) matrix [416]. This alloy was laser clad without preheat, i.e. cracks were allowed to form. Influence of preheating on crack elimination and sliding wear properties should be studied as well.

The results also indicated that intermixed Fe from the base material affected negatively on sliding wear resistance of Co-based alloys (Stellite 21, T-800). This was in accordance with the results reported in Refs. [184, 185, 330], where differently diluted carbide type Stellite SF20 and Stellite 6 were tested in various sliding conditions. In both cases studied here, considerable hardness drop was noticed in consequence of severe dilution. Due to significant difference in dilution the influence of the scale of the microstructure on microhardness and wear properties could not be studied here (laser vs. PTA).

As was shown by the results concerning Stellite 6 alloy, wear resistance is not always directly dependent on microhardness. Stellite 6 produced by laser cladding and HIPping exhibited significant difference in wear resistance despite similar initial microhardness. This behaviour can be attributed to the differences in microstructures. As the laser coating included interconnected network of interdendritic carbides, HIPped alloy contained tiny discrete carbides irregular or spherical in shape. The wear volume and block temperature measurements suggest that the network of hard interdendritic carbides characteristics for laser coating provided more rigid structure to support oxide layers and to resist plastic deformation than discrete tiny carbides. It was also noted that laser coating work-hardened more than HIPped alloys. Microhardness values measured from the work-hardened zones were 610-670 $HV_{0.3}$ for laser coating and 520-560 $HV_{0.3}$ for HIPped alloy. EDS point analyses taken from the matrices (laser: Co-23.9Cr-3.8W-2.4Ni-0.9Si-0.1Mo-2.0Fe, HIP: 20.8Cr-6.7W-2.2Ni-

1.0Si-0.4Mo-1.2Fe in wt.%) suggest that there were not considerable differences in alloying elements, which increase or decrease the stacking fault energy of Co matrix. On the basis of this, difference in microhardness values measured from the work-hardened zone originate from the different nominal contact stresses. As the HIPped alloy wore more than laser coating, nominal contact stress on the surface, under which the hardness was measured, was lower.

In practice, the test conditions used here where the two solid metal surfaces are in dry sliding contact can be encountered for example in lubricated machines at the start or in circumstances where the surfaces slide with so slow speed and high load that there is just boundary lubrication between them or when there is shortage of lubrication oil for some reason [394]. In this sense, higher load and slower speed could have been chosen. There may also exist applications where the use of liquid lubrication is limited due to too high or too low temperatures or for instance to cleanliness requirements [394].

4.6 Residual stresses

Tribaloy T-800 intermetallic type Co-based hardfacing alloy posses highly desired properties including high hardness at elevated temperatures and excellent sliding wear properties, which makes them potential candidates in applications like gas turbines, combustion chambers of diesel engines and various metal forming tools. Its extreme brittleness has, however, hindered its use as welded coatings since crack-free production on base materials excluding the thinnest ones is very difficult. In this study, such crack-free T-800 coatings were prepared on mild, martensitic (EN 1.4731) and austenitic (21-12N) stainless steels 20 mm in thickness with the help of elevated preheat and working temperatures (500°C). Nevertheless, there is not much use of initially crack-free coating layer if it cracks and fragments into pieces in real service conditions and in worst case destroy some expensive components nearby. For that reason, awareness of its residual stress state on various base materials, especially on used martensitic and austenitic SS grades, which are typical valve steels in combustion engines, was highly needed.

Residual stress measurements conducted with XRD and hole-drilling methods showed that large tensile residual stresses can be avoided in coatings on mild and martensitic stainless steels mainly due to small CTE difference between coating and base materials (T-800: 12.6 (20-500°C), Fe52: 12.7 (20-500°C) and mart. SS: 12.1 (20-600°C) x 10^{-6} K^{-1}). Also, relatively high preheat temperature, which was necessary to avoid cracking, decreases thermal stresses by lowering the temperature gradients (equation 7 in section 1.5.5), cooling and strain rates. From the fatigue endurance and stress corrosion cracking points of view, it was positive to note that grinding generated high compressive stresses on the surface of coating since fatigue and stress corrosion cracks frequently initiate on the surfaces of components under tension. On the other hand, due to counterbalancing effect, large tensile stresses generated below the region in compression. Meanwhile, T-800 on austenitic stainless steel possessed high compressive stresses throughout the whole coating thickness, which formed during cooling due to base material's larger shrinking (Aust. SS: 16.7 (20-600°C) x 10^{-6} K^{-1}). It was also noted in the manufacturing stage that its crack-free production on austenitic SS was much easier, i.e. higher cooling rates were tolerated.

About measuring techniques, T-800 consists approximately 54-57 vol.% of hcp-ordered Laves phases and 43-46 vol.% of Co-based solid solution. Owing to dual phase structure,

residual stresses could have been measured for both phases separately following the equation [350]:

$$^{m}\sigma_{ij} = (1 - f_m)\sigma_i(Laves) + f_m\sigma_j(Co) \qquad (25)$$

Where $^{m}\sigma_{ij}$ is macro-residual stress of T-800, σ_i (Laves) is residual stress of Laves phase, σ_j (Co) is residual stress of matrix and f_m is volume fraction of matrix. This kind of procedure would have, however, necessitated repositioning of detectors and calibration each time changing the phase to be measured since their suitable diffraction peaks (2θ-values) deviated a lot. Elastic constants (E, υ) for these were also unknown. For these reasons only Laves phases were considered. Residual stresses in Laves phases and Co-based solid solution could have differed due to differences in elastic constants and CTEs. For instance, during cooling Co-based matrix, which probably has higher CTE than Laves phase (Mo has low CTE), would have contracted more than Laves phase during cooling, thus creating compressive stress in Laves phase. Consequently, Laves phases would have restricted matrix's shrinkage causing additional tension in it. Despite of this Laves phase analysis only and the use of normal T-800 elastic constants for it, results were in good agreement with the macro-stress results obtained via hole-drilling method, which can be considered reliable when residual stresses are less than 60% of the yield strength of material. Yield strength of T-800 is unknown but due to its low ductility (elongation <1%) it can be expected to be near the ultimate tensile strength, which is 700 MPa [400].

For Stellite 21 coatings, which are substantially softer and more ductile than T-800, tensile residual stresses were much higher on austenitic and martensitic stainless steels compared with T-800. This can be attributed to the larger CTE of coating. Stellite 21 coatings were also clad without preheat because its crack-free production does not necessitate that. Therefore, the larger thermal gradients, faster cooling and strain rates took place compared with the T-800 processing.

4.7 Thermal fatigue properties

Alternating or cycling temperatures subjected to coating/base material pairs exert stresses on both materials if there is mismatch in CTEs. The magnitude and sign of these stresses depends on CTEs and mechanical properties of materials. With the used thermal fatigue test setup, where the heating and cooling were administered from the one side only, thermal gradients exert stresses as well. These kinds of situations where coating/base material pairs undergo stress changes due to temperature cycles are frequently encountered in combustion engines, gas turbines, moulds, rolls and other various metal forming tools in extrusion of non-ferrous metals etc. Also laser clad components, which are subsequently heat-treated undergo temperature changes. In these studies, low-cycle thermal fatigue tests were conducted for pairs comprising: 1) soft and ductile Inconel 625 on mild steel, 2) moderately hard high-Cr NiCr alloy SX-717 on mild steel and 3) hard and very brittle T-800 on mild and 4) austenitic (21-12N) stainless steels.

According to nominal CTEs of materials found from the literature, Inconel 625 has higher CTE than its base material (Inconel 625: 13.2 (20-500°C) vs. Fe52: 12.7 (20-500°C) x 10^{-6} K^{-1} [372]). In this situation, tensile stresses develop in coating layer during cooling. Due to very high ductility of Inconel 625 (elongation 50% [400]) and rather modest CTE mismatch (= low tensile stress during cooling), low diluted Inconel 625 laser coating survived at least 50

temperature cycles from RT to 685°C and back to RT. Internal structural discontinuities were absent except oxidized semi-molten powder particle detected near the coating/base material interface. As a potential stress raiser, it did not, however, act as initiation site for fatigue crack.

In the case of SX-717 on mild steel, stresses caused by the CTE mismatch could be expected to be low since CTE for SX-717 (11.7 x 10^{-6} K^{-1} (at 100°C) [374]) does not deviate much from the CTE of mild steel. For that reason and due to high enough ductility, low diluted laser coating survived the same amount of cycles as Inconel 625 laser coating. Even if the CTE mismatch was negligible, some tensile residual stresses were expected to develop in coating layer during cooling. Cooling of the sample was administered from the bottom side as was shown in Figure 37 in section 2.3.9. Thus, the coating side cooled slower than the bottom side, which led to the situation where still hot coating side tried to undergo shrinking on top of already cooled bottom side. As cooled bottom side tried to prevent the shrinkage of hotter coating side, tensile stresses developed on the coating side. It is still noteworthy to point out that micro-pores, which were probably shrinking cavities, found exclusively in interdendritic regions, did not initiate fatigue cracks in given conditions.

As the nominal CTE of T-800 does not differ much from the CTE of mild steel (T-800: 12.6 (20-500°C) [373] vs. Fe52: 12.7 (20-500°C) [372]), it was expected that T-800 laser coating, even if very brittle (elongation <1% [400]), would survive well in given conditions. It was, however, noted that heavily diluted coating (~30 wt.% Fe) survived surely just one cycle. During the next five cycles it cracked severely. These cracks appeared perpendicularly to the coating/base material interface and they did not propagate beyond the interface. This was positive together with the fact that cracks parallel to coating/base material interface were not detected. Apparently, the tensile stresses, which evolved mainly in consequence of one-sided cooling, i.e. thermal gradients, were high enough to cause cracks. Rather high Fe, i.e. lower volume fraction of Laves phases, content did not apparently increase the ductility of T-800 either. Tobar et al. [417] studied the influence of dilution (7 and 14 wt.% Fe) on cracking susceptibility of laser clad T-800. They concluded that no noticeable effect was found.

In the case of T-800 on austenitic SS, where the base material possess clearly higher CTE than coating (T-800: 12.6 (20-500°C) vs. Aust. SS: 16.7 (20-600°C) x 10^{-6} K^{-1}), tensile stresses were expected to develop during the heating and compressive stresses during the cooling period in coating, which was originally in compression. Similar to T-800 on mild steel, this low diluted T-800 (3-4 wt.% Fe) on austenitic SS survived surely one cycle and cracked heavily during the next 5 cycles. Due to low ductility of coating, it probably cracked during the heating period when the base material expanded more than coating. Cracks, which appeared perpendicular to coating/base material interface propagated beyond the interface to the depth of ~200 μm. Base material underneath the coating was initially in tension as was shown in Figure 156 enhancing the crack propagation cross the interface.

As the CTE of mild steel used in the experiments does not differ much from quenched & tempered, tool and martensitic stainless steels, the results obtained provide some information about laser coatings' applicability in combustion engines (Inconel 625, SX-717, T-800) and metal forming tools (T-800). Due to lower yield strength of the mild steel, some plastic flow in the vicinity of interface may, however, provide easier conditions for coatings to survive on mild steel compared with higher yield strength steels. Specimens used in these test (thickness 20 mm) did not have as high rigidity as more massive real applications. This made also

conditions somewhat easier. On the other hand, temperatures cycles (heating and cooling) were very rapid, probably not often encountered in real applications.

5 CONCLUSIONS

A wide variety of different metallic alloy coatings with and without refractory carbide reinforcements was produced on Fe-based base materials with short-wavelength industrial high power lasers (Neodymium:yttrium-aluminium-garnet (Nd:YAG) and direct high power diode laser (HPDL)) using 1-step blown powder method. Laser coatings together with the selected bulk alloys and coatings manufactured by rival coating techniques were characterized and tested. Characterization and testing included wet corrosion studies in chloride bearing environment, hot corrosion studies against molten sulphate-vanadate salts, high temperature stability, three-body abrasion wear studies using quartz sand as an abrasive, sliding wear studies in dry condition against quenched & tempered (QT) steels, residual stress measurements using X-ray diffraction (XRD) and hole-drilling methods as well as low-cycle thermal fatigue tests. Direction and magnitude of back reflection from the melt pool during direct HPDL cladding was defined by conducting temperature measurements on several locations including prisms inside the laser head.

Back reflection measurements conducted by using off-axis and coaxial type powder feeding configurations in cladding of Co-based hardfacing alloy on mild steel revealed that certain amount of reflected laser energy reached the prisms inside the laser head despite readily absorbed short-wavelength laser beam and rather long working distance of nearly 0.5 m. The amount of back reflection inside the laser head depended on the powder feeding nozzle type and incidence angle of laser beam with respect to surface of melt pool. As the leading edge of the melt pool reflects the beam forward towards the direction where cladding proceeds, laser head should be tilted towards “pushing” position in order to avoid additional heating inside the laser head. This is particularly true for single bead cladding. With used cladding parameters and obtained bead height, tilting as much as 5.0° towards the “pushing” direction fully eliminated the back reflection inside the laser head. During large area coating applications where the beads are deposited side by side with certain overlapping, height of the other end of the single bead increases and the melt pool becomes inclined due to overlapping. This changes the direction of back reflection more towards the direction where the inter-track advance proceeds resulting in less back reflection inside the laser head compared with single bead cladding. The coaxial type powder feeding nozzle blocked the back reflection more efficiently than off-axis nozzle did.

In wet corrosion studies in neutral chloride bearing aqueous solution (3.5 wt.% NaCl) at room temperature (RT), laser cladding process unlike high-velocity oxy-fuel (HVOF) spraying process proved to produce impervious Ni-, Cr-, and Co-based metallic corrosion barrier coatings, which isolated the less noble base materials completely from the surrounding environment. Both inhomogeneous distribution of alloying elements in micro-level caused by inevitable microsegregation and intermixed Fe from the base material in macro-level caused by insufficient homogenization of the melt led however to the preferentially dissolved areas, which were not detected in corresponding wrought alloy with more homogeneous composition. Limited amount of dilution by the intermixed Fe from the base material, characteristics for laser coatings, had a useful effect, particularly in preventing pitting and crevice corrosion. It was noted that Fe was detrimental to crevice corrosion in Ni-based Inconel 625 and to pitting corrosion resistance in Co-based Stellite 21. For these reasons, low diluted laser coatings were superior to heavily diluted plasma transferred arc (PTA) overlay welded coatings. Consequently, distribution of alloying elements in macro- and micro-level together with the magnitude of dilution dictates the corrosion performance of laser coatings and their relation to the corresponding wrought alloy. By careful control of these features as

was proved by the high traverse speed remelting experiment, corrosion properties equivalent to wrought alloy could be obtained in the specified test conditions.

Ni- and Cr-based laser coatings exposed in air atmosphere to molten sulphate-vanadate compounds at 650°C showed equivalent or better resistance than commonly used commercial Ni-based wrought alloys. Most importantly, low diluted Inconel 625 and SX-717 laser coatings outperformed wrought Nimonic 80A alloy widely used in applications subjected to molten salts. This was attributed to the more protective oxide layers, which formed on the exposed surfaces, at least partly due to higher Cr contents. Moreover, Inconel 625 laser coating was superior to wrought Inconel 625. As the chemical compositions for these two were nearly the same, difference in hot corrosion behaviour can be attributed to the differences in microstructure and distribution of alloying elements. In laser coating, Mo and Nb were strongly segregated to the interdendritic regions, whereas in the wrought alloy they were more homogeneously distributed. Reaction product layer studies showed that more Mo and Nb were transferred to the salt from the wrought alloy. This is known to increase melt acidity, which in turn increases corrosion. In addition, wrought alloy may have suffered from grain boundary attack in the Cr-depleted layer. Underneath that layer no grain boundary attack was detected. Compared with the uniform deterioration detected in Inconel 625, in Cr-based laser coatings Cr-rich phases were prone to molten salt attack. It was also observed that Cr-based laser coatings, which consisted of metastable bcc ordered α-Cr and fcc γ-Ni phases underwent transformation towards equilibrium during the long-term exposure to high temperature. In other words, the amount of α-Cr phases and their Cr content increased.

In low-stress three-body rubber wheel abrasion wear tests, metal matrix composite (MMC) laser coating produced from experimental powder prepared by self-propagating high-temperature synthesis (SHS) showed great potential. Abrasion wear resistance of this coating reinforced with high volume fraction (~64%) of very fine (<2μm) (Ti, Mo)C particulates approached the qualities of high volume fraction hard metals produced by sintering and HVOF spraying. In addition, initial carbide volume fraction in the powder corresponded well to the amount detected in the coating layer because individual powder particle contained both the matrix and carbides. This was not always the case when the mechanical powder mixtures were used. In general, production of MMCs is relatively easy and flexible by laser cladding. With used matrix and carbide combinations, none of the coatings exhibited carbide “pull-outs” due to wear, which proved that there was excellent bonding between carbide and matrix. Among monolithic laser coatings, V-rich Fe-based tool steel showed the best behaviour outperforming for instance several MMC laser coatings. In general, increased hardness of the matrix at the expense of reduced fracture toughness was an advantage in this type of test. As opposed to bulk alloys and sprayed coatings, laser coatings suffered from distinctive local differences in wear rates due to reheated zones associated with overlapping and inadequate homogenisation of the melt.

Under low-stress dry sliding conditions against QT steels, solid solution strengthened, carbide and intermetallic type Co-based laser coatings outperformed corresponding PTA coatings and hot isostatic pressed (HIP) material in wear resistance. These results can be attributed to the higher microhardness values due to lower amount of dilution by the Fe from the base material and differences in microstructure, which both affect the alloys ability to support the forming oxide layers. Novel Fe-based Nanosteel hardfacing alloy exhibited resistance equivalent to the best of Co-based intermetallic type alloys.

Residual stress studies conducted on brittle and ductile hardfacing alloys deposited on various Fe-based base materials indicated that mismatch in coefficients of thermal expansion (CTE) mainly dictates the final residual stress state in coating layer. Even if managed to produce crack-free coating layers from very brittle intermetallic type hardfacing alloy with suitably low CTE by using appropriate preheating, this alloy was very susceptible to cracking when subjected to alternating temperatures as evidenced by low-cycle thermal fatigue tests.

6 SUGGESTIONS FOR FUTURE WORK

Various coating characterization methods used here showed the potential of laser coatings in different wear and corrosion conditions. In future, harsher conditions should be used particularly in wet corrosion studies to get clearer differences between different alloys, corresponding wrought and laser clad alloys. Furthermore, concerning corrosion properties, microsegregation particularly in fine-scale microstructures produced with short interaction times should be determined with methods, which have higher spatial resolutions e.g. electron probe microanalysis (EPMA, spatial resolution around 1 μm) or scanning transmission electron microscopy (STEM, spatial resolution around 0.1 μm) [103]. Attempts to diminish the degree of detrimental microsegregation by alloying should also be undertaken. Recent publication has reported that small additions of W to Ni-based superalloys containing Mo decreased the microsegregation of Mo. In hot corrosion studies, reasons for the superiority of Inconel 625 laser coating over corresponding wrought alloy were not very clear. The influence of Mo and differences in its distribution on melt acidity should be defined by measuring oxide-ion activities from the melt as explained and showed in a few publications [327].

Concerning production of MMC laser coatings, apparently more research should be done on feeding techniques in order to produce coatings which reinforcement content corresponds better with the desired or planned volume fractions. Fluidized-bed powder feeders or separate feeding of reinforcements and matrix should be studied. In abrasion wear studies reliable ranking of MMCs based on volume losses was difficult. In order to get more accurate volume losses, the whole surface of the wear test specimen should be scanned before and after the test with some fast surface profiler equipped with software calculating volume losses. It is largely argued whether the results of rubber wheel abrasion tests can be utilized when selecting materials to real wear conditions. For this reason laser coatings should also be subjected to more realistic abrasion wear conditions, which would include more impact or some harder support for abrasives than just rubber. From the point of view of development of abrasion wear resistant laser coatings, SHS (Ti, Mo)C powders should be prepared in tool steel matrix, laser clad and tested in various wear conditions.

Due to high power densities and local heat input characteristics for laser cladding and unfavourable CTE mismatch, large tensile residual stresses evolve in the coating layer during cooling. It should be studied to what extent these tensile residual stresses could be diminished by subsequent stress-relief annealing in cases where $CTE_c > CTE_s$. Low- and high-cycle fatigue tests (axial, bending, torsion) should be also carried out on moderately large components, where the fraction of coating and HAZ is not too high with respect to base material to resemble more realistic conditions. These tests should be done to check the influence of tensile residual stresses, possible structural discontinuities, hardened HAZ and associated reduced ductility on fatigue endurance of laser clad component.

From the processing and the development of laser cladding process point of view, wide rectangular spot geometry characteristics for direct HPDL should be utilized in strip feeding as reported in section 1.2.2.3. Productivity could be increased further by introducing resistive or inductive heating on strip consumable. As the productivity is largely dependent on delivered laser power, the applicability of very powerful (~30 kW) fiber lasers should be examined in various cladding situations and develop powder, wire and strip feeding nozzles which resist high temperatures.

7 REFERENCES

[1] Davis, J. R., *Surface engineering for corrosion and wear resistance*, 2001 Woodhead Publishing, ISBN: 0871707004

[2] Schmidt, A. O., *Tools and engineering materials with hard, wear-resistant infusions*, Journal of Engineering for Industry, August 1969, 549-552

[3] Ion, J. C., *Laser processing of engineering materials – principles, procedure and industrial application*, Elsevier Butterworth-Heinemann, Oxford, UK, 2005

[4] Matthews, S. J., *Laser fusing of hardfacing alloy powders*, Lasers in Materials Processing, Conference Proceedings, Edited by E. A. Metzbower, ASM, Ohio, USA, 1983, 138-148

[5] MacIntyre, R. M., *Laser hardfacing of RB211 turbine blade shroud interlocks*, Applications of Lasers in Material Processing, ASM Conference, Los Angeles, 24-26th January, 1983, 230-

[6] Eboo, G. M. and Lindemanis, A. E., *Advances in laser cladding process technology*, ICALEO´83, SPIE Vol. 527, Applications of High Power Lasers, 1985, 86-94

[7] Alam, N. and Ion, J. C., *Extending life of components by laser beam cladding*, Australasian Welding Journal 47 (2002), 26-27

[8] Merchant, V., *The slow industrial acceptance of laser cladding*, Industrial Laser Solutions, June 2002

[9] Archambeault, J. and Dubourg, L., *Scientific and technological landscape of laser cladding: A bibliometric analysis of patents and publications*, CD-ROM Proceedings of ICALEO2005; 24th International Congress on Applications of Lasers & Electro-optics, Laser Institute of America, November 2005, Miami, FLA, USA

[10] Bachmann, F. and Takahashi, R., *Chances and limitations of high power diode lasers – Results of research and development in Germany*, The Review of Laser Engineering 31 (2003) 5, 313-317

[11] Brandt, M., Harris, J., Sun, S., Dempster, B., Alam, N. and Bishop, A., *In-situ cladding of leading edge of LP turbine blades using fibre delivered diode laser*, CD-ROM Proceedings of ICALEO2005; 24th International Congress on Applications of Lasers & Electro-optics, Laser Institute of America, November 2005, Miami, FLA, USA

[12] Verhaeghe, G., *The fiber laser – A newcomer for material welding and cutting*, Welding Journal, August 2005, 56-60

[13] Tucker, T. R., Clauer, A. H., Wright, I. G. and Stropki, J. T., *Laser-processed composite metal cladding for slurry erosion resistance*, Thin Solid Films 118 (1984), 73-84

[14] Kauppila, J., *Stelliittipinnoitus laserilla*, M.Sc. Thesis, 1988, Lappeenranta University of Technology, Lappeenranta, Finland

[15] Hinse-Stern, A., Burchards, D. and Mordike, B. L., *Laser cladding with preheated wires*, European Conference on Laser Treatment of Materials (ECLAT'92), edited by B. L. Mordike, 223–228

[16] Nowotny, S, Richter, A. and Beyer, E., *Laser cladding using high-power diode lasers*, Proceedings of ICALEO'98, 17th International Congress on Applications of Lasers and Electro-Optics, Laser Institute of America, November 1998, Orlando, FLA, USA, G68–G74

[17] Cederberg, M. and Ainasoja, E., *Laserpinnoitus kunnossapidon apuvälineenä*, Hitsaustekniikka 5 (2000), 15-18

[18] Schneider, M., *Laser cladding with powder – effect of some machining parameters on clad properties*, Ph.D. Thesis, University of Twente, The Netherlands, 1998, ISBN 9036510988

[19] Powell, J., Henry, P. S. and Steen, W. M., *Laser cladding with preplaced powder: analysis of thermal cycling and dilution effects*, Surface Engineering 4 (1988) 2, 141-149

[20] Gedda, H., *Laser cladding: An experimental and theoretical investigation*, Doctoral Thesis, Luleå University of Technology, Sweden, 2004

[21] Hirose, A. and Kobayashi, K. F., *Formation of hybrid clad layers by laser processing*, ISIJ International 35 (1995) 6, 757-763

[22] Hoadley, A. F. A., Frenk, A. and Marsden, C. F., *A process overview of laser hardfacing*, Surface Engineering, Processes and Applications (USA) 1995, 171-186

[23] Steen W. M., *Laser material processing*, 3rd edition, Springer-Verlag London Limited, 2003

[24] Gedda, H., Kaplan, A. and Powell, J., *Melt-solid interactions in laser cladding and laser casting*, Metallurgical and Materials Transactions 36B (2005), 683-689

[25] Mazumder, J. and Li, L. J., *A study of mechanism of laser cladding processes*", Report of the College of Engineering, University of Illinois, No. UILI-Eng 84-3610/110, July 1984

[26] Fujimagari, H., Hagiwara, M. and Kojima, T., *Laser cladding technology to small diameter pipes*, Nuclear Engineering and Design 195 (2000), 289-298

[27] Bruck, G. J., *High-power laser beam cladding*, Journal of Metals, February 1987, 10-13

[28] Volz, R., Reichelt, U., Wolf, S., Pei, Y. T. and Zuo, T. C., *Laser processing of aluminium automobile parts with powder technologies*, Proceedings of the 30th ISATA: Rapid prototyping/laser applications in the automotive industries, Croydon, England: Automotive Automation Ltd., edited by D. Roller, 1997, 393-400

[29] Weerasinghe, V. M. and Steen, W. M., *Computer simulation model laser cladding*, Transport Phenomena in Materials Processing, 1983, 15-23

[30] Picasso, M., Marsden, C. F., Wagniere, J. D., Frenk, A. and Rappaz, M., *A simple but realistic model for laser cladding*, Metallurgical and Materials Transactions 25B (1994), 281–291

[31] Lalas, C., Tsirbas, K., Salonitis, K. and Chryssolouris, G., *An analytical model of the laser clad geometry*, International Journal of Advanced Manufacturing Technology 32 (2007), 34-41

[32] Hoadley, A. F. A. and Rappaz, M., *A Thermal Model of Laser Cladding by Powder Injection*, Metallurgical Transactions 23B (1992), 631-642

[33] Li, W. B., Engström, H., Powell, J., Tan, Z. and Magnusson, C., *Modelling of the laser cladding process - Preheating of the blown powder material*, Lasers in Engineering 4 (1995), 329-341

[34] Lin, J., *Temperature analysis of the powder streams in coaxial laser cladding*, Optics and Laser Technology 31 (1999) 8, 565-570

[35] Pinkerton, A. J., and Li, L., *Rapid prototyping using direct laser deposition - the effect of powder atomisation type and flow rate*, Proceedings of the Institution of Mechanical Engineers, Part B: Journal of Engineering Manufacture 217 (2003) 6, 741-752

[36] Liu, C. Y. and Lin, J., *Thermal processes of a powder particle in coaxial laser cladding*, Optics and Laser Technology 35 (2003) 2, 81-86

[37] Chivel, Yu. A., *Cone-shaped beams in selective laser cladding*, Technical Physics Letters 31 (2005) 1, 1–3

[38] Becker, R. and Sepold, G., *Micro-coating by a laser powder feed process*, Advanced Powder Technology 2 (1991) 3, 181–189

[39] Burbaum, B., Albus, P. and Kelbassa, I., *Laser cladding of mesh structures on HPT liner and NGV parts*, oral presentation in ICALEO2008, 27th International Congress on Applications of Lasers & Electro-optics, Laser Institute of America, October 2008 Temecula, CA, USA

[40] Weerasinghe, V. M. and Steen, W. M., *Laser cladding with pneumatic powder delivery*, Applied Laser Tooling, ISBN 90-247-3486-X, edited by Soares, O. D. D., Perez-Amor, M., 1987, Martinus Nijhoff Publishers, Dordrecht, Netherlands, 183-211

[41] Weerasinghe, V. M. and Steen, W. M., *Laser cladding with blown powder*, Metal Construction, October 1987, 581-585

[42] Haferkamp, H., Schmidt, H., Gerken, J. and Püster, T., *Application of laser powder cladding and the risk of residual powder*, ECLAT´94, 475-483

[43] Wiklund, G. and Flinkfeldt, J., *Laserpåsvetsning kombinerad med MIG-utrustning*, Teknisk rapport 09/1997, Luleå Tekniska Universitet, ISSN: 1402-1536, ISRN: LTU-TR—97/09--SE

[44] Syed, W. U. H. and Li, L., *Effects of wire feeding direction and location in multiple layer diode laser direct metal deposition*, Applied Surface Science 248 (2005), 518-524

[45] Yelistratov, A. and Sciammarella, F., *Laser surfacing with wire feeding*, Welding Journal, December 2005, 36–39

[46] Haemers, T. A. M., Rickerby, D. G., Lanza, F., Geiger, F. and Mittemeijer, E .J., *Hardfacing of stainless steel with laser melted colmonoy*, Journal of Materials Science 35 (2000), 5691-5698

[47] Haemers, T. A. M., Rickerby, D. G., Lanza, F., Geiger, F. and Mittemeijer, E. J., *Laser cladding of stainless steel with Hastelloy*, Advanced Engineering Materials 3 2001 4, 242-245

[48] Kim, J. D., Kang, K. H. and Kim, J. N., *Nd:YAG laser cladding of marine propeller with Hastelloy C-22*, Applied Physics A79 (2004), 1583-1585

[49] Kim, J.-D. and Peng, Y., *Plunging method for Nd:YAG laser cladding with wire feeding,* Optics and Lasers in Engineering 33 (2000), 299-309

[50] Xue, L., Chen, J. Y., Hyatt, C. V. and Islam, M., *Laser Cladding with Continuous Ni-Al Bronze Wire Feeding for Repairing Marine Components*, Proceedings of ICALEO'99, 18th International Congress on Applications of Lasers and Electro-Optics, Laser Institute of America, November 1999, San Diego, CA, USA, F58-F67

[51] Adak, B., Nash, P., Chen, D. and Swiglo, A., *Microstructural characterization of laser cladding of Cu-30Ni*, Journal of Materials Science 40 (2005), 2051-2054

[52] Syed, W. U. H., Pinkerton, A. J. and Li, L., *Combining wire and coaxial powder feeding in laser direct metal deposition for rapid prototyping,* Applied Surface Science 252 (2006), 4803-4808

[53] Wang, F., Mei, J., Jiang, H. and Wu, X., *Laser fabrication of Ti6Al4V/TiC composites using simultaneous powder and wire feed,* Materials Science and Engineering A 445-446 (2007), 461-466

[54] Yelistratov, A., *Direct diode laser deposition with strip feeding*, Penton´s Welding Magazine 10/26/2006, http://www.weldingmag.com

[55] Luft, A., Löschau, W., Juch, K., Gassmann, R., Fux, V. and Reitzenstein, W., *Microstructures and Properties of Surface Layers Produced on Steels by Different*

Laser Melting Techniques, European Conference on Laser Treatment of Materials (ECLAT'92), edited by B. L. Mordike, 205-210

[56] Malin, V., Johnson, R. N. and Sciammarella, F. M., *Laser cladding helps refurbish US Navy ship components*, The AMPTIAC Quaterly 8 (2004) 3, 3-9

[57] Bouaifi, B. and Bartzsch, J., *Surface protection by laser beam deposition with hot wire addition*, Welding and Cutting 4/1993, E70–E72

[58] Nurminen, J., Riihimäki, J., Näkki, J. and Vuoristo, P., *Comparison of laser cladding with powder and hot and cold wire techniques*, CD-ROM Proceedings of ICALEO2006, 25th International Congress on Applications of Lasers and Electro-Optics, Laser Institute of America, October 2006, Scottsdale, AZ, USA

[59] Nurminen, J., Riihimäki, J., Näkki, J. and Vuoristo, P., *Hot-wire cladding process studies*, CD-ROM Proceedings of ICALEO2007, 26th International Congress on Applications of Lasers and Electro-Optics, Laser Institute of America, October 2007, Orlando, FLA, USA

[60] Beyer, E., Brenner, B. and Nowotny, S., *Overview of hybrid technology*, CD-ROM Proceedings of PICALO2004, 1st International Conference on Applications of Lasers and Optics, April 2004, Melbourne Australia

[61] Wetzig, A., Brenner, B., Fux, V. and Beyer, E., *Induction assisted laser-cladding a new and effective method for producing high wear resistant coatings on steel components*, Proceedings of ICALEO'98; 17th International Congress on Applications of Lasers & Electro-optics, Laser Institute of America, November 1998, Orlando, FLA, USA, D20-D28

[62] Theiler, C., Seefeld, T. and Sepold, G., *Deposition of graded metal matrix composites by laser beam cladding*, www.bias.uni-bremen.de

[63] Wilden, J., Bergmann, J, P. and Dolles, M., *Use of electromagnetic induced forces for active forming of coating geometry*, CD-ROM Proceedings of PICALO2006, 2nd International Conference on Applications of Lasers and Optics, April 2006, Melbourne Australia

[64] Velde, O., Techel, A. and Grundmann, R., *Suppression of the development of pores during laser-induced surface dispersion of TiC into aluminium, by means of a static magnetic field*, Surface and Coatings Technology 150 (2002), 170-176

[65] Eguchi, N., Zhou, Z., Shirasawa, H. and Ohmori, A., *NiCrAlY coating in YAG laser combined low pressure plasma spraying*, Proceedings of the 15th International Thermal Spray Conference (ITSC), 25-29 May 1998, Nice, France, 1517-1522

[66] Zieris, R., Nowotny, S., Berger, L.-M., Haubold, L. and Beyer, E., *Characterization of coatings deposited by laser-assisted atmospheric plasma spraying*, CD-ROM Proceedings of ITSC 2003, International Thermal Spray Conference, May 2003, Orlando, FLA, USA

[67] Suutala, J., Tuominen, J. and Vuoristo, P., *Laser-assisted spraying and laser treatment of thermally sprayed coatings*, Surface and Coatings Technology 201 (2006), 1981-1987

[68] Zhou, Z., Eguchi, N., Shirasawa, H. and Ohmori, A., *Microstructure and characterization of zirconia-yttria coatings formed in laser and hybrid spray process*, Journal of Thermal Spray Technology 8 (1999) 3, 405-413

[69] Montavon, G. and Coddet, C., *Modification of ceramic thermal spray deposit microstructure implementing laser treatment*, Thermal Spray 2001: New surfaces for a New Millennium, (Ed.) C. C. Berndt, K. A. Khor and E. F. Lugscheider, Published by ASM International, Materials Park, Ohio, USA, 2001, 1195-1202

[70] Ouyang, J. H. and Sasaki, S., *Microstructure and tribological characteristics of ZrO_2-Y_2O_3 ceramic coatings deposited by laser-assisted plasma hybrid spraying*, Tribology International 35 (2002), 255-264

[71] Antou, G., Montavon, G., Hlawka, F., Cornet, A., Coddet, C. and Machi, F., *Modification of ceramic thermal spray deposit microstructures implementing in situ laser remelting*, Surface and Coatings Technology 172 (2003), 279-290

[72] Li, L. and Steen, W. M., *A dual-frequence electromagnetic sensor for non-contact dilution evaluation in laser cladding and alloying processes*, Measuring Science and Technology 7 (1996), 650-660

[73] Ollier, B., Pirch, N. and Kreutz, E. W., *A numerical model of the one-step laser cladding process*, Laser und Optoelektronik 27 (1995) 1, 63-70

[74] Pelletier, J. M., Sahour, M. C., Pilloz, M. and Vannes, A. B., *Influence of processing conditions on geometrical features of laser claddings obtained by powder injection*, Journal of Materials Science 28 (1993), 5184-5188

[75] Watkins, K. G., *Laser cladding*, Course material of University of Liverpool, February 2001

[76] Komvopoulos, K. and Nagarathnam, K., *Processing and characterization of laser-cladded coating materials*, Journal of Engineering Materials and Technology 112 (1990), 131-143

[77] Qian, M., Lim, L. C., Chen, Z. D. and Chen, W. L., *Parametric studies of laser cladding processes*, Journal of Materials Processing Technology 63 (1997), 590-593

[78] Navas, C., Conde, A., Fernandez, B. J., Zubiri, F. and de Damborenea, J., *Laser coatings to improve wear resistance of mould steel*, Surface & Coatings Technology 194 (2005), 136-142

[79] Tuominen, J., Hayhurst, P., Eronen, V., Vuoristo, P. and Mäntylä, T., *Comparison of multi-feed and off-axis high power diode laser (HPDL) cladding*, CD-ROM Proceedings of Photonics West 2003, SPIE, January 2003, San Jose Convention Center, San Jose, CA, USA

[80] Seefeld, T., Theiler, C. and Sepold, G., *Laser beam cladding at high processing speed*, www.bias.uni-bremen.de

[81] Frenk, A. and Kurz, W., *High speed laser cladding: solidification conditions and microstructure of a cobalt-based alloy*, Materials Science and Engineering A173 (1993), 339-342

[82] de Damborenea, J. and Vazquez, A. J., *Laser cladding of high-temperature coatings*, Journal of Materials Science 28 (1993), 4775-4780

[83] Oliveira, de U., Ocelik, V. and De Hosson, J. Th. M., *Analysis of coaxial laser cladding processing conditions*, Surface & Coatings Technology 197 (2005), 127-136

[84] Kaplan, A. F. H. and Groboth, G., *Process analysis of laser beam cladding*, Trans. ASME: J. Manufacturing Sci. Eng. 123 (2001), 609-614

[85] Hu, Y. P., Chen, C. W. and Mukherjee, K., *Innovative laser-aided manufacturing of patterned stamping and cutting dies: processing parameters*, Materials and Manufacturing Processes 13 (1998) 3, 369-387

[86] Zhao, G., Cho, C. and Kim, J. -D., *Application of 3-D finite element method using Lagrangian formulation to dilution control in laser cladding*, International Journal of Mechanical Sciences 45 (2003) 5, 777-796

[87] Picasso, M. and Rappaz, M., *Laser-powder-material interactions in the laser cladding process*, Journal de Physique IV 4 (1994), C4-27 - C4-33

[88] Picasso, M. and Hoadley, A. F. A., *Finite element simulation of laser surface treatments including convection in the melt pool,* Int. J. Num. Meth. Heat Fluid Flow 4 (1994), 61-83

[89] Lepski, D., Eichler, H., Fux, V., Scharek, S. and Beyer, E., *Simulation of the powder injection laser beam cladding process*, 3rd International Conference "THE" Coatings in Manufacturing and Engineering, Thessaloniki, Greece, 2002

[90] Han, L., Liou, F. W. and Phatak, K. M., *Modeling of laser cladding with powder injection*, Metallurgical and Materials Transactions B 35B (2004), 1139-1150

[91] Lepski, D., Eichler, H., Scharek, S., Fux, V., Nowotny, S. and Beyer, E., *Simulation of laser beam cladding by powder injection*, Proceedings of the Second International WLT-Conference on Lasers in Manufacturing 2003, Munich, June 2003

[92] Lepski, D., Eichler, H., Fux, V., Scharek, S. and Beyer, E., *Calculating temperature field and single track bead shape in laser cladding with Marangoni flow using Rosenthal´s solution*, Lasers in Manufacturing 2001, Munich, June 2001, 167-177

[93] Cho, C., Zhao, G., Kwak, S. and Kim, C. B., *Computational mechanics of laser cladding process*, Journal of Materials Processing Technology 153-154 (2004), 494-500

[94] Martukanitz, R. P. and Babu, S. S., *Materials modeling for advanced coatings systems*, CD-ROM Proceedings of ICALEO2002; 21st International Congress on Applications of Lasers & Electro-optics, Laser Institute of America, October 2002, Scottsdale, AZ, USA

[95] Babu, S. S., Martukanitz, R. P., Parks, K. D. and David, S. A., *Towards prediction of microstructural evolution during laser surface alloying*, Metallurgical and Materials Transactions A 33A (2002), 1189-1200

[96] Miyamoto, I., Fujimori, S. and Itakura, K., *Mechanism of dilution in laser cladding with powder feeding*, Proceedings of ICALEO'97; 16th International Congress on Applications of Lasers & Electro-optics, Laser Institute of America, November 1997, San Diego, CA, USA, F1-F10

[97] Marsden, C. F., Frenk, A. and Wagniere, J.-D., *Power absorption during the laser cladding process*, European Conference on Laser Treatment of Materials (ECLAT'92), Edited by B.L. Mordike, DGM Informationsgesellschaft mbH, 1992, p. 375-380

[98] Frenk, A., Vandyoussefi, M., Wagniere, J.-D., Zryd, A. and Kurz, W., *Analysis of the laser-cladding process for Stellite on steel*, Metallurgical and Materials Transactions 28B (1997), 501-508

[99] Ollier, B., Pirch, N., Kreutz, E. W. and Schlüter, H., *Cladding with laser radiation: properties and analysis*, European Conference on Laser Treatment of Materials (ECLAT'92), Edited by B.L. Mordike, DGM Informationsgesellschaft mbH, 1992, 687-692

[100] Gutu, I., Petre, C., Mihailescu, I. N., Taca, M., Alexandrescu, E. and Ivanov, I., *Surface treatment with linearly polarized laser beam at oblique incidence*, Optics & Laser Technology 34 (2002), 381-388

[101] Bloehs, W., Grünenwald, B., Dausinger, F. and Hügel, H., *Recent progress in laser surface treatment: I. Implications of laser wavelength*, Journal of Laser Applications 8 (1996), 15-23

[102] Dausinger, F. and Shen, J., *Energy coupling efficiency in laser surface treatment*, ISIJ International 33 (1993) 9, 925-933

[103] Kou, S., *Welding Metallurgy – Second Edition*, a John Wiley & Sons, Inc., Publication, 2003, ISBN 0-471-43491-4

[104] Partes, K., Seefeld, T., Sepold, G. and Vollertsen, F., *High efficiency laser cladding at elevated processing speed*, CD-ROM Proceedings of ICALEO2005; 24th International Congress on Applications of Lasers & Electro-optics, Laser Institute of America, November 2005, Miami, FLA, USA

[105] Sears, J., *Measuring laser absorption coefficient during laser additive manufacturing of 316L stainless steel and Ti-6V-4Al alloys*, CD-ROM Proceedings of ICALEO2007, 26th International Congress on Applications of Lasers and Electro-Optics, Laser Institute of America, October 2007, Orlando, FLA, USA

[106] Li, Y., Liu, Y., Geng, H. and Nie, D., *Synthesis and cladding of Ni_3Al intermetallic on steel substrate by laser controlled reactive synthesis*, Journal of Materials Processing Technology 171 (2006), 405-410

[107] Department of Trade and Industry, *Wear Resistant Surfaces in Engineering – a guide to their production, properties and selection*, London, Her Majesty's Stationery Office, Crown copyright 1986, ISBN 0 11 513826 9, 142-160

[108] Sallamand, P. and Pelletier, J. M., *Laser cladding on aluminium-base alloys: microstructural features*, Materials Science and Engineering A171 (1993), 263-270

[109] Pelletier, J. M., Sallamand, P. and Criqui, B., *Microstructure and mechanical properties of some metal matrix composites produced on different materials by laser cladding*, Lasers in Engineering 3 (1994), 15-27

[110] Salehi, D. and Brandt, M., *Melt pool temperature control using LabVIEW in Nd:YAG laser blown powder cladding process*, Int. J. Adv. Manuf. Technol. (2006) 29, 273-278

[111] Doubenskaia, M., Bertrand, Ph. and Smurov, I., *Optical monitoring of Nd:YAG laser cladding*, Thin Solid Films 453-454 (2004), 477-485

[112] Bi, G., Gasser, A., Wissenbach, K. and Poprawe, R., *Temperature measurement and its application for monitoring and control in laser cladding*, Proceedings of the 3rd International WLT-Conference on Lasers in Manufacturing 2005, 143-148

[113] Bloehs, W., Grünenwald, B., Dausinger, F. and Hügel, H., *Recent progress in laser surface treatment: II. Adopted processing for high efficiency and quality*, Journal of Laser Applications 8 (1996), 65-77

[114] Salehi, D., Brandt, M., Kogel-Hollacher, M. and Schmid, J., *Fundamental investigations on process monitoring in the laser cladding process*, CD-ROM Proceedings of ICALEO2002; 21st International Congress on Applications of Lasers & Electro-optics, Laser Institute of America, October 2002, Scottsdale, AZ, USA

[115] Sun, S., Durandet, Y. and Brandt, M., *Correlation between melt pool temperature and clad formation in pulsed and continuous wave Nd:YAG laser cladding of Stellite 6*, CD-ROM Proceedings of PICALO2004, 1st International Conference on Applications of Lasers and Optics, April 2004, Melbourne Australia

[116] Grünenwald, B., Shen, J., Dausinger, F. and Hügel, H., *Laser cladding with composite powders using pyrometric temperature control and beam combining*, Proc. 26th ISATA, Aachen, 13-17 Sebtember 1993, 287-294

[117] Hu, D. and Kovacevic, R., *Finite element modelling of thermal behavior of molten pool in closed-loop controlled laser-based additive manufacturing*, CD-ROM Proceedings of ICALEO2002; 21st International Congress on Applications of Lasers & Electro-optics, Laser Institute of America, October 2002, Scottsdale, AZ, USA

[118] Sexton, C. L., Byrne, G. and Watkins, K. G., *Alloy development by laser cladding: An overview*, Journal of Laser Applications 13 (2001) 1, 2-11

[119] Brennan, M. S. and Gassmann, R. C., *Laser cladding of nickel and iron base alloys on boiler waterwall panels and tubes,* Corrosion 2000, Paper 00235/1-00235/10

[120] Fernandez, E., Garcia, J. R., Cuetos, J. M. and Higuera, V., *Behaviour of laser treated Cr, Ni coatings in the oxidative atmosphere of a steam boiler*, Surface & Coatings Technology 195 (2005), 1-7

[121] Coulon, P. A., Com-Nougue, J., Kerrand, E. and Thauvin, G., *Characterisation and wear resistance of cobalt base coatings deposited by CO_2 laser on steam turbine components*, European Conference on Laser Treatment of Materials (ECLAT'92), edited by B. L. Mordike, 181–186

[122] Kathuria, Y. P., *Some aspects of laser surface cladding in the turbine industry*, Surface and Coatings Technology 132 (2000), 262-269

[123] Jendrzejewski, R., Conde, A., de Damborenea, J. and Sliwinski, G., *Characterization of the laser-clad stellite layers for protective coatings*, Materials and Design 23 (2002), 83-88

[124] Sun, S., Durandet, Y. and Brandt, M., *Parametric investigation of pulsed Nd:YAG laser cladding of stellite 6 on stainless steel*, Surface & Coatings Technology 194 (2005), 225-231

[125] Duraiselvam, M., Galun, R., Wesling, V., Mordike, B. L., Reiter, R. and Oligmüller, J., *Cavitation erosion resistance of AISI 420 martensitic stainless steel laser-clad with nickel aluminide intermetallic composites and matrix composites with TiC reinforcement*, Surface and Coatings Technology 201 (2006), 1289-1295

[126] Lo, K. H., Cheng, F. T. and Man, H. C., *Laser transformation hardening of AISI 440C martensitic stainless steel for higher cavitation erosion resistance*, Surface and Coatings Technology 173 (2003), 96-104

[127] Kim, T. H. and Kim, B. C., *Chromium carbide laser-beam surface-alloying treatment on stainless steel*, Journal of Materials Science 27 (1992), 2967-2973

[128] Zhang, D., Lei, T. C. and Li, F. J., *Laser cladding of stainless steel with Ni-Cr_3C_2 for improved wear performance*, Wear 251 (2001), 1372-1376

[129] Ernst, G., Lüftenegger, A. and Ebner, R., *New laser reinforcement and refurbishing concepts for dies on the way to series application*, 5th Int. Conf. on Tooling (Tool steel in the next century), University of Leoben, Austria, 1999, 437-446

[130] Wang, S. H., Chen, J. Y. and Xue, L., *A study of the abrasive wear behaviour of laser-clad tool steel coatings*, Surface & Coatings Technology 200 (2006), 3446-3458

[131] Zhang, Y., Cherng, T. C., Yuan, X. and Zeng, X., *Wear and impact resistance of laser cladding steel for die cutting application*, Proceedings of ICALEO'97, 16th International Congress on Applications of Lasers & Electro-optics, Laser Institute of America, November 1997, San Diego, CA, USA, F138-F147

[132] Pirzada, D., Baburaj, E. G., Govindaraju, R. and Froes, F. H., *Laser surface coating of TiC on H13 die steel: effects on corrosion and erosion behaviour,* Surface Engineering 16 (2000) 2, 164-168

[133] Jiang, W. and Molian, P., *Nanocrystalline TiC powder alloying and glazing of H13 steel using a CO_2 laser for improved life of die-casting dies*, Surface and Coatings Technology 135 (2001), 139–149

[134] Shah, S. V. and Dahotre, N. B., *Laser-surface engineered vanadium carbide coating for extended die life*, Journal of Materials Processing Technology 124 (2002), 105-112

[135] Wiklund, G. and Kaplan, A., *Laser cladding of cast iron using 12 kW CO_2-laser combined with induction heating*, Proceedings of the 10th Nordic Laser Materials Processing Conference (NOLAMP), Luleå, Sweden, 2005, 217-224

[136] Park, H. I., Nakata, K. and Tomida, S., *In situ formation of TiC particulate composite layer on cast iron by laser alloying of thermal sprayed titanium coating*, Journal of Materials Science 35 (2000), 747-755

[137] Zhong, M., Liu, W., Li, F., Yang, L. and He, J., *Corrosion and wear resistance characteristics of laser alloyed NiCr coating on cast iron liner*, CD-ROM Proceedings of PICALO2004, 1st International Conference on Applications of Lasers and Optics, April 2004, Melbourne Australia

[138] Stanford, M. K. and Jain, V. K., *Friction and wear characteristics of hard coatings*, Wear 251 (2001), 990-996

[139] Yang, X., Zhong, M., Zheng, T. and Zhang, N., *Novel reduced-friction materials by laser cladding of copper alloy on cast iron*, Journal of Materials Science and Technology 9 (1993), 248-252

[140] Dubourg, L., Pelletier, H., Vaissiere, D., Hlawka, F. and Cornet, A., *Mechanical characterisation of laser surface alloyed aluminium-copper systems*, Wear 253 (2002), 1077-1085

[141] Almeida, A., Petrov, P., Nogueira, I. and Vilar, R., *Structure and properties of Al-Nb alloys produced by laser surface alloying*, Materials Science and Engineering A303 (2001), 273-280

[142] Kawasaki, M., Takase, K., Kato, S., Nakagawa, M. and Mori, K., *Development of engine valve seats directly deposited onto aluminum cylinder head by laser cladding process*, SAE Technical Paper Series 920571, International Congress & Exposition, Detroit, Michigan, USA, February 24-28, 1992, 1-15

[143] Matsuyama, H., Kano, M., Shibata, K. and Ninomiya, R., *Process and materials development for laser cladding valve seats on aluminium engine heads*, Proceedings of Global PowerTrain Conference GPC'99, 1999, 56-64

[144] Palumbo, G., Pinto, S. and Tricarico, L., *Numerical finite element investigation on laser cladding treatment of ring geometries*, Journal of Materials Processing Technology 155-156 (2004), 1443-1450

[145] Tomida, S., Nakata, K., Saji, S. and Kubo, T., *Formation of metal matrix composite layer on aluminum alloy with TiC-Cu powder by laser surface alloying process*, Surface and Coatings Technology 142-144 (2001), 585–589

[146] Ayers, J. D., *Wear behaviour of carbide-injected titanium and aluminum alloys*, Wear 97 (1984), 249-266

[147] Vreeling, J. A., *Laser Melt Injection of Ceramic Particles in Metals*, Ph.D. Thesis, 2001, Groningen University, Netherlands

[148] Ocelik, V., Matthews, D. and De Hosson, J. Th. M., *Sliding wear resistance of metal matrix composite layers prepared by high power laser*, Surface & Coatings Technology 197 (2005), 303-315

[149] Wang, A. H., Xie, C. S. and Nie, J. H., *Bond strength of a laser-clad iron-base alloy coating on Al-Si alloy substrate and its fracture behaviour*, Materials Characterization 47 (2001), 1-7

[150] Anandkumar, R., Colaco, R., Ocelik, V., De Hosson, J. Th. M. and Vilar, R., *Microstructure and abrasive wear studies of laser clad Al-Si/SiC composite coatings*, Materials Science Forum Vols. 537-538 (2007), 89-95

[151] Ghosh, K., McCay, M. H. and Dahotre, N. B., *Formation of a wear resistant surface on Al by laser aided in-situ synthesis of $MoSi_2$*, Journal of Materials Processing Technology 88 (1999), 169-179

[152] Durandet, Y., Kallage, P. and Brandt, M., *Control of dilution during laser cladding of Al 7075 substrates with Al-12Si aluminium alloy powder*, CD-ROM Proceedings of

PICALO2004, 1st International Conference on Applications of Lasers and Optics, April 2004, Melbourne Australia

[153] Meinert, K. C. and Bergan, P., *Refurbishment of Aluminum Alloys by Laser Cladding*, Proceedings of ICALEO'99, 18th International Congress on Applications of Lasers & Electro-optics, Laser Institute of America, November 1999, San Diego, CA, USA, F49-F57

[154] Hoebel, M., Fehrmann, B. and Schnell, A., *Robot guided laser repair of single crystal turbine blades*, Power-Gen Europe 2003, 6-8 May 2003, Düsseldorf, Germany, 1-17

[155] Gäumann, M., Henry, S., Cleton, F., Wagniere, J. D. and Kurz, W., *Epitaxial laser metal forming: analysis of microstructure formation*, Materials Science and Engineering A 271 (1999), 232-241

[156] Keutgen, S., Backes, G. M., Kreutz, E. W., Pirch, N., Krause, S. and Poprawe, R., *The Production of Layers Made of Inconel 738LC by Cladding with Nd:YAG Laser Radiation*, Proceedings of ICALEO2001, 20th International Congress on Applications of Lasers & Electro-Optics, Laser Institute of America, October 2001, Jacksonville, FLA, USA, 603-612

[157] Galvan, D., Ocelik, V., Pei, Y., Kooi, B. J. and De Hosson, J. T. M., *Microstructure and properties of TiB/Ti6Al4V coatings produced with laser treatments,* Proceedings of the 22nd Heat Treating Society Conference and the 2nd International Surface Engineering Congress, 15-17 September 2003, Indianapolis, Indiana, USA, 411-418

[158] Kloosterman, A. B., *Surface Modification of Titanium with Lasers*, Ph.D. Thesis, Groningen University, Netherlands, 1998

[159] Kelbassa, I., Gasser, A. and Wissenbach, K., *Laser cladding as a repair technique for blisks out of titanium and nickel base alloys used in aero engines*, CD-ROM Proceedings of PICALO2004, 1st International Conference on Applications of Lasers and Optics, April 2004, Melbourne Australia

[160] Nowotny, S., Scharek, S., Beyer, E. and Richter, K. H., *Laser beam build-up welding: precision in repair, surface cladding, and direct 3D metal deposition*, Journal of Thermal Spray Technology 16 (2007) 3, 344-348

[161] ASM Metals Reference Book, 3rd Edition, Editor M. Bauccio, 1993, ASM International, Materials Park, OH, ISBN 0-87170-478-1

[162] Yue, T. M., Mei, H. and Man, H. C., *Improvement of the corrosion resistance of magnesium ZM51 / SiC composite by laser cladding*, Journal of Materials Science Letters 20, 2001, 1479-1482

[163] Dutta Majumdar, J. D., Chandra, B. R., Galun, R., Mordike, B. L. and Manna, I., *Laser surface engineering of a magnesium alloy with $Al+Al_2O_3$*, Surface and Coatings Technology 179 (2004) 297-305

[164] Yang, Y., Hu, J. D., Wang, H. Y., Liu, S. Y., Li, Y. X. and Guo, Z. X., *Laser (Nd:YAG) cladding of AZ91D magnesium alloys with Al+Ti+C nanopowders*, Lasers in Engineering 16 (2006), 9-17

[165] Jun, Y., Sun, G. P., Wang, H. Y., Jia, S. Q. and Jia, S. S., *Laser (Nd:YAG) cladding of AZ91D magnesium alloys with $Al+Si+Al_2O_3$*, Journal of Alloys and Compounds 407 (2006), 201-207

[166] Lindroos, V., Sulonen, M. ja Veistinen, M., *Uudistettu Miekk'ojan metallioppi*, Kustannusosakeyhtiö Otava, 1986, ISBN 951-666-216-1

[167] Yue, T. M., Hu, Q. W., Mei, Z. and Man, H. C., *Laser cladding of stainless steel on magnesium ZK60/SiC composite*, Materials Letters 47 (2001), 165-170

[168] Dutta Majumdar, J. D., Chandra, B. R., Galun, R., Mordike, B. L. and Manna, I., *Laser composite surfacing of a magnesium alloy with silicon carbide*, Composites Science and Technology, Volume 63, 2003, 771-778

[169] Dutta Majumdar, J., Galun, R., Mordike, B. L., Ramesh Chandra, B. and Manna, I., *Laser composite surfacing of a magnesium alloy with chromium carbide*, Lasers in Engineering 16 (2006), 349-359

[170] Dehm, G., Medres, B., Shepeleva, L., Scheu, C., Bamberger, M., Mordike, B. L., Mordike, S., Ryk, G., Halperin, G. and Etsion, I., *Microstructure and tribological properties of Ni-based claddings on Cu substrates*, Wear 225-229 (1999), 18-26

[171] Leong, C. C., Lu, L., Fuh, Y. H. and Wong, Y. S., *In-situ formation of copper matrix composites by laser sintering*, Materials Science and Engineering A 338 (2002), 81-88

[172] Tam, K. F., Cheng, F. T. and Man, H. C., *Laser surfacing of brass with Ni-Cr-Al-Mo-Fe using various laser processing parameters*, Materials Science and Engineering A325 (2002), 365-374

[173] Tam, K. F., Cheng, F. T. and Man, H. C., *Enhancement of cavitation erosion and corrosion resistance of brass by laser surface alloying with Ni-Cr-Si-B*, Surface and Coatings Technology 149 (2002), 36-44

[174] Viswanadham, C. S., Goswami, G. L., Galun, R. and Mordike, B. L., *Laser melt injection of TiC particles into aluminium bronze*, Lasers in Engineering 16 (2006), 207-213

[175] Patent WO2007002017 200701004

[176] Govindaraju, M. R. and Molian, P. A., *Enhancement of wear and corrosion resistance of metal-matrix composites by laser coatings*, Journal of Materials Science 29 (1994), 3274-3280

[177] Mei, Z., Guo, L. F. and Yue, T. M., *The effect of laser cladding on the corrosion resistance of magnesium ZK60/SiC composite*, Journal of Materials Processing Technology 161 (2005), 462-466

[178] Bakkar, A., Galun, R. and Neubert, V., *Laser cladding of carbon/magnesium metal matrix composites*, Lasers in Engineering 15 (2005), 63-73

[179] Wang, A. H. and Yue, T. M., *YAG laser cladding of an Al-Si alloy onto an Mg/SiC composite for the improvement of corrosion resistance*, Composites Science and Technology 61 (2001), 1549-1554

[180] Li, H., Zeng, X. and Li, H., *Study on thick film resistor and electrode fabricated by laser micro-cladding electronic pastes*, Surface and Coatings Technology 200 (2006), 6832-6839

[181] Rombouts, M., Vanhulsel, A., Komp, A., Gedopt, J., Engelen, W. and Persoons, R., *Production of low-friction coatings by laser cladding*, CD-ROM Proceedings of ICALEO2008, 27th International Congress on Applications of Lasers & Electro-optics, October 2008, Temecula, CA, USA

[182] Atamert, S. and Stekly, J., *Microstructure, wear resistance, and stability of cobalt based and alternative iron based hardfacing alloys*, Surface Engineering 9 (1993) 3, 231-240

[183] Rogne, T., Berget, J., Fostervoll, H. and Nilsen, N. I., *Corrosion and wear properties of different weld overlays*, Thermal Spray 2001: New Surfaces for a New Millennium, (Ed.) C. C. Berndt, K. A. Khor and E. F. Lugsheider, Published by ASM International, Materials Park, Ohio, USA, 2001, 1329-1337

[184] Frenk, A. and Kurz, W., *Microstructural effects on the sliding wear resistance of a cobalt-based alloy*, Wear 174 (1994), 81-91

[185] De Hosson, J. T. M. and De Mol van Otterloo, L., *Surface Engineering with Lasers : Application to Co Based Materials*, Surface Engineering 13 (1997) 6, 471-481

[186] Persson, D. H. E., *On the mechanisms behind the tribological performance of stellites*, Doctoral Thesis, 2005, Uppsala Universitet, Sweden

[187] Frenk, A. and Wagniere, J. D., *Laser cladding with cobalt-based hardfacing alloys*, Journal de Physique IV 1 (1991), C7-65 - C7-68

[188] Anderson, T., *Practical aspects of laser cladding with high power lasers*, CD-ROM Proceedings of ICALEO2002; 21st International Congress on Applications of Lasers & Electro-optics, Laser Institute of America, October 2002, Scottsdale, AZ, USA

[189] Schlager, D., Theiler, C. and Kohn, H., *Protection against high temperature corrosion with laser welded claddings – Applied and tested on exhaust valve discs of large diesel engines burning heavy fuel oil*, Materials and Corrosion 53 (2002), 103-110

[190] Anjos, M. A., Vilar, R. and Qiu, Y. Y., *Laser Cladding of ASTM S 31254 Stainless Steel on a Plain Carbon Steel Substrate*, Surface and Coatings Technology 92 (1997), 142-149

[191] Weerasinghe, V. M., Steen, W. M. and West, D. R. F., *Laser deposited austenitic stainless steel clad layers*, Surface Engineering 3 (1987) 2, 147-153

[192] Li, R., Ferreira, M. G. S., Anjos, M. and Vilar, R., *Localized corrosion of laser surface cladded UNS S31254 superaustenitic stainless steel on mild steel*, Surface and Coatings Technology 88 (1996), 90-95

[193] Pan, Q. Y., Huang, W. D., Song, R. G., Zhou, Y. H. and Zhang, G. L., *The improvement of localized corrosion resistance in sensitized stainless steel by laser surface remelting,* Surface and Coatings Technology 102 (1998), 245-255

[194] Sha, C. K. and Tsai, H. L., *Hardfacing characteristics of S42000 stainless steel by using CO_2 laser*, Journal of Materials Engineering and Performance 10 (2001) 1, 37-41

[195] De Beurs, H. and De Hosson, J. Th. M., *Wear induced hardening of laser processed chromium-carbon steel*, Scripta Metallurgica 21 (1987), 627-632

[196] Li, R., Ferreira, M. G. S., Anjos, M. and Vilar, R., *Localized corrosion performance of laser surface cladded UNS S44700 superferritic stainless steel on mild steel*, Surface and Coatings Technology 88 (1996), 96-102

[197] Zhang, Y., Yuan, X. and Zeng, X., *Wear resistance and impact resistance of hardfacing alloys: laser cladding vs. hot isostatic pressing (HIP)*, Proceedings of ICALEO'99, 18th International Congress on Applications of Lasers & Electro-optics, Laser Institute of America, November 1999, San Diego, CA, USA, F241-F251

[198] Axen, N. and Zum Gahr, K.-H., *Abrasive wear of TiC-steel composite clad layers on tool steel*, Wear 157 (1992), 189-201

[199] Colaco, R., Gordo, E., Ruiz-Navas, E. M., Otasevic, M. and Vilar, R., *A comparative study of the wear behaviour of sintered and laser surface melted AISI M42 high speed steel diluted with iron*, Wear 260 (2006), 949-956

[200] Singh, J. and Mazumder, J., *Microstructure and wear properties of laser clad Fe-Cr-Mn-C alloys*, Metallurgical and Materials Transactions A 18 (1987), 312-322

[201] Choi, J. and Mazumder, J., *Non-equilibrium synthesis of Fe-Cr-C-W alloy by laser cladding*, Journal of Materials Science 29 (1994), 4460-4476

[202] Kagawa, A. and Ohta, Y., *Wear resistance of laser clad chromium carbide surface layers*, Materials Science and Technology 11 (1995), 515-519

[203] Wu, X. and Chen, G., *Nonequilibrium microstructures and their evolution in a Fe-Cr-W-Ni-C laser clad coating*, Materials Science and Engineering A270 (1999), 183-189

[204] Wu, X. and Hong, Y., *Microstructural evolution of a laser-cladded coating*, Scripta Materialia 43 (2000) 2, 123-127

[205] Colaco, R. and Vilar, R., *Development of Metal Matrix Composite Materials for Wear Resistant Coatings using a Laser Rapid-Alloy-Prototyping Technique*, Proceedings of ICALEO2000, 19th International Congress on Applications of Lasers & Electro-optics, Laser Institute of America, October 2000, Dearborn, MI, USA, D161-D170

[206] Choi, J., Choudhuri, S. K. and Mazumder, J., *Role of preheating and specific energy input on the evolution of microstructure and wear properties of laser clad Fe-Cr-C-W alloys*, Journal of Materials Science 35 (2000), 3213-3219

[207] Ocken, H., *Iron-base wear-resistant alloys*, Advanced Materials & Processes, June 2000, 103-104

[208] Kim, J. K. and Kim, S. J., *The temperature dependence of the wear resistance of iron-base NOREM 02 hardfacing alloy*, Wear 237 (2000), 217-222

[209] Grobner, P., Ohriner, E. K., Wada, T. and Whelan, E. P., *NOREM wear-resistant iron-based hardfacing alloys*, EPRI, Palo Alto, CA: 1989, NP-6466-M

[210] Osara, K., *Characterization of abrasion, impact-abrasion and impact wear of selected materials*, Doctoral Thesis, Institute of Materials Science, Tampere University of Technology 2001, Tampere, Finland

[211] Pelletier, J. M., Oucherif, F., Sallamand, P. and Vannes, A. B., *Hadfield steel coatings on low carbon steel by laser cladding*, Materials Science and Engineering A202 (1995), 142-147

[212] Pelletier, J. M., Sauger, E., Gachon, Y. and Vannes, A. B., *Mechanical and tribological properties of Hadfield steel coatings manufactured by laser processing*, Journal of Materials Science 34 (1999), 2955-2969

[213] Blank, E., Liechti, T. and Poire, L., *High performance coatings of aluminium alloys for improved wear resistance and load bearing capability*, High Performance Materials in Engine Technology, P. Vincenzini (Editor), 1995, 225-232

[214] Wang, A. H., Xie, C. S. and Nie, J. H., *Microstructural characteristics of iron based alloy laser clad on Al-Si alloy*, Materials Science and Technology 15 (1999), 957-964

[215] Galun, R., Bergmann, G. and Weinhausen, D., *Laser clads for application as bearing materials: microstructure and tribological properties*, CD-ROM Proceedings of ICALEO2005; 24th International Congress on Applications of Lasers & Electro-optics, Laser Institute of America, November 2005, Miami, FLA, USA

[216] Yakovlev, A., Bertrand, Ph. And Smurov, I., *Multimaterial laser cladding with coaxial powder injection*, CD-ROM Proceedings of ICALEO2007; 26th International Congress on Applications of Lasers & Electro-optics, Laser Institute of America, October 2007, Orlando, FLA, USA

[217] Zeng, D. W., Xie, C. S. and Wang, M. Q., *In situ synthesis and characterization of Fe_p/Cu composite coating on SAE 1045 carbon steel by laser cladding*, Materials Science and Engineering A 344 (2003) 1, 357-364

[218] Pei, Y. T. and De Hosson, J. T. M., *Functionally graded materials produced by laser cladding*, Acta materialia 48 (2000), 2617-2624

[219] Pei, Y. T., Ocelik, V. and De Hosson, J. T. M., *Interfacial adhesion of laser clad functionally graded materials*, Materials Science and Engineering A342 (2003), 192-200

[220] Almeida, A., Anjos, M., Vilar, R., Li, R., Ferreira, M. G. S., Steen, W. M. and Watkins, K. G., *Laser alloying of aluminium alloys with chromium*, Surface and Coatings Technology 70 (1995), 225-229

[221] Deuis, R. L., Yellup, J. M. and Subramanian, C., *Metal-matrix composite coatings by PTA surfacing*, Composites Science and Technology 58 (1998), 299-309

[222] Pierson, H. O., *Handbook of refractory carbides and nitrides: properties, characteristics, processing and applications*, Noyes Publications, 1996, USA

[223] Techel, A., Luft, A., Müller, A. and Nowotny, S., *Production of hard metal-like wear protection coatings by CO_2 laser cladding*, Optical and Quantum Electronics 27 (1995), 1313-1318

[224] Huang, S. W., Samandi, M. and Brandt, M., *Abrasive wear performance of laser clad WC/Ni layers*, Wear 256 (2004), 1095-1105

[225] Gassmann, R. C., *Laser cladding with ($WC+W_2C$)Co-Cr-C and ($WC+W_2C$)/Ni-B-Si composites for enhanced abrasive wear resistance*, Materials Science and Technology 12 (1996), 691-696

[226] Nowotny, S., Techel, A., Luft, A. and Reitzenstein, W., *Microstructure and wear properties of laser clad carbide coatings*, Proceedings of ICALEO'93, International Congress on Applications of Lasers and Electro-Optics, SPIE, October 1993, Orlando, FLA, USA, 985-993

[227] Lou, D., Hellman, J., Luhulima, D., Liimatainen, J. and Lindroos, V. K., *Interactions between tungsten carbide (WC) particulates and metal matrix in WC-reinforced composites*, Materials Science and Engineering A 340 (2003), 155-161

[228] Outokumpu HSC Chemistry Version 4.0, *Chemical Reaction and Equilibrium Software with Extensive Thermochemical Database*, 1999

[229] http://ocw.mit.edu, MIT PPT.presentation

[230] Gassmann, R., Nowotny, S., Luft, A., Reitzenstein, W. and Shen, J., *Laser cladding of hard particles rich alloys*, Proceedings of ICALEO'92, International Congress on Applications of Lasers and Electro-Optics, SPIE, October 1992, Orlando, FLA, USA, 288-300

[231] Pang, W., Man, H. C. and Yue, T. M., *Laser surface coating of Mo-WC metal matrix composite on Ti6Al4V alloy*, Materials Science and Engineering A 390 (2005), 144-153

[232] Wu, P., Zhou, C. Z. and Tang, X. N., *Microstructural characterization and wear behavior of laser cladded nickel-based and tungsten carbide composite coatings*, Surface and Coatings Technology 166 (2003), 84-88

[233] Li, Q., Lei, T. C. and Chen, W. Z., *Microstructural characterization of WCp reinforced Ni-Cr-B-Si-C composite coatings*, Surface and Coatings Technology 114 (1999), 285-291

[234] Herrera, Y., Grigorescu, I. C., Ramirez, J., Di Rauso, C. and Staia, M. H., *Microstructural characterization of vanadium carbide laser clad coatings*, Surface and Coatings Technology 108-109 (1998), 308-311

[235] Ebner, R., Kriszt, B. and Doppler, C., *Laser alloyed high speed steels*, European Conference on Laser Treatment of Materials (ECLAT'92), edited by B. L. Mordike, 187-192

[236] Shah, S. V. and Dahotre, N. B., *Laser-surface engineered vanadium carbide coating for extended die life*, Journal of Materials Processing Technology 124 (2002), 105-112

[237] Nurminen, J., Näkki, J. and Vuoristo, P., *On the wear properties of laser coatings with high carbide concentrations*, CD-ROM Proceedings of ICALEO2004; 23rd International Congress on Applications of Lasers & Electro-optics, Laser Institute of America, October 2004, San Francisco, CA, USA

[238] Tassin, C., Laroudie, F., Pons, M. and Lelait, L., *Carbide-reinforced coatings on AISI 316 L stainless steel by laser surface alloying*, Surface and Coatings Technology 76-77 (1995), 450-455

[239] Kim, T. H. and Kim, B. C., *Chromium carbide laser-beam surface-alloying treatment on stainless steel*, Journal of Materials Science 27 (1992), 2967-2973

[240] Kumar, S. and Goswami, G. L., *Wear behaviour of various Ni-based laser clad materials*, Lasers in Engineering 16 (2006), 305-315

[241] Colaco R. and Vilar R., *Abrasive wear of metallic matrix reinforced materials*, Wear 255 (2003), 643-650

[242] Liu, W. and DuPont, J. N., *Fabrication of functionally graded TiC/Ti composites by Laser Engineered Net Shaping*, Scripta Materialia 48 (2003), 1337-1342

[243] Shen, J. Nowotny, S., Dausinger, F. and Hügel, H., *Laser surface treatment of a low carbon steel by cladding with tungsten carbide composite powders*, Proceedings of LAMP'92, Nagaoka (June, 1992), 755-760

[244] Almeida, A., Eugenio, S., Livramento, V., Marques, M. T., Correia, J. B. and Vilar, R., *Laser cladding of Cu-NbC nanocomposite coatings*, CD-ROM Proceedings of ICALEO2006; 25th International Congress on Applications of Lasers & Electro-optics, Laser Institute of America, October 2006, Scottsdale, AZ, USA

[245] Jiang, W. and Molian, P., *Nanocrystalline TiC powder alloying and glazing of H13 steel using a CO_2 laser for improved life of die-casting dies*, Surface and Coatings Technology 135 (2001), 139–149

[246] Fasasi, A. Y., Pons, M., Tassin, C., Galerie, A., Sainfort, G. and Polak, C., *Laser surface melting of mild steel with submicronic titanium carbide powders*, Journal of Materials Science 29 (1994), 5121-5126

[247] Zhu, B., Zeng, X., Tao, Z., Yang, S. and Cui, K., *Coarse cemented WC particle ceramic-metal composite coatings produced by laser cladding*, Wear 170 (1993), 161-166

[248] Van Acker, K., Vanhoyweghen, D., Persoons, R. and Vangrunderbeek, J., *Influence of tungsten carbide particle size and distribution on the wear resistance of laser clad WC/Ni coatings*, Wear 258 (2005), 194-202

[249] Laroudie, F., Tassin, C. and Pons, M., *Hardening of 316L stainless steel by laser surface alloying*, Journal of Materials Science 30 (1995), 3652-3657

[250] Cerri, W., Martinella, R., Mor, G. P., Bianchi, P. and Angelo, D. D., *Laser deposition of carbide-reinforced coatings*, Surface and Coatings Technology 49 (1991), 40-45

[251] Hidouci, A., Simonin, F. and Pelletier, J. M., *Preparation by laser cladding and microstructural characterisation of $MoSi_2$ and ($MoSi_2$ + ZrO_2) coatings on steel and graphite substrates*, Lasers in Engineering 8 (1998), 17-34

[252] Wolfe, D. E., Singh, J., Senderson, S. and Zabinski, J., *Laser-clad composite coatings*, Advanced Materials and Processes, August 2000, 41-44

[253] Pei, Y. T., Ocelik, V. and De Hosson, J. T. M., *SiCp/Ti6Al4V functionally graded materials produced by laser melt injection*, Acta Materialia 50 (2002), 2035-2051

[254] De Hosson, J. Th. M. and Ocelik, V., *Functionally graded materials produced with high power lasers*, Materials Science Forum 426-432 (2003), 123-130

[255] Vreeling, J. A., Ocelik, V., Pei, Y. T., Van Agterveld, D. T. L. and De Hosson, J. T. M., *Laser melt injection in aluminum alloys: on the role of the oxide skin*, Acta mater. 48 (2000), 4225-4233

[256] Abboud, J. H. and West, D. R. F., *Ceramic-metal composites produced by laser surface treatment*, Materials Science and Technology 5 (1989), 725-728

[257] Abboud, J. H., West, D. R. F. and Rawlings, R. D., *Functionally gradient titanium-aluminide composites produced by laser cladding*, Journal of Materials Science 29 (1994), 3393-3398

[258] Syed, W. U. H., Pinkerton, A. J., Liu, Z. and Li, L., *Coincident wire and powder deposition by laser to form compositionally graded material*, Surface and Coatings Technology 201 (2007), 7083-7091

[259] Carvalho, P. A., Braz, N., Pontinha, M. M., Ferreira, M. G. S., Steen, W. M., Vilar, R. and Watkins, K. G., *Automated workstation for variable composition laser cladding - its use for rapid alloy scanning*, Surface and Coatings Technology 72 (1995), 62-70

[260] Xu, J., Liu, W. and Zhong, M., *Microstructure and dry sliding wear behavior of MoS_2/TiC/Ni composite coatings prepared by laser cladding*, Surface & Coatings Technology 200 (2006), 4227-4232

[261] Yakovlev, A., Bertrand, P. and Smurov, I., *Wear-resistant coatings with engineered structure by laser cladding*, Tribology Letters 17 (2004) 4, 705-708

[262] Courant, B., Hantzpergue, J. J. and Benayoun, S., *Surface treatment of titanium by laser irradiation to improve resistance to dry-sliding friction*, Wear 236 (1999), 39-46

[263] Liu, X. B., Wang, C. M., Yu, L. G. and Wang, H. M., *Microstructure of laser clad high-temperature self-lubricating wear-resistant composite coatings*, Proceedings of SPIE Vol. 3862 (1999), 423-427

[264] Liu, X. B., Wang, C. M., Yu, L. G. and Wang, H. M., *Laser cladding for high-temperature self-lubricating wear-resistant composite coatings on y-TiAl intermetallic alloy Ti-48Al-2Cr-2Nb*, Proceedings of SPIE Vol. 3888 (2000), 312-317

[265] Wang, H. M., Yu, Y. L. and Li, S. Q., *Microstructure and tribological properties of laser clad CaF_2/Al_2O_3 self-lubrication wear-resistant ceramic matrix composite coatings*, Scripta Materialia 47 (2002), 57-61

[266] Yang, S., Chen, N., Liu, W., Zhong, M., Wang, Z. and Kokawa, H., *Fabrication of nickel composite coatings reinforced with TiC particles by laser cladding*, Surface and Coatings Technology 183 (2004), 254-260

[267] Shehata, G. H., Moussa, A. M. A. and Molian, P. A., *Nd:YAG laser alloying of high-speed steel tools with BN and Ti/BN and the effects on turning performance*, Wear 170 (1993), 199-210

[268] Molian, P. A. and Hualun, L., *Laser cladding of Ti-6Al-4V with BN for improved wear performance*, Wear 130 (1989), 337-352

[269] Wang, K. L., Zhu, Y. M., Zhang, Q. B. and Sun, M. L., *Effect of rare earth cerium on the microstructure and corrosion resistance of laser cladded nickel-base alloy coatings*, Journal of Materials Processing Technology 63 (1997), 563-567

[270] Wang, K. L., Zhang, Q. B., Sun, M. L. and Zhu, Y. M., Effect *of laser surface cladding of ceria on the wear and corrosion of nickel-based alloys*, Surface and Coatings Technology 96 (1997), 267-271

[271] Wang, K. L., Zhang, Q. B., Sun, M. L., Wei, X. G. and Zhu, Y. M., *Rare earth elements modification of laser-clad nickel-based alloy coatings*, Applied Surface Science 174 (2001), 191-200

[272] Zhao, T., Cai, X., Wang, S. and Zheng, S., *Effect of CeO_2 on microstructure and corrosive wear behaviour of laser-cladded Ni/WC coatings*, Thin Solid Films 379 (2000), 128-132

[273] Wang, K. L., Zhang, Q. B., Sun, M. L. and Wei, X. G., *Microstructural characteristics of laser clad coatings with rare earth metal elements*, Journal of Materials Processing Technology 139 (2003), 448-452

[274] Li, M, He, Y. and Yuan, X., *Effect of nano-Y_2O_3 on microstructure of laser cladding cobalt-based alloy coatings*, Applied Surface Science 252 (2006), 2882-2887

[275] Ribaudo, C. and Mazumder, J., *Oxidation Behavior of a Laser-clad Nickel-based Alloy Containing Hafnium*, Materials Science and Engineering, A121 (1989), 531-538

[276] Duan, G. and Wang, H. M., *High-temperature wear resistance of a laser-clad y/Cr_3Si metal silicide composite coating*, Scripta Materialia 46 (2002), 107-111

[277] Jian, L. N. and Wang, H. M., *Microstructure and wear behaviours of laser-clad $Cr_{13}Ni_5Si_2$-based metal-silicide coatings on titanium alloy*, Surface & Coatings Technology 192 (2005), 305-310

[278] Cai, L. X. and Wang, H. M., *Microstructure and dry-sliding wear resistance of laser clad tungsten reinforced W_5Si_3/W_2Ni_3Si intermetallic coatings*, Applied Surface Science 235 (2004), 501-506

[279] Ignat, S., Sallamand, P., Nichici, A., Vannes, B., Grevey, D. and Cicala, E., *$MoSi_2$ laser cladding-elaboration, characterisation and addition of non-stabilized ZrO_2 powder particles*, Intermetallics 11 (2003), 931-938

[280] Lu, X. D. and Wang, H. M., *Corrosive sliding wear behavior of laser clad Mo_2Ni_3Si / NiSi intermetallic coating*, Applied Surface Science 245 (2005), 346-352

[281] Wang, H. M. and Liu, Y. F., *Microstructure and wear resistance of laser clad Ti5Si3/NiTi2 intermetallic composite coating on titanium alloy*, Materials Science and Engineering A 338 (2002), 126-132

[282] Hidouci, A., Simonin, F. and Pelletier, J. M., *Preparation by laser cladding and microstructural characterisation of $MoSi_2$ and ($MoSi_2$ + ZrO_2) coatings on steel and graphite substrates*, Lasers in Engineering 8 (1998), 17-34

[283] Duraiselvam, M., Galun, R., Wesling, V. and Mordike, B. L., *Laser clad WC reinforced Ni-based intermetallic-matrix composites to improve cavitation erosion resistance*, CD-ROM Proceedings of ICALEO2005; 24th International Congress on Applications of Lasers & Electro-optics, Laser Institute of America, November 2005, Miami, FLA, USA

[284] Chen, Y. and Wang, H. M., *Microstructure and wear resistance of a laser clad TiC reinforced nickel aluminides matrix composite coating*, Materials Science and Engineering A368 (2004), 80-87

[285] Corbin, S. F., Toyserkani, E. and Khajepour, A., *Cladding of an Fe-aluminide coating on mild steel using pulsed laser assisted powder deposition*, Materials Science and Engineering A354 (2003), 48-57

[286] Uenishi, K., Sukimoto, A. and Kobayashi, K F., *The formation of titanium aluminides on aluminium surfaces by CO_2 laser alloying*, Z. Metallkd. 83 (1992) 4, 241-245

[287] Kelbassa, I., Weisheit, A., Wissenbach, K. and Hermes, V., *Laser metal deposition TiAl alloys*, CD-ROM Proceedings of PICALO2006, 1nd International Conference on Applications of Lasers and Optics, April 2006, Melbourne Australia

[288] Cui, Z. D., Man, H. C., Cheng, F. T. and Yue, T. M., *Cavitation erosion-corrosion characteristics of laser surface modified NiTi shape memory alloy*, Surface and Coatings Technology 162 (2003), 147-153

[289] Yang, Y. Q. and Man, H. C., *Laser spray cladding of porous NiTi coatings on NiTi substrates*, Surface & Coatings Technology 201 (2007), 6928-6932

[290] Virtanen, S., Böhni, H., Busin, R., Marchione, T., Pierantoni, M. and Blank, E., *The effect of laser surface modification on the corrosion behaviour of Fe and Al base alloys,* Corrosion Science 36 (1994) 9, 1625-1644

[291] Wu, X. and Hong, Y., *Fe-based thick amorphous-alloy coating by laser cladding*, Surface and Coatings Technology 141 (2001), 141-144

[292] Wu, X., Xu, B. and Hong, Y., *Synthesis of thick Ni66Cr5Mo4Zr6P15B4 amorphous alloy coating and large glass-forming ability by laser cladding*, Materials Letters 56 (2002), 838-841

[293] Nowotny, S., Richter, A. and Tangermann, K., *Surface protection of light metals by one-step laser cladding with oxide ceramics,* Journal of Thermal Spray Technology 8 (1999) 2, 258-262

[294] Zhou, X. B. and De Hosson, J. T. M., *Metal-ceramic interfaces in laser coated aluminium alloys*, Acta metall. mater. 42(1994) 4, 1155-1162

[295] Lusquinos, F., Pou, J., Arias, J. L., Boutinguiza, M., Leon, B. and Perez-Amor, M., *Calcium phosphate coatings obtained by laser surface cladding*, Proceedings of ICALEO2001, 20th International Congress on Applications of Lasers & Electro-optics, Laser Institute of America, October 2001, Jacksonville, FLA, USA

[296] Lusquinos, F., De Carlos, A., Pou, J., Arias, J. L., Boutinguiza, M., Leon, B., Perez-Amor, M., Driessens, F. C. M., Hing, K., Gibson, I., Best, S. and Bonfield, W., *Calcium phosphate coatings obtained by Nd:YAG laser cladding: Physicochemical and biological properties*, J. Biomed. Mater. Res. 64A (2003), 630-637

[297] Lusquinos, F., Pou, J., Boutinguiza, M., Quintero, F., Soto, R., Leon, B. and Perez-Amor, M., *Main characteristics of calcium phosphate coatings obtained by laser cladding*, Applied Surface Science 247 (2005), 486-492

[298] Wang, Y., Li, Y., Yu, H., Ding, J., Tang, X., Li, J. and Zhou, Y., *In situ fabrication of bioceramic composite coatings by laser cladding*, Surface & Coatings Technology 200 (2005), 2080-2084

[299] Kurz, W. and Trivedi, R, *Rapid solidification processing and microstructure formation*, Materials Science and Engineering A179/A180 (1994), 46-51

[300] David, S. A., Vitek, J. M., Rappaz, M. and Boatner, L. A., *Microstructure of stainless steel single-crystal electron beam welds*, Metallurgical Transactions A 21A (1990), 1753-1766

[301] Frenk, A. and Kurz, W., *Microstructure formation in laser materials processing*, Lasers in Engineering 1 (1992), 193-212

[302] Gilgien, P. and Kurz, W., *Microstructure and phase selection in rapid laser processing*, Laser Processing: Surface Treatment and Film Deposition, ed. J. Mazumder, O. Conde, R. Vilar and W. Steen, NATO ASI Series, 1996, 78-91

[303] Pelletier, J. M., Renaud, L. and Fouquet, F., *Solidification microstructures induced by laser surface alloying: influence of the substrate*, Materials Science and Engineering, A134 (1991), 1283-1287

[304] Gäumann, M., Trivedi, R. and Kurz, W., *Nucleation ahead of the advancing interface in directional solidification*, Materials Science and Engineering A 226-228 (1997), 763-769

[305] Monson, P. E. J. and Steen, W. M., *Comparison of laser hardfacing with conventional processes*, Surface Engineering 6 (1990) 3, 185-193

[306] David, S. A. and Vitek, J. M., *Correlation between solidification parameters and weld microstructures*, International Materials Reviews 34 (1989) 5, 213-245

[307] Chande, T. and Mazumder, J., *Two-dimensional, transient model for mass transport in laser surface alloying*, Journal of Applied Physics 57 (1985) 6, 2226-2232

[308] Chan, C., Mazumder, J. and Chen, M. M., *A two-dimensional transient model for convection in laser melted pool*, Metallurgical Transaction A 15 (1984) 12, 2175-2184

[309] Takeda, T., Steen, W. M. and West, D. R. F., *Laser cladding with mixed power feed*, Proceedings of the Materials Processing Symposium, ICALEO'84, ed. J. Mazumder, Laser Institute of America, 1984, 151-158

[310] Chan, C., Mazumder, J. and Chen, M. M., *A model for surface tension driven fluid flow in laser surface alloying*, Lasers in Materials Processing, Conference Proceedings, Edited by E. A. Metzbower, ASM, Ohio, USA, 1983, 150-157

[311] Felberbaum, L., Voisey, K., Gäumann, M., Viguier, B. and Mortensen, A., *Thermal fatigue of single-crystalline superalloy CMSX-4: a comparison of epitaxial laser-deposited material with the base single crystal*, Materials Science and Engineering A 299 (2001), 152-156

[312] Belmondo, A. and Castagna, M., *Wear-resistant coatings by laser processing*, Thin Solid Films 64 (1979), 249-256

[313] Dutta Majumder, J., Pinkerton, A., Liu, Z., Manna, I. and Li, L., *Mechanical and electrochemical properties of multiple-layer diode laser cladding of 316L stainless steel*, Applied Surface Science 247 (2005), 373-377

[314] Cooper, K. P., Slebodnick, P. and Thomas, P., *Seawater corrosion behavior of laser surface modified Inconel 625 alloy*, Materials Science and Engineering A 206 (1996) 1, 138-149

[315] Kujanpää, V. P. and David, S. A., *Microsegregation in a laser and gas tungsten arc welded Mo austenitic stainless steel,* Proceedings of ICALEO'86, International Conference on Applications of Lasers and Electro-Optics, November 1986, Arlington, VA, USA, 63-69

[316] Nakao, Y. and Nishimoto, K., *Effects of laser surface melting on corrosion resistance of stainless steel and nickel-base alloy clad layers in cast bi-metallic pipes*, ISIJ International 33 (1993) 9, 934-940

[317] Escudero, M. L. and Bello, J. M., *Laser surface treatment and corrosion behaviour of martensitic stainless AISI 420 steel*, Materials Science and Engineering A 158 (1992) 2, 227-233

[318] Akgun, O. V. and Inal, O. T., *Laser surface melting and alloying of type 304L stainless steel – Part II Corrosion and wear resistance properties*, Journal of Materials Science 30 (1995), 6105-6112

[319] Pan, Q. Y., Huang, W. D., Song, R. G., Zhou, Y. H. and Zhang, G. L., *The improvement of localized corrosion resistance in sensitized stainless steel by laser surface melting,* Surface and Coatings Technology 102 (1998), 245-255

[320] Reitz, W. and Rawers, J., *Effect of laser surface melted zirconium alloys on microstructure and corrosion resistance*, Journal of Materials Science 27 (1992), 2437-2443

[321] Watkins, K. G., Liu, Z., McMahon, M., Vilar, R. and Ferreira, M. G. S., *Influence of the overlapped area on the corrosion behaviour of laser treated aluminium alloys*, Materials Science and Engineering A 252 (1998), 292-300

[322] Chong, P. H., Liu, Z., Skeldon, P. and Thompson, G. E., *Large area surface treatment of aluminium alloys for pitting corrosion protection*, Applied Surface Science 208-209 (2003), 399-404

[323] Crook, P., *The effects of dilution upon the corrosion and wear properties of cobalt-based weld overlays*, Corrosion Science 35 (1993) 1-4, 647-653

[324] Zhang, S., Man, H. C., Wu, W. and Wang, M., *Laser cladding of Co-based alloy on 2Cr13 stainless steel*, Proceedings of ICALEO2000, 19th International Congress on Applications of Lasers & Electro-optics, Laser Institute of America, October 2000, Dearborn, MI, USA, D200-D209

[325] Uusitalo, M., *High temperature corrosion and erosion-corrosion of coatings in chlorine-containing environments*, Doctoral Thesis, Tampere University of Technology, 2003, p. 45

[326] Longa, Y. and Takemoto, M., *Laser processing of high-chromium nickel-chromium coatings deposited by various thermal spraying methods*, Corrosion Science 50 (1994) 11, 827-837

[327] Longa-Nava, Y., Zhang, Y. S., Takemoto, M. and Rapp, R. A., *Hot corrosion of nickel-chromium and nickel-chromium-aluminum thermal-spray coatings by sodium sulphate-sodium metavanadate salt*, Corrosion Science 52 (1996) 9, 680-689

[328] Wang, M., Jin, Z. and Wu, W., *Hot corrosion behaviour of nickel-based superalloy irradiated with a laser beam*, Materials Science and Engineering 92 (1987), 145-151

[329] Hutchings, I. M., *Tribology – Friction and wear of engineering materials*, 4th Edition, 1996, Metallurgy & Materials Science Series, Arnold, ISBN 0 340 56184 X

[330] Xu, G., Kutsuna, M., Liu, Z. K. and Yamada, K., *Comparison between diode laser and TIG cladding of Co-based alloys on the SUS403 stainless steel*, Surface and Coatings Technology 201 (2006), 1138-1144

[331] Xu, G., Kutsuna, M., Liu, Z. K. and Zhang, H., *Characteristics of Ni-based coating layer formed by laser and plasma cladding processes*, Materials Science and Engineering A 417 (2006), 63-72

[332] Atamert, S. and Bhadeshia, H. K. D. H., *Comparison of the microstructures and abrasive wear properties of Stellite hardfacing alloys deposited by arc welding and laser cladding,* Metallurgical Transactions A 20 (1989), 1037-1054

[333] De Mol van Otterloo, J. L. and De Hosson, J. Th. M., *Microstructure and abrasive wear of cobalt-based laser coatings*, Scripta Materialia, 36 (1997) 2, 239-245

[334] Aihua, W., Zengyi, T. and Beidi, Z., *Laser beam cladding of seating surfaces on exhaust valves*, Welding Journal 70 (1991) 4, 106s-109s

[335] Weisheit, A. and Mordike, B. L., *Laser surface alloying of titanium with vanadium carbide and molybdenumdisilicide to improve wear resistance*, Proceedings of ICALEO'93, International Congress on Applications of Lasers & Electro-optics, Laser Institute of America, October 1993, Orlando, FLA, USA, 923-932

[336] Oberländer, B. C. and Lugscheider, E., *Comparison of properties of coatings produced by laser cladding and conventional methods*, Materials Science and Technology 8 (1992), 657-665

[337] Duraiselvam, M., Galun, R., Siegmann, S., Wesling, V. and Mordike, B. L., *Particle-laden liquid impact erosion characteristics of laser clad Ni-based intermetallic matrix composites with TiC and WC reinforcements*, Lasers in Engineering 15 (2005), 355–373

[338] Jiang, W. H. and Kovacevic, R., *Slurry erosion resistance of laser clad Fe-Cr-B-Si coatings*, Surface Engineering 20 (2004) 6, 464-468

[339] Wang, P., Yang, Y., Ding, G., Qu, J. and Shao, H., *Laser cladding coating against erosion-corrosion wear and its application to mining machine parts*, Wear 209 (1997), 96-100

[340] Zhang, D., Lei, T. C., Zhang, J. and Ouyang, J., *The effects of heat treatment on microstructure and erosion properties of laser surface-clad Ni-base alloy*, Surface and Coatings Technology 115 (1999), 176-183

[341] Zhang, D. and Zhang, X., *Laser cladding of stainless steel with Ni-Cr_3C_2 and Ni-WC for improving erosive-corrosive wear performance,* Surface & Coatings Technology 190 (2005), 212-217

[342] Lo, K. H., Cheng, F. T., Kwok, C. T. and Man, H. C., *Improvement of cavitation erosion resistance of AISI 316 stainless steel by laser surface alloying using fine WC powder*, Surface and Coatings Technology 165 (2003), 258-267

[343] Kwok, C. T., Cheng, F. T. and Man, H. C., *Laser surface modification of UNS S31603 stainless steel using NiCrSiB alloy for enhancing cavitation erosion resistance*, Surface and Coatings Technology 107 (1998), 31-40

[344] Man, H. C., Zhang, S., Yue, T. M. and Cheng, F. T., *Laser surface alloying of NiCrSiB on Al6061 aluminium alloy*, Surface and Coatings Technology 148 (2001), 136-142

[345] Kwok, C. T., Cheng, F. T. and Man, H. C., *Laser-fabricated Fe-Ni-Co-Cr-B austenitic alloy on steels. Part I. Microstructures and cavitation erosion behaviour*, Surface and Coatings Technology 145 (2001), 194-205

[346] Cheng, F. T., Kwok, C. T. and Man, H. C., *Cavitation erosion resistance of stainless steel laser-clad with WC-reinforced MMC,* Materials Letters 57 (2002), 969-975

[347] McMahon, M. A., Green, A., Watkins, K. G., Ferreira, M. G. S. and Vilar, R., *Effect of residual stress on the corrosion properties of CO_2 laser surface melted alloys*, Materials Science Forum 192-194 (1995), 789-796

[348] Davis, J. R., *Corrosion: Understanding the basics*, ASM International, Materials Park, OH, USA, 2000, ISBN 0-87170-641-5

[349] Dekumbis, R., *Controlling residual stresses in laser cladded coatings*, Proceedings of the 6th International Conference Lasers in Manufacturing, Birmingham, IFS 1989

[350] Kadolkar, P. B., Watkins, T. R. And Dahotre, N., *Residual stress characterization of particulate-reinforced composite coating using X-ray diffraction technique*, Proceedings from the 1st International Surface Engineering Congress and the 13th IFHTSE Congress, October 2002, Columbus, OH, USA, 593-603

[351] Chen, J. Y. and Xue, L., *Microstructural characteristics of laser-clad AISI P20 tool steel*, Proceedings from the 1st International Surface Engineering Congress and the 13th IFHTSE Congress, 7-10 October, 2002, Columbus, Ohio, USA, 198-205

[352] Van Brussel, B. A. and De Hosson, J. Th. M., *Residual stresses in the surface layer of laser-treated steels*, Materials Science and Engineering A161 (1993), 83-89

[353] Frenk, A., Marsden, C. F., Wagniere, J. D., Vannes, A. B., Laracine, M. and Lormand, M. Y., *Influence of an intermediate layer on the residual stress field in a laser clad*, Surface and Coatings Technology 45 (1991), 435-441

[354] Roth, M., *Residual stresses in laser treated surfaces*, Residual Stresses III, H. Fujiwara, T. Abe and K. Tanaka (editors), Elsevier Applied Science, London and New York, 1992, 845-851

[355] Prime, M. B. and Hellwig, C., *Residual stresses in a bi-material laser clad measured using compliance*, Proceedings of ICRS-5, June 16-18, 1997, Linköping, Sweden, 127-132

[356] Magnon, G., *Residual stresses in laser cladded layer*, LiTH-IKP, June 2001

[357] Hosseini, M. and Ericsson, T., *Residual stresses in laser cladded layers*, LiTH-IKP-Cr-014

[358] Hjörnhede, A. and Nylund, A., *Adhesion testing of thermally sprayed and laser deposited coatings*, Surface and Coatings Technology 184 (2004), 208-218

[359] Hidouci, A., Pelletier, J. M., Ducoin, F., Dezert, D. and El Guerjouma, R., *Microstructural and mechanical characteristics of laser coatings*, Surface and Coatings Technology 123 (2000), 17-23

[360] Cadenas, M., Vijande, R., Montes, H. J. and Sierra, J. M., *Wear behaviour of laser cladded and plasma sprayed WC-Co coatings*, Wear 212 (1997), 244-253

[361] Niederhauser, S., *Laser cladded steel – Microstructures and mechanical properties of relevance for railway applications*, Ph.D. Thesis, Chalmers University of Technology, Göteborg, Sweden 2005

[362] Wang, A. H., Nie, J. H. and Xie, C. S., *Fractural behavior in the transitional region of laser-clad Al-Fe bronze on Al-Si alloy under tensile loading*, Materials Letters 56 (2002), 822-826

[363] Wang, A. H., Xie, C. S. and Wang, W. Y., *Cracking behaviour in the transitional region of laser-clad coatings on Al-Si alloy under multiple impact loading*, Materials Characterization 49 (2003), 247-254

[364] Xue, L., Li, Y., Van Daam, T. and Bampton, C., *Investigation of laser consolidation for manufacturing functional net-shape components for potential rocket engine applications*, CD-ROM Proceedings of ICALEO2007; 26th International Congress on Applications of Lasers & Electro-optics, Laser Institute of America, November 2007, Orlando, FLA, USA

[365] Griffith, M. L., Ensz, M. T., Puskar, J. D., Robino, C. V., Brooks, J. A., Philliber, J. A., Smugeresky, J. E. and Hofmeister, W. H., *Understanding the microstructure and properties of components fabricated by laser engineered net shaping (LENS)*, Mat. Res. Soc. Symp. Proc. Vol. 625, 2000 Materials Research Society, 9-20

[366] Hedges, M., *Laser based additive manufacturing using LENS and M3D*, Proceedings of the LANE 2004, Laser Assisted Net Shape Engineering 4, Edited by: M. Geiger, A. Otto

[367] Galvan, D., Ocelik, V., Pei, Y., Kooi, B. J., De Hosson, J. T. M. and Ramous, E., *Microstructure and properties of TiB/Ti-6Al-4V coatings produced with laser treatments*, Journal of Materials Engineering and Performance 13 (2004) 4, 406-412

[368] Mehlmann, A., Dirnfeld, S. F. and Minkoff, I., *Laser-melt injection of B_4C on titanium*, Surface and Coatings Technology 42 (1990), 275-281

[369] Li, X. C., Stampfl, J. and Prinz, F. B., *Mechanical and thermal expansion behavior of laser deposited metal matrix composites of Invar and TiC*, Materials Science and Engineering A282 (2000), 86-90

[370] Kelbassa, I., Kreutz, E., Albus, P. and Zhu, L., *Mechanical properties of the laser cladded alloys Ti-6Al-4V and Inconel 718*, CD-ROM Proceedings of ICALEO2005, 24th International Congress on Applications of Lasers and Electro-Optics, Laser Institute of America, November 2005, Miami, FLA, USA

[371] Astapchik, S. A., Golubev, V. S., Vaganov, V. V. and Klindyik, A. P., *Laser Treatment of Thermal Sprayed Coatings on Titanium Base Alloys*, 2nd PLASMA-TECHNIK-SYMPOSIUM, Vol 1, 1991, 335-344

[372] Materials Property Database (MPDB), CD-ROM, Copyright © 2002 Jahm Software, Inc.

[373] Crook, P., *Cobalt and Cobalt Alloys*, Metals Handbook, 10th Edition, Vol. 2, ASM International, 1990, 446-454

[374] Tobe, S., Andoh, Y., Hidaka, K., Tanaka, K., Nishimura, S., Kawaharada, K. and Shirai, K., *High temperature corrosion resistance of newly developed Cr-based alloy coatings*, Proceedings of the United Thermal Spray Conference 1999, Düsseldorf, Germany, 296-300

[375] Roth, R. S., Negas, T. and Cook, L. P, *Phase diagrams for ceramists, Vol. IV*, Figure 5127, The American Ceramic Society, Columbus, OH, USA, 1981, p. 89

[376] Nanda, S. K. and Roskilly, A. P., *Exhaust valve failure under residual fuel operation*, Journal of Marine Design and Operations 2003 B2, 23-28

[377] Bryers, R. W., *Fireside slagging, fouling and high-temperature corrosion of heat-transfer surface due to impurities in steam-raising fuels*, Prog. Energy Combust. Sci. 22 (1996), 29-120

[378] Suryanarayana, C. and G Norton, M., *X-Ray Diffraction – A Practical Approach*, Plenum Press, 1998, New York, N.Y, USA, p. 223
[379] Schwarz, T. and Kockelmann, H., *The hole-drilling method – The best technique for the experimental determination of residual stresses in many fields of application*, MTB 29 (1993) 2, 33-38
[380] Al-Fozan, S. A. and Malik, A. U., *Effect of seawater level on corrosion behaviour of different alloys*, International Desalineation Association (IDA) World Congress Conference, Singapore, 2005
[381] Möller, H., *The corrosion behaviour of steel in seawater*, The Southern African Institute of Mining and Metallurgy, 8th International Corrosion Conference, 2006
[382] Pourbaix, M., *Atlas of Electrochemical Equilibria in Aqueous Solutions*, 2nd Edition, National Association of Corrosion Engineers (NACE), Houston, Texas, USA, 1974, p. 265
[383] DuPont, J. N., Robino, C. V. and Marder, A. R., *Modeling solute redistribution and microstructural development in fusion welds of Nb-bearing superalloys*, Acta Materialia 46 (1998), 4781-4790
[384] Tinoco, J., *On the spray forming of metals, the formation of porosity and the heat evolution during solidification*, Doctoral Thesis, Royal Institute of Technology, Casting of Metals, Stockholm, Sweden, November 2003
[385] Knorovsky, G. A., Cieslak, M. J., Headley, T. J., Roming, A. D. and Hammetter, W. F., *INCONEL 718: A solidification diagram*, Metallurgical Transactions A 20A (1989), 2149-2158
[386] Kingston-Jones, M. G., Thomas, J. R. and Radcliff, A. S., *Review of operating experience with current valve materials*, Diesel Engine Combustion Chamber Materials For Heavy Fuel Operation, The Institute of Marine Engineers, 1990, ISBN 0-907206-23-9
[387] Massalski, T. B., Murray, J. L., Bennett, L. H. and Baker, H., *Binary Alloy Phase Diagrams*, Vol. 1, American Society for Metals, Metals Park, OH, USA, 1986, p.842
[388] Tomita, T., Takatani, Y., Okita, K. and Harada, Y., *Improvement of wear property of NbC/high Cr-high Ni overlay alloy coating formed by plasma transferred arc welding process*, Proceedings of the 15th International Thermal Spray Conference, 25-29 May 1998, Nice, France, 253-258
[389] Ashby, M. F., *Selecting the components of composites*, Journal de Physique IV 3 (1993), 1595-1600
[390] Zum Gahr, K. H., *Microstructure and wear of materials*, Elsevier Science Publishers B. V., 1987, ISBN 0-444-42754-6, p. 69
[391] Luft, A., Techel, A., Nowotny, S. and Reitzenstein, W., *Microstructures and dissolution of carbides occurring during the laser cladding of steel with tungsten carbide reinforced Ni- and Co-hard alloys*, Praktische Metallographie 32 (1995) 5, 235-247
[392] Nowotny, S., Techel, A., Müller, A., Reitzenstein, W. and Uelze, A., *Influences on the wear resistance of carbide laser claddings*, European Conference on Laser Treatment of Materials,ECLAT´94, 1994, DGM Informationsgesellschaft mbH
[393] Wu, P., Du, H. M., Chen, X. L., Li, Z. Q., Bai, H. L. and Jiang, E. Y., *Influence of WC particle behaviour on the wear resistance properties of Ni-WC composite coatings*, Wear 257 (2004), 142-147
[394] Arnell, R. D., Davies, P. B., Halling, J. and Whomes, T. L., *Tribology: Principles and design applications*, New York, Springer-Verlag, 1991

[395] Bhansali, K. J., *Adhesive wear of nickel- and cobalt-base alloys*, Wear, 60 (1980), 95-110
[396] Frenk, A., Henchoz, N. and Kurz, W., *Laser cladding of a cobalt-based alloy: processing parameters and microstructure*, Z. Metallkd. 84 (1993), 886-892
[397] Halstead, A. and Rawlings, R. D., *Structure and hardness of Co-Mo-Cr-Si wear resistant alloys (Tribaloys)*, Metal Science 18 (1984), 491-500
[398] Gnanamuthu, D. S., *Laser surface treatment*, Optical Engineering 19 (1980) 5, 783-792
[399] Song, J. H. and Kim, H. J., *Sliding wear performance of cobalt-based alloys in molten-Al-added zinc bath*, Wear, 210 (1997), 291-298
[400] www.matweb.com
[401] Dent, A. H., Horlock, A. J., McCartney, D. G. and Harris, S. J., *The corrosion behavior and microstructure of high-velocity oxy-fuel sprayed nickel-base amorphous/nanocrystalline coatings*, Journal of Thermal Spray Technology 8 (1999) 3, 399-404
[402] Edris, H., McCartney, D. G. and Sturgeon, A. J., *Microstructural characterization of high velocity oxy-fuel sprayed coatings of Inconel 625*, Journal of Materials Science 32 (1997), 863-872
[403] Whitney, E., Williams, S. and Krantz, B., *Pitting resistance of laser clad alloys 625, C-276, 59 and 686*, CD-ROM Proceedings of ICALEO2005, 24th International Congress on Applications of Lasers & Electro-Optics, Laser Institute of America, October 2005, Miami, FLA, USA, 580-584
[404] Malayoglu, U., Neville, A. and Lovelock, H., *Assessing the kinetics and mechanisms of corrosion of cast and HIPped Stellite 6 in aqueous saline environments*, Corrosion Science 47 (2005), 1911-1931
[405] Lai, Y., *High-temperature corrosion of engineering alloys*, ASM International, Materials Park, OH, 1990, ISBN: 0-87170-411-0
[406] Rapp, R., *Corrosion by molten salts*, Corrosion: Fundamentals, Testing, and Protection, Vol. 13A, ASM Handbook, ASM International, 2003, 117-123
[407] Rapp, R., *Hot corrosion of materials: a fluxing mechanism*?, Corrosion Science (2002), 209-221
[408] Hwang, Y. S. and Rapp, R. A., *Thermochemistry and solubilities of oxides in sodium sulphate-vanadate solutions*, Corrosion Science 45 (1989) 11, 933-937
[409] Seiersten, M. and Kofstad, P., *Sodium vanadate-induced corrosion of nickel and MCrAlY coatings on Inconel 600*, Materials Science and Technology 3 (1987), 576-582
[410] Saunders, S. R. J., Spencer, S. J. and Nicholls, J. R., *The influence of fuel composition on lives of current valve materials for diesel engines – metallurgical and mechanistic studies*, Diesel Engine Combustion Chamber Materials for Heavy Fuel Operation, The Institute of Marine Engineers, 1990, ISBN 0-907206-23-9, 111-119
[411] Nicholls, J. R. and Stephenson, D. J., *Hot corrosion tests on candidate diesel valve materials*, Diesel Engine Combustion Chamber Materials for Heavy Fuel Operation, The Institute of Marine Engineers, 1990, ISBN 0-907206-23-9, 47-60
[412] Goebel, J. A., Pettit, F. S., and Goward, G. W., *Mechanisms for the hot corrosion of nickel-base alloys*, Metallurgical Transactions 4 (1973), 261-278
[413] Upadhyaya, G. S., *Cemented tungsten carbides, production, properties and testing*, Noyes Publications, USA, 1998, ISBN: 0-8155-1417-4
[414] Davis, J. R., *Hardfacing, Weld Cladding, and Dissimilar Metal Joining*, http://products.asminternational.org

[415] Aoh, J. N., Jeng, Y. R., Chu, E. L. and Wu, L. T., *On the wear behaviour of surface clad layers under high temperature*, Wear 225-229 (1999), 1114-1122
[416] Branagan, D. J., Marshall, M. C. and Meacham, B. E., *High toughness high hardness iron based PTAW weld materials*, Materials Science and Engineering A 428 (2006), 116-123
[417] Tobar, M. J., Amado, J. M., Alvarez, C., Garcia, A., Varela, A. and Yanez, A., *Characteristics of Tribaloy T-800 and T-900 coatings on steel substrates by laser cladding*, Surface & Coatings Technology 202 (2008), 2297-2301